Correlation of Tensile Strength to Flexural Rupture Modulus of GFRP Bars

by

Philip Lochan

A thesis

presented to the University of Waterloo

in fulfillment of the

thesis requirement for the degree of

Master of Applied Science

in

Civil Engineering

Waterloo, Ontario, Canada, 2021

Author's Declaration

I hereby declare that I am the sole author of this thesis. This is a true copy of the thesis, including any required final revisions, as accepted by my examiners.

I understand that my thesis may be made electronically available to the public.

Abstract

Glass fibre reinforcing polymer (GFRP) bars are becoming a more comparable alternative to steel rebar used as tensile reinforcement for concrete, due to their cost effectiveness compared to other alternatives. GFRP has material characteristics of being corrosion-resistant and low-impact to electromagnetic field interference. GFRP bars are also stronger but less stiff than traditional steel rebar. However, the biggest drawback of GFRP bars acting as reinforcement for concrete members is their brittle nature, where there is little-to-no warning of failure of a structural reinforced concrete element. As a result, it is crucial to successfully identify the tensile strength of such material prior to installment in construction projects. The most direct way to measure this quality is to perform a uniaxial, direct tensile test on GFRP bars. This test involves clamping the ends of the GFRP bar in a testing machine and pulling the bar apart with tensile force until failure. From this, the tensile stress and tensile elastic modulus of a GFRP bar can be obtained from the recorded force and displacement values.

The tensile test requires large capacity test frames. Typically, the bigger sized GFRP bars are very difficult to test to their ultimate tensile stress due to lack of access of a testing machine strong enough to break the GFRP bar. Another critical consideration that needs to be made is adequately preparing steel anchorages tubes at the ends of the GFRP bar such that the grips of the testing machine would not crush the GFRP material. A common problem with this setup is that the GFRP could de-bond from the steel tube mid-way through the test, if they are not properly bonded together. As a result, there needs to be ample anchorage length and threading of the insides of the anchorage tubes to promote bonding between the GFRP material and the steel anchorage tube. If an anchorage tube length is very long, this can cause the specimen to be quite heavy and difficult to maneuver when placing it inside of the testing machine. This test is direct in obtaining key parameters, but it involves significant time and effort to conduct, discouraging the completion of quality control tests for GFRP bars, which are needed to ensure the tensile strength of the reinforcement used in concrete.

An alternative test that has been investigated to obtain the tensile strength of a GFRP bar is conducting a flexural test, where the specimen is subjected to compressive and tensile stresses. Since the goal is to observe the tensile strength of the GFRP bar, the only preparations for this test that are required is having access to the proper flexural apparatus, and cutting the GFRP specimen to length and longitudinally in half to ensure tensile failure occurs first. From this test, the loading at which the tensile fibres first rupture can be converted into a rupture stress. Using Weibull's Weakest Link model to describe the failure distribution of the GFRP material based on its flaws, the rupture stress can be related to its tensile strength. To provide a more accurate result, the GFRP material is modelled as a bi-moduli material, where its compressive and tensile elastic moduli are different. Through these set of calculations, the flexural test of the GFRP material is an efficient method in obtaining the tensile strength.

This research investigates 3-point and 4-point bending tests of GFRP bars of size 8 mm, 13 mm, 16 mm, 20 mm, 25 mm, and 32 mm in diameter, to be used to determine tensile strength of these bars. Testing with two different flexural tests will examine if one of the tests yield a more accurate result for calculating the tensile strength of the GFRP bars compared to the other. Using varying sizes of GFRP bars will confirm whether the set of correlation calculations work for all sizes. Tensile testing of GFRP bars of sizes 8 mm, 13 mm, and 16 mm in diameter was completed, in order to validate the results from the flexural testing.

It was found that both 3-point and 4-point bending tests can be used to determine tensile strength. Both methods are comparably accurate, with 3-point bending being slightly faster to do. In comparison with results from tensile testing (for smaller specimens) and prior research, it was found that the correlated tensile capacities from the flexure tests had minor discrepancies, having an error of less than 19%. The flexural test holds great potential to be a successful standardized test that yields accurate results to determine the ultimate tensile strength of a GFRP bar. The purpose for such testing is for quality control and quality assurance of different batches of GFRP bars to be installed in concrete infrastructure.

Acknowledgements

First and foremost, I would like to give thanks to my supervisor, Professor Maria Anna Polak, for accepting me as a MASc student and for her continual guidance, support, and patience throughout my research work. Despite the several hinderances of my research program due to the COVID-19 implications, I am grateful for all the support and accommodations she was able to provide. I am truly thankful for an opportunity to explore the research field within civil engineering under her supervision and mentorship.

I would like to acknowledge the financial support from National Sciences and Engineering Research Council of Canada (NSERC) for this research work during my tenure as a graduate student.

I would like to thank Professor Maria Anna Polak, Professor Scott Walbridge, and Professor Bruce Hellinga for the time spent reviewing my thesis. Special thanks to Professor Scott Walbridge for giving me an opportunity that gave me an introduction to the research-side of civil engineering as a research assistant during latter half of my undergraduate studies.

I would also like to acknowledge material supply of GFRP from Fiberline Composites (Schöck Canada) for providing the GFRP rebar material used in the laboratory test completed within this research; the Engineering Machine Shop at the University of Waterloo for their co-operation and guidance regarding fabrication of items needed for my flexure lab tests; Phil's Precision Machining for their co-operation in threading the inner surface of the steel DOM tubes required for my tensile tests.

I would like to extend my gratitude to Paulina Arczewska, my predecessor whose research work I am furthering, and her willingness to co-operate and provide advice to complete my own research work.

I would also like to extend my gratitude to the CEE lab staff: Richard Morrison, Douglas Hirst, Peter Volcic, and Victor Lewis, for their assistance, guidance and support as I completed my lab experiments in a safe environment and assistance in procuring necessary equipment in a timely fashion. Special thanks to Peter Volcic for his supervision and guidance of my lab work.

Thank you to my research group, dubbed the Polak Army, for their support and guidance throughout my graduate studies. To Graeme Milligan and Ryan Barrage, for helping me solve problems that arose from my research work whether it be regarding mathematical derivations or discussing material science or engineering applications, or simply listening to my struggles; acting as mentors throughout different phases in my graduate studies life ranging from: coursework, researching information, writing research papers, and teaching assistant advice. To Colin Van Niejenhuis, for lending his advice and experience with GFRP research helping me to conduct my first set of lab tests and teaching assistant advice. To Tim Tedford, for his advice and encouragement throughout graduate studies and life as a master's researcher student. Also, thank you my roommates of past and present, and fellow classmates from my undergraduate Civil Engineering program who continued their studies pursuing a master's degree as well - for the encouragement and offering suggestions to my research struggles.

Lastly, I would like to give thanks to my family, for their unconditional love, financial and emotional support throughout my academic career. To my brother Johnathan Lochan, who was there to listen to my struggles throughout my studies and was always willing to spend time together even though I was quite busy at times. To my mom Mandy Lochan, who always ensure I was okay and healthy throughout my studies, would be overjoyed when seeing me, and cheering me on the entire time. To my dad Frank Lochan, who was there to listen to me any time of day whether I was feeling up or down, and to bounce

ideas off of regarding construction portions of my lab work, having a familiarity in the construction field and being *the* handyman that I grew up with.

Table of Contents

List of Figures

List of Tables

List of Symbols and Variables

Symbol	Name	Definition	First Referenced In
A	Cross-sectional Area of Specimen	(refer to "Name")	Section 5.2.1 - Equation 5.1; Defined in Section 5.3.3- Equation 5.18
A_c	Compressive (Stressed) Area/Zone	Portion of cross-sectional area subjected to compressive stress	Section 5.2.1 - Equation 5.1
A_t	Tensile (Stressed) Area/Zone	Portion of cross-sectional area subjected to tensile stress	Section 5.2.1 - Equation 5.1
b	y-intercept of the Weibull Strength Distribution Graphs	(refer to "Name")	Section 5.3.2 - Table 5.3
c	Location of Neutral Axis of cross-section (measured from top fibre of specimen)	(refer to "Name")	Section 5.2.1 – Figure 5.2 & Equation 5.3
d	Distance between radius and height of cross-sectional area for flexure specimen	Distance between original radius and current height of the cross-section of a flexure specimen. This portion was removed as a result of waterjet cutting GFRP bars longitudinally.	Section 5.3.3 – Equation 5.18
c_{flaw}	Flaw Size	Constant value used to describe the fracture stress of a material based on the flaw size of the material	Section 5.3 - Equation 5.6
E	Elastic Modulus	Constant of proportionality of the stress-strain relationship of specified material	Section 5.1 – Figure 5.1
E_c	Compressive Elastic Modulus	Elastic Modulus that describes the compressive stress-strain constant of proportionality	Section 5.1 – Figure 5.1
E_t	Tensile Elastic Modulus	Elastic Modulus that describes the tensile stress-strain constant of proportionality	Section 5.1 – Figure 5.1

F	Applied force from testing machine	Applied force from testing machine	For flexural tests: Section 3.2.1 – Equation 3.1 For tensile tests: Section 3.5.2 – Equation 3.4
F_{cr}	Critical Load of Specimen	Load at which tensile fibres begin to rupture for GFRP specimen subjected to bending	Section 5.2.2 – Table 5.2
$F_{loading\ nose}$	Force from a Loading Nose	Applied force exerted from a single loading nose	Section 3.2.1 – Equation 3.1
F_{max}	Maximum Force	Greatest applied force that was recorded during testing	For flexural tests: Section 3.5.1 – Table 3.6 For tensile tests: Section 3.5.2 – Table 3.7
h	Height of a specimen	(refer to "Name")	Section 5.2.1 – Figure 5.2 & Equation 5.3
i	Rank of Specimen's Strength Relative to Others	(refer to "Name")	Section 5.3.2 - Equation 5.16
K_{IC}	Resistance to Crack Propagation	Constant that represents the resistance to growth of cracking on specified material	Section 5.3 - Equation 5.6
L	Length of Specimen	(refer to "Name")	Section 5.2.2 – Table 5.2
$L_{ext-base}$	Gage Length of Extensometer	Gage Length of Extensometer; fixed value for all tensile tests	Section 3.5.2 – Equation 3.3
$L_{ext-off}$	Offset in Gage Length of Extensometer	Accidental amount of displacement that may have occurred due to movement of extensometer prior to start of tensile test	Section 3.5.2 – Equation 3.3
M	Bending moment of a specimen	(refer to "Name")	Section 5.2.1 – Figure 5.2 & Equation 5.3
m	Weibull Modulus	The shape parameter for the probability of failure based on "Weibull's Weakest Link" Model; rep	Section 5.3.1 - Equation 5.7

$\boldsymbol{n}$	Elastic Moduli Ratio	Ratio between $\frac{E_t}{E_c}$	Section 5.2.1 – Equation 5.4
$\boldsymbol{n_s}$	Number of Specimens	(refer to "Name")	Section 5.3.2 - Equation 5.17
$\boldsymbol{P_f}$	Probability of Failure	(refer to "Name")	Section 5.3.1 - Equation 5.7
$\boldsymbol{R^2}$	Coefficient of Determination	Tell how accurate the line-of-best-fit is for a plot of data points	Section 5.3.2 - Table 5.3
$\boldsymbol{r}$	Original Radius of Specimen	(refer to "Name")	Section 5.2.2 – Table 5.2
$\boldsymbol{V}$	Volume of Specimen	(refer to "Name")	Section 5.3.1 - Equation 5.7
$\boldsymbol{V_b}$	Tensile Volume due to Bending	Volume of GFRP specimen subjected to flexural tensile stress.	Section 5.3.1 - Equation 5.9
$\boldsymbol{V_{Eb}}$	Effective Tensile Volume due to Bending	Effective portion of volume of GFRP specimen subjected to tensile stress as a result of bending.	Section 5.3.1 - Equation 5.15
$\boldsymbol{V_{Eb,3pt}}$	Effective Tensile Volume due to 3-Point Bending	Effective portion of volume of GFRP specimen subjected to tensile stress as a result of a 3-point bending test.	Section 5.3.3 - Equation 5.21a
$\boldsymbol{V_{Eb,4pt}}$	Effective Tensile Volume due to 4-Point Bending	Effective portion of volume of GFRP specimen subjected to a tensile stress as a result of a 4-point bending test.	Section 5.3.3 - Equation 5.21b
$\boldsymbol{V_{Et}}$	Effective Tensile Volume due to Direct Tension	(refer to definition below)	Section 5.3.1 - Equation 5.16
$\boldsymbol{V_t}$	Tensile Volume due to Direct Tension	Portion of volume of GFRP specimen subjected to tensile stress as a result of bending (will equal specimen volume subjected to pure tension, since entire volume is placed in pure tension)	Section 5.3.1 - Equation 5.8
$\boldsymbol{x}$	Length of the Specimen	(refer to "Name")	Section 5.3.3 - Equation 5.19
$\boldsymbol{y}$	Height/Depth/Vertical Distance/ of the Specimen's cross-section	(refer to "Name")	Sections 5.2.1 & 5.3.3

y_d	Stress Density Factor	Coefficient describing the factor of stress distributed through the density of a material; used for finding the fracture stress of a material	Section 5.3 – Equation 5.6
z	Width/Horizontal Distance of the Specimen's cross-section	(refer to "Name")	Section 5.2.1 & 5.3.3
Δ	Flexural Deflection	Deflection from flexural tests	Section 3.2.1
δ	Axial Displacement	Displacement of GFRP specimen in tensile test, recorded by attached extensometer	Section 3.2.1 – Equation 3.3
ε	Strain of GFRP Specimen in Direct Tension	The strain of the GFRP specimen subjected to uniaxial direct tension.	Section 3.5.2 - Equation 3.4
ε_c	Compressive Strain of GFRP Specimen in Bending	The strain of the GFRP specimen subjected to bending exhibited at top of the cross-section, where it endures the maximum compressive strain.	Section 5.2.1
ε_t	Tensile Strain of GFRP Specimen in Bending	The strain of the GFRP specimen subjected to bending exhibited at bottom of the cross-section, where it endures the maximum tensile strain.	Section 5.2.1
σ	Applied Stress	Applied forced on a material, per area.	For tensile tests: Section 3.5.2 - Equation 3.4 For flexural tests: Section 5.3.1 - Equation 5.7
σ_b	Tensile Stress via Bending	The tensile stress of a GFRP bar subjected to bending. In the correlation calculations, this will equal the rupture modulus.	Section 5.3.1 – Equation 5.9
$\frac{\sigma_b}{\sigma_t}$	Tensile Stress Ratio	Ratio of the correlated tensile capacity to the tested/actual tensile capacity of a GFRP bar	Section 5.3.2 – Equation 5.16

σ_c	Compressive Stress	The stress of the GFRP specimen subjected to bending, located at the top fibre of the cross-section, where it endures the maximum compressive stress.	Section 5.2.1 – Figure 5.2 & Equation 5.3
σ_f	Fracture Stress	Stress at which material experiences fracture	Section 5.3 - Equation 5.6
σ_o	Normalizing Stress Factor	The scale parameter for the probability of failure based on "Weibull's Weakest Link" Model	Section 5.3.1 - Equation 5.7
σ_r	Rupture Modulus	The bending stress at which the tensile fibres begin to rupture – i.e. tensile failure of GFRP flexural specimen	Section 5.2.2 – Table 5.2 (term first referenced in Section 1.1)
σ_t	Tensile Strength/Capacity (unless stated otherwise, i.e. flexural stress)	The tensile strength of the GFRP, commonly found from uniaxial direct tensile testing	Section 5.2.1 – Figure 5.2 & Equation 5.3
$\sigma_{t,calc}$	Correlated Tensile Strength	The correlated tensile strength of GFRP bar based on correlation calculations from flexural testing	Section 5.4 - Table 5.10
σ_u	Zero-strength Stress Factor	Stress at which no failure occurs below this value	Section 5.3.1 - Equation 5.7

Note: symbols for filtering not shown in this list; refer to Section 4.1 Filtering Data using Single & Double Exponential Filtering.

List of Equations

Chapter 1 - Introduction

Glass fibre reinforced polymers (GFRP) bars are the most common and the cheapest alternative to convention steel reinforcing bars (rebar) in structural concrete elements. GFRP bars have been used in numerous structures and application (Balendran et. al, 2002) due to several of its unique benefits. Some of these include an increased lifespan of the structural element as a result of the GFRP's corrosion resistant nature, and low electromagnetic interference since it is not metallic. GFRP can also achieve higher tensile capacity while having a cost more comparable to steel rebar.

Despite these benefits of using GFRP bars as opposed to the convention steel rebar, there are a few downsides. One of the primary drawbacks of using a GFRP bar is its brittle failure behaviour. GFRP reinforced concrete members must rely on concrete compressive behaviour to provide any warning of failure. Therefore, it is paramount that the tensile strength and the quality of GFRP bars can be easily tested and verified. The current direct tensile method cannot be easily implemented for quality assurance testing of the GFRP bars. Therefore, an alternative test method for assessing the tensile capacity of a GFRP bar that is fast and simple, is needed. Such a method, namely flexural testing of GFRP bars, is proposed and presented in this thesis.

1.1 Research Motivation

The most direct way to determine tensile strength is to perform a uniaxial direct tension test on a sample of the same batch of GFRP rods. This method exists in current testing standards such as CSA S806-12 (Annex B & C) (CSA, 2012), ASTM D7205/D7205M-06 (ASTM Committee D30, 2016), ASTM D7264/D7264M-15 (ASTM Committee D30, 2015) , and ACI 440.3R-12 (Appendix A) (ACI Committee 440, 2012), and is utilized by other researchers (Johnson, 2014; Tripathi, 2003; Castro & Carino, 1998). This test involves placing the specimen in a testing machine used for a uniaxial direct tension test, but is quite cumbersome to setup. It requires both ends of the GFRP bar to be cast properly into steel tubes that are long enough and have adequate bonding, so slippage does not occur during testing. Before the testing phase is reached, it is challenging to maneuver and setup the specimen in the testing apparatus itself, since the specimen is long and slender. Even before overcoming the challenges of preparing and setting up the specimen, there is a need to have a strong enough, and high enough, testing machine to complete the uniaxial direct tension tests of the GFRP bars. This type of a bar can endure a high tensile capacity, achieving over 1000 kN for bars with a diameter of approximately 30 mm or larger. Conducting the actual test will take quite a significant amount of time per specimen (Arczewska, 2017).

An alternative to the tensile test can be using a flexure test to determine the tensile stress in GFRP bars, using the ASTM D4476/D4476M-14 (ASTM Committee D20, 2014) standard. Since a beam-element is subjected to compressive and tensile stresses while bending, the behaviour near failure of the specimen can be observed and analyzed to help look at the tensile strength of a material. Slicing the GFRP bar in half longitudinally to have cross section very similar to a semicircle ensures that the GFRP bar will fail in tension during the flexural test. Setting up and conducting this test is much quicker and more efficient since specimens do not require difficult preparation. A low capacity machine, up to a load of no more than 25 kN, with the appropriate testing apparatus can be used to conduct the testing (Arczewska, Polak, & Penlidis, 2019).

Once the flexure test has been completed and the critical load at which the GFRP specimen's tensile fibres rupture has been identified, calculating the flexural-tensile stress (will be referred to as "rupture

modulus" throughout this thesis) can be completed, and correlated to the GFRP bar's tensile capacity. This correlation is based on several concepts in material science and mechanics. One of these includes observing the relationship in fracture mechanics of brittle materials - specifically Weibull's weakest link model, which is the distribution that the tensile strength in GFRP bars. Another model that forms this correlation is the flexure formula for a beam, used to calculate stress based on the moment that the beam endures. It is also important to note that this method will be derived using the assumption that the GFRP material behaves linearly as a bi-moduli material, where the modulus of elasticity for tension and compression are not the same.

1.2 Research Scope & Objectives

The objectives of this research are as follows:

- To investigate correlating the rupture modulus to the tensile capacity of GFRP bars using a 3-point-bending flexural test.
- To seek options determining failure load from load-displacement responses of flexure tests.
- To verify the correlations work for larger GFRP bar sizes.
- To analyze the results of the 4-point-bending test to see if this test is more accurate and desirable compared to a 3-point-bending test to determine the tensile strength of a GFRP bar.

This research work follows on Paulina Arczewska's work (2017), completed at the University of Waterloo. Arczewska's scope of research only observed GFRP bars of 12mm (M12) and 16mm (M16) in diameter in 3-point bending (2019), whereas this research looks at the following GFRP bar sizes (length in diameter): 8mm (M8), 13mm (M13), 16mm (M15), 20mm (M20), 25mm (M25) and 32mm (M32) in both 3-point and 4-point bending.

1.3 Structure of Research Work & Methodology

This research will utilize the parameters obtained from a flexural test of GFRP bars, which can be correlated to the actual tensile strength of the GFRP bar. The steps in the presented thesis are outlined in Figure 1.1.

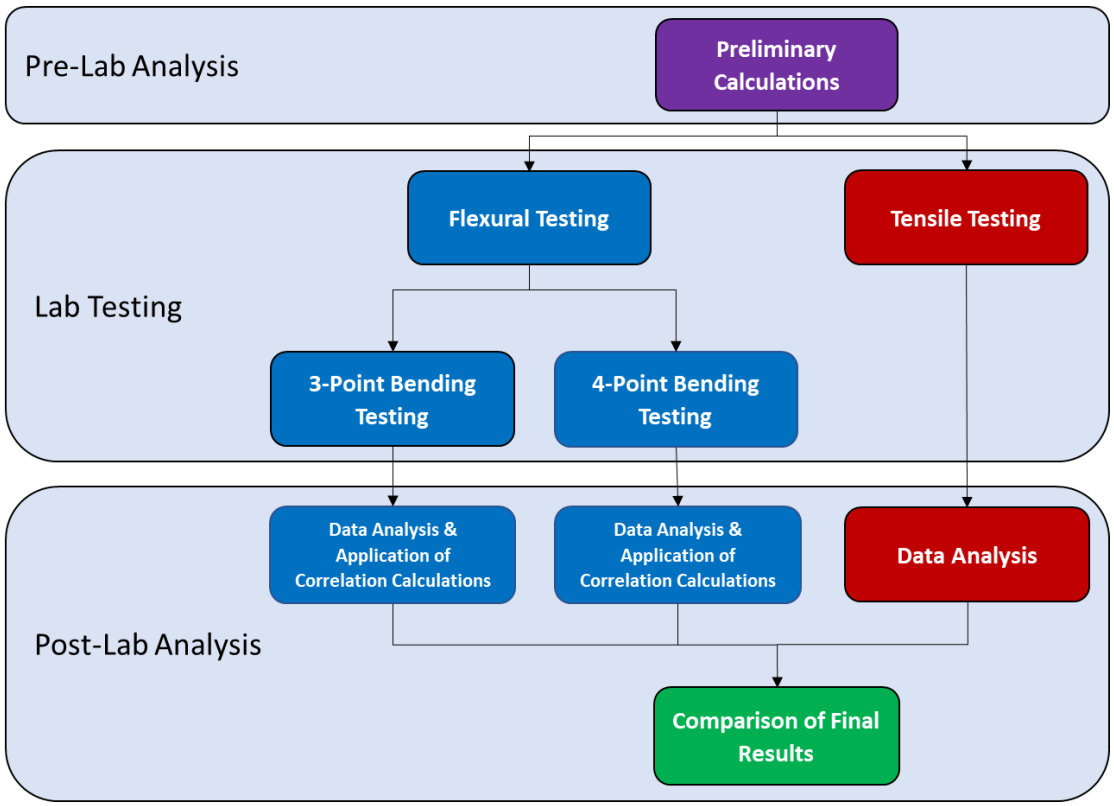

Figure 1.1: Structure of Research Work

Refining the procedures from a 3-point bending test is an essential part of this research work, following the work of Arczewska (2017). To expand on this research testing method, examining the results from a 4-point bending test was completed to see if it produces more accurate results compare to a 3-point bending test. In both methods, finding the maximum flexure load corresponding to cracking of the tensile fibres is a crucial task for the determination of the tensile strength. The rupture modulus versus tensile strength correlation calculations are provided afterwards. The first set of these calculations are to find the location of the neutral axis and the rupture modulus, which are calculated using equilibrium of forces and moments, and appropriate stress-strain relationships. The location of the neutral axis needed also to calculate the effective volumes of tensile stress in a GFRP bar when subjected to bending and direct tensile loads. These effective volume values are related to each other since they both represent the GFRP in a tensile failure state and they are linked using Weibull's "Weakest Link" Theory.

1.4 Thesis Outline

This thesis is formed into six chapters:

- Chapter 1 serves as the introduction to the thesis and provides a brief introduction for the importance of GFRP, the reason for seeking a new standardize testing for GFRP and the structure, scope and objectives of this research.
- Chapter 2 contains background information about what GFRP is and how it is manufactured and used, as well as what research work has been done to assess the quality and observe the tensile capacity of GFRP bars.
- Chapter 3 describes the lab testing procedures and observations of the GFRP specimens in the flexural tests and the uniaxial direct tension testing.

- Chapter 4 explains the methods used to identify the critical load point of tensile failure for the GFRP specimens in flexural testing.
- Chapter 5 analyzes the mechanics and statistical models used to form the set of correlation calculations use to rupture modulus to find the tensile capacity of the GFRP bars. Towards the end of this chapter, a comparison and discussion of the results is provided.
- Chapter 6 goes over the conclusion from this research and gives future recommendations for further research.

Chapter 2 - Background & Literature Review

This chapter provides a brief overview of the composite of GFRP bars, its use in civil engineering applications, and prior research completed to evaluate the tensile capacity.

2.1 GFRP Rebar Composition & Production

GFRP bars are composed of 2 main components: the glass fibres and the matrix. These glass fibres are produced through the extrusion of molten glass through a metal bushing and then rapidly cooled, where their strength is affected based on flaws and defects formed during this process. The main composition of glass fibres is silica (SiO_2), which what gives strength to these fibres. Although silica is a reactive compound, it is protected by the matrix of the GFRP material. The matrix of the material is a polymer, which not only does the matrix limit the damage done to the fibres, but it helps distribute the load between the fibres while keeping them in place. This serves a crucial function in the tensile capacity of the FRP bars (Arczewska, 2017); (Gardiner, 2020).

The product is formed through pultrusion: the process used for making straight GFRP bars. This involves glass fibers being pulled from their roving configuration, grouped together and are bathed in a resin tank, where the fibres are impregnated with the appropriate resin substance. The fibres are then squeezed through a bushing to be group in form of a bar, and outer-surface material may be applied as necessary (i.e. sand) (Benmokrane et. al, 1995). The material is pulled through a heated die, which forms the matrix of the bar as it is dried and hardened from the resin bath (Gardiner, 2020; Arczewska, 2017). The bar undergoes any other additional outer-surface alteration as needed (i.e. forming ribbed surface) and is cut to length. Figure 2.1 shows an image of the pultrusion process.

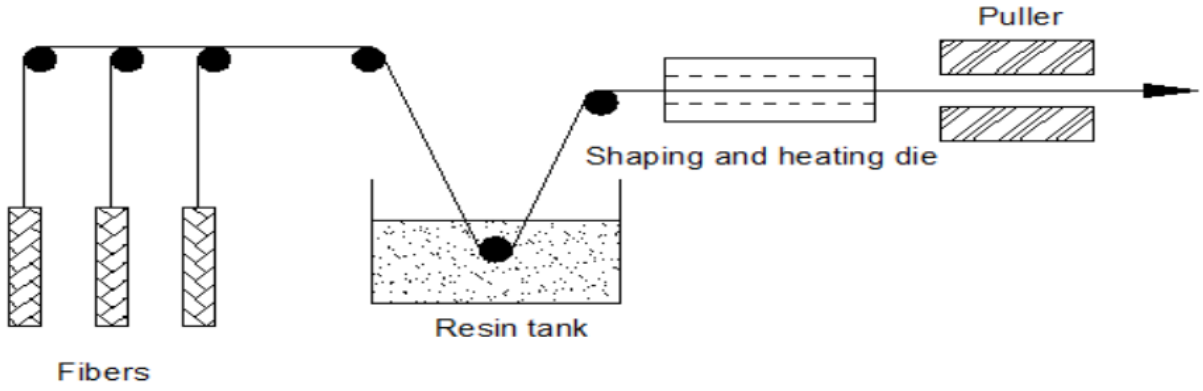

Figure 2.1: Pultrusion Process of GFRP Bar (Arczewska, 2017)

Being an anisotropic material, the tensile strength of the GFRP bar is the strongest in the longitudinal axis (Benmokrane et. al, 1995). This is attributed to the alignment of the glass fibres during the pultrusion process, in addition to the polymer matrix that consolidates the material. Imperfections during the formation of the glass fibres or pultrusion process directly affects the tensile capacity of the GFRP bar.

2.2 GFRP Used in Civil Engineering Applications

GFRP bars are used as tensile reinforcement of concrete structures, and is the most common alternative to traditional steel rebar due to their material properties. The availability and development of FRP can

be noted back to the 1940s (Gardiner, 2020; ACI Committee 440, 2015), but use of GFRP material as a rebar has been present since the 1970s and 1980s, due to demand of non-conductive and non-corrosive reinforcement in concrete (Arczewska, 2017; ACI Committee 440, 2015). The primary used for GFRP due to its corrosion-resistant nature of GFRP are in areas where reinforced concrete elements can be exposed to moisture such as bridges, parking garages, pedestrian platforms and other marine structures (Arczewska, 2017; ACI Committee 440, 2015). Examples of GFRP bars in used specifically for its benefit of having minimal electromagnetic interference are in such places as hospital rooms equipped with a magnetic resonance imaging (MRI) equipment, or power plants (ACI Committee 440, 2015). Figure 2.2 and Figure 2.3 show practical uses of GFRP installed in places where moisture will be present and could seep into concrete elements.

Figure 2.2: GFRP Installation for a Parking Garage Slab (Ahmed et al., 2016)

Figure 2.3: GFRP Installation for Water Treatment Plant Walls (Mohamed & Benmokrane, 2013)

Despite all these applications, further adoption of GFRP rebar use is hindered by the methods used to test the quality and strength of the product. One of the most commonly used methods to assess the quality and strength is through a uniaxial direct tension test.

2.3 Tensile Testing on GFRP Bars

Uniaxial tensile testing of the GFRP bars requires placing a specimen under uniform tensile stress as it is being pulled from both ends. This test is documented in testing standards such as:

- ASTM D7205 – Standard Test Method for Tensile Properties of Fiber Reinforced Polymer Matrix Composite Bars (ASTM Committee D30, 2016)
- CSA S806-12 Annex C - Test method for tensile properties of FRP reinforcements (CSA, 2012)
- and ACI 440.3 – Guide Test Method for Fiber-Reinforced Polymers (FRPs) for Reinforcing of Strengthening Concrete Structures (ACI Committee 440, 2012)

The tensile capacity of the GFRP bar can be found directly from testing based on the size of the bar and its failure load. As mentioned in 1.1 Research MotivationSection 1.1 of this thesis as a part of the motivation for this research work, there have been several studies done with this test method, such as observing the properties of GFRP bars prior to using as reinforcement in concrete elements (Johnson, 2014; Tripathi, 2003), and observing variables with the test setup itself to determine accurate results (Castro & Carino, 1998).

The test is conceptually simple; however, several issues exist which make the test impractical for repeated quality control testing. These are as follows:

- The specimens are long, slender, and heavy. It takes a substantial amount of time and effort to setup the GFRP specimens before testing, since it involves installing proper grips on the ends of the GFRP bars, as advised by testing procedures CSA S806-12 (Annex C) (CSA, 2012), ASTM D7205/D7205M-06 (ASTM Committee D30, 2016), and ACI 440.3R-12 (Appendix A) (ACI Committee 440, 2012). This installation involves ensuring that the end grip, which is usually specified as a steel drawn-over mandrel (DOM) tube, is long enough so that there is proper development length for the GFRP bar to bond to the tube. This task is difficult due to the long length of the GRFP bar, generally requiring to be anywhere from 800 mm up to 3000 mm (ASTM Committee D30, 2016). Also, since the specimens are slender and heavy, it increases the difficulty in maneuvering the specimen and properly setting it up in the testing machine.
- The specimens require specially constructed end grips. To aid with the bonding of the steel tube and the GFRP bar, the tube's inner surface should be roughened (i.e. threaded), to increase surface area of the bonding with the proper grout.
- The capacity of GFRP specimens are very high, requiring large capacity testing frames. The GFRP bars are much stronger than steel bars. The nominal strength of GFRP is around 1000 MPa which results in the capacity of (i.e. 30M bars of minimum of 700 kN). The actual capacities are in usually higher. This, combined with the fact that the specimens are long and heavy, prevents routine testing of these bars when quality control is an issue.

2.4 Flexural Testing on GFRP Bars

Past research that focused on the flexural properties of FRP bars using a 3-point or 4-point bending test (Benmokrane et. al, 2017; Maranan et. al, 2014; Benmokrane et al., 2006; Tripathi, 2003). These laboratory tests were based on one of the following testing procedures:

- ASTM D790-17 – Standard Test Methods for Flexural Properties of Unreinforced and Reinforced Plastics and Electrical Insulating Materials (ASTM Committee D20, 2017).
- ASTM 4476 – Standard Test Method for Flexural Properties of Fiber Reinforced Pultruded Plastic Rods (ASTM Committee D20, 2014)
- CSA S807-10 – Specification for fibre-reinforced polymers (CSA, 2010)

In these experiments, specimens with full cross-sections were tested which resulted in failures that were not consistently tension-driven. Figure 2.4 shows an example of a flexural test with an FRP specimen with the full cross section. In such testing, the compressive strength of the specimen (which is lower than tensile strength for GFRP bars) or debonding of the fibres from the matrix prompted the specimen failure (Maranan et. al, 2014).

Figure 2.4: FRP Specimen with Full Cross-section Tested in 3-Point Bending Test (Maranan et al., 2014)

Arczewska (2017) completed flexural testing of GFRP specimens where the cross section was cut into two parts, with almost half cross section present for each piece (half the cross section, minus the blade thickness), to enable failure of the tensile fibres before the compressive fibres. *Figure 2.5* and Figure 2.6 shows an example of a flexural test of a GFRP specimen cut longitudinally in half.

Figure 2.5: Side View 3-Point Bending Test Specimen Cut Longitudinally

Figure 2.6: Front View 3-Point Bending Test Specimen with Longitudinal Cut

2.5 Work by Arczewska (2017)

The research described in this thesis relates to testing GFRP bars in flexure to determine tensile strength. It is a continuation of the work initiated by Arczewska (2017). Arczewska's work involved several experiments observing the mechanical properties of GFRP bars, such as the tensile strength, compression strength, shear strength, and flexural strength, both with and without decay of the bars. She conducted flexural tests in 3-point bending on GFRP bars that were cut longitudinally to ensure that the bar failed under tensile stress, as shown in Figure 2.7, where rupture occurs in the bottom fibres placed under tension. These flexural tests specifically examined the determination of the rupture modulus (tensile stress at which the GFRP bar will fail), which is used for calculating the tensile strength of GFRP via calculations derived from: the brittle characteristics of GFRP, stress-strain equations, and relationships describing equilibrium for stress on a beam.

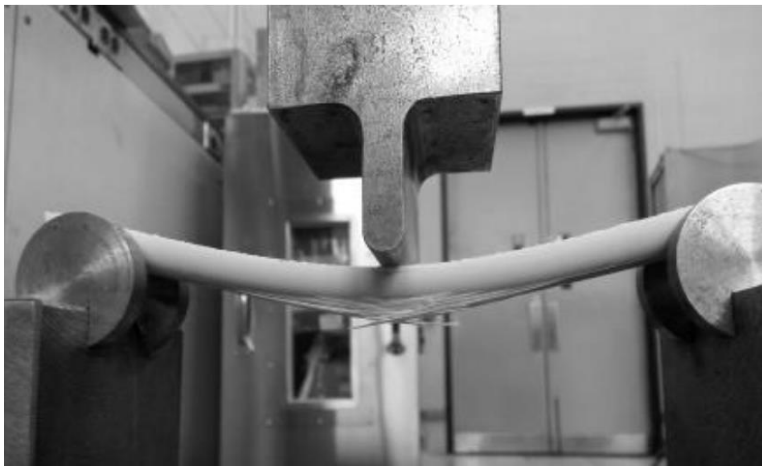

Figure 2.7: 3-Point Bending Test of GFRP Specimen (Arczewska, 2017)

Equations for stresses in the beam using equilibrium of forces and moments, along with stress-strain relationships along the cross section of the specimen were observed and used to isolate the tensile strength from the flexural test (i.e. rupture modulus). A critical assumption that was made to enhance the accuracy of the results from the calculations is modelling the GFRP as a bi-moduli material, meaning the material possesses different tensile and compressive elastic moduli. Arczewska clearly explains this phenomenon and concludes that if this was not accounted for, the correlation calculation (require to calculate the actual tensile strength) could have an error from about 0.5% to 9% (2017). Implementing the bi-moduli model was done by altering the stress-strain relationship, where the both elastic moduli for tensile and compression are required (i.e. it cannot be assumed that the elastic modulus in the compression and tension zone of the specimen's cross section will be the same value).

Utilization of Weibull's weakest link model was another crucial concept required to relate the rupture modulus to the tensile capacity of the GFRP bar. This is based on the brittle nature of the material represented by a failure distribution. Recognizing the probability of material failure from a flexure and tensile test is the same, the correlation between the rupture modulus and tensile capacity had been established. The details of this portion of the correlation calculations are presented in this thesis, and is further discussed in Chapter 5.

Arczewska compared the results of the correlated tensile capacity of the flexural-tested specimens to direct-tensile specimens of the same size and type of GFRP bar, which included: #4 (14 mm diameter)

and #5 (18 mm diameter) straight sand-coated bars, and M12 (12 mm diameter) and M16 (16 mm diameter) straight ribbed bars. This was accomplished by finding the ratio of the rupture modulus (denoted as σ_b) to the tensile capacity (denoted as σ_t) via correlation calculations, and comparing it to the ratio of rupture modulus and tensile capacity obtained from direct tensile tests. These ratios are listed in Table 2.1Table 2.1: Relative Error for Tensile-Flexure Strength Correlation , along with the percent error of the calculated ratio to the ratio of test parameters.

Table 2.1: Relative Error for Tensile-Flexure Strength Correlation (Arczewska, 2017)

GFRP Bar	σ_b/σ_t from calculations	σ_b/σ_t from tested valued	% Error
#4	1.35	1.39	2.8
#5	1.39	1.40	0.7
M12	1.66	1.64	1.0
M16	1.58	1.51	4.0

From Table 2.1, it was concluded that using the correlation calculations from 3-point bending tests results were effective in determining the tensile capacity of a GFRP bar because the error between the two ratios were very low, less than 5%. The research work presented in this thesis (discussed in Chapter 5) reviews the correlation calculations used, and observes if these correlations show similar results for bigger GFRP bar sizes and specimens subjected to 4-point bending.

Chapter 3 - Laboratory Testing

This chapter discusses details pertaining to the laboratory testing in this research program. Information for the specimens used in the tests are provided, followed by necessary preparations needed prior to testing. Test observations and results are then reported and discussed.

3.1 Specimen Details

The specimens used for the flexural and tensile testing are ComBAR, provided by Fiberline Composites (partnered with Schöck), where the GFRP bars are ribbed bars. The tested GFRP bars are of 8 mm (M8), 13 mm (M13), 16 mm (M15), 20 mm (M20), 25 mm (M25), and 32 mm (M32) in diameter. It should be noted that these specimens are not all from the same batch.

Table 3.1 indicates the dimensions of the GFRP used in this research program. All these bars were provided in lengths of 2 metres and were later cut to length required for flexural testing based on ASTM D7205/D7205M-06 (ASTM Committee D20, 2014). Appendix A contains important various parameters from the manufacturer's technical information brochure, as well as specification sheets for the M13, M15 and M20 bars, as those were the only ones available for the provided GFRP bars.

Table 3.1: Dimensions and Characteristics of GFRP Bars Used (Fiberline Composites, 2017)

Bar Designation	Core Diameter (mm)	Exterior Diameter (mm)	Cross-Section Area (mm^2)
M8	8	9	50.3
M13	13	14.5	132
M15	16	18	201
M20	20	22	314
M25	25	27	491
M32	32	34	804

For the flexure tests, 10 specimens of all GFRP bar sizes were tested in both types of flexure tests: 3-point and 4-point bending. However, due to limitations of the available testing machinery's capacity, only the M8, M13 and M15 GFRP bars were tested in direct tension. Due to testing errors, only 4 specimens have been tested for the M13 GFRP bars. For the M8 and M15 bars, 5 specimens were tested. Table 3.2 summarizes the number of specimens for each size of GFRP that were used in each test.

Table 3.2: Number of Specimens per Laboratory Test

Bar Designation	3-Point Bending Test	4-Point Bending Test	Direct Tensile Test
M8	10	10	4
M13	10	10	5
M15	10	10	5
M20	10	10	-
M25	10	10	-
M32	10	10	-

The labelling convention used for the specimens were based on the order of which they were measured, per each bar size. Appendix B has the full specifications and information on each of the flexure specimens, as identified and sorted by their individual specimen number (i.e. M13-20). Specimens for the direct tensile test are labelled in a similar fashion as the flexure specimens, but denoted with a "T" before associating a number to it, in order to distinguish the specimens used among the two types of lab testing (i.e. M15-T1). Appendix C provides specifications and information of each of the direct tensile specimens.

No other conditioning has been done on the specimens for these tests, other than the ones listed in the subsequent Sections of 3.2 Procedures for Laboratory Tests and 3.3 Specimen Preparation of this thesis (i.e. tests were completed at room temperature; corrosion or decay of the material is not within the scope of this research).

3.2 Procedures for Laboratory Tests

3.2.1 Flexure Tests

The procedure used for both 3-point and 4-point is based on ASTM D4476 – "Standard Test Method for Flexural Properties of Fiber Reinforced Pultruded Plastic Rods" (ASTM Committee D20, 2014) and CSA S807-10 – "Specification for fibre-reinforced polymers" (CSA, 2010). For the 4-point bending tests, ASTM D7264 – "Standard Test Method for Flexural Properties of Polymer Matrix Composite Materials" (ASTM Committee D30, 2015) was also consulted for reference. ASTM D4476 specifies the testing equipment required for a 3-point bending test, as shown in Figure 3.1, the parameters to set to administer the test, as well as the specifications to prepare the specimen for testing.

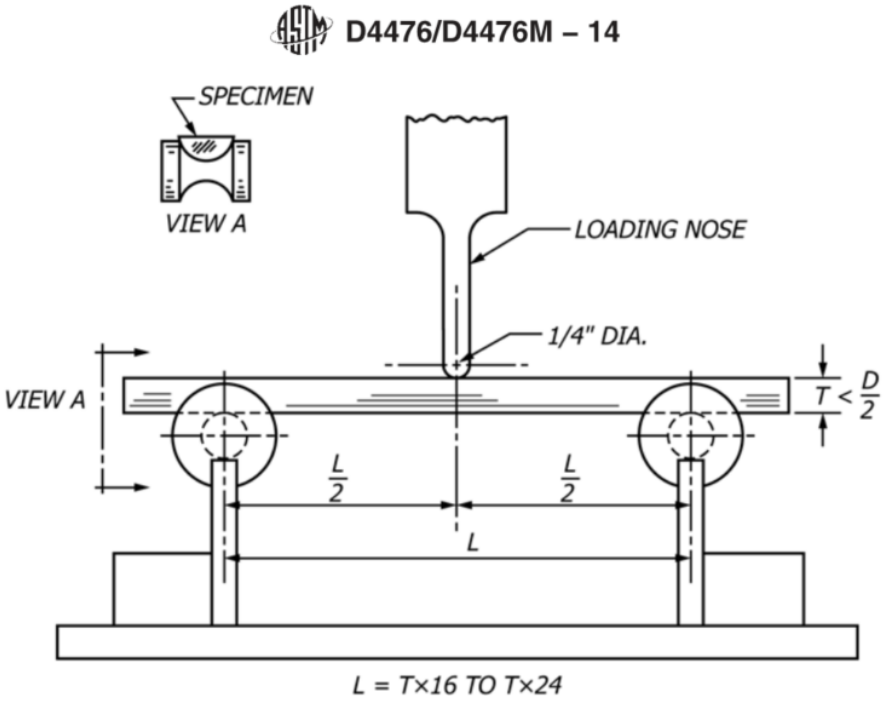

Figure 3.1: 3-Point Bending Testing Apparatus from ASTM 4476 (ASTM Committee D20, 2014)

The testing equipment used for this research is the same equipment used in previous work completed at the University of Waterloo by Arczewska (2017), and is composed of several parts as shown in Figure 3.2 for the 3-point bending tests and Figure 3.3 for the 4-point bending tests.

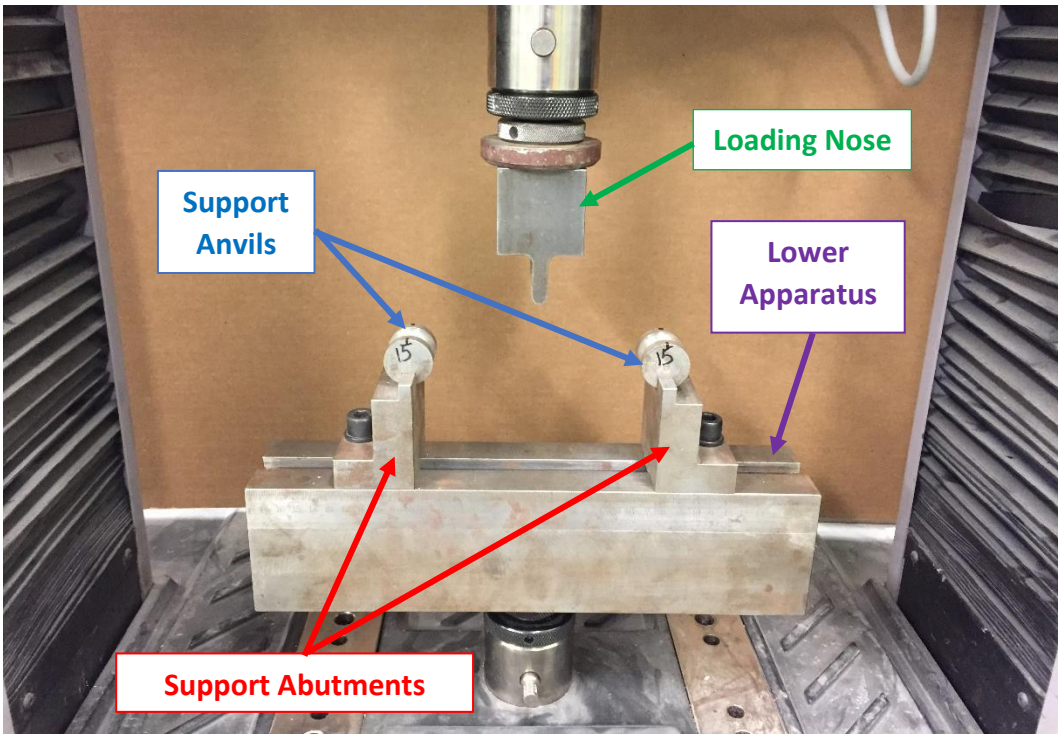

Figure 3.2: Flexural Testing Equipment Used for 3-Point Bending Tests

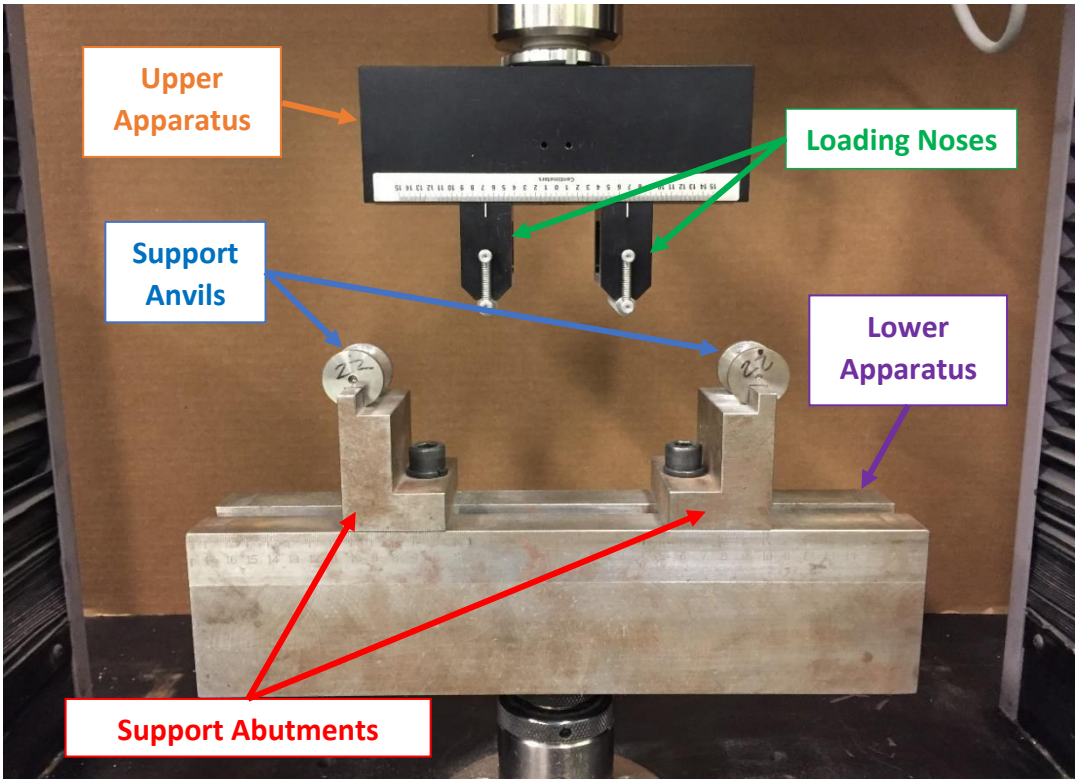

Figure 3.3: Flexural Testing Equipment Used for 4-Point Bending Tests

The bottom apparatus, which is the same one used for both 3-point and 4-point bending tests, is made from solid steel and is mounted in place on the machine. It allows the steel abutments to be adjusted to the desired location. These abutments hold the “anvil” supports for the specimen during the testing without inducing unwanted stress on the specimen as it bends. The top apparatus is attached to an MTS hydraulic machine, which is displacement-controlled and applies a downward force situated at the midspan of the specimen that is held in a stationary position by the bottom apparatus. The top apparatus for a 3-point bending test is a loading nose made of solid steel with a diameter of ⅜”. Although this is contrary to what was outlined in ASTM D4476, this was used to carry out the test in order to remain consistent with the previous research work of Arczewska’s (2017), as well as to prevent the loading nose from pre-emptively cutting into the GFRP specimen with a smaller diameter. The top apparatus that was used for the 4-point bending tests was an MTS apparatus that holds two adjustable loading noses, that can change the position and size of the loading nose tip. The loading nose tip sizes that were used for the 4-point bending tests are ⅜” in diameter, to maintain consistency with the rest of the completed lab tests. The locations of these loading noses are situated at one-third of the specimen’s clear span length.

The anvil supports are also made from steel, and has the appropriate curved dimensions to hold the specimen of the correct size without inducing unnecessary additional stresses on it as the test is being done. ASTM D4476 specifies the dimensions and specifications for these supports as indicated in Figure 3.4. From Arczewska’s previous work (2017), two pairs of these were used for the M13 and M15 bars. However, for the M8, M25, and M32 bars, new support pairs needed to be fabricated, following the specifications as outlined in ASTM D4476 (ASTM Committee D20, 2014). Certain dimensions based on ASTM D4476 (ASTM Committee D20, 2014) were altered to allow the support to be compatible for the available apparatus, such as the notch size for sitting on the abutments, and the length of the supports. Figure 3.5 and Figure 3.6 show the CAD drawings for the M8 and M32 bars, respectively.

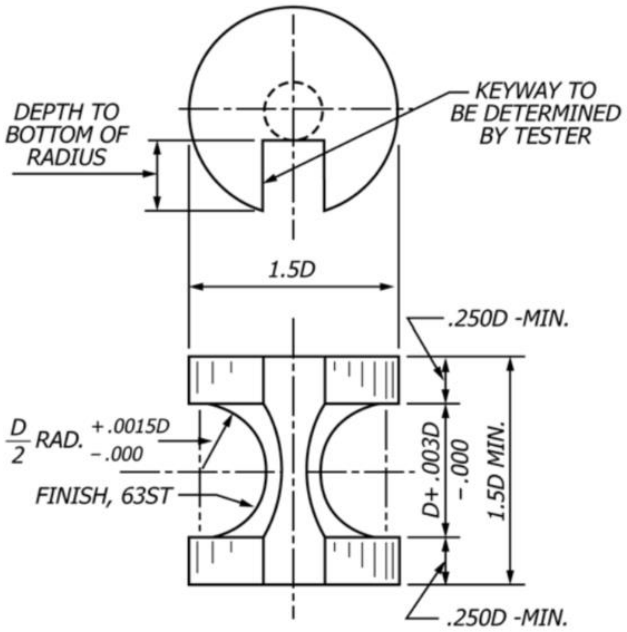

Figure 3.4: Specified Dimensions for “Anvil” Supports (ASTM Committee D20, 2014)

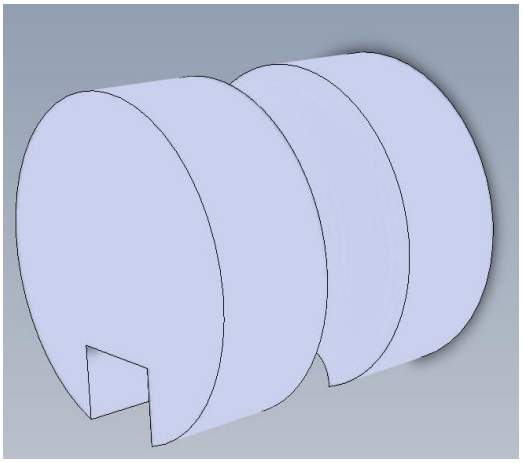

Figure 3.5: CAD Drawing for "Anvil" Support for M8 Bars

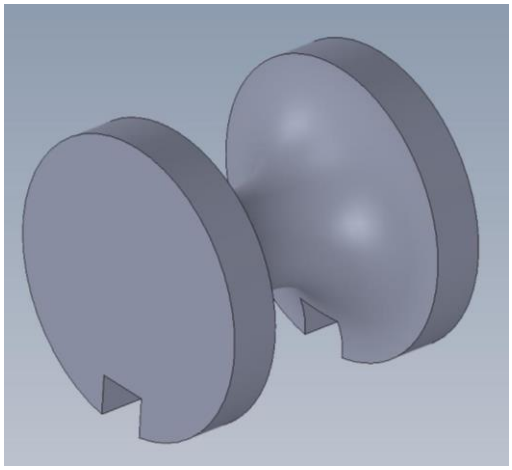

Figure 3.6: CAD Drawing for "Anvil" Support for M32 Bars

The parameters recorded during testing include the load and displacement for both the 3-point and 4-point bending tests. These readings are based on the downward displacement of the machine's crosshead, and the amount of force it exerts on the specimen. However, for the 4-point bending test, the actual loading and displacement information is different from the outputted values. Since there are two loading noses that distributed the applied force to the specimen, the recorded loading was divided by 2, as indicated in Equation 3.1.

$$F_{loading\ nose} = \frac{F}{2} \qquad \textit{Equation 3.1}$$

For the displacement, Equation 3.2 was used to convert the machine's crosshead displacement to represent the midspan displacement of the specimen, since the crosshead displacement is representative of the point of contact between the crosshead and the specimen are ends of the loading noses that apply loading to the specimen. The full derivation for this equation is found in Appendix D.

$$\Delta_{4pt,mid} = \frac{9}{8}\Delta_{crosshead} \qquad \textit{Equation 3.2}$$

For uniformity and simplicity of all flexure tests done in this program, a consistent loading rate of 3mm/min was used. This is slightly different from specifications outlined in the ASTM D4476 (ASTM Committee D20, 2014) standard, since it mentions to use a loading rate of: 3 mm/minute where the sample width falls between 6.35mm and 9.525 mm, or 6 mm/minute where the sample width falls between 9.525 mm and 12.7 mm. ASTM D4476 (ASTM Committee D20, 2014) also mentions that if the testing time is less than 20 seconds, the loading rate should be reduced, and vice versa, where the loading rate should increase if the testing time is greater than 20 seconds.

The test was completed until failure of the specimen, which complies with ASTM D4476 (ASTM Committee D20, 2014). The test was also stopped when the maximum applied load in dropped by 90% from peak loading.

3.2.2 Tensile Tests

The procedure for tensile testing is based off of ACI 440.3R-12 (Appendix A) (ACI Committee 440, 2015), ASTM D7205-06 (ASTM Committee D30, 2016), CSA S806-12 (Annex B & C) (CSA, 2012). Figure 3.7 from

CSA S806-12 shows a schematic of the test specimens that will be used to place the GFRP under tensile stress, where the GFRP bar is bonded to steel anchors, which are then placed between V-grips in the tensile testing machine.

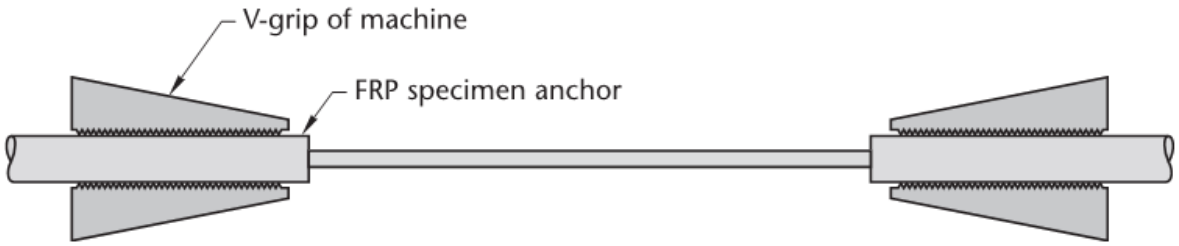

Figure 3.7: Required Testing Setup for Uniaxial Tensile Testing from CSA S806-12 (CSA, 2012)

Based on ASTM D7205-06 (ASTM Committee D30, 2016) and CSA S806-12 (CSA, 2012), the length of the GFRP specimen should be 40 times the bar diameter plus the length of the DOM tubes on both sides of the GFRP bar. The length of the DOM tubes vary from 300 mm (for smallest diameter of 6.4 mm) to 800 mm (for largest diameter of 800 mm), depending on the GFRP bar size. Figure 3.8 shows an image of the test apparatus used for the tensile tests, with zoomed in view of the crosshead on the left, and load cell and V-grips on the right.

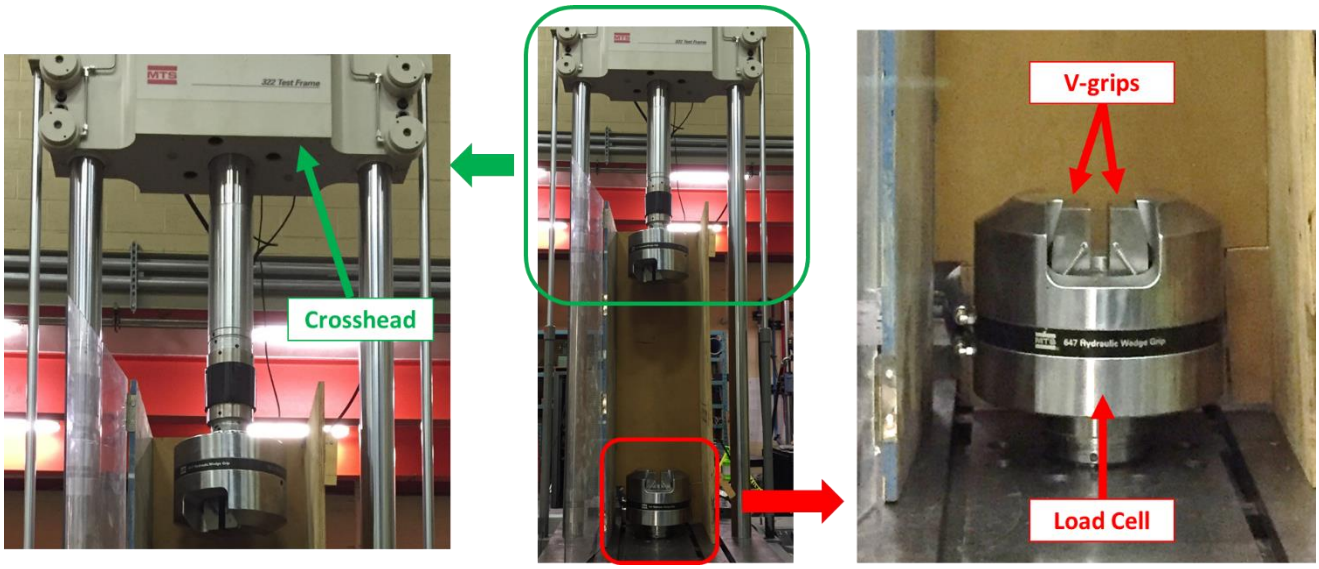

Figure 3.8: View of Direct Tensile Testing Machine

Tests were completed in a 500 kN capacity machine, with a loading rate of 300 MPa/min (same loading rate used by Arczewska (2017)). This translates to the following loading rates per bar size: 15kN/min for the M8 bars, 40 kN/min for the M13 bars, and 60 kN/min for the M15 bars. The recorded data are the force exerted by the machine, and the displacement of the specimen at midspan being tracked by an extensometer, and the displacement of the testing machine's crosshead. It should be noted that the extensometer was removed at 60% of the expected ultimate loading for the first test of a given bar size, and 75% after measuring the ultimate load of the first specimen.

3.3 Specimen Preparation

3.3.1 Flexure Tests

As specified in ASTM D4476 (ASTM Committee D20, 2014), the GFRP bars itself were cut longitudinally in half, via waterjet cutting, along the length to ensure that the specimen first fails in tension as it is being subjected to bending stresses. Due waterjet cutting, the heights of the specimen slightly vary by 1-2 mm. All specimens were measured before testing. The standard requires the specimen to have a clear span length between 16 times and 24 times the depth of the specimen, which is less than the radius of the bar. ASTM D4476 (ASTM Committee D20, 2014) also recommends that the specimen should have an overhang of about 10% of the specimen's length on each side of the bar. The method used to determine the length of the specimens in these tests was taking the average of the minimum and maximum clear lengths for the bar and rounding to the nearest 10mm, for ease of calculation. Afterwards, 20% of this clear span length was added to obtain the total specimen length, for testing purposes. However, due to the limitations of the waterjet cutting procedure, the maximum length of the bar that was permissible was 300mm. Figure 3.9 indicates the locations of the point load application and support placements for the specimens, while Table 3.3 presents the specified lengths of the specimens based on GFRP bar size. Figure 3.10 and Figure 3.11 show the GFRP bars cut to length, both before being cut longitudinally, while Figure 3.12 and Figure 3.13 show afterwards.

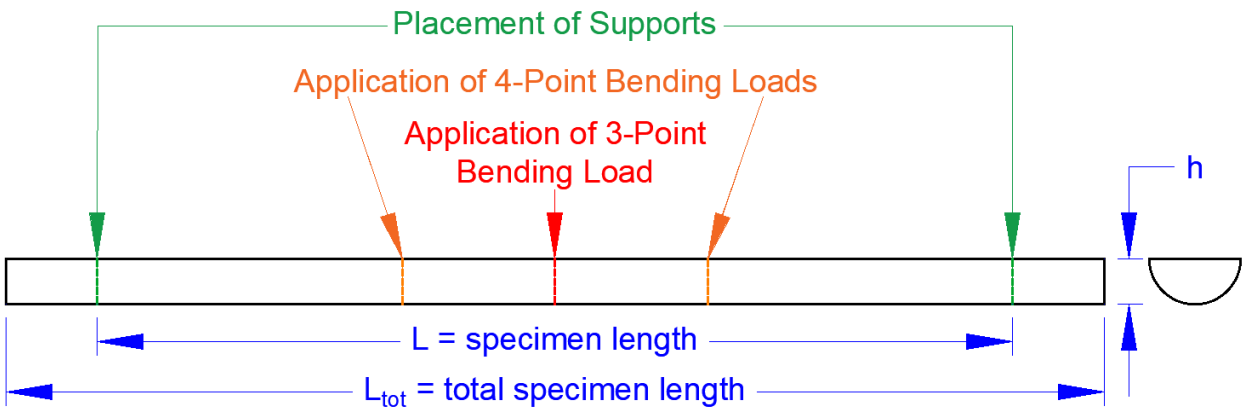

Figure 3.9: Point Load and Support Placement along Length of GFRP Specimen

Table 3.3: Length of GFRP Specimens

Bar Designation	L (mm)	L_{tot} (mm)
M8	80	96
M13	130	156
M15	160	192
M20	200	240
M25	250	300
M32	320	384

Figure 3.10: All GFRP Bars Cut to Length Prior to Longitudinal Cut

Figure 3.11: Close-up View of GFRP Bars Prior to Longitudinal Cut

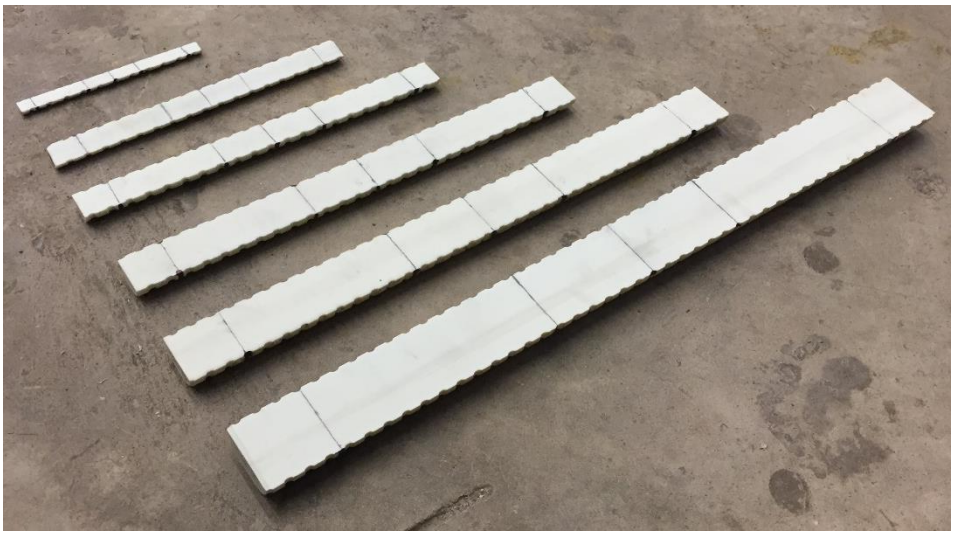

Figure 3.12: Cut-to-Length GFRP Bars Cut Post-Longitudinal Cut

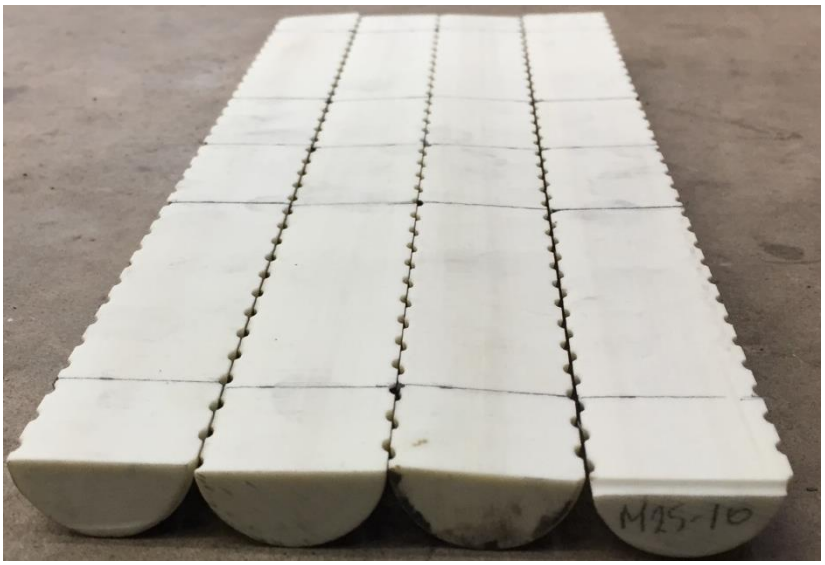

Figure 3.13: Close-up View of GFRP Bars Post-Longitudinal Cut

The locations of loading application and placement of supports were indicated on the specimens directly, for ease and time efficiency of setting up the specimen for testing, as seen in Figure 3.9, Figure 3.12 and Figure 3.13. For the 3-point bending tests, the load will be applied at the midspan of the specimen. For the 4-point bending tests, the load will be applied at one-third of the length from the support toward the midspan of the specimen, from each end.

It should be noted that, due to the availability of various "anvil" support sizing, a few of the specimens sizes that were unable to fit "snugly" without inducing unnecessary stresses to the specimen needed to have its width slightly reduced by a few millimetres to ensure this. This was completed using a Dremel rotary hand tool used as a sander, to remove a bit of the outer portion of the specimen that will be resting on the supports. This alteration mainly applied to the M25 and M32 bars. Since the failure did not occur at the support, this alteration did not influence the final test results.

3.3.2 Tensile Tests

The free length of the specimens used in the tensile test need to be about 40 times its diameter size, The total length includes the length of the DOM tubes that act as anchors on both ends of the specimen (ASTM Committee D30, 2016; CSA, 2012). The purpose of using steel DOM tubes as anchors are to enclose the GFRP specimen, so that the V-grips will not crush the GFRP fibres, as the test is being conducted. However, a common issue with casting steel DOM tube to the GFRP bar is de-bonding, where the specimen fails due to slipping out of the anchor. To address this, the longer length of 500 mm for all specimens was used, as opposed the recommended length of the anchorage listed in ASTM D7205 (ASTM Committee D30, 2016). Table 3.4 presents the GFRP bar length, anchorage length, and total length of the specimen. Additional details and key parameters to determine specimen dimensions are indicated in Appendix E.

Table 3.4: Direct Tensile Specimen Length

Bar Designation	Free Length (mm)	DOM Tube Length (mm)	Total Length of Specimen (mm)
M8	320	500	1320
M13	520	500	1520
M15	640	500	1640

The chosen diameters of the DOM tubes were based on the recommended dimensions listed in ASTM D7205 (ASTM Committee D30, 2016) per GFRP bar size. The wall thickness of the DOM tubes was set to 6.35 mm (1/4”), which satisfies having a minimum thickness of 5 mm listed by ASTM D7205 and CSA S806-12.

Table 3.5 indicates the dimensions for DOM tubes. To promote stronger bonding between the two materials, the inner surface of the DOM tubes were roughened in order to create a more suitable bonding surface. Further specifications of the DOM tubes used are provided in Appendix E.

Table 3.5: DOM Tube Anchorage Dimensions

Bar Designation	Outer Diameter (mm)	Wall Thickness (mm)	Length (mm)
M8	35	6.35	500
M13	42	6.35	500
M15	42	6.35	500

To bond the DOM tube and GFRP bar together, demolition expansive grout (Dexpan) was chosen bonding agent. While the DOM tube and GFRP bar were set in place on a wooden vertical casting stand, the grout was poured between the two materials, and was left to cure for at least 2-3 days. Wooden “washers” were machined to fit within the DOM tube to ensure that the GFRP bar stays aligned during the casting process. Silicon caulking was applied between the GFRP bar, wooden washer, and DOM tube to ensure that the expansive grout will not leak out of the DOM tube. Figure 3.14 shows the cross section of a specimen before casting.

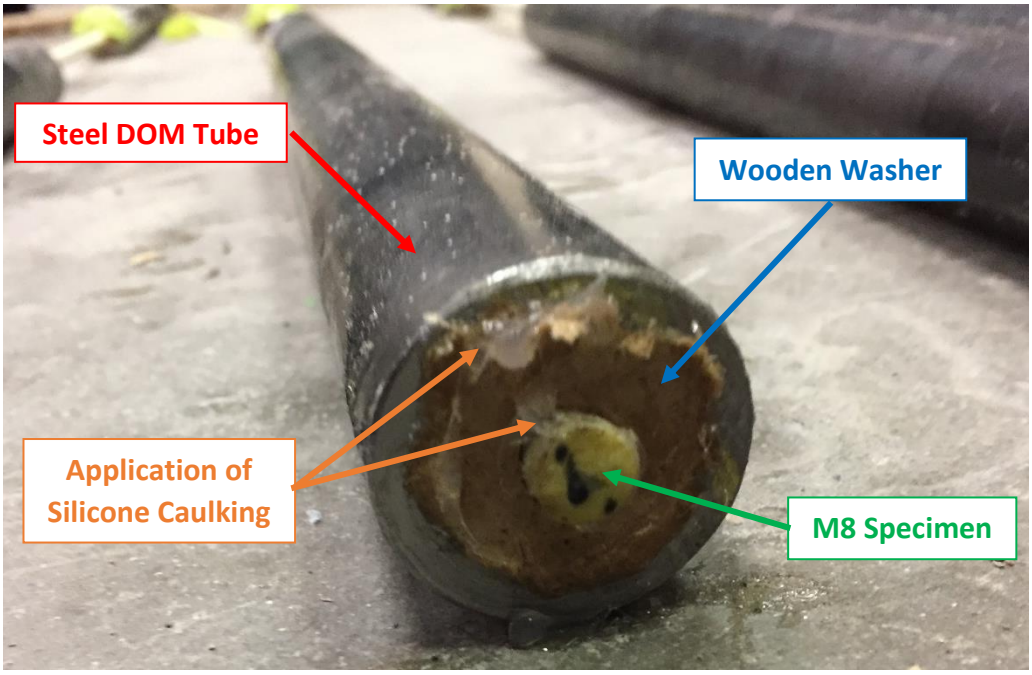

Figure 3.14: Cross-section of M8 GFRP Specimen Preparation Before Casting Expansive Grout

Figure 3.15 shows the cross section of a specimen after casting, where the wooden washer popped out of place after the expansive grout cured.

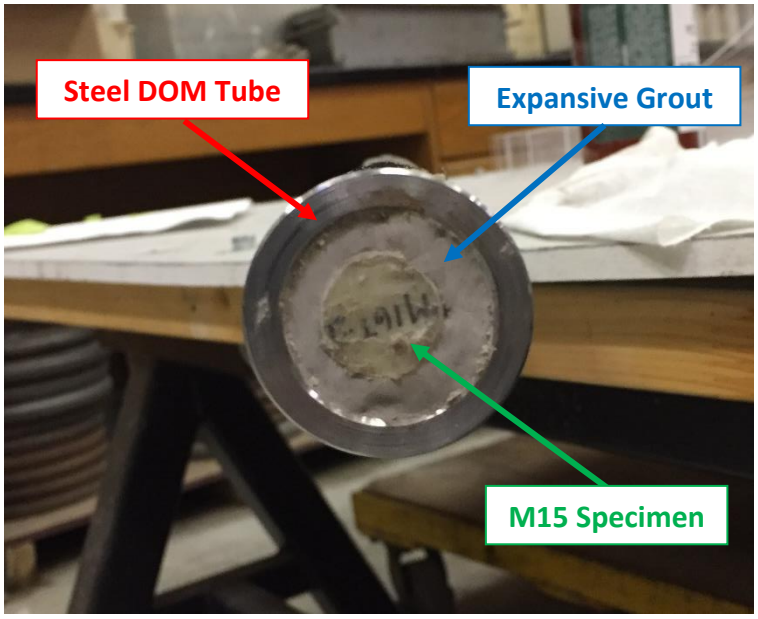

Figure 3.15: Cross-section of M15 GFRP Specimen Preparation After Casting Expansive Grout

Figure 3.16 displays GFRP bars held in place within casting stand, while the grout cures.

Figure 3.16: Tensile GFRP Specimens in Casting Stand

Figure 3.17 shows a GFRP specimen placed in the tensile testing machine prior to the beginning of testing, while Figure 3.18 shows the placement of a GFRP specimen being held by the bottom V-grips.

Figure 3.17: Tensile GFRP Specimens Testing Machine

Figure 3.18: V-Grips of Testing Machine

3.4 Test Observations

3.4.1 Flexure Tests

Similar general observations were noticed for both 3-point and 4-point bending tests. As the test starts, the specimen gradually bends due to the applied loading from the testing machine. Between 3-point and 4-point bending of the specimen, the deflected shape is different due to the locations of applied loading. Figures 3.19 to 3.22 show the examples of the specimens' deflected shapes in 3-point and 4-point bending near the begin and ends of the respective test. Figure 3.23 and Figure 3.24 show the failure GFRP specimen for the 3-point and 4-point bending tests, respectively. Figure 3.25 and Figure

3.26 show the theoretical deflected shape and bending moment diagram of a 3-point and 4-point bending test respectively. These are presented for ease of comparison between the theoretical behaviour and the different stages of the specimen testing.

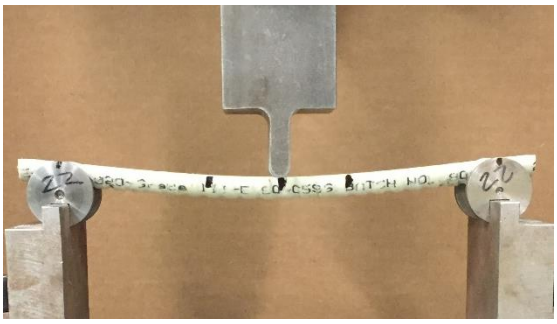

Figure 3.19: Deflected M20 Bar Shortly After Start of 3-Point Bending Test

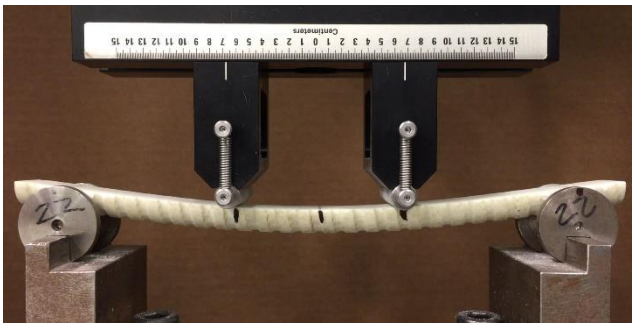

Figure 3.20: Deflected M20 Bar Shortly After Start of 4-Point Bending Test

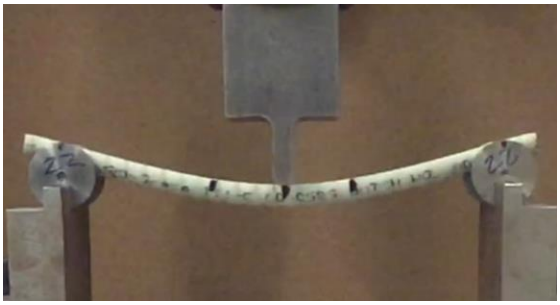

Figure 3.21: M20 Bar in 3-Point Bending Test Before Failure

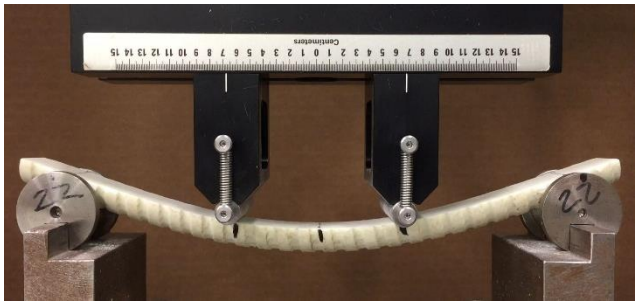

Figure 3.22: Deflected M20 Bar in 4-Point Bending Test Before Failure

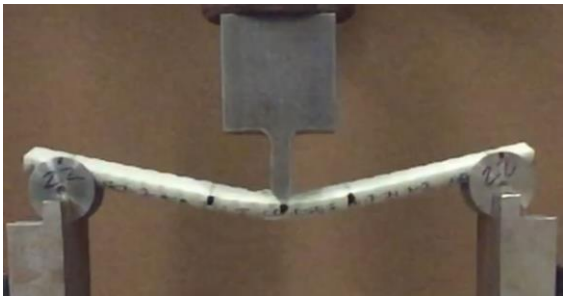

Figure 3.23: M20 Bar in 3-Point Bending Test After Failure

Figure 3.24: M20 Bar in 4-Point Bending Test After Failure

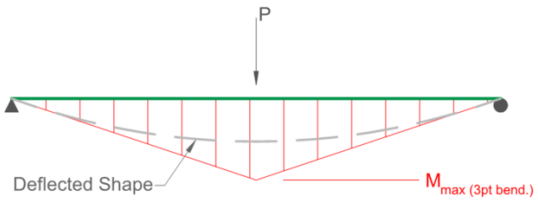

Figure 3.25: M20 Bar in 3-Point Bending Test After Failure

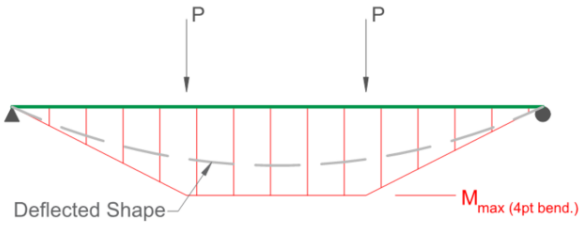

Figure 3.26: M20 Bar in 3-Point Bending Test After Failure

From Figures 3.19 to 3.26, it is evident that the deflected shapes are not similar, due to the variation in the point load positions. Transitioning from Figures 3.21 & 3.22 to Figures 3.23 & 3.24, the specimens can no longer hold their deflected shape without significant breakage. The segments between the point of rupture to the ends of the specimen appear to be quite linear in shape post-failure. However, a notable characteristic of the deflected shape is that between the point loads, the segment has entirely deformed into a non-linear shape. This indicates that this region of the specimen endures the most bending stress, clearly resembling the bending moment diagram for beam experiencing 4-point bending, as shown in Figure 3.26.

Signs of failure can be identified when tensile fibres fractures are visible, as shown in Figure 3.27 and 3.28. During the test, cracking noises (i.e. similar to cracking of ceramic material) can be heard from the specimen itself. Generally, subtle cracking noises were heard prior to visible damage. As the test proceeds past the point of first signs of tensile failure, pieces of the bottom of the GFRP specimen appear to break or peel off since the tensile fibres are being stretched out and cannot maintain its form. These pieces are usually the ribbed portions (outer diameter of the GFRP). Based on Figure 3.28, it is evident that these fractures of tensile fibres can be more easily seen in specimens for 4-point bending as opposed to 3-point bending.

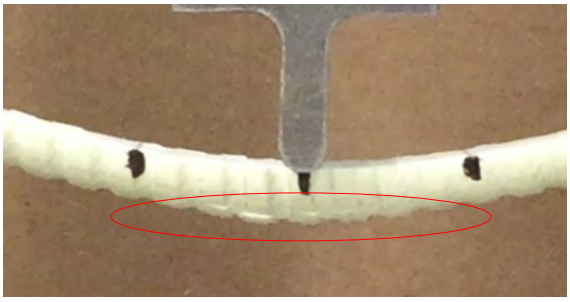

Figure 3.27: Close-up View of Tensile Fibre Rupture in M20 Bar in a 3-Point Bending Test

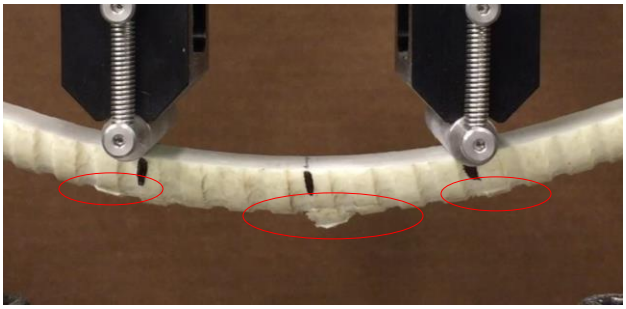

Figure 3.28: Close-up View of Tensile Fibre Rupture in M20 Bar in a 4-Point Bending Test

Since these tests have been conducted until the specimen reaches total failure, it can be seen in Figure 3.23 and Figure 3.24 that both the compressive and tensile fibres rupture. After the specimen were taken out of its position in the testing apparatus, signs of rupture were still evident on the specimen itself, even though it mostly reverts to its undeflected shape. This can be seen in Figures 3.29 to 3.34.

Figure 3.29: Close-up View of Bottom (Tensile-Stressed) Side of M20 Specimen Subjected to 3-Point Bending

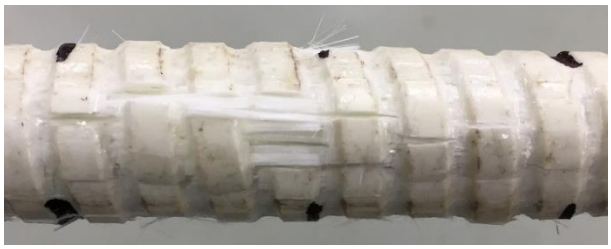

Figure 3.30: Close-up View of Bottom (Tensile-Stressed) Face of M20 Specimen in 4-Point Bending

Figure 3.31: Close-up View of Side Face of M20 Specimen Subjected to 3-Point Bending

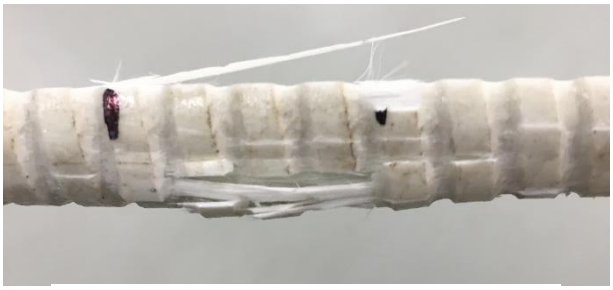

Figure 3.32: Close-up View of Side Face of M20 Specimen Subjected to 4-Point Bending

Figure 3.33: Close-up View of Top (Compressive-Stressed) Face of M20 Specimen Subjected to 3-Point Bending

Figure 3.34: Close-up View of Top (Compressive-Stressed) Face of M20 Specimen Subjected to 4-Point Bending

Similar to the comparison of Figure 3.23 and Figure 3.24 of the total failure of the specimen in the testing apparatus, it is evident that more damages are seen in specimens subjected to the 4-point bending test from Figures 3.29 to 3.30. In both cases, it appears that the signs of rupture are the same where delamination and breakage of fibres are notable, specifically with the missing pieces of ribs on the bottom, and the fractures along the sides and top of the specimen.

Although Figures 3.19 to 3.24 and Figures 3.29 to 3.34 only show a 20M specimen, the same failure behaviours were exhibited in the other bar sizes used in this test. The difference between tests with the smaller to larger bar sizes were that larger bars could endure more loading and undergo more deflection. An obvious observation was that the failure of larger bars more closely represented the nature of the GFRP material – being a brittle and sudden failure. Figures 3.35 to 3.44 display the side view of other GFRP bar sizes, post-failure.

Figure 3.35: Close-up View of Side Face of M8 Specimen Subjected to 3-Point Bending

Figure 3.36: Close-up View of Side Face of M8 Specimen Subjected to 4-Point Bending

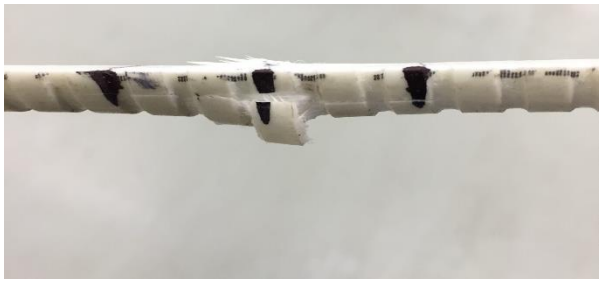

Figure 3.37: Close-up View of Side Face of M13 Specimen Subjected to 3-Point Bending

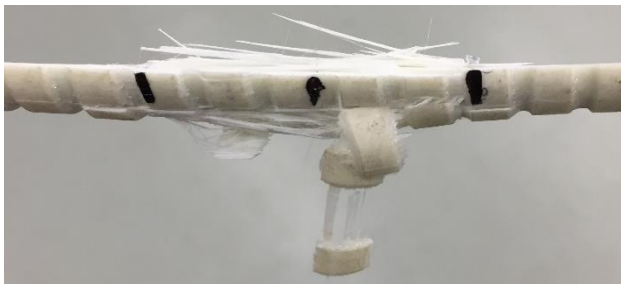

Figure 3.38: Close-up View of Side Face of M13 Specimen Subjected to 4-Point Bending

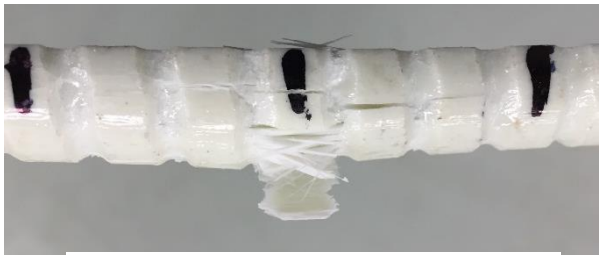

Figure 3.39: Close-up View of Side Face of M15 Specimen Subjected to 3-Point Bending

Figure 3.40: Close-up View of Side Face of M15 Specimen Subjected to 4-Point Bending

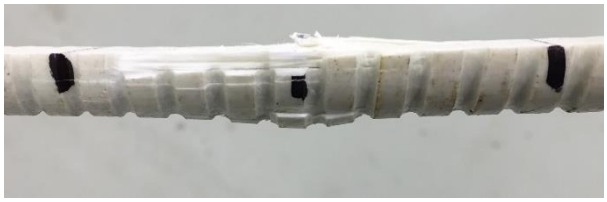

Figure 3.41: Close-up View of Side Face of M25 Specimen Subjected to 3-Point Bending

Figure 3.42: Close-up View of Side Face of M25 Specimen Subjected to 4-Point Bending

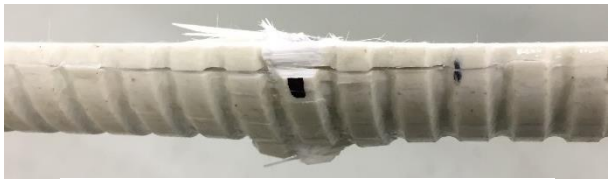

Figure 3.43: Close-up View of Side Face of M32 Specimen Subjected to 3-Point Bending

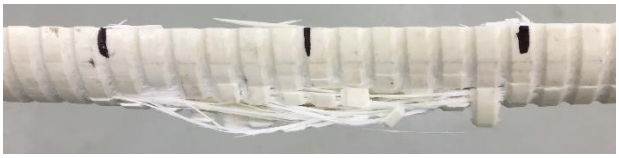

Figure 3.44: Close-up View of Side Face of M32 Specimen Subjected to 4-Point Bending

It is evident that the 4-point bending test is more destructive as opposed to a 3-point bending test, based on the appears of the GFRP bars displayed in Figures 3.35 to 3.44, regardless of size. In all cases, it is quite notable that the tensile fibres rupture and usually appear to have more damage compared to the compressive fibres, despite the GFRP specimens mostly reverting to their undeflected shape.

3.4.2 Tensile Tests

While conducting the tensile tests, the extensometer was removed approximately at 60% of the predicted ultimate load for the first 1-2 specimens, and at 75% for the rest of the specimens, after discovering the actual ultimate load. The gage length of the extensometer that was used is 165.8 mm.

As the loading increased and the GFRP specimen stretched, it was seen that the cross section of the diameter decreased. For most specimens, cracking was heard as the test approached its predicted failure load. There were a few specimens that showed minimal warning just before failure. Failure of a specimen was abrupt, where the glass fibre strands of the GFRP bar quickly tore apart from the rest of the cross section, until the entire cross section was severed. Using precaution and proper safety equipment is crucial when disposing the material in this condition.

None of the tests failed through pull-out, proving that using 500 mm long DOM tubes to act as anchorage on both ends of the GFRP bars is more than sufficient for ribbed GFRP bars. However, due to errors in test setup, only 4 specimens have been tested for the M13 bars. Due to data recording errors, one of the four specimens did not have the extensometer displacement recorded. However, for the M8 and M15 GFRP bar sizes, 5 specimens have been tested.

Figures 3.45 to 3.47 are three sets of 4 images of a M8, M13, and M15 tensile test specimen, respectively. The first image (a) shows the specimen at the beginning of the test. The second image (b) shows the specimen just before the first sign of rupture. The third image (c) shows the first sign of specimen rupture. The last image (d) shows the specimen post-failure.

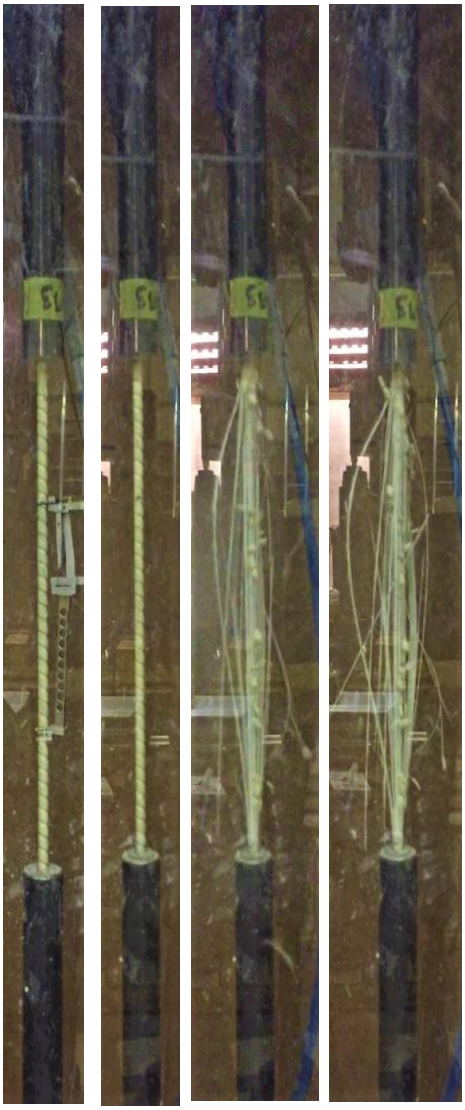

(a) (b) (c) (d)

Figure 3.45: Stages of testing for Specimen M8-T3

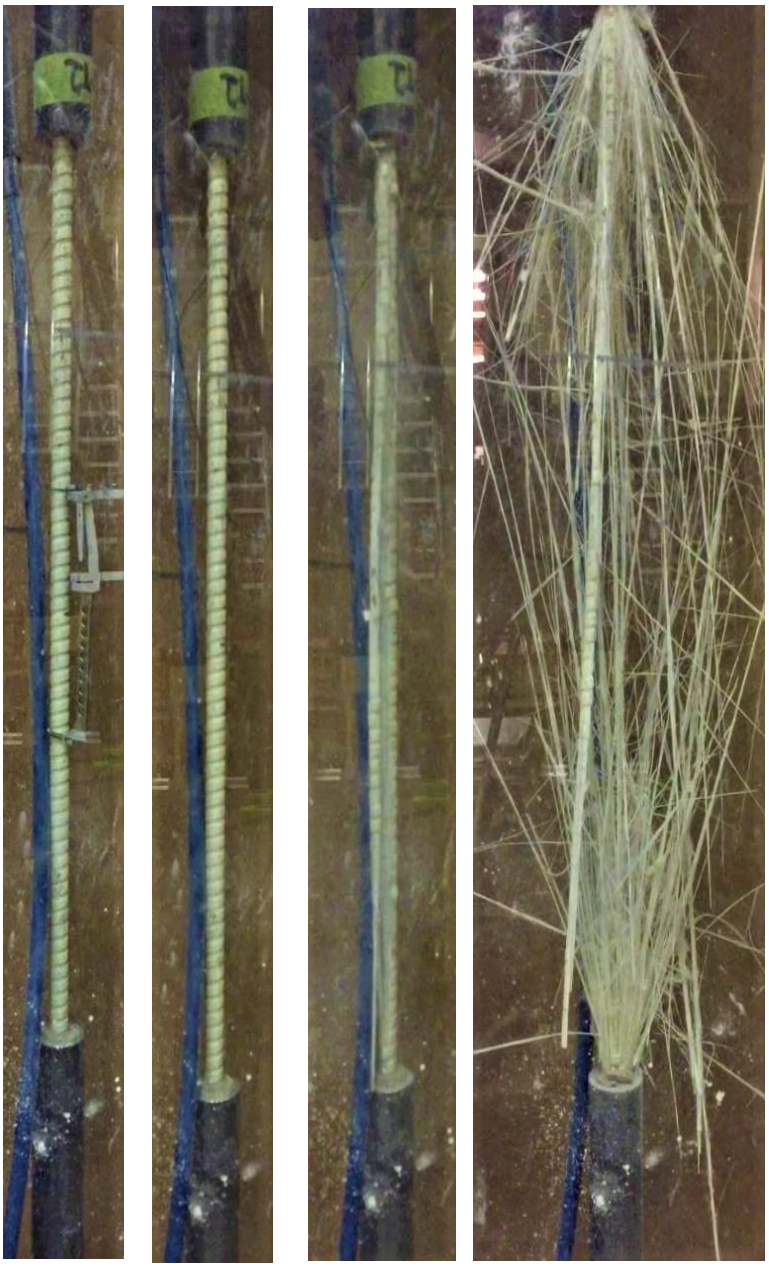

(a) (b) (c) (d)

Figure 3.46: Stages of testing for Specimen M13-T2

(a *(b)* *(c)* *(d)*

Figure 3.47: Stages of testing for Specimen M15-T2

Based on Figures 3.45 to 3.47, the elongation of the GFRP bar is more evident as the bar size is larger, and can be seen when comparing image (a) and (b) to each other. The amount of damage is more profound with the bigger sized specimens as well, where the glass fibres are very scattered as the GFRP bar fails for the M15 bar, unlike the M8 bar where the failure is more subtle. Rupture of the GFRP bars start with a portion of the cross section breaking off from the rest of it, which is indicated in Figures 3.46c and 3.47c.

3.5 Test Results and Discussion

3.5.1 Flexure Tests

A majority of the specimens exhibit a fairly linear-elastic trend for most of the duration of testing, which immediately turns non-linear when peak loading is about to be reached. When the load-displacement curve appears to be curved, it meant that the specimen was approaching its ultimate load. The nonlinearity was initiated by cracking of the fibres on the tensile side of the specimens, followed by crushing of fibres on the compressive side. The determination of this onset of nonlinearity is one of the important aspects studied in this research and described in detail in Chapter 4. The point represents the tensile rupture strength of bars in bending.

Figure 3.48 shows an example of a 3-point and 4-point bending load-displacement plot for a small diameter M8 specimens. Figure 3.49 shows an example of a 3-point and 4-point bending load-displacements plot for M32 specimens. The data for smaller diameters has more “noise” than the obvious linear behaviour of the larger diameters.

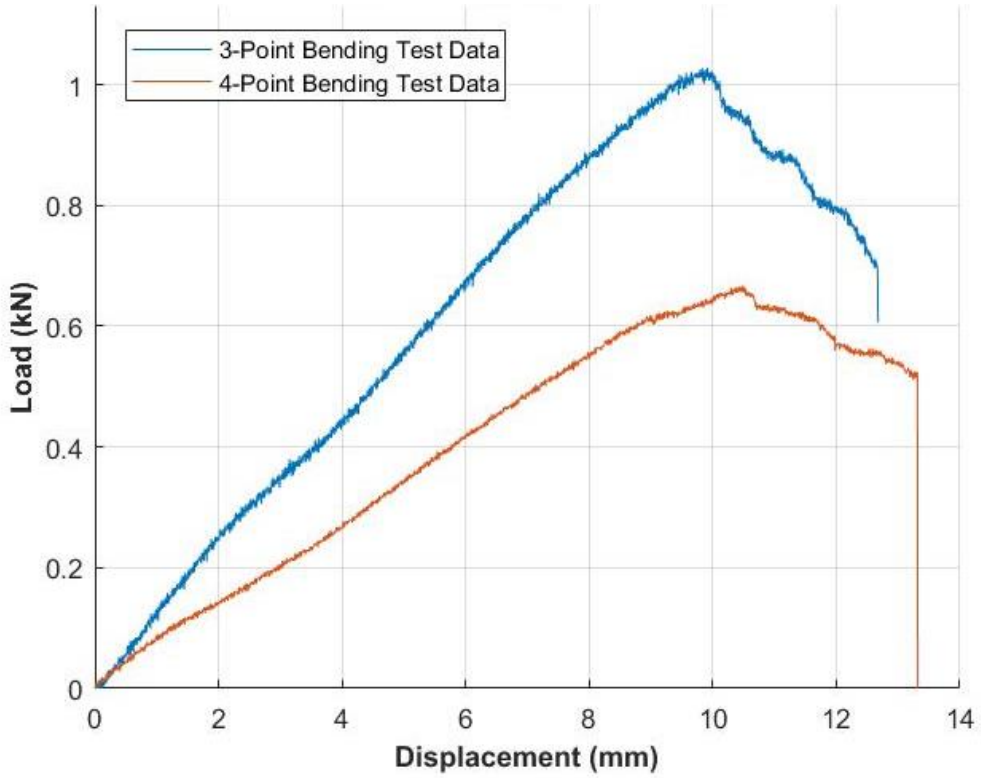

Figure 3.48: Load-Displacement Plot for M8-1 (in 3-Point Bending) & M8-17 (in 4-Point Bending)

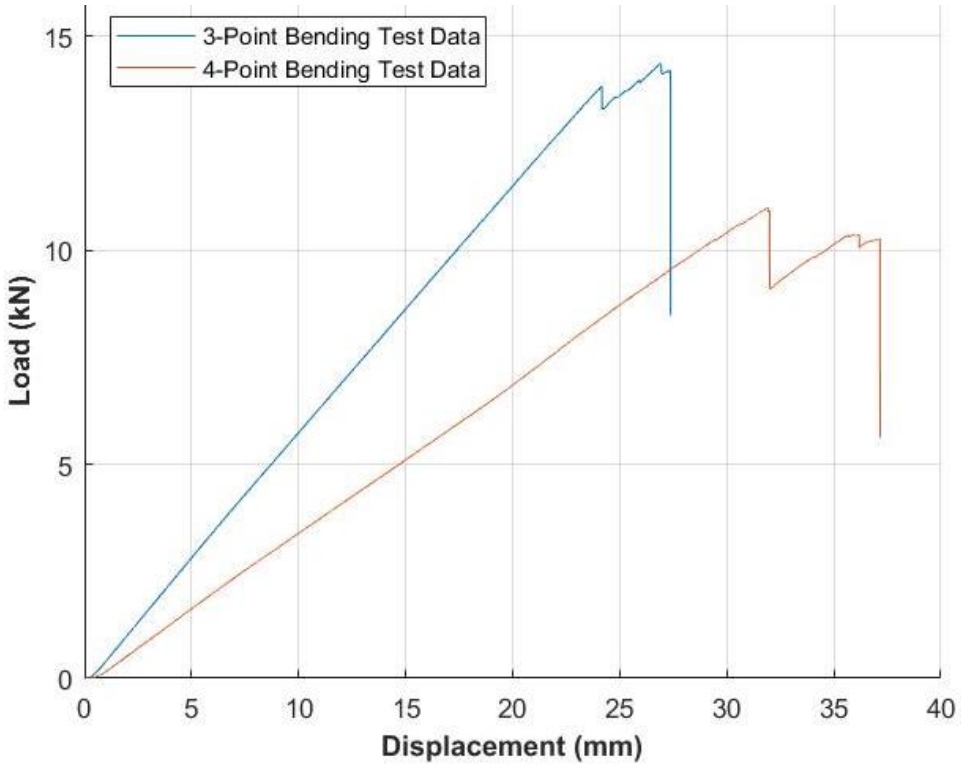

Figure 3.49: Load-Displacement Plot for M32-3 (in 3-Point Bending) & M32-14 (in 4-Point Bending)

The overall behaviours are quite similar for both 3-point and 4-point bending tests. It should be noted that the bars showed a variety of load-displacement behaviours. While some showed very clear linearity where the peak load corresponds to fibres cracking, others had more complex behaviour before cracking. However, the overall behaviour was always the same; initial linearity (or almost linearity) followed by more or less abrupt stiffness change. Figures 3.50 to 3.53 display examples of load-displacement plots for M13, M15, M20, and M25 specimens, respectively.

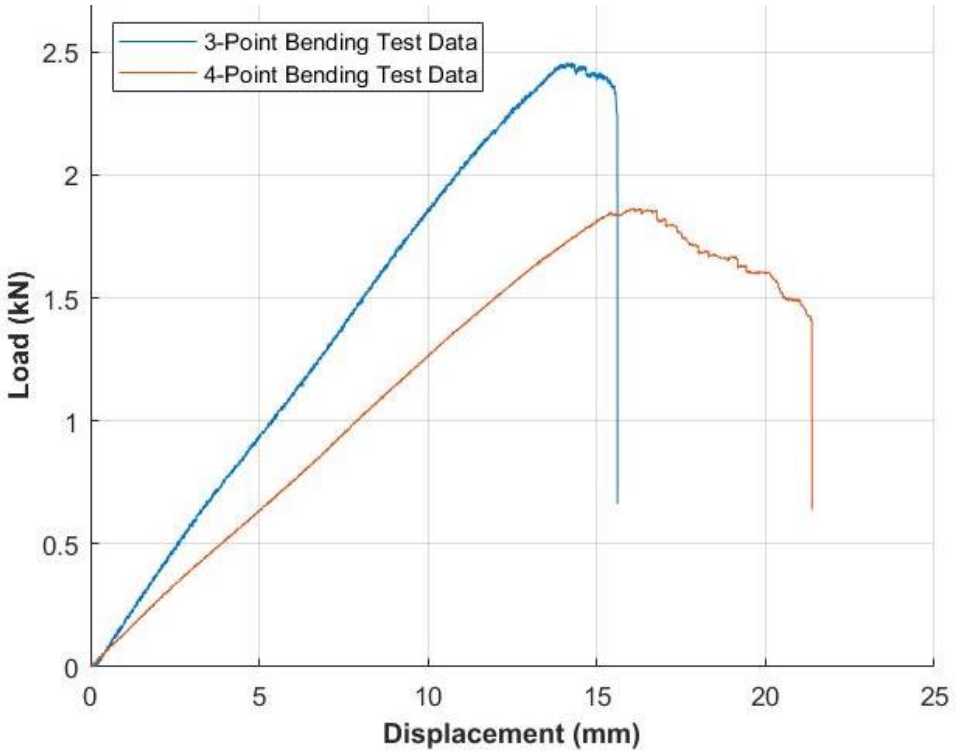

Figure 3.50: Load-Displacement Plot for M13-20 (in 3-Point Bending) & M13-16 (in 4-Point Bending)

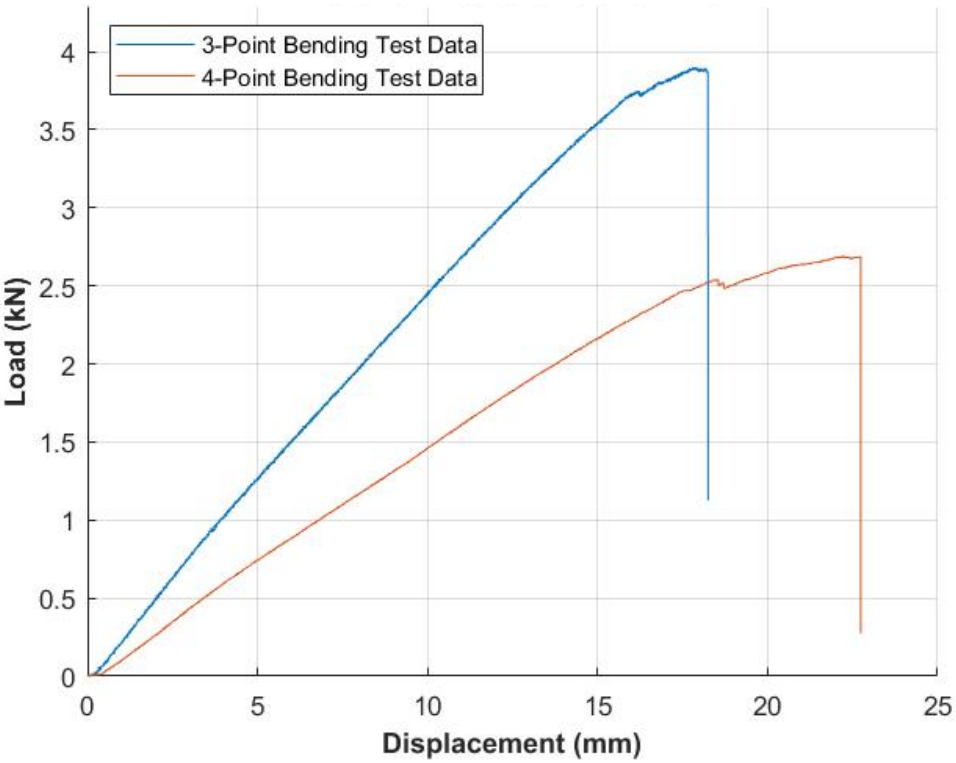

Figure 3.51: Load-Displacement Plot for M15-29 (in 3-Point Bending) & M15-10 (in 4-Point Bending)

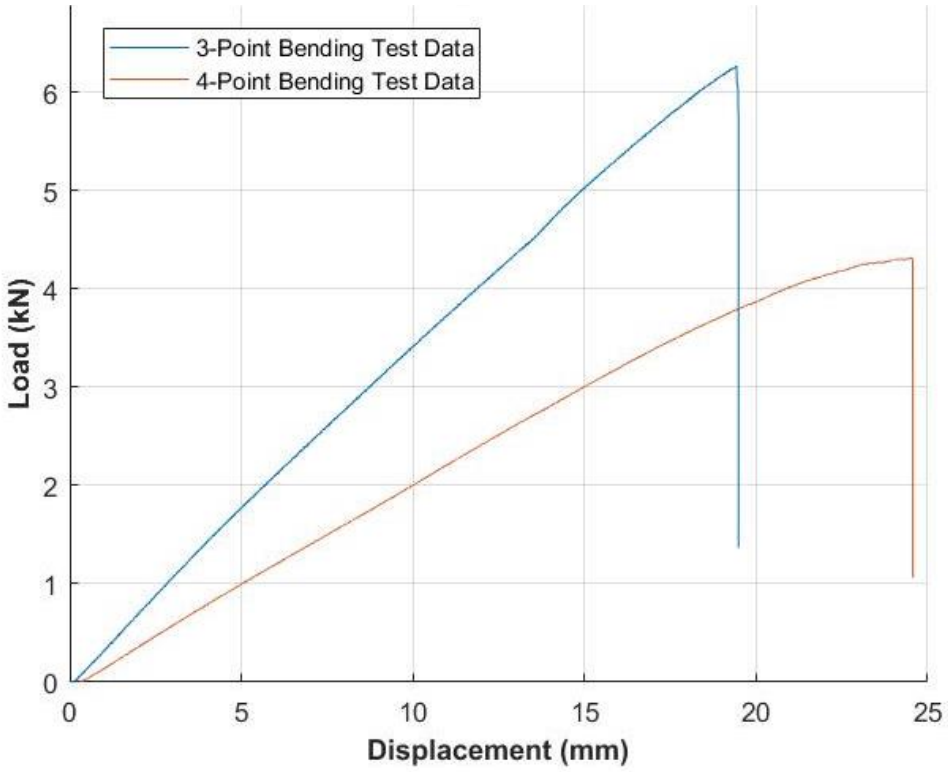

Figure 3.52: Load-Displacement Plot for M20-12 (in 3-Point Bending) & M20-7 (in 4-Point Bending)

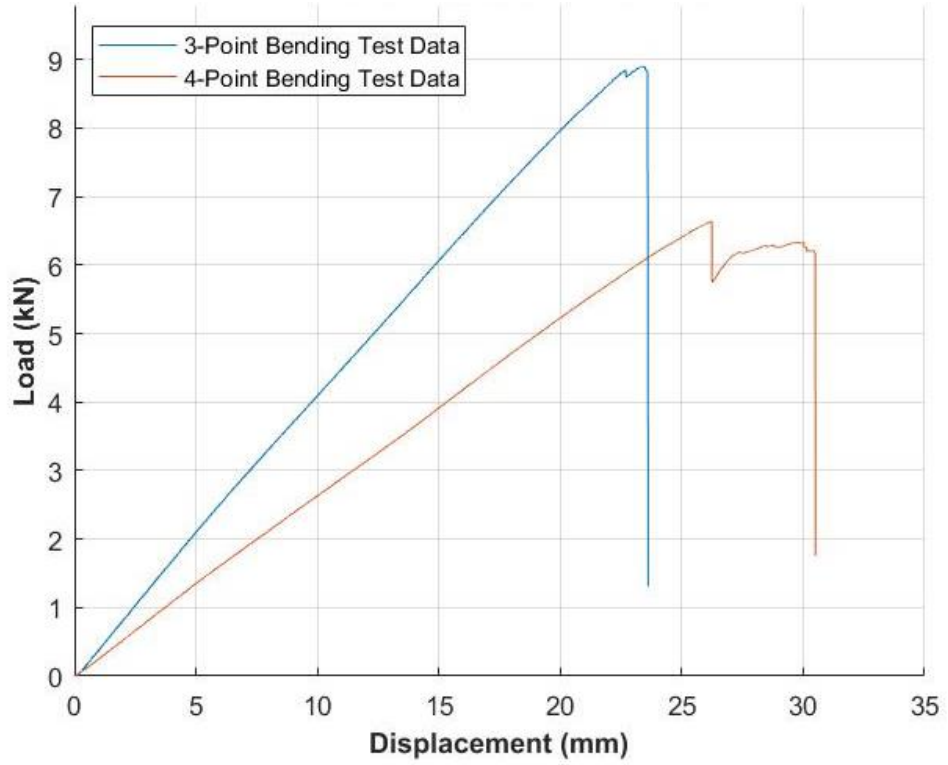

Figure 3.53: Load-Displacement Plot for M25-8 (in 3-Point Bending) & M25-4 (in 4-Point Bending)

The peak load varies depending on the size of the GFRP, as well as the type of testing. As noted in Section 3.2.1, the loading and displacement values provided from testing need to be altered to accurately represent 4-point bending. Even between the different specimens of the same size and flexure test, there are slightly differences; due to specimens being of different batches and different dimensions, which depend on longitudinal cutting. Table 3.6 displays the average maximum load per loading nose and the displacement value at maximum loading. These are the absolute maximum loads recorded during testing, which are not the ones used for calculation of cracking load.

Table 3.6: Average Maximum Loading per Loading Nose and Corresponding Displacement

Bar Size	Parameter	3-Point Bending			4-Point Bending		
		Average	Standard Deviation	Coefficient of Variation	Average	Standard Deviation	Coefficient of Variation
M8	F_{max} (kN)	0.903	0.111	0.123	0.690	0.060	0.086
	Δ at F_{max} (mm)	9.792	0.649	0.066	13.439	0.885	0.066
M13	F_{max} (kN)	2.542	0.119	0.047	1.815	0.103	0.057
	Δ at F_{max} (mm)	14.243	0.318	0.022	19.967	0.589	0.029
M15	F_{max} (kN)	3.960	0.083	0.021	2.782	0.107	0.038
	Δ at F_{max} (mm)	17.313	0.707	0.041	24.109	1.685	0.070
M20	F_{max} (kN)	6.183	0.246	0.040	4.495	0.138	0.031
	Δ at F_{max} (mm)	20.044	0.562	0.028	28.963	0.927	0.032
M25	F_{max} (kN)	8.759	0.359	0.041	6.602	0.293	0.044
	Δ at F_{max} (mm)	22.300	1.003	0.045	34.084	1.511	0.044
M32	F_{max} (kN)	14.132	0.511	0.036	10.634	1.400	0.132
	Δ at F_{max} (mm)	26.652	1.519	0.057	38.315	2.756	0.072

The individual specimen maximum loads and deflections are provided in Appendix B. The individual load-displacement plots for each specimen are provided in Appendix C. For the correlation calculations that will be outlined in Chapter 5, the maximum loading will not be used. The primary reason for this is that the maximum load corresponds to the highest loading which the specimen can take before it completely fails. This research examines tensile strength of the bar, as opposed to its flexural strength; therefore, the loading which corresponds to the first potential sign of rupture of the tensile fibres will be used the calculations. Chapter 4 of this thesis will go through the methodology and procedures completed to identify this loading.

3.5.2 Tensile Tests

The displacement from the extensometer represents the displacement of the specimen, unlike the displacement of the testing machine's crosshead. However, since the extensometer had to be removed before the ultimate load of the specimen was reached to avoid damage, the load-displacement plots using the crosshead displacement are provided as reference to observe characteristics of the specimen throughout the entire duration of the test.

The total gage length for each test was the base gage length of the extensometer, in addition to accounting for any offset in distance imposed between contact blades of extensometer if there was slight movement before testing began. The strain for the specimen was calculated by dividing this total length by the sum of the total length and the displacement during testing, which is represented in Equation 3.3.

$$\varepsilon = \frac{L_{ext-base} + L_{ext-off}}{\delta + \left(L_{ext-base} + L_{ext-off}\right)} \qquad \textit{Equation 3.3}$$

The stress is calculated from taking the load data and dividing it by the specimen's cross section, as shown in Equation 3.4.

$$\sigma = \frac{F}{A} \qquad \textit{Equation 3.4}$$

All the specimens exhibit a linear-elastic behaviour, until they approach their respective ultimate load where it becomes more non-linear in nature. For all specimens, there is a notable point of slope change that occurs at approximately 30% of the ultimate load of the specimen. This phenomenon is shown in plots for the M8 and M13 specimens, and less evident in the M15 specimens.

For all plots, the region which corresponds to the portion of stress-strain plot used to calculate the tensile elastic modulus is displayed. The starting and ending points for this region corresponds to strain values of 0.001 and 0.003, respectively (ASTM Committee D30, 2016). The load-crosshead displacement plots also show the display the maximum load, point when the extensometer was removed during the test. This is noted in Figures 3.54 to 3.62, where one specimen of each size has its load-crosshead displacement, load-extensometer displacement, and stress-strain plots displayed.

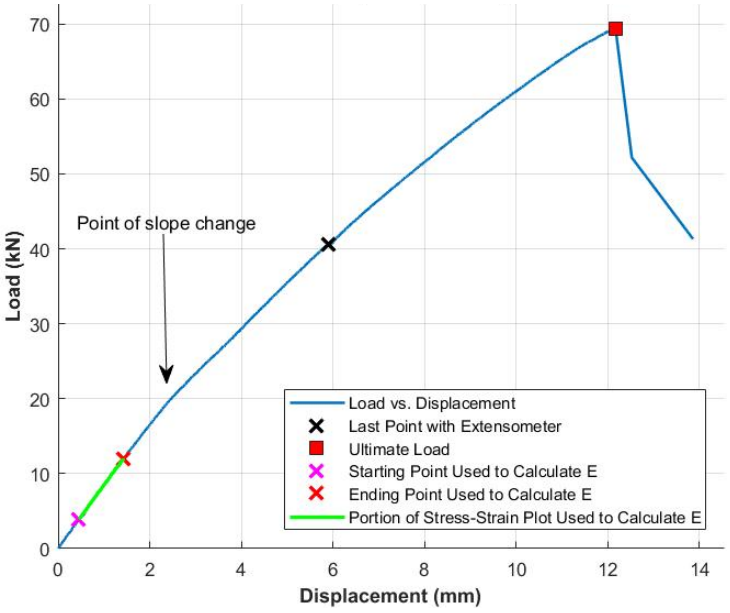

Figure 3.54: Load-Crosshead Displacement Plot for M8-T1

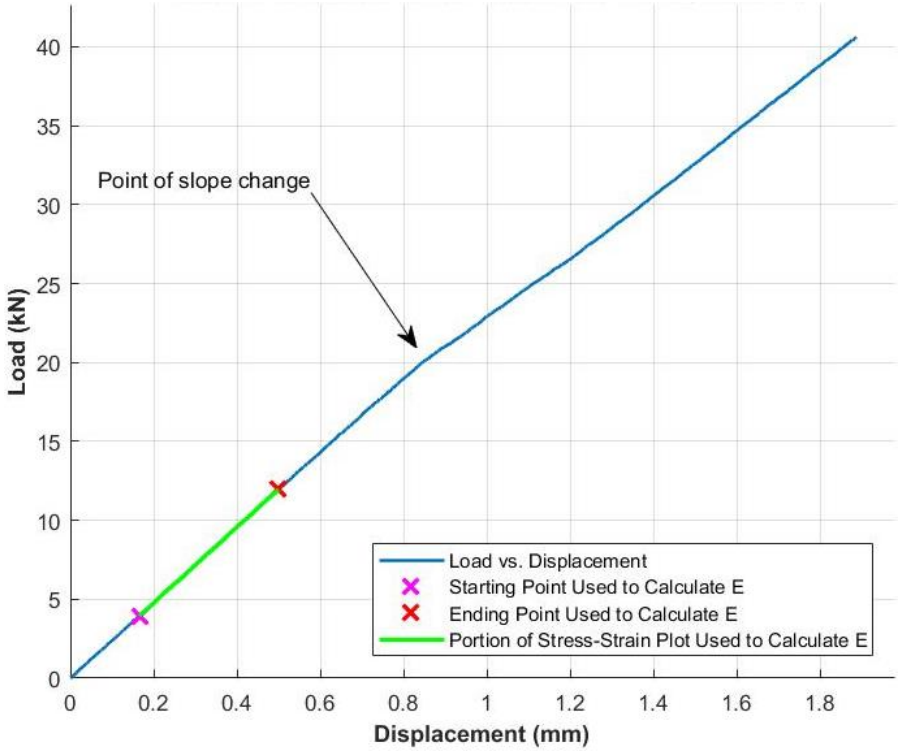

Figure 3.55: Load-Extensometer Displacement Plot for M8-T1

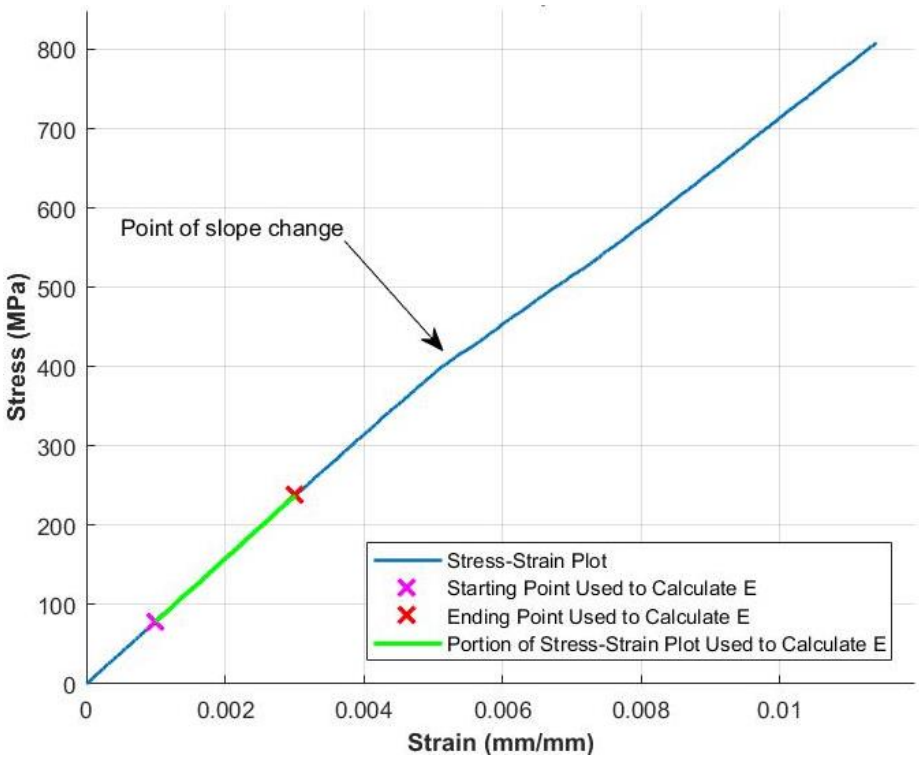

Figure 3.56: Stress-Strain Plot for M8-T1

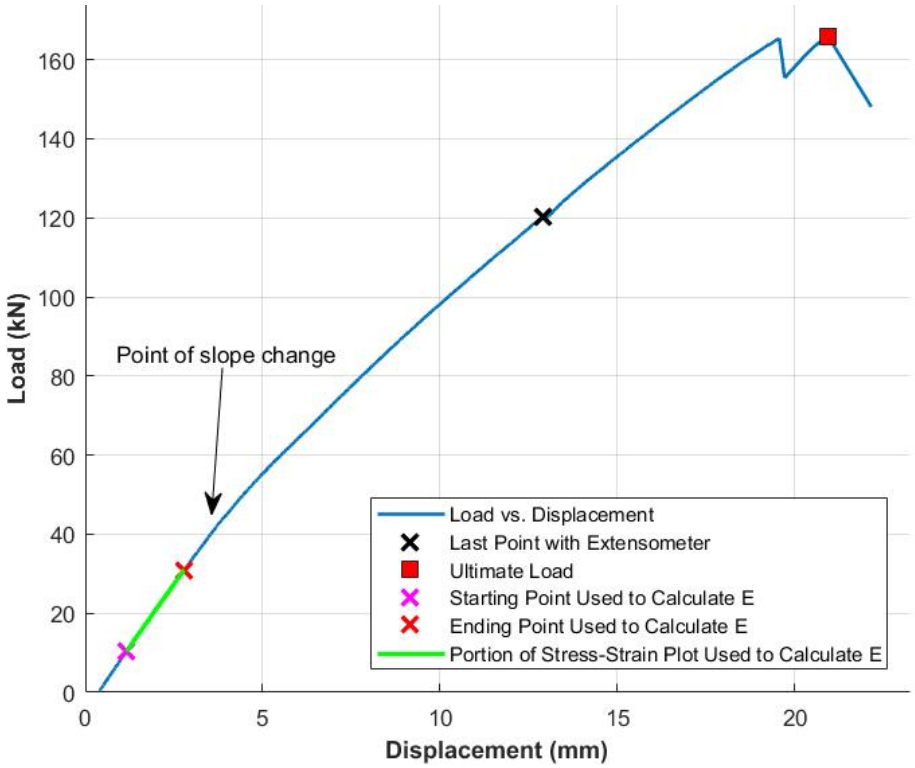

Figure 3.57: Load-Crosshead displacement Plot for M13-T2

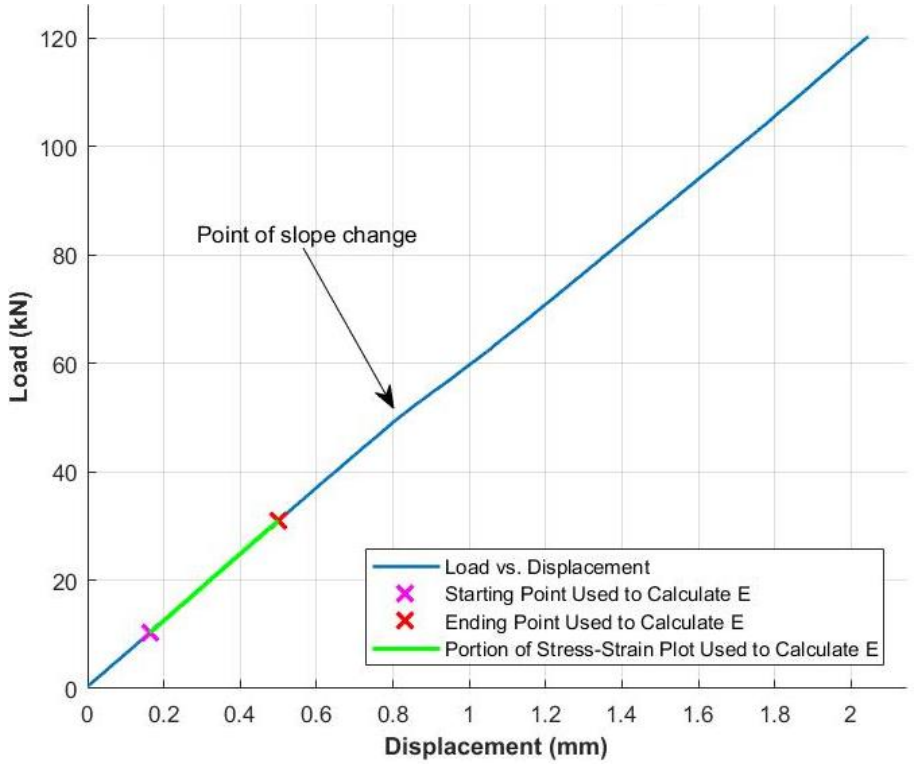

Figure 3.58: Load-Extensometer Displacement Plot for M13-T2

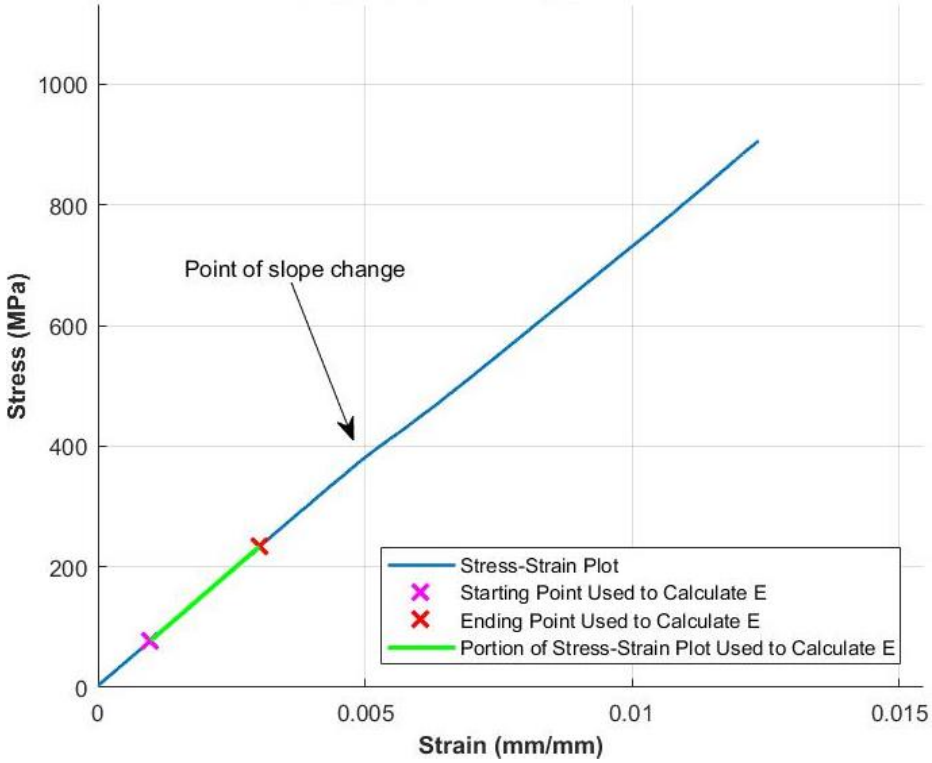

Figure 3.59: Stress-Strain Plot for M13-T2

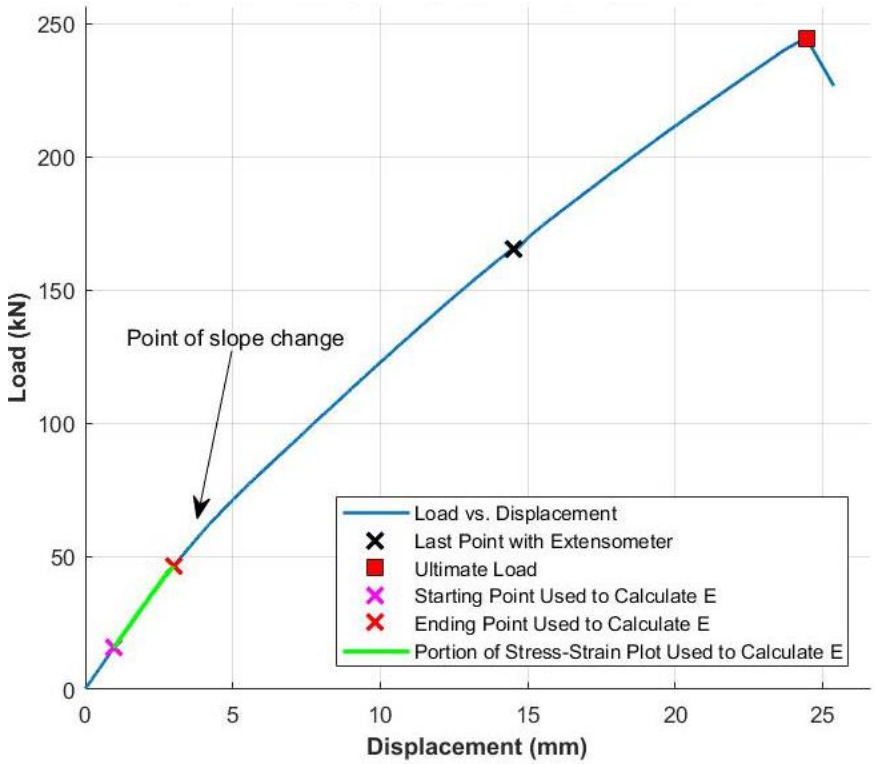

Figure 3.60: Load-Crosshead displacement Plot for M15-T3

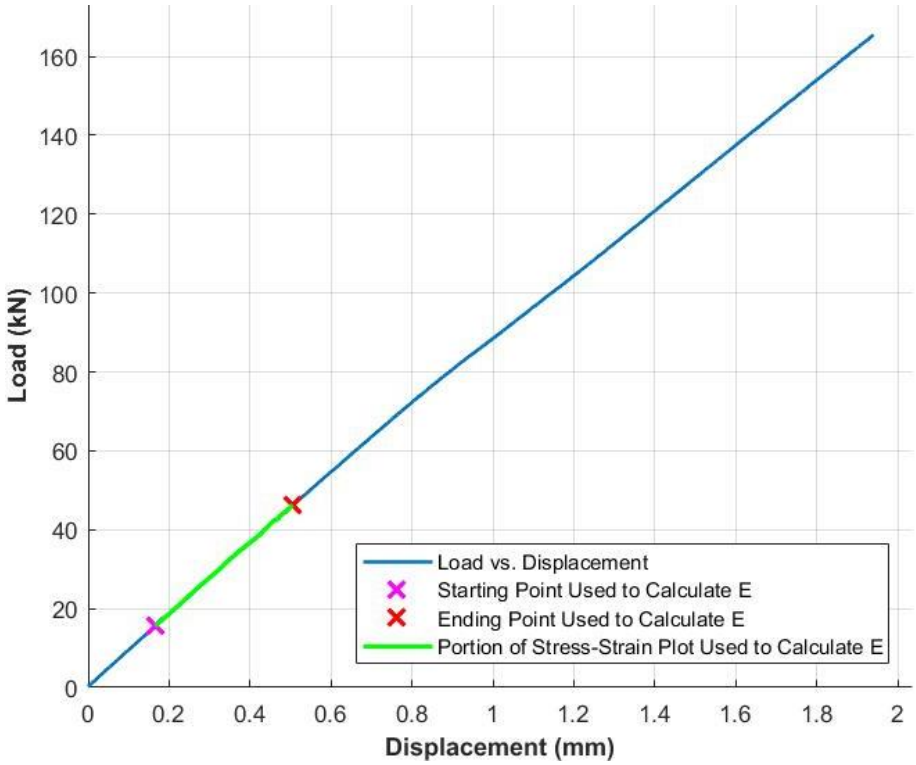

Figure 3.61: Load-Extensometer Displacement Plot for M15-T3

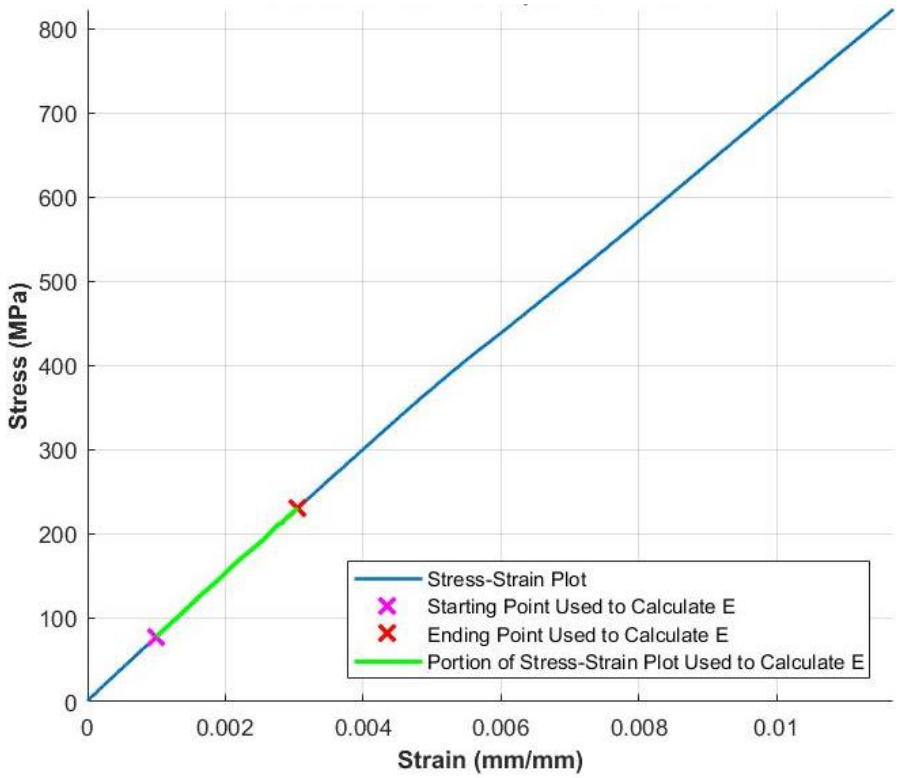

Figure 3.62: Stress-Strain Plot for M15-T3

Throughout all plots in Figure 3.54 to 3.62, all the corresponding graphs are quite similar in behaviour, where they have linear slopes, and a sudden specimen failure. Table 3.7 shows a summary of averages for the maximum loads, ultimate tensile capacities, and tensile elastic modulus for each specimen size. Outliers have been identified as two specimens with either: defects during casting the DOM tube anchors and testing errors, or omission of specimens with the lowest and highest load. Averages that were made excluding outliers include three specimens.

Table 3.7: Summary of Tensile Testing Information

Bar Size	Parameter	All Specimens			Excluding Outliers		
		Average	Standard Deviation	Coefficient of Variation	Average	Standard Deviation	Coefficient of Variation
M8	F_{max} (kN)	65.83	5.79	0.09	67.57	1.66	0.02
	σ_t (MPa)	1309.67	115.28	0.09	1344.35	33.04	0.02
	E_t (MPa)	79897.19	1918.43	0.02	80874.23	1891.31	0.02
M13	F_{max} (kN)	162.27	3.43	0.02	163.42	3.11	0.02
	σ_t (MPa)	1222.57	25.81	0.02	1231.23	23.45	0.02
	E_t (MPa)	76847.85	471.23	0.01	76847.85	471.23	0.01
M15	F_{max} (kN)	247.07	14.92	0.06	243.10	4.50	0.02
	σ_t (MPa)	1228.82	74.19	0.06	1209.08	22.39	0.02
	E_t (MPa)	75243.02	849.08	0.01	74968.56	488.08	0.01

From Table 3.7, it is evident that the smaller the GFRP bar, the more stiff it is and the higher the ultimate stress it can endure. Even though the M8 specimens have the smallest ultimate load average, its tensile stress capacity is the highest. For the M13 and M15 specimens, the tensile capacities and elastic moduli are similar, although the M15 bars can endure much more tensile load.

Appendix E contains more details for each of the tensile specimens, while Appendix F display relevant plots from tensile testing data. The average ultimate stress values that exclude outliers will be used in comparison to the results from the flexural test. This will be further discussed in Chapter 5 of this thesis.

Chapter 4 - Identifying Cracking Flexure Load for Tested Specimens

Determination of the correct maximum flexure load considered for the tensile strength calculations is presented in this chapter. This load corresponds to the end of the linear response of the load-displacement curve (see Figure 4.5 for an example of this). The maximum point load is higher, as there is a portion of nonlinear response after cracking of the bottom tensile fibres before crushing of the top compressive fibres, which results in errors in the correlations to the tensile capacity. Therefore, the maximum loading at which the tensile fibres of the specimen break needs to be determined in order to calculate the correlated tensile capacity with minimal errors. This is considered to be the maximum load along the linear portion of the load-deflection graph, right before a significant change in slope. This indicates that the tensile fibres of the specimen are starting to rupture, which results in a change of the load-displacement trend exhibited by the specimen, due to having less of the cross-section intact to resist bending stresses.

Three methods were used to determine this maximum loading point, known as "cracking load" herein. These methods are 1) visual inspection, 2) lines-of-best-fit, and 3) numerical differentiation. For each of these methods to be properly conducted, the data sets must be filtered to reduce the noise within the data set. Tables and figures presented in this chapter use the following specimens: M8-30, M15-25, and M32-16. These specimens will be referred to as: M8, M15, and M32, respectively. These are used to show example on how the calculations are done. The described procedures were applied to all bars to calculate flexure cracking load.

4.1 Filtering Data using Single & Double Exponential Filtering

Filtering is commonly used for signal processing applications, where a substantial amount of noise is present in the signal (i.e. data set). By filtering data, noise in the data set is reduced, decreasing the variability of the response. Since all the flexural testing data has some noise present, albeit minimal, it is difficult to define a relationship for the data set such that the slope can be found.

One of the most common methods used for filtering is "single exponential filtering" (addressed as SES onward). However, this filtering method is not ideal for representing data that follows a trend (Performity LLC/Greg Stanley and Associates, n.d.). Therefore, a closely related filtering method that is more suited to filter data following trends is "double exponential filtering" (addressed as DES onward). To understand how DES works, it is important to understand how SES operates, which will be briefly described in Subsection 4.1.1.

4.1.1 Background

SES is represented by Equation 4.1:

$$f_{new}(x_i) = (1-\alpha) f_{new}(x_{i-1}) + \alpha f(x_{i-1}) \qquad \textit{Equation 4.1}$$

where:

- $f_{new}(x)$ = new, filtered y-value (i.e. filtered loading)
- $f(x)$ = old, unfiltered y-value (i.e. raw loading from lab testing results)
- α = exponential filter factor for estimated value of f(x), also called the "smoothing constant"; a value between 0 and 1
- x_i = represent the currently observed x-value (i.e. displacement)
- x_{i-1} = represent the previous observed x-value (i.e. displacement)

This filtering method works by applying a smoothing factor, which can be thought of as a weighted average factor, to the previous unfiltered data point, while adding the previous "smoothed" data value multiplied by the remaining weight from the factor (out of 100%). The term that observes the previous filtered data is also be influenced by similar weighed factors; hence, making this equation exponential. The higher (i.e. closer to 1) the exponential filter constant, the closer the filtered value will be based off the actual value. Inversely, the lower the exponential filter constant (i.e. closer to 0), the closer it will be to the previous filtered value and less based on the actual value.

DES is very similar to SES, except it includes a function to account for the trend that the data set follows. DES is represented by Equation 4.2 and Equation 4.3:

$$f_{new}(x_i) = [1-\alpha][f_{new}(x_{i-1}) + g(x_{i-1})] + \alpha f(x_i) \quad \text{Equation 4.2}$$

$$g(x_i) = [1-\gamma]g(x_{i-1}) + \gamma[f_{new}(x_i) - f_{new}(x_{i-1})] \quad \text{Equation 4.3}$$

where:

- $g(x_i)$ = equation that represents estimated trend at x-values (i.e. displacement)
- γ = a second exponential factor to estimate the trend that the data set follows; a value between 0 and 1

Equation 4.2 is the smoothing function, where it still has an exponential factor that behaves as a weighed factor between the previous actual value and involves summing the filtered valued and previous estimated trend value, much like SES. However, it differs from SES since it utilizes the previous value of the estimated trend and adjusts it with the previous value of the filtered value (NIST/SEMATECH, 2013). This estimated trend value, represented in Equation 4.3, also has its own exponential factor, where is applies to the difference between adjacent filtered values (i.e. most recent estimated trend of filtered data) (Performity LLC/Greg Stanley and Associates, n.d.), and the previously estimated trend.

Since the initial values of the data cannot be applied to these formulae since they depend on prior data, there are a few recommendations to set for them as follows in Equation 4.4 and Equation 4.5. For filtering calculations used in this research, the first condition in Equation 4.5 is used.

$$f_{new}(x_1) = f(x_1) \quad \text{Equation 4.4}$$

$$g(x_1) = \begin{cases} f(x_2) - f(x_1) \\ \frac{1}{3}\left[[f(x_2) - f(x_1)] + [f(x_3) - f(x_4)] + [f(x_4) - f(x_3)]\right] \\ \frac{f(x_n) - f(x_1)}{n-1} \end{cases} \quad \text{Equation 4.5}$$

where:

- n = total number of points

The values of α and γ can be assigned any value between and including, 0 to 1. The higher γ is, the more the filtered data set remains close to trend of the original data set. The smaller γ is, the further the filtered data is from the trend of the original data set. Regarding α, higher value it is, the closer the filtered data represents the shape of the original data. It is also an indication that it has more influence

(than γ) over the general shape and trend of the filtered data. The smaller α is, the smoother the function is as a result of the degree of filtering on the filtered data set.

4.1.2 Methodology & Application

In all the following calculations, DES filtering has been applied to the raw lab data for loading, since the load-displacement data sets follows a trend. The chosen values for the exponential factors are 0.1 for both α and γ. This means that there heavy filtering applied to the data, which may result in some slight misrepresentations around points in the data set that represent breakage in the specimen during testing. For example, Figure 4.1 and Figure 4.2 shows data for specimen M32 not being represented correctly due to heavy filtering of data. However, since the cracking load will not be a minima value, this has minimal effect on the analyses from utilizing the three different methods.

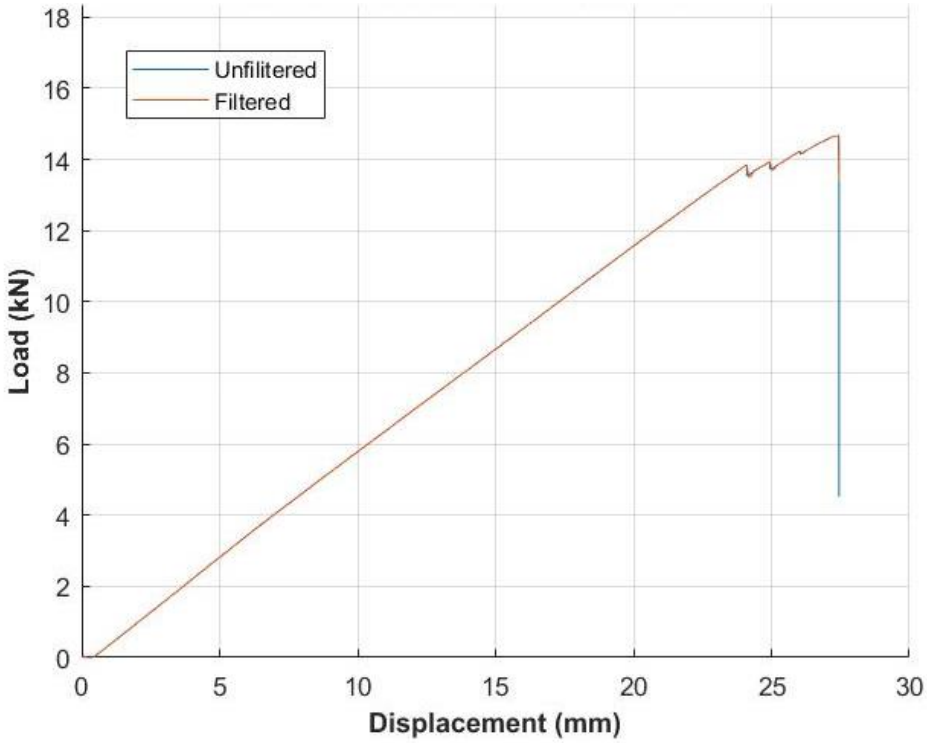

Figure 4.1: Load-Displacement Plot for Specimen M32

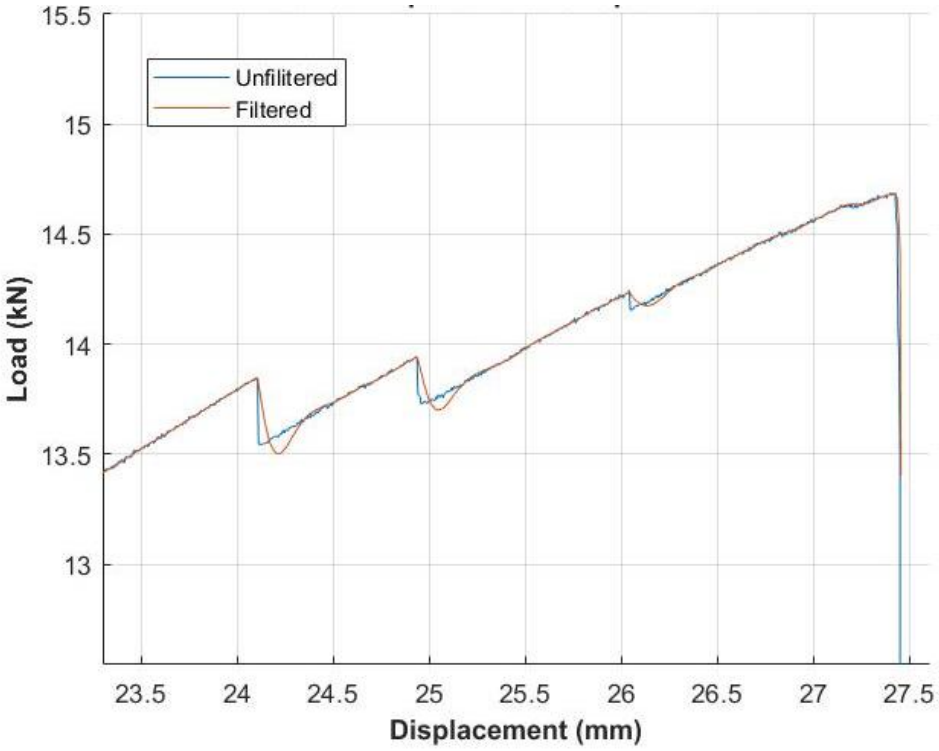

Figure 4.2: Zoomed in Load-displacement Plot for Specimen M32 with Heavy-Over-Filtered Data (α = 0.1)

It should be noted that for the filtering of the differentiated load data of the first and second order (from numerical differentiation, which is the third method outlined in this chapter), SES was used to filter the results, since the numerical differentiated data points have values that are approximately the same (i.e. constant value trend). The value of the alpha exponential factor used in both cases is 0.01. More details of the procedure for completing numerical differentiation and filtering will be discussed later in Section 4.4.

4.2 Visual Inspection

Generally, using visual inspection to determine the maximum loading point for the tensile stress is not recommended due to its high subjectivity. However, it is described herein and compared to computerized methods. It requires finding the region of where this maximum loading point can be identified, which is based on the viewer's judgement to choose an adequate region that represents the end segment of linear portion of the load-displacement graph. Once the region has been selected along the graph, the view is then zoomed in on that region, so that point can be visually identified. To conduct this method, data was imported into MATLAB, where the unfiltered loading was plotted against the recorded deflected data. From this plot, the cracking load was found by visual inspection. An example of this is shown in Figure 4.3, where it shows the load-deflection curve for a M15 specimen with the highlighted region being the estimated portion of the graph that best represents the ending of the linear trend. This highlight region is determined by visual inspection, since there is slight peak located here.

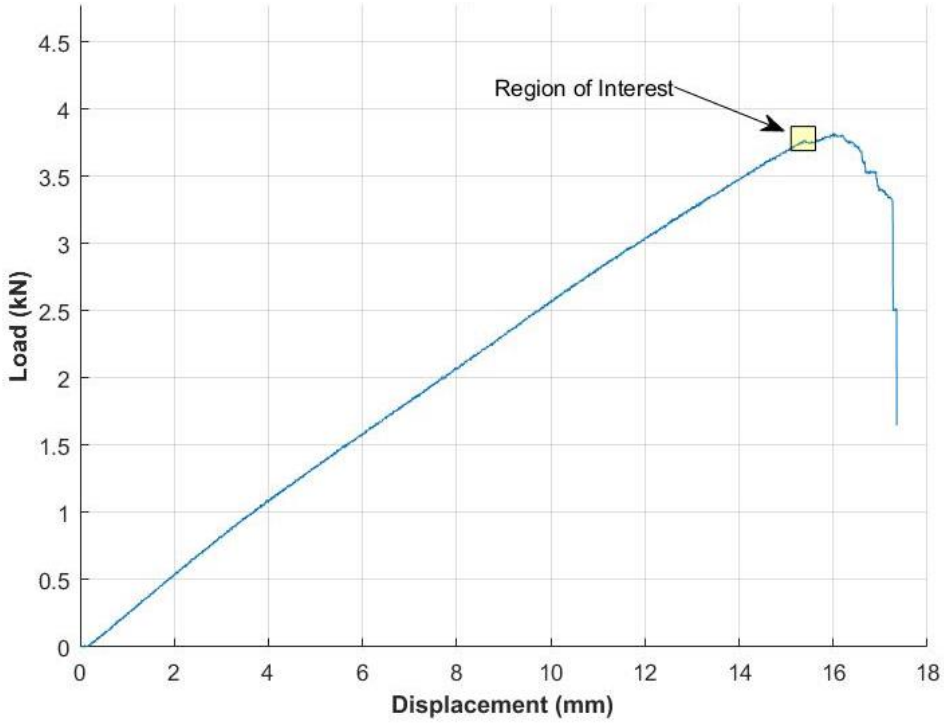

Figure 4.3: Maximum Load Region for Linear Portion of Load-Displacement Graph of M15 Specimen

The peak data point is selected and identified for this region. From its place in the data set, the corresponding point is found on the filtered load data, which can then be identified and included on the plot that MATLAB generates, as shown in Figure 4.4.

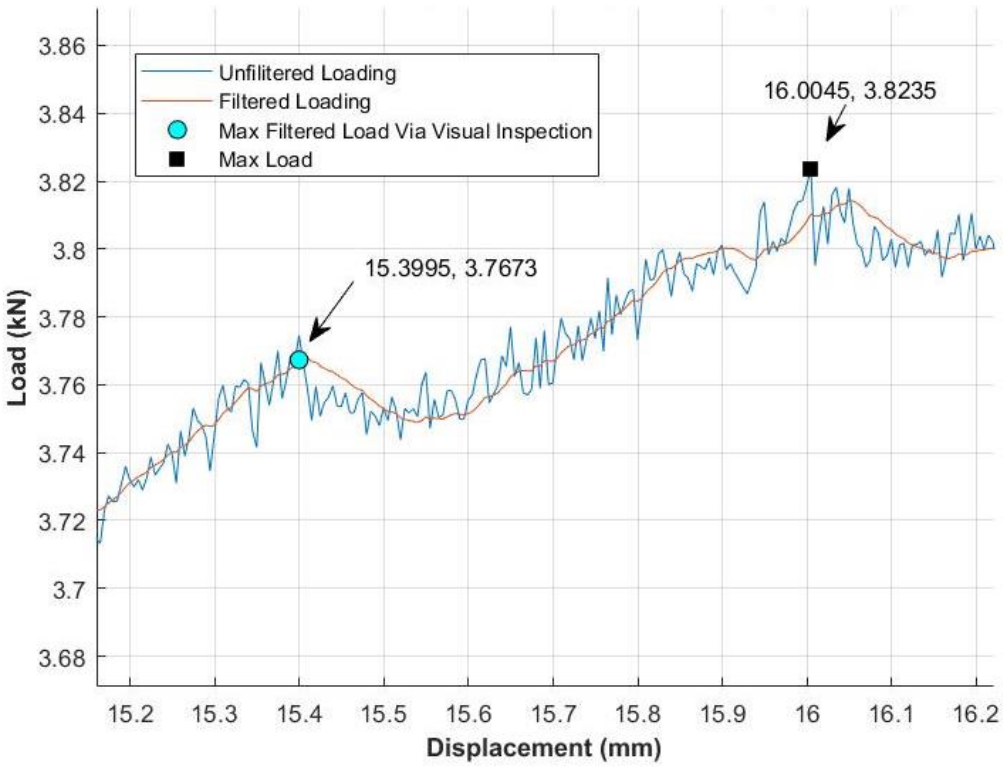

Figure 4.4: Zoomed-in View of Maximum Load Region for Linear Portion of Load-Displacement Graph of M15 Specimen

From Figure 4.4, it is evident that the lab data is noisy, since there are numerous localized peaks on the plot. Right before the specimen reaches a displacement of approximately 15.4 mm, there is a slight downward response present. This is an indication that the tensile fibre for this specimen has endured its maximum load just before it broke. The maximum load is taken at the point before this decline, as indicated by the cyan marker in Figure 4.4. This corresponds to a displacement of about 15.4 mm and loading of about 3.77 kN.

Figure 4.5 and Figure 4.6 are examples where the cracking load is easier to point out, using a M32 specimen, where the plots appears to be quite linear.

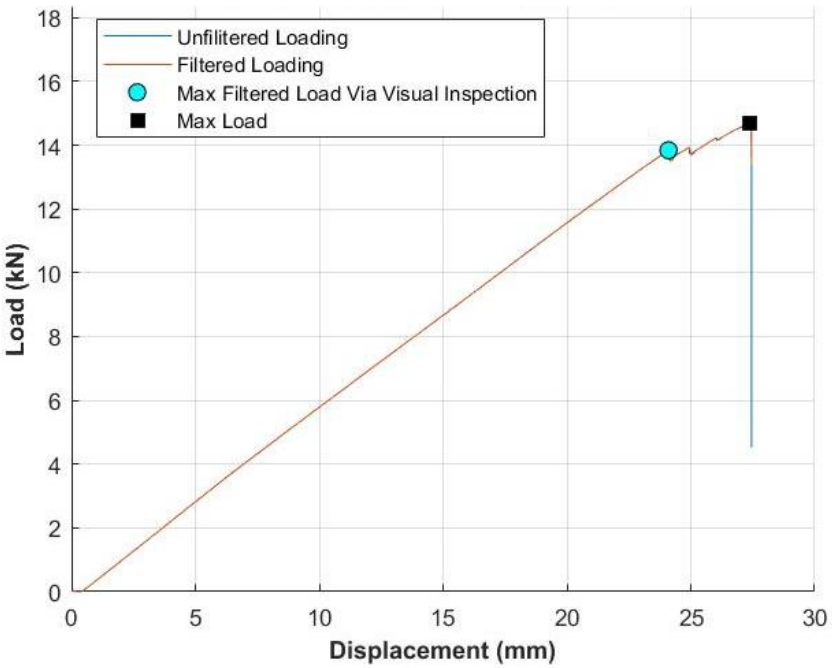

Figure 4.5: Load-Displacement Data for Specimen M32

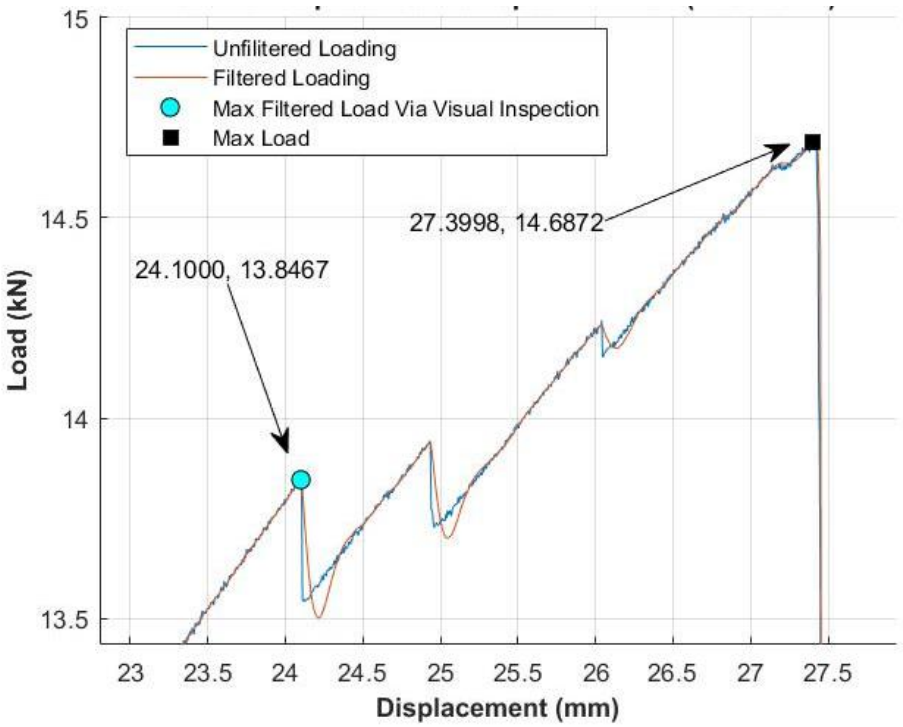

Figure 4.6: Zoomed-in View of Maximum Load Region for Linear Portion of Load-Displacement Graph of M32 Specimen

Figure 4.7 and Figure 4.8 shows an example of a lab data specimen where it is not as clear to identify where the cracking load is located be due to the plot's non-linear nature, using a M8 specimen.

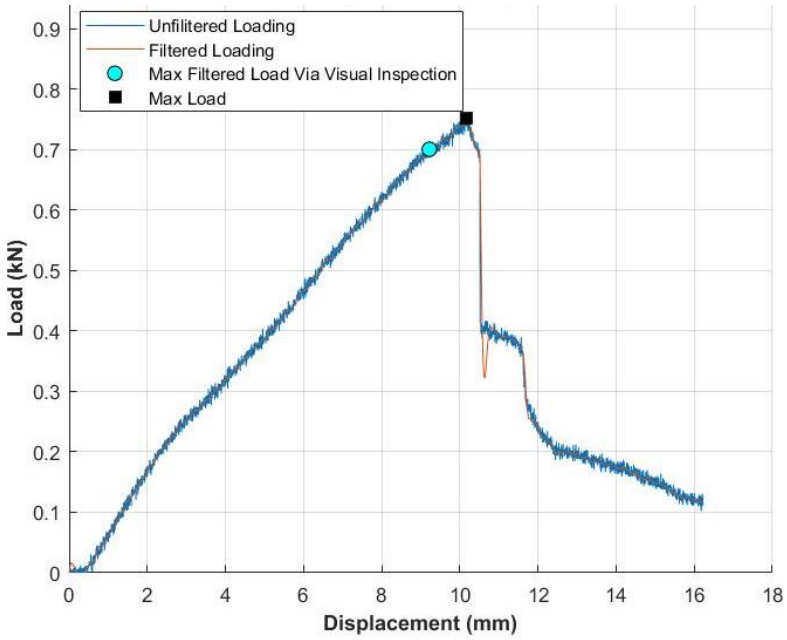

Figure 4.7: Load-Displacement Data for Specimen M8

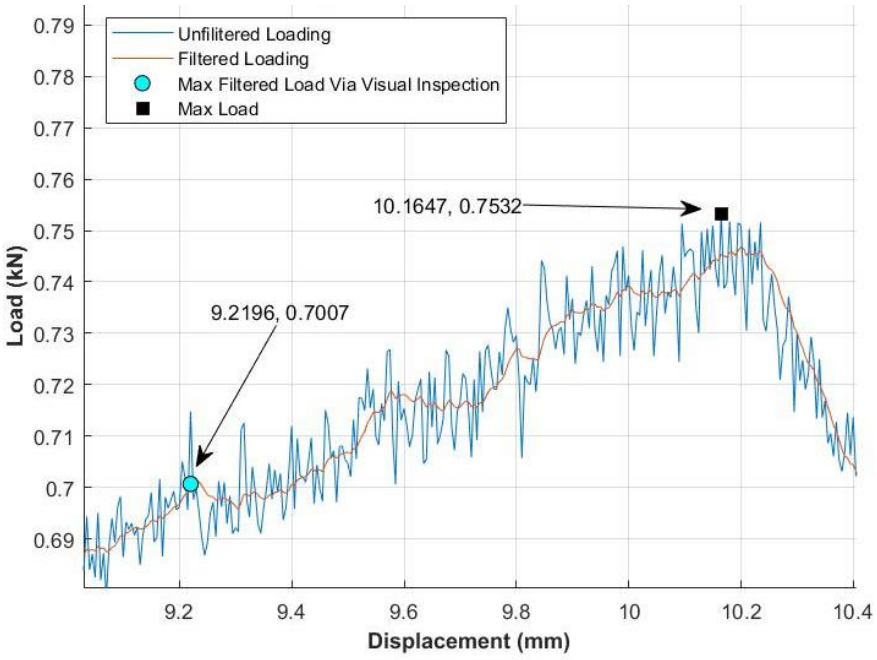

Figure 4.8: Zoomed-in View of Maximum Load Region for Linear Portion of Load-Displacement Graph of M8 Specimen

As shown in Figure 4.8, there are several potential cracking loads. Using visual inspection to identify the cracking load depends on the user's decision on which one to use point to use.

In conclusion, while identifying the region at the end of the linear segment of this load-displacement graph from Figure 4.6 was not difficult, other regions may not be as easily identifiable for other lab data. This process is simple and straight-forward, but it requires input and judgement from the viewer of the load-deflection graphs, especially in selecting the end-region of the linear trend. Since there are over 100 specimens for all flexure tests (3-point-bending & 4-point-bending), applying this for all data sets will be quite time-consuming and might not be objective. If all the load-displacement curves had minimal noise and it were obvious where the maximum load of the linear portion of the data set is, this method could have been utilized for efficiency in identifying the cracking loads.

4.3 Lines-of-Best-Fit

4.3.1 Background

The method of lines-of-best-fit uses lines that best represent the filtered lab data from specimen testing. Once lines have been formed, observations of their slopes relative to one another are made to identify the cracking load. If there is a significant reduction in slope between each of the line segments, the cracking load is identified as the point between the line segments.

4.3.2 Methodology & Application

A MATLAB script was created to go through the data set and to form a line-of-best-fit through a series of points. It does so by enabling the user to specify a minimum number of points required for the program to form a line of best fit, then looks at all the possible lines of best fit using every successive point afterward. The line with the highest coefficient of determination value, R^2, is chosen by the MATLAB program to be included as an "established trend line segment" representing the series of points for the rest of the analysis. The starting point of the next line will be the last point of the previous line segment.

There needs to be a minimum number of points to represent a line segment for this analysis in the MATLAB script. This is to ensure that the program correctly forms a line with multiple points, instead of establishing a line segment between two consecutive ones, since the lab data points can be made entirely of 2-pointed line segments. The chosen minimum number of points to use for this method is 100 points, because average of the R^2 values for established line segments were higher compared to lower minimum number of points (i.e. 10 points), after testing several values. An example comparison of using different number of minimum points to form a line will be made with Figures 4.10 to 4.12.

The MATLAB script forms a short list of potential cracking loads corresponding to the starting point of a line segment that meets all the specified conditions mentioned below. The desired cracking load is the first occurrence of a point that meets the conditions, since this will be the first sign that indicates the load-displacement plot exhibits a non-linear response. These conditions are as follows:

- The R^2 value for the targeted line segment must be higher than 0.9, indicating that the current line segment is correctly representing data points with high accuracy.
- The percent change must be lower (greater negative value) than -10% (since the slopes between the established line segments are decreasing between each other). Observation of the percent change between slopes can be completed since non-linear trends can still be represented by smaller lines-of-best-fit with different slopes, just at different slopes. Percent change was used to characterize this criterion since it is primarily used to compare an old value to a new one, as represented by Equation 4.6.

$$\% \, change = \left(\frac{(new - old)}{abs(old)} \right) \times 100\% \qquad \text{Equation 4.6}$$

- The starting point of a line-of-best-fit segment must be within 75% of the maximum loading of the data set. The reason for this is to limit the analysis to regions close to maximum loading
- Automatically considering the last point of a line-of-best-fit segment, if there is discontinuity (i.e. a break, with significant and sudden decrease in loading) in the data set. This enables the MATLAB script to neglect the above conditions for points that are after a break, so they are not considered. This condition specifically applies to the M32 plots (refer to Figure 4.5 and Figure 4.6). There are several sub-conditions that are used to represent this current condition, which include:
    - Identifying a discontinuity (i.e. break) in the data to be a load difference of 0.2 kN between two consecutive points. This value was determined via calibration using the filtered loading data for the M8, M15, and M32 specimens.
    - Using a R^2 value of 0.99 or higher for the current line segment (where the program is looking for the end point) in consideration. Since this condition was made for the data for M32 specimens where the trends are fairly linear, the strict threshold for the R^2 value is to ensure that the line segment follows the linear trend that already exists within the data set.
    - The percent change of the slope of the current line segment must be less than 10%.
    - The R^2 value for the next line segment must be less than 0.99, to indicate that there is a break or change in slope, since the new line segment uses the last point of the previous line segment, which should be before the discontinuity. Since this next line segment will have a severe change in trend, the, R^2 value will be less than 0.99.

The following example using lines-of-best-fit will be demonstrated below with two different analyses. Figure 4.9 shows the raw and filtered lab data for the M15 specimen. Figure 4.10 shows the lines-of-best-fit the program has formed using a minimum of 5 points to form a line-of-best-fit, which will be considered Analysis 1 for the purpose of this comparison. Figure 4.11 shows the lines-of-best-fit formed from using a minimum of 100 points per line segment, and will be identified as Analysis 2. In both Figures 4.10 and 4.11, the line segments have been labelled for ease of identification, and all potential cracking loads that the program has identified has been displayed. The first potential cracking load in this shortlist is the "chosen" cracking load the program decides, as represented by the larger data point marker. Tables 4.1 and 4.2 present the potential cracking loads identified by the respective analysis.

It should be noted that the vertical lines between each of the lines-of-best-fit are not line segments generated by the program; they are only shown to connect each of the lines-of-best-fit together. Also, the potential cracking loads identified on the graphs correspond to the filtered load, as opposed to the actual starting point of the line-of-best-fit to which it belongs.

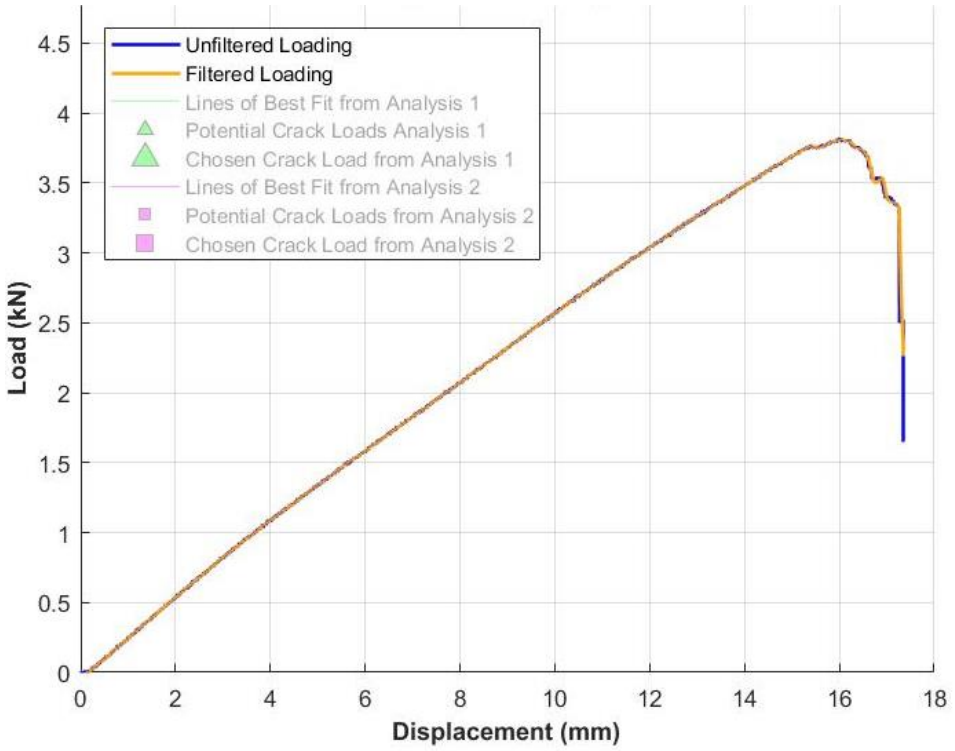

Figure 4.9: Load-Displacement Plot for M15 Specimen

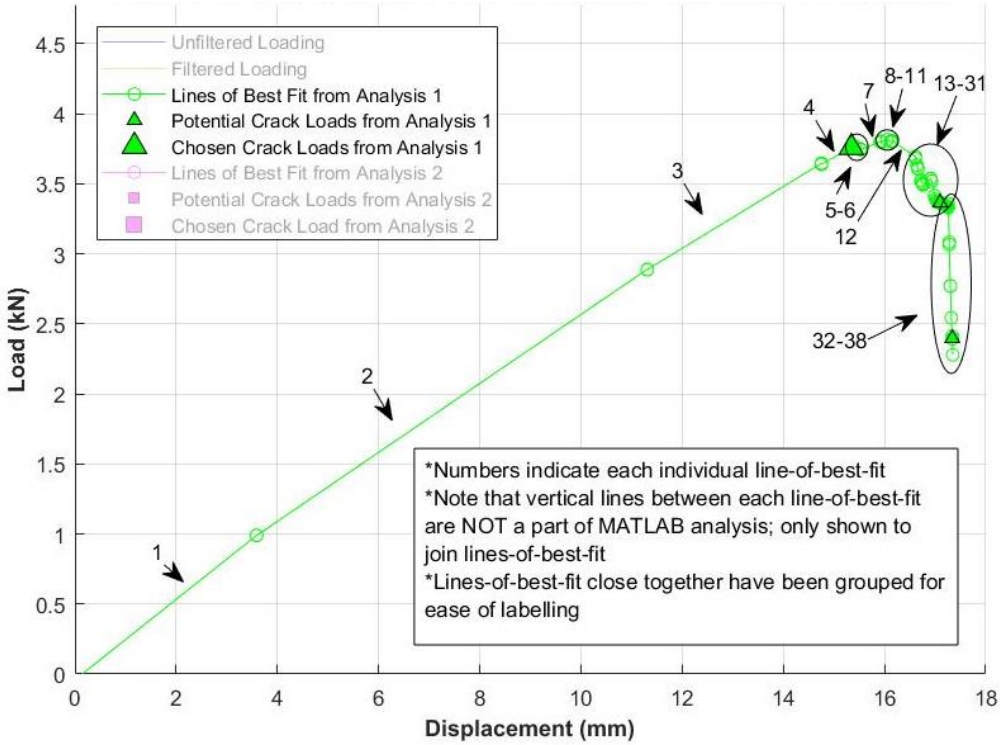

Figure 4.10: Load-Displacement Plot for M15 Specimen as Represented by Minimum of 5 Points per Lines-of-Best-Fit

Table 4.1: Potential Points-of-Interest & Accuracy from Analysis 1

Line Segment # with Potential Cracking Load (Starting Point)	Point #	Displacement (mm)	Filtered Load (kN)
5	3069	15.344	3.759
26	3420	17.100	3.365
38	3468	14.340	2.397
R^2 Average		**0.9548**	
R^2 Average (without last line segment)		**0.9578**	

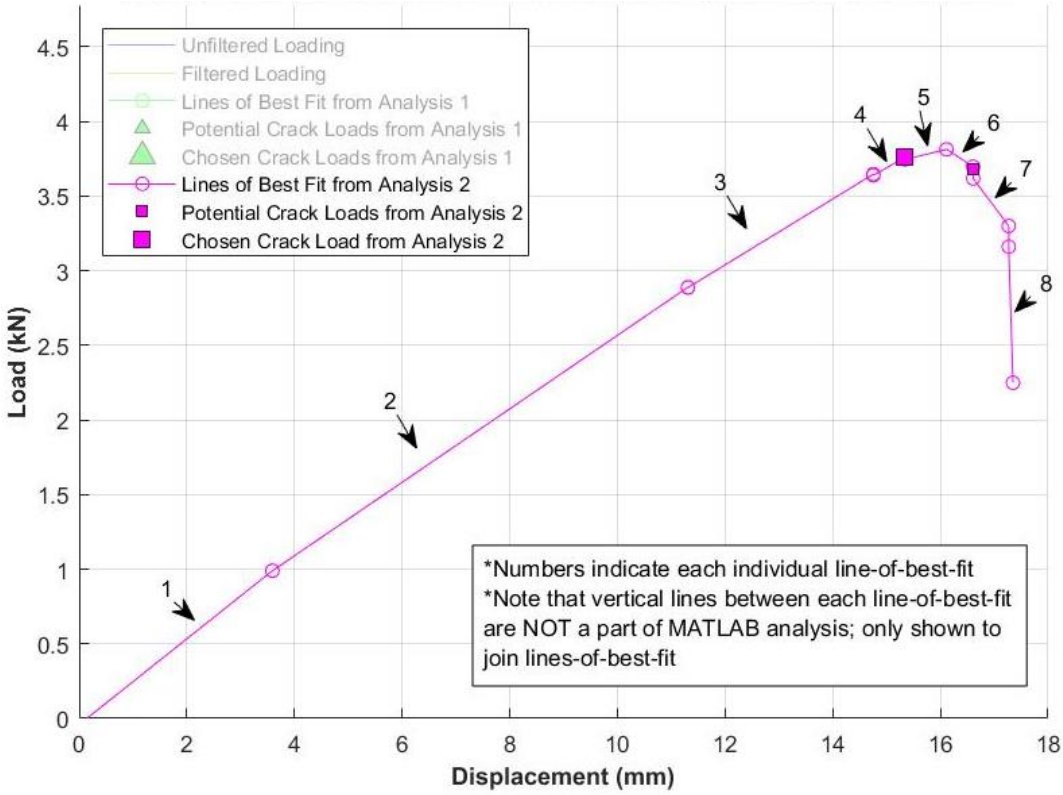

Figure 4.11: Load-Displacement Plot for M15 Specimen as Represented by Minimum of 5 Points per Lines-of-Best-Fit

Table 4.2: Potential Points-of-Interest & Accuracy from Analysis 2

Line Segment # with Potential Cracking load (Starting Point)	Point #	Displacement (mm)	Filtered Load (kN)
5	3069	15.344	3.759
7	3322	16.609	3.681
R^2 Average		**0.9565**	
R^2 Average (without last line segment)		**0.9531**	

To easily compare these analyses on how well they work, Figure 4.12 shows them plotted over top the raw and filtered lab data.

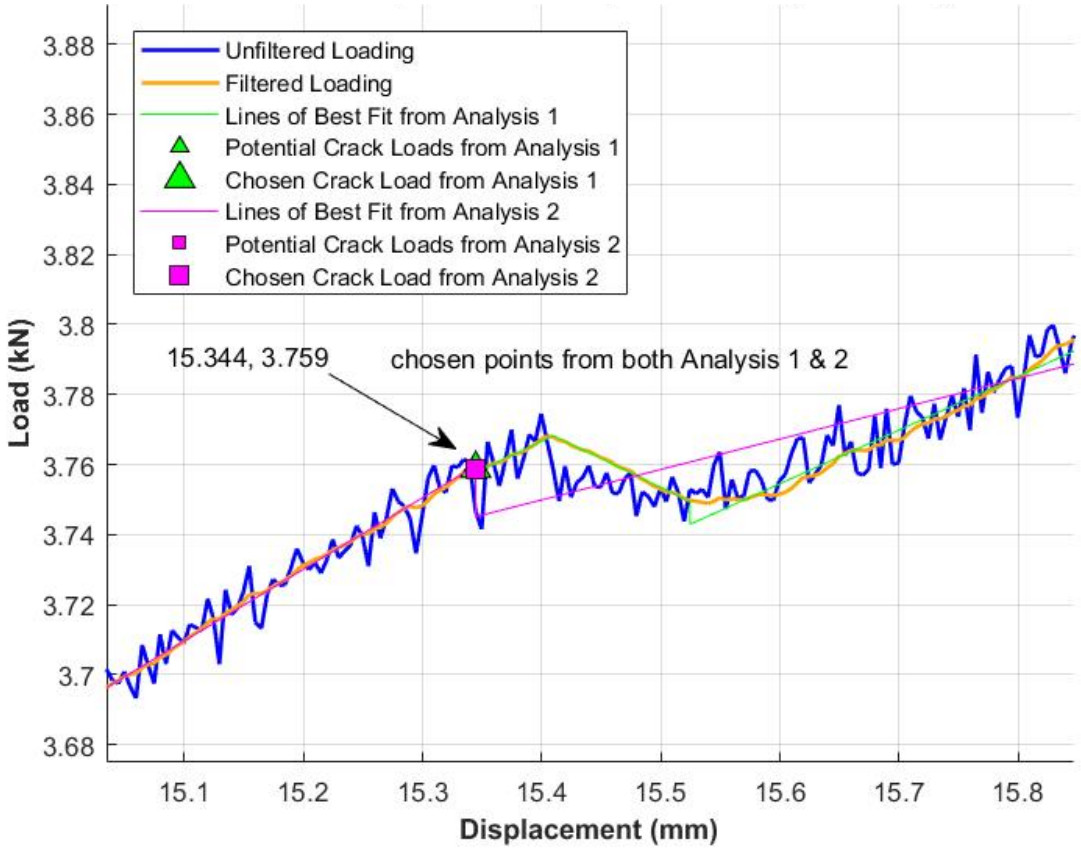

Figure 4.12: Zoomed-in Load-Displacement Plot for M15 Specimen with Lines-of-Best-Fit using 5 (Analysis 1) and 100 (Analysis 2) Data Points

From Figure 4.12, it is evident that the lines-of-best-fit from Analysis 1 (green line) follows filtered loading (orange line) more closely compared to Analysis 2 (magenta line), since the line segments are smaller. It should also be noted that the chosen cracking load points from Analysis 1 and 2 are the same, which is the first instance of a cracking load meeting all conditions, as specified above. This proves that both analyses are accurate, despite using different minimum number of points. The larger number of points required to form a line is a more accurate analysis to identify the cracking load correctly because it will return less potential cracking points due to requiring a greater number of points to form a line-of-best-fit. This is shown more clearly in Table 4.1 and Table 4.2, where Analysis 1 returned three potential cracking loads, versus Analysis 2 only outputting two.

The average R^2 value for all lines-of-best-fit is presented as well, to check the accuracy of each line. It is advised to consider the R^2 value of all the lines except for the last one, since the formation of the last line-of-best-fit is forced due to lack of remaining data points to form a line-of-best-fit as accurate as the previous segments (i.e. it is all dependent on what the last point was to form the second-to-last line of best fit used). It is evident that both analyses are quite accurate, as their R^2 values are very similar.

4.3.3 Conclusion

The method of using lines-of-best-fit is much better than visual inspection since it eliminates a significant amount of subjectivity but requires numerous computations. However, since the experimental data sets are large, these computations have a long processing time with the MATLAB script – especially with the M32 specimen data. There are still numerous decisions that need to be made in the formation of the MATLAB script to run this program, such as: changing the specified minimum number of points the programs uses to make lines-of-best-fit, altering the required value for R^2 for any corresponding conditions it pertains to, modifying the value of percent change the program looks for to identify a potential cracking load, and changing the value of load difference to indicate what the program considers to be a discontinuity in the data set.

4.4 Numerical Differentiation

4.4.1 Background

Numerical differentiation can be used to provide the values for the slope (from 1st derivative of the data set), as well as the rate of change of the slope and the behaviour of the trend which the data follows (2nd derivative of data set). A simple and efficient way to find potential cracking loads using numerical differentiation is by taking the 2nd derivative of the filtered data set, and finding all the results that are very close to zero. Values of the 2nd order derivative that are very close to zero indicate that the trend of the load-displacement data points is linear. The reason for this is that for linear trends, the first derivative should be a constant non-zero value, whereas the second derivative should be zero. Therefore, the cracking load should simply be last point which is very close to zero. To determine what "very close to zero" is, a threshold range needs to be defined, which is explained in the following Subsection 4.4.2.

4.4.2 Methodology & Application

A MATLAB program was made to complete the numerical differentiation. The raw data was filtered using DES (refer to the Section 4.1 that discusses the filtering methodology), and the first derivative of the filtered data was taken using MATLAB's gradient function. This gradient function applies forward difference approximation, backward difference approximation, and centre difference approximation, all represented by Equation 4.7, Equation 4.8, Equation 4.9 respectively. Forward difference approximation requires the input of two consecutive points, where the second point succeeds the first targeted point. Backward different approximation is the opposite, where two consecutive points are also required, but the second point precedes the first targeted point. Centre difference approximate requires two input points as well, but uses one-point immediately before and after the targeted point. Using all three of these equations for differentiation utilizes all points of a filtered data set.

$$f'(x_i) = \frac{f(x_{i+1}) - f(x_i)}{x_{i+1} - x_i} \qquad \textit{Equation 4.7}$$

$$f'(x_i) = \frac{f(x_i) - f(x_{i-1})}{x_i - x_{i-1}} \qquad \textit{Equation 4.8}$$

$$f'(x_i) = \frac{f(x_{i+1}) - f(x_{i-1})}{x_{i+1} - x_{i-1}} \qquad \textit{Equation 4.9}$$

Figure 4.13 and Figure 4.14 shows regular and zoomed view for slope of load (1st derivative)-displacement plot for filtered and unfiltered data for specimen M15.

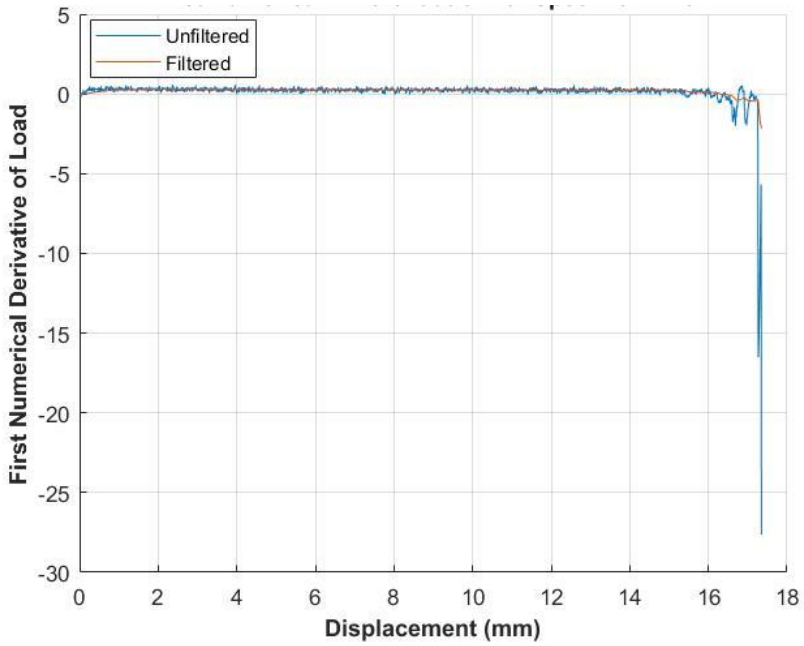

Figure 4.13: 1st Numerical Derivative of Load-Displacement Plot for M15 Specimen with Unfiltered and Filtered Data

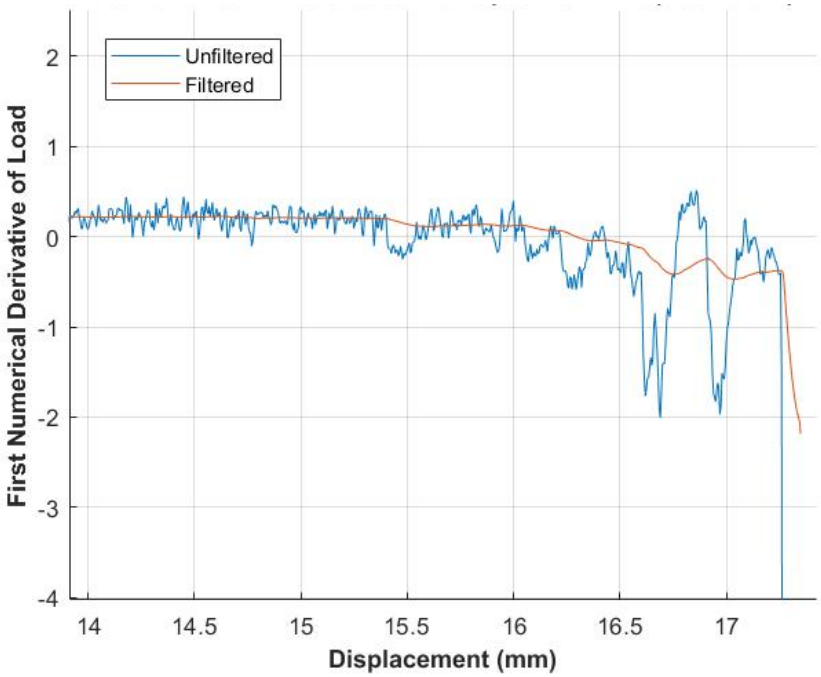

Figure 4.14: Zoomed-in View of 1st Numerical Derivative of Load-Displacement Plot for M15 specimen with Unfiltered and Filtered Data

Values toward end of data set for 1st derivative are very large negative values, which signify significant slope changes compared to the rest of the data set, since the specimen experiences complete failure of the cross section. Since the first numerical differentiation of the filtered loading data has much more of a constant trend as opposed to a linear, SES was used to filter these values to reduce the noise, so that the second numerical derivative can be completed with accuracy.

The program finds the cracking load within the second-order differentiated data set using a set of criteria, as follows:

- The cracking load must be within 75% of the maximum loading, so the analysis does not consider points of interest near the beginning of the data set.
- The cracking load must not be past a discontinuity (i.e. break) in the data with a load difference of 0.2 kN between two consecutive points. This value was determined via calibration using the filtered loading data for the M8, M15, and M32 specimens
- The cracking load must be within the threshold of ± 0.02 of the second order numerically differentiated filtered load data. The values ± 0.02 were determined by calibration using specimens M8, M15, and M32.

Figure 4.15 & Figure 4.16 show all the points of the unfiltered and filtered change of slope of load (2nd derivative) that are within the specified threshold.

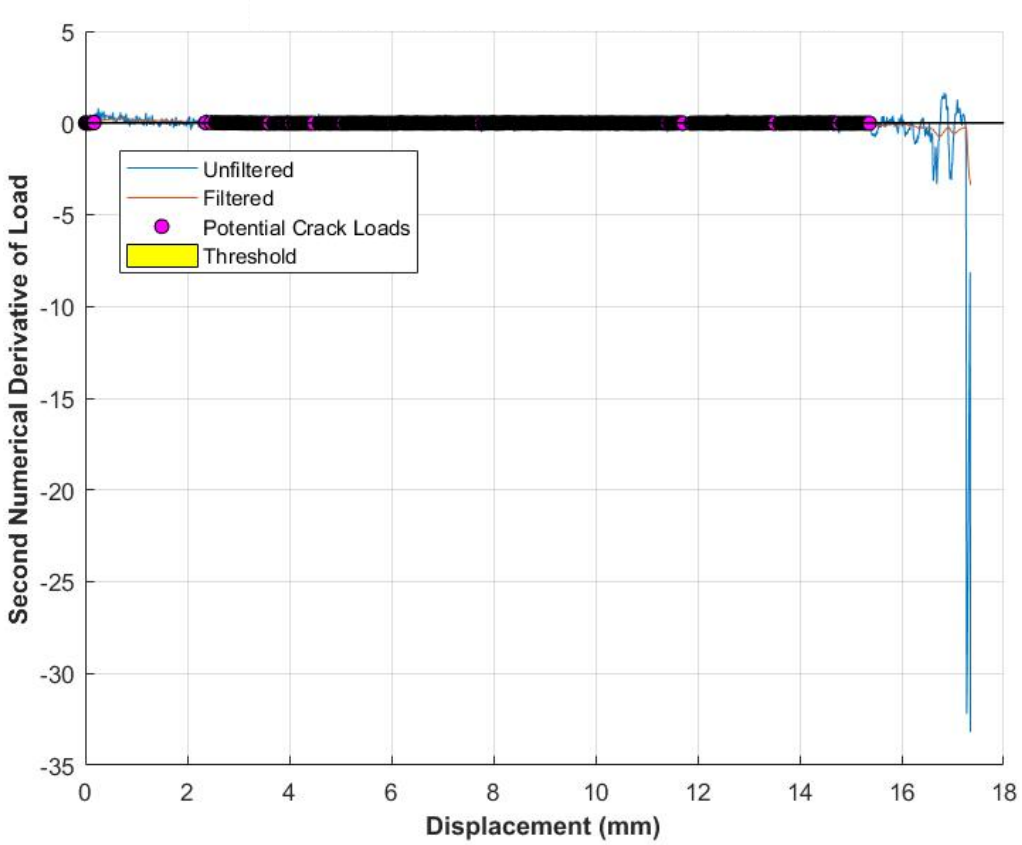

Figure 4.15: 2nd Numerical Derivative of Load-Displacement Plot for M15 Specimen with Unfiltered and Filtered Data and Threshold of Potential Cracking Loads

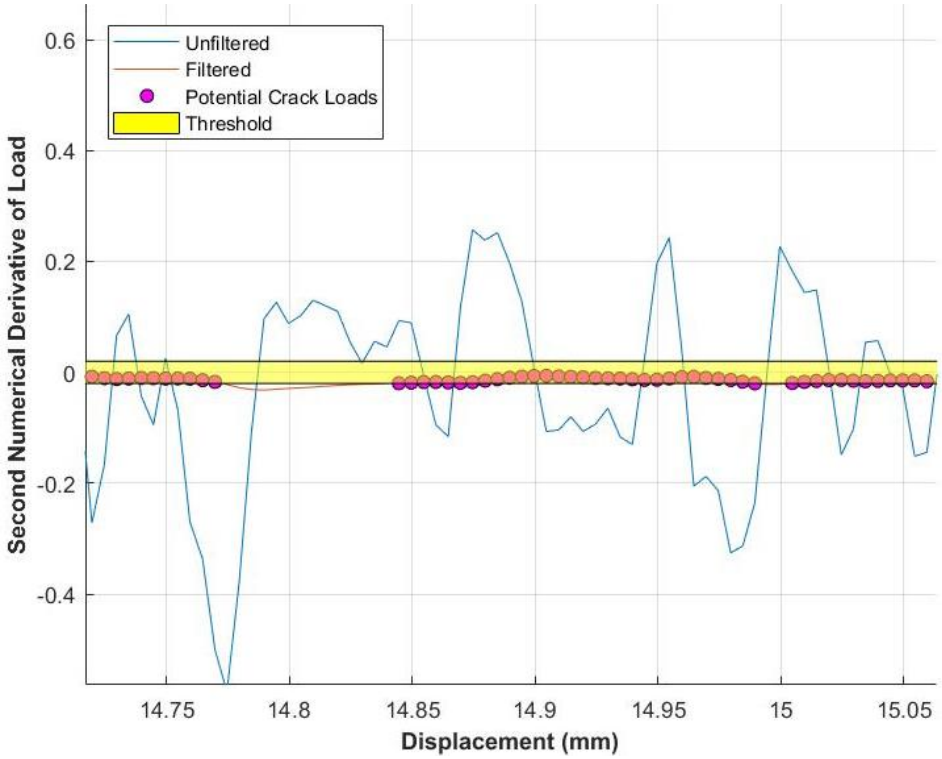

Figure 4.16: Zoomed-in View of 2nd Numerical Derivative of Load-Displacement Plot for M15 Specimen with Unfiltered and Filtered Data and Threshold of Potential Cracking Loads

In Figure 4.16, there are multiple "gaps" in the data that do not lie within the threshold, as indicated by the yellow zone between -0.02 and +0.02. This means that there are changes in the curvature of the filtered load-displacement plot.

The cracking load is normally the first occurrence of the last point of a series of points inside the threshold, which corresponds to the last point of a linear portion of the in the load-displacement plot before an abrupt slope change. However, since this is test data, the first occurrence of a series of points inside the threshold (i.e. before a gap that is present in the threshold) does not necessarily correlate to the correct cracking load. To avoid the MATLAB program from returning an incorrect cracking load, a set of conditions were made as MATLAB checks the various series of points within the threshold. The program checks if there are a specific amount of points behind the last point in the series (i.e. checking that there are 10 points behind a potential cracking load that fall within the threshold) that are within the specified range behind the last point in the series (i.e. in a 20-point range/window behind potential cracking load) to ensure that the data trend has an abrupt change in. The reason that the number of required points preceding potential cracking load and the search-range are not the same value is to account for some points trend that are outside of the threshold zone (i.e. "gaps" in the series of data points that are within the threshold).

Determination of number of points preceding the cracking load, and search-range of preceding points involved using trial-and-error to see what the best combination of the calibrated conditions is. The more preceding points that are involved in these conditions validates that the MATLAB script is returning a cracking load that follows a linear trend, while also making this check more stringent since it requires a bigger region of the data set to fall within the threshold. Having a bigger "tolerance" between the

required preceding points and the search-range for counting the number of preceding points makes it easier for the program to pass this check. Alternatively, seeking to minimize this “tolerance” between the required number of preceding points and search-range for this check could potentially be another way to validate that the required points involved in the check does exhibit a linear-behaviour. However, it was found that the search-range will be minimized as well; therefore, effectively minimizing the required number of points that MATLAB script seeks for this check. The chosen number of preceding points that MATLAB looks for behind a potential points-of-interest are 150, and the range to look for behind this point is 175, allowing for a 25-data point “tolerance” in the check. These values were found after calibrating and analyzing results for M8, M15, and M32 specimens.

Figure 4.17 and Figure 4.18 show the chosen cracking load on the 2nd derivative plot for the M15 specimen, as indicated by a red square marker.

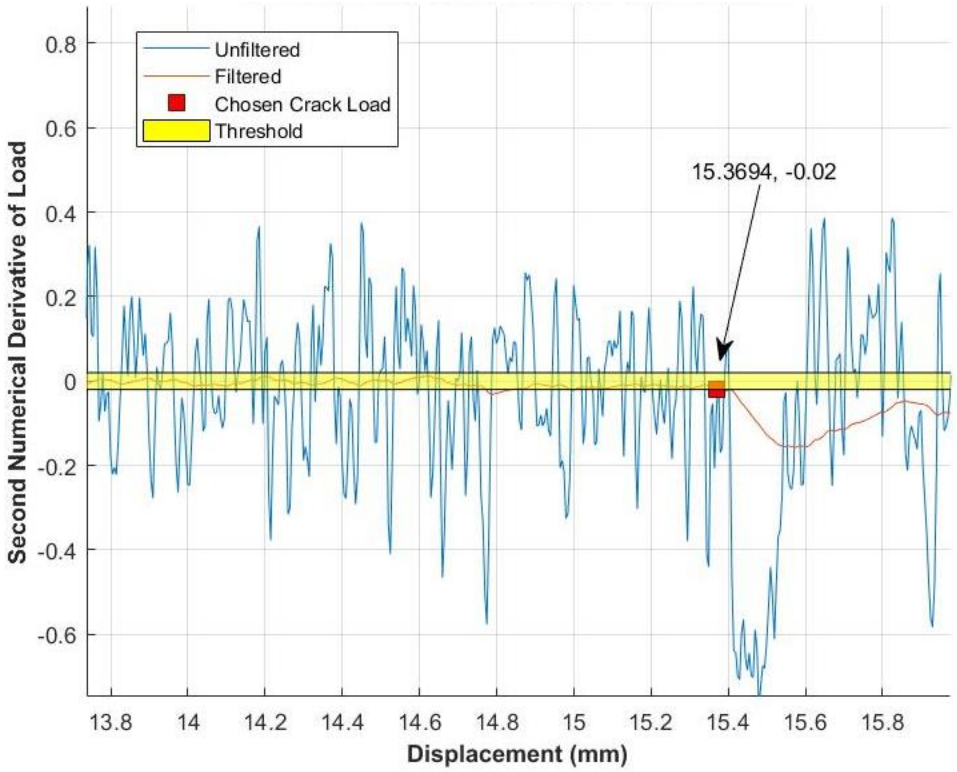

Figure 4.17: 2nd Numerical Derivative of Load-Displacement Plot for M15 Specimen with Chosen Cracking Load

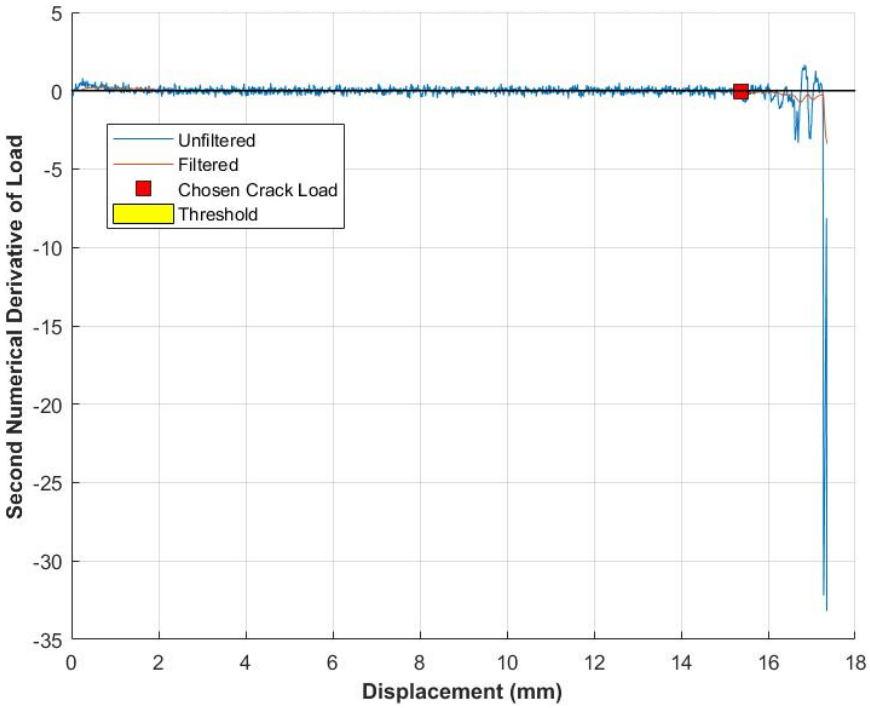

Figure 4.18: Zoomed-in view of 2nd Numerical Derivative of Load-Displacement Plot for M15 Specimen with Chosen Cracking Load

Similarly, and Figure 4.20 show the chosen cracking load on the load-displacement graph.

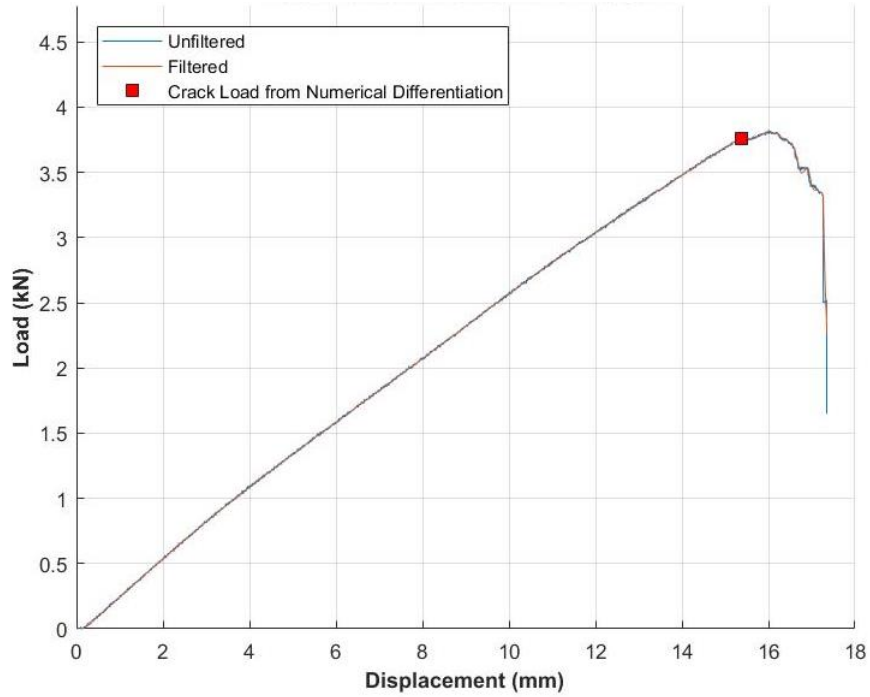

Figure 4.19: Chosen Cracking Load on Load-Displacement Plot for M15 Specimen

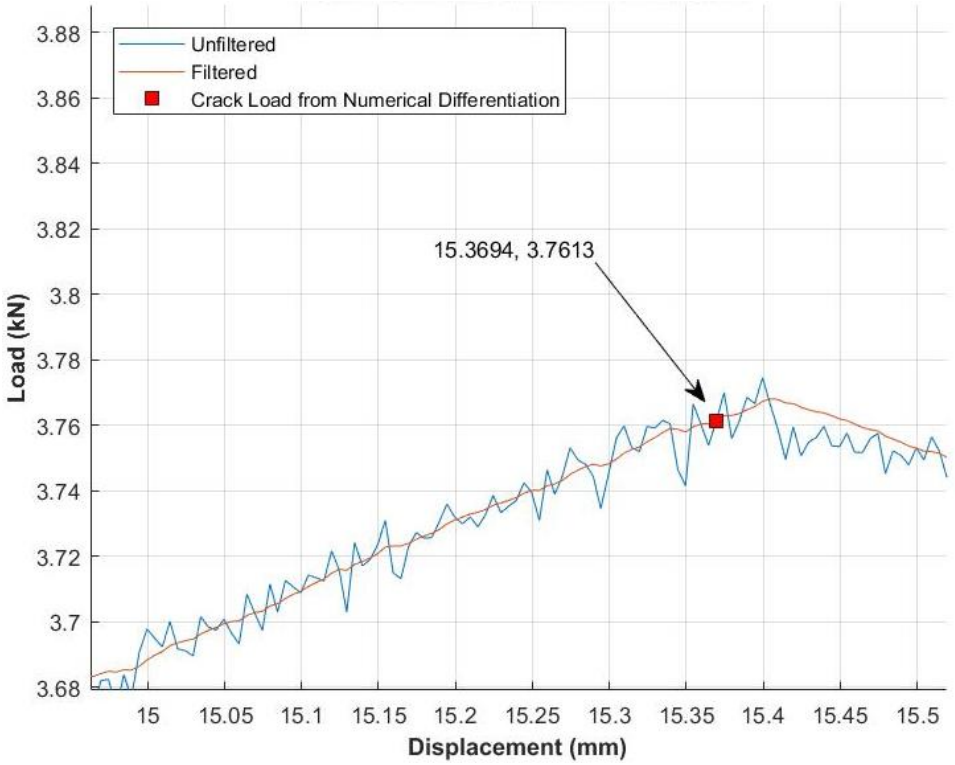

Figure 4.20: Zoomed-in View of Chosen Cracking Load on Load-Displacement Plot for M15 Specimen

4.4.3 Conclusion

This method is quite compact and efficient, as it does not require a lot of computations. There are also less decisions that need to be made, reducing the subjectivity and bias of this method. The only decisions that needed to be made are determining the threshold limit and figuring out the number of required preceding points and the search-range for these points, that need to be considered to determine the cracking load. The threshold limit could be narrower, but risks making the targeted cracking load lower than it actually is. The number of preceding points to the cracking load and the search-range for these points could be altered to provide a potentially more accurate result, but should be noted that poor selection of these values for the condition leads to an improper check that MATLAB completes for this method. Both of these alterations can be completed via trial and error.

4.5 Conclusion & Chosen Method of Determining the Cracking load on Methods

4.5.1 Summary

To compare the results of all the methods with the three bar sizes of M8, M15, and M32, Figure 4.21 and Figure 4.22 display all the chosen points of interest laid out over top the load-displacement data for specimen M15. The points of interest for each method are summarized in Table 4.3.

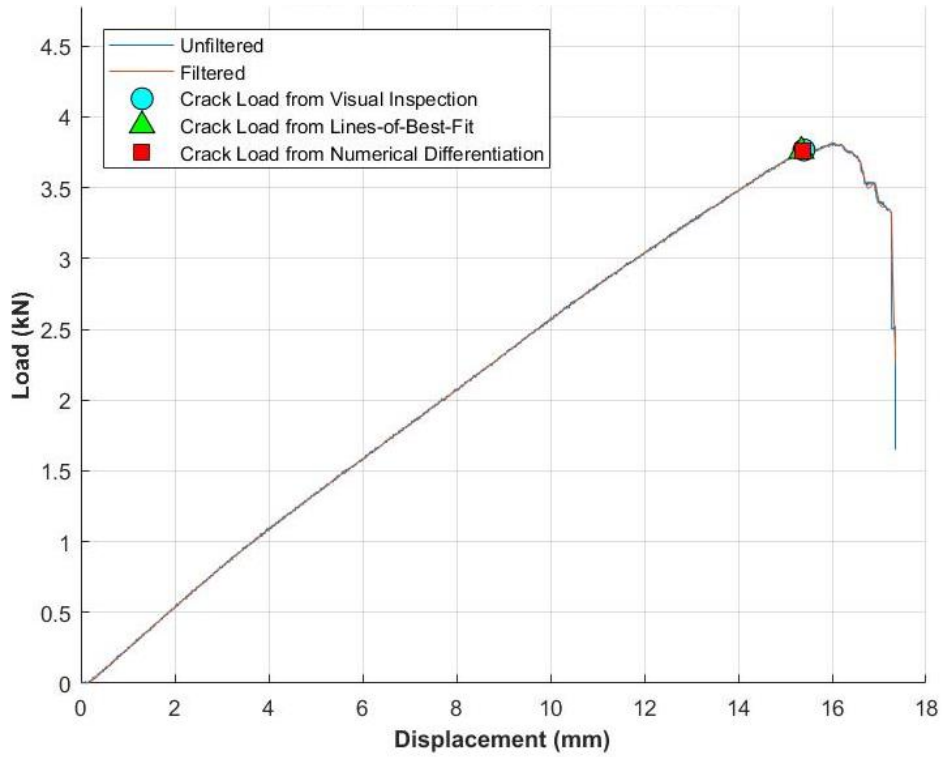

Figure 4.21: Load-Displacement Plot of M15 Specimen with Cracking Loads from All Methods

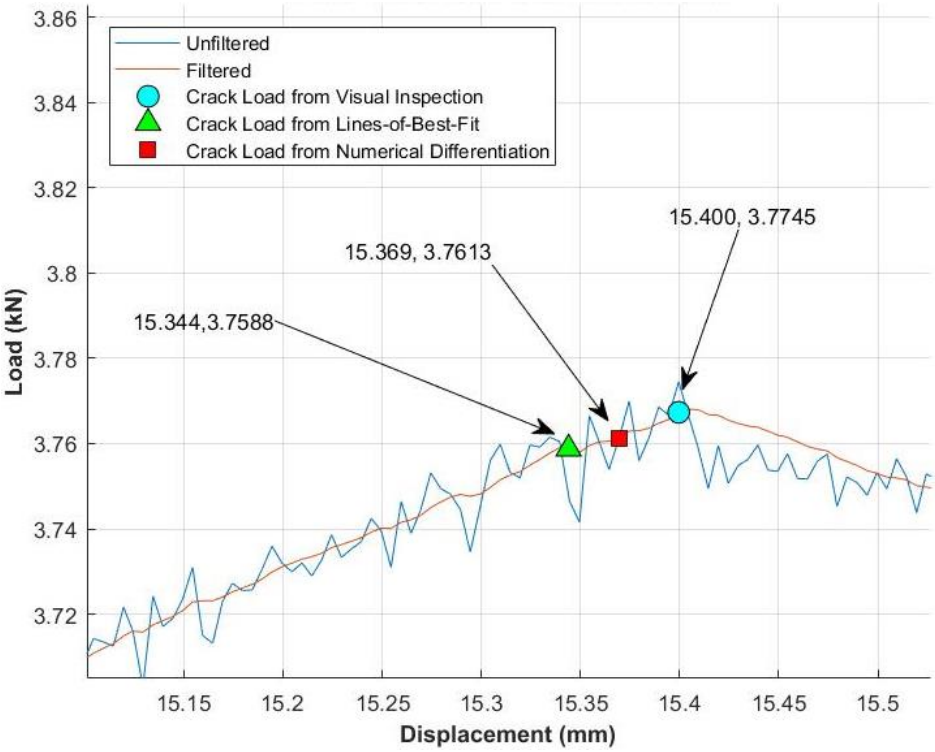

Figure 4.22: Zoomed-in View of Load-Displacement plot of M15 Specimen with Cracking Loads from All Methods

Table 4.3: Summary and Comparison for Cracking Loads from All Methods for M15 Specimens

Point #	Method Used	Displacement (mm)	Filtered Load (kN)
3080	Visual Inspection	15.400	3.767
3069	Lines-of-Best-Fit	15.344	3.759
3074	Numerical Differentiation	15.369	3.761

From Figure 4.22 and Table 4.3, it is evident that all three methods yield similar results. The cracking load from the lines-of-best-fit method is the lowest cracking-point. This is based on how the MATLAB script broke up the data for the analysis – which does not mean this method is the most restrictive. The cracking load from visual inspection returns the highest cracking load, indicating that this method is the possibly the least restrictive. The chosen cracking load from numerical differentiation is in between the two other chosen points-of-interest from the other alternatives.

For other specimens, these analyses do not return the exact same patterns between chosen points-of-interest, but are close to each other. Data for the M8 specimen is examined and shown in Figure 4.23 & Figure 4.24 and Table 4.4; data for the M32 specimen is shown in Figure 4.25 & Figure 4.26 and Table 4.5.

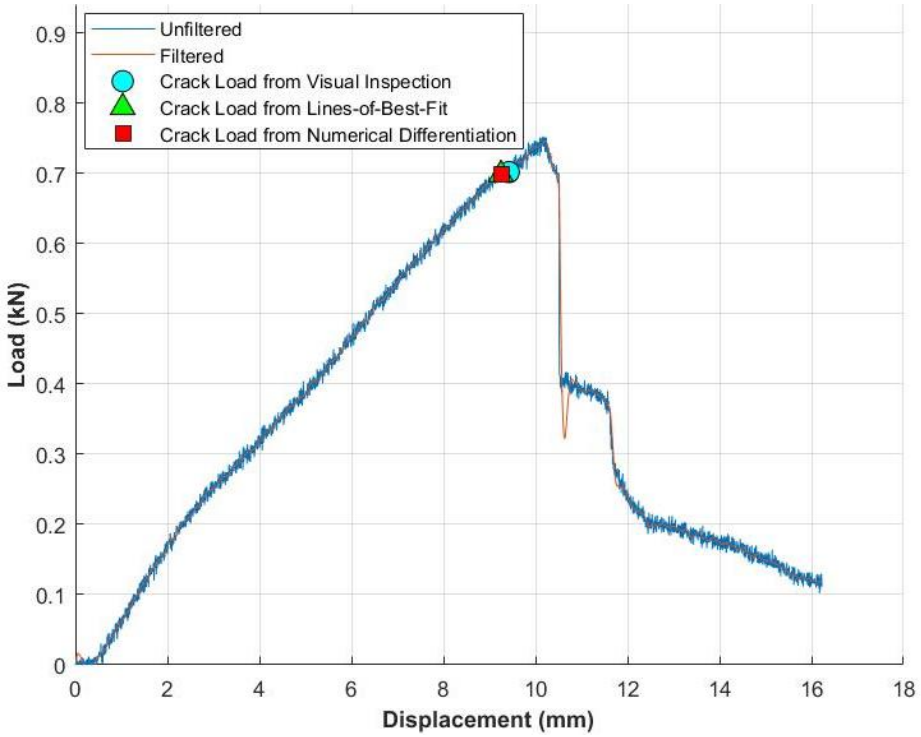

Figure 4.23: Load-Displacement Plot of M8 Specimen with Cracking Loads from All Methods

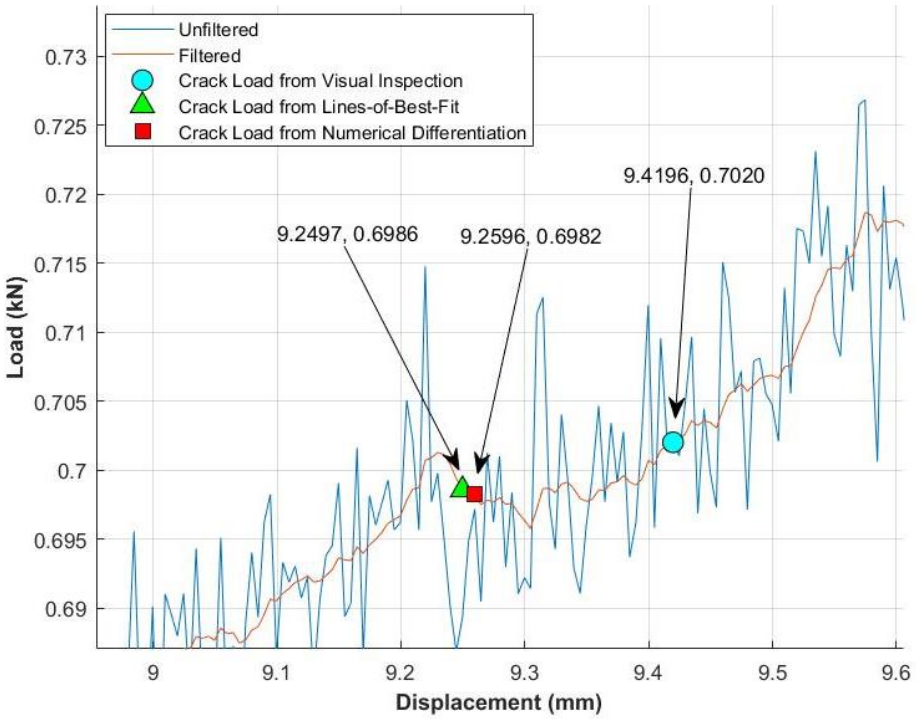

Figure 4.24: Zoomed-in View of Load-Displacement Plot of M8 Specimen with Cracking Loads from All Methods

Table 4.4: Summary and Comparison for Cracking Loads from All Methods for M8 Specimen

Point #	Method Used	Displacement (mm)	Filtered Load (kN)
1884	Visual Inspection	9.420	0.702
1850	Lines-of-Best-Fit	9.250	0.699
1852	Numerical Differentiation	9.260	0.688

The important characteristic to note between Figure 4.23 and Figure 4.21 is that the M8 load-displacement plot follows a linear-behaviour to a lesser extent compared to the M15 plot. Despite this, the results from M15 outlined in Figure 4.21 & Figure 4.22 and Table 4.3, the results for M8 in Figure 4.23 & Figure 4.24 and Table 4.4 exhibit similar patterns. The cracking load chosen from lines-of-best-fit is the “earliest” of the three options, and inversely, the cracking load chosen from visual inspection is the “latest”. The chosen cracking load from the numerical differentiation is between the two other chosen points-of-interest, but it is evident in Figure 4.24 that this point is very close to the chosen point from the lines-of-best-fit method. This indicates that both these methods are accurate and reliable on successfully identifying the true cracking load.

For a final comparison of these methods, Figure 4.25 & Figure 4.26 and Table 4.5 displays the results for M32 specimen, which also has a different load-displacement behaviour compared to M8 and M15.

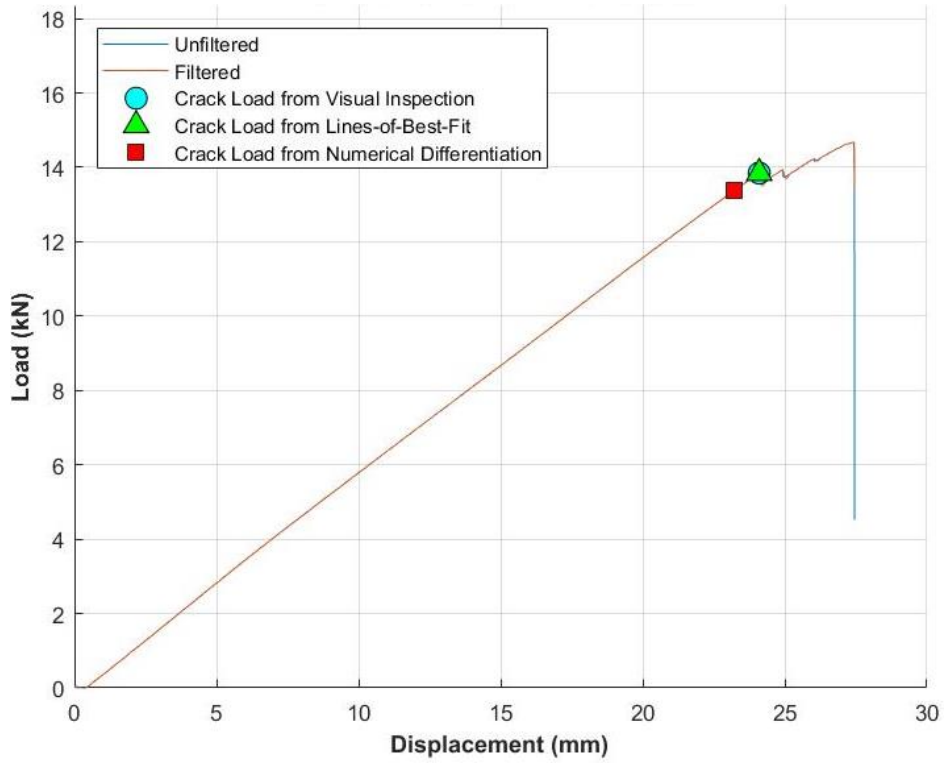

Figure 4.25: Load-Displacement Plot of Specimen M32 with Cracking Loads from All Methods

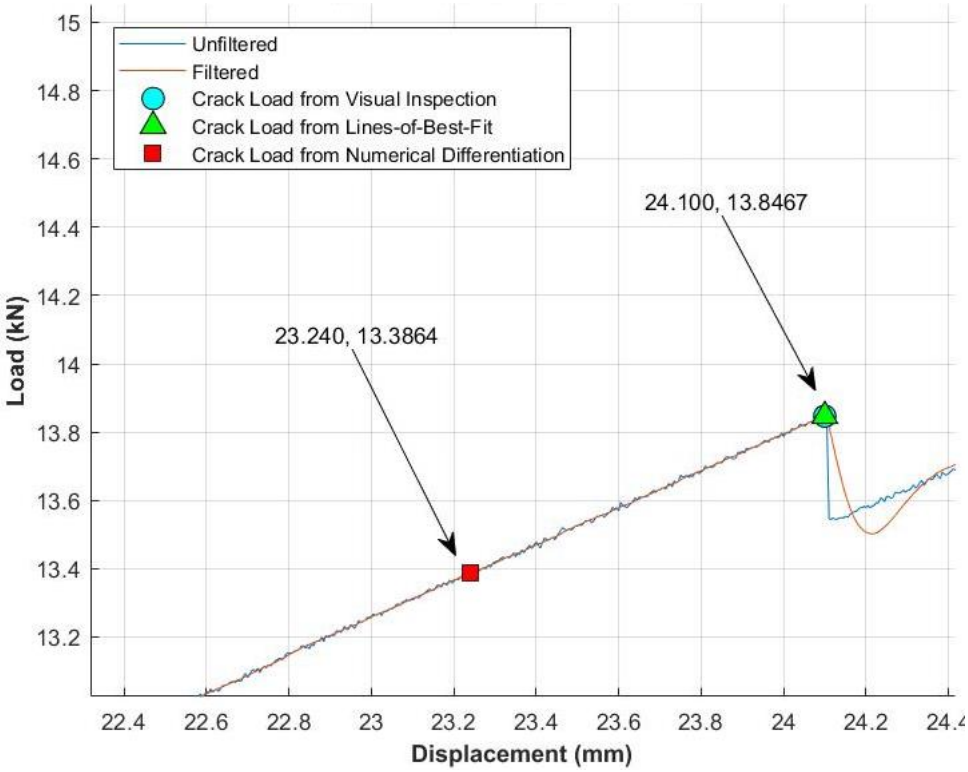

Figure 4.26: Zoomed-in View of Load-Displacement Plot of Specimen M32 with Cracking Loads from All Methods

Table 4.5: Summary and Comparison for Cracking Loads from All Methods for M32 Specimen

Point #	Method Used	Displacement (mm)	Filtered Load (kN)
4820	Visual Inspection	24.100	13.847
4820	Lines-of-Best-Fit	24.100	13.847
4637	Numerical Differentiation	23.240	13.386

The behaviour of the M32 specimen as it is being loaded is quite linear, as seen in Figure 4.25. From using visual inspection and the MATLAB program for lines-of-best fit methods, the identification of the same point was made, which is the first notable peak before there is a break in the specimen (identified by the drop in load right after this point). This shows the feasibility and effectiveness of using both methods for a graph that clearly exhibits a linear behaviour. However, with the numerical differentiation method, it identified an "earlier" point, which matches the results from the M8 and M15 specimens, and shown in Figure 4.24 and Figure 4.22, respectively. Since the lab data for this M32 specimen is not truly linear, this "earlier" point should not be disregarded. It should also be noted that these points are still close together, as noted on Figure 4.25, proving the usefulness for all methods.

4.5.2 Chosen Method of Determining the Cracking load on Methods

The chosen method to determine the cracking load is numerical differentiation, after consideration of filtering the data and using the three different test methods. This method requires the least amount of bias and decision making and was the easiest method to automate, compared to the other two methods. While visual inspection is quick to complete for one test, it is very time consuming to do for all tests, and is highly subjective. The lines-of-best-fit technique requires several inputs from the user to implement and is not the easiest to automate, relative to numerical differentiation. Table 4.6 shows the chosen cracking load for each of the specimens used in this chapter. Appendix B indicates the critical load that was used for each individual specimen.

Table 4.6: Chosen Cracking Load for Each GFRP Size

GFRP Size	Displacement (mm)	Filtered Load (kN)
M8	9.260	0.688
M15	15.369	3.761
M32	23.240	13.386

Chapter 5 - Calculation of Tensile Strength from Rupture Modulus

In this section, the relationships and equations that are used to correlate the rupture modulus from the flexural test, to the tensile strength of the GFRP bars are provided and discussed.

5.1 Bi-Moduli Behaviour

The proposed testing method is based on ASTM D4476-14 (ASTM Committee D20, 2014). However, the relationships and procedures derived in this standard assume that the GFRP material exhibits a uni-modular elastic behaviour in both tension and compression.

Research has shown that, while GFRP can be modelled in this manner, there is a small error in strength because of the difference in its tensile and compressive elastic moduli (Medri, 1982; Jones, 1978; Jones, 1977). Researchers have shown that the ratio of tensile to compressive elastic moduli is typically 1.2 to 1.25 (Jones, 1978; Jones, 1977), although exact values will vary due to the variations of batches during manufacturing. One possible explanation for this is due to the differences in the fibre stiffness versus the matrix stiffness where if the fibres tend to contact each other or buckle, it results in a more or less stiff composite, respectively (Jones, 1977). Figure 5.1 shows the differences between using a single elastic modulus to dual elastic moduli compared to the actual stress-strain behaviour of GFRP (Jones, 1977).

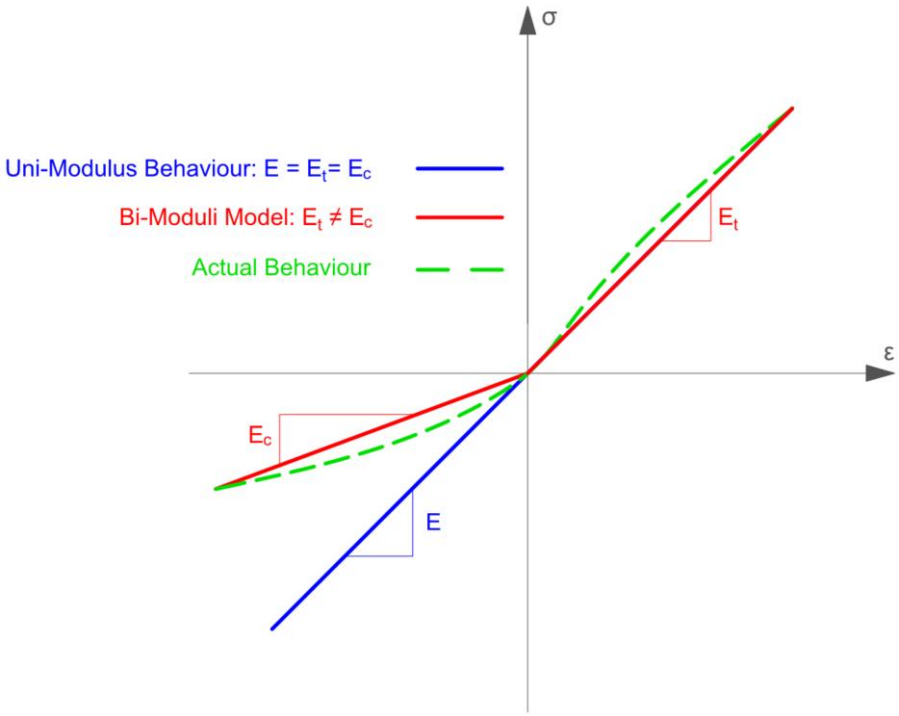

Figure 5.1:Comparison of Uni and Bi-Moduli vs. Actual Stress-Strain Behaviour of GFRP

When using the incorrect model to analyze the stress-strain behaviour of GFRP, the rupture modulus found from the load-displacement data of a flexural test can be inaccurately calculated, ending in skewed results. Due to this, new relationships need to be derived to incorporate the bi-moduli behaviour of the GFRP material.

5.2 Flexural/Bending Moment Relationships

5.2.1 Determining Rupture Modulus

The basis for equations and relationships shown is the bi-elastic moduli behaviour. The equilibrium of forces and moments is used along with stress-strain relationships to describe the stresses that develop along the specimen's cross section as it is being bent, represented as Equations 5.1 to 5.3 respectively (Beer et al., 2012). Figure 5.2 provides a graphical representation of the stress and strain distributions along the cross-section of a typical specimen in bending (Arczewska, 2017).

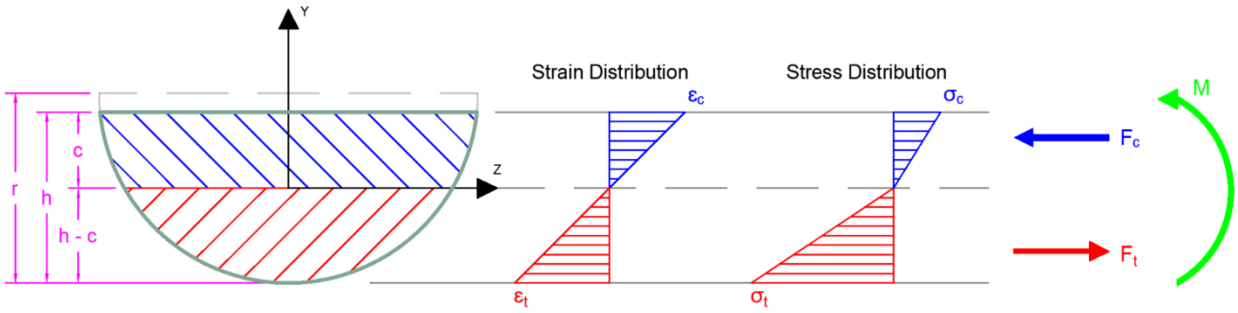

Figure 5.2: Distribution of Bending Stresses and Strains of GFRP Material Along Height of Cross-section

$$\int_{A_t} \sigma_t \, dA + \int_{A_c} \sigma_c \, dA = 0 \qquad \textit{Equation 5.1}$$

$$\int_{A_t} -y\sigma_t \, dA + \int_{A_c} -y\sigma_c \, dA = M \qquad \textit{Equation 5.2}$$

$$\frac{\sigma_t}{E_t(h\text{-}c)} = \frac{\sigma_c}{E_c c} \qquad \textit{Equation 5.3}$$

where:

- σ_t and σ_c refers to the peak tensile and compressive stress produced from bending, respectively
- A_t and A_c refers to tensile and compressive areas from bending, respectively
- E_t and E_c refer to the tensile and compressive elastic modulus, respectively
- M represents the bending moment
- h represents the height/depth of the specimen
- c represents the location of the neutral axis from the top surface of the specimen

It should be noted from Figure 5.2 that because of the different elastic moduli, the slope of the stress distribution are different for tension and compression, and is appropriately adjusted in Equation 5.3. The height, h, the radius r, and the length of the specimen must be measured prior to testing. It should be mentioned that slight variations in measurements for the height, radius and length of the specimens were noted, have minimal effects on the results since the differences are a few millimetres apart. The moment produced by the cracking load in Equation 5.2 (expressed as M) is calculated based on the test results and procedures outlined in Chapter 4.

The elastic moduli should be measured via the appropriate testing (i.e. direct tension or compression), or obtained from the GFRP manufacturer, if available. However, it is more common for a GFRP

manufacturer to provide only the tensile elastic modulus for the material, which is insufficient on its own for the completion of these calculations. More importantly, it is noted that the two different elastic moduli can be represented as a ratio $\frac{E_t}{E_c}$, signifying that the distinct values of the tensile and compressive stiffness do not need to be known explicitly. To represent this in the calculations, Equation 5.3 is simplified into Equation 5.4, where n represents the ratio $n = \frac{E_t}{E_c}$.

$$\frac{\sigma_t}{n(h\text{-}c)} = \frac{\sigma_c}{c} \qquad \textit{Equation 5.4}$$

The importance of Equation 5.4 is that this relationship is dependent on the ratio between the tensile and compressive elastic moduli of the GFRP material, as opposed to their actual values. Based on Jones' research (1977; 1978), this ratio be assumed to be between 1.2 and 1.25, if the tensile and compressive elastic moduli are both unavailable.

This leaves three parameters that remain unknown for Equations 5.1 to 5.3, which are: flexural-tensile stress, the flexural-compressive stress, and the location of the neutral axis. Solving for these unknowns is not a trivial task because the cross section is similar, but not exact, to a semi-circular shape (for each specimen, exact dimensions must be used) and the calculations need to include the bi-modular material behaviour. The equilibrium of forces and sum of moment relationships both require the use of the cross-sectional area in order to calculate forces and moments. Similarly, with calculating other areas of typical cross sections, an integral equation was developed, but required use of a software to calculate the result, as hand calculations are difficult to complete.

From here onward, the tensile stress due to bending will be referred to as the "rupture modulus" σ_r, to avoid confusion with the overall tensile capacity, σ_t, of the GFRP bar. Appendix G contains derivations and descriptions on how the unknowns were solved with Equations 5.1 to 5.3.

5.2.2 Rupture Modulus from Testing

Due to the lack of information on the compressive stiffness of the tested GFRP material and for the purposes of this research work, the correlation calculations have been carried out using two different n values. Using the extremes of the range provided from Jones' research (1977; 1978), $n = 1.25$ and 1.2 are used for Method 1 and Method 2 of the calculations, respectively.

Provided for reference, the tensile elastic moduli provided from the manufacturer and calculated from tensile testing (refer to Section 3.5.2, using tensile elastic moduli calculated from excluding outliers) are provided in Table 5.1. The manufacturer's specification sheets for M13, M15 and M20 bars are found in Appendix A. It should be noted that not all the bars from the M13 specimens are of the same batch. The M15 and M20 bars are of the same batch, and its properties should be accurately represented by their corresponding specification sheet.

Table 5.1: Tensile Elastic Modulus (MPa) of GFRP Specimens

Source	M8	M13	M15	M20	M25	M32
Fiberline Specification Sheets	-	62220	65300	60900	-	-
Uniaxial Direct Tensile Testing	80874.23	76847.85	74968.56	-	-	-

From Table 5.1, there Is a notable difference in the tensile stiffness between the specification sheets and the direct tensile testing for the M13 and M15 specimens, where it is apparent they are stiffer from the tensile testing conducted within this research. Reasons for this could be the result of having specimens from various batches for the M13 and M15 bars that were specifically used in the direct tensile testing, or discrepancies in stiffness measuring methods. It should be noted that these values are not directly used in the calculations in this work. The value used is the tensile to compressive elastic moduli ratio $n = \frac{E_t}{E_c}$.

From here onward, important calculated parameters will indicate a percentage difference between the values, just to provide an ease of comparing the calculations between the two methods, although this is not a primary objective of this research. The percent difference calculation used is as follows in Equation 5.5.

$$\%\ Difference = \frac{|Value\ 1 - Value\ 2|}{\left|\frac{Value\ 1 + Value\ 2}{2}\right|} \times 100\% \qquad \textit{Equation 5.5}$$

Due to the complexity of calculating the areas of the compressive and tensile regions of the cross-section by integration, and the computations to find the rupture modulus, MATLAB was used for this process. The results from these computations provides three values of the tensile stress due to bending (rupture modulus), compressive stress due to bending, and the location of the neutral axis. A full derivation of these equations is found in Appendix G.

Table 5.2 shows a summary of the averages of all the specimens' dimensions and physical properties, along with the computed values for the rupture modulus, the compressive stress, and the location of the neutral axis, based on their corresponding test method. Appendix B displays the full list of specimens, their properties, and the results from the calculations.

Table 5.2: Summary of Specimen Variable Averages of 10 Specimens

Average for Specimen Variables		Type of Bending Test	M8	M13	M15	M20	M25	M32
Measure Values (Pre-Testing and During Testing)	Radius, r (mm)	3-Point	4	6.5	8	10	12.5	16
		4-Point	4	6.5	8	10	12.5	16
	Height, h (mm)	3-Point	3.40	6.02	7.58	9.56	11.87	15.42
		4-Point	3.38	5.98	7.51	9.53	11.74	15.39
	Unsupported Length, L (mm)	3-Point	80	130	160	200	250	320
		4-Point	80	130	160	200	250	320
	Critical Point Load per Loading nose, F_{cr} (N)	3-Point	877.13	2392.35	3790.41	5732.04	8387.49	13390.03
		4-Point	655.92	1707.41	2521.89	3852.06	6045.81	9673.32
Post-Testing Calculations - Method 1 (n =1.25)	Location of Neutral Axis, c (mm)	3-Point	1.51	2.69	3.40	4.29	5.32	6.92
		4-Point	1.50	2.67	3.36	4.27	5.26	6.90
	Rupture (Tensile) Stress, σ_r (MPa)	3-Point	2228.23	1887.74	1875.55	1774.18	1688.31	1591.46
		4-Point	2257.15	1828.35	1697.76	1604.67	1664.93	1539.79
		% Difference	*1.29%*	*3.20%*	*9.95%*	*10.03%*	*1.39%*	*3.30%*
	Compressive Stress, σ_c (MPa)	3-Point	1428.17	1221.73	1217.20	1152.89	1096.10	1035.15
		4-Point	1445.76	1182.21	1100.62	1042.19	1079.41	1001.29
	Maximum Bending Moment, M (Nmm)	3-Point	1.75E+04	7.78E+04	1.52E+05	2.87E+05	5.24E+05	1.07E+06
		4-Point	1.75E+04	7.40E+04	1.35E+05	2.57E+05	5.04E+05	1.03E+06
Post-Testing Calculations - Method 2 (n = 1.2)	Location of Neutral Axis, c (mm)	3-Point	1.50	2.67	3.36	4.24	5.26	6.84
		4-Point	1.49	2.64	3.33	4.22	5.20	6.83
	Rupture (Tensile) Stress, σ_r (MPa)	3-Point	2203.25	1866.51	1854.44	1754.25	1669.28	1573.53
		4-Point	2231.84	1807.80	1678.67	1586.65	1646.21	1522.40
		% Difference	*1.29%*	*3.20%*	*9.95%*	*10.03%*	*1.39%*	*3.30%*
	Compressive Stress, σ_c (MPa)	3-Point	1443.57	1234.89	1230.30	1165.27	1107.92	1046.29
		4-Point	1461.35	1194.94	1112.46	1053.37	1091.02	1012.09
	Maximum Bending Moment, M (Nmm)	3-Point	1.75E+04	7.78E+04	1.52E+05	2.87E+05	5.24E+05	1.07E+06
		4-Point	1.75E+04	7.40E+04	1.35E+05	2.57E+05	5.04E+05	1.03E+06
% Difference Between Rupture Modulus from Method 1 & 2		*3-Point*	*1.13%*	*1.13%*	*1.13%*	*1.13%*	*1.13%*	*1.13%*
		4-Point	*1.13%*	*1.13%*	*1.13%*	*1.13%*	*1.13%*	*1.14%*

Upon examining the rupture modulus from Table 5.2, it is evident that as the GFRP bar size increases, the rupture modulus generally decreases, as expected from a material with a brittle nature. This phenomenon can be explained by the larger number of flaws introduced in a higher volume (size) of GFRP material.

Another observation that is made about the rupture moduli between the flexural tests are that the average rupture modulus is smaller for all sizes, except for the M8 specimens, for the 4-point bending values relative to the 3-point bending values. This is because the 4-point bending test subjects more of the material to maximum bending moment, engaging more flaws in the material, which ultimately lowers the rupture modulus. Despite this difference, the rupture moduli between the 3-point to 4-point bending tests are quite close to each other, having about 10% difference (4% difference for all specimens, excluding M15 and M20 specimens). Such a small percentage difference between the

rupture moduli is a possible indication that a 4-point bending test is not much more effective compared to a 3-point bending test, when correlating the rupture modulus of a GFRP to its tensile strength. However, using a 4-point bending test will yield a more conservative (lower) correlated tensile value, which will be further explained in this chapter.

Lastly, the percentage difference between the rupture moduli using Method 1 and 2 are very small, less than 2%, and are almost the same for both the 3-point and 4-point bending tests. It shows that the difference in the n (which is the $\frac{E_t}{E_c}$ ratio) between Method 1 and 2 show little impact on the results. This is also reflected in yielding the same percentage differences between the 3-point and 4-point bending tests in Method 1 and 2.

5.3 Relationship between Rupture Modulus and Tensile Strength of GFRP using Weibull's "Weakest Link" Model

The rupture modulus of the GFRP specimens is larger than its direct tensile strength. This is a known phenomenon for brittle materials since the strength is related to the number of flaws in the tested cross section.

Studies completed by Griffith (1921) and Irwin (1956) suggest that the size of the crack, or flaw in the material, will end up dictating the strength of the material. This is represented in form of Equation 5.6.

$$\sigma_f = \frac{K_{IC}}{y_d\sqrt{c_{flaw}}} \qquad \textit{Equation 5.6}$$

where:

- σ_f represents the fracture stress
- K_{IC} represents the resistance to crack propagation
- y_d represents the stress density factor (dimensionless)
- c_{flaw} depends on the flaw size

Flaws are introduced into a material based on the impurities in the material's composition and size due to processing; they are distributed throughout the material's volume. From Equation 5.6, it is evident that the larger the flaw size, the lesser the fracture stress is for the material. Therefore, the material's strength depends on its "weakest link", and will be described as the Weibull's "Weakest Link" model.

5.3.1 Utilizing Weibull's "Weakest Link" Model to Describing Tensile Stress of GFRP

This model statistically describes the failure distribution of brittle materials, such as like GFRP, where the strength of the material is determined by the size of flaws in the specimen (Quinn & Quinn, 2010; Weil & Daniel, 1964). The probability of brittle material failure is described in the form of Equation 5.7.

$$P_f = 1 - \exp\left(-\int_V \left(\frac{\sigma - \sigma_u}{\sigma_o}\right)^m dV\right) \qquad \textit{Equation 5.7}$$

where:

- V represents the volume of the specimen
- σ represents the applied stress

- σ_u represents the zero-strength stress where no failure occurs below this stress (which is usually assumed to be zero)
- σ_o is the normalizing factor (the scale parameter)
- m is the Weibull modulus (shape parameter), which will be discussed in Section 5.3.2

Since GFRP is a brittle material, this model is applied to determine its tensile strength in both the flexural and tensile tests, enabling the correlation of the tensile strength of a GFRP specimen to its rupture modulus. To reflect this, Equation 5.7 is altered to describe the failure of the GFRP specimens in flexure and direct tension as shown in Equation 5.8 and Equation 5.9 respectively, where σ_t refers to tensile stress from direct tension (which will be equated to the tensile strength of GFRP material, σ_t) and σ_b refers to tensile stress from bending (which will be equated to rupture modulus, σ_r).

$$P_f = 1 - \exp\left(-\int_V \left(\frac{\sigma_t - \sigma_u}{\sigma_o}\right)^m dV_t\right) \qquad \text{Equation 5.8}$$

$$P_f = 1 - \exp\left(-\int_V \left(\frac{\sigma_b - \sigma_u}{\sigma_o}\right)^m dV_b\right) \qquad \text{Equation 5.9}$$

where:

- V_t and V_b represent the volume experiencing tensile stress in exerted from uniaxial direct tensile test and a flexural test, respectively. Figure 5.3 presents a visual representation of V_t and V_b, where red regions shows the tensile stressed area, and the blue region shows the compressive stressed area.

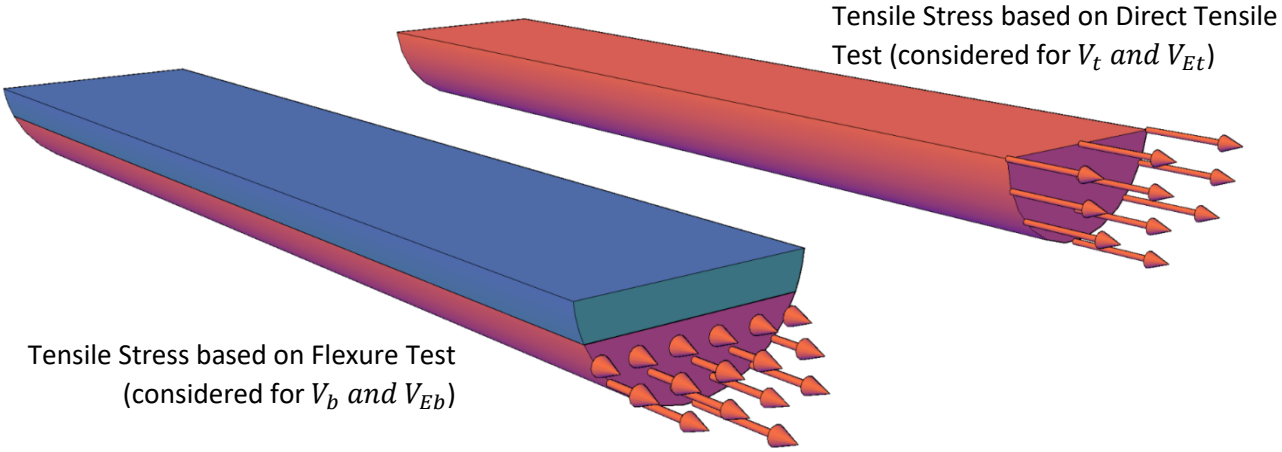

Figure 5.3: Direct Tensile and Flexure Tensile Stress Distribution on a Flexure Specimen

Considering the probability of failure for both of these tests are the same, equating Equation 5.8 and Equation 5.9 and simplifying, forms Equation 5.10.

$$\int_V \left(\frac{\sigma_t - \sigma_u}{\sigma_o}\right)^m dV_t = \int_V \left(\frac{\sigma_b - \sigma_u}{\sigma_o}\right)^m dV_b \qquad \text{Equation 5.10}$$

Since σ_u is assumed to be zero, and after the completing integration over the specimen for either tension or flexure, Equation 5.10 is reduced to Equation 5.11 and Equation 5.12, which represents the left and right sides of Equation 5.10 respectively. The form of Equation 5.12 was derived for the failure of brittle materials for a 3-point and 4-point flexural test as shown (Quinn, et al., 2009; Quinn G. D., 2003; Weil & Daniel, 1964). Finally, Equation 5.11 and Equation 5.12 are substituted back into Equation 5.10, which results in Equation 5.13.

$$\int_V \left(\frac{\sigma_t - \sigma_u}{\sigma_o}\right)^m dV_t = V_t \left(\frac{\sigma_t}{\sigma_o}\right)^m \quad \textit{Equation 5.11}$$

$$\int_V \left(\frac{\sigma_b - \sigma_u}{\sigma_o}\right)^m dV_b = \begin{cases} V_b \left(\frac{\sigma_b}{\sigma_o}\right)^m \left(\frac{1}{2(m+1)^2}\right) \leftarrow for\ 3pt.bending \\ V_b \left(\frac{\sigma_b}{\sigma_o}\right)^m \left(\frac{(m+3)}{6(m+1)^2}\right) \leftarrow for\ 4pt.bending \end{cases} \quad \textit{Equation 5.12}$$

$$V_t \left(\frac{\sigma_t}{\sigma_o}\right)^m = \begin{cases} V_b \left(\frac{\sigma_b}{\sigma_o}\right)^m \left(\frac{1}{2(m+1)^2}\right) \leftarrow for\ 3pt.bending \\ V_b \left(\frac{\sigma_b}{\sigma_o}\right)^m \left(\frac{(m+3)}{6(m+1)^2}\right) \leftarrow for\ 4pt.bending \end{cases} \quad \textit{Equation 5.13}$$

Rearranging Equation 5.13 to solve for the ratio between the rupture modulus and the tensile strength gives Equation 5.14. Equation 5.15 introduces a new term, describing the effective tensile volume experience by a material following the "weakest link" model that is subjected to bending (Quinn, et al., 2009; Quinn G. D., 2003). The effective tensile volume subjected to direct tension is simply the volume of a flexure specimen subjected to pure tension. Equation 5.14 can then be simplified into Equation 5.16, which provides a general form describing the ratio between two different stresses of materials that follow Weibull's weakest link model (Quinn, et al., 2009; Quinn G. D., 2003; Weil & Daniel, 1964). This will be described as the "tensile stress ratio" herein.

$$\frac{\sigma_b}{\sigma_t} = \begin{cases} \left(\frac{2V_t(m+1)^2}{V_b}\right)^{\frac{1}{m}} \leftarrow for\ 3pt.bending \\ \left(\frac{6V_t(m+1)^2}{V_b(m+3)}\right)^{\frac{1}{m}} \leftarrow for\ 4pt.bending \end{cases} \quad \textit{Equation 5.14}$$

$$V_{Eb} = \begin{cases} \frac{V_b}{2(m+1)^2} \leftarrow for\ 3pt.bending \\ \frac{V_b(m+3)}{6(m+1)^2} \leftarrow for\ 4pt.bending \end{cases} \quad \textit{Equation 5.15}$$

$$\frac{\sigma_b}{\sigma_t} = \left(\frac{V_{Et}}{V_{Eb}}\right)^{\frac{1}{m}} \quad \textit{Equation 5.16}$$

where:

- V_{Et} and V_{Eb} refer to the effective volumes of tensile stress in a uniaxial direct tensile test and a flexural test, respectively.

The tensile strength of GFRP bars is found after obtaining the rupture modulus from flexural testing and calculating Weibull modulus and the effective volumes, noted in Equation 5.16.

5.3.2 Determining Weibull Modulus

The Weibull modulus, m, also known as the shape parameter, is used to describe the distribution of GFRP material failure, which is linked to the flaws present in the material. The higher this value, the more uniformly the material defects are distributed throughout the volume (Arczewska, Polak, & Penlidis, 2019). This parameter's value is obtained by using the Weibull strength distribution graph, where the natural logarithm of the rupture modulus is taken and plotted against the double natural logarithm of its respective probability of failure in the list of samples, using Equation 5.17, where "n_s" represents the total number of specimens and "i" represents the rank of the specimen's strength relative to the others, in order from least to greatest.

$$P_f = \frac{i - 0.5}{n_s} \qquad \textit{Equation 5.17}$$

From these transformed points of data, a line of best fit is plotted against the dataset, from which the Weibull modulus is found by simply finding the slope of the line of best fit. It should be noted that this value becomes more accurate with having more sample data, as well as eliminating any outliers that may skew the line of best fit. Figure 5.4 shows the Weibull strength distribution graph for M13 specimens in the 3-point bending tests, while Table 5.3 shows the sorted data with its strength and appropriate transformations to form the graph (from Method 1). Likewise, Figure 5.5 represents the information in Table 5.4 for the M13 specimens in 4-point bending (from Method 1). The remaining Weibull graphs and related tables are displayed in Appendix D.

Table 5.3: Data for Weibull Strength Distribution Graph for M13 Data in 3-Point Bending (All Specimens)

Rank, i	Test No.	Specimen No.	Rupture Modulus, σ_r (MPa)	$P_f = \frac{(i - 0.5)}{n}$	$x = \ln(\sigma_r)$	$y = \ln\left(ln\left(\frac{1}{1 - P_f}\right)\right)$
1	42	M13-14	1760.66	0.05	7.47	-2.97
2	45	M13-11	1760.96	0.15	7.47	-1.82
3	10	M13-20	1799.78	0.25	7.50	-1.25
4	41	M13-10	1884.86	0.35	7.54	-0.84
5	7	M13-3	1889.01	0.45	7.54	-0.51
6	9	M13-15	1907.54	0.55	7.55	-0.23
7	44	M13-20	1909.38	0.65	7.55	0.05
8	43	M13-13	1953.11	0.75	7.58	0.33
9	6	M13-1	1973.10	0.85	7.59	0.64
10	8	M13-18	2039.01	0.95	7.62	1.10
	m =	**24.00**		**b =**	**-181.56**	**R^2 =** **0.9139**

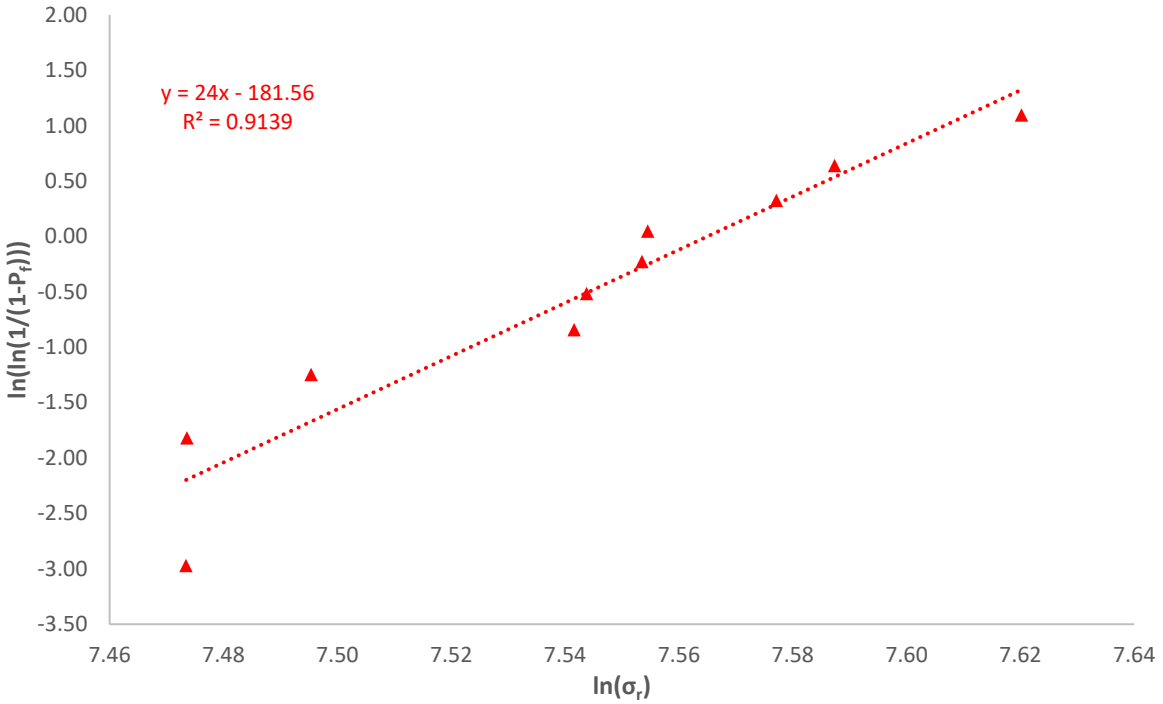

Figure 5.4: Weibull Strength Distribution Graph for M13 Specimens in 3-Point Bending (All Specimens)

Table 5.4: Data for Weibull Strength Distribution Graph for M13 Data in 4-Point Bending (All Specimens)

Rank, i	Test No.	Specimen No.	Rupture Modulus, σ_r (MPa)	$P_f = \frac{(i-0.5)}{n}$	$x = \ln(\sigma_r)$	$y = \ln\left(ln\left(\frac{1}{1-P_f}\right)\right)$
1	76	M13-12	1647.30	0.05	7.41	-2.97
2	78	M13-16	1665.56	0.15	7.42	-1.82
3	74	M13-4	1697.21	0.25	7.44	-1.25
4	75	M13-8	1811.85	0.35	7.50	-0.84
5	77	M13-17	1822.47	0.45	7.51	-0.51
6	79	M13-5	1844.93	0.55	7.52	-0.23
7	81	M13-9	1860.01	0.65	7.53	0.05
8	73	M13-7	1935.90	0.75	7.57	0.33
9	82	M13-19	1961.16	0.85	7.58	0.64
10	80	M13-6	2037.11	0.95	7.62	1.10
	m =	**16.51**		**b =**	**-124.55**	**R^2 =** **0.9242**

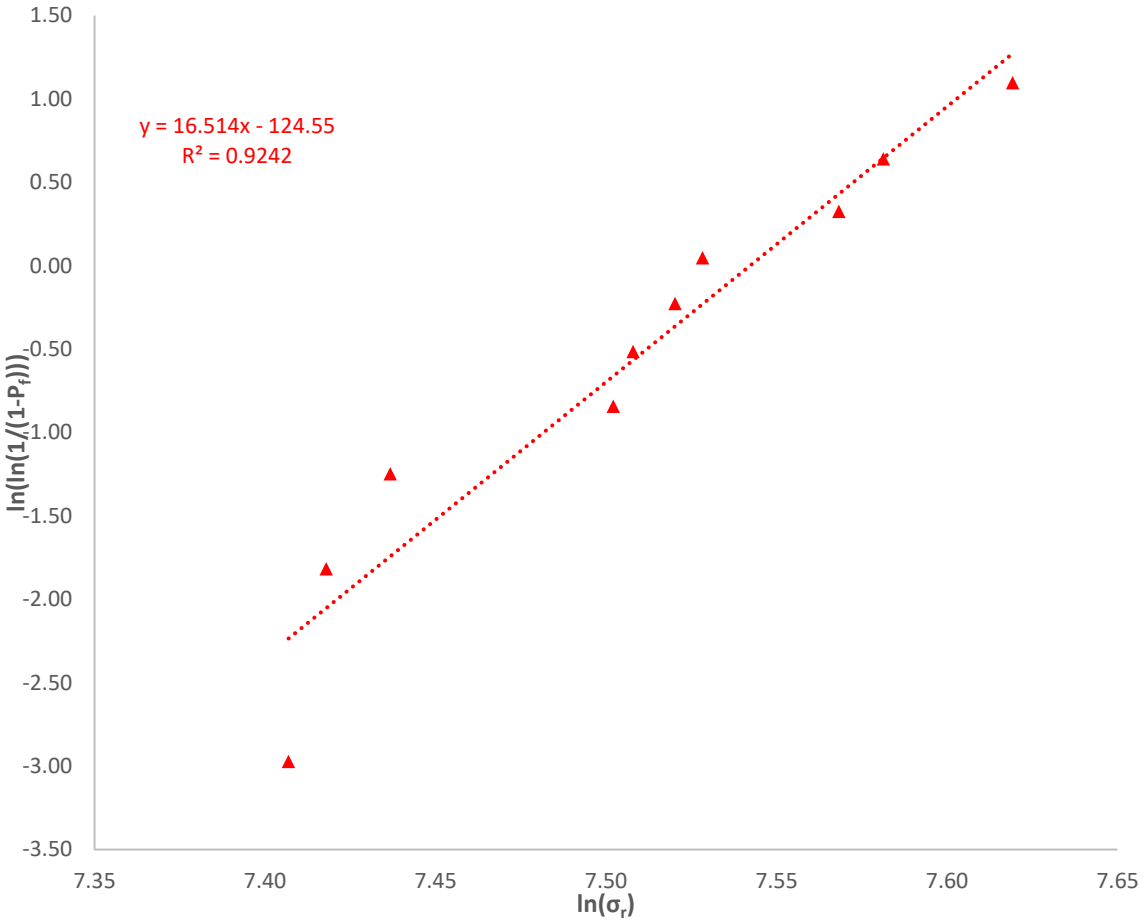

Figure 5.5: Weibull Strength Distribution Graph for M13 Specimens in 4-Point Bending (All Specimens)

While the data and plots shown in the above tables and figures are accurate, as indicated by the coefficient of determination, R^2, they include all specimens where none are treated as outliers. A second analysis of the Weibull moduli was conducted to exclude potential outliers among the 10 specimens for each size per flexural test. These outliers were the specimens had the lowest and highest rupture moduli. For comparison, Table 5.5, Figure 5.6, Table 5.6, and Figure 5.7 display the same data and plots as above, except the inclusion of the first and last data points of the Weibull graph (which have not been removed from the respective table, but has be indicated in red), where the following plots use 8 specimens, instead of all 10.

Table 5.5: Data for Weibull Strength Distribution Graph for M13 Data in 3-Point Bending (Except First and Last Data Points)

Rank, i	Test No.	Specimen No.	Rupture Modulus, σ_r (MPa)	$P_f = \frac{(i-0.5)}{n}$	$x = \ln(\sigma_r)$	$y = \ln\left(ln\left(\frac{1}{1-P_f}\right)\right)$
1	42	M13-14	1760.66	0.05	7.47	-2.97
2	45	M13-11	1760.96	0.15	7.47	-1.82
3	10	M13-20	1799.78	0.25	7.50	-1.25
4	41	M13-10	1884.86	0.35	7.54	-0.84
5	7	M13-3	1889.01	0.45	7.54	-0.51
6	9	M13-15	1907.54	0.55	7.55	-0.23
7	44	M13-20	1909.38	0.65	7.55	0.05
8	43	M13-13	1953.11	0.75	7.58	0.33
9	6	M13-1	1973.10	0.85	7.59	0.64
10	8	M13-18	2039.01	0.95	7.62	1.10
	m =	**20.74**		**b =**	**-156.82**	**R^2 =** **0.9436**

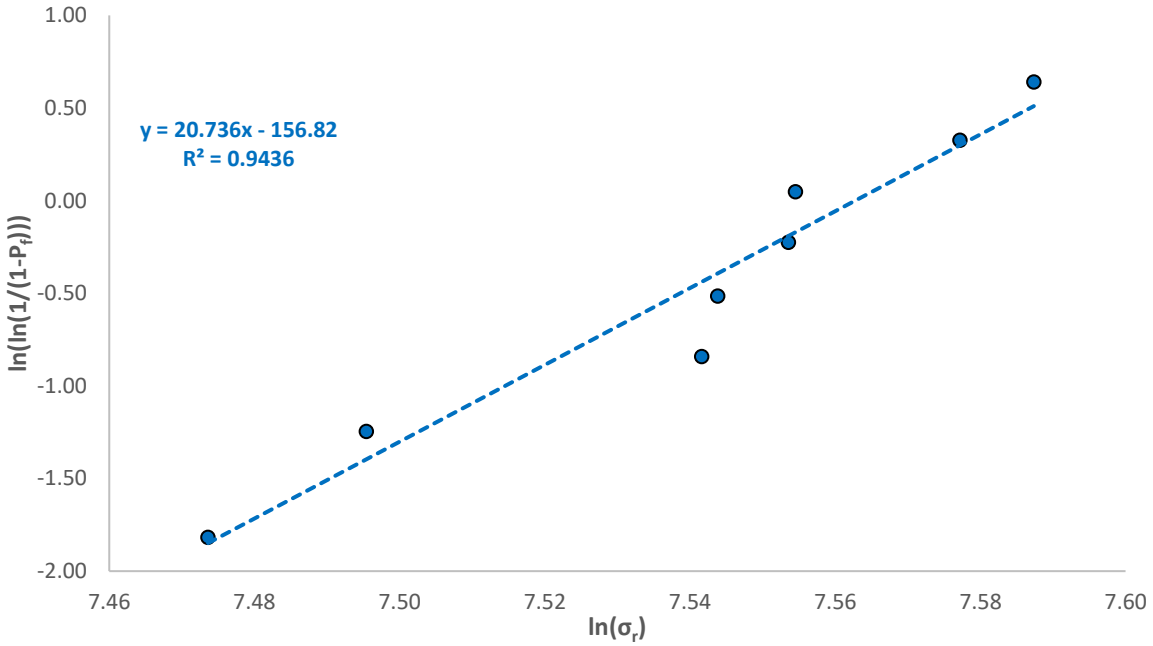

Figure 5.6: Weibull Strength Distribution Graph for M13 Data in 3-Point Bending (Except First and Last Data Points)

Table 5.6: Data for Weibull Strength Distribution Graph for M13 Data in 4-Point Bending (Except First and Last Data Points)

Rank, i	Test No.	Specimen No.	Rupture Modulus, σ_r (MPa)	$P_f = \frac{(i-0.5)}{n}$	$x = \ln(\sigma_r)$	$y = \ln\left(ln\left(\frac{1}{1-P_f}\right)\right)$
1	76	M13-12	1647.30	0.05	7.41	-2.97
2	78	M13-16	1665.56	0.15	7.42	-1.82
3	74	M13-4	1697.21	0.25	7.44	-1.25
4	75	M13-8	1811.85	0.35	7.50	-0.84
5	77	M13-17	1822.47	0.45	7.51	-0.51
6	79	M13-5	1844.93	0.55	7.52	-0.23
7	81	M13-9	1860.01	0.65	7.53	0.05
8	73	M13-7	1935.90	0.75	7.57	0.33
9	82	M13-19	1961.16	0.85	7.58	0.64
10	80	M13-6	2037.11	0.95	7.62	1.10
m =	**14.11**			**b =**	**-106.42**	**R^2 =** **0.9560**

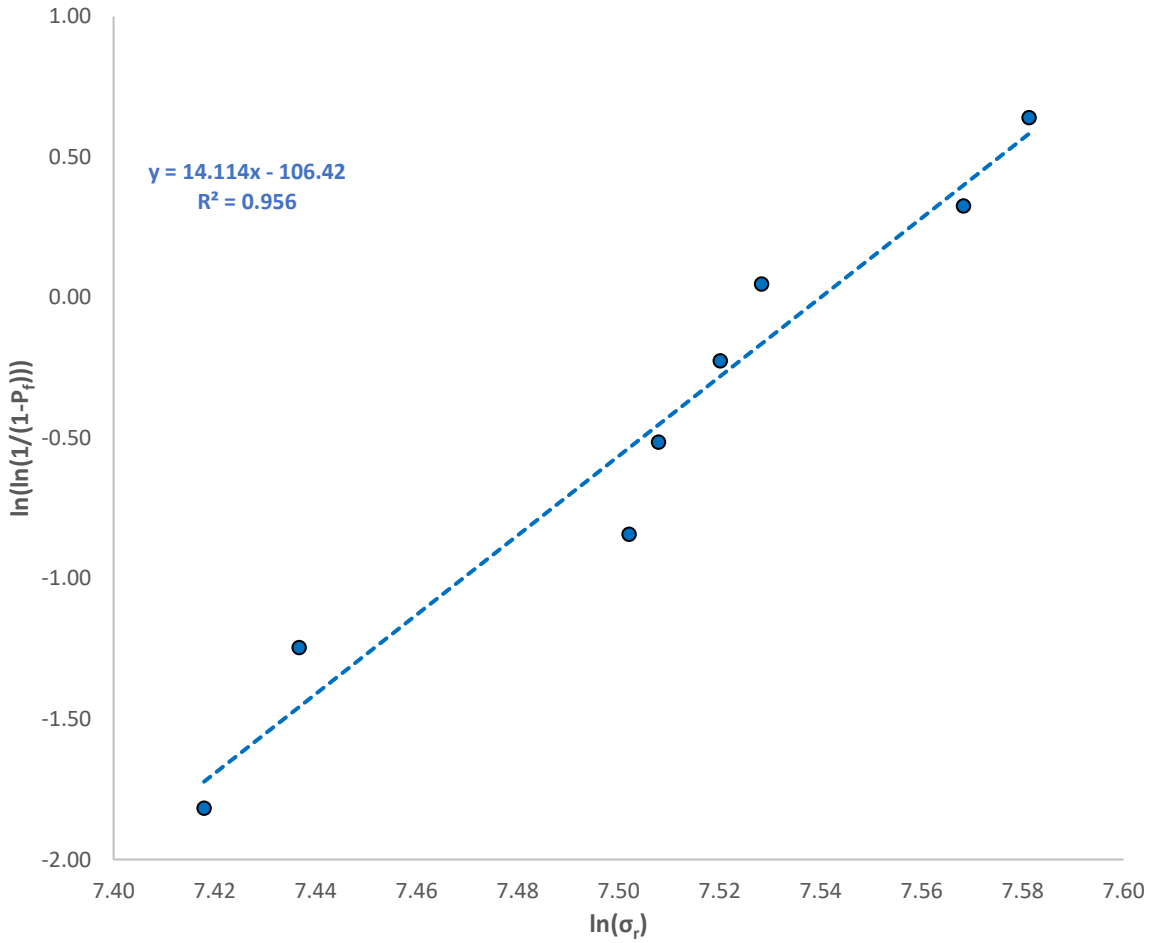

Figure 5.7: Weibull Strength Distribution Graph for M13 Data in 4-Point Bending (Except First and Last Data Points)

Based on Table 5.5 to Table 5.6 (or Figure 5.6 to Figure 5.7) and for other specimens (shown in Appendix D), the coefficient of determination increases for most of the specimens when excluding the first and last data points used in the Weibull graph. Regardless of the coefficient of determination for these specimens, the variance among the rupture modulus from the different specimens are lower, making the values more reasonably comparable with each other.

Since there is a difference in the Weibull modulus based on the data points in the Weibull graph, the decision to use the 8-specimen plot and analysis was made for the rest of the calculations presented in this research. Using these 8-specimens in the Weibull strength distribution graph to find the Weibull modulus will be known as Variation B for the set of calculations. Variation A will include the calculations for using all 10 specimens to determine the Weibull modulus. The Variation A calculations and associated graphs are provided in Appendix B and C respectively, displaying the calculated results for each set of test specimens; the corresponding Weibull graphs and Weibull modulus found are provided in Appendix D.

Table 5.7 contains the summary of the calculated Weibull moduli for both Variations A & B. It should be noted that the displayed Weibull moduli have been rounded to the nearest fifth of a tenth (i.e. “0.5”), for the ease of completing the following numerical computations for the equations displayed in this section.

Table 5.7: Weibull Modulus for Each Specimen Size Per Flexure Test

Variation	Point Load for Testing	M8	M13	M15	M20	M25	M32
A (all specimens)	3	22	24	18	26	30.5	17
	4	16.5	16.5	14.5	15	17.5	20
B (excluding outliers)	3	20.5	20.5	15	22	23.5	21
	4	18	14	17	13	15.5	21.5

It is evident that, for both Variations displayed in Table 5.7, the Weibull moduli are not drastically different. However, it is obvious that almost all the Weibull moduli are unique, which means the spread of the flaws throughout the material vary considerably.

It should also be noted Method 1 and Method 2 yield the same results for the Weibull moduli calculation. This is because the Weibull modulus depends on the distribution of failure loads and not the subsequent calculations of the rupture strengths.

5.3.3 Effective Volume Under Tensile Stress

The calculation for the effective volume for direct tensile testing is the volume of the entire flexure specimen, as mentioned in Section 5.3.1 for the description of Equation 5.14 and Equation 5.16. The calculation of the cross-sectional area for a flexure specimen is shown in Equation 5.18. The volume is calculated by multiplying the cross-sectional area by the length of the specimen, as shown in Equation 5.19. The parameters represented in Equation 5.19 and Equation 5.19 are shown in Figure 5.8 and Figure 5.9 displaying the length and cross-section of the flexure specimen, respectively.

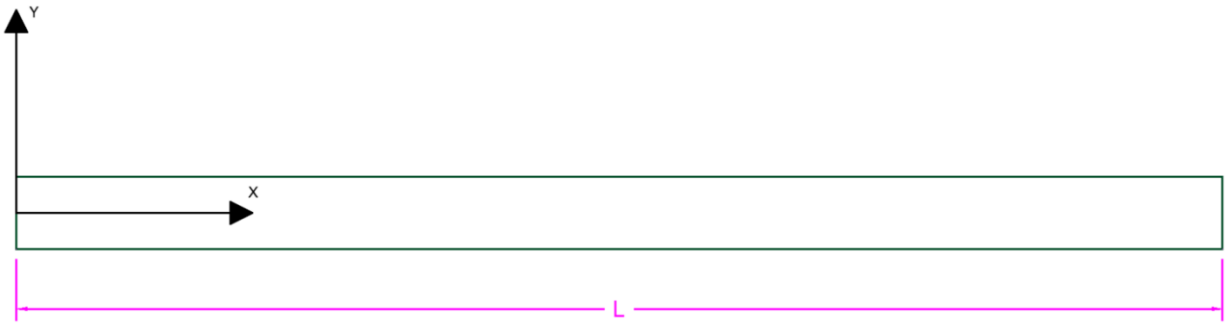

Figure 5.8: Length of Flexure GFRP Specimen

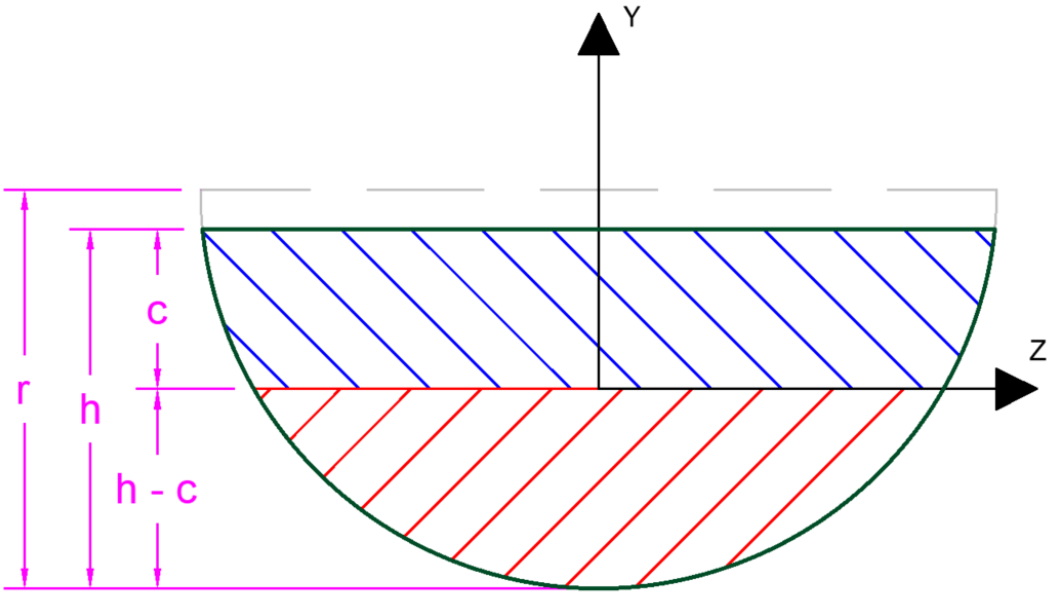

Figure 5.9: Cross Section of Flexure GFRP Specimen

$$A = r\left(r \times \cos^{-1}\left(\frac{d}{r}\right) - d \times \sqrt{1 - \frac{d^2}{r^2}}\right) \qquad \textit{Equation 5.18}$$

Where $d = r - h$

$$V_{Et} = V_t = A \times L \qquad \textit{Equation 5.19}$$

where:

- L is the length of the specimen,
- r is the original radius of the specimen

The calculation for effective volume for flexural testing, is not as trivial. Similar to the concerns in Section 5.2.1 addressed with solving for the unknown expressions with Equation 5.1 to Equation 5.3, the bounds of the cross-section are not easy to work with, due to its “semi-circular-like” nature where the width varies non-linearly along the depth. In addition, the stress distribution is not perfectly linear,

which complicates formulating an equation to represent the effective tensile volume due to bending for the shape of the specimen used in this research.

Starting with Equation 5.12, factors that contribute to the stress calculation are substituted in for the maximum tensile stress achieved in a flexural test, σ_b. The tensile bending stress on the bottom portion of the cross-section, along the length of the specimen is represented as Equation 5.20, which describes the bending moment diagram for the respective flexural loading. This is represented in Figure 5.7, where x represents the length of the flexure specimen.

$$\sigma_{b,bottom}(x) = \begin{cases} \left(\frac{x}{L/2}\right)\sigma_{t,max} = \left(\frac{2x}{L}\right)\sigma_{t,max} \leftarrow for\ 3pt\ bending \\ \begin{cases} \sigma_{t,max}\ for \frac{L}{3} < x < \frac{2L}{3} \\ \left(x \Big/ \left(\frac{L}{3}\right)\right)\sigma_{t,max}\ for\ 0 < x < \frac{L}{3}\ ;\ \frac{2L}{3} < x < L \end{cases} \leftarrow for\ 4pt\ bending \end{cases} \quad \text{Equation 5.20}$$

Equation 5.21 builds off of Equation 5.19, where a linear function factor for the bending stress distribution along the depth of the cross section is introduced (not the same linear slope as compressive stress, due to the bi-moduli behaviour of the material) from zero at the neutral axis, until the bottommost fibre of the GFRP specimen. This is represented in Figure 5.8, where y represents depth along the cross-section of the GFRP specimen, respectively.

$$\sigma_b(x,y) = \begin{cases} -\left(\frac{y}{h-c}\right)\left(\frac{2x}{L}\right)\sigma_{t,max} \leftarrow for\ 3pt\ bending \\ \begin{cases} -\left(\frac{y}{h-c}\right)\sigma_{t,max}\ for\ \frac{L}{3} < x < \frac{2L}{3} \\ -\left(\frac{y}{h-c}\right)\left(\frac{3x}{L}\right)\sigma_{t,max}\ for\ 0 < x < \frac{L}{3}\ ;\ \frac{2L}{3} < x < L \end{cases} \leftarrow for\ 4pt\ bending \end{cases} \quad \text{Equation 5.21}$$

This bending stress expressions represented in Equation 5.21 are then substituted into the left-side of Equation 5.12 for flexural tensile stress to form Equation 5.22 (because there are two functions at different bounds for a 4-point bending test, the corresponding integral splits into two, as shown in Equation 5.21). Expanding the equation further via integration presents Equation 5.23, which enables solving for effective volume experiencing tensile stress for a 3-point and 4-point bending test. Appendix G displays the full derivation, complete with steps, for formulating the equation for the effective tensile volume for 3-point bending and 4-point bending tests.

a) $$V_{Eb,3ptbnd} = 2\int_{V_b}\left(\frac{-\left(\frac{y}{h-c}\right)\left(\frac{2x}{L}\right)\sigma_{t,max}}{\sigma_{t,max}}\right)^m dV_b = -2\int_{V_b}\left(\left(\frac{y}{h-c}\right)\left(\frac{2x}{L}\right)\right)^m dV_b$$

b) $$V_{Eb,4ptbnd} = 2\int_0^{\frac{L}{6}}\int_{A_t}\left(-\left(\frac{y}{h-c}\right)\left(\frac{\sigma_{t,max}}{\sigma_{t,max}}\right)\right)^m dA_t dx + 2\int_0^{\frac{L}{3}}\int_{A_t}\left(-\left(\frac{y}{h-c}\right)\left(\frac{3x}{L}\right)\left(\frac{\sigma_{t,max}}{\sigma_{t,max}}\right)\right)^m dA_t dx \quad \text{Equation 5.22}$$

a) $$V_{Eb,3ptbnd} = \left(-\frac{2^{m+1}}{((h-c)L)^m}\right)\int_0^{L/2}\int_0^{-(h-c)}\int_{-\sqrt{r^2-\left(y-(r-(h-c))\right)^2}}^{\sqrt{r^2-\left(y-(r-(h-c))\right)^2}} y^m x^m \, dz\, dy\, dx$$

b) $$V_{Eb,4ptbnd} = \left(\frac{2(-1)^m}{(h-c)^m}\right)\int_0^{\frac{L}{6}}\int_0^{-(h-c)}\int_{-\sqrt{r^2-\left(y-(r-(h-c))\right)^2}}^{\sqrt{r^2-\left(y-(r-(h-c))\right)^2}} y^m dz dy dx + \left(\frac{2(-1)^m(3)^m}{(h-c)^m L^m}\right)\int_0^{\frac{L}{3}}\int_0^{-(h-c)}\int_{-\sqrt{r^2-\left(y-(r-(h-c))\right)^2}}^{\sqrt{r^2-\left(y-(r-(h-c))\right)^2}} y^m x^m dz dy dx$$

Equation 5.23

where:

- L is the length of the specimen,
- r is the original radius of the specimen,
- z-coordinate refers to the width of the cross section,
- y-coordinate refers to the height/depth of the cross-section, and the
- x-coordinate refers to the length of the cross-section.

Due to the complexity of Equation 5.23, the calculations were completed using software (MATLAB and Maple) to evaluate the integral after all the cross-sectional parameters were measured directly from the specimens, and the location of the neutral axis was obtained after completing the testing. Table 5.8 indicates a summary of the average effective volumes under tensile stress due to flexural and direct tensile testing.

Table 5.8: Average Effective Volumes for 8 Specimens Per Test

Effective Tensile Volume	Type of Bending Test	M8	M13	M15	M20	M25	M32
Direct Tension, V_{Et} (mm^3)	3-Point	1661.63	7780.40	15018.34	29758.95	57388.77	121885.50
	4-Point	1608.78	7766.74	14745.19	29539.18	56581.33	122876.59
Bending, V_{Eb} (mm^3)	3-Point	0.49	2.29	7.41	7.42	12.24	33.92
	4-Point	4.44	31.41	44.80	133.75	197.61	264.59

From Table 5.8, the effective volumes under tensile stress due to bending from the 3-point bending and 4-point bending tests are quite different; the effective volumes for 4-point bending are much larger. This is obvious, since the amount of the GFRP specimen's volume subjected to the maximum bending moment is greater compared to a 3-point bending test, and therefore, the volume of tensile stress increases as a result.

It should also be noted that the effective volumes are the essentially same for both Methods 1 and 2 of the calculation; it is slightly off due to the minimal variations for the flexural specimen dimensions. Since the difference in the $\frac{E_t}{E_c}$ ratios between the two Methods is very small, it has minimal impact on the results for effective volume (calculations were completed for $\frac{E_t}{E_c} = 1$, and the difference in the effective volume results were more notable). This indicates that a $\frac{E_t}{E_c}$ ratio between 1.2 and 1.25 (Jones, 1978; Jones, 1977) will produce similar results.

While the effective volumes describe how much of the material is experiencing tensile stress, they are directly used in the few final calculations for obtaining the tensile strength of the GFRP material. Appendix B displays all the specimens' information pertaining to their effective volumes.

5.4 Determining Tensile Strength

Equation 5.16 is used to solve the tensile stress ratio of GFRP bars, once the effective volumes are calculated. Table 5.9 displays a summary of the averages for the tensile stress ratio of a flexure test to a direct tensile test.

Table 5.9: Average $\sigma_b/\sigma_t = (V_{Et}/V_{Eb})^{1/m}$ for 8 Specimens Per Test

Type of Bending Test	M8	M13	M15	M20	M25	M32
3-Point	1.49	1.49	1.64	1.46	1.43	1.48
4-Point	1.39	1.48	1.41	1.51	1.44	1.33
% Difference	6.97%	0.31%	15.22%	3.81%	0.53%	10.41%

From Table 5.9, there is little difference in tensile stress ratio values between a 3-point and 4-point bending test, since all percent differences are about 15% or less. This is another indication that there is no significant difference between using 3-point or 4-point bending test to determine the tensile capacity of a GFRP bar. Table 5.9 also presents the results for both Methods 1 and 2, as there is no difference since the effective volumes presented in Table 5.8 do not change between the two Methods as well.

To calculate the tensile strength, the rupture modulus found in the flexural testing divided by the tensile stress ratio, outlined from Section 5.2.2. Table 5.10 presents a summary of the correlated tensile strength for each specimen, based on their respective flexural test.

Table 5.10: Average Tensile Strength for (Eight) Specimen Per Test

Method	Type of Bending Test	M8	M13	M15	M20	M25	M32
1 (n = 1.25)	3-Point	1508.51	1271.24	1146.89	1214.69	1176.08	1088.80
	4-Point	1623.39	1231.10	1217.12	1062.09	1150.69	1199.34
	% Difference	7.34%	3.21%	5.94%	13.41%	2.18%	9.66%
2 (n = 1.2)	3-Point	1491.58	1253.30	1133.97	1201.04	1162.82	1076.51
	4-Point	1605.19	1217.26	1203.44	1050.14	1137.73	1185.81
	% Difference	7.34%	2.92%	5.94%	13.41%	2.18%	9.66%
% Difference Between Method 1 & 2	*3-Point*	*1.13%*	*1.42%*	*1.13%*	*1.13%*	*1.13%*	*1.14%*
	4-Point	*1.13%*	*1.13%*	*1.13%*	*1.13%*	*1.13%*	*1.13%*

From Table 5.10, it is evident that the correlated tensile capacity generally decreases as the size of the GFRP bar increases, which is an indication that the correlation calculations work for large-sized GFRP bars. This trend is not observed for the correlated tensile capacities for the M15 and M20 specimens for

both 3-point and 4-point bending tests. A possible reason for this is that the batch for these specimens could be stronger (i.e. less flaws present) than they usually are.

It should also be noted that the resulting tensile strength values from the 3-point bending and 4-point bending calculations are not drastically different, since the percent difference between the two flexural tests for both methods are under 10%, with the exception of the M20 specimens for both methods of the calculations being slightly above 13%. Overall, this indicates minor differences of the correlated tensile strength between 3-point bending test to a 4-point bending test, showing that there is no obvious benefit of one test over the other.

Much similar to the percent difference trends between Methods 1 and 2 noticed in Table 5.2 for the rupture modulus, the percent differences between the two Methods for the respective flexural test are almost the same.

5.5 Discussion and Comparison of Results

This section of the thesis will focus on the comparison of the correlated tensile results between other sources within and outside of this research, to show the effectiveness of the correlation calculations.

5.5.1 Comparison of Correlated Tensile Capacities to Tensile Strength Obtain from Direct Tensile Tests & Specification Sheets

Other sources within this research have provided tensile strength values of some of the GFRP specimens used in the flexural tests, which will be used for comparison to the correlated tensile capacities. Fiberline has provided the specification sheets for the M13, M15, and M20 bars, while direct tensile testing was completed for M8, M13, and M15 bars. Figure 5.10 provides a visual comparison of correlated tensile capacities of the relevant GFRP bar sizes compared to their corresponding tensile capacities reported from tensile testing or specification sheets. This graph is further discussed below, in which the presented tables display differences in the results.

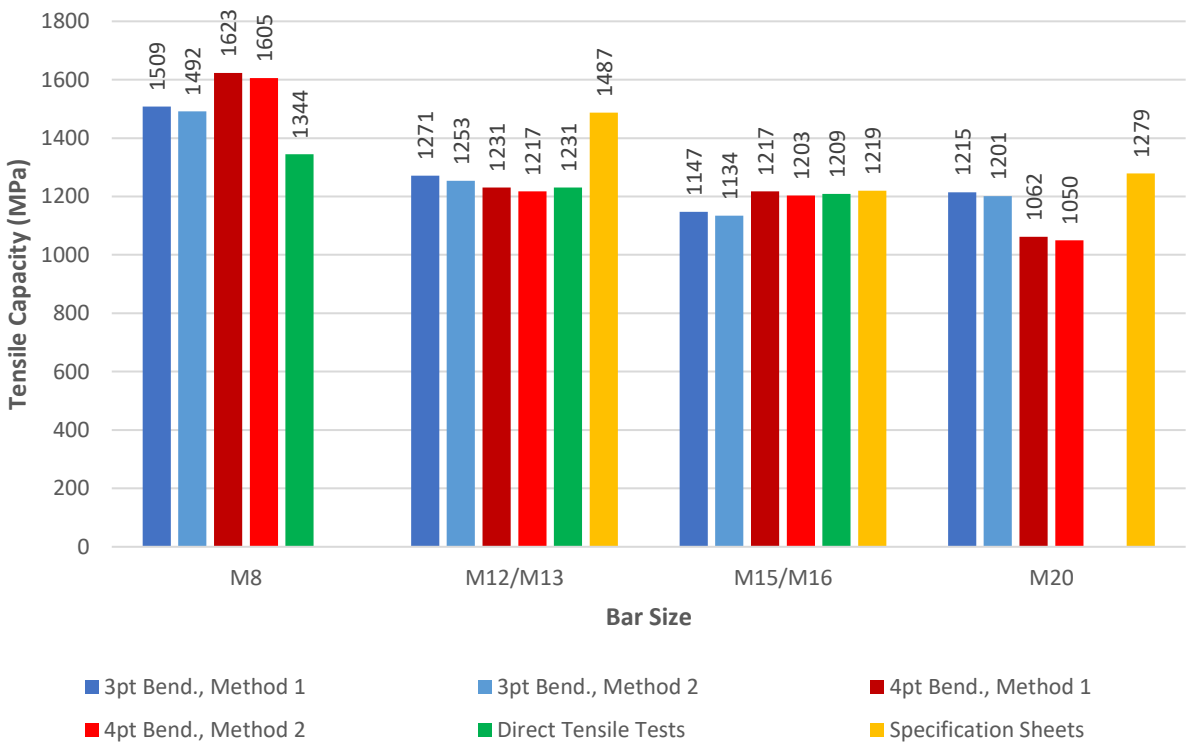

Figure 5.10: Comparison of Correlated Tensile Capacities versus Internal Sources

Table 5.11 shows a summary of the tensile stiffness and the tensile strength of the GFRP bars from the respective source.

Table 5.11: Summary of Average Tensile Elastic Modulus & Capacity from Direct Tensile Tests and Specification Sheets

Source	Parameter	M8	M13	M15	M20	M25	M32
Direct Tensile Tests	E_t (MPa)	80874.23	76847.85	74968.56	-	-	-
	σ_t (MPa)	1344.347	1231.229	1209.08	-	-	-
Specification Sheets	E_t (MPa)	-	62220	65300	60900	-	-
	σ_t (MPa)	-	1487.4	1219.4	1278.8	-	-

As noted in Table 5.11, there are some discrepancies between the tensile elastic moduli and tensile strength between the M13 and M15 specimens from the specification sheets and the tensile tests. The tensile test specimens are stiffer compared to the reported values in the specification sheets. However, the ultimate tensile strength values for the M13 and M15 values are quite similar, where values the manufacturer's specification sheets are higher in comparison with the results from testing. Reasons for this could lie with deviations in testing methods completed by the manufacturer versus the direct tensile tests completed in this research.

Table 5.12 displays the tensile strength ratios $\frac{\sigma_b}{\sigma_t}$ from the calculations shown in this work, from tensile testing done in this work and form the specification sheets supplied by the manufacturers.

Table 5.12: Comparison of σ_b/σ_t from Correlated and Test Values

σ_t Values Used	Method	Type of Bending Test	M8	M13	M15	M20	M25	M32
Calculated Ratios	1 & 2	3-Point	1.49	1.49	1.64	1.46	1.43	1.48
		4-Point	1.39	1.48	1.41	1.51	1.44	1.33
From Test Values	1	3-Point	1.40	1.52	1.47	-	-	-
		4-Point	1.36	1.38	1.33	-	-	-
	2	3-Point	1.39	1.51	1.45	-	-	-
		4-Point	1.34	1.36	1.31	-	-	-
Specification Sheets	1	3-Point	-	1.27	1.54	1.39	-	-
		4-Point	-	1.23	1.39	1.25	-	-
	2	3-Point	-	1.25	1.52	1.37	-	-
		4-Point	-	1.22	1.38	1.24	-	-

It is evident that the tensile stress ratio values from the Method 1 using tensile capacities from the tensile testing results and specification sheets are slightly closer to the correlated stress ratios calculated from the flexural test. This indicates using an elastic moduli ratio of 1.25 is more accurate.

Table 5.13 provides a summary of the tensile capacities from the correlation calculations, direct tensile testing, and specification sheets. Table 5.14 and Table 5.15 present the percentage difference of the tensile strengths from the tensile testing and specification sheets to the correlation calculations, respectively.

Table 5.13: Comparison of Tensile Capacities from Correlations, Testing and Specification Sheets

Method/ Source	Type of Flexural Test	M8	M13	M15	M20	M25	M32
1	3-Point	1508.51	1271.24	1146.89	1214.69	1176.08	1088.80
	4-Point	1623.39	1231.10	1217.12	1062.09	1150.69	1199.34
2	3-Point	1491.58	1253.30	1133.97	1201.04	1162.82	1076.51
	4-Point	1605.19	1217.26	1203.44	1050.14	1137.73	1185.81
Direct Tensile Testing		1344.35	1231.23	1209.08	-	-	-
Specification Sheets		-	1487.40	1219.40	1278.80	-	-

Table 5.14: Percentage Difference of Tensile Capacity from Direct Tensile Tests

Method/ Source	Type of Flexural Test	M8	M13	M15	M20	M25	M32
1	3-Point	11.51%	3.20%	5.28%	-	-	-
	4-Point	18.81%	0.01%	0.66%	-	-	-
2	3-Point	10.38%	1.78%	6.41%	-	-	-
	4-Point	17.69%	1.14%	0.47%	-	-	-

Table 5.15: Percentage Difference of Tensile Capacity from Specification Sheets

Method/ Source	Type of Flexural Test	M8	M13	M15	M20	M25	M32
1	3-Point	-	15.67%	6.13%	5.14%	-	-
	4-Point	-	18.86%	0.19%	18.52%	-	-
2	3-Point	-	17.08%	7.26%	6.27%	-	-
	4-Point	-	19.98%	1.32%	19.64%	-	-

As noted from Table 5.14, the differences are low, less than 7% across both Methods, excluding the results from the M8 specimens, having a difference up to 19%. This proves that flexural test can yield adequate results for obtaining the tensile capacity of a GFRP specimen. The differences are lower for the M13 and M15 specimens placed under 4-point bending compared to 3-point bending, indicating that a 4-point bending is more accurate than a 3-point bending test.

From Table 5.15, there is a significant percentage difference between the tensile capacities from the correlation calculations and the specification sheets, up to 20%. Such a large difference could be a result of deviations and imperfections in testing methods, or specimens belonging to different batches (like for the M13 specimens). Also, since the differences are lower in the Method 1 calculations (i.e. $\frac{E_t}{E_c} = 1.25$), compared to Method 2 (i.e. $\frac{E_t}{E_c} = 1.2$), this could mean that the assumed elastic moduli ratio is slightly incorrect, and could be higher than anticipated within these two Methods,. It is also evident that the difference of the tensile capacities from the specimens under 3-point bending are generally lower than the results from the specimens of the 4-point bending test, with the exception of the M15 specimens. Since there are only three specimens for this comparison, it is difficult to make a definite conclusion, but it is seen that the 3-point bending tests yields a stronger correlation than the 4-point bending test.

5.5.2 Comparison with Arczewska's (2017) Work

Tensile and flexural tests were completed for M12 and M16 bars by Arczewska (2017), which allows for comparison with the tests in this research for the M13 and M15 bars. Since the M12 bar from Arczewska's research is very close to the M13 bars in size, the sets of parameters and results will be compared. Table 5.16 to Table 5.23 shows the comparisons between the M13 bars from this research and the M12 bars from Arczewska's research, and the M15 bars from both research works (in Arczewska's work, the bars with the designation of M16 actually had the same dimensions as the M15 bars in this research), using both Methods 1 and 2 of correlated calculations. Figure 5.11 provides a visual comparison of correlated tensile capacities of the relevant GFRP bar sizes compared to Arczewska's results, which is further discussed below, in which the presented tables display differences in the results.

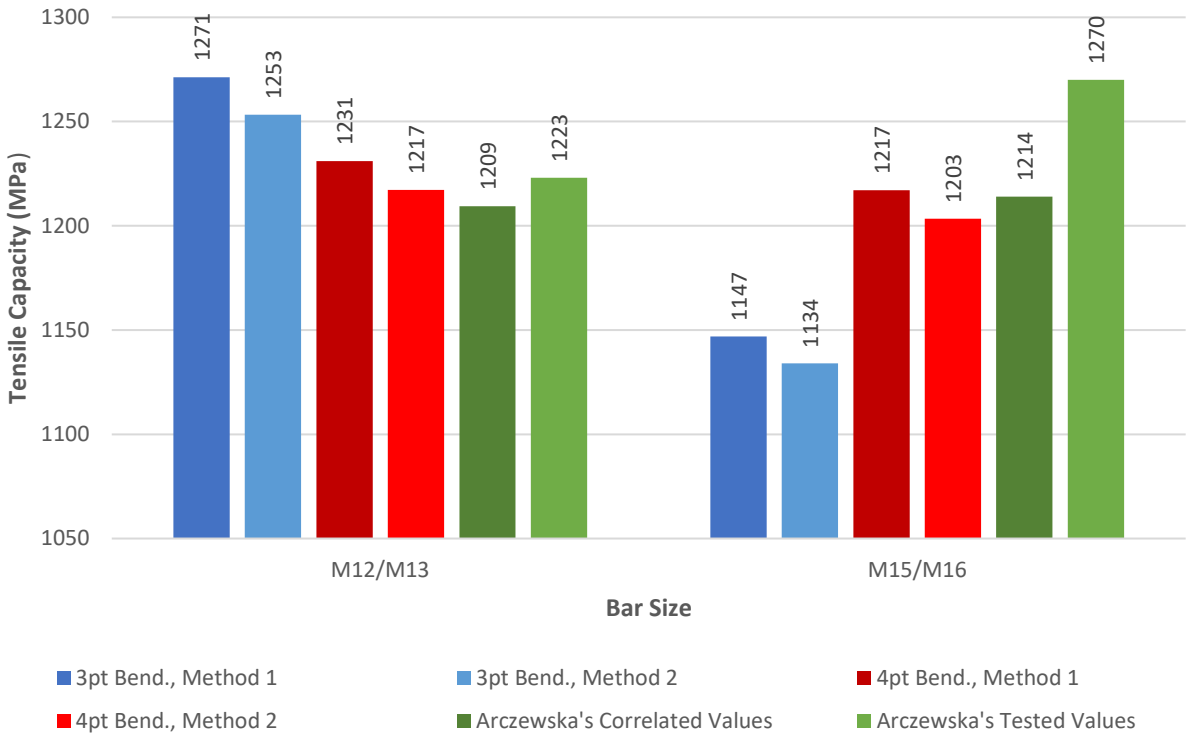

Figure 5.11: Comparison of Correlated Tensile Capacities versus Arczewska's (2017) Results

Table 5.16 to Table 5.19 show a summary of key parameters, the percentage difference between those key parameters, percentage difference between the tensile stress ratio from correlations and tests, and tensile strengths from correlations and tests, respectively. Arczewska tested bars only in 3-point bending. For completeness of the comparison, both 3-point and 4-point bending results from this research are presented.

Table 5.16: Comparison of Key Parameters from Current Researched M13 and Previously Researched M12 GFRP Bars

Specimen Size	Type of Flexural Test	M13 - Method 1	M13 - Method 2	Arczewska's M12
Rupture (Tensile) Stress, σ_r (MPa)	3-Point	1887.74	1866.51	2010.00
	4-Point	1828.35	1807.80	-
V_{Eb} (mm^3)	3-Point	2.29	2.29	1.28
	4-Point	31.41	31.41	-
V_{Et} (mm^3)	3-Point	7780.40	7780.40	54259.20
	4-Point	7766.74	7766.74	-
Weibull Modulus, m	3-Point	20.50	20.50	21
	4-Point	20.50	20.50	-
$\sigma_b/\sigma_t = (V_{Et}/V_{Eb})^{1/m}$	3-Point	1.49	1.49	1.66
	4-Point	1.48	1.48	-
Correlated Tensile Strength, $\sigma_{t,calc}$ (MPa)	3-Point	1271.24	1253.30	1209.39
	4-Point	1231.10	1217.26	-
σ_b/σ_t from testing	3-Point	1.52	1.51	1.64
	4-Point	1.38	1.36	-

Table 5.17: Difference for Key Parameters Between based on Current Research Work and Arczewska (2017) and Previous Research for M13 GFRP Bars

Parameters	Type of Flexural Test	M13 - Method 1	M13 - Method 2
Rupture (Tensile) Stress, σ_r (MPa)	3-Point	6.27%	7.40%
	4-Point	9.46%	10.59%
$\sigma_b/\sigma_t = (V_{Et}/V_{Eb})^{1/m}$	3-Point	11.00%	11.00%
	4-Point	11.31%	11.31%
Correlated Tensile Strength, $\sigma_{t,calc}$ (MPa)	3-Point	4.99%	3.57%
	4-Point	1.78%	0.65%
σ_b/σ_t from testing	3-Point	7.38%	8.51%
	4-Point	17.30%	18.42%

(Calculated based on % differences between values by Arczewska (2017) and 3-Point or 4-Point Bending using Method 1 or Method 2 Calculations from this research work)

Table 5.18: Percentage Difference for σ_b/σ_t Between Current and Previous Research for M13 GFRP Bars

σ_t values used from Arczewska's Research	Type of Flexural Test	M13 - Method 1	M13 - Method 2
Correlated	3-Point	11.00%	11.00%
	4-Point	11.31%	11.31%
Tested	3-Point	9.79%	9.79%
	4-Point	10.10%	10.10%
(Calculated based on % differences between values by Arczewska (2017) and 3-Point or 4-Point Bending using Method 1 or Method 2 Calculations from this research work)			

Table 5.19: Percentage Difference for Tensile Capacities Between Current and Previous Research for M13 GFRP Bars

σ_t values used from Arczewska's Research	Type of Flexural Test	M13 - Method 1	M13 - Method 2
Correlated	3-Point	4.99%	3.57%
	4-Point	1.78%	0.65%
Tested	3-Point	3.87%	2.45%
	4-Point	0.66%	0.47%
(Calculated based on % differences between values by Arczewska (2017) and 3-Point or 4-Point Bending using Method 1 or Method 2 Calculations from this research work)			

From Tables 5.17 to 5.19, it is evident that the difference is small for all compared values for the M12/13 specimens, indicating the results are very similar, further proving the accuracy of the correlation calculations. With the correlated tensile capacities for the M13 specimens from this research, it is shown that they are close to Arczewska's M12 correlated tensile strength values, having a difference of almost less than 5%. It is important to note that in Arczewska's correlation calculations, the effective volume of a direct tensile test was calculated using a GFRP bar size used as a direct tensile test specimen, where the full cross-section is intact. This varies with the effective volume of a direct tensile test calculation presented in this thesis, where the volume was calculated modelling the volume of a flexure specimen. Even when comparing to Arczewska's tested M12 strength from direct tensile testing, the percentage difference below 4% as well.

It is evident that results from 3-point bending for all parameters are closer to Arczewska's results compared to 4-point bending. This could be an indication that 3-point bending yields better correlations to 4-point bending. However, for the comparison of the correlated values, it should be noted that Arczewska only completed 3-point bending tests, which could be why the corresponding percentage differences in correlated tensile capacities are very small.

Discrepancies between Arczewska's results and the results presented in this research is the result of notable difference in procedure such as:

- Using different effective volume of tensile stress of direct tensile calculations, where Arczewska uses the typical volume of the free length of tensile specimen, based on ASTM D7205 specifications (ASTM Committee D30, 2016). This research uses the volume of the flexure specimen, based on ASTM D4476 (ASTM Committee D20, 2014).
- The GFRP bar sizes that were compared are of different batches that are formed years apart, in addition to having different core diameters. The M12 bars tested by Arczewska had a core diameter of 12 mm, and the M13 bar tested in this research program has a core diameter of 13 mm.

Table 5.20 to Table 5.23 also has a similar comparison of parameters and results for the M15 specimens to Arczewska's M16 specimens.

Table 5.20: Comparison of Key Parameters from Current Researched M15 and Previously Researched M16 GFRP Bars

Specimen Size	Type of Flexural Test	M15 - Method 1	M15 - Method 2	Arczewska's M16
Rupture (Tensile) Stress, σ_r (MPa)	3-Point	1875.55	1854.44	1923.00
	4-Point	1697.76	1678.67	-
V_{Eb} (mm^3)	3-Point	7.41	7.41	2.08
	4-Point	44.80	44.80	-
V_{Et} (mm^3)	3-Point	15018.34	15018.34	128614.40
	4-Point	14745.19	14745.19	-
Weibull Modulus, m	3-Point	15	15	24
	4-Point	15	15	-
$\sigma_b/\sigma_t = (V_{Et}/V_{Eb})^{1/m}$	3-Point	1.64	1.64	1.58
	4-Point	1.41	1.41	-
Correlated Tensile Strength, $\sigma_{t,calc}$ (MPa)	3-Point	1146.89	1133.97	1214.02
	4-Point	1217.12	1203.44	-
σ_b/σ_t from testing	3-Point	1.47	1.45	1.51
	4-Point	1.33	1.31	-

Table 5.21: Difference for Key Parameters Between based on Current Research Work and Arczewska (2017) and Previous Research for M15 GFRP Bars

Parameters	Type of Flexural Test	M15 - Method 1	M15 - Method 2
Rupture (Tensile) Stress, σ_r (MPa)	3-Point	2.50%	3.63%
	4-Point	12.44%	13.57%
$\sigma_b/\sigma_t = (V_{Et}/V_{Eb})^{1/m}$	3-Point	3.60%	3.60%
	4-Point	11.63%	11.63%
Correlated Tensile Strength, $\sigma_{t,calc}$ (MPa)	3-Point	5.69%	6.82%
	4-Point	0.25%	0.88%
σ_b/σ_t from testing	3-Point	2.86%	3.99%
	4-Point	12.89%	14.01%
(Calculated based on % differences between values by Arczewska (2017) and 3-Point or 4-Point Bending using Method 1 or Method 2 Calculations from this research work)			

Table 5.22: Difference for σ_b/σ_t Between Current and Previous Research for M15 GFRP Bars

σ_t values used from Arczewska's Research	Type of Flexural Test	M15 - Method 1	M15 - Method 2
Correlated	3-Point	3.60%	3.60%
	4-Point	11.63%	11.63%
Tested	3-Point	8.13%	8.13%
	4-Point	7.11%	7.11%
(Calculated based on % differences between values by Arczewska (2017) and 3-Point or 4-Point Bending using Method 1 or Method 2 Calculations from this research work)			

Table 5.23: Percentage Difference for Tensile Capacities Between Current and Previous Research for M15 GFRP Bars

σ_t values used from Arczewska's Research	Type of Flexural Test	M15 - Method 1	M15 - Method 2
Correlated	3-Point	5.69%	6.82%
	4-Point	0.25%	0.88%
Tested	3-Point	10.19%	11.32%
	4-Point	4.25%	5.38%
Calculated based on % differences between values by Arczewska (2017) and 3-Point or 4-Point Bending using Method 1 or Method 2 Calculations from this research work)			

The differences are higher than with the comparison of the M13 specimens to Arczewska's M12. However, this could be attributed to the different batch of each type of specimen. The percentage

differences of the tensile capacities are not drastically different from one another, since the percentage difference between both results are no more than 12%. It is evident that the 4-point bending test results and correlations for the M15 bars have a less percentage difference when compare to Arczewska's M16 correlated tensile strength, indicating that 4-point bending is more accurate than 3-point bending.

5.5.3 Comparison with Others' Research Work

Due to the lack of present data for the tensile capacity of GFRP bars to be compared to this research, data from other researchers were sought out. However, due to lack of similarity between tensile tests from these researchers, only the straight 15mm diameter bars from Johnson (2014) was suitable to compare this research work to. The dimensions and specifications of this bar are listed in Table 5.24. Figure 5.12 provides a visual comparison of correlated tensile capacities of the relevant GFRP bar sizes compared to Johnson's results, which is further discussed below, in which the presented tables display differences in the results.

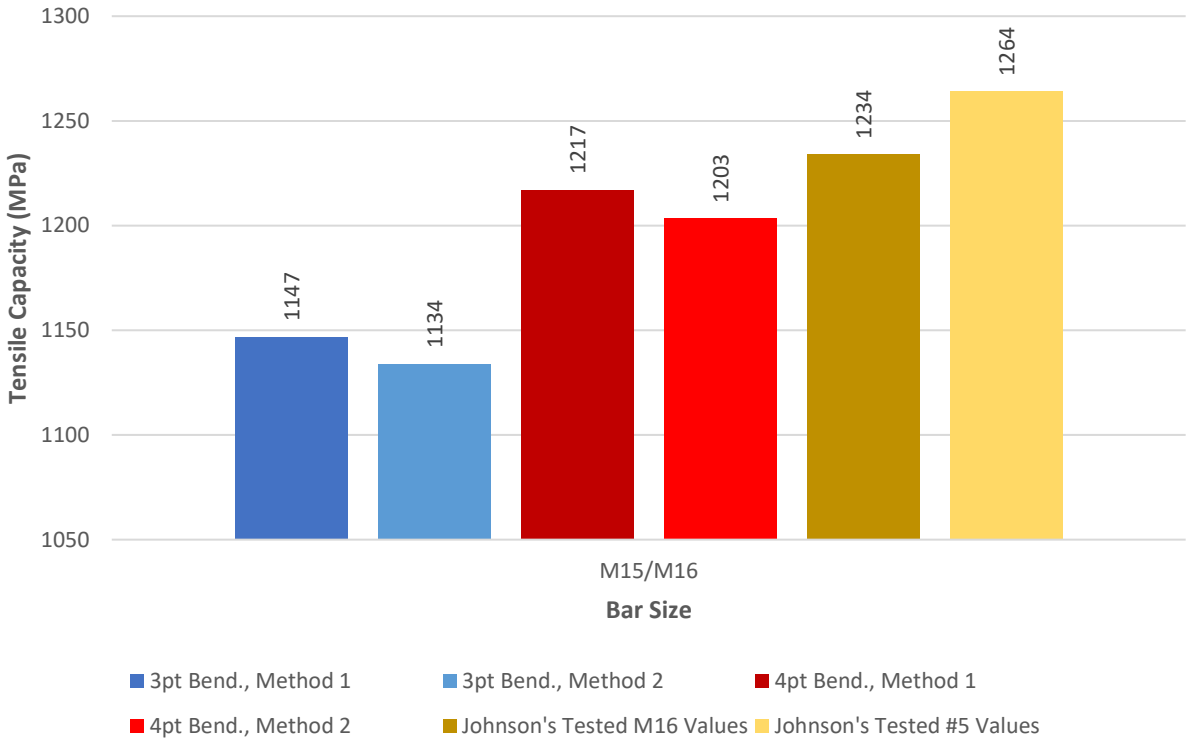

Figure 5.12: Comparison of Correlated Tensile Capacities versus Johnson's (2014) Results

Table 5.25 contains a summary of the tensile stiffness and strength of the M15 bars and Johnson's specimens.

Table 5.24: Dimensions of GFRP Specimens from Johnson's (2014) Research Work

Type of Bar	Bar Designation	Inner Diameter (mm)	Outer Diameter (mm)	Area (mm^2)
Ribbed	M15	16.3	18	200
Sand-Coated	#5 B1	17.5	19.2	197.9

Table 5.25: Comparison of Tensile Elastic Modulus and Capacity from Current Researched M15 and Johnson's M16 Specimens

Specimen	Modulus of Elasticity (MPa)	Tested Tensile Strength (MPa)	Correlated Tensile Strength - Method 1 (MPa)	Correlated Tensile Strength - Method 2 (MPa)
M15 (3-Point Bending)	74968.56	1209.08	1146.89	1133.97
M15 (4-Point Bending)			1217.12	1203.44
Johnson's M16	61000	1234	---	---
Johnson's #5 B1	71000	1264	---	---

From Table 5.24, it should be noted that the M15 bars are ribbed, much similar to the M15 bars contained in this research, which makes a desirable comparison. For the other set of bars however, they are sand-coated and have slightly different inner diameters than 16mm. Despite these two changes, comparisons will be made with the M15 bars from this research, which will provide insight on how well the correlation calculations work for bars that are clearly not the same type. Table 5.26 provides the percentage difference between the tensile stiffnesses and tensile capacities from both research works.

Table 5.26: Percentage Error Between Tensile Strength from Johnson's (2014) Research

Specimen	Method 1		Method 2	
	M16 (3-Point Bending)	M16 (4-Point Bending)	M16 (3-Point Bending)	M16 (4-Point Bending)
Johnson's M16	7.32%	1.38%	8.45%	2.51%
Johnson's #5 B1	9.72%	3.78%	10.84%	4.91%

It is evident that there is a correlation between the tensile strength of the M15 specimens from this research in both methods compared to the M15 and #5 B1 specimens from Johnson's research, as the errors are less than 11% overall. These percentage differences are about the same from Table 5.23 with Arczewska's M16 bars, indicating that the comparisons are very similar; the correlated calculations work are comparable to values from direct tensile tests, showing this method works, albeit with minor errors. Between 3-point and 4-point bending, the percentage errors indicate that the 4-point bending tests are slightly more accurate compared to 3-point bending.

This comparison provides further indication that the correlations from the rupture modulus can apply not only to different batches of the similar type of GFRP (i.e. ribbed) bar of the same size, but to other

types as well (i.e. sand-coated). More research and testing should be completed for GFRP bars of different batches and different types to further investigate and valid the effectiveness of the correlation calculations from flexural testing to obtain the tensile strength.

Chapter 6 - Conclusion

The primary purpose of the presented work is to find an efficient and easy method of quality control testing of GFRP bars to assess their tensile capacity. This is necessary to enable more frequent usage of the material in practice. While completing a uniaxial direct tension test is the most direct and reliable way of getting tensile strength, it requires a lot of time and intricacies to set up the test properly, while having limitations based on the testing machine's capability to test a GFRP bar up to a certain size.

6.1 Summary and Conclusions

The research presented herein involves flexural testing of GFRP bars. The bars are cut longitudinally into two half sections to ensure tensile failure during flexural testing. Accurate measurements of the specimens' dimensions are crucial to capture the rupture modulus of the specimen, which is obtained after identifying the cracking load. The bi-moduli behaviour of the material is considered through the elastic moduli ratio of the specimens, which is also required to calculate the rupture modulus. Two methods of calculation were completed based on having a elastic moduli ratio of $\frac{E_t}{E_c} = 1.25$ and 1.2 respectively, to demonstrate the accuracy of using these ratio values from prior research (Jones, 1978; Jones, 1977), as well as showing the difference in results.

The resulting rupture moduli of each specimen size are analyzed using Weibull's weakest link theory, which considers the probability of failure and flaw distribution in the GFRP bars. Using this statistical model, this enabled linking the failure of a GFRP bar from a flexural test to a tensile test, based on the effective volume of the specimen placed under tensile stress. The effective volume of a specimen subjected to bending is less for uniform tension, which is also reflected by the rupture modulus being larger than the direct tensile strength of a bar. Less volume means a smaller number of internal imperfections, and thus the discrepancy. This is a well-known phenomenon for brittle materials (Quinn & Quinn, 2010; Weil & Daniel, 1964).

The calculations of the effective volume vary based on the type of test, specimen dimensions and material flaw distribution based on the results of the Weibull plots. The resulting statistical relationship results in the formation of the ratio between rupture modulus to the tensile capacity of a GFRP bar. Calculating the correlated tensile capacity is the product of this ratio and the rupture modulus.

The results of comparing the correlated tensile capacities (from flexure tests) to the direct tensile tests conducted on available specimens of M8, M13 and M15 GFRP bar sizes shows a difference of 7% for the M13 and M15 specimens. Since this difference is low, this validates the accuracy in using a flexural test to seek a GFRP bar's tensile strength. However, for the difference between the correlated and tested tensile capacities for the M8 specimens reach up to 19%, which could be a result of variations and errors in test methods. All results from 3-point bending calculations were noted to have lower differences compared to results from 4-point bending.

Due to the lack of available information and resources to obtain the measured tensile capacity of the of larger sized GFRP bars like the M25 and M32, comparisons to the correlated tensile strengths presented in this thesis have not been made. However, in comparison to Fiberline's technical information (2017),

the correlated strength of these bars are confirmed to be over 1000 MPa, as listed. Furthermore, it is clearly shown that the correlated tensile capacity of these larger bars is less than the smaller sized bars, which appeals to the nature of brittle of materials and validates the application of the correlation calculations for bigger sized GFRP bars. Additional research should be done to compare and validate the correlated tensile strengths of these bars to measured tensile strengths. It should be noted that direct tensile testing of these large diameter bars is difficult because the bars are very strong, which require high capacity testing frames. Also, for large bar diameters, the length of the tensile specimens must be very long, which required very tall testing frames.

Examining the tensile capacities from other sources, the following observations are made:

- In comparison with the specification sheets (indicated in Table 5.15) provided from Fiberline, the percentage differences between the reported tensile capacity of the GFRP bars compared to the correlated tensile strengths are no greater than 20%, for both results from 3-point and 4-point bending tests.
- In comparison with Arczewska's (2017) correlated tensile capacities (indicated in Table 5.19 and Table 5.23), the percentage differences are low. There is a 4.99% difference between the correlated tensile strength of the M13 bars in this research to the correlated and tested tensile capacities from the M12 specimens (2017). Likewise, there is a 11.32% difference between the corelated strengths of the M15 bars in this research to the correlated and tested tensile capacities of from the M16 specimens. In the comparisons of the Arczewska's M12 specimens to the M13 specimens (2017). The differences with the correlated tensile capacities from 4-point bending tests are lower than the correlated tensile capacities from 3-point bending for all comparisons.
- The percentage difference between Johnson's (2014) M16 specimens in direct tension testing versus the correlated tensile capacity of the M15 GFRP bars are about 11%. The percentage difference of the 4-point bending correlated tensile strengths is lower compared to the 3-point bending.

Based on the researched conducted in this thesis, the following conclusions can be offered:

- The flexure testing of GFRP bars is a simple and efficient methodology for determination of tensile strength of GFRP bars.
    - The advantage in using flexure tests instead of direct tensile tests is its simplicity and cost. Computation procedures based on the Weibull's Weakest Link Model are used to determine the tensile strength. It can be successfully used for quality control of the GFRP bars; allowing for safer utilization of the bars in concrete construction.
    - As outlined in this research, the difference between the correlated tensile capacities to tested tensile capacities are generally low, proving the accuracy for bars of the same size, as well as different types and batches potentially.
- Both 3-point and 4-point bending tests can be used for correlating rupture moduli with the corresponding tensile strength of the GFRP bars.
    - The results from both a 3-point and 40point bending tests prove to exceed the manufacturer's guaranteed tensile capacity of 1000 MPa, indicating that the correlations from both types of test are accurate.

    - The 4-point bending tests of GFRP bars have a larger volume under tensile stress compared to 3-point bending. Also, the area of maximum stresses is larger. For this reason, it is often preferred over the 3-point bending test, for the determination of tensile strength of brittle materials. The results of the correlated tensile strength of a GFRP bar from 4-point bending to 3-point bending are similar, having a percent difference of less than 10% (shown in Table 5.10).
    - In comparison with GFRP tensile strengths from other sources, there this no clear indication on whether the correlated tensile capacities of a 3-point bending test is better than a 4-bending test. This is based on the varying differences being larger for 3-point in comparison to results from other research works (Arczewska, 2017; Johnson, 2014), but lower in comparison to the results from direst tensile tests and specification sheets. It should also be noted that the discrepancies from results of 3-point bending are consistently lower compared to the results from 4-point bending.
    - A 3-point bending test is an adequate configuration for the determination of tensile strength of GFRP bars. It can be argued that it is easier to conduct than 4-point bending, and thus can be preferable without jeopardizing the accuracy of results.
- Proper adoption of the ratio of elastic moduli in tension and compression is important for accuracy of the results.
    - In comparing results from the two different methods of calculation of tensile capacity from the flexural test, Methods 1 and 2, various sets of data outlined in Chapter 5 indicate that it is unclear on which Method of calculation is more accurate. Method 1 has a lower differences in some of the comparisons with the direct tensile results (Table 5.14), specification sheets (Table 5.15), and a part of some external sources (Johnson, 2014), while displaying a higher difference with all other comparisons (Arczewska, 2017).

6.2 Future Work, Comments & Recommendations

There are several recommendations that should be considered for future work to further validate and improve testing. Some of these recommendations are as follows:

- Include LVDTs for more accurate displacement values of GFRP specimen in flexural tests. This could enable more accurately analyses utilizing the displacements in the flexural tests.
- Test as many sizes as possible in direct tension, especially with the larger bars, in order to validate the results.
- Test GFRP bars from other manufacturers and different sizes, others than ones specified in this thesis– in order to see if the correlation calculations, hold true for all types of GFRP bars, regardless of manufacturer. The ratio of the tensile and compressive elastic moduli should be the same among the tested GFRP bars, to maintain consistency.
- Test straight segments from curved or hooked GFRP bars, since those bars are formed in a different manner compared to straight GFRP bars.
- Complete testing with the same size and batch of bar, to eliminate the variability.
- Complete testing on different bar sizes to validate the correlation calculations working for various types of GFRP bars.
- Compressive testing could be completed to see the actual ratio of tensile to compressive elastic moduli.

- For tensile testing, ensure that alignment rings are well fastened and snugged-tightly in the anchor, to ensure no expansive grout leaks after pouring, and the GFRP bar will not misalign due to alignment ring displacement due to curing of expansive grout (pushing alignment ring out).
- Complete correlation calculations using a tensile elastic moduli ratio of $\frac{E_t}{E_c} > 1.25$ and $\frac{E_t}{E_c} < 1.2$, and compare it to other results.
- Complete comparisons using the maximum possible loading from the flexure test, while modifying correlation calculations necessary to minimize errors in the correlation.
- Complete comparisons and analyzes of the GFRP strengths observing the 95th percentile of the tests, since this is reliability threshold used in engineering design work.

Another possible improvement could be utilizing the deflection equations of the GFRP bars in the flexural testing to calculate the elastic moduli ratio. Completing this task would enable an easier method of obtaining the elastic moduli, and would make the flexural testing a self-contained method to obtain all required variables for this set of correlation calculations. In addition to correlation concepts outlined in this thesis, this method of using deflection uses findings from other research work to relate the flexure elastic modulus to the elastic moduli ratio of GFRP (Mujika et al., 2006). This task was a possible objective of this research work; however, an issue arose where the returned values from the elastic moduli appeared to be too different that what a normal GFRP bar would exhibit.

The result of this is due to oversimplification in the calculations from the flexural test setup and lack of information. One assumption made was that the supports are frictionless, which in reality is not true, and directly affects the deflections. Also, the assumption of small deflections does not apply to bending of half section of GFRP bars. Further development of capturing the realistic characteristics of the flexural test may lead to the improvement of using this method to calculate the rupture modulus. Appendix G outlines the set of equations used in to describe this analysis. These equations are provided for information only, as they would lead to determination of correct equations to conduct this analysis. In the calculations presented in this thesis, a constant ratio of $n = \frac{E_t}{E_c}$ was used.

Letters of Copyright Permission

The letters/agreements that provided permission for the use of figures reproduced from other publications are provided in the following pages:

INSERT Letters of copyright – PAGE 1 OF 10

INSERT Letters of copyright – PAGE 2 OF 10

INSERT Letters of copyright – PAGE 4 OF 10

INSERT Letters of copyright – PAGE 5 OF 10

INSERT Letters of copyright – PAGE 10 OF 10

References

ACI Committee 440. (2012). ACI 440.3R-12 - Guide Test Methods for Fiber-Reinforced Polymers (FRPs) for Reinforcing or Strengthening Concrete Structures. United States of America: American Concrete Institute.

ACI Committee 440. (2015). ACI 440.1R-15 Guide for the Design and Construction of Structural Concrete Rinforced with Fiber-Reinforced Polymer (FRP) Bars. Farmington Hills, Michigan, United States of America: American Concrete Institute.

ACI Committee E-701. (2000). ACI Education Bulletin E2-00 - Reinforcement for Concrete - Materials and Applications. United States of America: American Concrete Institute.

Ahmed, E. A., Benmokrane, B., & Sansfaçon, M. (2016, March 9). Case Study: Design, Construction, and Performance of the La Chancelière Parking Garage's Concrete Flat Slabs Reinforced with GFRP Bars. American Society of Civil Engineers. doi:https://doi.org/10.1061/(ASCE)CC.1943-5614.0000656

Aimran, A. (2014). A comparison between single exponential smoothing (SES), double exponential smoothing (DES), holt's (brown) and adaptive response rate exponential smoothing (ARRES) techniques in forecasting Malaysia population. *Global Journal of Mathematical Analysis*, 276-280.

Arczewska, P. (2017). *Practical Performance Criteria and Durability Prediction Modeling of Glass Fiber Reinforced Polymer (GFRP) Bars.* University of Waterloo, Department of Civil and Environmental Engineering. Waterloo: University of Waterloo.

Arczewska, P., Polak, M., & Penlidis, A. (2019). Relation between Tensile Strength and Modulus of Rupture for GFRP Reinforcing Bars. *Journal of Material in Civil Engineering, 31*(2). doi:10.1061/(ASCE)MT.1943-5533.0002575

ASTM Committee D20. (2014, May). ASTM D4476/D4476M-14 - Standard Test Method for Flexural Properties of Fiber Reinforced Pultruded Plastic Rods. West Conshokocken, Pennsylvania, United States of America: American Society for Testing and Materials. doi:10.1520/D4476_D4476M-14

ASTM Committee D20. (2017, July). ASTM D790-17 - Standard Test Methods for Flexural Properties of Unreinforced and Reinforced Plastics and Electrical Insulating Materials. West Conshohocken, Pennsylvania, United States of America: American Society for Testing and Materials. doi:10.1520/D0790-17

ASTM Committee D30. (2015, May). ASTM D7264/D7264M-15 - Standard Test Method for Flexural Properties of Polymer Matrix Composite Materials. West Conshohocken, Pennsylvania, United States of America: American Society for Testing and Materials. doi:10.1520/D7264_D7264M-15

ASTM Committee D30. (2016, November). ASTM D7205/D7205M-06 - Standard Test Method for Tensile Properties of Fiber Reinforced Polymer Matrix Composite Bars. West Conshohocken, Pennsylvania, United States of America: American Society for Testing and Materials. doi:10.1520/D7205_D7205M-06R16

Balendran, R. V., Rana, T. M., Maqsood, T., & Tang, W. C. (2002). Application of FRP bars as reinforcement in civil engineering structures. *Structural Survey Vol. 20 No. 2*, 62-72.

Beer, F. P., Johnston, E. R., Dewolf, J. T., & Mazurek, D. F. (2012). *Mechanics of Materials* (6th ed.). New York, United States of America: McGraw-Hill.

Benmokrane, B., Ali, A. H., Mohamed, H. M., ElSafty, A., & Manlo, A. (2017, February). Laboratory Assessment and durability performacne of vinyl-ester polyester, and epoxy glass-FRP bars for concrete structures. *Composites Part B*(114), 163-174. doi:10.1016

Benmokrane, B., Chaallal, O., & Masmoudi, R. (1995, February 1). Glass fibre reinforced plastic (GFRP) rebars for concrete structures. *Construction and Building Materials, 9*(6), 353-364.

Benmokrane, B., Masmoudi, R., & Zhang, B. (2006, July). New Method for Testing Fiber-reinforced Polymer Rods Under Flexure. *Journal of Testing and Evaluation, 35*(2), 171-176.

Castro, P. F., & Carino, N. J. (1998). Tensile and Nondestructive Testing of FRP Bars. *Journal of Composite For Construction*, 17-27.

CSA. (2010, March). CSA S807-10 Specification for fibre-reinforced polymers. Mississauga, Ontario, Canada: Canadian Standards Association.

CSA. (2012, March). CSA S806-12 - Design and construction of building structures with fibre-reinforced polymers. Mississauga, Ontario, Canada: Canadian Standards Association.

El-Salakawy, E., & Rubiat, M. (2014, January 21). Repair of GFRP-Reinforced Concrete Bridge Barriers. *Journal of Bridge Engineering, 19*(6). doi:https://doi.org/10.1061/(ASCE)BE.1943-5592.0000584

Erki, M. A., & Rizkalla, S. H. (1993). Anchorage For FRP. *Concrete International, 15*(6), 54-59.

Fiberline Composites. (2017). ComBAR® by Fiberline Technical Information. Retrieved 2019

Fiberline Composites. (n.d.). ComBAR® by Fiberline Technical Information. Retrieved from www.fiberline.com

Gardiner, G. (2009, 25 3). The Making of Glass Fiber. CompositesWorld. Retrieved September 7, 2019, from https://www.compositesworld.com/articles/the-making-of-glass-fiber

Gardiner, G. (2020, June 1). *The making of glass fiber*. Retrieved from CompositesWorld: https://www.compositesworld.com/articles/the-making-of-glass-fiber

Griffith, A. A. (1921). The phenomena of rupture and flow in solids. *Philosophical Transactions of the Royal Society of London. Series A, Containing Papers of a Mathematical or Physical Character, 221*, 163-198. doi:https://doi.org/10.1098/rsta.1921.0006

Johnson, D. T. (2014). *Investigation of Glass Fibre Reinforced Polymer (GFRP) Bars as Internal Reinforcement for Concrete Structures.* University of Toronto, Department of Civil Engineering. Toronto: University of Toronto.

Jones, R. M. (1977). Stress-Strain Relations for Materials with Different Moduli in Tension and Compression. *AIAA Journal, 15*(1), 16-23.

Jones, R. M. (1978). *Mechanics of Composite Materials With Different Moduli in Tension and Compression.* Southern Methodist University, Civil and Mechanical Engineering Department. Dallas: Air Force Office of Scientific Research.

Kocaoz, S., Samaranayake, V. A., & Nanni, A. (2004, August 5). Tensile characterization of glass FRP bars. *Composites Part B: Engineering*, 127-134. doi:10.1016/j.compositesb.2004.05.004

Koch, M., & Lupton, D. (2006, October 24). Design and Manufacture of Bushings for Glass Fibre Production. Hanau, Hesse, Germany: W. C. Heraeus GmbH, Engineered Materials Division.

Loewenstein, K. L. (1993). The Manufacture of Continuous Glass Fibres. 3rd revised ed. Elsevier.

Maranan, G. B., Manalo, A. C., Karunasena, W., Benmokrane, B., & Lutze, D. (2014). Flexural behaviour of glass fibre reinforced polymers (GFRP) bars sujected to elevated temperature. *23rd Australasian Conference on the Mechanics of Structures and Materials. 1*, pp. 187-192. Lismore: Southern Cross University.

Medri, G. (1982, January). A Nonlinear Elastic Model for Isotropic Materials With Different Behavior in Tension and Compression. *Journal of Engineering Materials and Technology, 104*(1), 26-28.

Mohamed, H. M., & Benmokrane, B. (2013, October 3). Design and Performance of Reinforced Concrete Water Chloration Tank Totally Reinforced with GFRP: Case Study. *Image*. American Society of Civil Engineers. doi:https://doi.org/10.1061/(ASCE)CC.1943-5614.0000429

Mujika, F., Carbajal, N., Arrese, A., & Mondragon, I. (2006). Determination of tensile and compressive moduli by flexural tests. *Polymer Testing, 25*, 766-771. doi:10.1016/j.polymertesting.2006.05.003

NC State University. (2011, January 25). *Double Exponential Smoothing: Approaches to Forecasting : A Tutorial*. Retrieved from NC State University: https://scm.ncsu.edu/scm-articles/article/double-exponential-smoothing-approaches-to-forecasting-a-tutorial#1

NIST/SEMATECH. (2013, October 30). *Double Exponential Smoothing*. Retrieved from e-Handbook of Statistical Methods: https://www.itl.nist.gov/div898/handbook/pmc/section4/pmc433.htm

Performity LLC/Greg Stanley and Associates. (n.d.). *A Guide to Filtering of Single Variables*. Retrieved from Greg Stanley and Associates: https://gregstanleyandassociates.com/whitepapers/FaultDiagnosis/Filtering/filtering.htm

Pierce, R. (2017, July 7). *Percentage Difference, Percentage Error, Percentage Change*. Retrieved from Math Is Fun: http://www.mathsisfun.com/data/percentage-difference-vs-error.html

Quinn, G. D. (2003). Weibull Strength Scaling for Standardized Rectangular Flexure Specimens. *Journal of the American Ceramic Society, 86*(3), 508-510.

Quinn, G. D., Sparenberg, B. T., Koshy, P., Ives, L. K., Jahanmir, S., & Arola, D. D. (2009). Flexural Strength of Ceramic and Glass Rods. *Journal of Testing and Evaluation, 37*(3), 222-244. doi:10.1520/JTE101649

Quinn, J. B., & Quinn, G. D. (2010). A practical and systematic review of Weibull statistics for reporting strengths of dental materials. *Dental Materials, 26*, 135-147. doi:10.1016/j.dental.2009.09.006

Stephanie. (2018, June 7). *Exponential Smoothing: Definition of Simple, Double and Triple*. Retrieved from Statistics How To: https://www.statisticshowto.com/exponential-smoothing/

Tripathi, V. K. (2003). *Standardization of Test Methods for Property Evaluation of FRP Bars.* West Virginia University, Department of Civil and Environmental Engineering. Morgantown: West Virginia University.

Tu, J. W., Guo, D. L., Mei, S. T., Jiang, H. C., & Li, X. P. (2015). Three-parameter Weibull distribution model for tensile strength of GFRP bars bases on experimental tests. *Materials Research Innovations, 19*(5), 1191-1196. doi:10.1179/1432891714Z.0000000001276

Tuf-Bar. (n.d.). Advantages of Using Glass Fiber Reinforced Polymer (GFRP) Rebar. Retrieved September 8, 2019, from https://www.tuf-bar.com/advantages-of-using-glass-fiber-reinforced-polymer-gfrp-rebar/

Tuf-Bar. (n.d.). What are the Constituents of Fiber Reinforced Polymers (FRP) Bars? Retrieved September 8, 2019, from https://www.tuf-bar.com/what-are-the-constituents-of-fiber-reinforced-polymer-frp-bars/

Weil, N. A., & Daniel, I. M. (1964). Analysis of Fracture Probabilities in Nonuniformly Stressed Brittle Materials. *Journal of The American Ceramic Society, 47*(6), 268-274.

Appendix A - GFRP Bar Information

Product description

ComBAR® was conceptualized as internal reinforcement in concrete members. The mechanical properties and bond properties are comparable to those of steel rebar. The material properties were determined for predominantly static loads in central European and North American climates. They are certified for a design service life of 100 years.

ComBAR® bars are linearly elastic up to failure. For all bar diameters it occurs at stresses well above 1,000 MPa. As a result of the comparatively low modulus of elasticity of ComBAR® (≥ 60 GPa), the failure of ComBAR® reinforced concrete members is preceded by large deflections. When the load is removed the deflection returns to near zero.

ComBAR® bars with end heads can be installed where geometric constraints require reduced development lengths. Double headed bars are ideally suited as shear and punching shear reinforcement in beams and slabs.

ComBAR® bars can not be permanently deformed or bent. If a straight bar is bent it returns to its original shape as soon as the applied force is removed. Bars with small diameters can be bent elastically (circular tunnel cross-sections). Customised bent bars and stirrups are prefabricated at the shop.

ComBAR® bent bars have been durability-tested for a service life up to 100 years.

Material characteristics Fields of application

• high corrosion resistance	=>	open and underground parking garages, bridge caps, barrier walls, curbs, sidewalks, approach slabs, wing walls, slim facade elements, shore line stabilization, hydraulic engineering
• high chemical resistance	=>	industrial floors, industrial containers, sewage-treatment plants, agricultural facilities
• electrically non-conductive	=>	transformers, reactors / inductors, machinery with high field-strengths, non ballasted rail slabs (signals and switches of railways)
• non-magnetic	=>	sensitive electronic equipment, structural biology, nano technology, quantum physics, MRIs, non ballasted rail slabs
• ease of machining	=>	shaft walls in tunnelling, formwork anchors, temporary structures
• very low thermal conductivity	=>	energy conservation in housing construction

Comparison reinforcement materials

property	steel rebar	stainless steel rebar	Fiberline ComBAR®
ultimate tensile strength (MPa)	> 500[1)]	655	> 1,000
ultimate elongation (‰)	> 25[1)]	50	> 16.7
elastic modulus E (GPa)	200	190	> 60
bond strength (MPa)	13.7	13.7	12.2[2)]
min. required concrete cover (mm)	40 (exposed) 30 (unexposed)	< 30	d_b + 10 mm
density (g/cm3)	7.85	7.92	2.2
thermal conductivity (W/mK)	60	16	< 0.5
coefficient of thermal expansion (1/K)	0.8 to 1.2 x 10^{-5}	1.73 x 10^{-5}	0.6 x 10^{-5} (axial) 2.2 x 10^{-5} (radial)
specific resistance (μΩcm)	1 – 2 x 10^{-5}	7.2 x 10^{-5}	> 10^{12}
magnetism	yes	slightly	no

[1)] for grade 400R steel rebar
[2)] values for 16 mm ComBAR® bars (certification of compliance with ISIS specifications/CSA S807, University of Toronto)
Sources for material values of steel and stainless steel on request.

Product data sheet of straight bars

Bar sizes, dimensions, weights, ultimate tensile strength

ComBAR® bar	designated diameter (ACI/CSA)	core diameter (mm)	exterior diameter (mm)	cross-sectional area[1] (mm^2)	specific weight (kg/m)
ø 8	M8	8	9	50.3	0.13
ø 13	M13	13	14.5	132	0.34
ø 16	M15	16	18	201	0.53
ø 20	M20	20	22	314	0.80
ø 25	M25	25	27	491	1.22
ø 32	M32	32	34	804	1.93

[1] Determination of load-bearing cross-sectional area:
The load bearing cross-sectional area of ComBAR® bars is the area of the core. The ribs are not included, as they do not contribute to the tensile capacity of the bars. To determine the load-bearing core cross-sectional area of the perfectly round ComBAR® bars the exterior diameter is measured using callipers. Twice the depth of the ribs, measured with callipers, is subtracted from this value to determine the core diameter.

Material properties of straight bars

properties	terms	values	comments
ultimate tensile strength	f_u	> 1,000 MPa	all bar diameters
1,000 hour tensile strength [1]	F_{k1000h}	950 MPa	5th percentile
logarithmic temporal slope [1]	R_{10}	< 15 %	5th percentile
modulus of elasticity	E_f	> 63.5 GPa	8, 12, 16, 25 mm [2]
ultimate elongation	ε_{Fu}	1.67%	ø 16mm bar [2]
bond strength	τ_F	12.2 MPa	ø 16mm bar
bar surface profile factor (bond)	k5	≤ 1.0	(CSA S806 9.3)
bond coefficient	k_b	0.6 [3]	(CHBDC 16.8.2.3)
bar surface factor	k_4	≤ 0.8	(CHBDC 16.8.4.1)
transverse shear strength [4]	t	≥ 180 MPa	acc. CSA / ACI
min. concrete cover	min. c	d + 10 mm/d + 5 mm (pre-cast)	min. cover for load transfer
fibre content	–	> 75% (vol.)	no secondary fibres or fillers
void ratio	–	< 1%	–

[1] values for determination of design value of tensile strength according to durability concept of fib defining time-to-failure lines (see page 15)
[2] values for 16mm ComBAR® bars (certification of compliance with ISIS specifications/CSA S807, University of Toronto); certifications for 8, 12, 16, 25 mm bars completed
[3] value determined for ComBAR® bars of all diameters
[4] values in tests according to CSA / ACI not for design of dowels. Ongoing test series show substantially higher values.

The Quality of all components of the ComBAR® reinforcement system is continuously tested as part of the Quality Control program of Fiberline Composites

FIBERLINE COMPOSITES

Quality Control Certificate - ComBAR GFRP

GFRP Reinforcement, supplied by Fiberline Composites Canada Inc.

Diameter (mm)		**13**	**Straight**
Grade			III
Type of Resin			Vinyl-Ester
Primary Fibre Type			EC-R Glass
Fibre Content (by Volume)			≥75%
Type of Manufacturing Process			Pultrusion
Lot Identification			Change of Resin/Additive…
GFRP Lot No.:			**8033245**
Resin Lot. No.:			8033246
Production Period:	**07-02-2016**	**to**	**16-03-2016**
Total Length in this Lot (m)			25,000

	Cross-Sectional Area *(Core Area Measurement)*				
	Specimen	***Area (mm^2)***	***Min. Value***	***Ave. Value***	***St. Dev.***
1	1	140.10	138.40	139.30	0.620
	2	139.10			
	3	139.40			
	4	139.50			
	5	138.40			

	Longitudinal Tensile Strength (*CSA-S806 Annex C)*				
	Specimen	***Tensile Strength (MPa)***	***Min. Value***	***Ave. Value***	***St. Dev.***
2	1	1,566.00	1,363.00	1,487.40	79.63
	2	1,497.00			
	3	1,544.00			
	4	1,467.00			
	5	1,363.00			

	Longitudinal Tensile Modulus (*CSA-S806 Annex C)*				
	Specimen	***Longitudinal E (GPa)***	***Min. Value***	***Ave. Value***	***St. Dev.***
3	1	63.50	61.20	62.22	1.139
	2	61.30			
	3	61.70			
	4	63.40			
	5	61.20			

	Longitudinal Ultimate Elongation *(CSA-S806 Annex C)*				
	Specimen	***Ultimate Elongation (%)***	***Min. Value***	***Ave. Value***	***St. Dev.***
4	1	2.50	2.20	2.38	0.130
	2	2.40			
	3	2.50			
	4	2.30			
	5	2.20			

5	***Transverse Shear Strength*** *(CSA-S806 Annex N)*				
	Specimen	***Shear Strength (MPa)***	***Min. Value***	***Ave. Value***	***St. Dev.***
	1	261.00	215.00	244.80	25.36
	2	239.00			
	3	215.00			
	4	230.00			
	5	279.00			

6	***Fibre Content*** *(by weight, ASTM D2584)*				
	Specimen	***Fibre Content (%)***	***Min. Value***	***Ave. Value***	***St. Dev.***
	1	86.40	86.30	86.36	0.055
	2	86.40			
	3	86.40			
	4	86.30			
	5	86.30			

7	***Void Content*** *(ASTM D2734)*				
	Specimen	***Void Content (%)***	***Max. Value***	***Ave. Value***	***St. Dev.***
	1	0.5	0.9	0.82	0.179
	2	0.9			
		0.9			
		0.9			
	3	0.9			

0.96

8	***Water Absorption*** *(ASTM D570)*					
	Specimen	***Water Absorption (%)***		***Max. Value***	***Ave. Value***	***St. Dev.***
	1	Short Term (24h)	-	0.03	0.014	0.013
	2		-			
	3		0.02			
	4		0.03			
	5		0.02			
	1	Long Term (7 days)	0.01	0.38	0.09	0.162
	2		0.01			
	3		0.02			
	4		0.03			
	5		0.38			

9	***Cure Ratio*** *(CSA-S807 Appendix A)*				
	Specimen	***Cure Ratio (%)***	***Min. Value***	***Ave. Value***	***St. Dev.***
	1	99.7	97.9	99.2	0.787
	2	99.4			
	3	99.1			
	4	97.9			
	5	99.9			

10	***Wet Glass Transitition Temperature*** *(ASTM E1640)*				
	Specimen	***WGTT (°C)***	***Min. Value***	***Ave. Value***	***St. Dev.***
	1	168.00	158	164.2	4.494
	2	164.00			
	3	169.00			
	4	162.00			
	5	158.00			

FIBERLINE COMPOSITES

Quality Control Certificate - ComBAR GFRP

GFRP Reinforcement, supplied by Fiberline Composites Canada Inc.

Diameter (mm)			**16**	**Straight**
Grade				III
Type of Resin				Vinyl-Ester
Primary Fibre Type				EC-R Glass
Fibre Content (by Volume)				≥75%
Type of Manufacturing Process				Pultrusion
Lot Identification				Change of Resin/Additive…
GFRP Lot No.:				**8051973**
Resin Lot. No.:				8051974
Production Period:	**01-11-2016**	**to**	**22-11-2016**	
Total Length in this Lot (m)				85,055

	Cross-Sectional Area *(Core Area Measurement)*				
	Specimen	***Area (mm²)***	***Min. Value***	***Ave. Value***	***St. Dev.***
1	1	207.91	204.09	206.43	1.866
	2	208.67			
	3	206.12			
	4	205.36			
	5	204.09			

	Longitudinal Tensile Strength (*CSA-S806 Annex C)*				
	Specimen	***Tensile Strength (MPa)***	***Min. Value***	***Ave. Value***	***St. Dev.***
2	1	1,190.00	1,187.00	1,219.40	34.67
	2	1,246.00			
	3	1,209.00			
	4	1,187.00			
	5	1,265.00			

	Longitudinal Tensile Modulus (*CSA-S806 Annex C)*				
	Specimen	***Longitudinal E (GPa)***	***Min. Value***	***Ave. Value***	***St. Dev.***
3	1	61.06	61.06	65.30	2.626
	2	64.69			
	3	66.72			
	4	67.84			
	5	66.17			

	Longitudinal Ultimate Elongation *(CSA-S806 Annex C)*				
	Specimen	***Ultimate Elongation (%)***	***Min. Value***	***Ave. Value***	***St. Dev.***
4	1	1.90	1.70	1.84	0.089
	2	1.90			
	3	1.80			
	4	1.70			
	5	1.90			

5

Transverse Shear Strength *(CSA-S806 Annex N)*

Specimen	*Shear Strength (MPa)*	*Min. Value*	*Ave. Value*	*St. Dev.*
1	251.00			
2	234.30			
3	245.20	234.30	250.74	12.65
4	254.40			
5	268.80			

6

Fibre Content *(by weight, ASTM D2584)*

Specimen	*Fibre Content (%)*	*Min. Value*	*Ave. Value*	*St. Dev.*
1	87.01			
2	86.78			
3	86.70	86.70	86.88	0.134
4	86.98			
5	86.93			

7

Void Content *(ASTM D2734)*

Specimen	*Void Content (%)*	*Max. Value*	*Ave. Value*	*St. Dev.*
1	0.39			
2	0.44			
	0.30	0.95	0.50	0.257
	0.42			
3	0.95			

0.96

8

Water Absorption *(ASTM D570)*

Specimen	*Water Absorption (%)*		*Max. Value*	*Ave. Value*	*St. Dev.*
1	Short Term (24h)	0.06			
2		0.07			
3		0.02	0.07	0.044	0.021
4		0.03			
5		0.04			
1	Long Term (7 days)	0.21			
2		0.11			
3		0.06	0.21	0.102	0.064
4		0.06			
5		0.07			

9

Cure Ratio *(CSA-S807 Appendix A)*

Specimen	*Cure Ratio (%)*	*Min. Value*	*Ave. Value*	*St. Dev.*
1	99.27			
2	99.80			
3	98.38	98.38	99.12	0.533
4	99.30			
5	98.85			

10

Wet Glass Transitition Temperature *(ASTM E1640)*

Specimen	*WGTT (°C)*	*Min. Value*	*Ave. Value*	*St. Dev.*
1	159.82			
2	162.69			
3	159.70	159.7	162.52	3.193
4	162.83			
5	167.56			

FIBERLINE COMPOSITES

Quality Control Certificate - ComBAR GFRP

GFRP Reinforcement, supplied by Fiberline Composites Canada Inc.

Diameter (mm)			**20**	**Straight**
Grade				III
Type of Resin				Vinyl-Ester
Primary Fibre Type				EC-R Glass
Fibre Content (by Volume)				75%
Type of Manufacturing Process				Pultrusion
Lot Identification				Change of Resin/Additive…
GFRP Lot No.:				**032012**
Resin Lot. No.:				232912
Production Period:	***Bars:***	**23-03-2012**	**to**	**29-03-2012**

Total Length in this Lot (m) 29,000

	Cross-Sectional Area *(Core Diameter Measurement)*				
	Specimen	***Area (mm^2)***	***Min. Value***	***Ave. Value***	***St. Dev.***
1	1	323.50	322.22	325.06	2.44
	2	322.22			
	3	328.29			
	4	324.61			
	5	326.69			

	Longitudinal Tensile Strength (*CSA-S806 Annex C)*				
	Specimen	***Tensile Strength (MPa)***	***Min. Value***	***Ave. Value***	***St. Dev.***
2	1	1,278.00	1,264.00	1,278.80	9.12
	2	1,264.00			
	3	1,280.00			
	4	1,284.00			
	5	1,288.00			

	Longitudinal Tensile Modulus (*CSA-S806 Annex C)*				
	Specimen	***Longitudinal E (GPa)***	***Min. Value***	***Ave. Value***	***St. Dev.***
3	1	61.20	60.65	60.90	0.21
	2	60.80			
	3	60.65			
	4	61.00			
	5	60.85			

	Longitudinal Ultimate Elongation *(CSA-S806 Annex C)*				
	Specimen	***Ultimate Elongation (%)***	***Min. Value***	***Ave. Value***	***St. Dev.***
4	1	2.00	2.00	2.08	0.08
	2	2.10			
	3	2.20			
	4	2.10			
	5	2.00			

	Transverse Shear Strength *(CSA-S806 Annex N)*				
	Specimen	***Shear Strength (MPa)***	***Min. Value***	***Ave. Value***	***St. Dev.***
5	1	190.00	180	188	6.0
	2	180.00			
	3	184.00			
	4	195.00			
	5	191.00			

	Fibre Content (by weight)				
	Specimen	***Fibre Content (%)***	***Min. Value***	***Ave. Value***	***St. Dev.***
6	1	88.50	88.4	88.6	0.2
	2	88.40			
	3	88.40			
	4	88.90			
	5	88.70			

FIBERLINE COMPOSITES

Quality Control Certificate - ComBAR GFRP

GFRP Reinforcement, supplied by Fiberline Composites Canada Inc.

Diameter (mm)			**20**	**Straight**
Grade				III
Type of Resin				Vinyl-Ester
Primary Fibre Type				EC-R Glass
Fibre Content (by Volume)				75%
Type of Manufacturing Process				Pultrusion
Lot Identification				Change of Resin/Additive...
GFRP Lot No.:				**032012**
Resin Lot. No.:				232912
Production Period:	***Bars:***	**23-03-2012**	**to**	**29-03-2012**

Total Length in this Lot (m) 29,000

7 — ***Void Content*** *(ASTM D2734)*

Specimen	*Void Content (%)*	*Max. Value*	*Ave. Value*	*St. Dev.*
1	0.41	0.67	0.48	0.12
2	0.37			
3	0.67			
4	0.50			
5	0.44			

8 — ***Water Absorption*** *(ASTM D570)*

Specimen		*Water Absorption (%)*	*Max. Value*	*Ave. Value*	*St. Dev.*
1	Short Term (24h)	0.09	0.11	0.09	0.015
2		0.11			
3		0.08			
4		0.08			
5		0.07			
1	Long Term (7 days)	0.11	0.39	0.17	0.124
2		0.12			
3		0.39			
4		0.11			
5		0.11			

9 — ***Cure Ratio*** *(CSA-S807 Appendix A)*

Specimen	*Cure Ratio (%)*	*Min. Value*	*Ave. Value*	*St. Dev.*
1	98.7	97.9	98.7	0.515
2	97.9			
3	99.2			
4	99.1			
5	98.6			

10 — ***Wet Glass Transitition Temperature*** *(ASTM E1640)*

Specimen	*WGTT (°C)*	*Min. Value*	*Ave. Value*	*St. Dev.*
1	133.00	130.00	133.6	2.302
2	130.00			
3	134.00			
4	135.00			
5	136.00			

Appendix B - Flexure Specimen Parameters

B.1 M8 Specimens in 3-Point Bending

Variation A – Parameters calculated using all 10 specimens

Variation B – Parameters calculated using 8 specimens (omitting outliers)

Orange text denotes outliers

GFRP Parameters and Information			M8 Specimens										Using All Specimens			Excluding Lowest and Highest Rupture Modulus		
GFRP Admin Info	Specimen Number		M8-10	M8-9	M8-33	M8-24	M8-1	M8-25	M8-7	M8-21	M8-3	M8-30	Avg.	Std Dev.	C.O.V.	Avg.	Std Dev.	C.O.V.
	Test Number		11	12	13	14	15	31	32	33	34	35						
	Type of Flexural Test		3-point bending															
	Date of Test		September 25, 2020						October 2, 2019									
	Batch		All specimens cut from single bar, batch dated March 10, 2010															
	Additional Notes																	
Specimen Dimensions	Measured Height (excluding rib thickness; top of specimen to core; mm)	End 1	3.66	3.55	3.44	3.28	3.48	3.61	3.26	3.27	3.33	3.25						
		End 2	3.62	3.44	3.41	3.02	3.59	3.73	3.06	3.27	3.54	3.25						
		Avg.	3.64	3.495	3.425	3.15	3.535	3.67	3.16	3.27	3.435	3.25	3.403	0.188	6%	3.453	0.176	5%
	Measured Total Length (mm)		96	96	95	96	96	96	95	95	96	98	95.9	0.876	1%	95.75	0.463	0%
	Orginial Radius of GFRP, r (mm) =		4	4	4	4	4	4	4	4	4	4						
	Height of Specimen, h (mm) =		3.64	3.495	3.425	3.15	3.535	3.67	3.16	3.27	3.435	3.25	3.403	0.188	6%	3.4525	0.176	5%
	Length of Specimen, L (mm) =		80	80	80	80	80	80	80	80	80	80						
Test Data Information	Maximum Load per Loading Nose (kN)		0.996	0.973	0.925	0.735	1.028	1.009	0.791	0.847	0.970	0.753	0.903	0.111	12%	0.935	0.099	11%
	Deflection at Maximum Load (mm)		9.640	9.955	9.780	9.510	9.915	8.142	10.510	10.195	10.110	10.165	9.792	0.649	7%	9.656	0.653	7%
	Data Point of Maximum Loading		1928	1991	1956	1902	1983	1628	2102	2039	2022	2033						
	Maximum Deflection (mm)		9.910	36.280	18.035	24.425	12.675	8.582	16.690	13.615	16.150	16.225	17.259	8.027	47%	17.459	9.089	52%
	Total Data Points		1982	7256	3607	4885	2535	1717	3338	2723	3230	3249						
	Chosen Filtered Critical Point Load, P_{cr} (N)		982.940	941.208	902.467	708.162	1005.689	998.814	771.150	826.656	936.009	698.223	877.132	117.890	13%	912.743	101.204	11%
Method 1, Et/Ec = 1.25																		
Calculation of Unknown Values	Location of Neutral Axis from top of specimen, c (mm) =		1.626	1.557	1.524	1.395	1.576	1.640	1.400	1.451	1.529	1.442	1.514	0.089	6%	1.537	0.083	5%
	Rupture (Tensile) Stress, σ_t (MPa) =		2136.627	2252.595	2266.121	2170.702	2342.856	2129.441	2345.914	2317.596	2334.128	1986.366	2228.234	119.339	5%	2243.758	87.750	4%
	Compressive Stress, σ_c (MPa) =		1379.811	1447.862	1453.322	1380.424	1507.818	1376.535	1492.326	1479.191	1497.409	1267.013	1428.171	76.109	5%	1440.296	54.602	4%
	Maximum Bending Moment, M (Nmm) =		1.97E+04	1.88E+04	1.80E+04	1.42E+04	2.01E+04	2.00E+04	1.54E+04	1.65E+04	1.87E+04	1.40E+04	1.75E+04	2.36E+03	13%	1.83E+04	2024.086	11%
Variation A																		
Effective Tensile Volume Calculations	Chosen Weibull Modulus, m		22	22	22	22	22	22	22	22	22	22						
	Effective Tensile Volume Under Bending Stress, V_{eb} (mm^3)		0.441	0.417	0.405	0.359	0.423	0.446	0.361	0.379	0.406	0.376	0.401	0.032	8%	0.410	0.030	7%
	Effective Tensile Volume Under Direct Tensile Stress, V_{Et} (mm^3)		1780.531	1688.280	1643.891	1470.742	1713.691	1799.659	1476.997	1546.026	1650.225	1533.447	1630.349	119.067	7%	1661.631	111.392	7%
	$\sigma_b/\sigma_t = (V_{Et}/V_{Eb})^{1/m}$		1.458	1.459	1.459	1.459	1.459	1.458	1.459	1.459	1.459	1.459	1.459	0.000	0%	1.459	0.000	0%
Tensile Strength, σt (MPa)			1464.956	1544.164	1553.290	1487.341	1606.126	1460.089	1607.417	1588.244	1599.926	1361.217	1527.277	81.762	5%	1538.017	60.053	4%
Variation B																		
Effective Tensile Volume Calculations	Chosen Weibull Modulus, m		20.5	20.5	20.5	20.5	20.5	20.5	20.5	20.5	20.5	20.5						
	Effective Tensile Volume Under Bending Stress, V_{Eb} (mm^3)		0.523	0.493	0.479	0.426	0.501	0.529	0.427	0.449	0.481	0.445	0.475	0.037	8%	0.485	0.035	7%
	Effective Tensile Volume Under Direct Tensile Stress, V_{Et} (mm^3)		1780.531	1688.280	1643.891	1470.742	1713.691	1799.659	1476.997	1546.026	1650.225	1533.447	1630.349	119.067	7%	1661.631	111.392	7%
	$\sigma_b/\sigma_t = (V_{Et}/V_{Eb})^{1/m}$		1.487	1.487	1.487	1.488	1.487	1.487	1.488	1.488	1.487	1.488	1.488	0.000	0%	1.487	0.000	0%
Tensile Strength, σ_t (MPa)			1436.873	1514.542	1523.483	1458.764	1575.321	1432.103	1576.534	1557.745	1569.226	1335.075	1497.967	80.191	5%	1508.507	58.894	4%
Method 2, Et/Ec = 1.2																		
Calculation of Unknown Values	Location of Neutral Axis from top of specimen, c (mm)		1.609	1.541	1.508	1.380	1.560	1.623	1.385	1.436	1.513	1.427	1.498	0.088	6%	1.521	0.082	5%
	Rupture Stress, σ_t (MPa)		2112.623	2227.331	2240.687	2146.431	2316.583	2105.513	2319.705	2291.611	2307.915	1964.105	2203.250	118.009	5%	2218.587	86.768	4%
	Compressive Stress, σ_c (MPa)		1394.668	1463.458	1469.005	1395.322	1524.049	1391.353	1508.416	1495.173	1513.576	1280.699	1443.572	76.928	5%	1455.825	55.197	4%
	Maximum Bending Moment, M (Nmm)		19658.797	18824.157	18049.332	14163.250	20113.783	19976.280	15423.001	16533.111	18720.179	13964.452	17542.634	2357.796	13%	18254.861	2024.086	11%
Variation A																		
Effective Tensile Volume Calculations	Chosen Weibull Modulus, m		22	22	22	22	22	22	22	22	22	22						
	Effective Tensile Volume Under Bending Stress, V_{Eb} (mm^3)		0.441	0.417	0.405	0.359	0.423	0.446	0.361	0.379	0.406	0.376	0.401	0.032	8%	0.410	0.030	7%
	Effective Tensile Volume Under Direct Tensile Stress, V_{Et} (mm^3)		1780.531	1688.280	1643.891	1470.742	1713.691	1799.659	1476.997	1546.026	1650.225	1533.447	1630.349	119.067	7%	1661.631	111.392	7%
	$\sigma_b/\sigma_t = (V_{Et}/V_{Eb})^{1/m}$		1.458	1.459	1.459	1.459	1.459	1.458	1.459	1.459	1.459	1.459	1.459	0.000	0%	1.459	0.000	0%
Tensile Strength, σt (MPa)			1448.498	1526.846	1535.857	1470.711	1588.115	1443.682	1589.459	1570.436	1581.959	1345.962	1510.152	80.850	5%	1520.763	59.381	4%
Variation B																		
Effective Tensile Volume Calculations	Chosen Weibull Modulus, m		20.5	20.5	20.5	20.5	20.5	20.5	20.5	20.5	20.5	20.5						
	Effective Tensile Volume Under Bending Stress, V_{eb} (mm^3)		0.523	0.493	0.479	0.426	0.501	0.529	0.427	0.449	0.481	0.445	0.475	0.037	8%	0.485	0.035	7%
	Effective Tensile Volume Under Direct Tensile Stress, V_{Et} (mm^3)		1780.531	1688.280	1643.891	1470.742	1713.691	1799.659	1476.997	1546.026	1650.225	1533.447	1630.349	119.067	7%	1661.631	111.392	7%
	$\sigma_b/\sigma_t = (V_{Et}/V_{Eb})^{1/m}$		1.487	1.487	1.487	1.488	1.487	1.487	1.488	1.488	1.487	1.488	1.488	0.000	0%	1.487	0.000	0%
Tensile Strength, σ_t (MPa)			1420.724	1497.543	1506.397	1442.444	1557.635	1416.002	1558.912	1540.297	1551.625	1320.124	1481.170	79.296	5%	1491.583	58.241	4%

B.2 M8 Specimens in 4-Point Bending

Variation A – Parameters calculated using all 10 specimens

Variation B – Parameters calculated using 8 specimens (omitting outliers)

Orange text denotes outliers

GFRP Parameters and Information			M8 Specimens										Using All Specimens			Excluding Lowest and Highest Rupture Modulus		
GFRP Admin Info	Specimen Number		M8-6	M8-4	M8-15	M8-8	M8-17	M8-32	M8-27	M8-11	M8-23	M8-14	Avg.	Std Dev.	C.O.V.	Avg.	Std Dev.	C.O.V.
	Test Number		83	84	85	86	87	88	89	90	91	92						
	Type of Flexural Test		4 -point bending															
	Date of Test		January 10, 2020															
	Batch		All specimens cut from single bar, batch dated March 10, 2010															
	Additional Notes																	
Specimen Dimensions	Measured Height (excluding rib thickness; top of specimen to core; mm)	End 1	3.35	3.39	3.34	3.33	3.39	3.45	3.44	3.29	3.54	3.42						
		End 2	3.39	3.34	3.37	3.29	3.55	3.51	3.4	3.18	3.47	3.25						
		Avg.	3.37	3.365	3.355	3.31	3.47	3.48	3.42	3.235	3.505	3.335	3.385	0.084	2%	3.369	0.088	3%
	Measured Total Length (mm)		96	96	96	96	95	96	97	96	96	96	96	0.471	0%	96	0	0%
	Orginial Radius of GFRP, r (mm) =		4	4	4	4	4	4	4	4	4	4						
	Height of Specimen, h (mm) =		3.37	3.365	3.355	3.31	3.47	3.48	3.42	3.235	3.505	3.335	3.385	0.084	2%	3.369375	0.087522956	3%
	Length of Specimen, L (mm) =		80	80	80	80	80	80	80	80	80	80						
Test Data Information	Maximum Load per Loading Nose (kN)		0.733	0.667	0.652	0.619	0.667	0.747	0.775	0.595	0.741	0.708	0.690	0.060	9%	0.683	0.058	9%
	Deflection at Maximum Load (mm)		13.909	13.472	13.820	13.707	13.706	11.979	13.092	14.561	11.897	14.244	13.439	0.885	7%	13.449	0.990	7%
	Data Point of Maximum Loading		2198	2129	2184	2166	2166	1893	2069	2301	1880	2251	2123.7	139.844	7%	2125.25	156.3912219	7%
	Maximum Deflection (mm)		14.393	14.267	16.229	15.320	16.902	12.343	13.714	16.532	12.039	14.408	14.615	1.661	11%	14.441	1.628	11%
	Total Data Points		2275	2255	2565	2421	2166	1951	2168	2301	1903	2277	2228.2	197.564	9%	2243.5	221.0100192	10%
	Chosen Filtered Critical Point Load, P_{cr} (N)		676.049	607.392	622.779	583.246	613.685	720.735	762.841	594.969	712.290	665.183	655.917	61.042	9%	647.830	53.179	8%
Method 1, Et/Ec = 1.25																		
Calculation of Unknown Values	Location of Neutral Axis from top of specimen, c (mm) =		1.498	1.496	1.491	1.470	1.545	1.550	1.522	1.435	1.562	1.482	1.505	0.040	3%	1.498	0.041	3%
	Rupture (Tensile) Stress, σ_t (MPa) =		2352.230	2120.852	2189.999	2117.981	1991.947	2323.498	2562.900	2281.866	2257.620	2372.635	2257.153	161.128	7%	2252.085	99.742	4%
	Compressive Stress, σ_c (MPa) =		1505.946	1357.564	1401.428	1353.453	1279.309	1492.720	1643.395	1454.835	1451.557	1517.357	1445.756	103.333	7%	1441.857	64.600	4%
	Maximum Bending Moment, M (Nmm) =		1.80E+04	1.62E+04	1.66E+04	1.56E+04	1.64E+04	1.92E+04	2.03E+04	1.59E+04	1.90E+04	1.77E+04	1.75E+04	1.63E+03	9%	1.73E+04	1.42E+03	8%
Variation A																		
Effective Tensile Volume Calculations	Chosen Weibull Modulus, m		16.5	16.5	16.5	16.5	16.5	16.5	16.5	16.5	16.5	16.5						
	Effective Tensile Volume Under Bending Stress, V_{eb} (mm^3)		5.064	5.053	5.032	4.936	5.279	5.300	5.171	4.778	5.354	4.989	5.096	0.180	4%	5.063	0.187	4%
	Effective Tensile Volume Under Direct Tensile Stress, V_{Et} (mm^3)		1609.093	1605.933	1599.615	1571.219	1672.414	1678.759	1640.724	1524.021	1694.630	1586.988	1618.340	53.318	3%	1608.782	55.329	3%
	$\sigma_b/\sigma_t = (V_{Et}/V_{Eb})^{1/m}$		1.418	1.418	1.418	1.418	1.418	1.418	1.418	1.418	1.418	1.418	1.418	0.000	0%	1.418	0.000	0%
Tensile Strength, σt (MPa)			1658.970	1495.770	1544.512	1493.604	1405.118	1639.022	1807.709	1608.966	1592.621	1673.259	1591.955	113.646	7%	1588.341	70.384	4%
Variation B																		
Effective Tensile Volume Calculations	Chosen Weibull Modulus, m		18	18	18	18	18	18	18	18	18	18						
	Effective Tensile Volume Under Bending Stress, V_{Eb} (mm^3)		4.443	4.434	4.415	4.331	4.631	4.650	4.537	4.192	4.698	4.378	4.471	0.158	4%	4.442	0.164	4%
	Effective Tensile Volume Under Direct Tensile Stress, V_{Et} (mm^3)		1609.093	1605.933	1599.615	1571.219	1672.414	1678.759	1640.724	1524.021	1694.630	1586.988	1618.340	53.318	3%	1608.782	55.329	3%
	$\sigma_b/\sigma_t = (V_{Et}/V_{Eb})^{1/m}$		1.387	1.387	1.387	1.387	1.387	1.387	1.387	1.388	1.387	1.387	1.387	0.000	0%	1.387	0.000	0%
Tensile Strength, σ_t (MPa)			1695.580	1528.780	1578.600	1526.577	1436.107	1675.168	1847.589	1644.503	1627.738	1710.192	1627.083	116.154	7%	1623.392	71.934	4%
Method 2, Et/Ec = 1.2																		
Calculation of Unknown Values	Location of Neutral Axis from top of specimen, c (mm)		1.482	1.480	1.475	1.455	1.529	1.534	1.506	1.420	1.546	1.466	1.489	0.039	3%	1.482	0.041	3%
	Rupture Stress, σ_t (MPa)		2325.863	2097.050	2165.454	2094.251	1969.597	2297.426	2534.157	2256.317	2232.281	2346.047	2231.844	159.324	7%	2226.836	98.626	4%
	Compressive Stress, σ_c (MPa)		1522.190	1372.226	1416.545	1368.056	1293.101	1508.812	1661.117	1470.540	1467.202	1533.727	1461.352	104.446	7%	1457.412	65.292	4%
	Maximum Bending Moment, M (Nmm)		18027.969	16197.109	16607.429	15553.222	16364.944	19219.597	20342.418	15865.838	18994.404	17738.214	17491.114	1627.790	9%	17275.473	1418.102	8%
Variation A																		
Effective Tensile Volume Calculations	Chosen Weibull Modulus, m		16.5	16.5	16.5	16.5	16.5	16.5	16.5	16.5	16.5	16.5						
	Effective Tensile Volume Under Bending Stress, V_{eb} (mm^3)		5.064	5.053	5.032	4.936	5.279	5.300	5.171	4.778	5.354	4.989	5.096	0.180	4%	5.063	0.187	4%
	Effective Tensile Volume Under Direct Tensile Stress, V_{Et} (mm^3)		1609.093	1605.933	1599.615	1571.219	1672.414	1678.759	1640.724	1524.021	1694.630	1586.988	1618.340	53.318	3%	1608.782	55.329	3%
	$\sigma_b/\sigma_t = (V_{Et}/V_{Eb})^{1/m}$		1.418	1.418	1.418	1.418	1.418	1.418	1.418	1.418	1.418	1.418	1.418	0.000	0%	1.418	0.000	0%
Tensile Strength, σt (MPa)			1640.374	1478.983	1527.201	1476.870	1389.352	1620.630	1787.436	1590.951	1574.746	1654.508	1574.105	112.374	7%	1570.533	69.597	4%
Variation B																		
Effective Tensile Volume Calculations	Chosen Weibull Modulus, m		18	18	18	18	18	18	18	18	18	18						
	Effective Tensile Volume Under Bending Stress, V_{eb} (mm^3)		4.443	4.434	4.415	4.331	4.631	4.650	4.537	4.192	4.698	4.378	4.471	0.158	4%	4.442	0.164	4%
	Effective Tensile Volume Under Direct Tensile Stress, V_{Et} (mm^3)		1609.093	1605.933	1599.615	1571.219	1672.414	1678.759	1640.724	1524.021	1694.630	1586.988	1618.340	53.318	3%	1608.782	55.329	3%
	$\sigma_b/\sigma_t = (V_{Et}/V_{Eb})^{1/m}$		1.387	1.387	1.387	1.387	1.387	1.387	1.387	1.388	1.387	1.387	1.387	0.000	0%	1.387	0.000	0%
Tensile Strength, σ_t (MPa)			1676.574	1511.623	1560.907	1509.473	1419.993	1656.370	1826.869	1626.090	1609.469	1691.028	1608.840	114.853	7%	1605.192	71.129	4%

B.3 M13 Specimens in 3-Point Bending

Variation A – Parameters calculated using all 10 specimens

Variation B – Parameters calculated using 8 specimens (omitting outliers)

Orange text denotes outliers

GFRP Parameters and Information			M13 Specimens										Using All Specimens			Excluding Lowest and Highest Rupture Modulus		
GFRP Admin Info	Specimen Number		M13-1	M13-3	M13-18	M13-15	M13-20	M13-10	M13-14	M13-13	M13-2	M13-11	Avg.	Std Dev.	C.O.V.	Avg.	Std Dev.	C.O.V.
	Test Number		6	7	8	9	10	41	42	43	44	45						
	Type of Flexural Test		3 -point bending															
	Date of Test		September 25, 2019					October 10, 2019										
	Batch		All specimens (for 3 and 4-point bending) cut from 2 bars of different batch. First bar batch no.: 8033245 Second bar batch no.: unknown															
	Additional Notes																	
Specimen Dimensions	Measured Height (excluding rib thickness; top of specimen to core; mm)	End 1	6.04	5.87	5.79	5.88	6	6.27	6.53	5.96	5.78	6.09						
		End 2	5.97	5.93	6	6.08	5.82	6.12	6.19	5.88	6.01	6.27						
		Avg.	6.005	5.9	5.895	5.98	5.91	6.195	6.36	5.92	5.895	6.18	6.024	0.164	3%	5.998125	0.123257498	2%
	Measured Total Length (mm)		157	157	157	158	157	157	157	157	157	157	157.1	0.316	0%	157.125	0.353553391	0%
	Orginial Radius of GFRP, r (mm) =		6.5	6.5	6.5	6.5	6.5	6.5	6.5	6.5	6.5	6.5						
	Height of Specimen, h (mm) =		6.005	5.9	5.895	5.98	5.91	6.195	6.36	5.92	5.895	6.18	6.024	0.164	3%	5.998125	0.123257498	2%
	Length of Specimen, L (mm) =		130	130	130	130	130	130	130	130	130	130						
Test Data Information	Maximum Load per Loading Nose (kN)		2.554	2.528	2.491	2.519	2.458	2.737	2.753	2.427	2.395	2.561	2.542	0.119	5%	2.522	0.106	4%
	Deflection at Maximum Load (mm)		13.821	14.275	13.865	14.690	14.145	14.346	14.260	14.670	14.479	13.880	14.243	0.318	2%	14.288	0.328	2%
	Data Point of Maximum Loading		2764	2855	2773	2938	2829	2869	2852	2934	2896	2776	2848.6	63.708	2%	2857.625	65.62869037	2%
	Maximum Deflection (mm)		16.319	15.642	14.549	15.024	15.615	14.698	15.111	14.797	15.023	15.140	15.192	0.530	3%	15.282	0.541	4%
	Total Data Points		3264	3129	2910	3005	3123	2940	3023	2960	3005	3029	3038.8	106.004	3%	3056.875	108.020418	4%
	Chosen Filtered Critical Point Load, P_{cr} (N)		2483.947	2281.039	2457.238	2377.873	2182.009	2553.585	2537.290	2377.383	2301.027	2372.150	2392.354	118.049	5%	2366.127	116.313	5%
Method 1, Et/Ec = 1.25																		
Calculation of Unknown Values	Location of Neutral Axis from top of specimen, c (mm) =		2.685	2.635	2.633	2.673	2.640	2.776	2.855	2.644	2.633	2.769	2.694	0.078	3%	2.682	0.059	2%
	Rupture (Tensile) Stress, σ_t (MPa) =		1973.104	1889.009	2039.008	1907.536	1799.781	1884.860	1760.663	1953.111	1909.384	1760.957	1887.741	91.453	5%	1884.718	71.881	4%
	Compressive Stress, σ_c (MPa) =		1276.550	1219.531	1316.236	1233.498	1162.161	1224.288	1147.639	1261.426	1232.561	1143.445	1221.734	56.712	5%	1219.183	45.471	4%
	Maximum Bending Moment, M (Nmm) =		8.07E+04	7.41E+04	7.99E+04	7.73E+04	7.09E+04	8.30E+04	8.25E+04	7.73E+04	7.48E+04	7.71E+04	7.78E+04	3.84E+03	5%	7.69E+04	3.78E+03	5%
Variation A																		
Effective Tensile Volume Calculations	Chosen Weibull Modulus, m		24	24	24	24	24	24	24	24	24	24						
	Effective Tensile Volume Under Bending Stress, V_{eb} (mm^3)		1.573	1.534	1.533	1.564	1.538	1.644	1.705	1.542	1.533	1.638	1.580	0.061	4%	1.571	0.046	3%
	Effective Tensile Volume Under Direct Tensile Stress, V_{Et} (mm^3)		7791.858	7615.041	7606.627	7749.737	7631.870	8112.338	8391.017	7648.701	7606.627	8087.017	7824.083	276.121	4%	7780.399	207.783	3%
	$\sigma_b/\sigma_t = (V_{Et}/V_{Eb})^{1/m}$		1.425	1.426	1.426	1.425	1.426	1.425	1.425	1.426	1.426	1.425	1.425	0.000	0%	1.425	0.000	0%
Tensile Strength, σt (MPa)			1384.192	1325.089	1430.304	1338.168	1262.508	1322.481	1235.500	1370.076	1339.377	1235.532	1324.323	64.054	5%	1322.178	50.381	4%
Variation B																		
Effective Tensile Volume Calculations	Chosen Weibull Modulus, m		20.5	20.5	20.5	20.5	20.5	20.5	20.5	20.5	20.5	20.5						
	Effective Tensile Volume Under Bending Stress, V_{Eb} (mm^3)		2.291	2.235	2.232	2.277	2.240	2.393	2.483	2.245	2.232	2.385	2.301	0.088	4%	2.287	0.066	3%
	Effective Tensile Volume Under Direct Tensile Stress, V_{Et} (mm^3)		7791.858	7615.041	7606.627	7749.737	7631.870	8112.338	8391.017	7648.701	7606.627	8087.017	7824.083	276.121	4%	7780.399	207.783	3%
	$\sigma_b/\sigma_t = (V_{Et}/V_{Eb})^{1/m}$		1.487	1.487	1.487	1.487	1.487	1.487	1.486	1.487	1.487	1.487	1.487	0.000	0%	1.487	0.000	0%
Tensile Strength, σ_t (MPa)			1327.011	1270.333	1371.200	1282.885	1210.340	1267.880	1184.514	1313.465	1313.465	1184.518	1272.561	62.849	5%	1271.237	50.785	4%
Method 2, Et/Ec = 1.2																		
Calculation of Unknown Values	Location of Neutral Axis from top of specimen, c (mm)		2.657	2.608	2.605	2.645	2.612	2.747	2.826	2.617	2.605	2.740	2.666	0.078	3%	2.654	0.058	2%
	Rupture Stress, σ_t (MPa)		1950.916	1867.781	2016.095	1886.089	1779.554	1863.643	1740.829	1931.160	1887.928	1741.134	1866.513	90.436	5%	1863.526	71.079	4%
	Compressive Stress, σ_c (MPa)		1290.297	1232.668	1330.415	1246.782	1174.680	1237.462	1159.978	1275.014	1245.838	1155.751	1234.888	57.327	5%	1232.311	45.962	4%
	Maximum Bending Moment, M (Nmm)		8.07E+04	7.41E+04	7.99E+04	7.73E+04	7.09E+04	8.30E+04	8.25E+04	7.73E+04	7.48E+04	7.71E+04	7.78E+04	3.84E+03	5%	7.69E+04	3.78E+03	5%
Variation A																		
Effective Tensile Volume Calculations	Chosen Weibull Modulus, m		24	24	24	24	24	24	24	24	24	24						
	Effective Tensile Volume Under Bending Stress, V_{Eb} (mm^3)		1.573	1.534	1.533	1.564	1.538	1.644	1.705	1.542	1.533	1.638	1.580	0.061	4%	1.571	0.046	3%
	Effective Tensile Volume Under Direct Tensile Stress, V_{Et} (mm^3)		7791.858	7615.041	7606.627	7749.737	7631.870	8112.338	8391.017	7648.701	7606.627	8087.017	7824.083	276.121	4%	7780.399	207.783	3%
	$\sigma_b/\sigma_t = (V_{Et}/V_{Eb})^{1/m}$		1.425	1.426	1.426	1.425	1.426	1.425	1.425	1.426	1.426	1.425	1.425	0.000	0%	1.425	0.000	0%
Tensile Strength, σt (MPa)			1368.626	1310.198	1414.231	1323.123	1248.319	1307.595	1221.583	1354.678	1324.326	1221.624	1309.430	63.342	5%	1307.311	49.819	4%
Variation B																		
Effective Tensile Volume Calculations	Chosen Weibull Modulus, m		20.5	20.5	20.5	20.5	20.5	20.5	20.5	20.5	20.5	20.5						
	Effective Tensile Volume Under Bending Stress, V_{eb} (mm^3)		2.291	2.235	2.232	2.277	2.240	2.393	2.483	2.245	2.232	2.385	2.301	0.088	4%	2.287	0.066	3%
	Effective Tensile Volume Under Direct Tensile Stress, V_{Et} (mm^3)		7791.858	7615.041	7606.627	7749.737	7631.870	8112.338	8391.017	7648.701	7606.627	8087.017	7824.083	276.121	4%	7780.399	207.783	3%
	$\sigma_b/\sigma_t = (V_{Et}/V_{Eb})^{1/m}$		1.487	1.487	1.487	1.487	1.487	1.487	1.486	1.487	1.487	1.487	1.487	0.000	0%	1.487	0.000	0%
Tensile Strength, σ_t (MPa)			1312.087	1256.058	1355.791	1268.460	1196.737	1253.607	1171.166	1298.703	1269.601	1171.184	1255.339	60.711	5%	1253.304	47.754	4%

B.4 M13 Specimens in 4-Point Bending

Variation A – Parameters calculated using all 10 specimens

Variation B – Parameters calculated using 8 specimens (omitting outliers)

Orange text denotes outliers

GFRP Parameters and Information			M13 Specimens										Using All Specimens			Excluding Lowest and Highest Rupture Modulus		
GFRP Admin Info	Specimen Number		M13-7	M13-4	M13-8	M13-12	M13-17	M13-16	M13-5	M13-6	M13-9	M13-19	Avg.	Std Dev.	C.O.V.	Avg.	Std Dev.	C.O.V.
	Test Number		73	74	75	76	77	78	79	80	81	82						
	Type of Flexural Test		4 -point bending															
	Date of Test		January 10, 2019															
	Batch		All specimens (for 3 and 4-point bending) cut from 2 bars of different batch. First bar batch no.: 8033245 Second bar batch no.: unknown															
	Additional Notes																	
Specimen Dimensions	Measured Height (excluding rib thickness; top of specimen to core; mm)	End 1	5.89	6.01	5.85	5.83	6.34	6.09	6.22	5.88	5.89	6.2						
		End 2	6.13	5.75	5.89	5.99	5.71	6.24	6.05	5.98	5.69	5.89						
		Avg.	6.01	5.88	5.87	5.91	6.025	6.165	6.135	5.93	5.79	6.045	5.976	0.121	2%	5.99	0.132449451	2%
	Measured Total Length (mm)		157	157	157	157	157	157	156	157	158	158	157.1	0.568	0%	157.125	0.640869944	0%
	Orginial Radius of GFRP, r (mm) =		6.5	6.5	6.5	6.5	6.5	6.5	6.5	6.5	6.5	6.5						
	Height of Specimen, h (mm) =		6.01	5.88	5.87	5.91	6.025	6.165	6.135	5.93	5.79	6.045	5.976	0.121	2%	5.99	0.132449451	2%
	Length of Specimen, L (mm) =		130	130	130	130	130	130	130	130	130	130						
Test Data Information	Maximum Load per Loading Nose (kN)		1.926	1.705	1.735	1.676	1.803	1.866	1.942	1.883	1.703	1.909	1.815	0.103	6%	1.824	0.100	5%
	Deflection at Maximum Load (mm)		19.776	20.332	20.401	18.927	19.794	19.541	19.553	20.876	20.641	19.831	19.967	0.589	3%	19.984	0.416	2%
	Data Point of Maximum Loading		3125	3213	3224	2991	3128	3088	3090	3299	3262	3134	3155.4	93.088	3%	3158	65.77667845	2%
	Maximum Deflection (mm)		21.255	24.577	23.109	23.832	23.608	25.495	26.072	23.253	27.844	25.174	24.422	1.835	8%	24.642	2.007	8%
	Total Data Points		3359	3884	3652	3766	3731	4029	4121	3675	4401	3979	3859.7	290.223	8%	3894.5	317.4640587	8%
	Chosen Filtered Critical Point Load, P_{cr} (N)		1831.424	1524.790	1621.245	1497.859	1734.317	1673.137	1832.156	1867.151	1611.158	1880.913	1707.415	142.365	8%	1713.642	126.869	7%
Method 1, Et/Ec = 1.25																		
Calculation of Unknown Values	Location of Neutral Axis from top of specimen, c (mm) =		2.687	2.625	2.621	2.640	2.694	2.762	2.747	2.649	2.583	2.704	2.671	0.058	2%	2.678	0.063	2%
	Rupture (Tensile) Stress, σ_t (MPa) =		1935.897	1697.213	1811.853	1647.300	1822.474	1665.562	1844.929	2037.109	1860.056	1961.157	1828.355	129.464	7%	1824.893	103.090	6%
	Compressive Stress, σ_c (MPa) =		1252.607	1095.266	1169.011	1063.701	1179.613	1081.162	1196.844	1315.944	1198.123	1269.868	1182.214	83.657	7%	1180.312	66.579	6%
	Maximum Bending Moment, M (Nmm) =		7.94E+04	6.61E+04	7.03E+04	6.49E+04	7.52E+04	7.25E+04	7.94E+04	8.09E+04	6.98E+04	8.15E+04	7.40E+04	6.17E+03	8%	7.43E+04	5.50E+03	7%
Variation A																		
Effective Tensile Volume Calculations	Chosen Weibull Modulus, m		16.5	16.5	16.5	16.5	16.5	16.5	16.5	16.5	16.5	16.5						
	Effective Tensile Volume Under Bending Stress, V_{eb} (mm^3)		24.785	24.033	23.975	24.206	24.872	25.688	25.513	24.322	23.514	24.988	24.590	0.699	3%	24.671	0.768	3%
	Effective Tensile Volume Under Direct Tensile Stress, V_{Et} (mm^3)		7800.284	7581.390	7564.568	7631.870	7825.564	8061.700	8011.073	7665.535	7430.089	7859.277	7743.135	203.107	3%	7766.743	223.098	3%
	$\sigma_b/\sigma_t = (V_{Et}/V_{Eb})^{1/m}$		1.417	1.417	1.417	1.417	1.417	1.417	1.417	1.417	1.417	1.417	1.417	0.000	0%	1.417	0.000	0%
Tensile Strength, σt (MPa)			1366.133	1197.527	1278.401	1162.347	1286.115	1175.562	1302.117	1437.430	1312.295	1384.012	1290.194	91.352	7%	1287.770	72.738	6%
Variation B																		
Effective Tensile Volume Calculations	Chosen Weibull Modulus, m		14	14	14	14	14	14	14	14	14	14						
	Effective Tensile Volume Under Bending Stress, V_{Eb} (mm^3)		31.555	30.599	30.525	30.819	31.666	32.703	32.480	30.966	29.939	31.814	31.307	0.889	3%	31.410	0.976	3%
	Effective Tensile Volume Under Direct Tensile Stress, V_{Et} (mm^3)		7800.284	7581.390	7564.568	7631.870	7825.564	8061.700	8011.073	7665.535	7430.089	7859.277	7743.135	203.107	3%	7766.743	223.098	3%
	$\sigma_b/\sigma_t = (V_{Et}/V_{Eb})^{1/m}$		1.482	1.483	1.483	1.482	1.482	1.482	1.482	1.482	1.483	1.482	1.482	0.000	0%	1.482	0.000	0%
Tensile Strength, σ_t (MPa)			1306.023	1144.809	1222.121	1111.183	1229.529	1123.868	1244.852	1374.163	1254.504	1323.123	1233.417	87.331	7%	1231.103	69.536	6%
Method 2, Et/Ec = 1.2																		
Calculation of Unknown Values	Location of Neutral Axis from top of specimen, c (mm)		2.659	2.598	2.593	2.612	2.667	2.733	2.719	2.622	2.556	2.676	2.643	0.057	2%	2.650	0.063	2%
	Rupture Stress, σ_t (MPa)		1914.125	1678.169	1791.514	1628.786	1802.001	1646.813	1824.166	2014.211	1839.141	1939.097	1807.802	128.004	7%	1804.378	101.924	6%
	Compressive Stress, σ_c (MPa)		1266.097	1107.048	1181.593	1075.159	1192.301	1092.799	1209.727	1330.118	1211.050	1283.541	1194.943	84.561	7%	1193.020	67.300	6%
	Maximum Bending Moment, M (Nmm)		7.94E+04	6.61E+04	7.03E+04	6.49E+04	7.52E+04	7.25E+04	7.94E+04	8.09E+04	6.98E+04	8.15E+04	7.40E+04	6.17E+03	8%	7.43E+04	5.50E+03	7%
Variation A																		
Effective Tensile Volume Calculations	Chosen Weibull Modulus, m		16.5	16.5	16.5	16.5	16.5	16.5	16.5	16.5	16.5	16.5						
	Effective Tensile Volume Under Bending Stress, V_{Eb} (mm^3)		24.785	24.033	23.975	24.206	24.872	25.688	25.513	24.322	23.514	24.988	24.590	0.699	3%	24.671	0.768	3%
	Effective Tensile Volume Under Direct Tensile Stress, V_{Et} (mm^3)		7800.284	7581.390	7564.568	7631.870	7825.564	8061.700	8011.073	7665.535	7430.089	7859.277	7743.135	203.107	3%	7766.743	223.098	3%
	$\sigma_b/\sigma_t = (V_{Et}/V_{Eb})^{1/m}$		1.417	1.417	1.417	1.417	1.417	1.417	1.417	1.417	1.417	1.417	1.417	0.000	0%	1.417	0.000	0%
Tensile Strength, σt (MPa)			1350.769	1184.090	1264.051	1149.284	1271.667	1162.330	1287.463	1421.273	1297.539	1368.444	1275.691	90.322	7%	1273.294	71.916	6%
Variation B																		
Effective Tensile Volume Calculations	Chosen Weibull Modulus, m		14	14	14	14	14	14	14	14	14	14						
	Effective Tensile Volume Under Bending Stress, V_{eb} (mm^3)		31.555	30.599	30.525	30.819	31.666	32.703	32.480	30.966	29.939	31.814	31.307	0.889	3%	31.410	0.976	3%
	Effective Tensile Volume Under Direct Tensile Stress, V_{Et} (mm^3)		7800.284	7581.390	7564.568	7631.870	7825.564	8061.700	8011.073	7665.535	7430.089	7859.277	7743.135	203.107	3%	7766.743	223.098	3%
	$\sigma_b/\sigma_t = (V_{Et}/V_{Eb})^{1/m}$		1.482	1.483	1.483	1.482	1.482	1.482	1.482	1.482	1.483	1.482	1.482	0.000	0%	1.482	0.000	0%
Tensile Strength, σ_t (MPa)			1291.338	1131.948	1208.392	1098.697	1215.721	1111.223	1230.849	1358.719	1240.384	1308.240	1219.551	86.347	7%	1217.262	68.752	6%

B.5 M15 Specimens in 3-Point Bending

Variation A – Parameters calculated using all 10 specimens

Variation B – Parameters calculated using 8 specimens (omitting outliers)

Orange text denotes outliers

GFRP Parameters and Information			M15 Specimens										Using All Specimens			Excluding Lowest and Highest Rupture Modulus		
GFRP Admin Info	Specimen Number		M15-5	M15-3	M15-26	M15-19	M15-29	M15-18	M15-25	M15-30	M15-14	M15-8	Avg.	Std Dev.	C.O.V.	Avg.	Std Dev.	C.O.V.
	Test Number		1	2	3	4	5	36	37	38	39	40						
	Type of Flexural Test		3-point bending															
	Date of Test		September 24, 2019					October 2, 2019										
	Batch		All specimens cut from multiple bars of the same batch. Batch No.: 8051973 Batch Date: November 11 to 22, 2016															
	Additional Notes																	
Specimen Dimensions	Measured Height (excluding rib thickness; top of specimen to core; mm)	End 1	7.41	7.45	7.41	7.5	7.51	7.5	7.63	7.72	7.45	7.67						
		End 2	7.68	7.45	7.39	8.06	7.86	7.58	7.49	7.64	7.57	7.63						
		Avg.	7.545	7.45	7.4	7.78	7.685	7.54	7.56	7.68	7.51	7.65	7.580	0.117	2%	7.583125	0.116708963	2%
	Measured Total Length (mm)		192	192	191	193	195	192	193	193	193	194	192.8	1.135	1%	192.625	0.916125381	0%
	Orginial Radius of GFRP, r (mm) =		8	8	8	8	8	8	8	8	8	8	8	0	0%	8	0	0%
	Height of Specimen, h (mm) =		7.545	7.45	7.4	7.78	7.685	7.54	7.56	7.68	7.51	7.65	7.580	0.117	2%	7.583125	0.116708963	2%
	Length of Specimen, L (mm) =		160	160	160	160	160	160	160	160	160	160	160	0	0%	160	0	0%
Test Data Information	Maximum Load per Loading Nose (kN)		4.027	4.036	3.919	3.909	3.902	4.047	3.824	3.935	3.921	4.083	3.960	0.083	2%	3.958	0.086	2%
	Deflection at Maximum Load (mm)		17.654	17.025	16.939	17.884	17.804	17.394	16.005	16.449	17.664	18.314	17.313	0.707	4%	17.288	0.772	4%
	Data Point of Maximum Loading		3531	3405	3388	3577	3561	3567	3201	3290	3533	3663	3471.6	145.206	4%	3468.75	159.135836	5%
	Maximum Deflection (mm)		17.698	17.061	17.073	18.000	18.250	17.832	17.349	16.622	17.736	18.944	17.656	0.669	4%	17.657	0.689	4%
	Total Data Points		3540	3413	3415	3601	3650	3567	3470	3329	3552	3789	3532.6	133.051	4%	3532.875	136.9227493	4%
	Chosen Filtered Critical Point Load, P_{cr} (N)		3899.202	3976.041	3822.763	3651.754	3515.429	3718.967	3761.346	3722.872	3836.959	3998.738	3790.407	148.421	4%	3801.575	111.604	3%
Method 1, Et/Ec = 1.25																		
Calculation of Unknown Values	Location of Neutral Axis from top of specimen, c (mm) =		3.378	3.333	3.309	3.491	3.446	3.376	3.386	3.443	3.362	3.429	3.395	0.056	2%	3.397	0.056	2%
	Rupture (Tensile) Stress, σ_t (MPa) =		1947.524	2046.099	1998.719	1697.010	1681.501	1860.405	1869.903	1783.452	1937.543	1933.316	1875.547	122.426	7%	1878.484	98.620	5%
	Compressive Stress, σ_c (MPa) =		1263.275	1325.092	1293.325	1105.227	1093.327	1206.662	1213.234	1159.517	1256.057	1256.308	1217.202	77.413	6%	1219.201	62.011	5%
	Maximum Bending Moment, M (Nmm) =		1.56E+05	1.59E+05	1.53E+05	1.46E+05	1.41E+05	1.49E+05	1.50E+05	1.49E+05	1.53E+05	1.60E+05	1.52E+05	5.94E+03	4%	1.52E+05	4.46E+03	3%
Variation A																		
Effective Tensile Volume Calculations	Chosen Weibull Modulus, m		18	18	18	18	18	18	18	18	18	18						
	Effective Tensile Volume Under Bending Stress, V_{eb} (mm^3)		5.956	5.851	5.795	6.217	6.111	5.950	5.972	6.106	5.917	6.072	5.995	0.130	2%	5.998	0.130	2%
	Effective Tensile Volume Under Direct Tensile Stress, V_{Et} (mm^3)		14920.783	14678.064	14550.396	15521.825	15278.763	14908.004	14959.123	15265.973	14831.339	15189.240	15010.351	299.283	2%	15018.335	298.368	2%
	$\sigma_b/\sigma_t = (V_{Et}/V_{Eb})^{1/m}$		1.545	1.545	1.545	1.544	1.544	1.545	1.545	1.544	1.545	1.544	1.545	0.000	0%	1.545	0.000	0%
Tensile Strength, σt (MPa)			1260.832	1324.546	1293.821	1098.863	1088.735	1204.426	1210.595	1154.741	1254.334	1251.742	1214.264	79.161	7%	1216.169	63.751	5%
Variation B																		
Effective Tensile Volume Calculations	Chosen Weibull Modulus, m		15	15	15	15	15	15	15	15	15	15						
	Effective Tensile Volume Under Bending Stress, V_{Eb} (mm^3)		9.104	8.944	8.859	9.504	9.342	9.096	9.130	9.333	9.045	9.282	9.164	0.199	2%	9.169	0.198	2%
	Effective Tensile Volume Under Direct Tensile Stress, V_{Et} (mm^3)		14920.783	14678.064	14550.396	15521.825	15278.763	14908.004	14959.123	15265.973	14831.339	15189.240	15010.351	299.283	2%	15018.335	298.368	2%
	$\sigma_b/\sigma_t = (V_{Et}/V_{Eb})^{1/m}$		1.638	1.638	1.638	1.638	1.638	1.638	1.638	1.638	1.638	1.638	1.638	0.000	0%	1.638	0.000	0%
Tensile Strength, σ_t (MPa)			1189.036	1249.059	1220.076	1036.290	1026.723	1135.800	1141.621	1088.969	1182.859	1180.440	1145.087	74.637	7%	1146.886	60.107	5%
Method 2, Et/Ec = 1.2																		
Calculation of Unknown Values	Location of Neutral Axis from top of specimen, c (mm)		3.343	3.298	3.275	3.455	3.410	3.341	3.350	3.408	3.327	3.393	3.360	0.056	2%	3.362	0.055	2%
	Rupture Stress, σ_t (MPa)		1925.607	2023.024	1976.312	1677.890	1662.565	1839.469	1848.858	1763.368	1915.742	1911.550	1854.438	121.057	7%	1857.349	97.533	5%
	Compressive Stress, σ_c (MPa)		1276.874	1339.397	1307.209	1117.117	1105.092	1219.652	1226.293	1171.994	1269.579	1269.826	1230.303	78.250	6%	1232.318	62.674	5%
	Maximum Bending Moment, M (Nmm)		1.56E+05	1.59E+05	1.53E+05	1.46E+05	1.41E+05	1.49E+05	1.50E+05	1.49E+05	1.53E+05	1.60E+05	1.52E+05	5.94E+03	4%	1.52E+05	4.46E+03	3%
Variation A																		
Effective Tensile Volume Calculations	Chosen Weibull Modulus, m		18	18	18	18	18	18	18	18	18	18						
	Effective Tensile Volume Under Bending Stress, V_{Eb} (mm^3)		5.956	5.851	5.795	6.217	6.111	5.950	5.972	6.106	5.917	6.072	5.995	0.130	2%	5.998	0.130	2%
	Effective Tensile Volume Under Direct Tensile Stress, V_{Et} (mm^3)		14920.783	14678.064	14550.396	15521.825	15278.763	14908.004	14959.123	15265.973	14831.339	15189.240	15010.351	299.283	2%	15018.335	298.368	2%
	$\sigma_b/\sigma_t = (V_{Et}/V_{Eb})^{1/m}$		1.545	1.545	1.545	1.544	1.544	1.545	1.545	1.544	1.545	1.544	1.545	0.000	0%	1.545	0.000	0%
Tensile Strength, σt (MPa)			1246.643	1309.608	1279.316	1086.482	1076.474	1190.872	1196.970	1141.737	1240.220	1237.650	1200.597	78.276	7%	1202.486	63.049	5%
Variation B																		
Effective Tensile Volume Calculations	Chosen Weibull Modulus, m		15	15	15	15	15	15	15	15	15	15						
	Effective Tensile Volume Under Bending Stress, V_{eb} (mm^3)		9.104	8.944	8.859	9.504	9.342	9.096	9.130	9.333	9.045	9.282	9.164	0.199	2%	9.169	0.198	2%
	Effective Tensile Volume Under Direct Tensile Stress, V_{Et} (mm^3)		14920.783	14678.064	14550.396	15521.825	15278.763	14908.004	14959.123	15265.973	14831.339	15189.240	15010.351	299.283	2%	15018.335	298.368	2%
	$\sigma_b/\sigma_t = (V_{Et}/V_{Eb})^{1/m}$		1.638	1.638	1.638	1.638	1.638	1.638	1.638	1.638	1.638	1.638	1.638	0.000	0%	1.638	0.000	0%
Tensile Strength, σ_t (MPa)			1175.612	1235.009	1206.375	1024.613	1015.159	1123.018	1128.772	1076.704	1169.549	1167.130	1132.194	73.802	7%	1133.971	59.435	5%

B.6 M15 Specimens in 4-Point Bending

Variation A – Parameters calculated using all 10 specimens

Variation B – Parameters calculated using 8 specimens (omitting outliers)

Orange text denotes outliers

GFRP Parameters and Information			M15 Specimens										Using All Specimens			Excluding Lowest and Highest Rupture Modulus		
GFRP Admin Info	Specimen Number		M1659	M15-31	M15-7	M15-20	M15-10	M15-4	M15-27	M15-13	M15-21	M15-15	Avg.	Std Dev.	C.O.V.	Avg.	Std Dev.	C.O.V.
	Test Number		63	64	65	66	67	68	69	70	71	72						
	Type of Flexural Test		4-point bending															
	Date of Test		December 18, 2019	January 8, 2020														
	Batch		All specimens cut from multiple bars of the same batch. Batch No.: 8051973 Batch Date: November 11 to 22, 2016															
	Additional Notes																	
Specimen Dimensions	Measured Height (excluding rib thickness; top of specimen to core; mm)	End 1	7.29	7.39	7.36	7.47	7.72	7.62	7.76	7.61	7.5	7.46						
		End 2	7.4	7.54	7.4	7.43	7.42	7.4	7.97	7.56	7.62	7.36						
		Avg.	7.345	7.465	7.38	7.45	7.57	7.51	7.865	7.585	7.56	7.41	7.514	0.148	2%	7.47625	0.092842032	1%
	Measured Total Length (mm)		190	193	193	193	193	191	190	193	192	193	192.1	1.287	1%	192.25	1.164964745	1%
	Orginial Radius of GFRP, r (mm) =		8	8	8	8	8	8	8	8	8	8	8	0	0%	8	0	0%
	Height of Specimen, h (mm) =		7.345	7.465	7.38	7.45	7.57	7.51	7.865	7.585	7.56	7.41	7.514	0.148	2%	7.47625	0.092842032	1%
	Length of Specimen, L (mm) =		160	160	160	160	160	160	160	160	160	160	160	0	0%	160	0	0%
Test Data Information	Maximum Load per Loading Nose (kN)		2.805	2.920	2.648	2.818	2.694	2.871	2.587	2.818	2.880	2.777	2.782	0.107	4%	2.789	0.081	3%
	Deflection at Maximum Load (mm)		25.143	24.763	25.040	22.958	25.527	24.027	19.851	25.090	23.780	24.913	24.109	1.685	7%	24.560	0.876	4%
	Data Point of Maximum Loading		3973	3913	3957	3628	4034	3797	3137	3965	3758	3937	3809.9	266.259	7%	3881.125	138.3757178	4%
	Maximum Deflection (mm)		25.789	25.335	25.897	27.542	26.119	24.445	33.581	25.753	26.708	25.815	26.698	2.549	10%	26.008	0.883	3%
	Total Data Points		4075	4004	4093	4353	4128	3883	5307	4070	4221	4080	4221.4	400.996	9%	4112.875	134.7860076	3%
	Chosen Filtered Critical Point Load, P_{cr} (N)		2267.665	2743.958	2353.522	2465.253	2469.742	2553.462	2335.446	2702.885	2780.322	2546.611	2521.887	177.681	7%	2517.433	168.989	7%
Method 1, Et/Ec = 1.25																		
Calculation of Unknown Values	Location of Neutral Axis from top of specimen, c (mm) =		3.283	3.340	3.299	3.333	3.390	3.362	3.532	3.398	3.386	3.314	3.364	0.071	2%	3.345	0.044	1%
	Rupture (Tensile) Stress, σ_t (MPa) =		1608.942	1873.839	1651.150	1691.516	1631.946	1719.223	1410.644	1777.733	1842.934	1769.669	1697.759	133.739	8%	1711.639	81.059	5%
	Compressive Stress, σ_c (MPa) =		1040.154	1213.839	1068.154	1095.457	1059.063	1114.526	920.091	1153.922	1195.736	1145.303	1100.624	85.603	8%	1109.039	53.419	5%
	Maximum Bending Moment, M (Nmm) =		1.21E+05	1.46E+05	1.26E+05	1.31E+05	1.32E+05	1.36E+05	1.25E+05	1.44E+05	1.48E+05	1.36E+05	1.35E+05	9.48E+03	7%	1.34E+05	9.01E+03	7%
Variation A																		
Effective Tensile Volume Calculations	Chosen Weibull Modulus, m		14.5	14.5	14.5	14.5	14.5	14.5	14.5	14.5	14.5	14.5						
	Effective Tensile Volume Under Bending Stress, V_{eb} (mm^3)		55.425	56.703	55.800	56.543	57.827	57.183	61.002	57.986	57.718	56.117	57.230	1.588	3%	56.825	0.991	2%
	Effective Tensile Volume Under Direct Tensile Stress, V_{Et} (mm^3)		14410.030	14716.376	14499.345	14678.064	14984.685	14831.339	15739.371	15023.031	14959.123	14575.925	14841.729	378.550	3%	14745.193	237.147	2%
	$\sigma_b/\sigma_t = (V_{Et}/V_{Eb})^{1/m}$		1.467	1.467	1.467	1.467	1.467	1.467	1.467	1.467	1.467	1.467	1.467	0.000	0%	1.467	0.000	0%
Tensile Strength, σt (MPa)			1096.457	1277.133	1125.264	1152.851	1112.387	1171.806	961.827	1211.777	1256.189	1206.068	1157.176	91.086	8%	1166.600	55.303	5%
Variation B																		
Effective Tensile Volume Calculations	Chosen Weibull Modulus, m		17	17	17	17	17	17	17	17	17	17						
	Effective Tensile Volume Under Bending Stress, V_{Eb} (mm^3)		43.697	44.705	43.993	44.579	45.592	45.085	48.099	45.718	45.507	44.243	45.122	1.253	3%	44.802	0.782	2%
	Effective Tensile Volume Under Direct Tensile Stress, V_{Et} (mm^3)		14410.030	14716.376	14499.345	14678.064	14984.685	14831.339	15739.371	15023.031	14959.123	14575.925	14841.729	378.550	3%	14745.193	237.147	2%
	$\sigma_b/\sigma_t = (V_{Et}/V_{Eb})^{1/m}$		1.406	1.406	1.406	1.406	1.406	1.406	1.406	1.406	1.406	1.406	1.406	0.000	0%	1.406	0.000	0%
Tensile Strength, σ_t (MPa)			1143.959	1332.440	1174.008	1202.778	1160.543	1222.544	1003.425	1264.234	1310.572	1258.307	1207.281	95.040	8%	1217.118	57.690	5%
Method 2, Et/Ec = 1.2																		
Calculation of Unknown Values	Location of Neutral Axis from top of specimen, c (mm)		3.249	3.305	3.265	3.298	3.355	3.327	3.496	3.362	3.350	3.279	3.329	0.070	2%	3.311	0.044	1%
	Rupture Stress, σ_t (MPa)		1590.852	1852.760	1632.725	1672.427	1613.610	1699.879	1394.745	1757.723	1822.192	1749.802	1678.672	132.234	8%	1692.401	80.128	5%
	Compressive Stress, σ_c (MPa)		1051.357	1226.908	1079.568	1107.291	1070.442	1126.524	929.984	1166.342	1208.607	1157.614	1112.464	86.530	8%	1120.968	54.001	5%
	Maximum Bending Moment, M (Nmm)		1.21E+05	1.46E+05	1.26E+05	1.31E+05	1.32E+05	1.36E+05	1.25E+05	1.44E+05	1.48E+05	1.36E+05	1.35E+05	9.48E+03	7%	1.34E+05	9.01E+03	7%
Variation A																		
Effective Tensile Volume Calculations	Chosen Weibull Modulus, m		14.5	14.5	14.5	14.5	14.5	14.5	14.5	14.5	14.5	14.5						
	Effective Tensile Volume Under Bending Stress, V_{Eb} (mm^3)		55.425	56.703	55.800	56.543	57.827	57.183	61.002	57.986	57.718	56.117	57.230	1.588	3%	56.825	0.991	2%
	Effective Tensile Volume Under Direct Tensile Stress, V_{Et} (mm^3)		14410.030	14716.376	14499.345	14678.064	14984.685	14831.339	15739.371	15023.031	14959.123	14575.925	14841.729	378.550	3%	14745.193	237.147	2%
	$\sigma_b/\sigma_t = (V_{Et}/V_{Eb})^{1/m}$		1.467	1.467	1.467	1.467	1.467	1.467	1.467	1.467	1.467	1.467	1.467	0.000	0%	1.467	0.000	0%
Tensile Strength, σt (MPa)			1084.129	1262.766	1112.708	1139.841	1099.889	1158.621	950.987	1198.137	1242.051	1192.528	1144.166	90.061	8%	1153.488	54.668	5%
Variation B																		
Effective Tensile Volume Calculations	Chosen Weibull Modulus, m		17	17	17	17	17	17	17	17	17	17						
	Effective Tensile Volume Under Bending Stress, V_{eb} (mm^3)		43.697	44.705	43.993	44.579	45.592	45.085	48.099	45.718	45.507	44.243	45.122	1.253	3%	44.802	0.782	2%
	Effective Tensile Volume Under Direct Tensile Stress, V_{Et} (mm^3)		14410.030	14716.376	14499.345	14678.064	14984.685	14831.339	15739.371	15023.031	14959.123	14575.925	14841.729	378.550	3%	14745.193	237.147	2%
	$\sigma_b/\sigma_t = (V_{Et}/V_{Eb})^{1/m}$		1.406	1.406	1.406	1.406	1.406	1.406	1.406	1.406	1.406	1.406	1.406	0.000	0%	1.406	0.000	0%
Tensile Strength, σ_t (MPa)			1131.097	1317.451	1160.907	1189.205	1147.504	1208.788	992.116	1250.003	1295.829	1244.181	1193.708	93.971	8%	1203.439	57.029	5%

B.7 M20 Specimens in 3-Point Bending

Variation A – Parameters calculated using all 10 specimens

Variation B – Parameters calculated using 8 specimens (omitting outliers)

Orange text denotes outliers

GFRP Parameters and Information			M20 Specimens										Using All Specimens			Excluding Lowest and Highest Rupture Modulus		
GFRP Admin Info	Specimen Number		M20-1	M20-21	M20-22	M20-19	M20-12	M20-9	M20-6	M20-8	M20-14	M20-10	Avg.	Std Dev.	C.O.V.	Avg.	Std Dev.	C.O.V.
	Test Number		21	22	23	24	25	56	57	58	59	60						
	Type of Flexural Test		3-point bending															
	Date of Test		September 26, 2020					October 17, 2019										
	Batch		All specimens cut from multiple bars of the same batch. Batch No.: 032012 Batch Date: March 23 to 29, 2012															
	Additional Notes																	
Specimen Dimensions	Measured Height (excluding rib thickness; top of specimen to core; mm)	End 1	9.69	9.43	9.47	9.36	9.87	9.65	9.65	9.45	9.61	9.48						
		End 2	9.55	9.45	9.46	9.41	9.56	9.53	9.67	9.54	9.59	9.52						
		Avg.	9.62	9.44	9.465	9.385	9.715	9.59	9.66	9.495	9.6	9.5	**9.547**	**0.106**	**1%**	**9.566875**	**0.108888459**	**1%**
	Measured Total Length (mm)		239	240	240	239	239	238	239	239	239	239	**239.1**	**0.568**	**0%**	**239**	**0.534522484**	**0%**
	Orginial Radius of GFRP, r (mm) =		10	10	10	10	10	10	10	10	10	10						
	Height of Specimen, h (mm) =		9.62	9.44	9.465	9.535	9.715	9.59	9.66	9.495	9.6	9.5	**9.562**	**0.089**	**1%**	**9.585625**	**0.082912928**	**1%**
	Length of Specimen, L (mm) =		200	200	200	200	200	200	200	200	200	200						
Test Data Information	Maximum Load per Loading Nose (kN)		6.019	6.048	6.297	6.717	6.274	6.048	6.430	5.904	6.024	6.070	**6.183**	**0.246**	**4%**	**6.235**	**0.248**	**4%**
	Deflection at Maximum Load (mm)		19.709	19.779	19.834	21.144	19.424	19.396	19.864	20.244	20.704	20.344	**20.044**	**0.562**	**3%**	**20.053**	**0.624**	**3%**
	Data Point of Maximum Loading		3942	3956	3967	4229	3885	3879	3973	4049	4141	4069	**4009.0**	**112.377**	**3%**	**4010.625**	**124.9159003**	**3%**
	Maximum Deflection (mm)		19.759	20.467	20.425	21.237	19.489	19.742	19.953	23.002	20.757	20.454	**20.528**	**1.017**	**5%**	**20.227**	**0.593**	**3%**
	Total Data Points		3952	4094	4086	4248	3898	3949	3991	4601	4152	4091	**4106.2**	**203.559**	**5%**	**4045.875**	**118.82693**	**3%**
	Chosen Filtered Critical Point Load, P_{cr} (N)		5626.147	5971.304	5500.525	6067.140	5813.629	5926.133	5881.950	5301.595	5521.839	5710.125	**5732.039**	**242.922**	**4%**	**5755.936**	**201.425**	**3%**
Method 1, Et/Ec = 1.25																		
Calculation of Unknown Values	Location of Neutral Axis from top of specimen, c (mm) =		4.314	4.227	4.239	4.273	4.359	4.299	4.333	4.254	4.304	4.256	**4.286**	**0.043**	**1%**	**4.297**	**0.040**	**1%**
	Rupture (Tensile) Stress, σ_t (MPa) =		1716.520	1904.616	1743.563	1890.106	1733.241	1821.277	1777.151	1668.034	1692.959	1794.381	**1774.185**	**79.505**	**4%**	**1771.150**	**63.847**	**4%**
	Compressive Stress, σ_c (MPa) =		1116.312	1235.591	1131.494	1227.765	1128.669	1184.067	1156.381	1082.922	1100.686	1164.982	**1152.887**	**51.185**	**4%**	**1151.295**	**41.099**	**4%**
	Maximum Bending Moment, M (Nmm) =		2.81E+05	2.99E+05	2.75E+05	3.03E+05	2.91E+05	2.96E+05	2.94E+05	2.65E+05	2.76E+05	2.86E+05	**2.87E+05**	**1.21E+04**	**4%**	**2.88E+05**	**1.01E+04**	**3%**
Variation A																		
Effective Tensile Volume Calculations	Chosen Weibull Modulus, m		26	26	26	26	26	26	26	26	26	26						
	Effective Tensile Volume Under Bending Stress, V_{Eb} (mm^3)		5.011	4.879	4.897	4.948	5.080	4.989	5.040	4.919	4.996	4.923	**4.968**	**0.065**	**1%**	**4.986**	**0.061**	**1%**
	Effective Tensile Volume Under Direct Tensile Stress, V_{Et} (mm^3)		29896.292	29177.098	29276.948	29556.597	30276.081	29776.386	30056.189	29396.785	29816.353	29416.760	**29664.549**	**357.336**	**1%**	**29758.951**	**331.362**	**1%**
	$\sigma_b/\sigma_t = (V_{Et}/V_{Eb})^{1/m}$		1.397	1.397	1.397	1.397	1.397	1.397	1.397	1.397	1.397	1.397	**1.397**	**0.000**	**0%**	**1.397**	**0.000**	**0%**
Tensile Strength, σt (MPa)			1228.651	1363.171	1247.917	1352.846	1240.675	1303.618	1272.073	1193.875	1211.775	1284.308	**1269.891**	**56.888**	**4%**	**1267.733**	**45.684**	**4%**
Variation B																		
Effective Tensile Volume Calculations	Chosen Weibull Modulus, m		22	22	22	22	22	22	22	22	22	22						
	Effective Tensile Volume Under Bending Stress, V_{Eb} (mm^3)		7.455	7.260	7.287	7.363	7.558	7.423	7.499	7.319	7.433	7.325	**7.392**	**0.097**	**1%**	**7.418**	**0.090**	**1%**
	Effective Tensile Volume Under Direct Tensile Stress, V_{Et} (mm^3)		29896.292	29177.098	29276.948	29556.597	30276.081	29776.386	30056.189	29396.785	29816.353	29416.760	**29664.549**	**357.336**	**1%**	**29758.951**	**331.362**	**1%**
	$\sigma_b/\sigma_t = (V_{Et}/V_{Eb})^{1/m}$		1.458	1.458	1.458	1.458	1.458	1.458	1.458	1.458	1.458	1.458	**1.458**	**0.000**	**0%**	**1.458**	**0.000**	**0%**
Tensile Strength, σ_t (MPa)			1177.250	1306.123	1195.695	1296.240	1188.780	1249.078	1218.859	1143.917	1161.078	1230.567	**1216.759**	**54.504**	**4%**	**1214.693**	**43.770**	**4%**
Method 2, Et/Ec = 1.2																		
Calculation of Unknown Values	Location of Neutral Axis from top of specimen, c (mm)		4.269	4.184	4.195	4.228	4.314	4.255	4.288	4.210	4.260	4.212	**4.241**	**0.042**	**1%**	**4.253**	**0.039**	**1%**
	Rupture Stress, σ_t (MPa)		1697.208	1883.259	1724.014	1868.825	1713.712	1800.920	1757.092	1649.333	1673.934	1774.235	**1754.253**	**78.617**	**4%**	**1751.242**	**63.136**	**4%**
	Compressive Stress, σ_c (MPa)		1128.311	1248.842	1143.626	1240.979	1140.811	1196.713	1168.848	1094.529	1112.505	1177.487	**1165.265**	**51.734**	**4%**	**1163.660**	**41.540**	**4%**
	Maximum Bending Moment, M (Nmm)		2.81E+05	2.99E+05	2.75E+05	3.03E+05	2.91E+05	2.96E+05	2.94E+05	2.65E+05	2.76E+05	2.86E+05	**2.87E+05**	**1.21E+04**	**4%**	**2.88E+05**	**1.01E+04**	**3%**
Variation A																		
Effective Tensile Volume Calculations	Chosen Weibull Modulus, m		26	26	26	26	26	26	26	26	26	26						
	Effective Tensile Volume Under Bending Stress, V_{Eb} (mm^3)		5.011	4.879	4.897	4.948	5.080	4.989	5.040	4.919	4.996	4.923	**4.968**	**0.065**	**1%**	**4.986**	**0.061**	**1%**
	Effective Tensile Volume Under Direct Tensile Stress, V_{Et} (mm^3)		29896.292	29177.098	29276.948	29556.597	30276.081	29776.386	30056.189	29396.785	29816.353	29416.760	**29664.549**	**357.336**	**1%**	**29758.951**	**331.362**	**1%**
	$\sigma_b/\sigma_t = (V_{Et}/V_{Eb})^{1/m}$		1.397	1.397	1.397	1.397	1.397	1.397	1.397	1.397	1.397	1.397	**1.397**	**0.000**	**0%**	**1.397**	**0.000**	**0%**
Tensile Strength, σt (MPa)			1214.827	1347.885	1233.925	1337.614	1226.696	1289.047	1257.715	1180.490	1198.157	1269.889	**1255.625**	**56.252**	**4%**	**1253.484**	**45.175**	**4%**
Variation B																		
Effective Tensile Volume Calculations	Chosen Weibull Modulus, m		22	22	22	22	22	22	22	22	22	22						
	Effective Tensile Volume Under Bending Stress, V_{Eb} (mm^3)		7.455	7.260	7.287	7.363	7.558	7.423	7.499	7.319	7.433	7.325	**7.392**	**0.097**	**1%**	**7.418**	**0.090**	**1%**
	Effective Tensile Volume Under Direct Tensile Stress, V_{Et} (mm^3)		29896.292	29177.098	29276.948	29556.597	30276.081	29776.386	30056.189	29396.785	29816.353	29416.760	**29664.549**	**357.336**	**1%**	**29758.951**	**331.362**	**1%**
	$\sigma_b/\sigma_t = (V_{Et}/V_{Eb})^{1/m}$		1.458	1.458	1.458	1.458	1.458	1.458	1.458	1.458	1.458	1.458	**1.458**	**0.000**	**0%**	**1.458**	**0.000**	**0%**
Tensile Strength, σ_t (MPa)			1164.005	1291.477	1182.288	1281.646	1175.385	1235.117	1205.102	1131.093	1148.030	1216.751	**1203.089**	**53.896**	**4%**	**1201.040**	**43.282**	**4%**

B.8 M20 Specimens in 4-Point Bending

Variation A – Parameters calculated using all 10 specimens

Variation B – Parameters calculated using 8 specimens (omitting outliers)

Orange text denotes outliers

GFRP Parameters and Information			M20 Specimens										Using All Specimens			Excluding Lowest and Highest Rupture Modulus		
GFRP Admin Info	Specimen Number		M20-18	M20-26	M20-5	M20-11	M20-24	M20-7	M20-20	M20-3	M20-23	M20-17	Avg.	Std Dev.	C.O.V.	Avg.	Std Dev.	C.O.V.
	Test Number		113	114	115	116	117	118	119	120	121	122						
	Type of Flexural Test		4-point bending															
	Date of Test		January 16, 2020															
	Batch		All specimens cut from multiple bars of the same batch. Batch No.: 032012 Batch Date: March 23 to 29, 2012															
	Additional Notes																	
Specimen Dimensions	Measured Height (excluding rib thickness; top of specimen to core; mm)	End 1	9.5	9.5	9.65	9.45	9.36	9.51	9.64	9.42	9.53	9.57						
		End 2	9.57	9.6	9.55	9.46	9.41	9.68	9.44	9.43	9.68	9.55						
		Avg.	9.535	9.55	9.6	9.455	9.385	9.595	9.54	9.425	9.605	9.56	9.525	0.077	1%	9.530625	0.082654077	1%
	Measured Total Length (mm)		240	239	238	239	239	239	240	239	240	238	239.1	0.738	0%	239.125	0.83452296	0%
	Orginial Radius of GFRP, r (mm) =		10	10	10	10	10	10	10	10	10	10						
	Height of Specimen, h (mm) =		9.535	9.55	9.6	9.455	9.385	9.595	9.54	9.425	9.605	9.56	9.525	0.077	1%	9.530625	0.082654077	1%
	Length of Specimen, L (mm) =		200	200	200	200	200	200	200	200	200	200						
Test Data Information	Maximum Load per Loading Nose (kN)		4.664	4.715	4.633	4.440	4.318	4.320	4.460	4.136	4.500	4.404	4.459	0.178	4%	4.429	0.175	4%
	Deflection at Maximum Load (mm)		29.785	30.348	29.349	28.931	29.551	28.375	27.241	28.121	29.108	27.830	28.864	0.961	3%	28.670	0.911	3%
	Data Point of Maximum Loading		4707	4796	4638	4572	4670	4484	4305	4444	4600	4398	4561.4	151.919	3%	4530.75	143.9491478	3%
	Maximum Deflection (mm)		30.247	30.780	30.346	29.670	35.449	28.407	29.038	33.611	30.293	28.848	30.669	2.212	7%	30.780	2.476	8%
	Total Data Points		4780	4864	4796	4689	5602	4490	4589	5312	4787	4559	4846.8	349.468	7%	4864.375	391.24013	8%
	Chosen Filtered Critical Point Load, P_{cr} (N)		3636.403	3359.959	3519.093	4216.590	3999.864	4043.766	3968.045	3651.164	4063.072	4062.624	3852.058	285.520	7%	3868.004	225.710	6%
Method 1, Et/Ec = 1.25																		
Calculation of Unknown Values	Location of Neutral Axis from top of specimen, c (mm) =		4.273	4.280	4.304	4.234	4.201	4.302	4.275	4.220	4.306	4.285	4.268	0.037	1%	4.271	0.040	1%
	Rupture (Tensile) Stress, σ_t (MPa) =		1510.473	1390.494	1438.574	1786.548	1724.648	1655.081	1646.197	1558.601	1658.915	1677.152	1604.668	126.663	8%	1608.705	96.592	6%
	Compressive Stress, σ_c (MPa) =		981.165	903.415	935.296	1159.232	1118.006	1075.986	1069.402	1010.913	1078.627	1089.809	1042.185	81.861	8%	1044.901	62.445	6%
	Maximum Bending Moment, M (Nmm) =		2.42E+05	2.24E+05	2.35E+05	2.81E+05	2.67E+05	2.70E+05	2.65E+05	2.43E+05	2.71E+05	2.71E+05	2.57E+05	1.90E+04	7%	2.58E+05	1.50E+04	6%
Variation A																		
Effective Tensile Volume Calculations	Chosen Weibull Modulus, m		15	15	15	15	15	15	15	15	15	15						
	Effective Tensile Volume Under Bending Stress, V_{eb} (mm^3)		108.339	108.578	109.375	107.067	105.956	109.295	108.418	106.590	109.455	108.737	108.181	1.227	1%	108.271	1.315	1%
	Effective Tensile Volume Under Direct Tensile Stress, V_{Et} (mm^3)		29556.597	29616.534	29816.353	29237.006	28957.478	29796.370	29576.576	29117.195	29836.337	29656.495	29516.694	308.297	1%	29539.175	330.192	1%
	$\sigma_b/\sigma_t = (V_{Et}/V_{Eb})^{1/m}$		1.453	1.453	1.453	1.454	1.454	1.453	1.453	1.454	1.453	1.453	1.453	0.000	0%	1.453	0.000	0%
Tensile Strength, σt (MPa)			1039.254	956.715	989.835	1229.125	1186.473	1138.803	1132.641	1072.275	1141.450	1153.957	1104.053	87.122	8%	1106.836	66.439	6%
Variation B																		
Effective Tensile Volume Calculations	Chosen Weibull Modulus, m		13	13	13	13	13	13	13	13	13	13						
	Effective Tensile Volume Under Bending Stress, V_{Eb} (mm^3)		133.834	134.129	135.113	132.264	130.894	135.014	133.933	131.677	135.211	134.326	133.640	1.515	1%	133.750	1.622	1%
	Effective Tensile Volume Under Direct Tensile Stress, V_{Et} (mm^3)		29556.597	29616.534	29816.353	29237.006	28957.478	29796.370	29576.576	29117.195	29836.337	29656.495	29516.694	308.297	1%	29539.175	330.192	1%
	$\sigma_b/\sigma_t = (V_{Et}/V_{Eb})^{1/m}$		1.515	1.515	1.515	1.515	1.515	1.515	1.515	1.515	1.515	1.515	1.515	0.000	0%	1.515	0.000	0%
Tensile Strength, σ_t (MPa)			997.237	918.038	949.824	1179.422	1138.487	1092.769	1086.850	1028.911	1095.310	1107.307	1059.415	83.597	8%	1062.087	63.751	6%
Method 2, Et/Ec = 1.2																		
Calculation of Unknown Values	Location of Neutral Axis from top of specimen, c (mm)		4.229	4.236	4.259	4.191	4.157	4.257	4.231	4.176	4.262	4.241	4.224	0.037	1%	4.227	0.039	1%
	Rupture Stress, σ_t (MPa)		1493.526	1374.880	1422.394	1766.515	1705.267	1636.485	1627.734	1541.100	1640.266	1658.335	1586.650	125.246	8%	1590.638	95.510	6%
	Compressive Stress, σ_c (MPa)		991.687	913.110	945.348	1171.662	1130.026	1087.538	1080.865	1021.770	1090.213	1101.495	1053.371	82.738	8%	1056.118	63.115	6%
	Maximum Bending Moment, M (Nmm)		2.42E+05	2.24E+05	2.35E+05	2.81E+05	2.67E+05	2.70E+05	2.65E+05	2.43E+05	2.71E+05	2.71E+05	2.57E+05	1.90E+04	7%	2.58E+05	1.50E+04	6%
Variation A																		
Effective Tensile Volume Calculations	Chosen Weibull Modulus, m		15	15	15	15	15	15	15	15	15	15						
	Effective Tensile Volume Under Bending Stress, V_{eb} (mm^3)		108.339	108.578	109.375	107.067	105.956	109.295	108.418	106.590	109.455	108.737	108.181	1.227	1%	108.271	1.315	1%
	Effective Tensile Volume Under Direct Tensile Stress, V_{Et} (mm^3)		29556.597	29616.534	29816.353	29237.006	28957.478	29796.370	29576.576	29117.195	29836.337	29656.495	29516.694	308.297	1%	29539.175	330.192	1%
	$\sigma_b/\sigma_t = (V_{Et}/V_{Eb})^{1/m}$		1.453	1.453	1.453	1.454	1.454	1.453	1.453	1.454	1.453	1.453	1.453	0.000	0%	1.453	0.000	0%
Tensile Strength, σt (MPa)			1027.594	945.973	978.702	1215.343	1173.140	1126.007	1119.938	1060.235	1128.617	1141.010	1091.656	86.148	8%	1094.405	65.695	6%
Variation B																		
Effective Tensile Volume Calculations	Chosen Weibull Modulus, m		13	13	13	13	13	13	13	13	13	13						
	Effective Tensile Volume Under Bending Stress, V_{eb} (mm^3)		133.834	134.129	135.113	132.264	130.894	135.014	133.933	131.677	135.211	134.326	133.640	1.515	1%	133.750	1.622	1%
	Effective Tensile Volume Under Direct Tensile Stress, V_{Et} (mm^3)		29556.597	29616.534	29816.353	29237.006	28957.478	29796.370	29576.576	29117.195	29836.337	29656.495	29516.694	308.297	1%	29539.175	330.192	1%
	$\sigma_b/\sigma_t = (V_{Et}/V_{Eb})^{1/m}$		1.515	1.515	1.515	1.515	1.515	1.515	1.515	1.515	1.515	1.515	1.515	0.000	0%	1.515	0.000	0%
Tensile Strength, σ_t (MPa)			986.010	907.701	939.141	1166.117	1125.712	1080.491	1074.613	1017.329	1082.976	1094.838	1047.493	82.655	8%	1050.139	63.039	6%

B.9 M25 Specimens in 3-Point Bending

Variation A – Parameters calculated using all 10 specimens

Variation B – Parameters calculated using 8 specimens (omitting outliers)

Orange text denotes outliers

GFRP Parameters and Information			M25 Specimens										Using All Specimens			Excluding Lowest and Highest Rupture Modulus		
GFRP Admin Info	Specimen Number		M25-1	M25-2	M25-13	M25-12	M25-8	M25-20	M25-15	M25-19	M25-9	M25-18	Avg.	Std Dev.	C.O.V.	Avg.	Std Dev.	C.O.V.
	Test Number		16	17	18	19	20	46	47	48	49	50						
	Type of Flexural Test		3-point bending															
	Date of Test		Septmeber 25, 2019		Septmeber 26, 2019		October 10, 2019											
	Batch		All specimens (from 3 and 4-point bending) cut from multiple bars of the same batch. Batch number and date are unknown.															
	Additional Notes				grinded ends a bit				grinded ends a bit									
Specimen Dimensions	Measured Height (excluding rib thickness; top of specimen to core; mm)	End 1	11.84	12.02	11.47	11.8	11.74	12.17	11.76	11.59	11.94	11.75						
		End 2	12.04	12.06	11.52	11.9	11.97	11.98	12.06	11.7	11.97	12.14						
		Avg.	11.94	12.04	11.495	11.85	11.855	12.075	11.91	11.645	11.955	11.945	**11.871**	**0.177**	**1%**	**11.864375**	**0.198843756**	**2%**
	Measured Total Length (mm)		299	299	299	299	298	299	300	299	299	299	**299**	**0.471**	**0%**	**299.125**	**0.353553391**	**0%**
	Orginial Radius of GFRP, r (mm) =		12.5	12.5	12.5	12.5	12.5	12.5	12.5	12.5	12.5	12.5						
	Height of Specimen, h (mm) =		11.94	12.04	11.495	11.85	11.855	12.075	11.91	11.645	11.955	11.945	**11.871**	**0.177**	**1%**	**11.864375**	**0.198843756**	**2%**
	Length of Specimen, L (mm) =		250	250	250	250	250	250	250	250	250	250						
Test Data Information	Maximum Load per Loading Nose (kN)		8.569	9.599	8.488	8.640	8.904	8.850	8.855	8.407	8.379	8.900	**8.759**	**0.359**	**4%**	**8.765**	**0.396**	**5%**
	Deflection at Maximum Load (mm)		21.474	22.934	22.691	21.939	23.489	21.059	22.239	20.984	24.024	22.164	**22.300**	**1.003**	**4%**	**22.254**	**0.995**	**4%**
	Data Point of Maximum Loading		4295	4587	4538	4388	4698	4212	4448	4197	4805	4433	**4460.1**	**200.510**	**4%**	**4451**	**199.0405558**	**4%**
	Maximum Deflection (mm)		21.742	23.789	22.830	22.049	23.613	21.995	22.262	22.896	26.322	22.538	**23.004**	**1.347**	**6%**	**23.085**	**1.430**	**6%**
	Total Data Points		4349	4758	4566	4410	4723	4400	4453	4580	5265	4508	**4601.2**	**269.368**	**6%**	**4617.5**	**285.9740248**	**6%**
	Chosen Filtered Critical Point Load, P_{cr} (N)		8169.722	9084.514	8126.482	8333.259	8813.248	8505.074	8225.344	7920.059	8232.270	8464.954	**8387.493**	**345.495**	**4%**	**8361.494**	**346.453**	**4%**
Method 1, Et/Ec = 1.25																		
Calculation of Unknown Values	Location of Neutral Axis from top of specimen, c (mm) =		5.351	5.399	5.138	5.308	5.310	5.416	5.337	5.210	5.358	5.354	**5.318**	**0.085**	**2%**	**5.315**	**0.095**	**2%**
	Rupture (Tensile) Stress, σ_t (MPa) =		1622.069	1768.672	1764.597	1684.261	1779.505	1644.604	1642.807	1667.936	1629.668	1679.032	**1688.315**	**60.479**	**4%**	**1685.197**	**53.636**	**3%**
	Compressive Stress, σ_c (MPa) =		1053.901	1150.417	1140.974	1093.233	1155.118	1070.132	1067.025	1080.237	1059.013	1090.971	**1096.102**	**38.599**	**4%**	**1094.000**	**34.038**	**3%**
	Maximum Bending Moment, M (Nmm) =		5.11E+05	5.68E+05	5.08E+05	5.21E+05	5.51E+05	5.32E+05	5.14E+05	4.95E+05	5.15E+05	5.29E+05	**5.24E+05**	**2.16E+04**	**4%**	**5.23E+05**	**2.17E+04**	**4%**
Variation A																		
Effective Tensile Volume Calculations	Chosen Weibull Modulus, m		30.5	30.5	30.5	30.5	30.5	30.5	30.5	30.5	30.5	30.5						
	Effective Tensile Volume Under Bending Stress, V_{eb} (mm^3)		6.617	6.695	6.272	6.547	6.551	6.722	6.594	6.388	6.629	6.621	**6.563**	**0.137**	**2%**	**6.558**	**0.154**	**2%**
	Effective Tensile Volume Under Direct Tensile Stress, V_{Et} (mm^3)		57860.403	58484.881	55084.755	57298.563	57329.771	58703.493	57673.101	56019.651	57954.061	57891.622	**57430.030**	**1104.698**	**2%**	**57388.766**	**1240.640**	**2%**
	$\sigma_b/\sigma_t = (V_{Et}/V_{Eb})^{1/m}$		1.347	1.347	1.347	1.347	1.347	1.347	1.347	1.347	1.347	1.347	**1.347**	**0.000**	**0%**	**1.347**	**0.000**	**0%**
Tensile Strength, σt (MPa)			1204.571	1313.483	1310.226	1250.719	1321.449	1221.359	1219.959	1238.514	1210.220	1246.874	**1253.737**	**44.887**	**4%**	**1251.419**	**39.800**	**3%**
Variation B																		
Effective Tensile Volume Calculations	Chosen Weibull Modulus, m		23.5	23.5	23.5	23.5	23.5	23.5	23.5	23.5	23.5	23.5						
	Effective Tensile Volume Under Bending Stress, V_{Eb} (mm^3)		12.350	12.495	11.707	12.219	12.227	12.546	12.306	11.923	12.372	12.357	**12.250**	**0.256**	**2%**	**12.241**	**0.288**	**2%**
	Effective Tensile Volume Under Direct Tensile Stress, V_{Et} (mm^3)		57860.403	58484.881	55084.755	57298.563	57329.771	58703.493	57673.101	56019.651	57954.061	57891.622	**57430.030**	**1104.698**	**2%**	**57388.766**	**1240.640**	**2%**
	$\sigma_b/\sigma_t = (V_{Et}/V_{Eb})^{1/m}$		1.433	1.433	1.433	1.433	1.433	1.433	1.433	1.433	1.433	1.433	**1.433**	**0.000**	**0%**	**1.433**	**0.000**	**0%**
Tensile Strength, σ_t (MPa)			1132.058	1234.425	1231.303	1175.418	1241.890	1147.850	1146.517	1163.927	1137.369	1171.815	**1178.257**	**42.178**	**4%**	**1176.078**	**37.397**	**3%**
Method 2, Et/Ec = 1.2																		
Calculation of Unknown Values	Location of Neutral Axis from top of specimen, c (mm)		5.295	5.343	5.085	5.253	5.255	5.360	5.281	5.156	5.303	5.298	**5.263**	**0.084**	**2%**	**5.260**	**0.094**	**2%**
	Rupture Stress, σ_t (MPa)		1603.705	1748.751	1744.681	1665.317	1759.491	1626.078	1624.257	1649.210	1611.318	1660.018	**1669.283**	**59.811**	**4%**	**1666.204**	**53.026**	**3%**
	Compressive Stress, σ_c (MPa)		1065.307	1162.796	1153.310	1104.991	1167.540	1081.646	1078.543	1091.845	1070.409	1102.781	**1107.917**	**39.010**	**4%**	**1105.790**	**34.412**	**3%**
	Maximum Bending Moment, M (Nmm)		510607.651	567782.125	507905.111	520828.697	550827.970	531567.126	514083.982	495003.690	514516.868	529059.610	**5.24E+05**	**2.16E+04**	**4%**	**5.23E+05**	**2.17E+04**	**4%**
Variation A																		
Effective Tensile Volume Calculations	Chosen Weibull Modulus, m		30.5	30.5	30.5	30.5	30.5	30.5	30.5	30.5	30.5	30.5						
	Effective Tensile Volume Under Bending Stress, V_{Eb} (mm^3)		6.617	6.695	6.272	6.547	6.551	6.722	6.594	6.388	6.629	6.621	**6.563**	**0.137**	**2%**	**6.558**	**0.154**	**2%**
	Effective Tensile Volume Under Direct Tensile Stress, V_{Et} (mm^3)		57860.403	58484.881	55084.755	57298.563	57329.771	58703.493	57673.101	56019.651	57954.061	57891.622	**57430.030**	**1104.698**	**2%**	**57388.766**	**1240.640**	**2%**
	$\sigma_b/\sigma_t = (V_{Et}/V_{Eb})^{1/m}$		1.347	1.347	1.347	1.347	1.347	1.347	1.347	1.347	1.347	1.347	**1.347**	**0.000**	**0%**	**1.347**	**0.000**	**0%**
Tensile Strength, σt (MPa)			1190.934	1298.689	1295.438	1236.651	1306.587	1207.601	1206.184	1224.610	1196.593	1232.755	**1239.604**	**44.391**	**4%**	**1237.315**	**39.348**	**3%**
Variation B																		
Effective Tensile Volume Calculations	Chosen Weibull Modulus, m		23.5	23.5	23.5	23.5	23.5	23.5	23.5	23.5	23.5	23.5						
	Effective Tensile Volume Under Bending Stress, V_{eb} (mm^3)		12.350	12.495	11.707	12.219	12.227	12.546	12.306	11.923	12.372	12.357	**12.250**	**0.256**	**2%**	**12.241**	**0.288**	**2%**
	Effective Tensile Volume Under Direct Tensile Stress, V_{Et} (mm^3)		57860.403	58484.881	55084.755	57298.563	57329.771	58703.493	57673.101	56019.651	57954.061	57891.622	**57430.030**	**1104.698**	**2%**	**57388.766**	**1240.640**	**2%**
	$\sigma_b/\sigma_t = (V_{Et}/V_{Eb})^{1/m}$		1.433	1.433	1.433	1.433	1.433	1.433	1.433	1.433	1.433	1.433	**1.433**	**0.000**	**0%**	**1.433**	**0.000**	**0%**
Tensile Strength, σ_t (MPa)			1119.242	1220.521	1217.406	1162.198	1227.923	1134.919	1133.571	1150.860	1124.562	1158.546	**1164.975**	**41.712**	**4%**	**1162.823**	**36.972**	**3%**

B.10 M25 Specimens in 4-Point Bending

Variation A – Parameters calculated using all 10 specimens

Variation B – Parameters calculated using 8 specimens (omitting outliers)

Orange text denotes outliers

GFRP Parameters and Information			M25 Specimens										Using All Specimens			Excluding Lowest and Highest Rupture Modulus		
GFRP Admin Info	Specimen Number		M25-6	M25-11	M25-14	M25-17	M25-4	M25-3	M25-10	M25-5	M25-16	M25-7	Avg.	Std Dev.	C.O.V.	Avg.	Std Dev.	C.O.V.
	Test Number		93	94	95	96	97	98	99	100	101	102						
	Type of Flexural Test		4-point bending															
	Date of Test		January 13, 2020															
	Batch		All specimens (from 3 and 4-point bending) cut from multiple bars of the same batch. Batch number and date are unknown.															
	Additional Notes																	
Specimen Dimensions	Measured Height (excluding rib thickness; top of specimen to core; mm)	End 1	11.68	11.78	11.73	11.77	11.88	11.61	11.62	11.73	11.83	11.89						
		End 2	11.93	11.96	11.73	11.44	12.07	11.42	11.72	11.62	11.47	11.95						
		Avg.	11.805	11.87	11.73	11.605	11.975	11.515	11.67	11.675	11.65	11.92	11.742	0.147	1%	11.735	0.164924225	1%
	Measured Total Length (mm)		299	299	299	300	300	300	299	299	299	298	299.2	0.632	0%	299.25	0.707106781	0%
	Orginial Radius of GFRP, r (mm) =		12.5	12.5	12.5	12.5	12.5	12.5	12.5	12.5	12.5	12.5						
	Height of Specimen, h (mm) =		11.805	11.87	11.73	11.605	11.975	11.515	11.67	11.675	11.65	11.92	11.742	0.147	1%	11.735	0.164924225	1%
	Length of Specimen, L (mm) =		250	250	250	250	250	250	250	250	250	250						
Test Data Information	Maximum Load per Loading Nose (kN)		6.703	6.449	6.917	5.995	6.641	6.337	6.580	6.606	6.790	7.004	6.602	0.293	4%	6.550	0.302	5%
	Deflection at Maximum Load (mm)		33.988	35.354	34.790	33.031	30.442	36.005	34.024	34.391	34.245	34.575	34.084	1.511	4%	34.008	1.690	5%
	Data Point of Maximum Loading		5371	5587	5498	5220	4811	5690	5377	5435	5412	5464	5386.5	238.748	4%	5374.5	267.0425327	5%
	Maximum Deflection (mm)		34.140	37.947	38.116	43.058	35.253	36.198	35.252	35.039	35.043	34.605	36.465	2.673	7%	36.550	2.832	8%
	Total Data Points		5395	5997	6024	6805	5571	5720	6319	5538	5924	5469	5876.2	438.020	7%	5917.875	456.6118819	8%
	Chosen Filtered Critical Point Load, P_{cr} (N)		5593.056	6121.504	6768.294	5737.117	6222.149	5483.079	5720.084	6404.663	6304.476	6103.665	6045.809	405.638	7%	6012.092	326.194	5%
Method 1, Et/Ec = 1.25																		
Calculation of Unknown Values	Location of Neutral Axis from top of specimen, c (mm) =		5.286	5.318	5.250	5.191	5.368	5.148	5.222	5.224	5.212	5.342	5.256	0.070	1%	5.253	0.079	2%
	Rupture (Tensile) Stress, σ_t (MPa) =		1520.722	1643.113	1868.214	1624.106	1635.880	1580.939	1598.092	1787.558	1768.515	1622.199	1664.934	107.611	6%	1657.550	77.151	5%
	Compressive Stress, σ_c (MPa) =		986.700	1066.757	1211.039	1051.368	1063.283	1022.480	1035.255	1158.039	1145.390	1053.755	1079.407	69.532	6%	1074.541	49.859	5%
	Maximum Bending Moment, M (Nmm) =		4.66E+05	5.10E+05	5.64E+05	4.78E+05	5.19E+05	4.57E+05	4.77E+05	5.34E+05	5.25E+05	5.09E+05	5.04E+05	3.38E+04	7%	5.01E+05	2.72E+04	5%
Variation A																		
Effective Tensile Volume Calculations	Chosen Weibull Modulus, m		17.5	17.5	17.5	17.5	17.5	17.5	17.5	17.5	17.5	17.5						
	Effective Tensile Volume Under Bending Stress, V_{eb} (mm^3)		166.398	167.676	164.904	162.436	169.760	160.669	163.718	163.815	163.322	168.668	165.137	2.910	2%	165.008	3.261	2%
	Effective Tensile Volume Under Direct Tensile Stress, V_{Et} (mm^3)		57017.721	57423.399	56549.777	55770.265	58078.946	55209.359	56175.546	56206.727	56050.829	57735.533	56621.810	918.073	2%	56581.325	1028.916	2%
	$\sigma_b/\sigma_t = (V_{Et}/V_{Eb})^{1/m}$		1.396	1.396	1.396	1.396	1.396	1.396	1.396	1.396	1.396	1.396	1.396	0.000	0%	1.396	0.000	0%
Tensile Strength, σt (MPa)			1089.433	1177.151	1338.314	1163.366	1172.036	1132.391	1144.771	1280.496	1266.837	1162.200	1192.699	77.076	6%	1187.406	55.258	5%
Variation B																		
Effective Tensile Volume Calculations	Chosen Weibull Modulus, m		15.5	15.5	15.5	15.5	15.5	15.5	15.5	15.5	15.5	15.5						
	Effective Tensile Volume Under Bending Stress, V_{Eb} (mm^3)		199.272	200.802	197.484	194.532	203.296	192.417	196.066	196.182	195.591	201.988	197.763	3.483	2%	197.609	3.903	2%
	Effective Tensile Volume Under Direct Tensile Stress, V_{Et} (mm^3)		57017.721	57423.399	56549.777	55770.265	58078.946	55209.359	56175.546	56206.727	56050.829	57735.533	56621.810	918.073	2%	56581.325	1028.916	2%
	$\sigma_b/\sigma_t = (V_{Et}/V_{Eb})^{1/m}$		1.440	1.440	1.440	1.441	1.440	1.441	1.441	1.441	1.441	1.440	1.440	0.000	0%	1.440	0.000	0%
Tensile Strength, σ_t (MPa)			1055.752	1140.762	1296.932	1127.384	1135.813	1097.361	1109.369	1240.897	1227.658	1126.277	1155.820	74.691	6%	1150.690	53.548	5%
Method 2, Et/Ec = 1.2																		
Calculation of Unknown Values	Location of Neutral Axis from top of specimen, c (mm)		5.232	5.262	5.196	5.137	5.312	5.094	5.168	5.170	5.158	5.286	5.202	0.070	1%	5.198	0.078	2%
	Rupture Stress, σ_t (MPa)		1503.715	1624.610	1847.258	1605.828	1617.459	1563.127	1580.133	1767.472	1748.630	1603.866	1646.210	106.409	6%	1638.891	76.300	5%
	Compressive Stress, σ_c (MPa)		997.254	1078.243	1224.036	1062.696	1074.725	1033.514	1046.389	1170.492	1157.716	1065.140	1091.020	70.276	6%	1086.114	50.386	5%
	Maximum Bending Moment, M (Nmm)		466088.017	510125.329	564024.483	478093.075	518512.395	456923.268	476673.637	533721.951	525373.026	508638.717	503817.390	33803.170	7%	501007.675	27182.802	5%
Variation A																		
Effective Tensile Volume Calculations	Chosen Weibull Modulus, m		17.5	17.5	17.5	17.5	17.5	17.5	17.5	17.5	17.5	17.5						
	Effective Tensile Volume Under Bending Stress, V_{Eb} (mm^3)		166.398	167.676	164.904	162.436	169.760	160.669	163.718	163.815	163.322	168.668	165.137	2.910	2%	165.008	3.261	2%
	Effective Tensile Volume Under Direct Tensile Stress, V_{Et} (mm^3)		57017.721	57423.399	56549.777	55770.265	58078.946	55209.359	56175.546	56206.727	56050.829	57735.533	56621.810	918.073	2%	56581.325	1028.916	2%
	$\sigma_b/\sigma_t = (V_{Et}/V_{Eb})^{1/m}$		1.396	1.396	1.396	1.396	1.396	1.396	1.396	1.396	1.396	1.396	1.396	0.000	0%	1.396	0.000	0%
Tensile Strength, σt (MPa)			1077.250	1163.895	1323.302	1150.273	1158.838	1119.632	1131.907	1266.108	1252.593	1149.065	1179.286	76.214	6%	1174.039	54.648	5%
Variation B																		
Effective Tensile Volume Calculations	Chosen Weibull Modulus, m		15.5	15.5	15.5	15.5	15.5	15.5	15.5	15.5	15.5	15.5						
	Effective Tensile Volume Under Bending Stress, V_{eb} (mm^3)		199.272	200.802	197.484	194.532	203.296	192.417	196.066	196.182	195.591	201.988	197.763	3.483	2%	197.609	3.903	2%
	Effective Tensile Volume Under Direct Tensile Stress, V_{Et} (mm^3)		57017.721	57423.399	56549.777	55770.265	58078.946	55209.359	56175.546	56206.727	56050.829	57735.533	56621.810	918.073	2%	56581.325	1028.916	2%
	$\sigma_b/\sigma_t = (V_{Et}/V_{Eb})^{1/m}$		1.440	1.440	1.440	1.441	1.440	1.441	1.441	1.441	1.441	1.440	1.440	0.000	0%	1.440	0.000	0%
Tensile Strength, σ_t (MPa)			1043.926	1127.916	1282.384	1114.712	1123.023	1085.063	1096.864	1226.904	1213.833	1113.548	1142.817	73.847	6%	1137.733	52.935	5%

B.11 M32 Specimens in 3-Point Bending

Variation A – Parameters calculated using all 10 specimens

Variation B – Parameters calculated using 8 specimens (omitting outliers)

Orange text denotes outliers

GFRP Parameters and Information			M32 Specimens										Using All Specimens			Excluding Lowest and Highest Rupture Modulus		
GFRP Admin Info	Specimen Number		M32-16	M32-12	M32-4	M32-11	M32-5	M32-9	M32-15	M32-20	M32-3	M32-8	Avg.	Std Dev.	C.O.V.	Avg.	Std Dev.	C.O.V.
	Test Number		26	27	28	29	30	51	52	53	54	55						
	Type of Flexural Test		3-point bending															
	Date of Test		September 30, 2019					October 10, 2019										
	Batch		All specimens (from 3 and 4-point bending) cut from multiple bars of the same batch. Batch number and date are unknown.															
	Additional Notes		grinded sides of location of support placements															
Specimen Dimensions	Measured Height (excluding rib thickness; top of specimen to core; mm)	End 1	15.67	15.1	15.11	15.59	15.54	15.61	15.05	15.04	15.51	15.14						
		End 2	15.44	15.04	14.91	15.53	15.6	15.64	15.21	15.15	15.52	15.12						
		Avg.	15.555	15.07	15.01	15.56	15.57	15.625	15.13	15.095	15.515	15.13	15.326	0.255	2%	15.33625	0.248420007	2%
	Measured Total Length (mm)		384	383	384	384	384	383	383	384	384	383	383.6	0.516	0%	383.5	0.534522484	0%
	Orginial Radius of GFRP, r (mm) =		16	16	16	16	16	16	16	16	16	16						
	Height of Specimen, h (mm) =		15.555	15.07	15.96	15.56	15.57	15.625	15.13	15.095	15.515	15.13	15.421	0.298	2%	15.33625	0.248420007	2%
	Length of Specimen, L (mm) =		320	320	320	320	320	320	320	320	320	320						
Test Data Information	Maximum Load per Loading Nose (kN)		14.687	13.334	14.055	14.720	14.241	14.632	14.231	13.526	14.361	13.532	14.132	0.511	4%	14.068	0.530	4%
	Deflection at Maximum Load (mm)		27.400	25.363	27.649	24.968	24.198	25.758	29.113	27.458	26.888	27.723	26.652	1.519	6%	26.738	1.553	6%
	Data Point of Maximum Loading		5480	5073	5530	4994	4840	5152	5823	5492	5378	5545	5330.7	303.872	6%	5347.875	310.6672255	6%
	Maximum Deflection (mm)		27.454	26.595	28.644	26.767	24.679	27.338	29.174	28.312	27.377	27.896	27.424	1.257	5%	27.353	1.324	5%
	Total Data Points		5491	5319	5729	5354	4936	5468	5835	5663	5476	5580	5485.1	251.500	5%	5471	264.8460469	5%
	Chosen Filtered Critical Point Load, P_{cr} (N)		13386.447	13283.660	12274.745	14698.646	13243.459	13278.656	13385.543	13416.465	13751.143	13181.575	13390.034	594.056	4%	13365.868	175.304	1%
Method 1, Et/Ec = 1.25																		
Calculation of Unknown Values	Location of Neutral Axis from top of specimen, c (mm) =		6.980	6.747	7.176	6.983	6.987	7.014	6.776	6.759	6.961	6.776	6.916	0.143	2%	6.875	0.119	2%
	Rupture (Tensile) Stress, σ_t (MPa) =		1556.380	1663.877	1343.659	1707.654	1536.144	1527.661	1661.022	1673.964	1608.479	1635.712	1591.455	106.669	7%	1607.905	60.161	4%
	Compressive Stress, σ_c (MPa) =		1013.596	1079.104	878.182	1112.162	1000.712	995.499	1077.800	1085.876	1047.160	1061.377	1035.147	67.453	7%	1045.140	36.995	4%
	Maximum Bending Moment, M (Nmm) =		1.07E+06	1.06E+06	9.82E+05	1.18E+06	1.06E+06	1.06E+06	1.07E+06	1.07E+06	1.10E+06	1.05E+06	1.07E+06	4.75E+04	4%	1.07E+06	1.40E+04	1%
Variation A																		
Effective Tensile Volume Calculations	Chosen Weibull Modulus, m		17	17	17	17	17	17	17	17	17	17						
	Effective Tensile Volume Under Bending Stress, V_{eb} (mm^3)		56.823	54.355	58.900	56.848	56.905	57.181	54.659	54.482	56.618	54.659	56.143	1.520	3%	55.710	1.265	2%
	Effective Tensile Volume Under Direct Tensile Stress, V_{Et} (mm^3)		124123.423	119161.800	128270.036	124174.603	124276.965	124839.987	119775.227	119417.379	123713.996	119775.227	122752.864	3049.509	2%	121885.500	2541.553	2%
	$\sigma_b/\sigma_t = (V_{Et}/V_{Eb})^{1/m}$		1.572	1.572	1.572	1.572	1.572	1.572	1.572	1.572	1.572	1.572	1.572	0.000	0%	1.572	0.000	0%
Tensile Strength, σt (MPa)			990.112	1058.273	854.939	1086.349	977.251	971.872	1056.485	1064.700	1023.238	1040.386	1012.361	67.759	7%	1022.790	38.163	4%
Variation B																		
Effective Tensile Volume Calculations	Chosen Weibull Modulus, m		21	21	21	21	21	21	21	21	21	21						
	Effective Tensile Volume Under Bending Stress, V_{Eb} (mm^3)		34.596	33.091	35.862	34.611	34.645	34.814	33.277	33.168	34.471	33.277	34.181	0.927	3%	33.917	0.771	2%
	Effective Tensile Volume Under Direct Tensile Stress, V_{Et} (mm^3)		124123.423	119161.800	128270.036	124174.603	124276.965	124839.987	119775.227	119417.379	123713.996	119775.227	122752.864	3049.509	2%	121885.500	2541.553	2%
	$\sigma_b/\sigma_t = (V_{Et}/V_{Eb})^{1/m}$		1.477	1.477	1.476	1.477	1.477	1.477	1.477	1.477	1.477	1.477	1.477	0.000	0%	1.477	0.000	0%
Tensile Strength, σ_t (MPa)			1053.993	1126.595	910.070	1156.439	1040.300	1034.571	1124.686	1133.434	1089.259	1107.548	1077.689	72.149	7%	1088.798	40.646	4%
Method 2, Et/Ec = 1.2																		
Calculation of Unknown Values	Location of Neutral Axis from top of specimen, c (mm)		6.908107112	6.677092266	7.102044415	6.910495022	6.91527139	6.941552462	6.705672339	6.689004229	6.88852226	6.705663659	6.844	0.142	2%	6.804	0.118	2%
	Rupture Stress, σ_t (MPa)		1538.842976	1645.123657	1328.505608	1688.412436	1518.963806	1510.444498	1642.321864	1655.107285	1590.234291	1617.293989	1573.525	105.463	7%	1589.792	59.464	4%
	Compressive Stress, σ_c (MPa)		1024.500068	1090.738758	887.6224671	1124.12638	1011.397443	1006.207662	1089.405228	1097.575696	1058.503712	1072.806348	1046.288	68.191	7%	1056.392	37.416	4%
	Maximum Bending Moment, M (Nmm)		1.07E+06	1.06E+06	9.82E+05	1.18E+06	1.06E+06	1.06E+06	1.07E+06	1.07E+06	1.10E+06	1.05E+06	1.07E+06	4.75E+04	4%	1.07E+06	1.40E+04	1%
Variation A																		
Effective Tensile Volume Calculations	Chosen Weibull Modulus, m		17	17	17	17	17	17	17	17	17	17						
	Effective Tensile Volume Under Bending Stress, V_{eb} (mm^3)		56.823	54.355	58.900	56.848	56.905	57.181	54.659	54.482	56.618	54.659	56.143	1.520	3%	55.710	1.265	2%
	Effective Tensile Volume Under Direct Tensile Stress, V_{Et} (mm^3)		124123.423	119161.800	128270.036	124174.603	124276.965	124839.987	119775.227	119417.379	123713.996	119775.227	122752.864	3049.509	2%	121885.500	2541.553	2%
	$\sigma_b/\sigma_t = (V_{Et}/V_{Eb})^{1/m}$		1.572	1.572	1.572	1.572	1.572	1.572	1.572	1.572	1.572	1.572	1.572	0.000	0%	1.572	0.000	0%
Tensile Strength, σt (MPa)			978.956	1046.345	845.298	1074.109	966.321	960.919	1044.591	1052.707	1011.631	1028.672	1000.955	66.992	7%	1011.268	37.721	4%
Variation B																		
Effective Tensile Volume Calculations	Chosen Weibull Modulus, m		21	21	21	21	21	21	21	21	21	21						
	Effective Tensile Volume Under Bending Stress, V_{eb} (mm^3)		34.596	33.091	35.862	34.611	34.645	34.814	33.277	33.168	34.471	33.277	34.181	0.927	3%	33.917	0.771	2%
	Effective Tensile Volume Under Direct Tensile Stress, V_{Et} (mm^3)		124123.423	119161.800	128270.036	124174.603	124276.965	124839.987	119775.227	123713.996	119417.379	119775.227	122752.864	3049.509	2%	121885.500	2541.553	2%
	$\sigma_b/\sigma_t = (V_{Et}/V_{Eb})^{1/m}$		1.477	1.477	1.476	1.477	1.477	1.477	1.477	1.477	1.477	1.477	1.477	0.000	0%	1.477	0.000	0%
Tensile Strength, σ_t (MPa)			1042.112	1113.830	899.805	1143.412	1028.655	1022.883	1111.958	1076.991	1120.599	1095.013	1065.526	71.320	7%	1076.505	40.151	4%

B.12 M32 Specimens in 4-Point Bending

Variation A – Parameters calculated using all 10 specimens

Variation B – Parameters calculated using 8 specimens (omitting outliers)

Orange text denotes outliers

GFRP Parameters and Information			M32 Specimens										Using All Specimens			Excluding Lowest and Highest Rupture Modulus		
GFRP Admin Info	Specimen Number		M32-19	M32-7	M32-2	M32-10	M32-18	M32-13	M32-17	M32-14	M32-6	M32-1	Avg.	Std Dev.	C.O.V.	Avg.	Std Dev.	C.O.V.
	Test Number		103	104	105	106	107	108	109	110	111	112						
	Type of Flexural Test		4-point bending															
	Date of Test		15-Jan-20								16-Jan-20							
	Batch		All specimens (from 3 and 4-point bending) cut from multiple bars of the same batch. Batch number and date are unknown.															
	Additional Notes		grinded sides of location of support placements															
Specimen Dimensions	Measured Height (excluding rib thickness; top of specimen to core; mm)	End 1	15.35	15.64	15.15	15.13	15.4	15.44	15.7	15.59	15.67	15.02						
		End 2	15.37	15.46	15.09	15.02	15.58	15.76	15.08	15.5	15.72	15.04						
		Avg.	15.36	15.55	15.12	15.075	15.49	15.6	15.39	15.545	15.695	15.03	15.386	0.236	2%	15.433125	0.224879928	1%
	Measured Total Length (mm)		383	383	384	384	383	383	383	383	383	384	383.3	0.483	0%	383.25	0.46291005	0%
	Orginial Radius of GFRP, r (mm) =		16	16	16	16	16	16	16	16	16	16						
	Height of Specimen, h (mm) =		15.36	15.55	15.12	15.075	15.49	15.6	15.39	15.545	15.695	15.03	15.386	0.236	2%	15.433125	0.224879928	1%
	Length of Specimen, L (mm) =		320	320	320	320	320	320	320	320	320	320						
Test Data Information	Maximum Load per Loading Nose (kN)		6.703	11.130	10.578	11.232	11.014	11.345	11.065	10.993	11.360	10.916	10.634	1.400	13%	11.090	0.250	2%
	Deflection at Maximum Load (mm)		33.988	39.281	37.946	43.869	36.332	37.079	40.782	36.314	37.842	39.712	38.315	2.756	7%	38.681	2.581	7%
	Data Point of Maximum Loading		5371	6208	5997	6933	5742	5860	6445	5739	5980	6276	6055.1	435.626	7%	6113	407.8375027	7%
	Maximum Deflection (mm)		34.140	42.079	44.582	44.685	39.982	38.790	45.494	42.218	42.938	39.964	41.487	3.411	8%	42.596	2.347	6%
	Total Data Points		5395	6650	7046	7062	6319	6130	7189	6672	6786	6316	6556.5	539.051	8%	6731.75	370.8210003	6%
	Chosen Filtered Critical Point Load, P_{cr} (N)		5593.056	10248.646	10233.853	9873.529	10095.275	10370.130	9833.466	10248.303	9894.354	10342.598	9673.321	1447.237	15%	10099.694	206.888	2%
Method 1, Et/Ec = 1.25																		
Calculation of Unknown Values	Location of Neutral Axis from top of specimen, c (mm) =		6.886	6.978	6.771	6.749	6.949	7.002	6.901	6.976	7.048	6.728	6.900	0.120	2%	6.922	0.108	2%
	Rupture (Tensile) Stress, σ_t (MPa) =		893.122	1589.951	1695.788	1647.637	1580.441	1596.719	1563.062	1591.099	1501.914	1738.146	1611.640	71.474	4%	1595.826	57.152	4%
	Compressive Stress, σ_c (MPa) =		580.667	1035.412	1100.373	1068.682	1028.684	1040.271	1016.494	1036.114	979.316	1126.914	1048.029	44.498	4%	1038.168	35.537	3%
	Maximum Bending Moment, M (Nmm) =		5.97E+05	1.09E+06	1.09E+06	1.05E+06	1.08E+06	1.11E+06	1.05E+06	1.09E+06	1.06E+06	1.10E+06	1.08E+06	2.24E+04	2%	1.08E+06	2.21E+04	2%
Variation A																		
Effective Tensile Volume Calculations	Chosen Weibull Modulus, m		20	20	20	20	20	20	20	20	20	20						
	Effective Tensile Volume Under Bending Stress, V_{eb} (mm^3)		292.378	297.460	286.001	284.799	295.853	298.800	293.180	297.326	301.349	283.598	293.152	6.657	2%	294.346	5.998	2%
	Effective Tensile Volume Under Direct Tensile Stress, V_{Et} (mm^3)		122127.783	124072.243	119672.980	119212.914	123458.120	124584.062	122434.749	124021.063	125556.624	118752.923	122418.409	2553.716	2%	122876.594	2300.822	2%
	$\sigma_b/\sigma_t = (V_{Et}/V_{Eb})^{1/m}$		3.343	3.342	3.344	3.345	3.343	3.342	3.343	3.342	3.342	3.345	3.343	0.001	0%	3.343	0.001	0%
Tensile Strength, σt (MPa)			267.139	475.701	507.044	492.612	472.813	477.762	467.543	476.041	449.460	519.635	482.068	21.218	4%	477.372	16.962	4%
Variation B																		
Effective Tensile Volume Calculations	Chosen Weibull Modulus, m		21.5	21.5	21.5	21.5	21.5	21.5	21.5	21.5	21.5	21.5						
	Effective Tensile Volume Under Bending Stress, V_{Eb} (mm^3)		262.818	267.387	257.083	256.002	265.943	268.592	263.538	267.267	270.884	254.922	263.513	5.986	2%	264.587	5.394	2%
	Effective Tensile Volume Under Direct Tensile Stress, V_{Et} (mm^3)		122127.783	124072.243	119672.980	119212.914	123458.120	124584.062	122434.749	124021.063	125556.624	118752.923	122418.409	2553.716	2%	122876.594	2300.822	2%
	$\sigma_b/\sigma_t = (V_{Et}/V_{Eb})^{1/m}$		1.331	1.331	1.331	1.331	1.331	1.331	1.331	1.331	1.330	1.331	1.331	0.000	0%	1.331	0.000	0%
Tensile Strength, σ_t (MPa)			671.208	1194.975	1274.330	1238.126	1187.803	1200.083	1174.699	1195.836	1128.866	1306.117	1211.204	53.620	4%	1199.340	42.873	4%
Method 2, Et/Ec = 1.2																		
Calculation of Unknown Values	Location of Neutral Axis from top of specimen, c (mm)		6.815	6.906	6.701	6.679	6.877	6.930	6.829	6.903	6.975	6.658	6.829	0.119	2%	6.850	0.107	2%
	Rupture Stress, σ_t (MPa)		882.994	1572.032	1676.681	1629.021	1562.643	1578.701	1545.455	1573.169	1484.885	1718.466	1593.451	70.665	4%	1577.824	56.525	4%
	Compressive Stress, σ_c (MPa)		586.960	1046.554	1112.232	1080.234	1039.748	1051.477	1027.434	1047.263	989.913	1139.123	1059.331	44.990	4%	1049.357	35.916	3%
	Maximum Bending Moment, M (Nmm)		596592.662	1093188.951	1091610.937	1053176.424	1076829.343	1106147.225	1048902.999	1093152.339	1055397.737	1103210.411	1.08E+06	2.24E+04	2%	1.08E+06	2.21E+04	2%
Variation A																		
Effective Tensile Volume Calculations	Chosen Weibull Modulus, m		20	20	20	20	20	20	20	20	20	20						
	Effective Tensile Volume Under Bending Stress, V_{eb} (mm^3)		292.378	297.460	286.001	284.799	295.853	298.800	293.180	297.326	301.349	283.598	293.152	6.657	2%	294.346	5.998	2%
	Effective Tensile Volume Under Direct Tensile Stress, V_{Et} (mm^3)		122127.783	124072.243	119672.980	119212.914	123458.120	124584.062	122434.749	124021.063	125556.624	118752.923	122418.409	2553.716	2%	122876.594	2300.822	2%
	$\sigma_b/\sigma_t = (V_{Et}/V_{Eb})^{1/m}$		1.352	1.352	1.352	1.352	1.352	1.352	1.352	1.352	1.352	1.352	1.352	0.000	0%	1.352	0.000	0%
Tensile Strength, σt (MPa)			653.0015571	1162.650381	1239.849751	1204.585273	1155.680092	1167.604819	1142.925088	1163.488828	1098.257798	1270.702899	1178.416	52.161	4%	1166.880	41.721	4%
Variation B																		
Effective Tensile Volume Calculations	Chosen Weibull Modulus, m		21.5	21.5	21.5	21.5	21.5	21.5	21.5	21.5	21.5	21.5						
	Effective Tensile Volume Under Bending Stress, V_{eb} (mm^3)		262.818	267.387	257.083	256.002	265.943	268.592	263.538	267.267	270.884	254.922	263.513	5.986	2%	264.587	5.394	2%
	Effective Tensile Volume Under Direct Tensile Stress, V_{Et} (mm^3)		122127.783	124072.243	119672.980	119212.914	123458.120	124584.062	122434.749	124021.063	125556.624	118752.923	122418.409	2553.716	2%	122876.594	2300.822	2%
	$\sigma_b/\sigma_t = (V_{Et}/V_{Eb})^{1/m}$		1.331	1.331	1.331	1.331	1.331	1.331	1.331	1.331	1.330	1.331	1.331	0.000	0%	1.331	0.000	0%
Tensile Strength, σ_t (MPa)			663.596	1181.508	1259.972	1224.137	1174.426	1186.541	1161.467	1182.360	1116.067	1291.405	1197.543	53.030	4%	1185.810	42.403	4%

Appendix C - Flexural Load-Displacement Graphs

This section of the papers includes the load-displacement plots of all the flexural specimens using the raw data and the filtered data, which have been plotted using MATLAB. The chosen load used (i.e. point-of-interest; refer to Chapter 4) is also indicated on the graphs, for reference. These plots are organized by the sequence of their testing number order, not their specimen number.

C1.0 Load-Displacement Graphs for GFRP Specimens Subjected to 3-Point Bending

C1.1 M8 Specimens

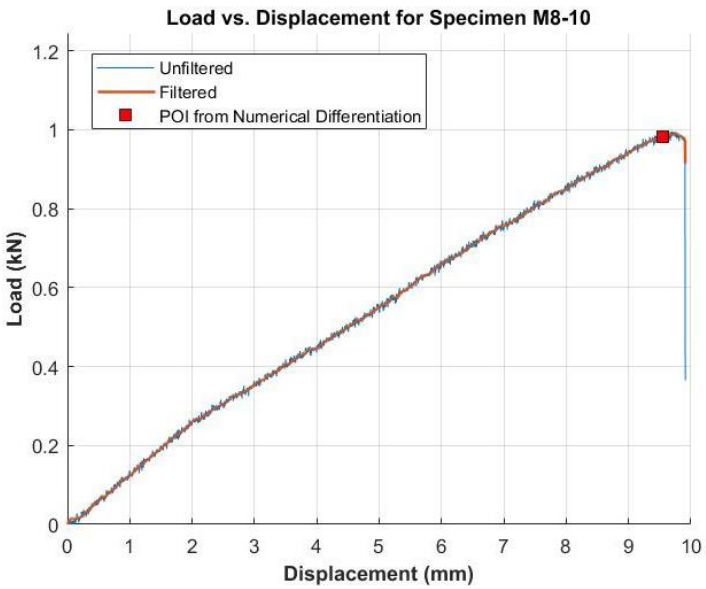

Figure C1.1: Load-displacement plot for Specimen M8-10

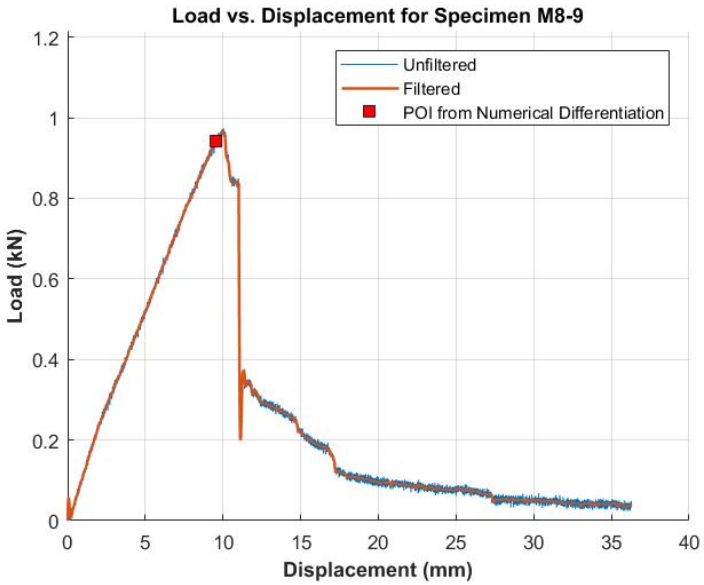

Figure C1.2: Load-displacement plot for Specimen M8-9

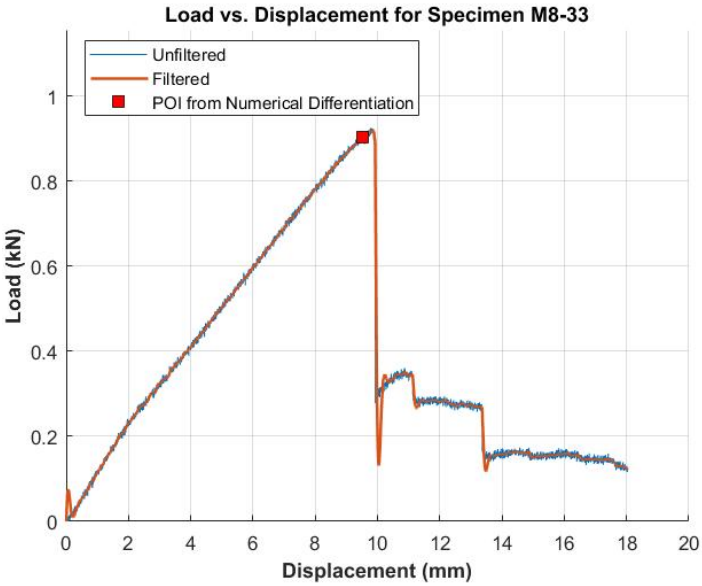

Figure C1.3: Load-displacement plot for Specimen M8-33

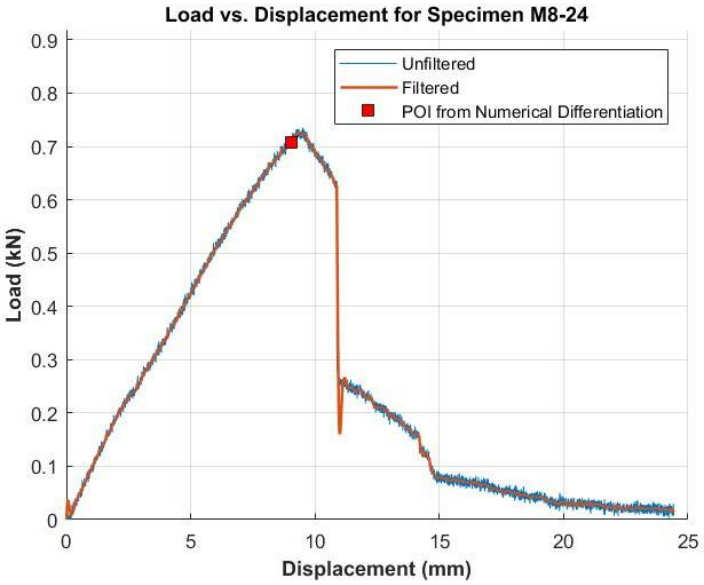

Figure C1.4: Load-displacement plot for Specimen M8-24

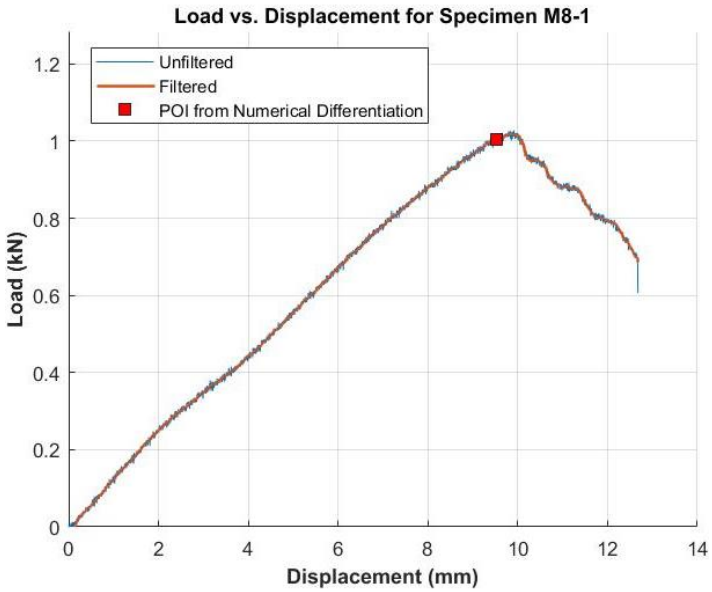

Figure C1.5: Load-displacement plot for Specimen M8-1

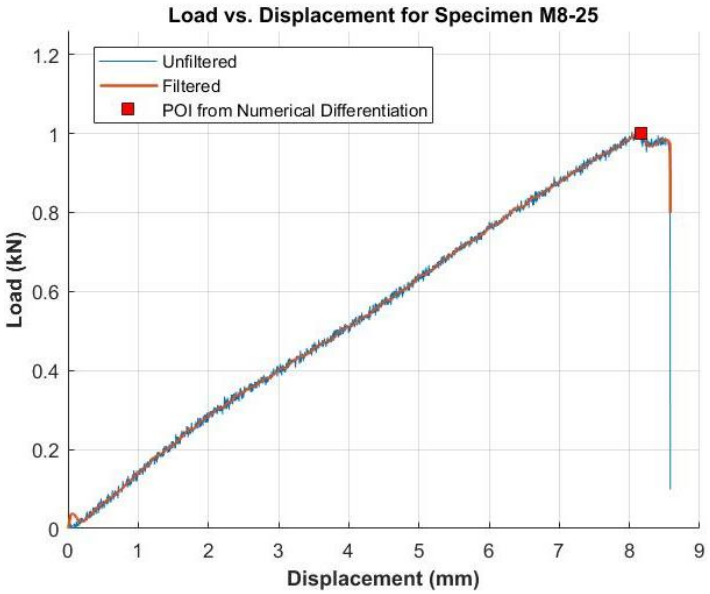

Figure C1.6: Load-displacement plot for Specimen M8-25

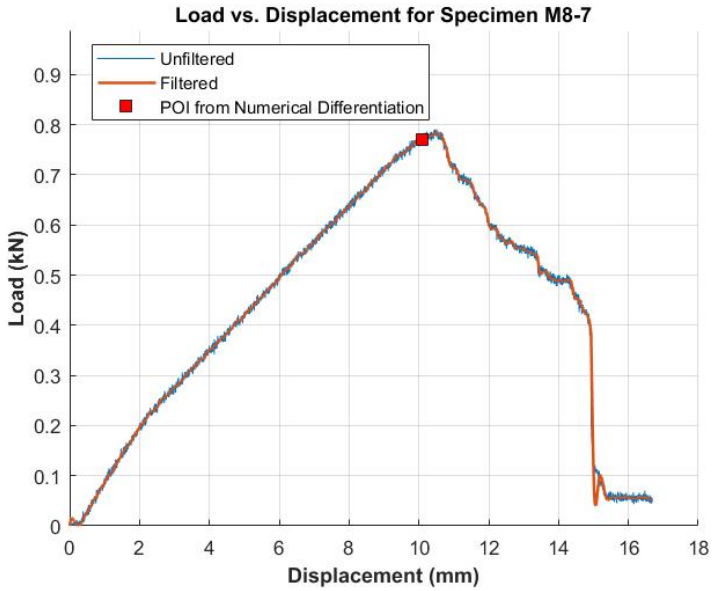

Figure C1.7: Load-displacement plot for Specimen M8-7

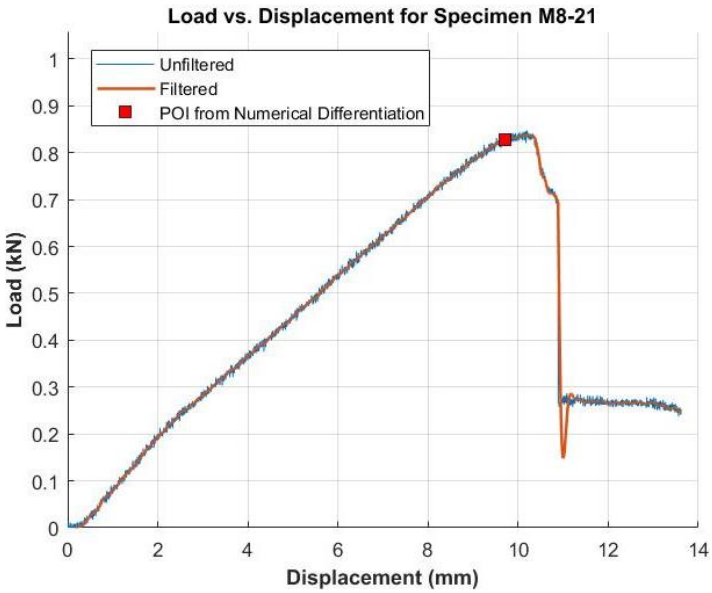

Figure C1.8: Load-displacement plot for Specimen M8-21

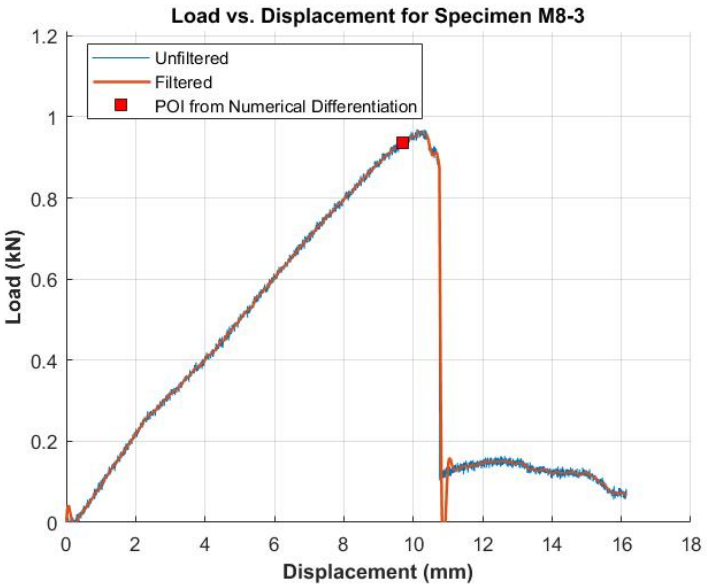

Figure C1.9: Load-displacement plot for Specimen M8-3

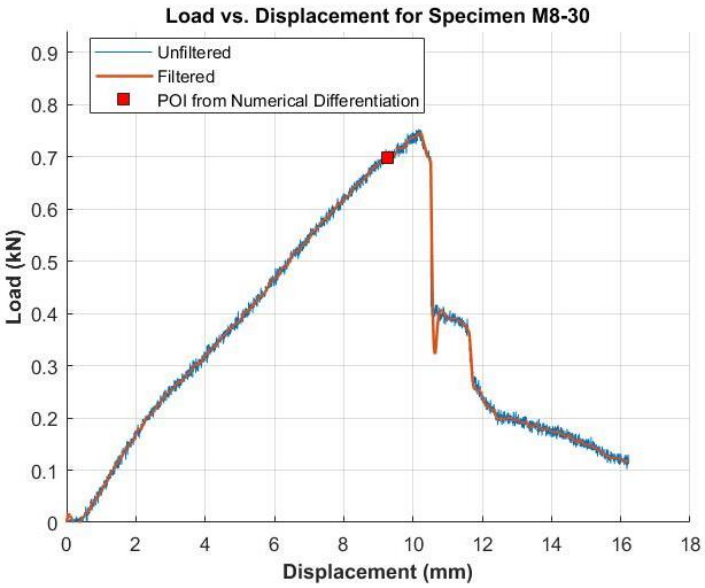

Figure C1.10: Load-displacement plot for Specimen M8-30

C1.2 M13 Specimens

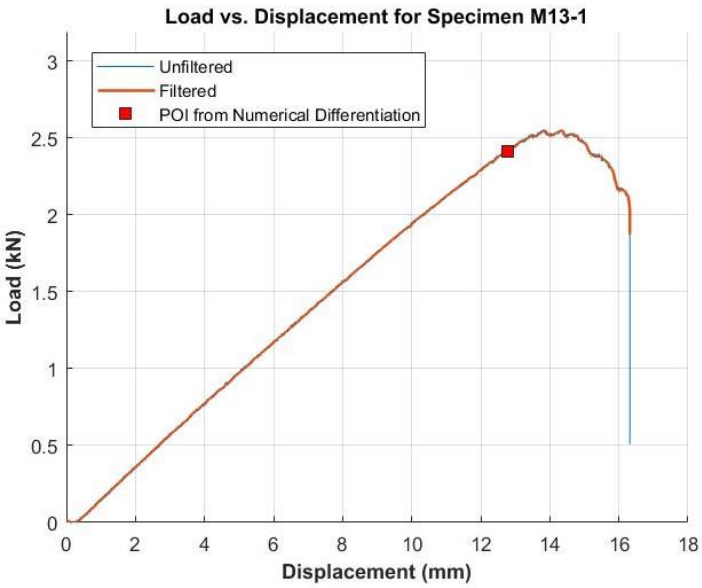

Figure C1.11: Load-displacement plot for Specimen M13-1

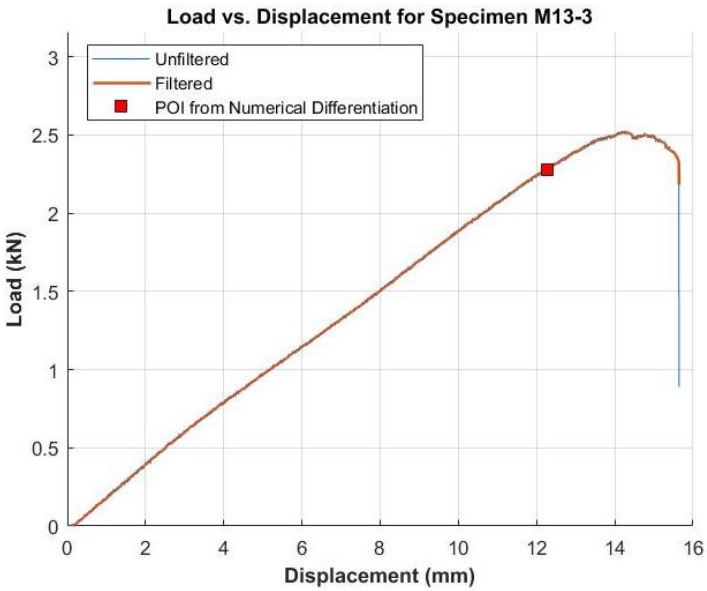

Figure C1.12: Load-displacement plot for Specimen M13-3

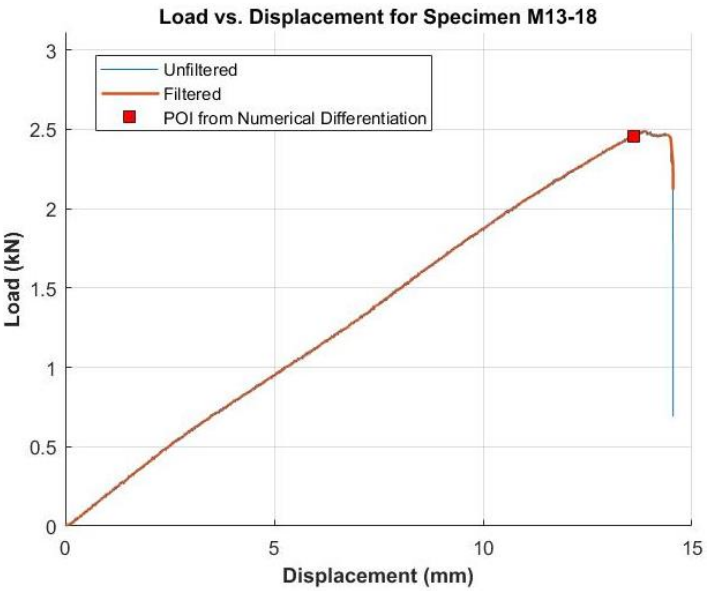

Figure C1.13: Load-displacement plot for Specimen M13-18

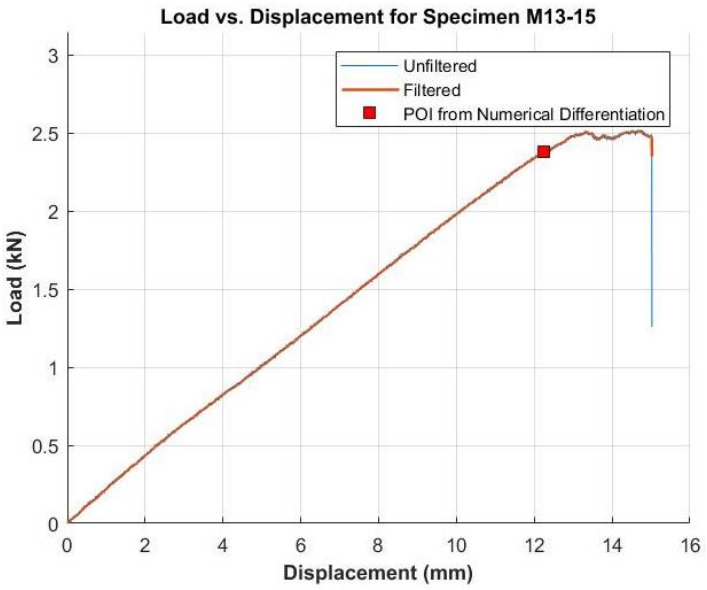

Figure C1.14: Load-displacement plot for Specimen M13-15

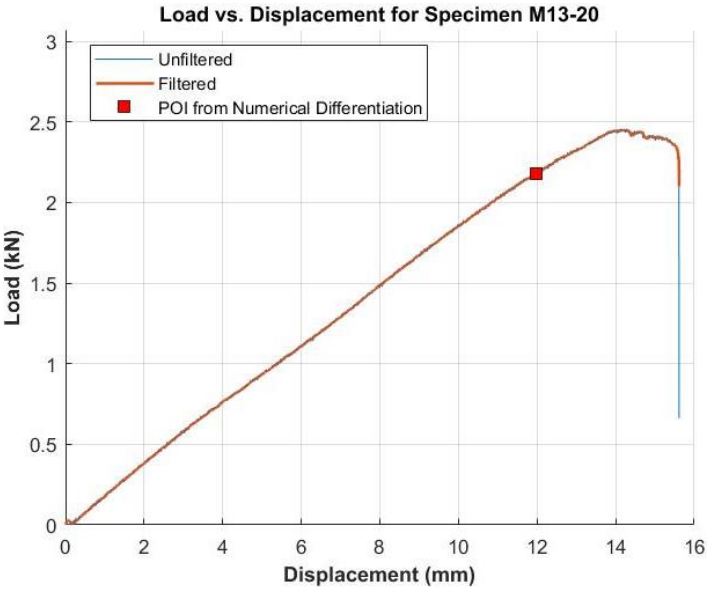

Figure C1.15: Load-displacement plot for Specimen M13-20

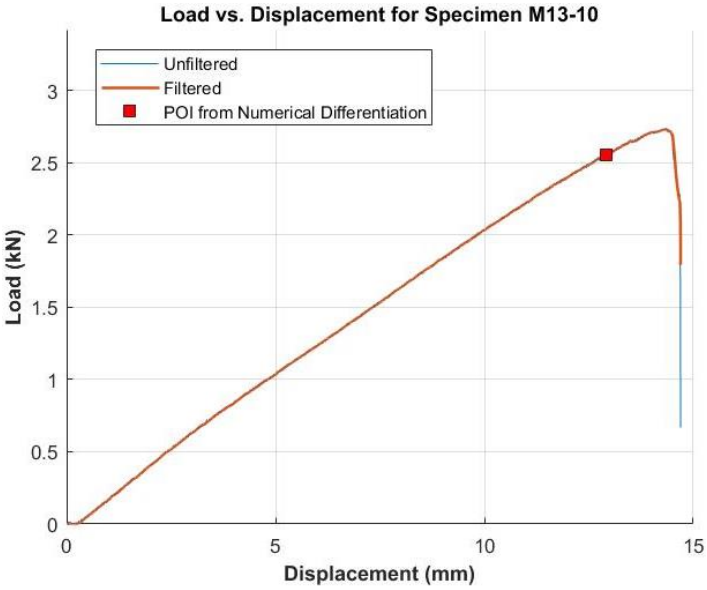

Figure C1.16: Load-displacement plot for Specimen M13-10

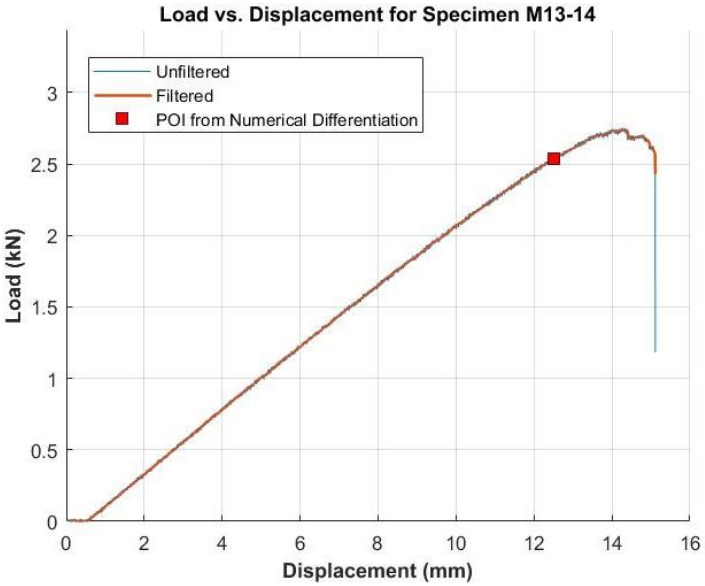

Figure C1.17: Load-displacement plot for Specimen M13-14

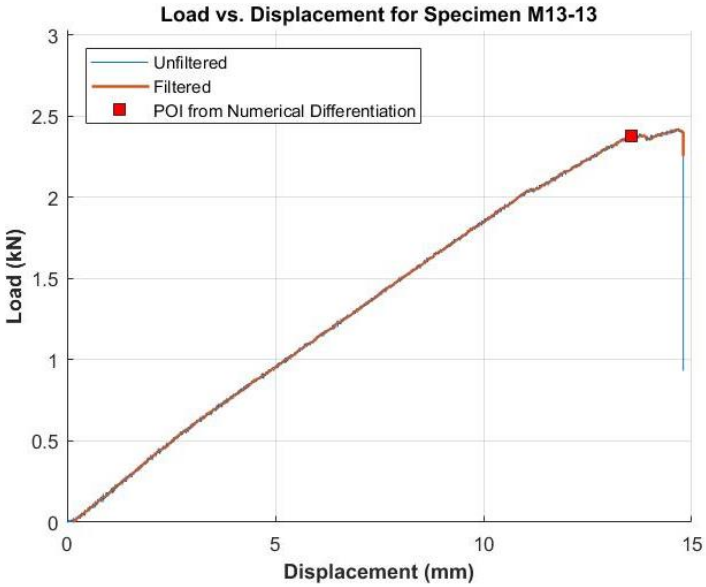

Figure C1.18: Load-displacement plot for Specimen M13-13

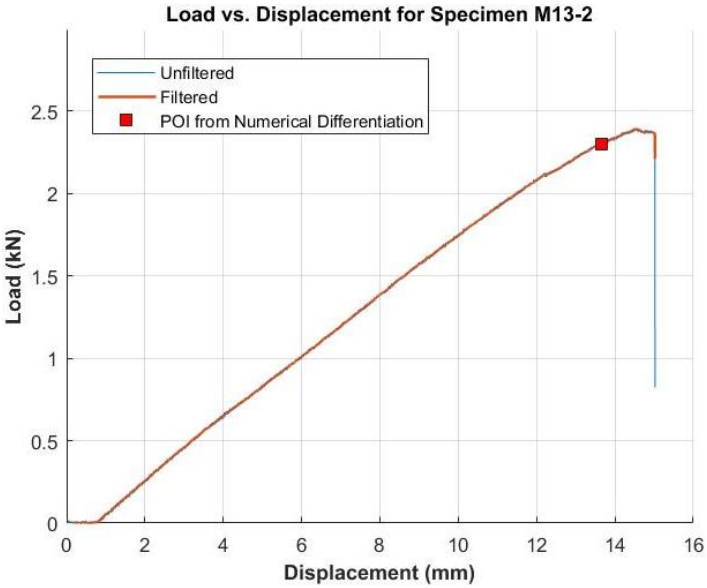

Figure C1.19: Load-displacement plot for Specimen M13-2

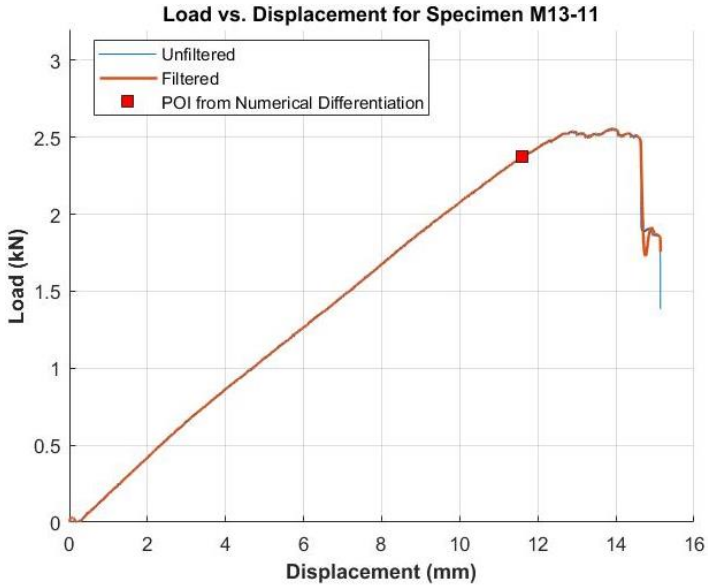

Figure C1.20: Load-displacement plot for Specimen M13-11

C1.3 M15 Specimens

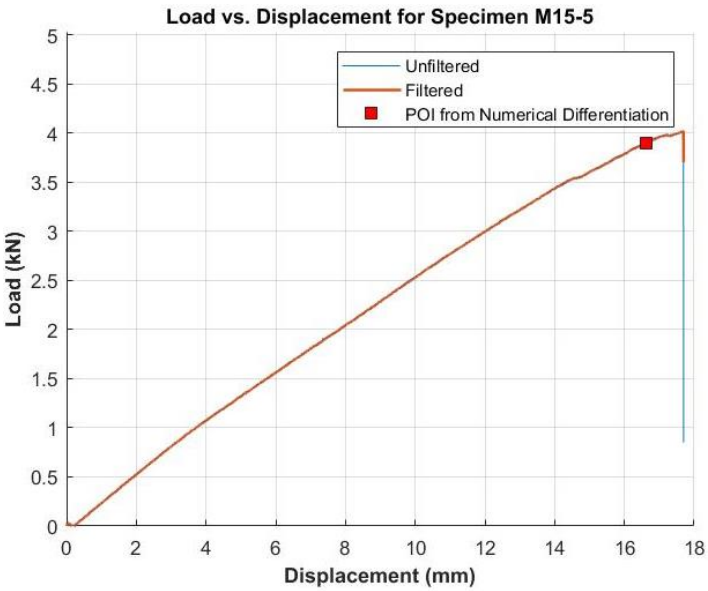

Figure C1.21: Load-displacement plot for Specimen M15-5

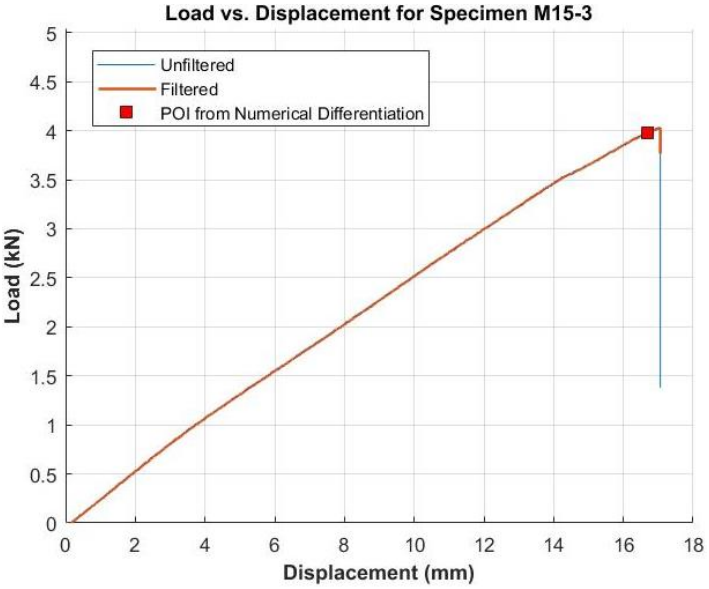

Figure C1.22: Load-displacement plot for Specimen M15-3

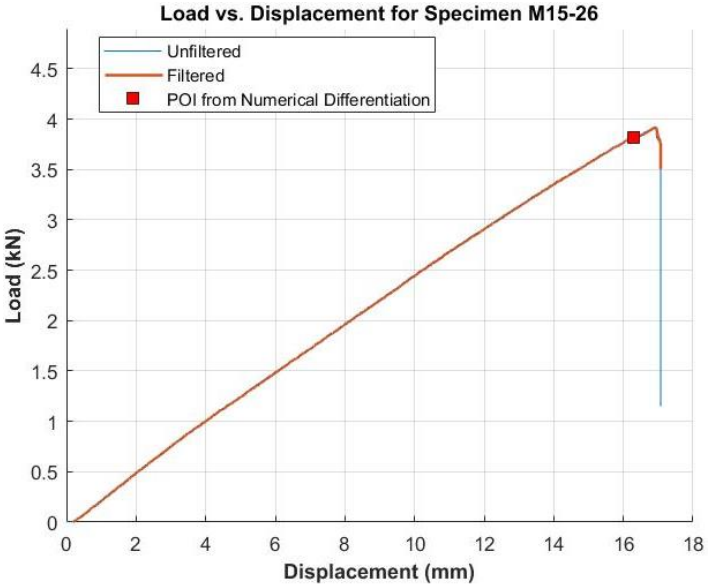

Figure C1.23: Load-displacement plot for Specimen M15-26

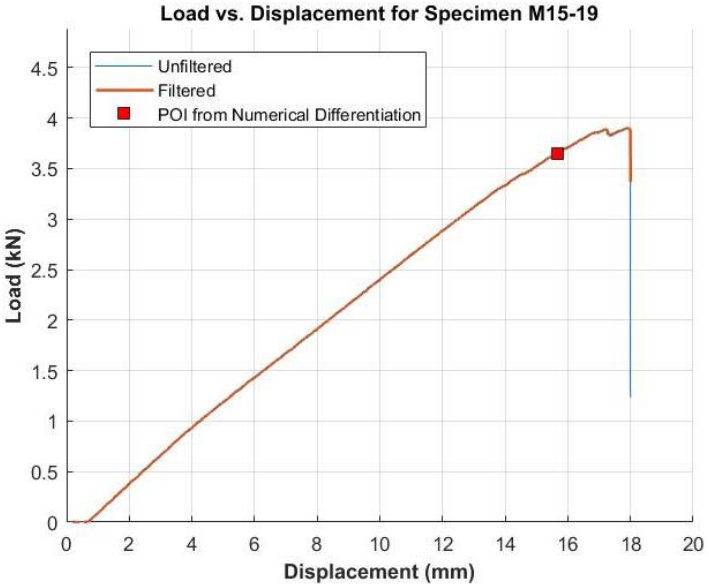

Figure C1.24: Load-displacement plot for Specimen M15-19

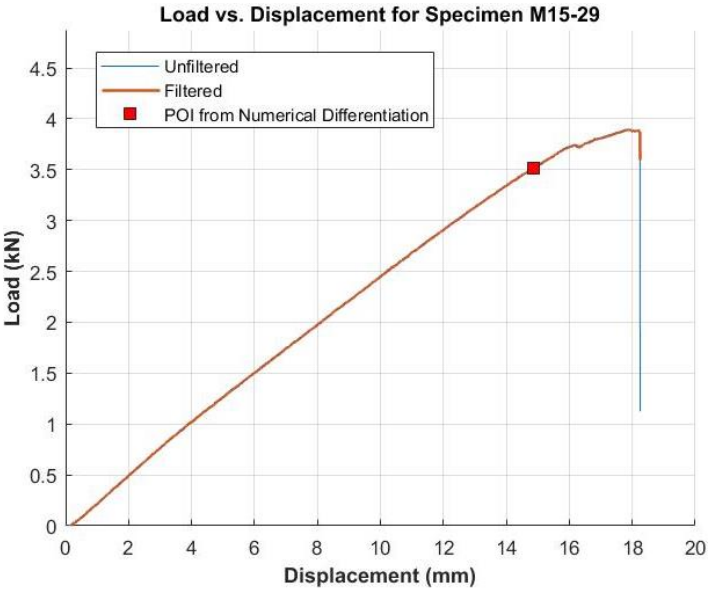

Figure C1.25: Load-displacement plot for Specimen M15-29

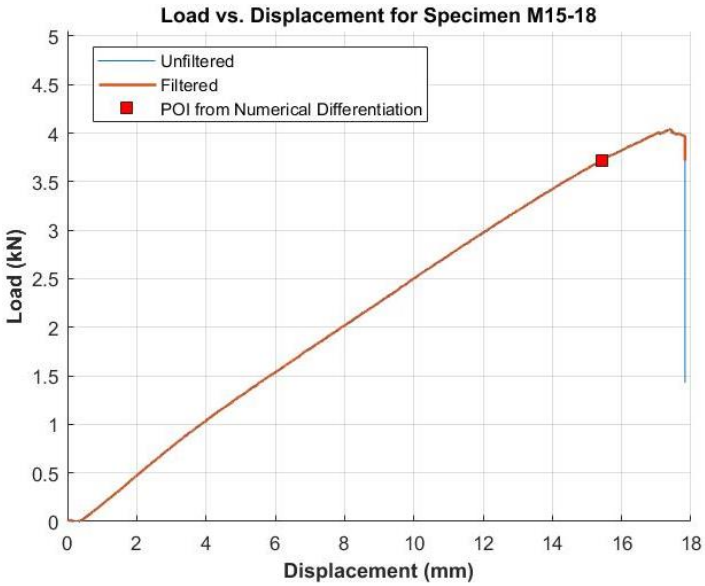

Figure C1.26: Load-displacement plot for Specimen M15-18

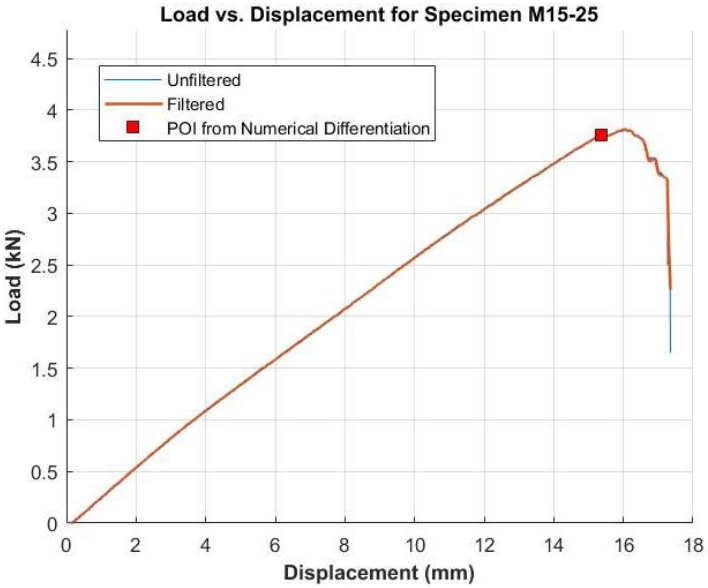

Figure C1.27: Load-displacement plot for Specimen M15-25

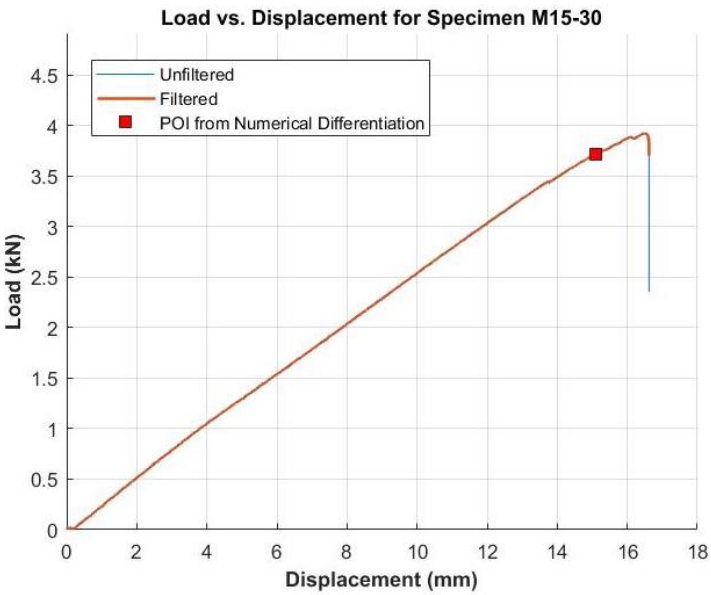

Figure C1.28: Load-displacement plot for Specimen M15-30

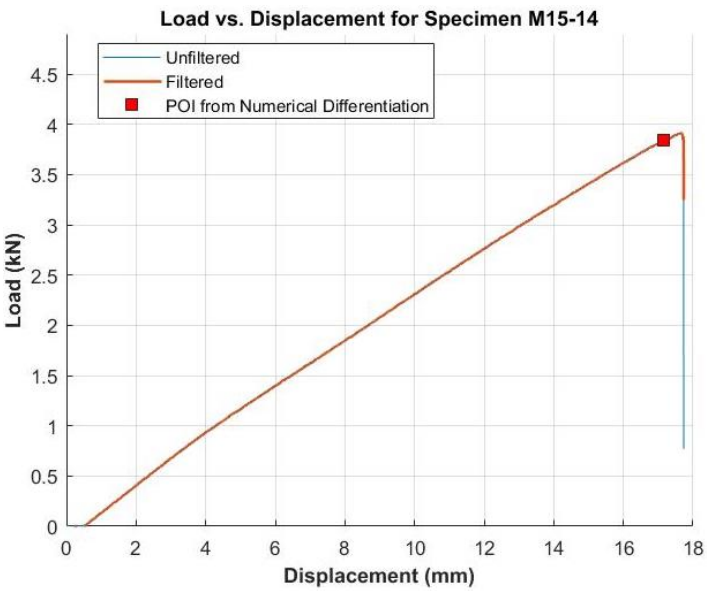

Figure C1.29: Load-displacement plot for Specimen M15-14

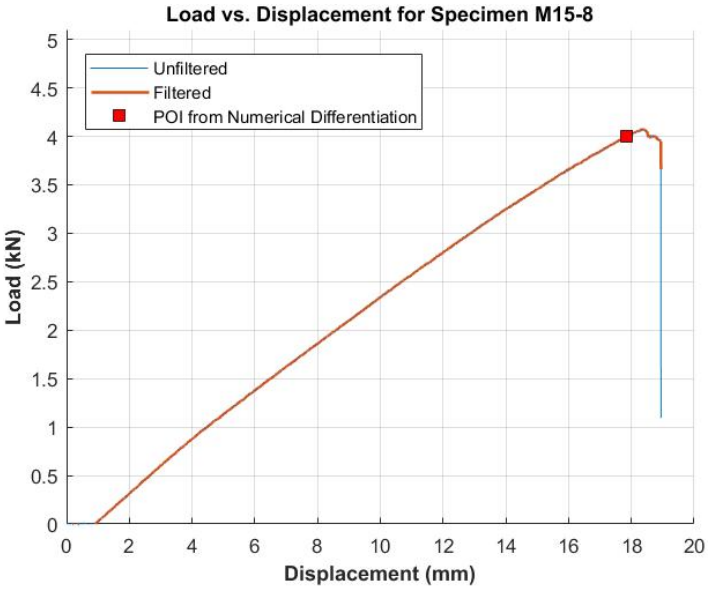

Figure C1.30: Load-displacement plot for Specimen M15-8

C1.4 M20 Specimens

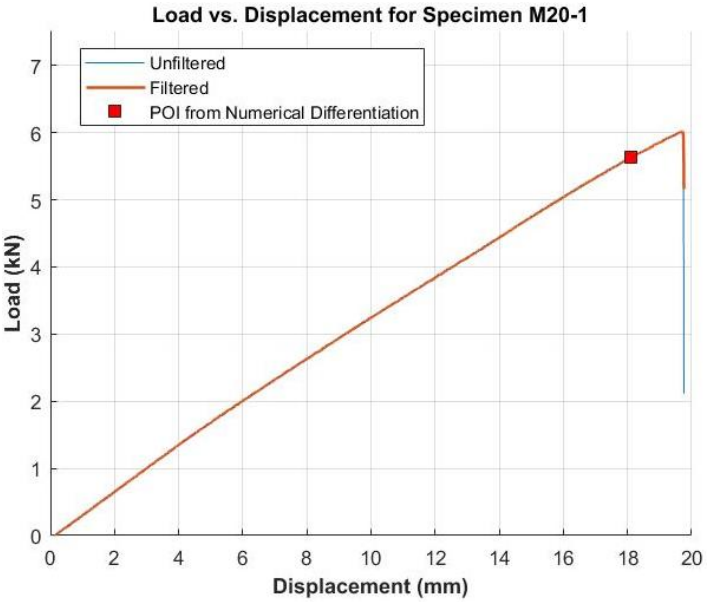

Figure C1.31: Load-displacement plot for Specimen M20-1

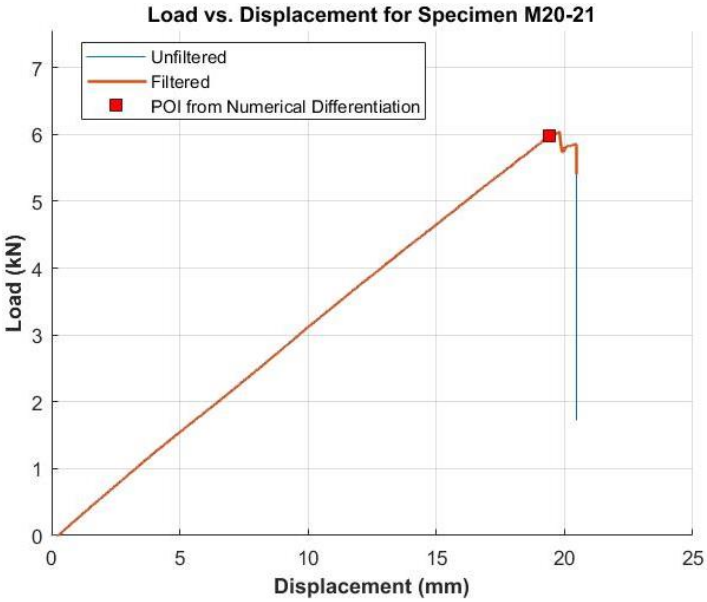

Figure C1.32: Load-displacement plot for Specimen M20-21

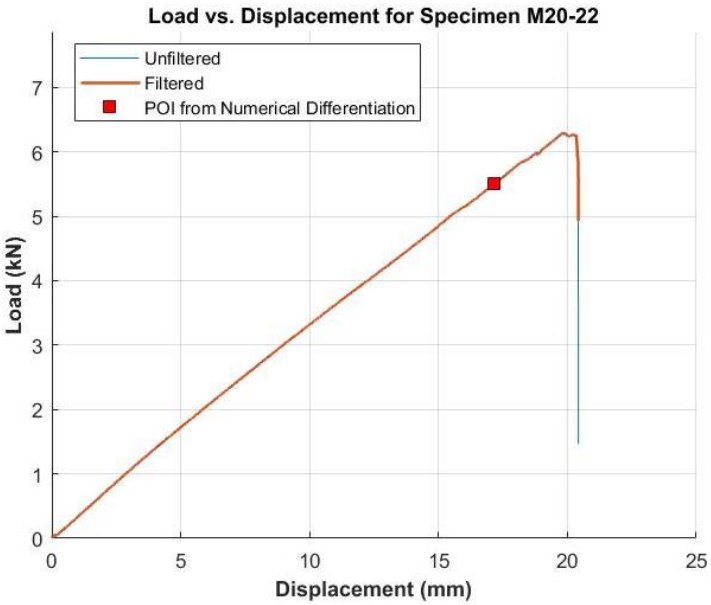

Figure C1.33: Load-displacement plot for Specimen M20-22

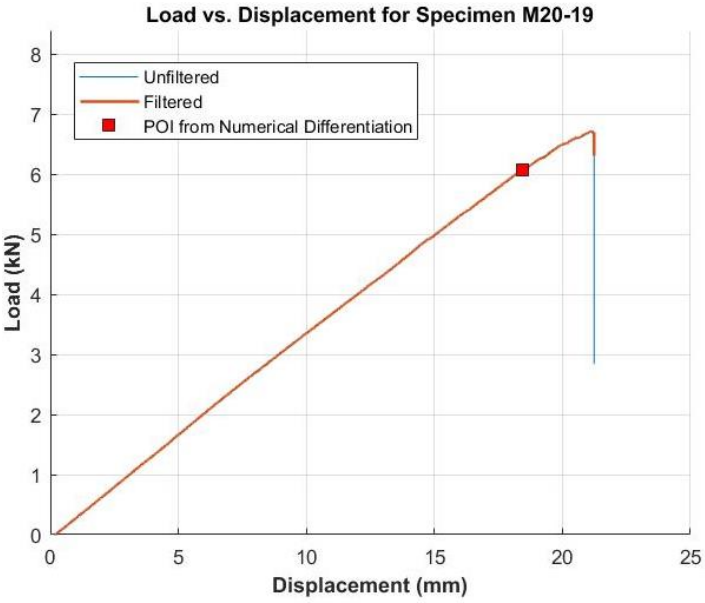

Figure C1.34: Load-displacement plot for Specimen M20-19

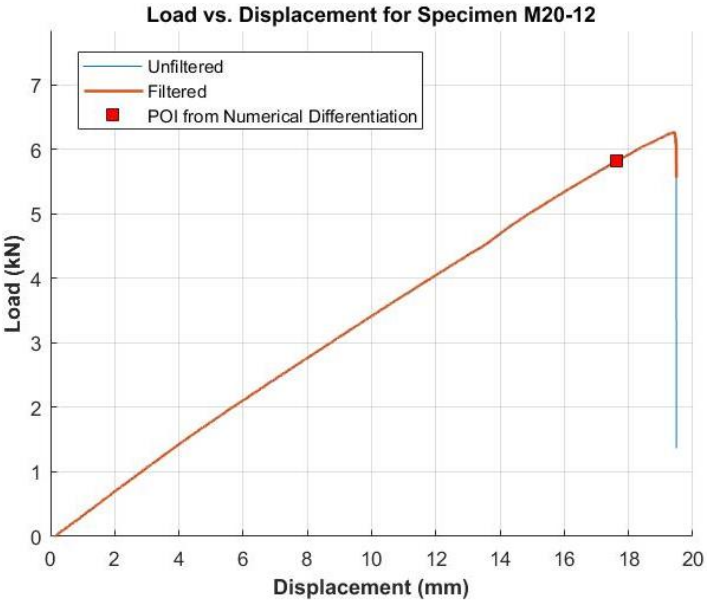

Figure C1.35: Load-displacement plot for Specimen M20-12

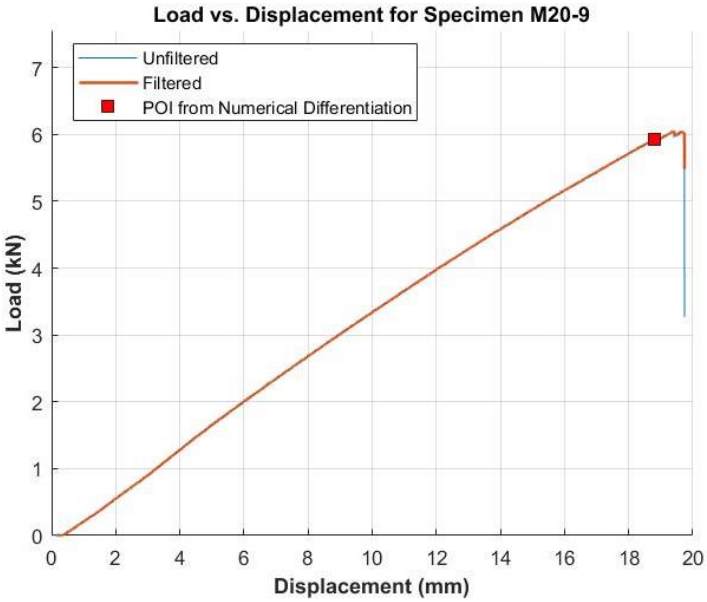

Figure C1.36: Load-displacement plot for Specimen M20-9

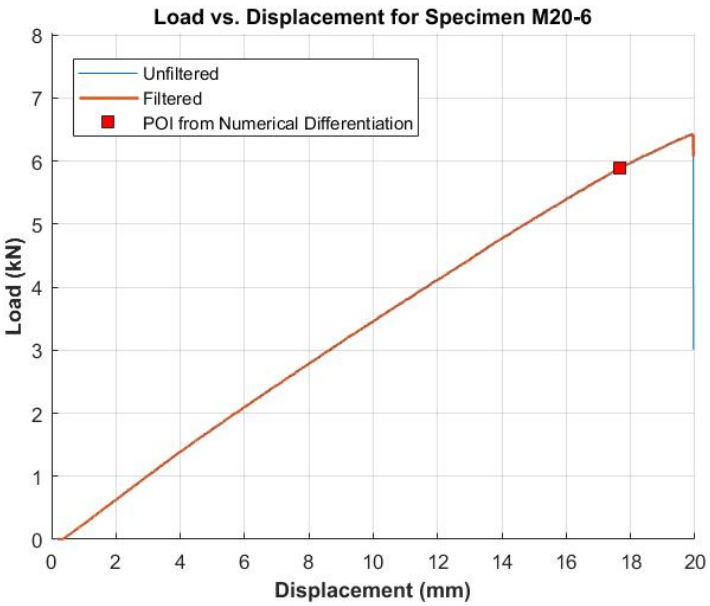

Figure C1.37: Load-displacement plot for Specimen M20-6

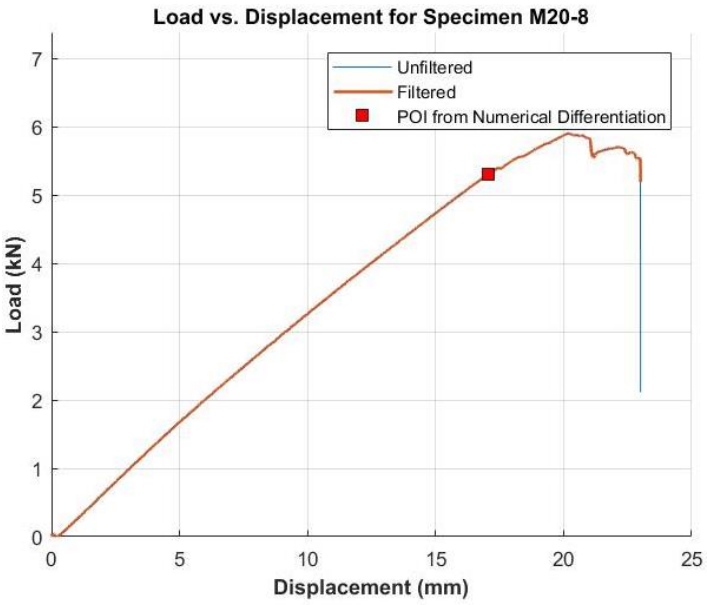

Figure C1.38: Load-displacement plot for Specimen M20-8

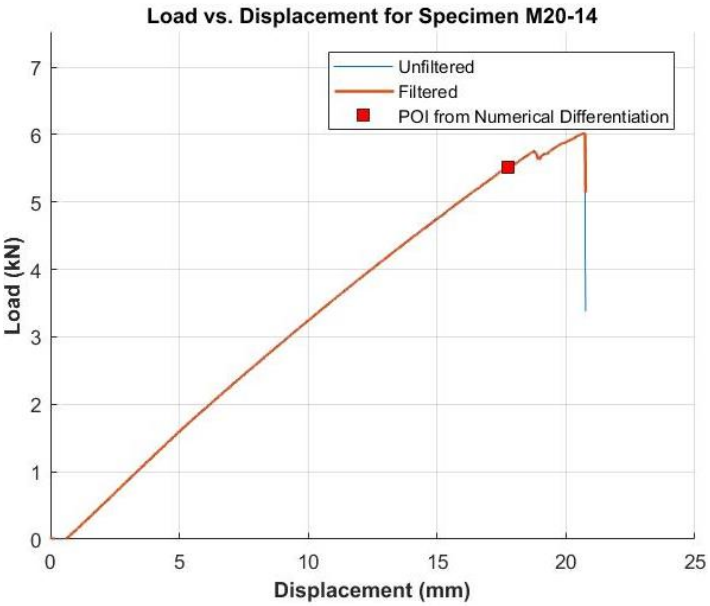

Figure C1. 39: Load-displacement plot for Specimen M20-14

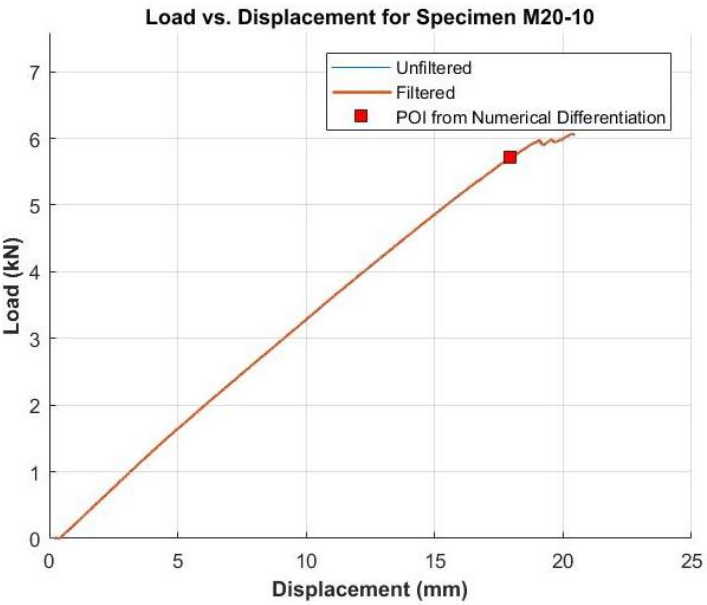

Figure C1.40: Load-displacement plot for Specimen M20-10

C1.5 M25 Specimens

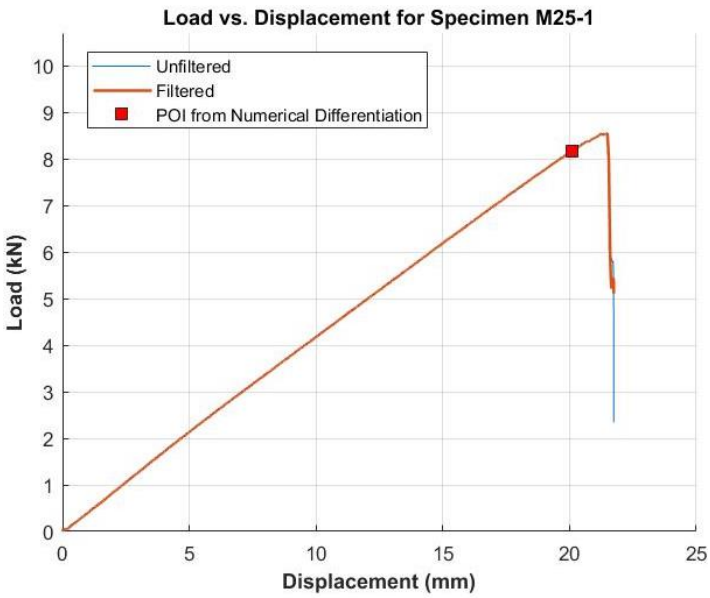

Figure C1.41: Load-displacement plot for Specimen M25-1

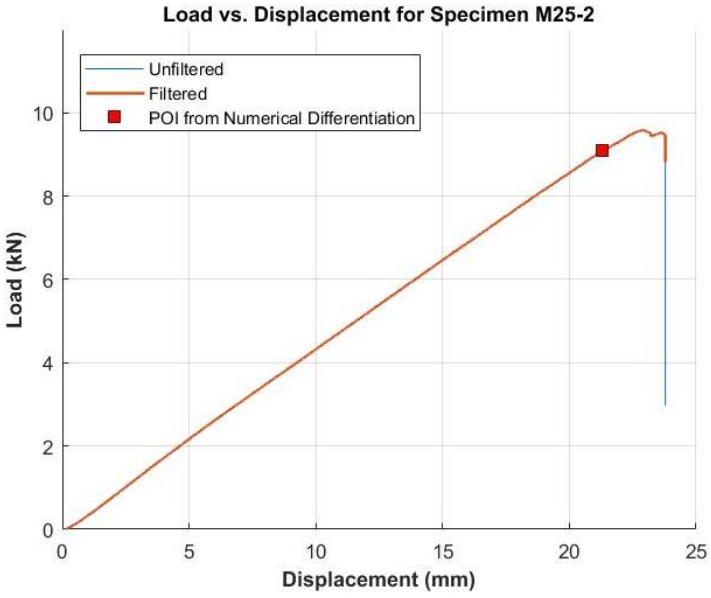

Figure C1.42: Load-displacement plot for Specimen M25-2

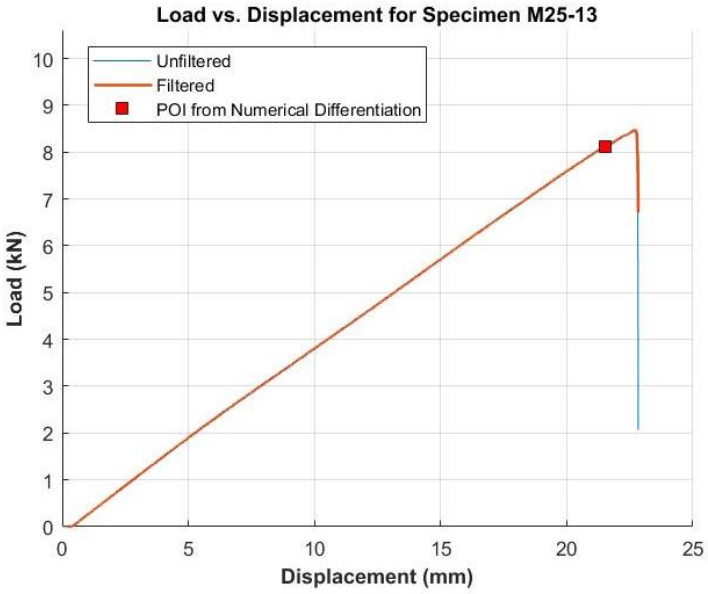

Figure C1.43: Load-displacement plot for Specimen M25-13

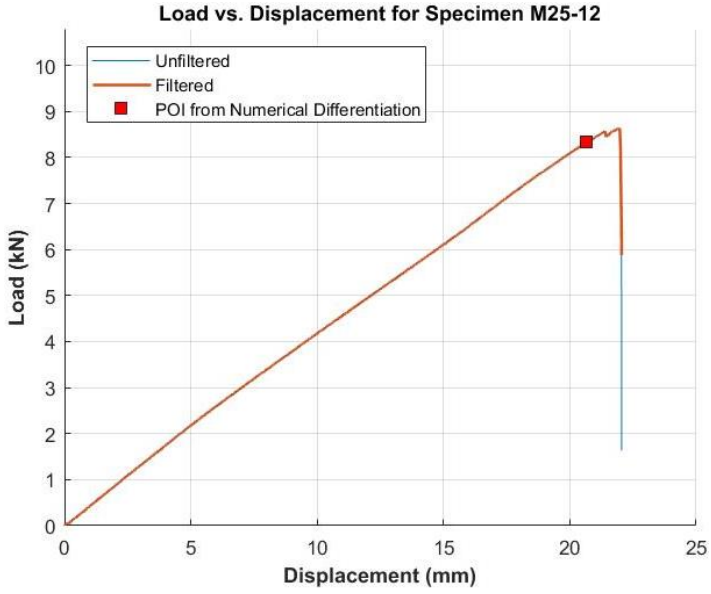

Figure C1.44: Load-displacement plot for Specimen M25-12

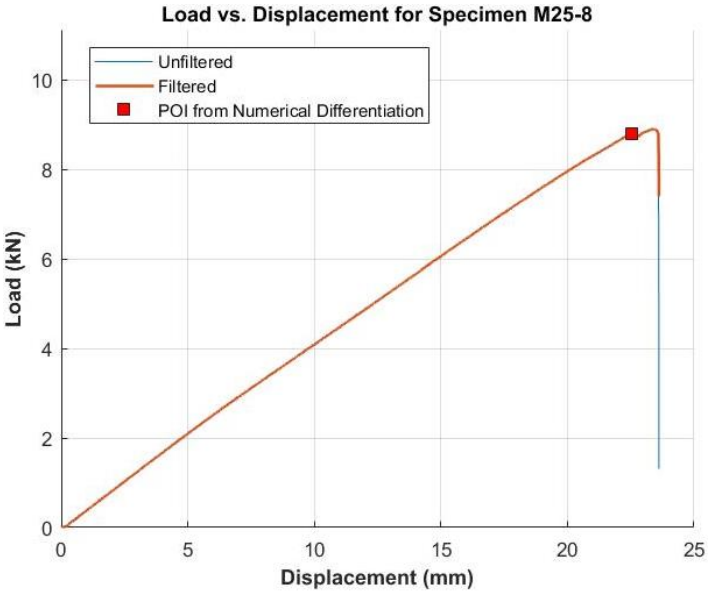

Figure C1.45: Load-displacement plot for Specimen M25-8

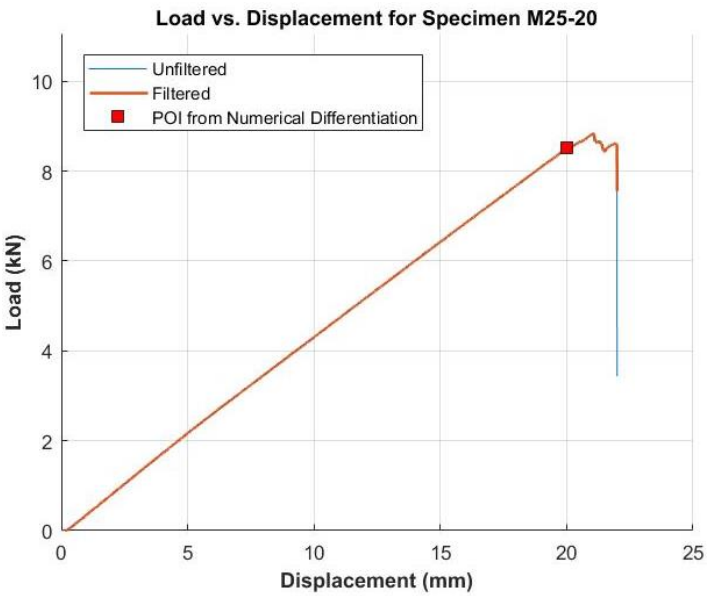

Figure C1.46: Load-displacement plot for Specimen M25-20

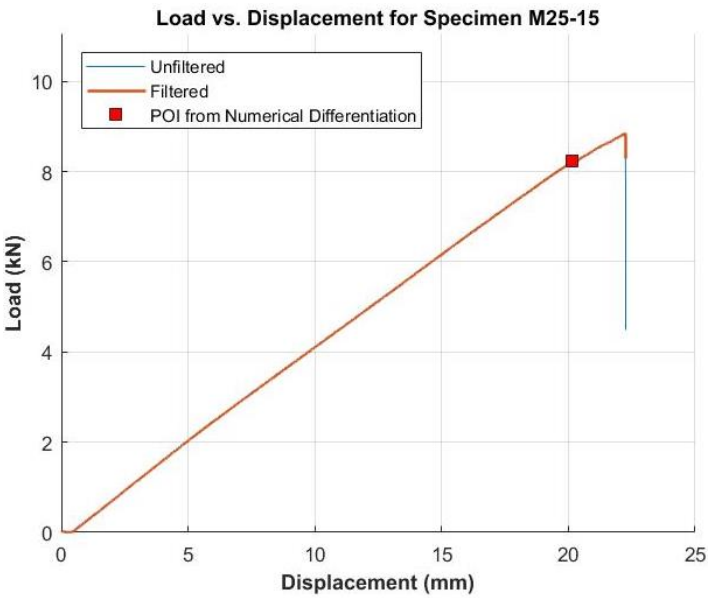

Figure C1.47: Load-displacement plot for Specimen M25-15

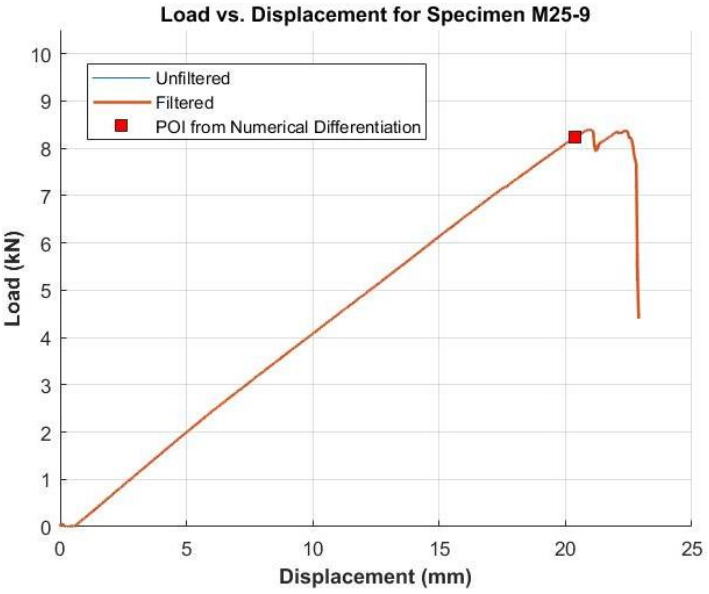

Figure C1.48: Load-displacement plot for Specimen M25-9

Figure C1.49: Load-displacement plot for Specimen M25-19

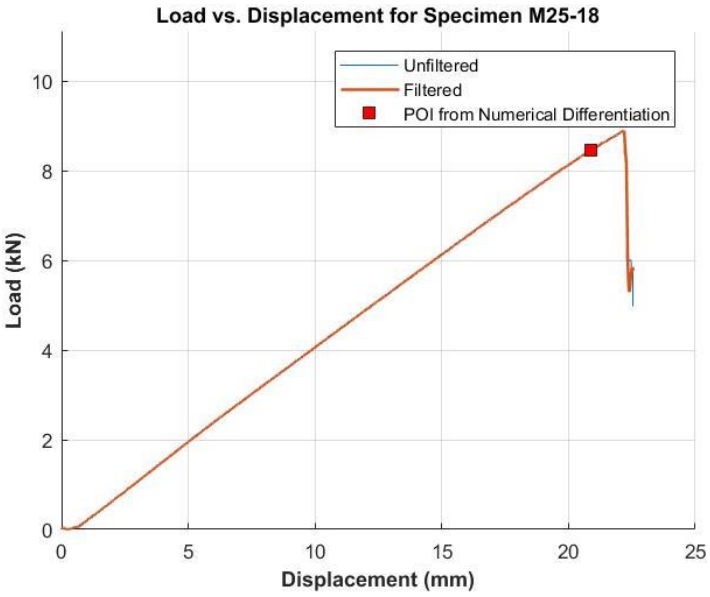

Figure C1.50: Load-displacement plot for Specimen M25-18

C1.6 M32 Specimens

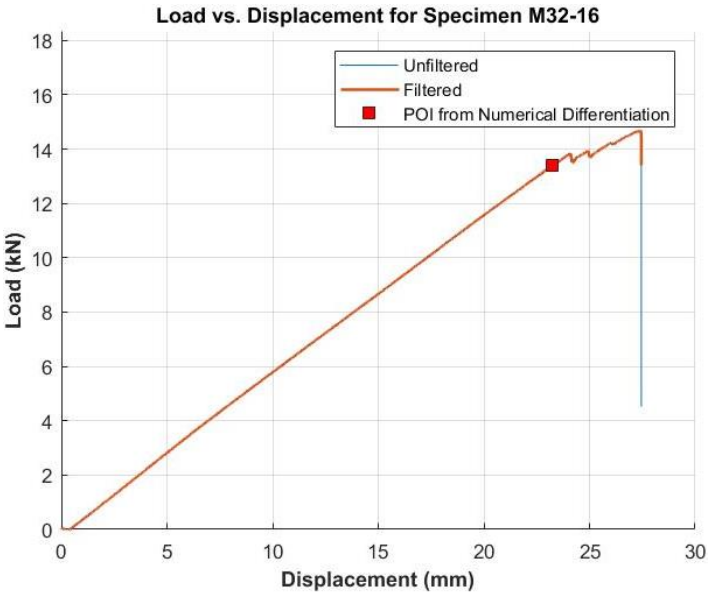

Figure C1.51: Load-displacement plot for Specimen M32-16

Figure C1.52: Load-displacement plot for Specimen M32-12

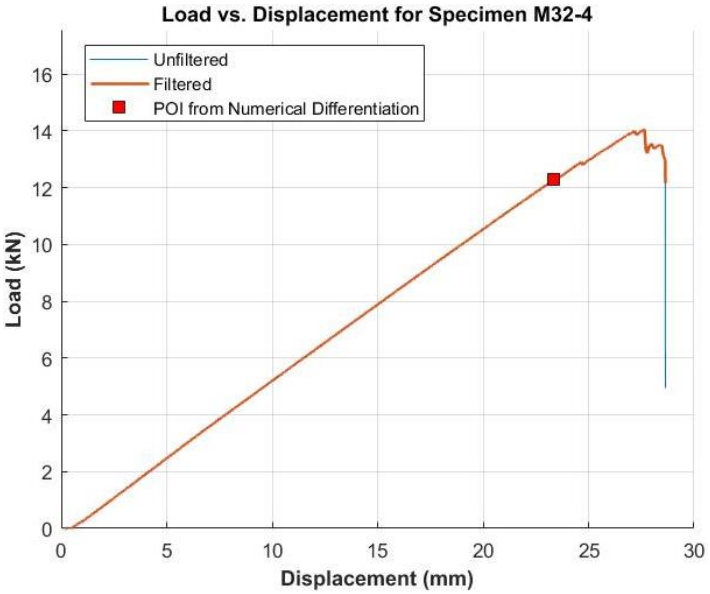

Figure C1.53: Load-displacement plot for Specimen M32-4

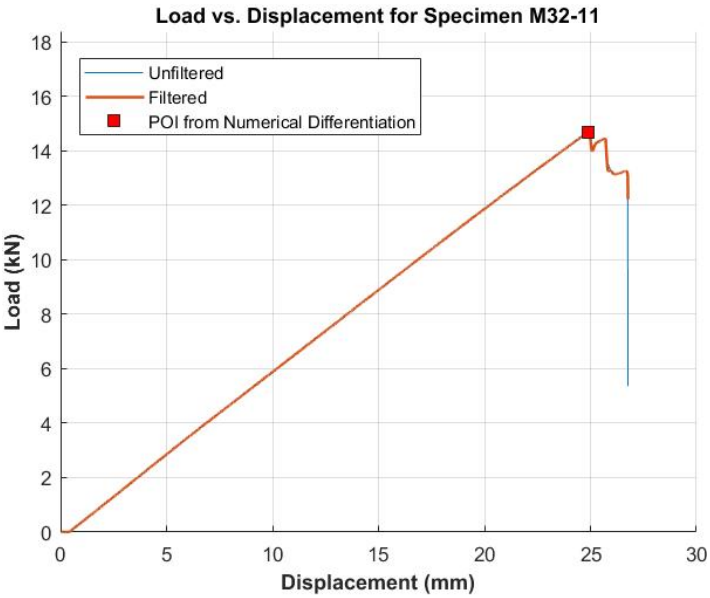

Figure C1.54: Load-displacement plot for Specimen M32-11

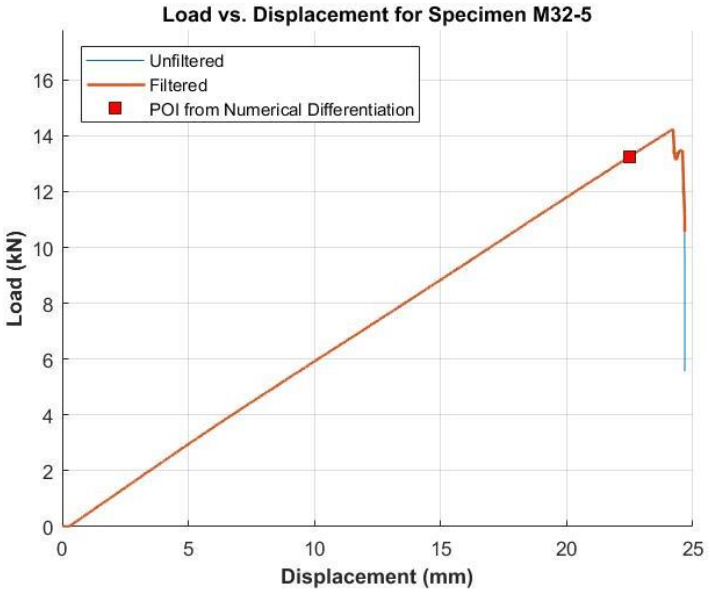

Figure C1.55: Load-displacement plot for Specimen M32-5

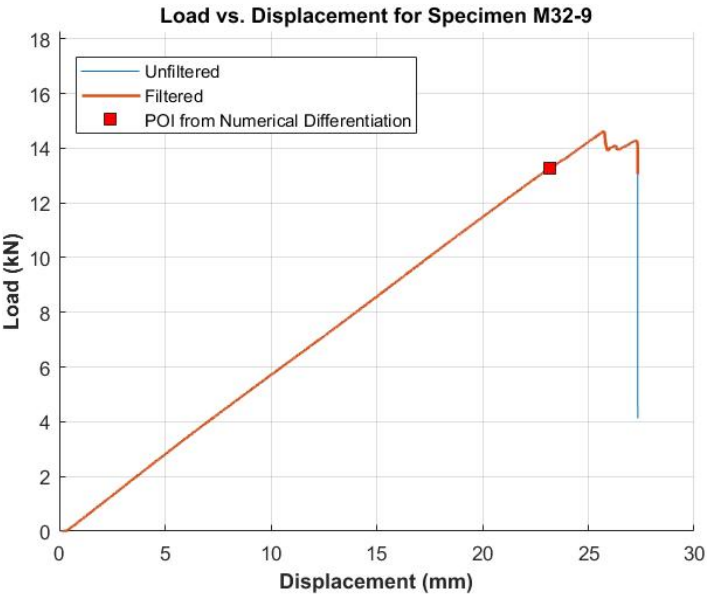

Figure C1.56: Load-displacement plot for Specimen M32-9

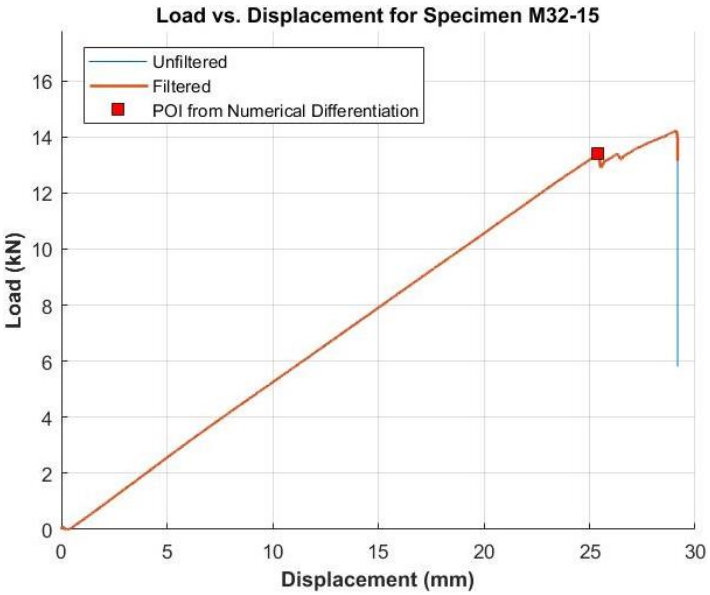

Figure C1.57: Load-displacement plot for Specimen M32-15

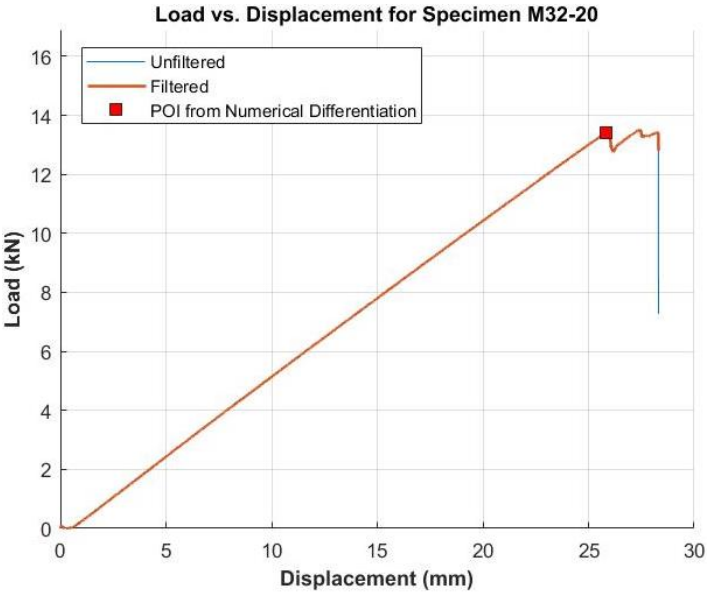

Figure C1.58: Load-displacement plot for Specimen M32-20

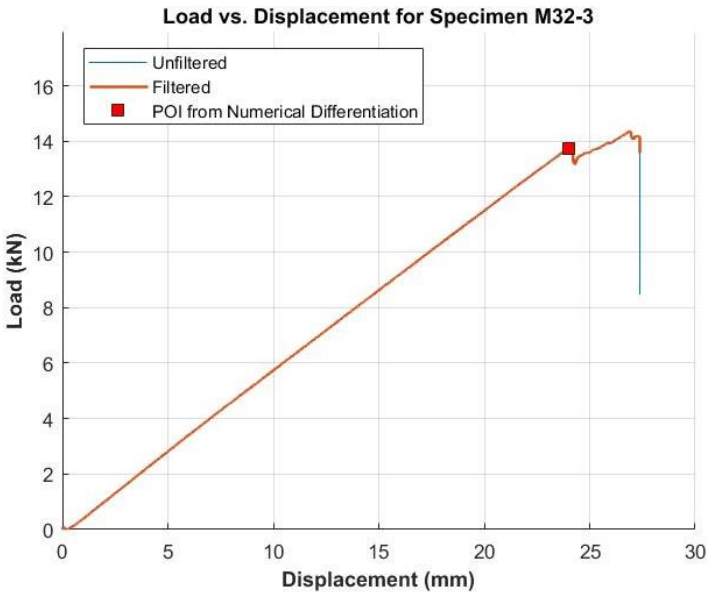

Figure C1.59: Load-displacement plot for Specimen M32-3

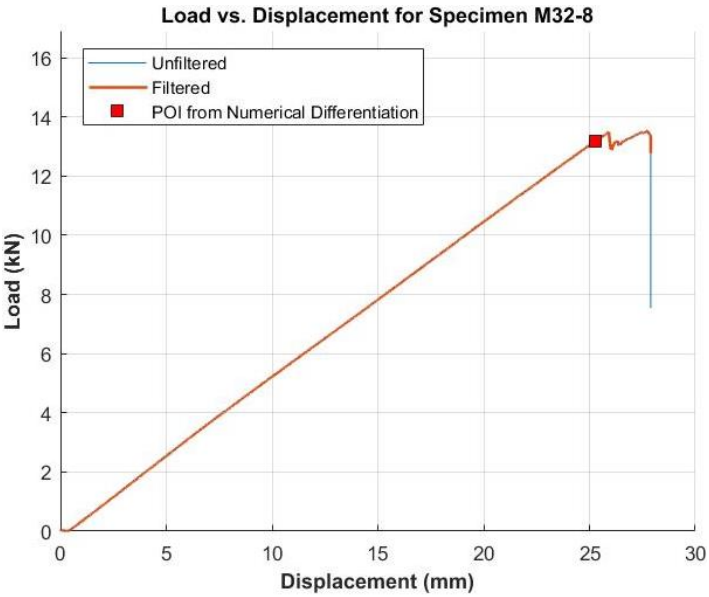

Figure C1.60: Load-displacement plot for Specimen M32-8

C2.0 Load-Displacement Graphs for GFRP Specimens Subjected to 4-Point Bending

C2.1 M8 Specimens

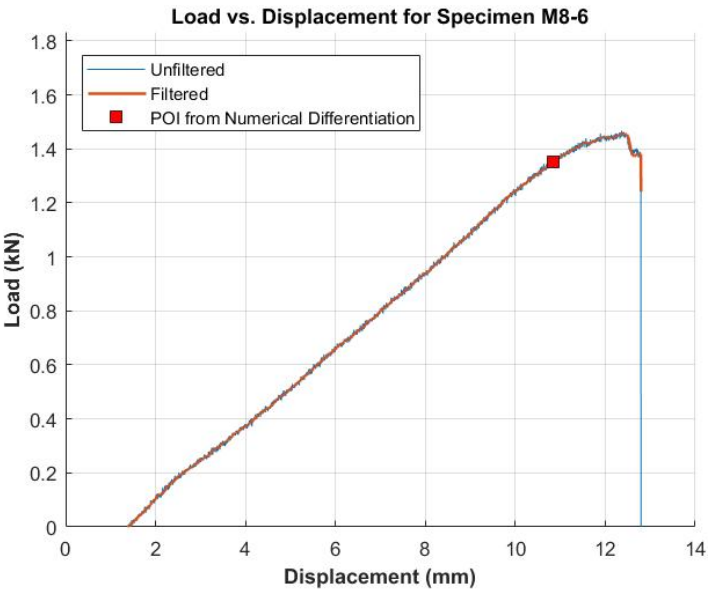

Figure C2.61: Load-displacement plot for Specimen M8-6

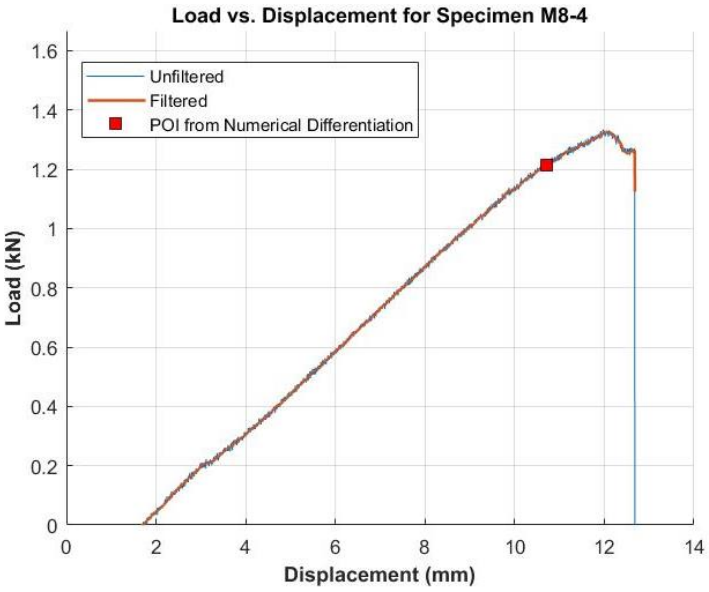

Figure C2.2: Load-displacement plot for Specimen M8-4

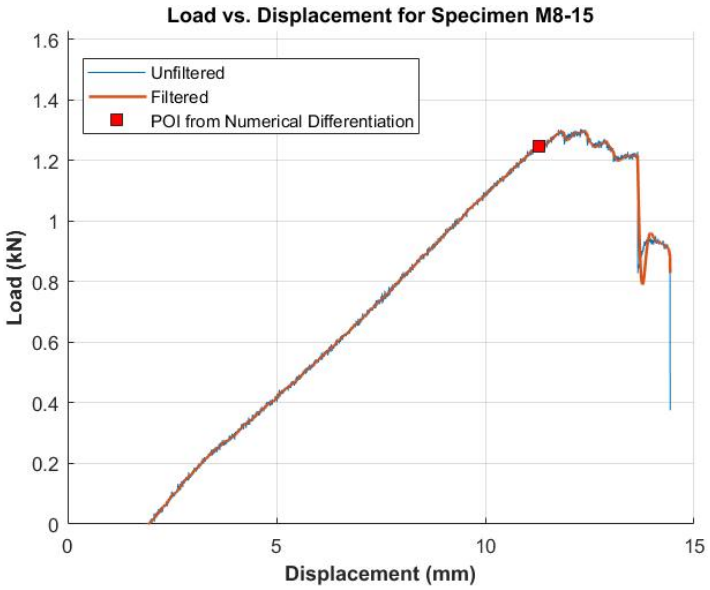

Figure C2.3: Load-displacement plot for Specimen M8-15

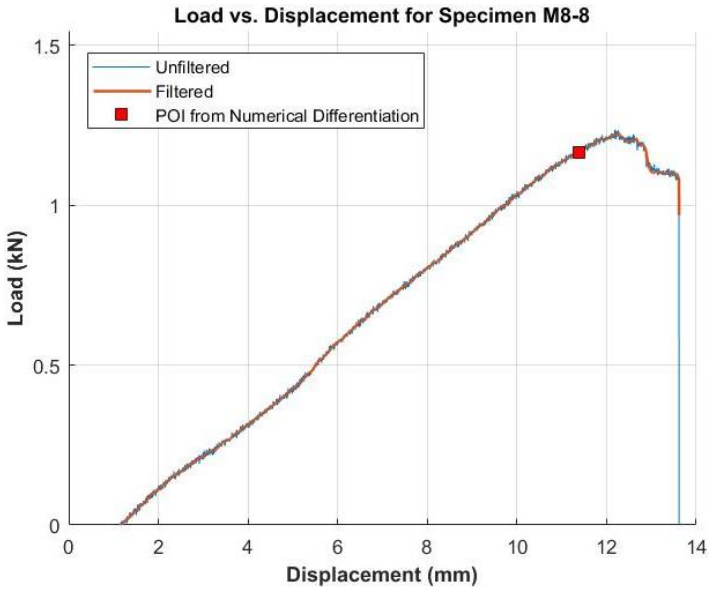

Figure C2.4: Load-displacement plot for Specimen M8-8

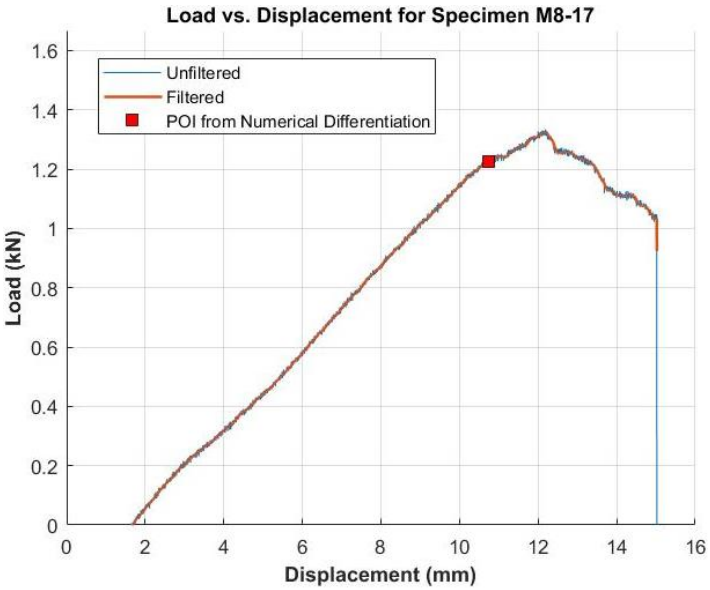

Figure C2.5: Load-displacement plot for Specimen M8-17

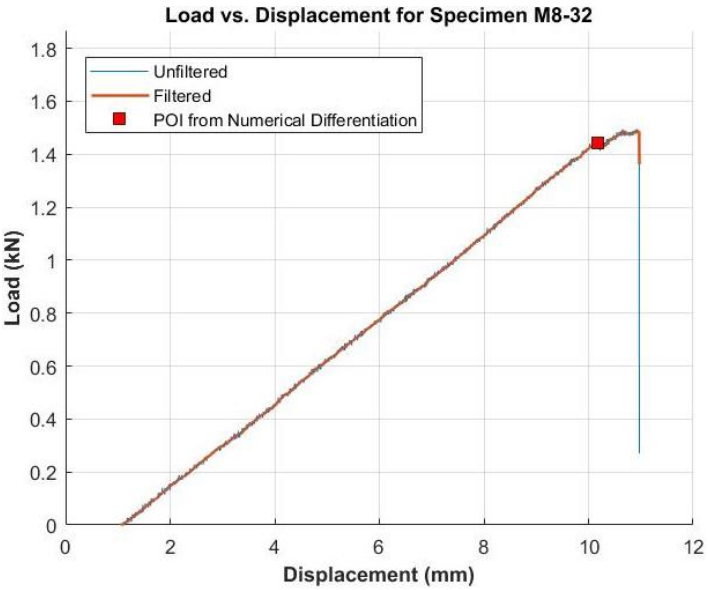

Figure C2.6: Load-displacement plot for Specimen M8-32

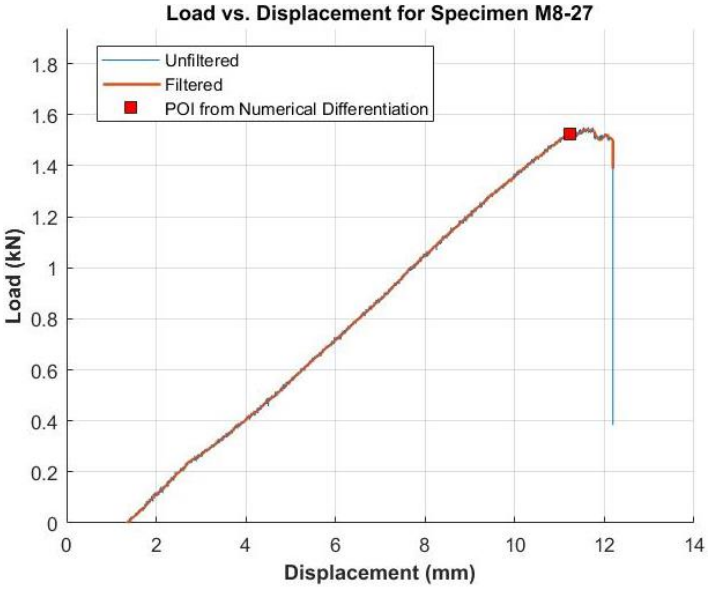

Figure C2.7: Load-displacement plot for Specimen M8-27

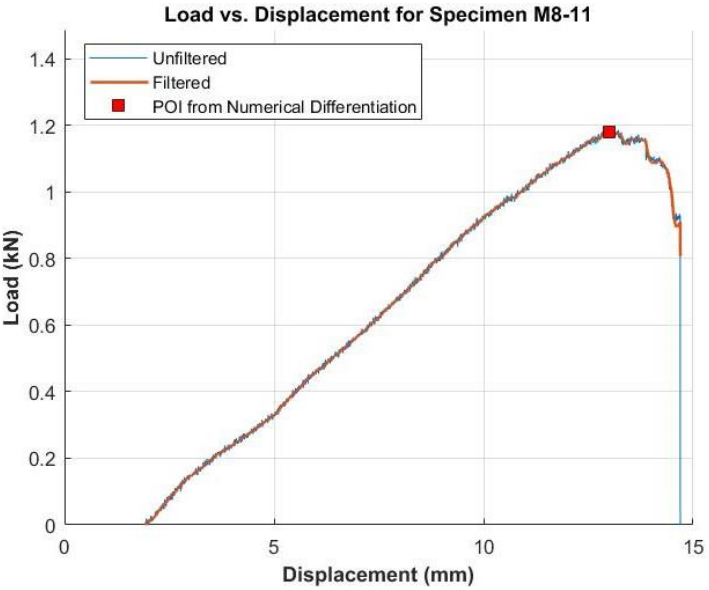

Figure C2.8: Load-displacement plot for Specimen M8-11

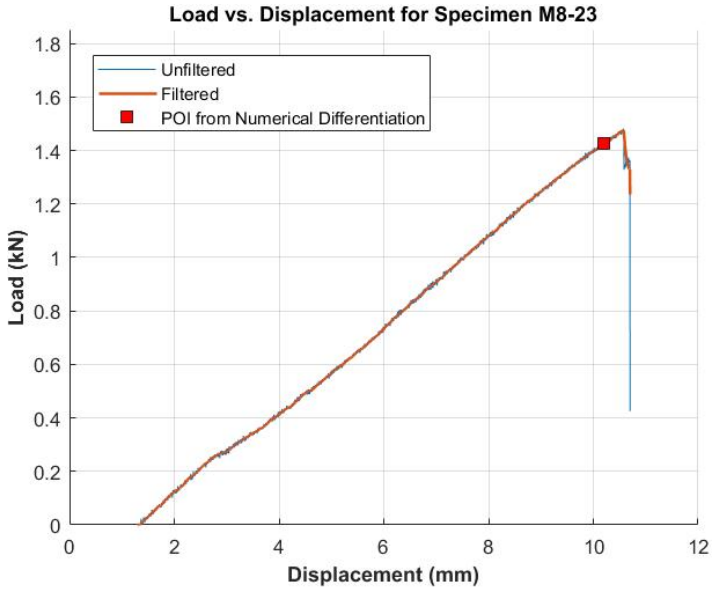

Figure C2.9: Load-displacement plot for Specimen M8-23

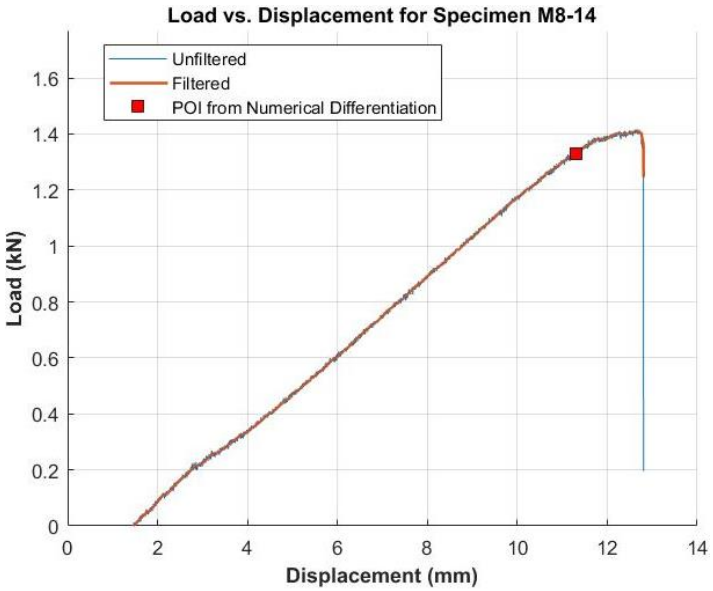

Figure C2.10: Load-displacement plot for Specimen M8-14

C2.2 M13 Specimens

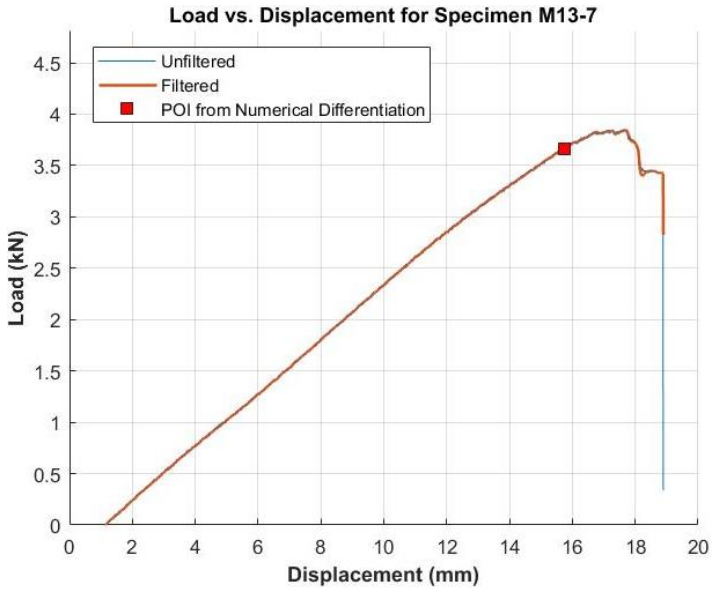

Figure C2.11: Load-displacement plot for Specimen M13-7

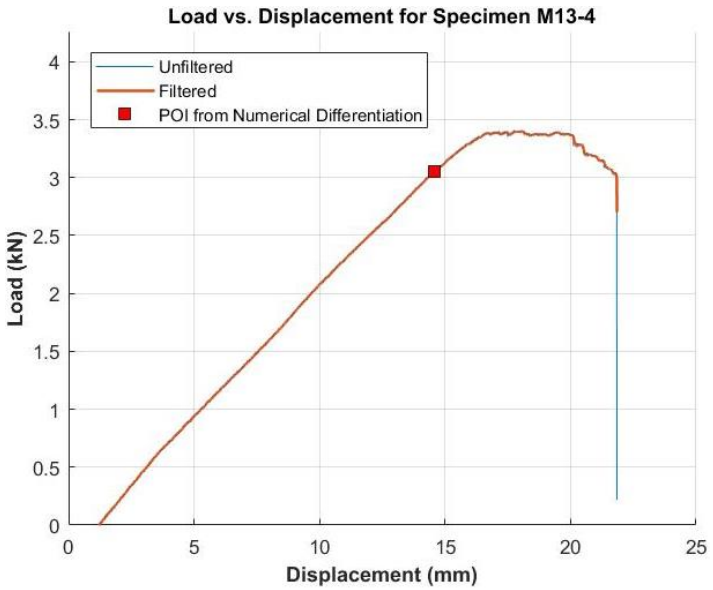

Figure C2.12: Load-displacement plot for Specimen M13-4

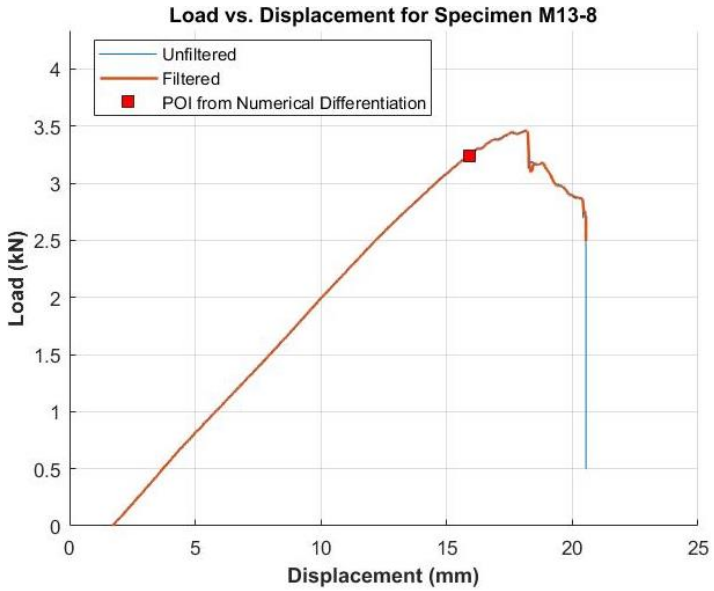

Figure C2.13: Load-displacement plot for Specimen M13-8

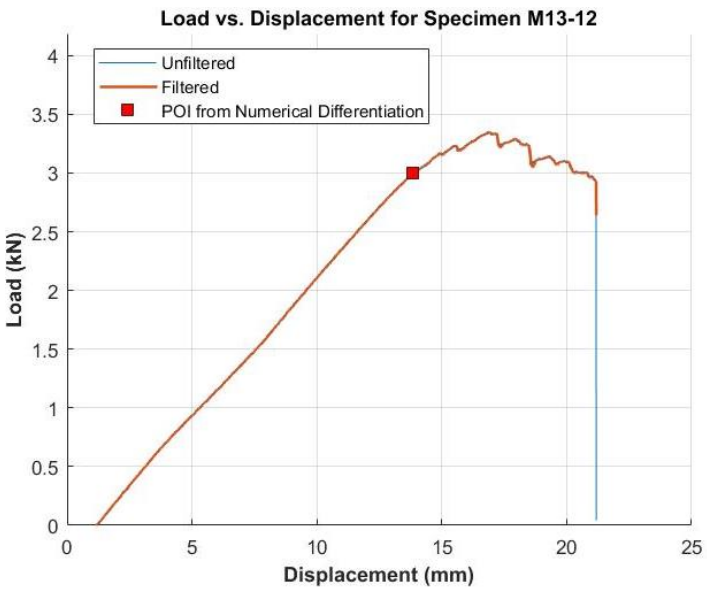

Figure C2.14: Load-displacement plot for Specimen M13-12

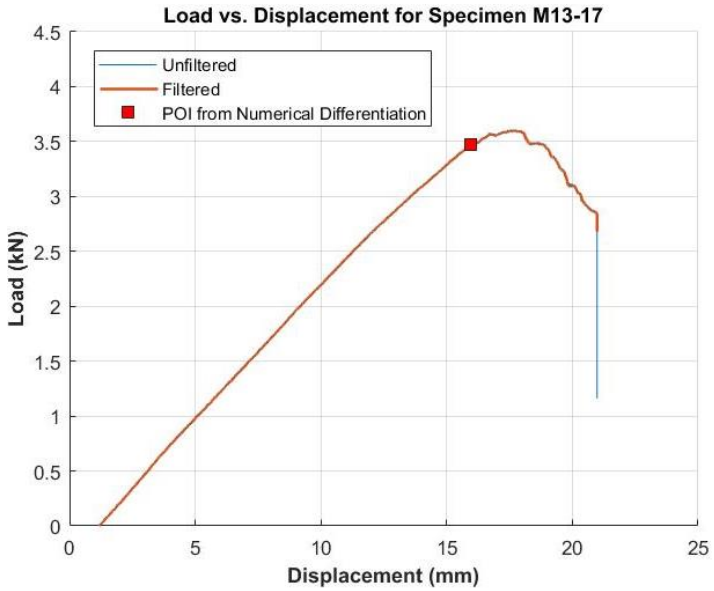

Figure C2.15: Load-displacement plot for Specimen M13-17

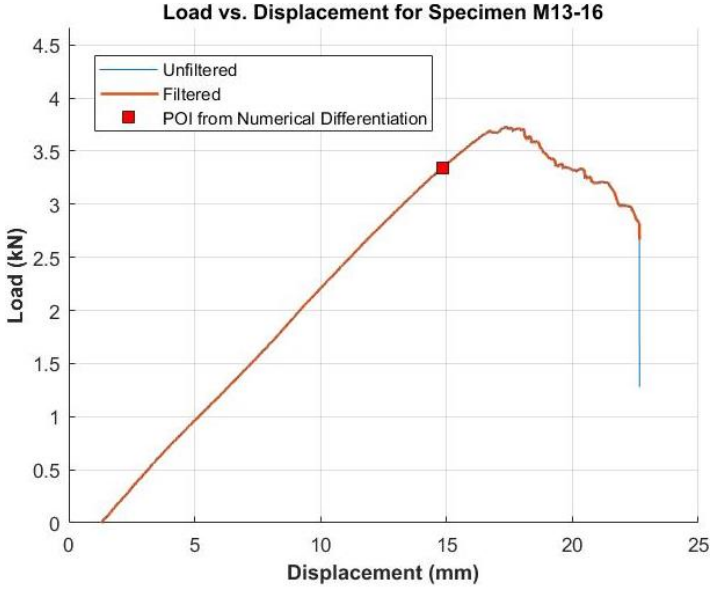

Figure C2.16: Load-displacement plot for Specimen M13-16

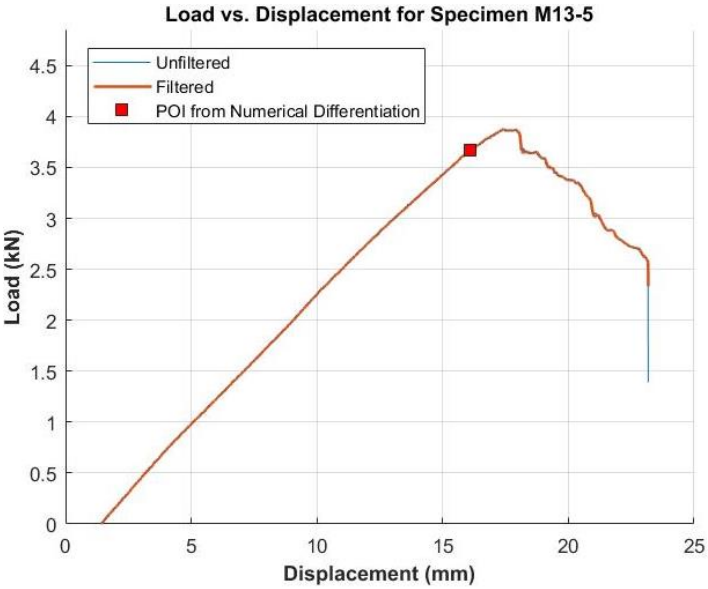

Figure C2.17: Load-displacement plot for Specimen M13-5

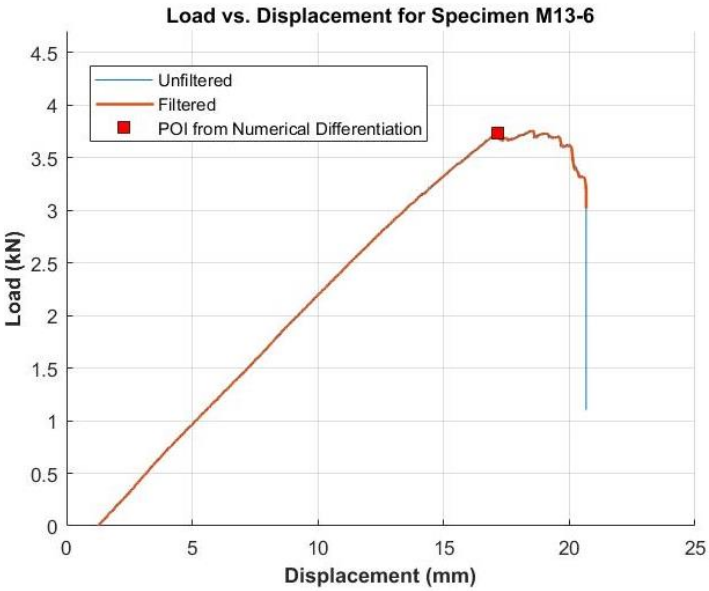

Figure C2.18: Load-displacement plot for Specimen M13-6

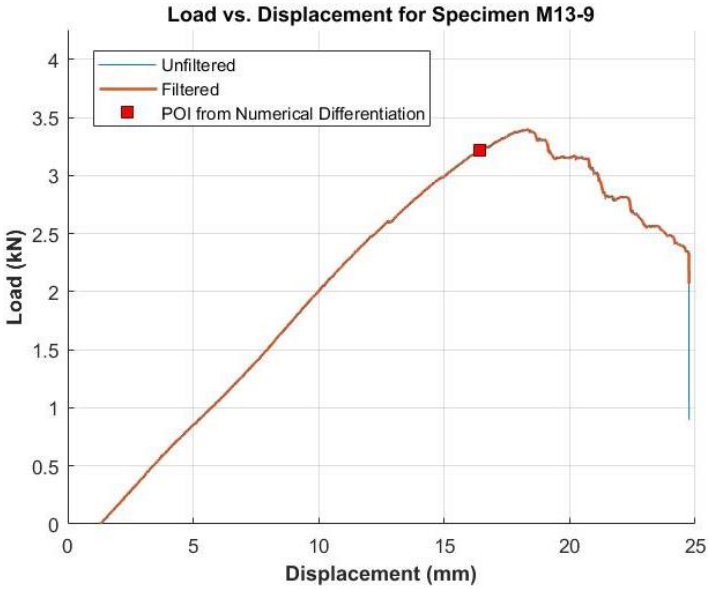

Figure C2.19: Load-displacement plot for Specimen M13-9

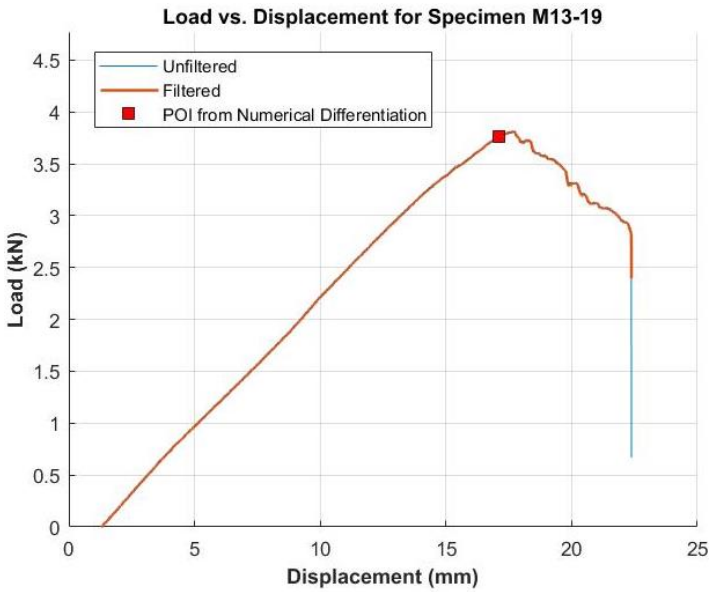

Figure C2.20: Load-displacement plot for Specimen M13-19

C2.3 M15 Specimens

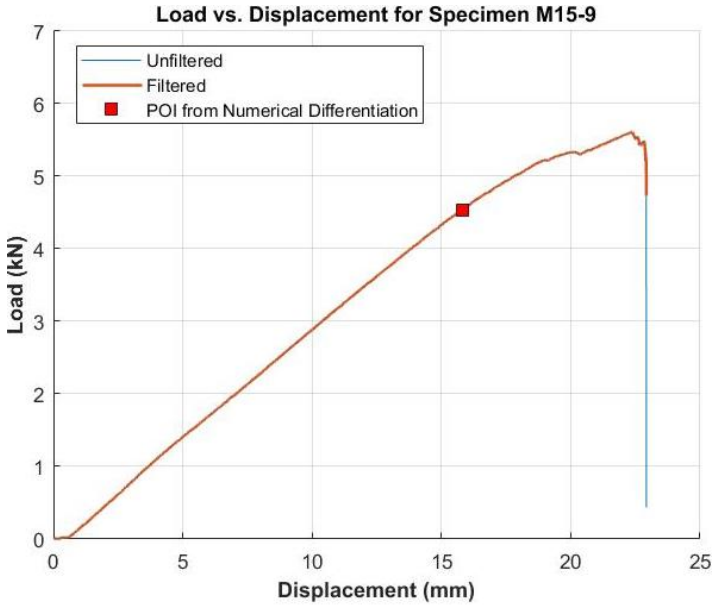

Figure C2.21: Load-displacement plot for Specimen M15-9

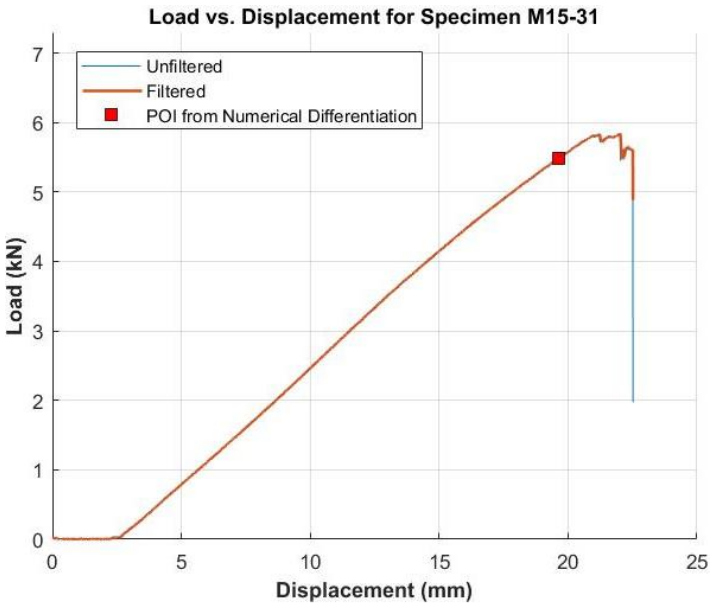

Figure C2.22: Load-displacement plot for Specimen M15-31

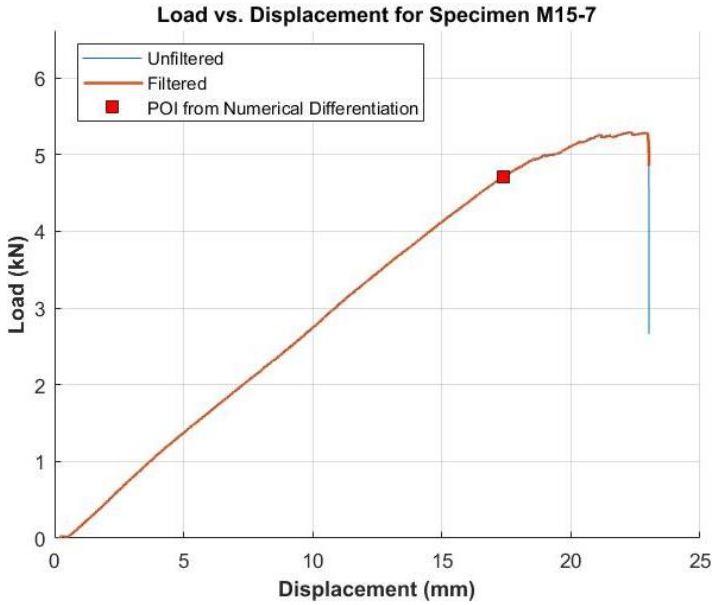

Figure C2.23: Load-displacement plot for Specimen M15-7

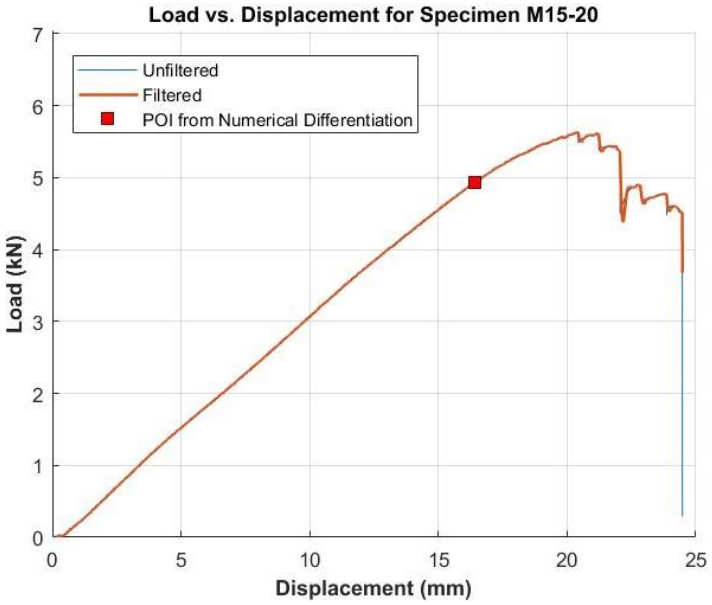

Figure C2.24: Load-displacement plot for Specimen M15-20

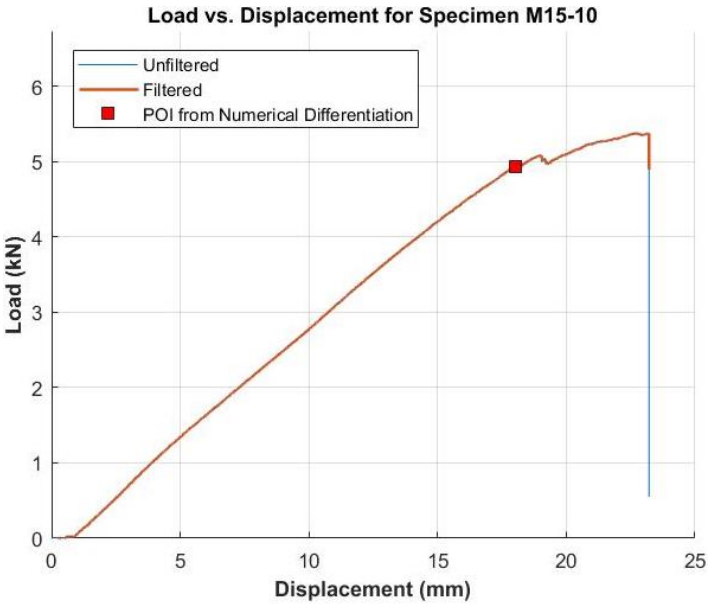

Figure C2.25: Load-displacement plot for Specimen M15-10

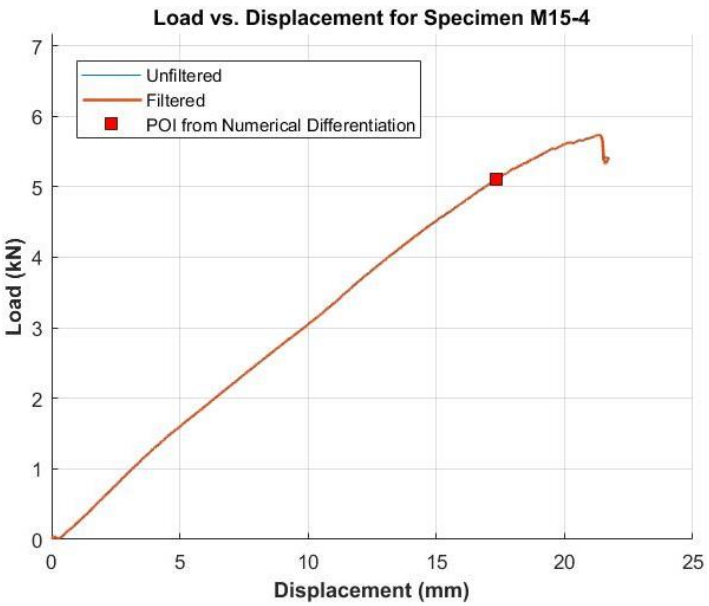

Figure C2.26: Load-displacement plot for Specimen M15-4

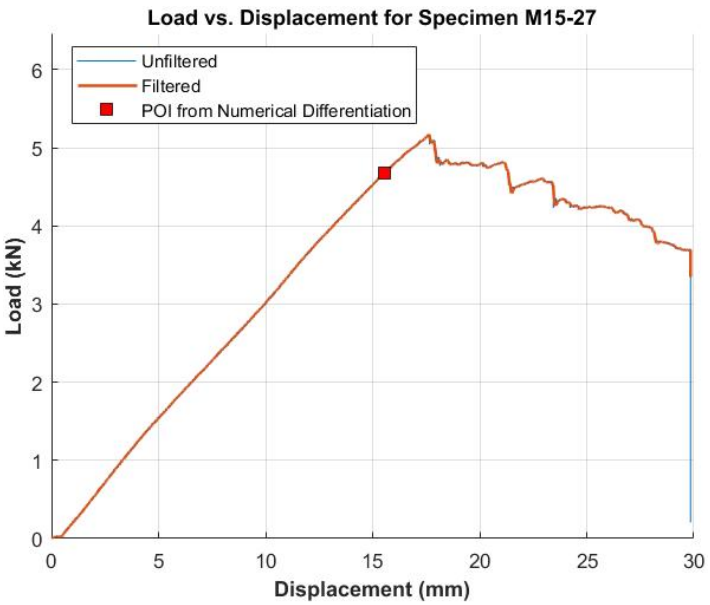

Figure C2.27: Load-displacement plot for Specimen M15-27

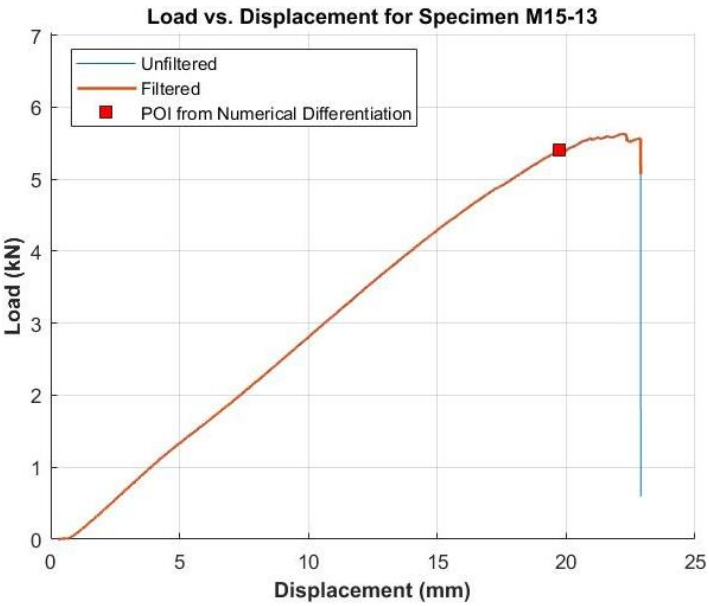

Figure C2.28: Load-displacement plot for Specimen M15-13

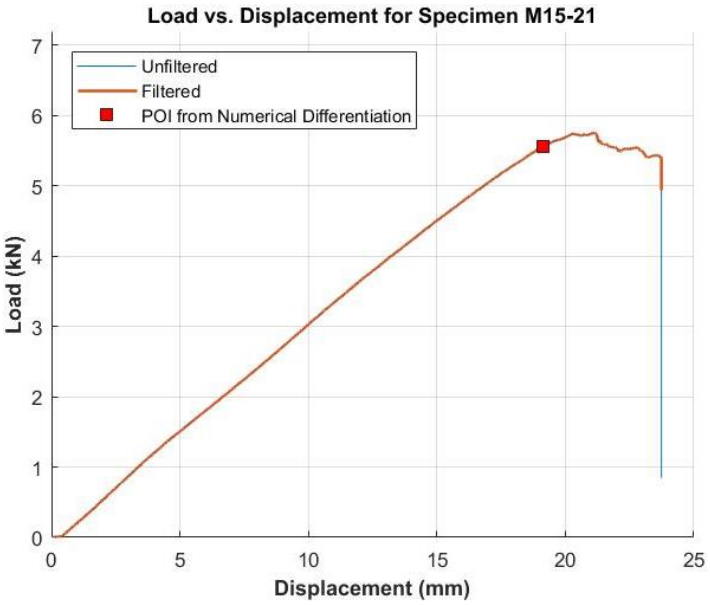

Figure C2.29: Load-displacement plot for Specimen M15-21

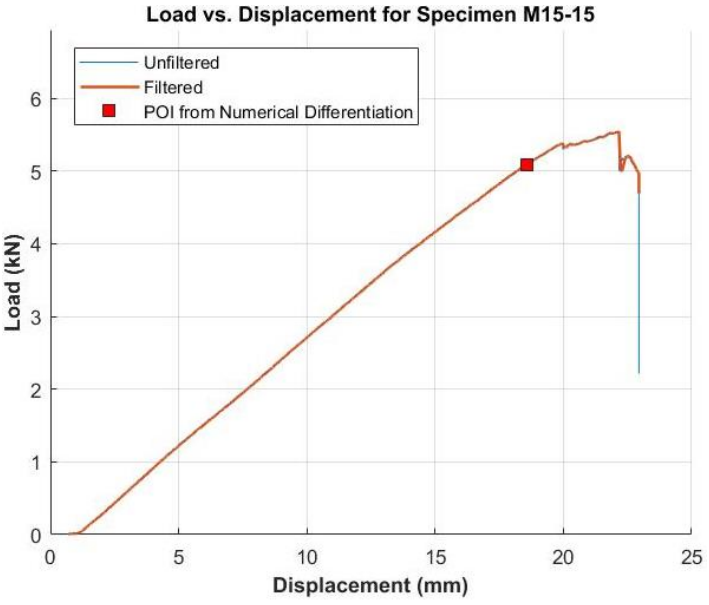

Figure C2.30: Load-displacement plot for Specimen M15-15

C2.4 M20 Specimens

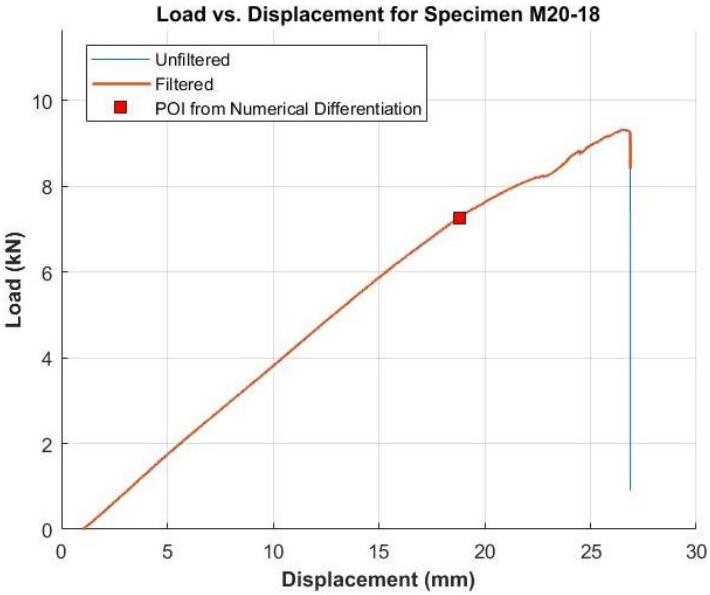

Figure C2.31: Load-displacement plot for Specimen M20-18

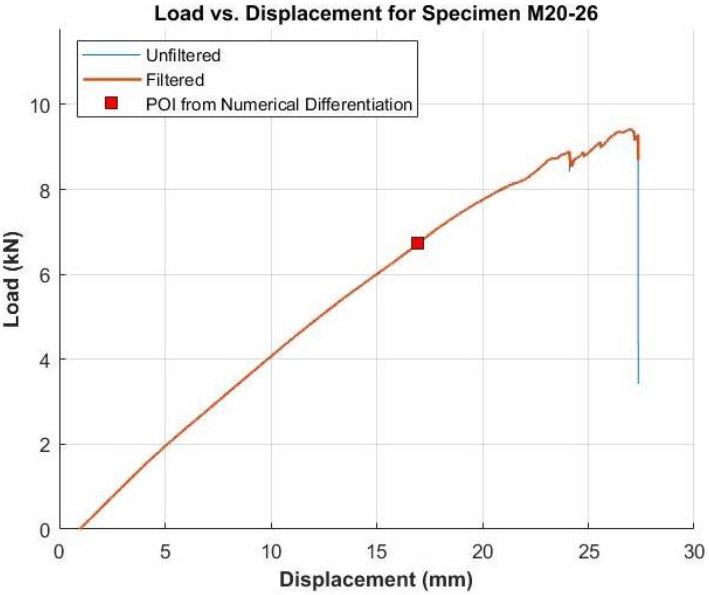

Figure C2.32: Load-displacement plot for Specimen M20-26

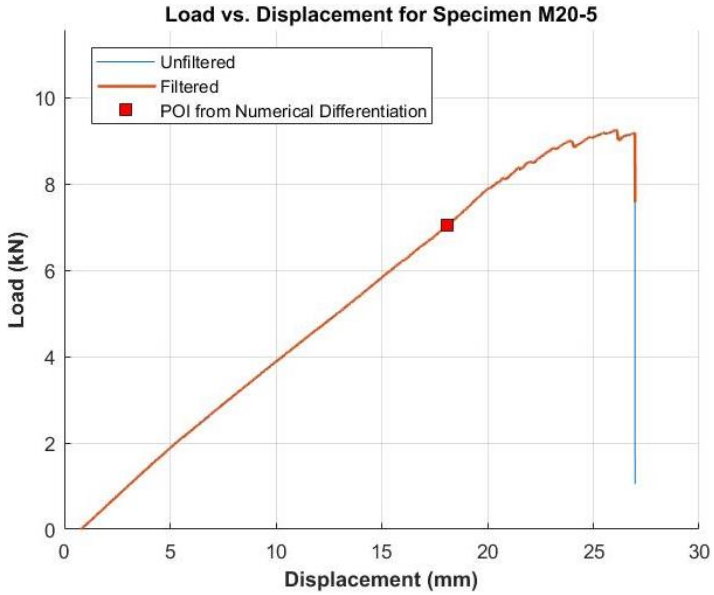

Figure C2.33: Load-displacement plot for Specimen M20-5

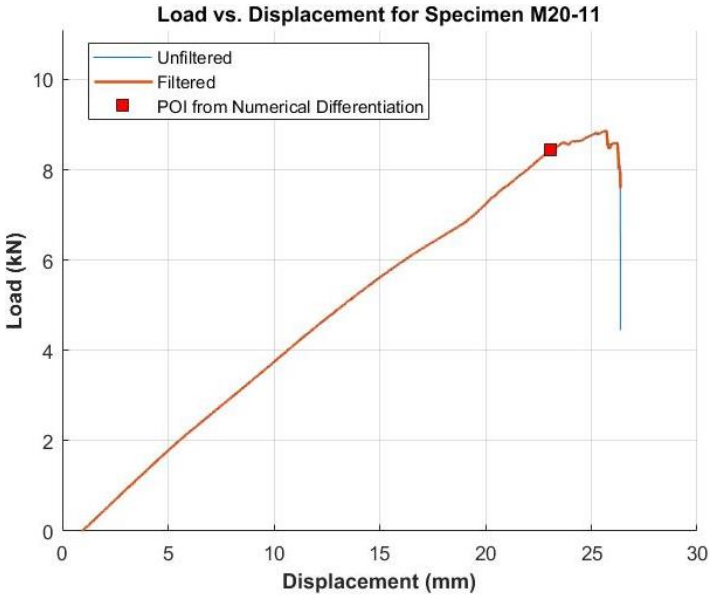

Figure C2.34: Load-displacement plot for Specimen M20-11

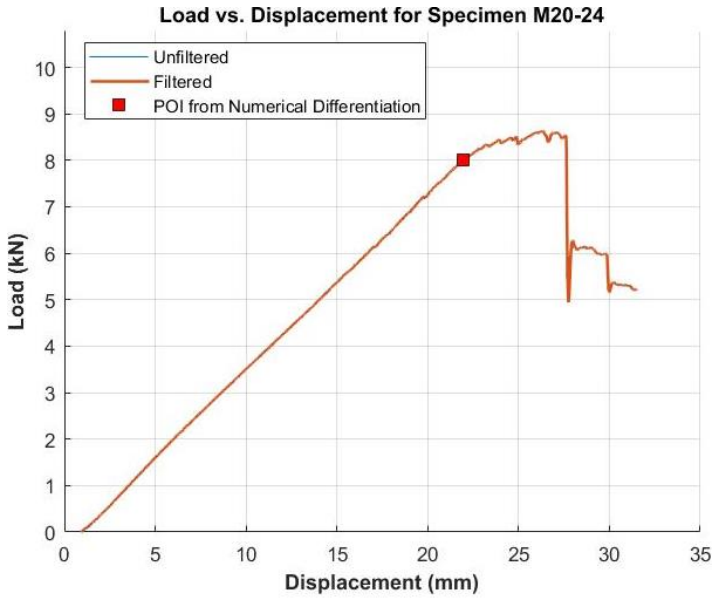

Figure C2.35: Load-displacement plot for Specimen M20-24

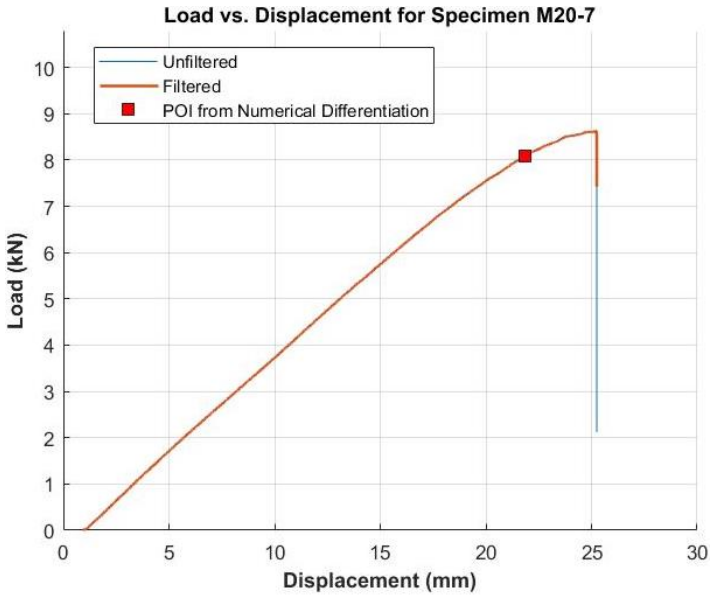

Figure C2.36: Load-displacement plot for Specimen M20-7

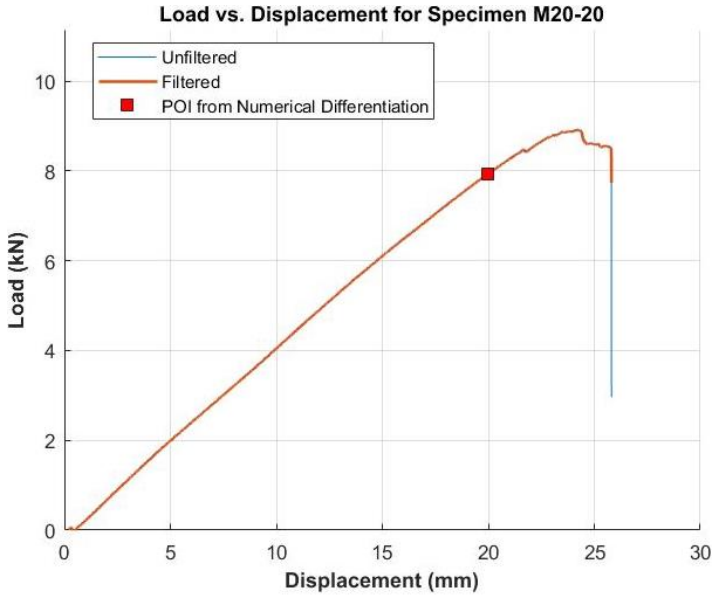

Figure C2.37: Load-displacement plot for Specimen M20-20

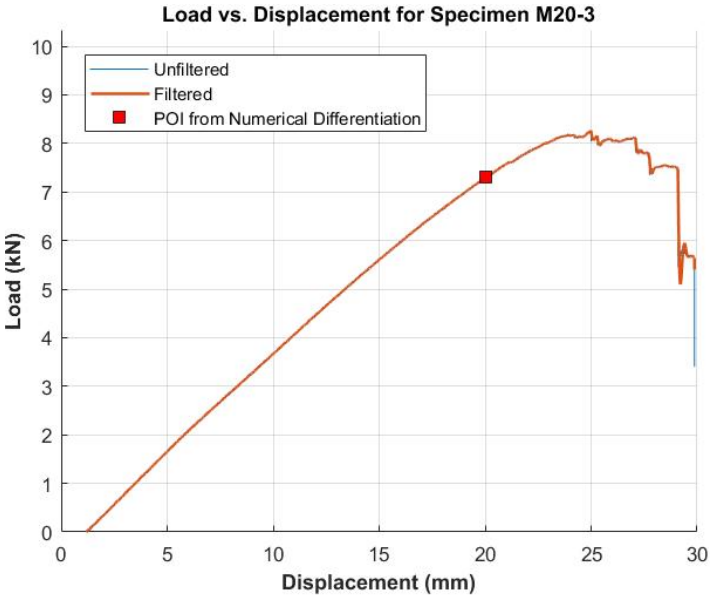

Figure C2.38: Load-displacement plot for Specimen M20-3

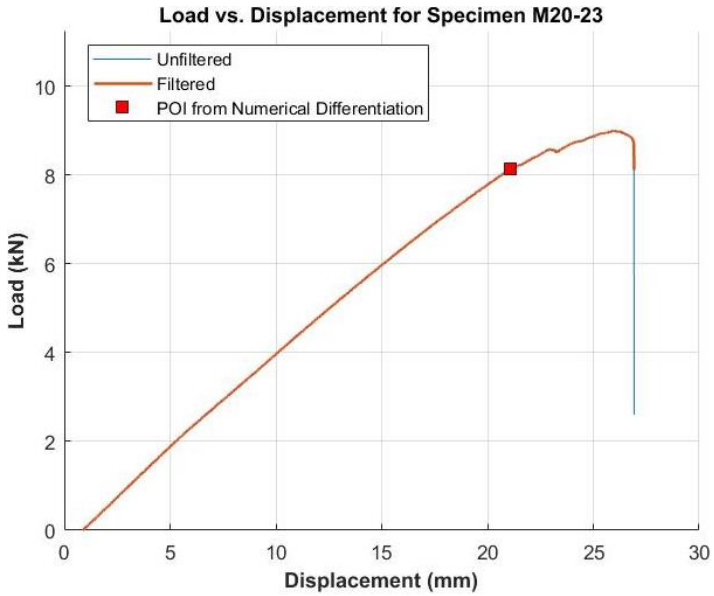

Figure C2.39: Load-displacement plot for Specimen M20-23

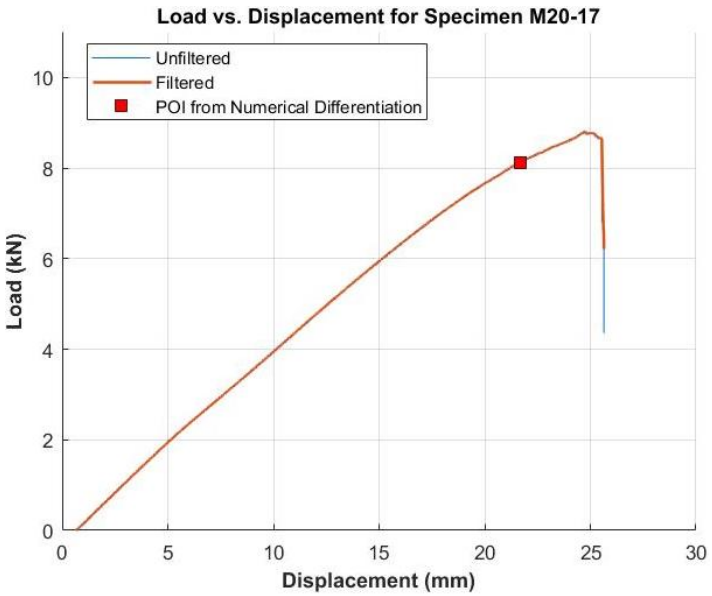

Figure C2.40: Load-displacement plot for Specimen M20-17

C2.5 M25 Specimens

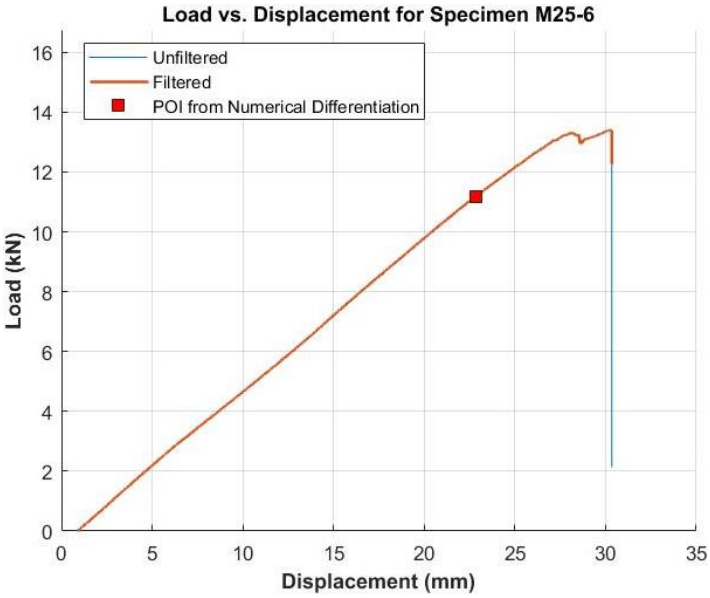

Figure C2.41: Load-displacement plot for Specimen M25-6

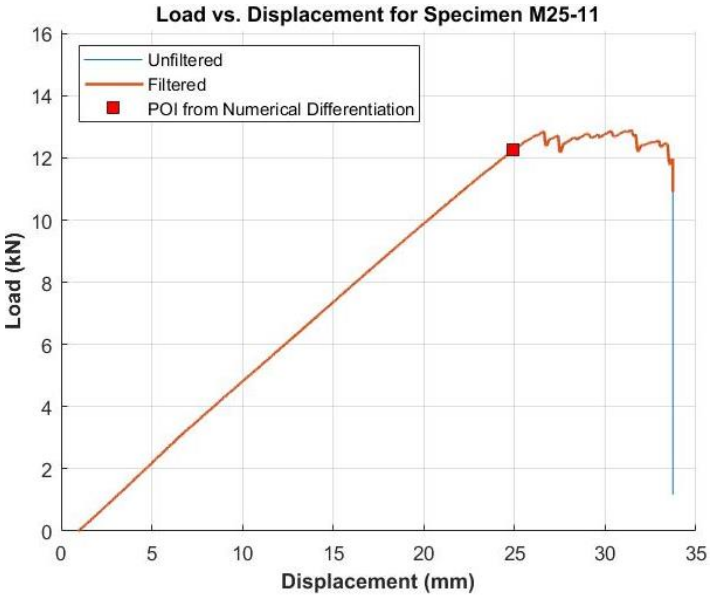

Figure C2.42: Load-displacement plot for Specimen M25-11

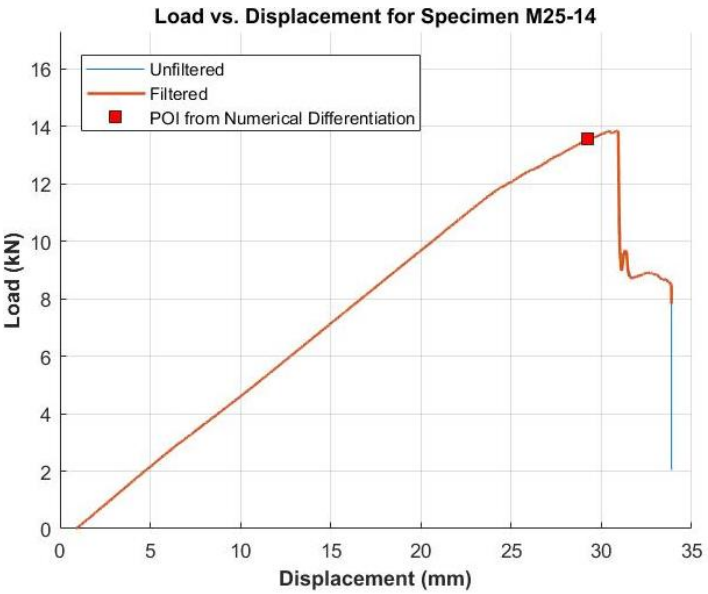

Figure C2.43: Load-displacement plot for Specimen M25-14

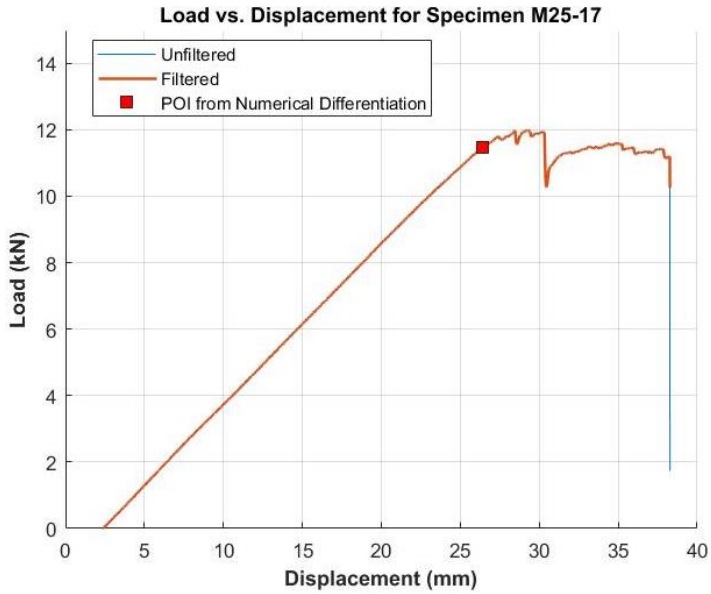

Figure C2.44: Load-displacement plot for Specimen M25-17

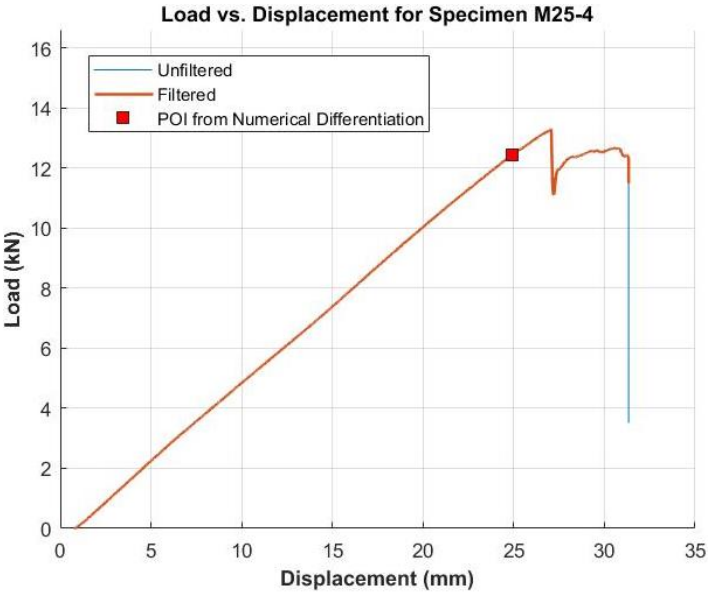

Figure C2.45: Load-displacement plot for Specimen M25-4

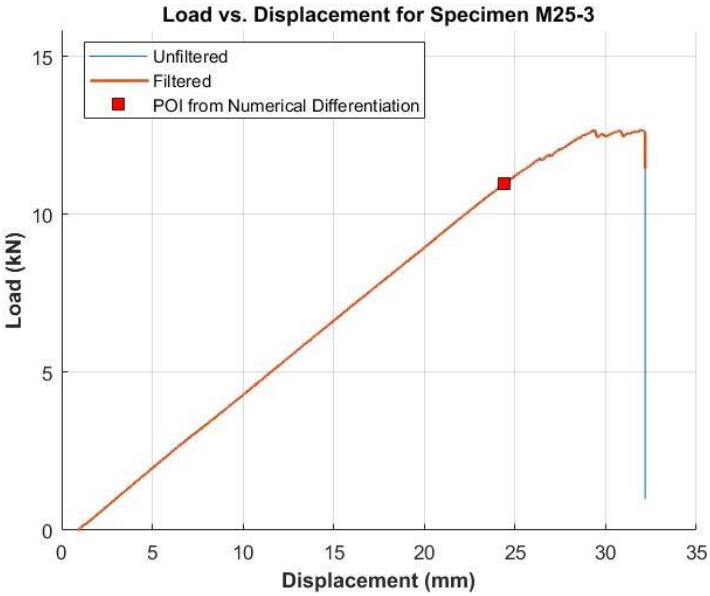

Figure C2.46: Load-displacement plot for Specimen M25-3

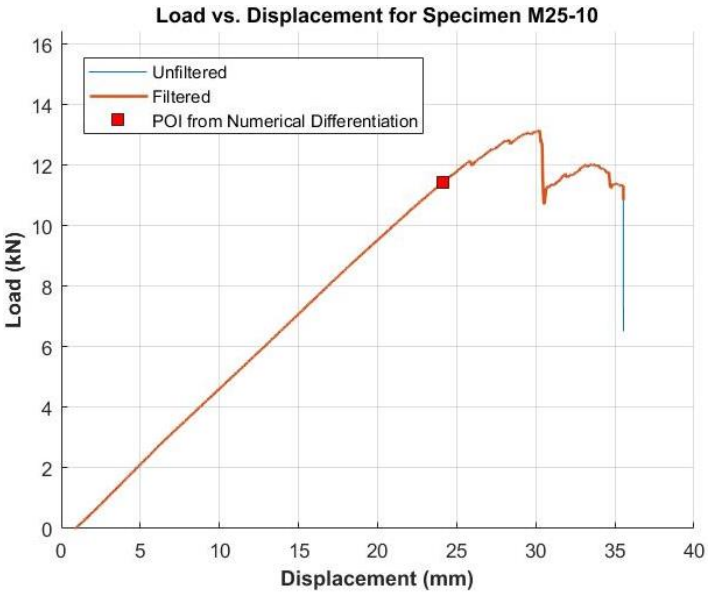

Figure C2.47: Load-displacement plot for Specimen M25-10

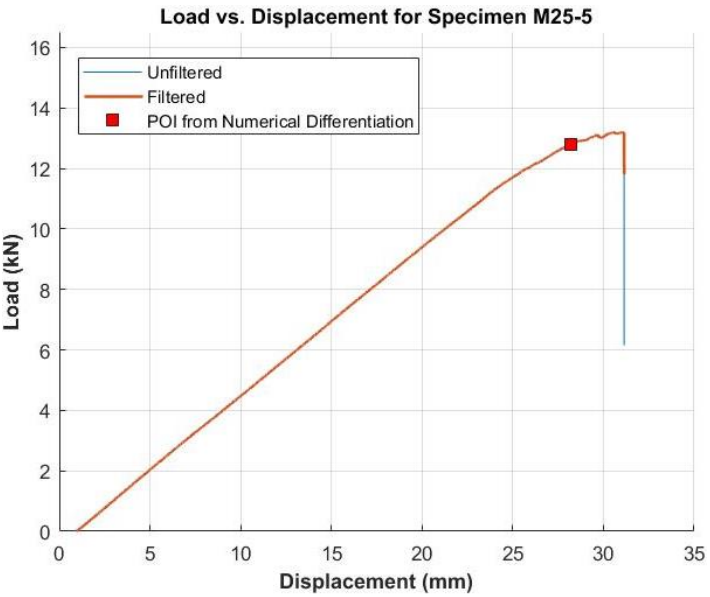

Figure C2.48: Load-displacement plot for Specimen M25-5

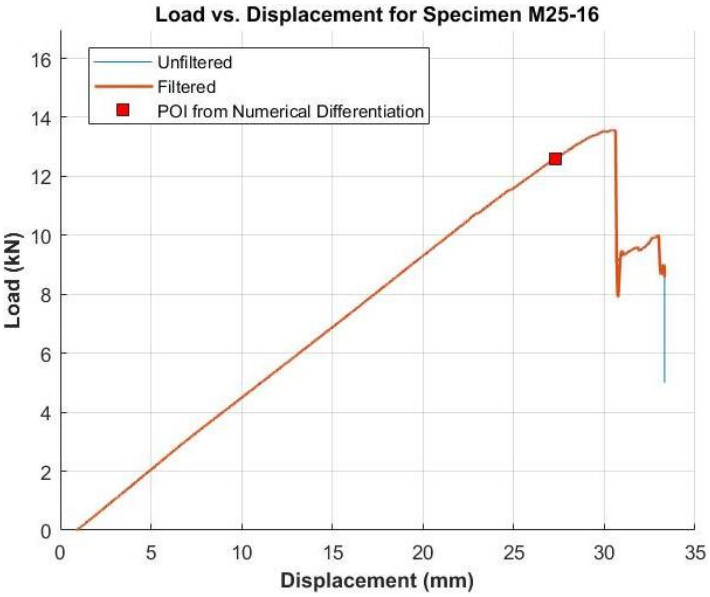

Figure C2.49: Load-displacement plot for Specimen M25-16

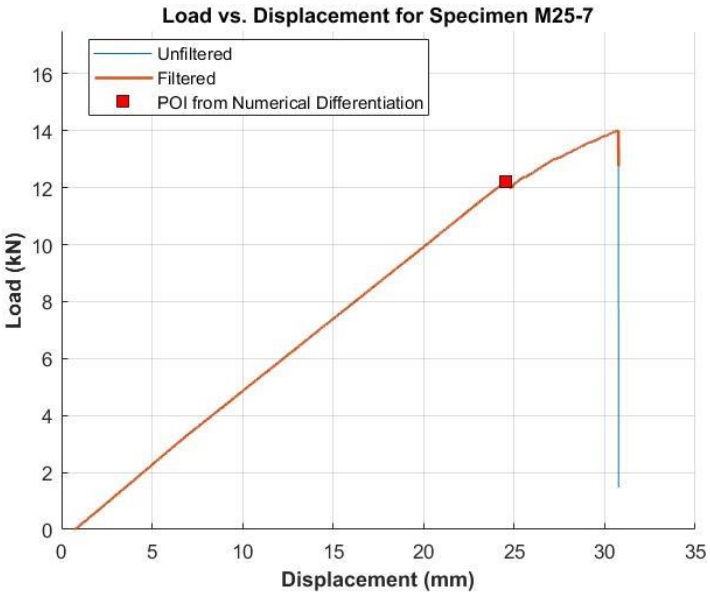

Figure C2.50: Load-displacement plot for Specimen M25-7

C2.6 M32 Specimens

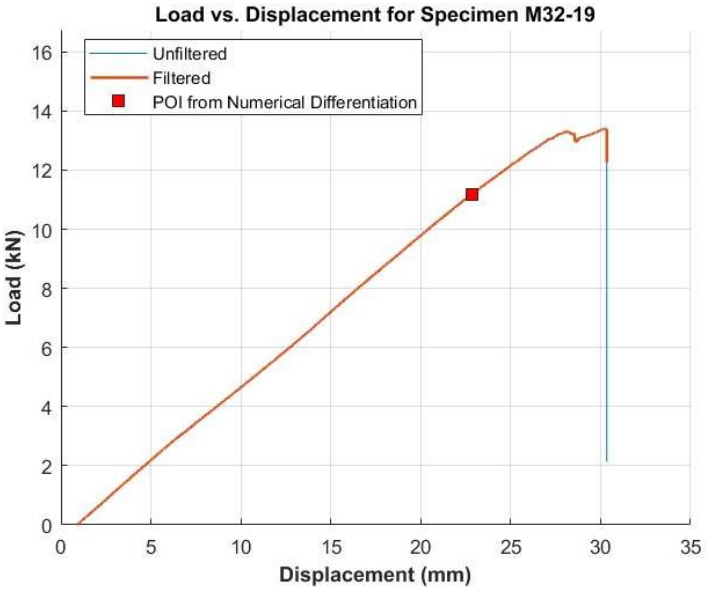

Figure C2.51: Load-displacement plot for Specimen M32-19

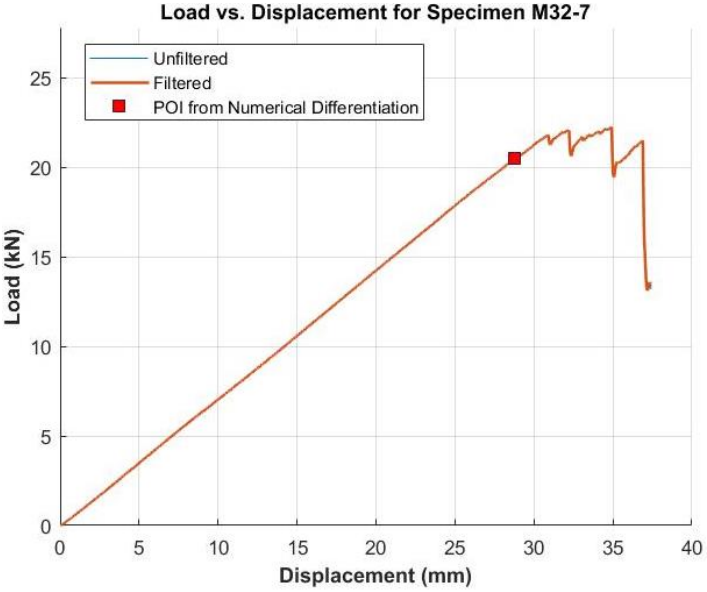

Figure C2.52: Load-displacement plot for Specimen M32-7

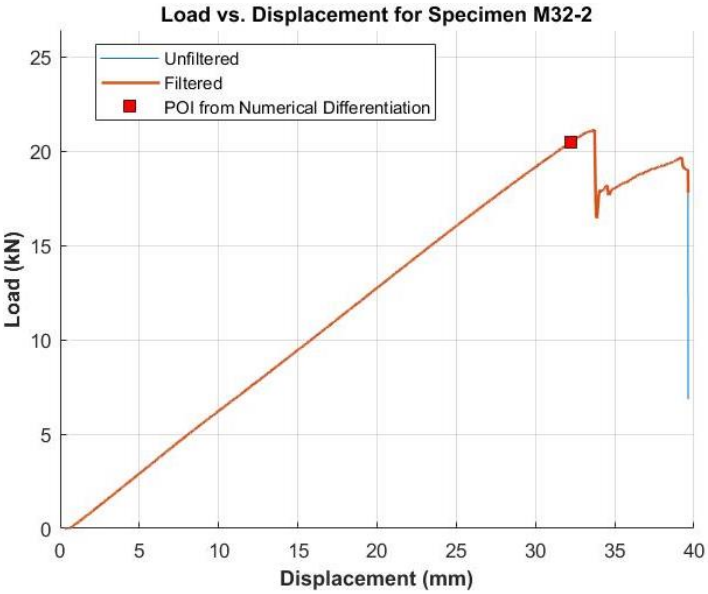

Figure C2.53: Load-displacement plot for Specimen M32-2

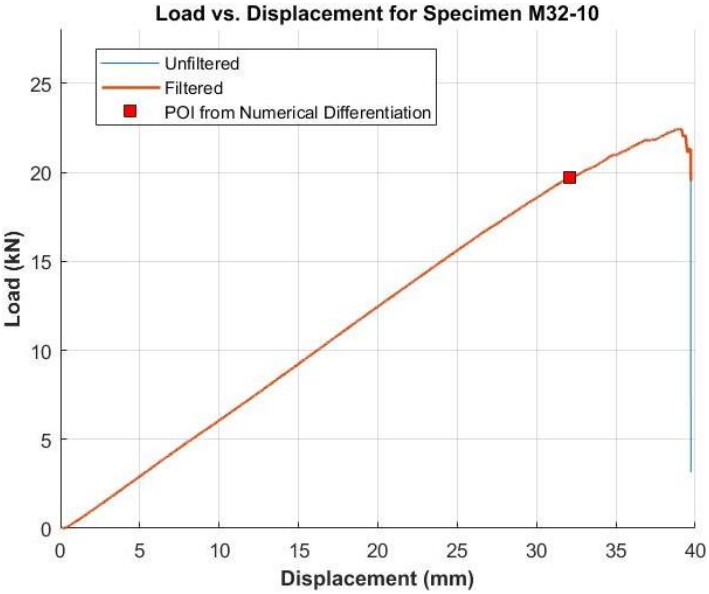

Figure C2.54: Load-displacement plot for Specimen M32-10

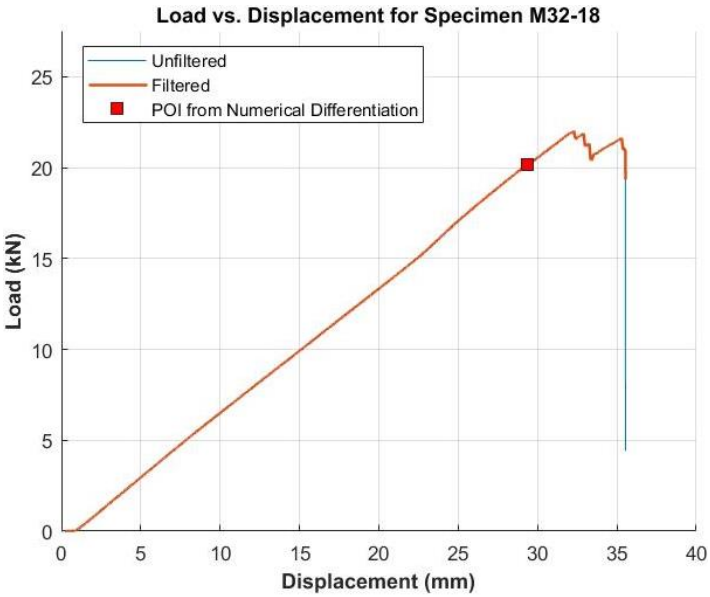

Figure C2.55: Load-displacement plot for Specimen M32-18

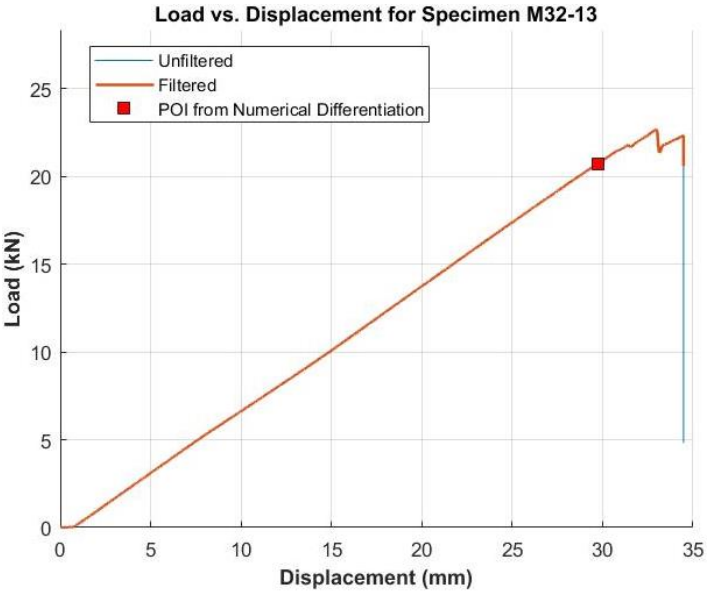

Figure C2.56: Load-displacement plot for Specimen M32-13

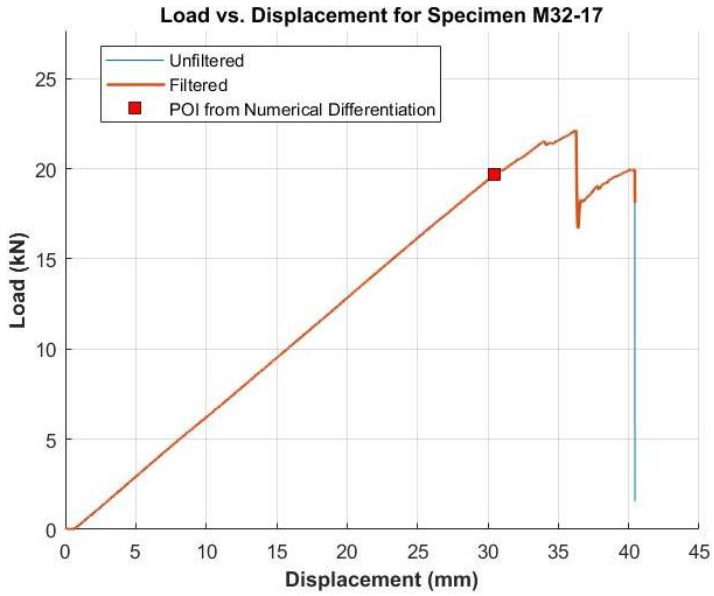

Figure C2.57: Load-displacement plot for Specimen M32-17

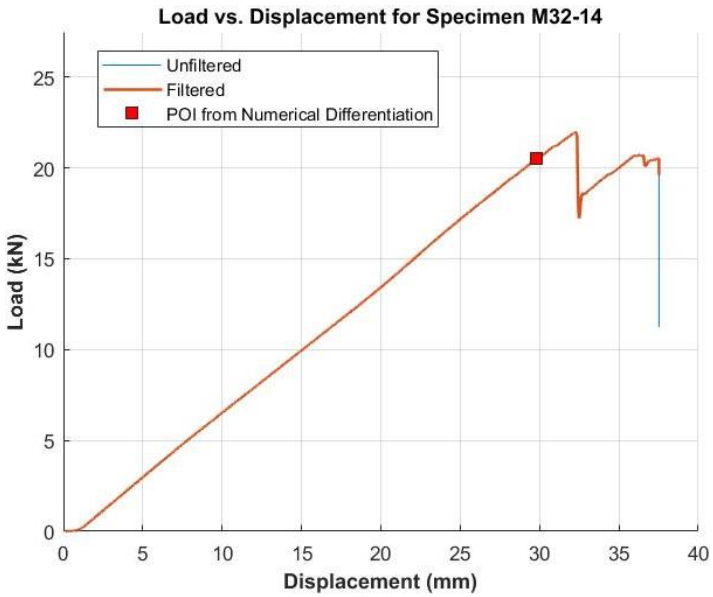

Figure C2.58: Load-displacement plot for Specimen M32-14

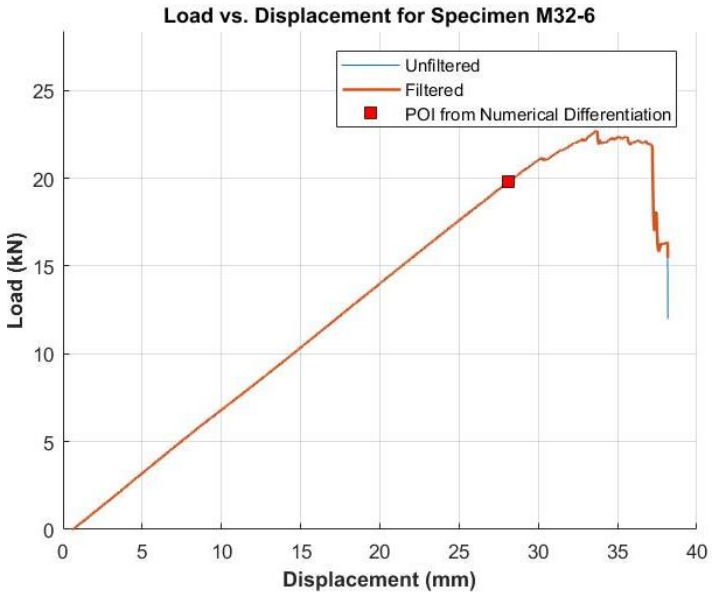

Figure C2.59: Load-displacement plot for Specimen M32-6

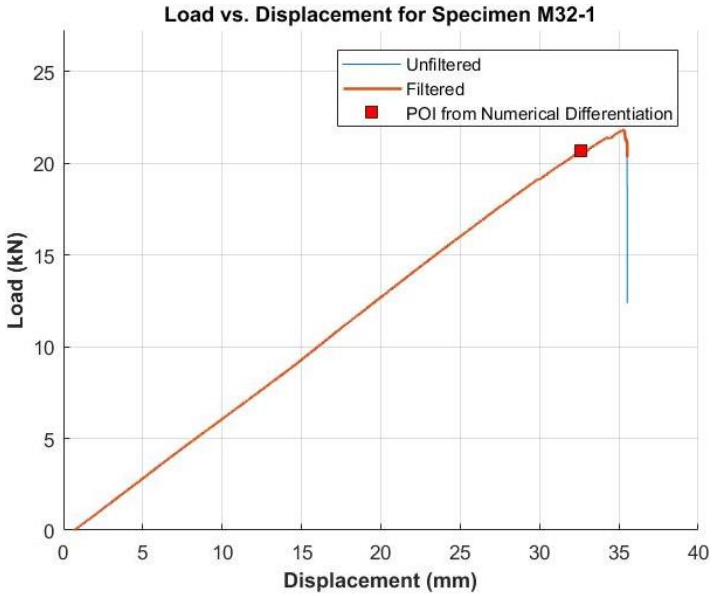

Figure C2.60: Load-displacement plot for Specimen M32-1

Appendix D – Weibull Strength Distribution Graphs

In Section 5.3.3 of this thesis, Variation B of the data analysis was presented, where the specimens with the lowest and highest rupture modulus for each size of specimens per flexural test has been omitted. The reason for this is to reduce the variance of the specimens' rupture modulus, as specimens with the lowest and highest rupture moduli can alter the results from the Weibull graph, which directly affect the Weibull modulus used in the correlation calculations. Variation A will be utilizing all the specimens to form the Weibull strength distribution graph and calculate the Weibull modulus, m.

Throughout the main parts of the thesis, the results from Variation B are used in comparisons and conclusions. The outliers and any parameters and calculated values associated with Variation B are highlighted in red in the following graphs and tables in this section.

D1.0 Weibull Graphs for Method 1 of the Correlation Calculations

D1.1 3-Point Bending

Table D1.1: Data for Weibull Strength Distribution Graph for M8 Data in 3-Point Bending

Rank, i	Test No.	Specimen No.	Rupture Modulus, σ_r (MPa)	$P_f = \frac{(i-0.5)}{n}$	$x = \ln(\sigma_r)$	$y = \ln\left(ln\left(\frac{1}{1-P_f}\right)\right)$
1	35	M8-30	1986.37	0.05	7.59	-2.97
2	31	M8-25	2129.44	0.15	7.66	-1.82
3	11	M8-10	2136.63	0.25	7.67	-1.25
4	14	M8-24	2170.70	0.35	7.68	-0.84
5	12	M8-9	2252.59	0.45	7.72	-0.51
6	13	M8-33	2266.12	0.55	7.73	-0.23
7	33	M8-21	2317.60	0.65	7.75	0.05
8	34	M8-3	2334.13	0.75	7.76	0.33
9	15	M8-1	2342.85	0.85	7.76	0.64
10	32	M8-7	2345.95	0.95	7.76	1.10
Trendline for All Specimens			m = 21.77		b = -168.38	R^2 = 0.9541
Trendline with No Outliers			**m = 20.29**		**b = -156.98**	**R^2 = 0.9364**

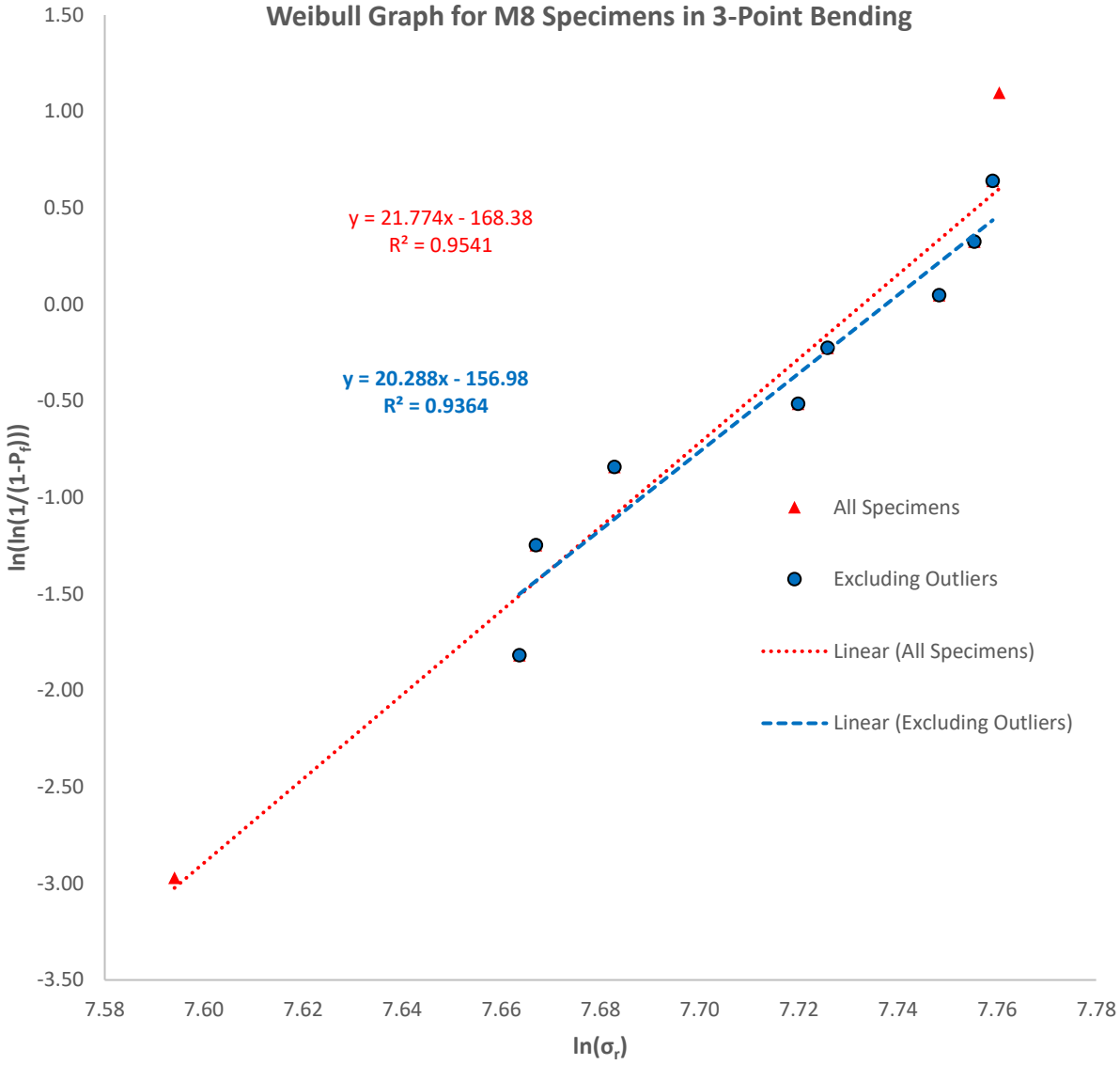

Figure D1.1: Weibull Strength Distribution Graph for M8 Specimens in 3-Point Bending

Table D1.2: Data for Weibull Strength Distribution Graph for M8 Data in 3-Point Bending

Rank, i	Test No.	Specimen No.	Rupture Modulus, σ_r (MPa)	$P_f = \frac{(i-0.5)}{n}$	$x = \ln(\sigma_r)$	$y = \ln\left(ln\left(\frac{1}{1-P_f}\right)\right)$
1	42	M13-14	1760.66	0.05	7.47	-2.97
2	45	M13-11	1760.96	0.15	7.47	-1.82
3	10	M13-20	1799.78	0.25	7.50	-1.25
4	41	M13-10	1884.86	0.35	7.54	-0.84
5	7	M13-3	1889.01	0.45	7.54	-0.51
6	9	M13-15	1907.54	0.55	7.55	-0.23
7	44	M13-20	1909.38	0.65	7.55	0.05
8	43	M13-13	1953.11	0.75	7.58	0.33
9	6	M13-1	1973.10	0.85	7.59	0.64
10	8	M13-18	2039.01	0.95	7.62	1.10
Trendline for All Specimens			m = 24.00		b = -181.56	R^2 = 0.9139
Trendline with No Outliers			**m = 20.74**		**b = -156.82**	**R^2 = 0.9436**

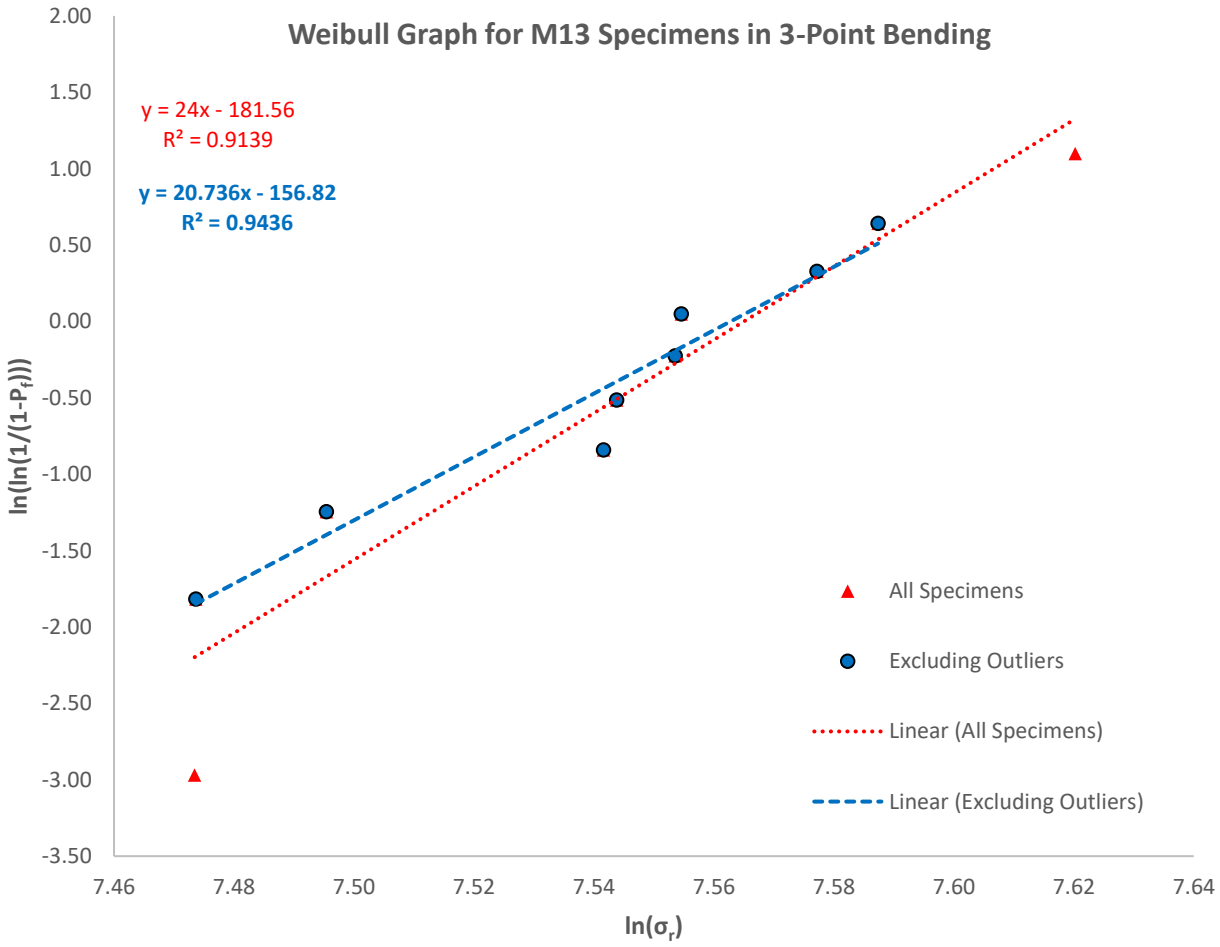

Figure D1.2: Weibull Strength Distribution Graph for M13 Specimens in 3-Point Bending

Table D1.3: Data for Weibull Strength Distribution Graph for M15 Data in 3-Point Bending

Rank, i	Test No.	Specimen No.	Rupture Modulus, σ_r (MPa)	$P_f = \frac{(i-0.5)}{n}$	$x = \ln(\sigma_r)$	$y = \ln\left(ln\left(\frac{1}{1-P_f}\right)\right)$
1	5	M15-29	1681.50	0.05	7.43	-2.97
2	4	M15-19	1697.01	0.15	7.44	-1.82
3	38	M15-30	1783.45	0.25	7.49	-1.25
4	36	M15-18	1860.40	0.35	7.53	-0.84
5	37	M15-25	1869.90	0.45	7.53	-0.51
6	40	M15-8	1933.32	0.55	7.57	-0.23
7	39	M15-14	1937.54	0.65	7.57	0.05
8	1	M15-5	1947.52	0.75	7.57	0.33
9	3	M15-26	1998.72	0.85	7.60	0.64
10	2	M15-3	2046.10	0.95	7.62	1.10
Trendline for All Specimens			m = 17.96		b = -135.86	R^2 = 0.9515
Trendline with No Outliers			**m = 15.05**		**b = -113.88**	**R^2 = 0.9560**

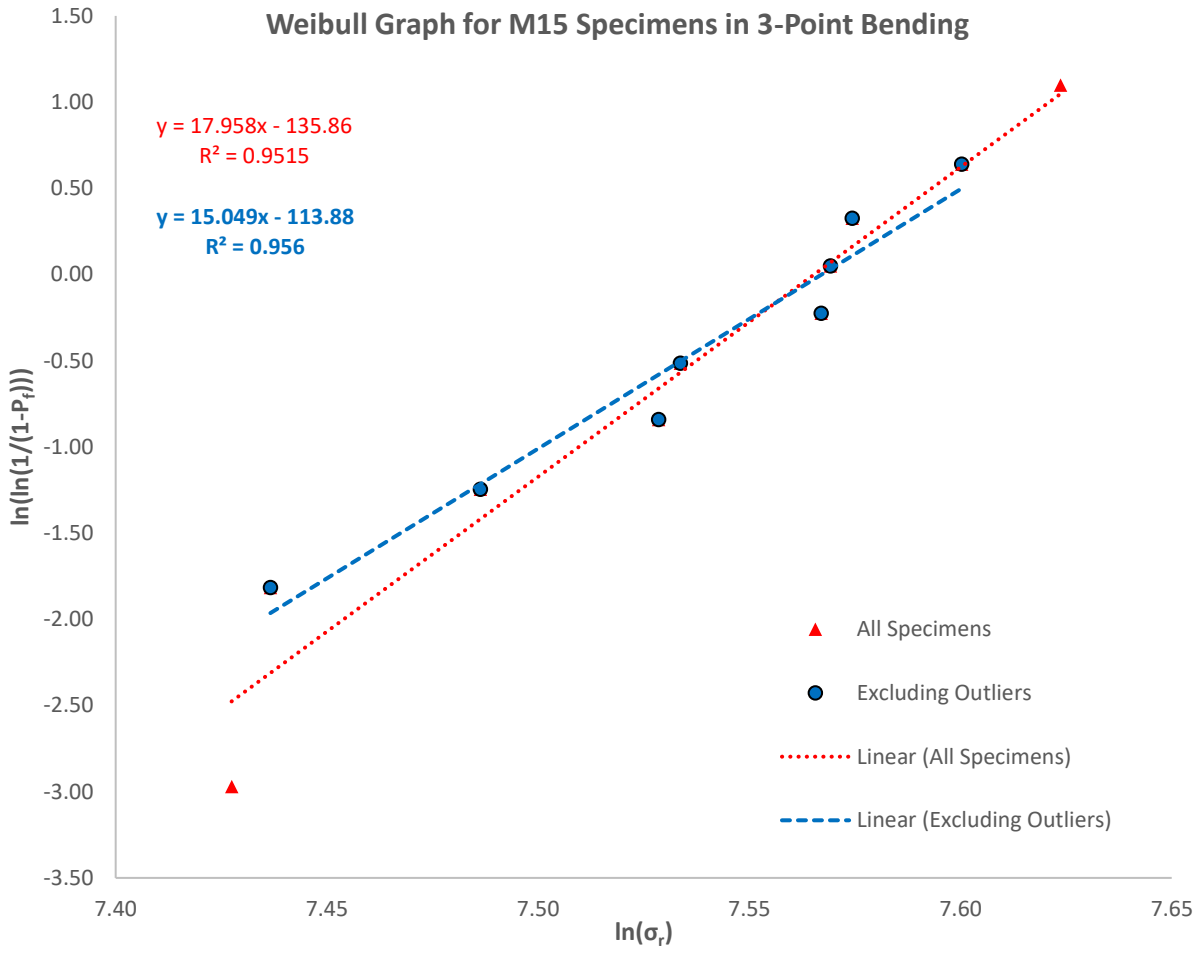

Figure D1.3: Weibull Strength Distribution Graph for M15 Specimens in 3-Point Bending

Table D1.4: Data for Weibull Strength Distribution Graph for M20 Data in 3-Point Bending

Rank, i	Test No.	Specimen No.	Rupture Modulus, σ_r (MPa)	$P_f = \frac{(i-0.5)}{n}$	$x = \ln(\sigma_r)$	$y = \ln\left(ln\left(\frac{1}{1-P_f}\right)\right)$
1	58	M20-8	1668.03	0.05	7.42	-2.97
2	59	M20-14	1692.96	0.15	7.43	-1.82
3	21	M20-1	1716.52	0.25	7.45	-1.25
4	25	M20-12	1733.24	0.35	7.46	-0.84
5	23	M20-22	1743.56	0.45	7.46	-0.51
6	57	M20-6	1777.15	0.55	7.48	-0.23
7	60	M20-10	1794.38	0.65	7.49	0.05
8	56	M20-9	1821.28	0.75	7.51	0.33
9	24	M20-19	1890.11	0.85	7.54	0.64
10	22	M20-21	1904.62	0.95	7.55	1.10
Trendline for All Specimens			m = 25.88		b = -194.12	R^2 = 0.8893
Trendline with No Outliers			**m = 21.97**		**b = -164.78**	**R^2 = 0.9062**

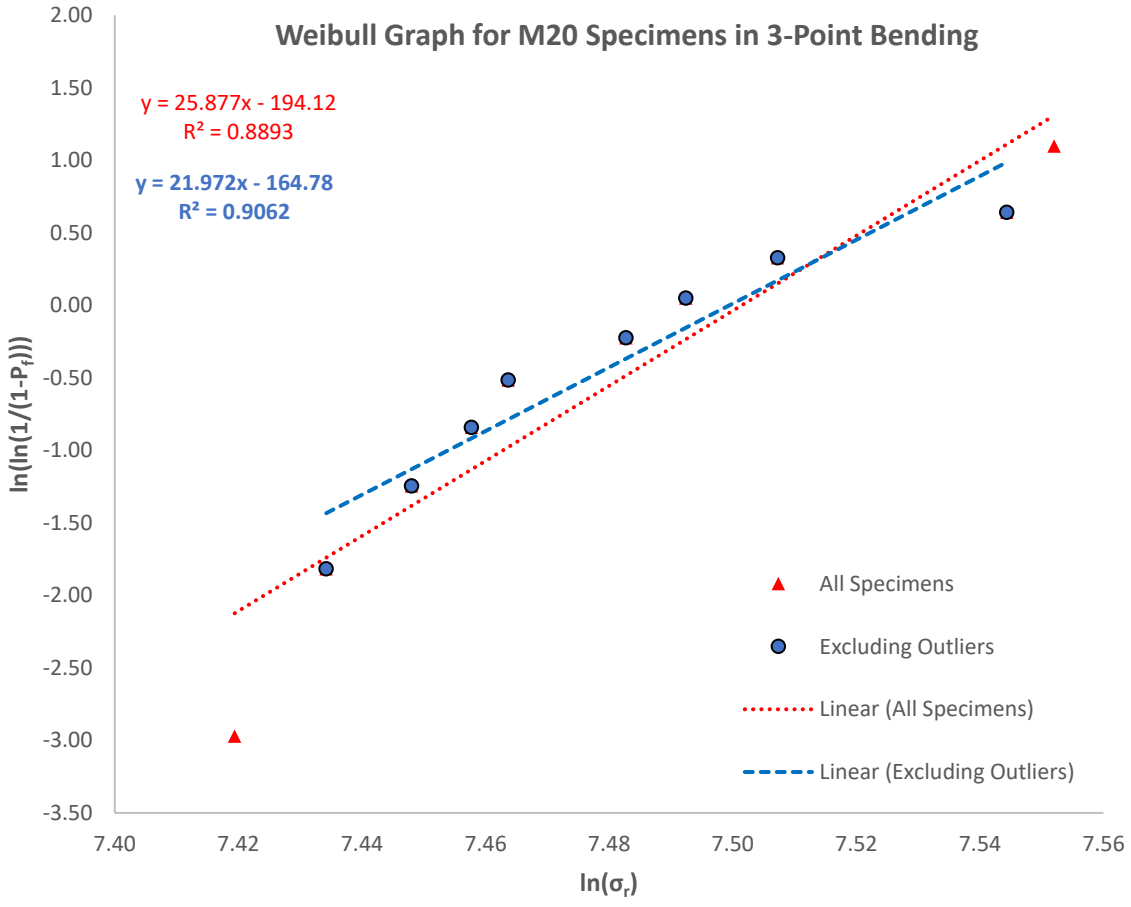

Figure D1.4: Weibull Strength Distribution Graph for M20 Specimens in 3-Point Bending

Table D1.5: Data for Weibull Strength Distribution Graph for M25 Data in 3-Point Bending

Rank, i	Test No.	Specimen No.	Rupture Modulus, σ_r (MPa)	$P_f = \frac{(i-0.5)}{n}$	$x = \ln(\sigma_r)$	$y = \ln\left(ln\left(\frac{1}{1-P_f}\right)\right)$
1	16	M25-1	1622.07	0.05	7.39	-2.97
2	49	M25-9	1629.67	0.15	7.40	-1.82
3	47	M25-15	1642.81	0.25	7.40	-1.25
4	46	M25-20	1644.60	0.35	7.41	-0.84
5	48	M25-19	1667.94	0.45	7.42	-0.51
6	50	M25-18	1679.03	0.55	7.43	-0.23
7	19	M25-12	1684.26	0.65	7.43	0.05
8	18	M25-13	1764.60	0.75	7.48	0.33
9	17	M25-2	1768.67	0.85	7.48	0.64
10	20	M25-8	1779.51	0.95	7.48	1.10
Trendline for All Specimens			m = 30.43		b = -226.71	R^2 = 0.7848
Trendline with No Outliers			**m = 23.58**		**b = -175.61**	**R^2 = 0.8121**

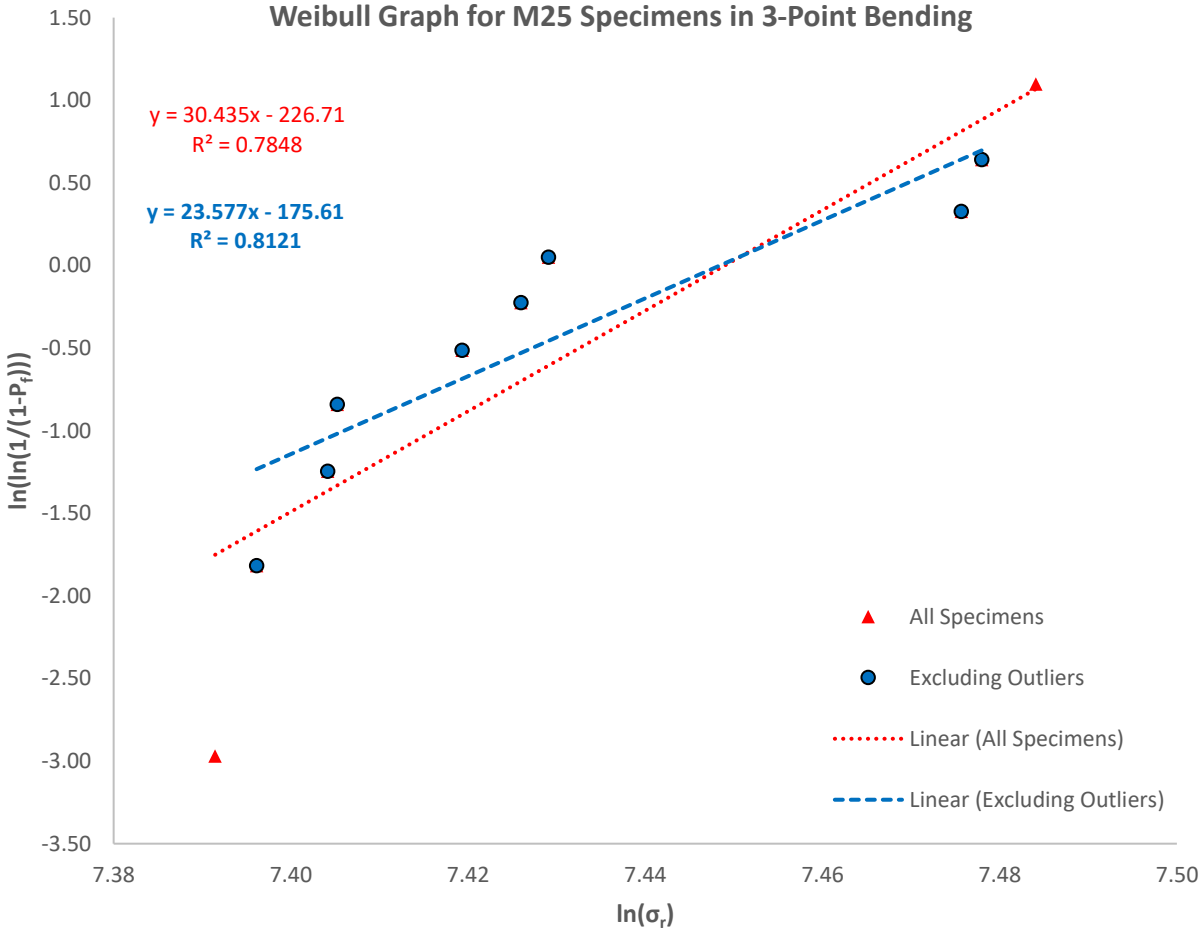

Figure D1.5: Weibull Strength Distribution Graph for M25 Specimens in 3-Point Bending

Table D1.6: Data for Weibull Strength Distribution Graph for M32 Data in 3-Point Bending

Rank, i	Test No.	Specimen No.	Rupture Modulus, σ_r (MPa)	$P_f = \frac{(i-0.5)}{n}$	$x = \ln(\sigma_r)$	$y = \ln\left(ln\left(\frac{1}{1-P_f}\right)\right)$
1	28	M32-4	1343.66	0.05	7.20	-2.97
2	51	M32-9	1527.66	0.15	7.33	-1.82
3	30	M32-5	1536.27	0.25	7.34	-1.25
4	26	M32-16	1556.38	0.35	7.35	-0.84
5	54	M32-3	1608.48	0.45	7.38	-0.51
6	55	M32-8	1635.71	0.55	7.40	-0.23
7	52	M32-15	1661.02	0.65	7.42	0.05
8	27	M32-12	1663.88	0.75	7.42	0.33
9	53	M32-20	1673.96	0.85	7.42	0.64
10	29	M32-11	1707.65	0.95	7.44	1.10
Trendline for All Specimens			m = 16.80		b = -124.35	R^2 = 0.9313
Trendline with No Outliers			**m = 21.17**		**b = -156.72**	**R^2 = 0.9335**

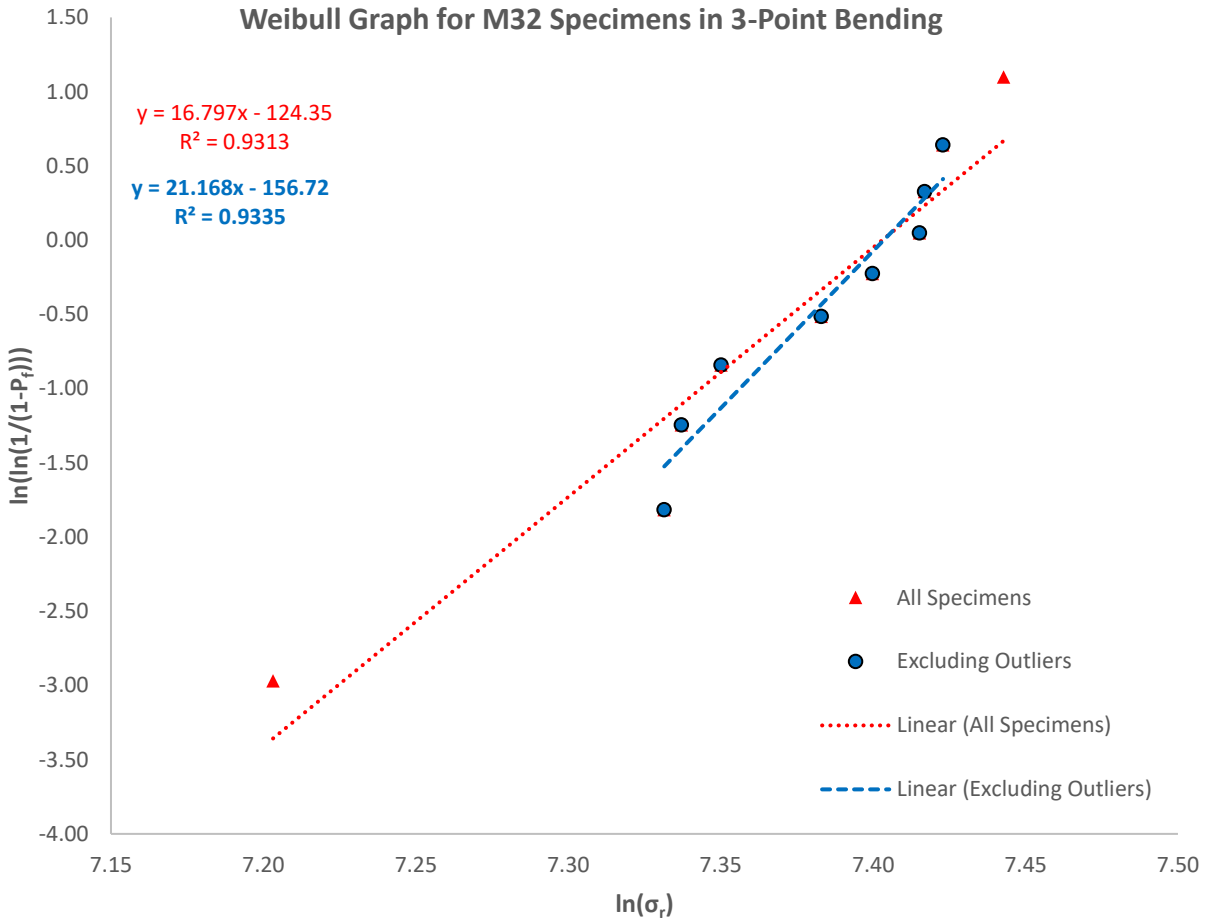

Figure D1.6: Weibull Strength Distribution Graph for M32 Specimens in 3-Point Bending

D1.2 4-Point Bending

Table D1.7: Data for Weibull Strength Distribution Graph for M8 Data in 4-Point Bending

Rank, i	Test No.	Specimen No.	Rupture Modulus, σ_r (MPa)	$P_f = \frac{(i-0.5)}{n}$	$x = \ln(\sigma_r)$	$y = \ln\left(ln\left(\frac{1}{1-P_f}\right)\right)$
1	87	M8-17	1991.95	0.05	7.60	-2.97
2	86	M8-8	2117.98	0.15	7.66	-1.82
3	84	M8-4	2120.85	0.25	7.66	-1.25
4	85	M8-15	2190.00	0.35	7.69	-0.84
5	91	M8-23	2257.62	0.45	7.72	-0.51
6	90	M8-11	2281.87	0.55	7.73	-0.23
7	88	M8-32	2323.50	0.65	7.75	0.05
8	83	M8-6	2352.23	0.75	7.76	0.33
9	92	M8-14	2372.63	0.85	7.77	0.64
10	89	M8-27	2562.90	0.95	7.85	1.10
Trendline for All Specimens			m = 16.65		b = -129.10	R^2 = 0.9460
Trendline with No Outliers			**m = 18.09**		**b = -140.05**	**R^2 = 0.9580**

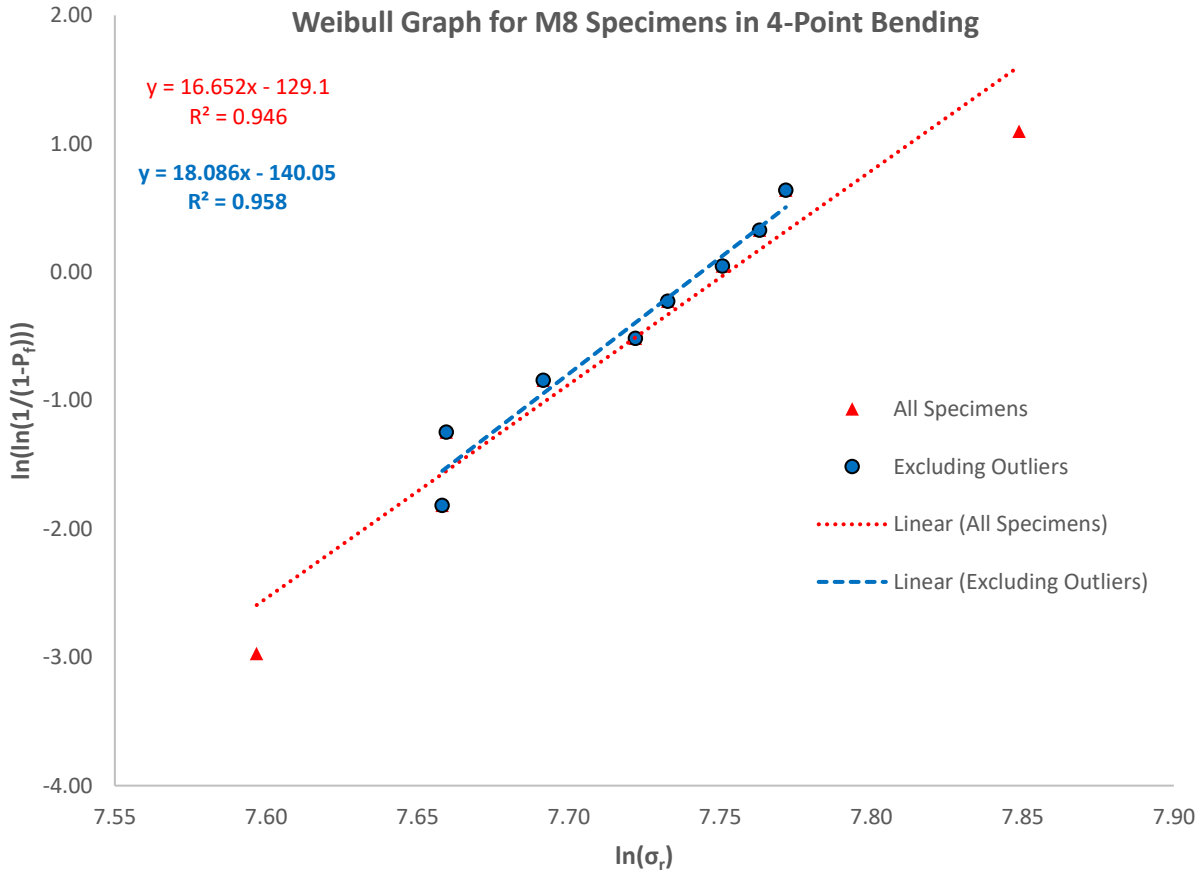

Figure D1.7: Weibull Strength Distribution Graph for M8 Specimens in 4-Point Bending

Table D1.8: Data for Weibull Strength Distribution Graph for M13 Data in 4-Point Bending

Rank, i	Test No.	Specimen No.	Rupture Modulus, σ_r (MPa)	$P_f = \frac{(i-0.5)}{n}$	$x = \ln(\sigma_r)$	$y = \ln\left(ln\left(\frac{1}{1-P_f}\right)\right)$
1	76	M13-12	1647.30	0.05	7.41	-2.97
2	78	M13-16	1665.56	0.15	7.42	-1.82
3	74	M13-4	1697.21	0.25	7.44	-1.25
4	75	M13-8	1811.85	0.35	7.50	-0.84
5	77	M13-17	1822.47	0.45	7.51	-0.51
6	79	M13-5	1844.93	0.55	7.52	-0.23
7	81	M13-9	1860.01	0.65	7.53	0.05
8	73	M13-7	1935.90	0.75	7.57	0.33
9	82	M13-19	1961.16	0.85	7.58	0.64
10	80	M13-6	2037.11	0.95	7.62	1.10
Trendline for All Specimens			m = 16.51		b = -124.55	R^2 = 0.9242
Trendline with No Outliers			**m = 14.11**		**b = -106.42**	**R^2 = 0.9560**

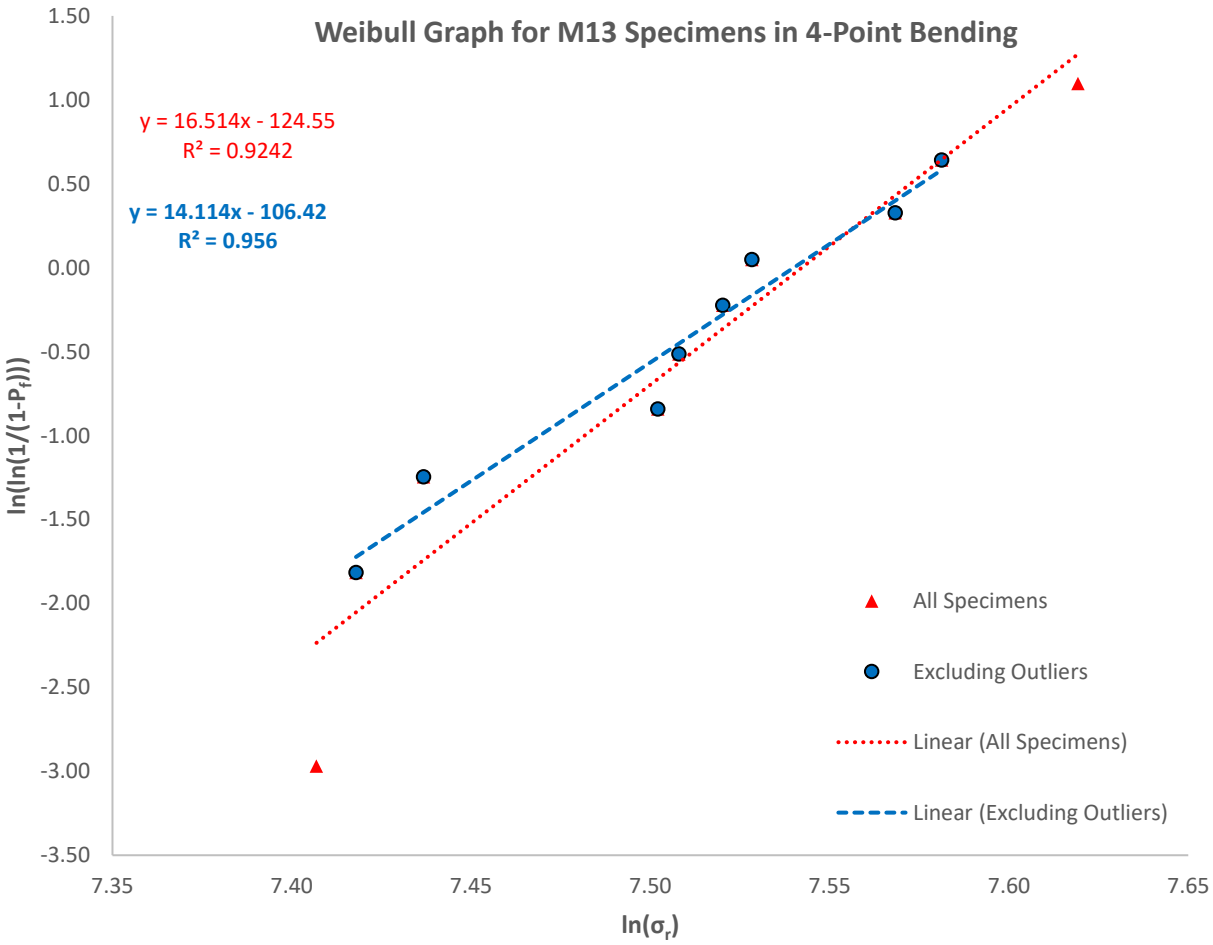

Figure D1.8: Weibull Strength Distribution Graph for M13 Specimens in 4-Point Bending

Table D1.9: Data for Weibull Strength Distribution Graph for M15 Data in 4-Point Bending

Rank, i	Test No.	Specimen No.	Rupture Modulus, σ_r (MPa)	$P_f = \frac{(i-0.5)}{n}$	$x = \ln(\sigma_r)$	$y = \ln\left(ln\left(\frac{1}{1-P_f}\right)\right)$
1	69	M15-27	1410.64	0.05	7.25	-2.97
2	63	M15-9	1608.94	0.15	7.38	-1.82
3	67	M15-10	1631.95	0.25	7.40	-1.25
4	65	M15-7	1651.15	0.35	7.41	-0.84
5	66	M15-20	1691.52	0.45	7.43	-0.51
6	68	M15-4	1719.22	0.55	7.45	-0.23
7	72	M15-15	1769.67	0.65	7.48	0.05
8	70	M15-13	1777.73	0.75	7.48	0.33
9	71	M15-21	1842.93	0.85	7.52	0.64
10	64	M15-31	1873.84	0.95	7.54	1.10
Trendline for All Specimens			m = 14.70		b = -109.87	R^2 = 0.9675
Trendline with No Outliers			**m = 17.03**		**b = -127.26**	**R^2 = 0.9501**

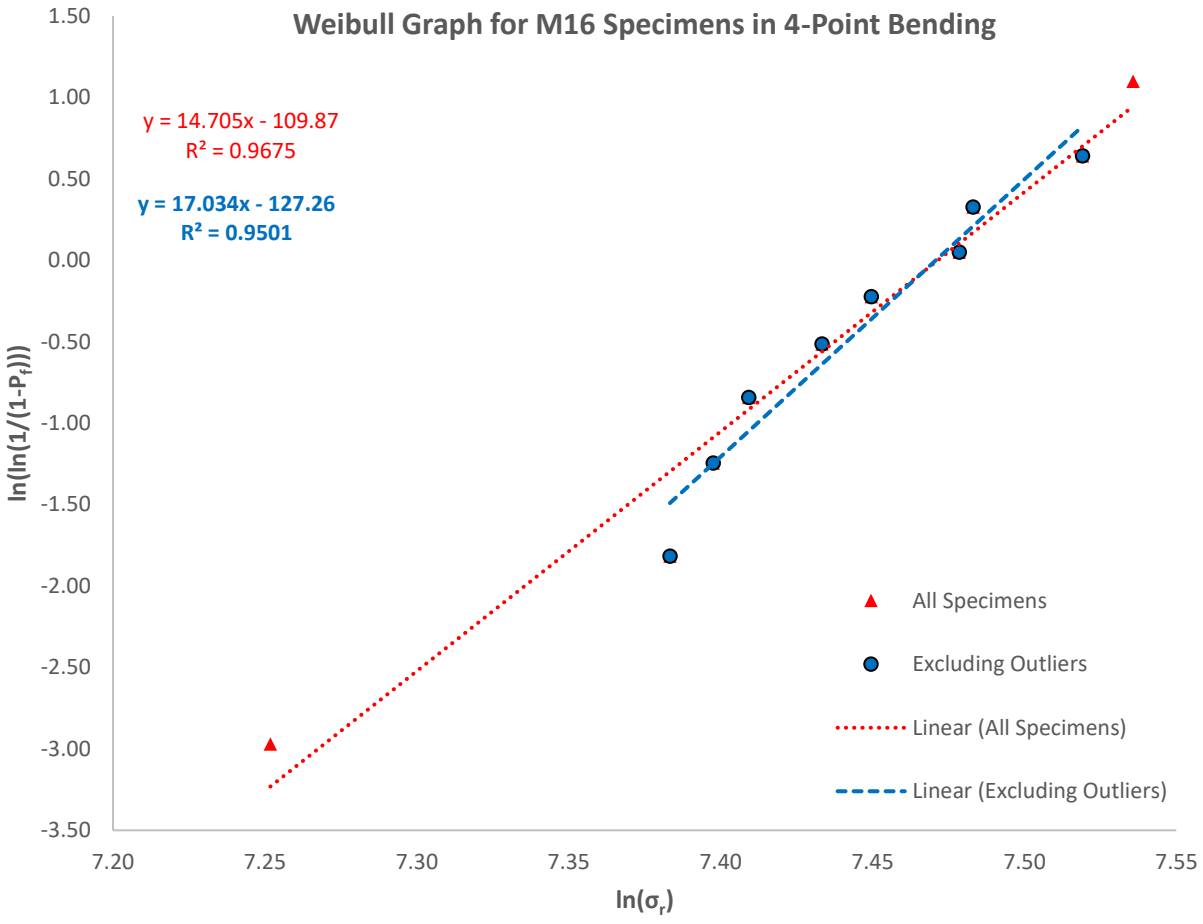

Figure D1.9: Weibull Strength Distribution Graph for M15 Specimens in 4-Point Bending

Table D1.10: Data for Weibull Strength Distribution Graph for M20 Data in 4-Point Bending

Rank, i	Test No.	Specimen No.	Rupture Modulus, σ_r (MPa)	$P_f = \frac{(i-0.5)}{n}$	$x = \ln(\sigma_r)$	$y = \ln\left(ln\left(\frac{1}{1-P_f}\right)\right)$
1	114	M20-26	1390.49	0.05	7.24	-2.97
2	115	M20-5	1438.57	0.15	7.27	-1.82
3	113	M20-18	1510.47	0.25	7.32	-1.25
4	120	M20-3	1558.60	0.35	7.35	-0.84
5	119	M20-20	1646.20	0.45	7.41	-0.51
6	118	M20-7	1655.08	0.55	7.41	-0.23
7	121	M20-23	1658.92	0.65	7.41	0.05
8	122	M20-17	1677.15	0.75	7.42	0.33
9	117	M20-24	1724.65	0.85	7.45	0.64
10	116	M20-11	1786.55	0.95	7.49	1.10
Trendline for All Specimens			m = 14.89		b = -110.43	R^2 = 0.9651
Trendline with No Outliers			**m = 13.07**		**b = -96.92**	**R^2 = 0.9456**

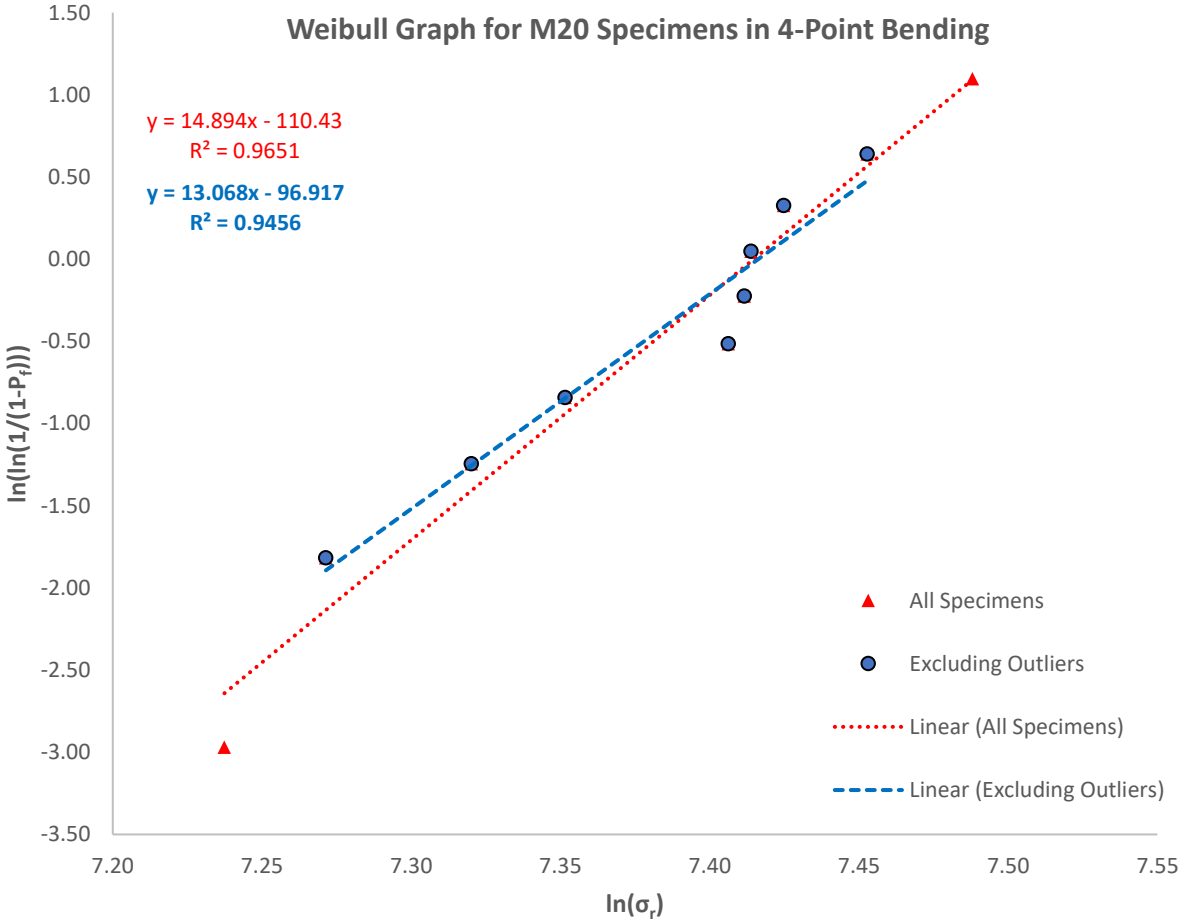

Figure D1.10: Weibull Strength Distribution Graph for M20 Specimens in 4-Point Bending

Table D1.11: Data for Weibull Strength Distribution Graph for M25 Data in 4-Point Bending

Rank, i	Test No.	Specimen No.	Rupture Modulus, σ_r (MPa)	$P_f = \frac{(i-0.5)}{n}$	$x = \ln(\sigma_r)$	$y = \ln\left(ln\left(\frac{1}{1-P_f}\right)\right)$
1	93	M25-6	1520.72	0.05	7.33	-2.97
2	98	M25-3	1580.94	0.15	7.37	-1.82
3	99	M25-10	1598.09	0.25	7.38	-1.25
4	102	M25-7	1622.20	0.35	7.39	-0.84
5	96	M25-17	1624.11	0.45	7.39	-0.51
6	97	M25-4	1635.88	0.55	7.40	-0.23
7	94	M25-11	1643.11	0.65	7.40	0.05
8	101	M25-16	1768.51	0.75	7.48	0.33
9	100	M25-5	1787.56	0.85	7.49	0.64
10	95	M25-14	1868.21	0.95	7.53	1.10
Trendline for All Specimens			m = 17.47		b = -130.11	R^2 = 0.8265
Trendline with No Outliers			**m = 15.68**		**b = -116.65**	**R^2 = 0.7550**

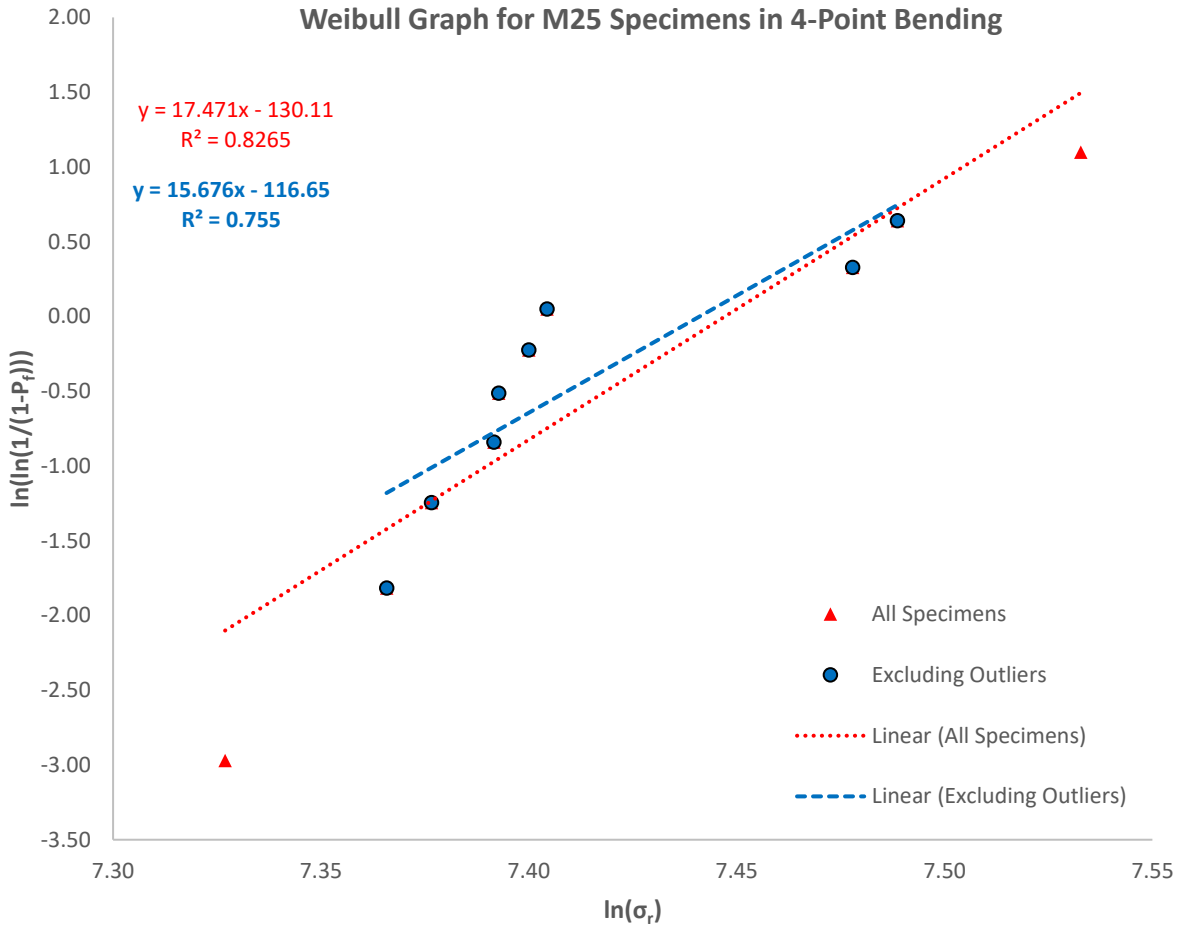

Figure D1.11: Weibull Strength Distribution Graph for M25 Specimens in 4-Point Bending

Table D1.12: Data for Weibull Strength Distribution Graph for M32 Data in 4-Point Bending

Rank, i	Test No.	Specimen No.	Rupture Modulus, σ_r (MPa)	$P_f = \frac{(i-0.5)}{n}$	$x = \ln(\sigma_r)$	$y = \ln\left(ln\left(\frac{1}{1-P_f}\right)\right)$
1	103	M32-19	893.12	0.05	6.79	-2.97
2	111	M32-6	1501.91	0.15	7.31	-1.82
3	109	M32-17	1563.06	0.25	7.35	-1.25
4	107	M32-18	1580.44	0.35	7.37	-0.84
5	104	M32-7	1589.95	0.45	7.37	-0.51
6	110	M32-14	1591.10	0.55	7.37	-0.23
7	108	M32-13	1596.72	0.65	7.38	0.05
8	106	M32-10	1647.64	0.75	7.41	0.33
9	105	M32-2	1695.79	0.85	7.44	0.64
10	112	M32-1	1738.15	0.95	7.46	1.10
Trendline for All Specimens			m = 5.30		b = -39.37	R^2 = 0.6879
Trendline for All Specimens			m = 20.16		b = -149.15	R^2 = 0.9150
Trendline with No Outliers			**m = 21.72**		**b = -160.66**	**R^2 = 0.8876**

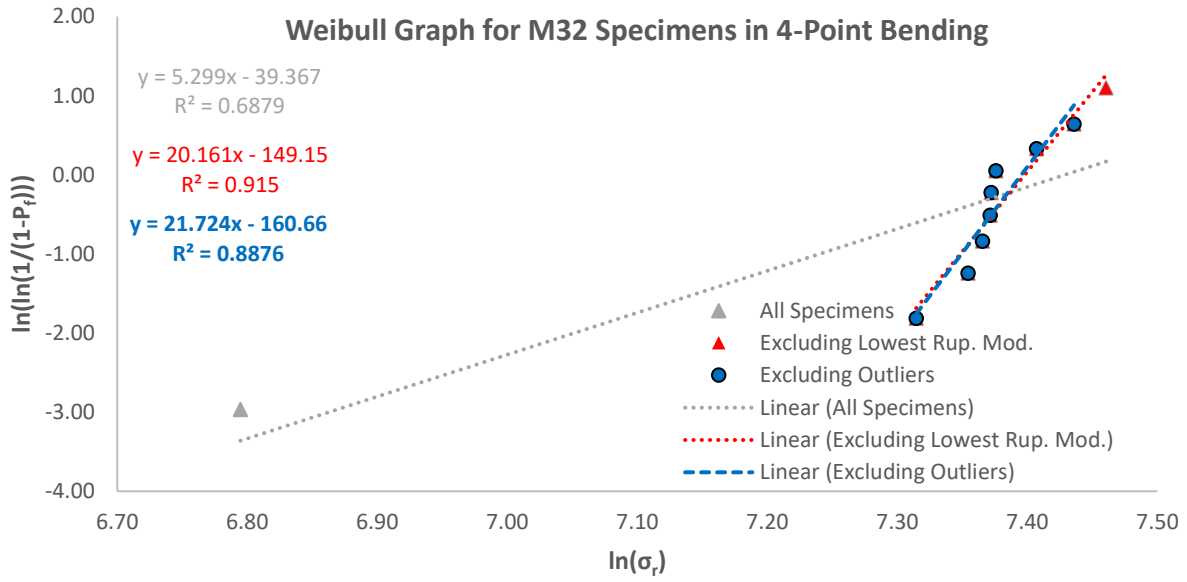

Figure D1.12: Weibull Strength Distribution Graph for M32 Specimens in 4-Point Bending

Note that the Weibull graph and data for the M32 specimen in 4-point bending, points correspond to using all specimens in the Weibull (grey triangle data points) , whereas the red triangular data correspond to using all the specimens except the first data point (which is the specimen with the lowest rupture modulus). The reason for distinguishing between the two data sets are to show that the first data point heavily skews the results from the Weibull graph for the for the gray square data points. Therefore, the red triangular data points are treated as the primary data set, similar to the rest of the graphs, even though it does not contain all data points.

D2.0 Weibull Graphs for Method 2 of Correlation Calculations

D2.1 3-Point Bending

Table D2.1: Data for Weibull Strength Distribution Graph for M8 Data in 3-Point Bending

Rank, i	Test No.	Specimen No.	Rupture Modulus, σ_r (MPa)	$P_f = \frac{(i-0.5)}{n}$	$x = \ln(\sigma_r)$	$y = \ln\left(ln\left(\frac{1}{1-P_f}\right)\right)$
1	35	M8-30	1964.11	0.05	7.58	-2.97
2	31	M8-25	2105.51	0.15	7.65	-1.82
3	11	M8-10	2112.62	0.25	7.66	-1.25
4	14	M8-24	2146.43	0.35	7.67	-0.84
5	12	M8-9	2227.33	0.45	7.71	-0.51
6	13	M8-33	2240.69	0.55	7.71	-0.23
7	33	M8-21	2291.61	0.65	7.74	0.05
8	34	M8-3	2307.91	0.75	7.74	0.33
9	15	M8-1	2316.58	0.85	7.75	0.64
10	32	M8-7	2319.71	0.95	7.75	1.10
Trendline for All Specimens			m = 21.77		b = -168.14	R^2 = 0.9542
Trendline with No Outliers			**m = 20.29**		**b = -156.75**	**R^2 = 0.9365**

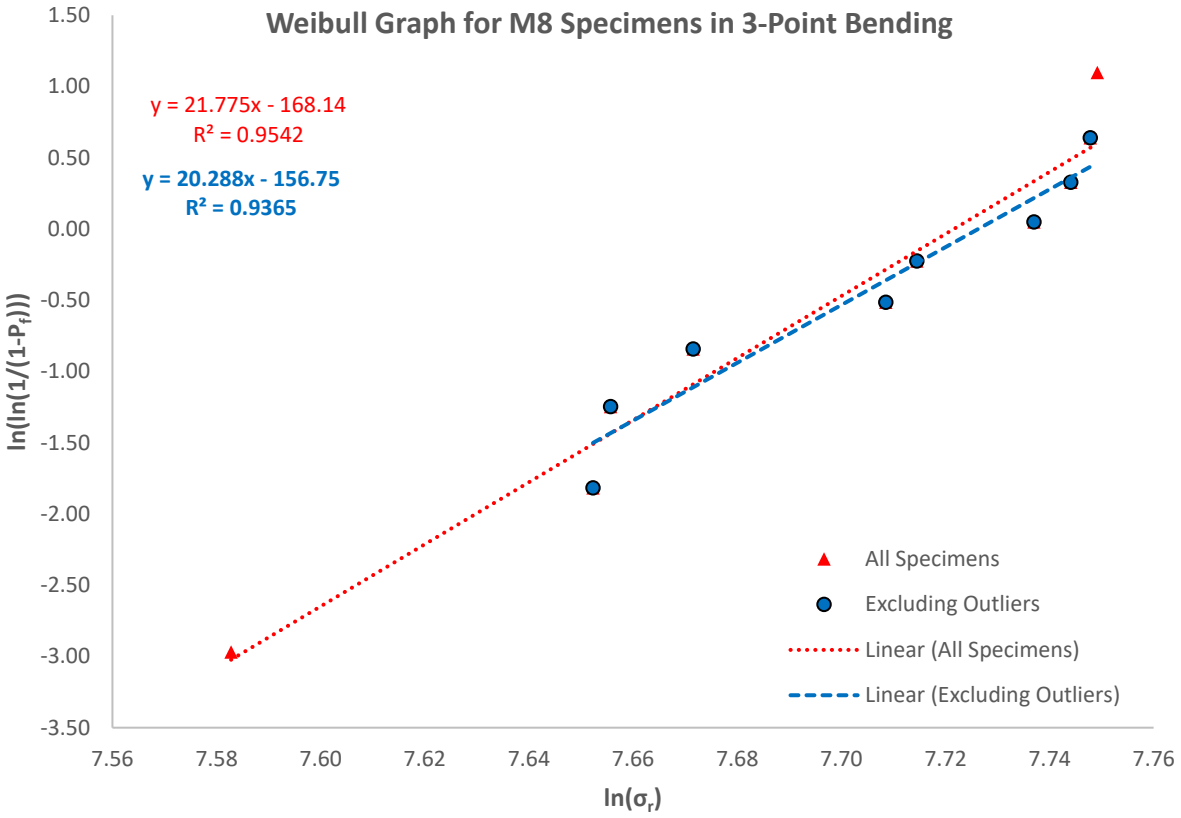

Figure D2.1: Weibull Strength Distribution Graph for M8 Specimens in 3-Point Bending

Table D2.2: Data for Weibull Strength Distribution Graph for M13 Data in 3-Point Bending

Rank, i	Test No.	Specimen No.	Rupture Modulus, σ_r (MPa)	$P_f = \frac{(i-0.5)}{n}$	$x = \ln(\sigma_r)$	$y = \ln\left(ln\left(\frac{1}{1-P_f}\right)\right)$
1	42	M13-14	1740.83	0.05	7.46	-2.97
2	45	M13-11	1741.13	0.15	7.46	-1.82
3	10	M13-20	1779.55	0.25	7.48	-1.25
4	41	M13-10	1863.64	0.35	7.53	-0.84
5	7	M13-3	1867.78	0.45	7.53	-0.51
6	9	M13-15	1886.09	0.55	7.54	-0.23
7	44	M13-20	1887.93	0.65	7.54	0.05
8	43	M13-13	1931.16	0.75	7.57	0.33
9	6	M13-1	1950.92	0.85	7.58	0.64
10	8	M13-18	2016.10	0.95	7.61	1.10
Trendline for All Specimens			m = 24.00		b = -181.27	R^2 = 0.9139
Trendline with No Outliers			**m = 20.73**		**b = -156.58**	**R^2 = 0.9436**

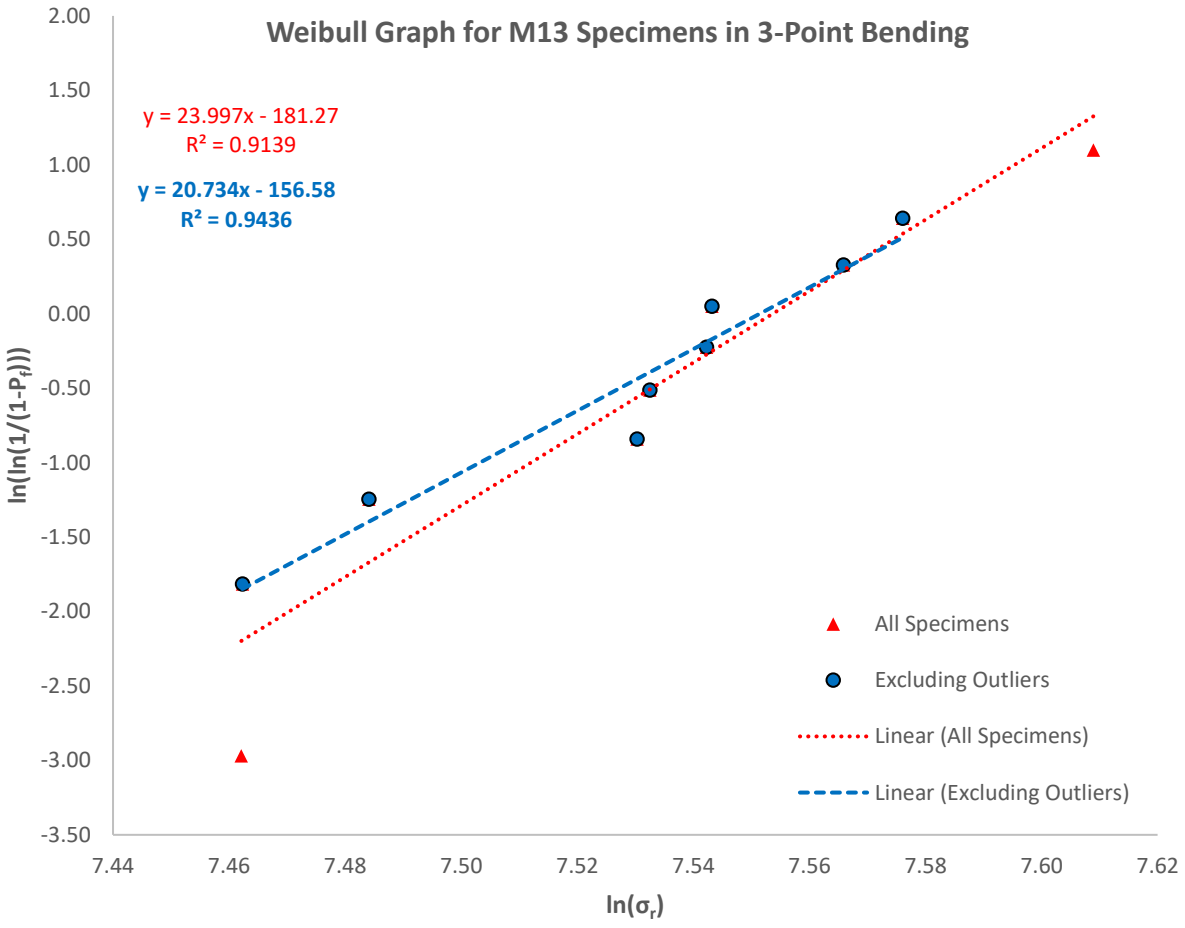

Figure D2.2: Weibull Strength Distribution Graph for M13 Specimens in 3-Point Bending

Table D2.3: Data for Weibull Strength Distribution Graph for M15 Data in 3-Point Bending

Rank, i	Test No.	Specimen No.	Rupture Modulus, σ_r (MPa)	$P_f = \frac{(i-0.5)}{n}$	$x = \ln(\sigma_r)$	$y = \ln\left(ln\left(\frac{1}{1-P_f}\right)\right)$
1	5	M15-29	1662.56	0.05	7.42	-2.97
2	4	M15-19	1677.89	0.15	7.43	-1.82
3	38	M15-30	1763.37	0.25	7.47	-1.25
4	36	M15-18	1839.47	0.35	7.52	-0.84
5	37	M15-25	1848.86	0.45	7.52	-0.51
6	40	M15-8	1911.55	0.55	7.56	-0.23
7	39	M15-14	1915.74	0.65	7.56	0.05
8	1	M15-5	1925.61	0.75	7.56	0.33
9	3	M15-26	1976.31	0.85	7.59	0.64
10	2	M15-3	2023.02	0.95	7.61	1.10
Trendline for All Specimens			m = 17.96		b = -135.65	R^2 = 0.9515
Trendline with No Outliers			**m = 15.05**		**b = -113.68**	**R^2 = 0.9561**

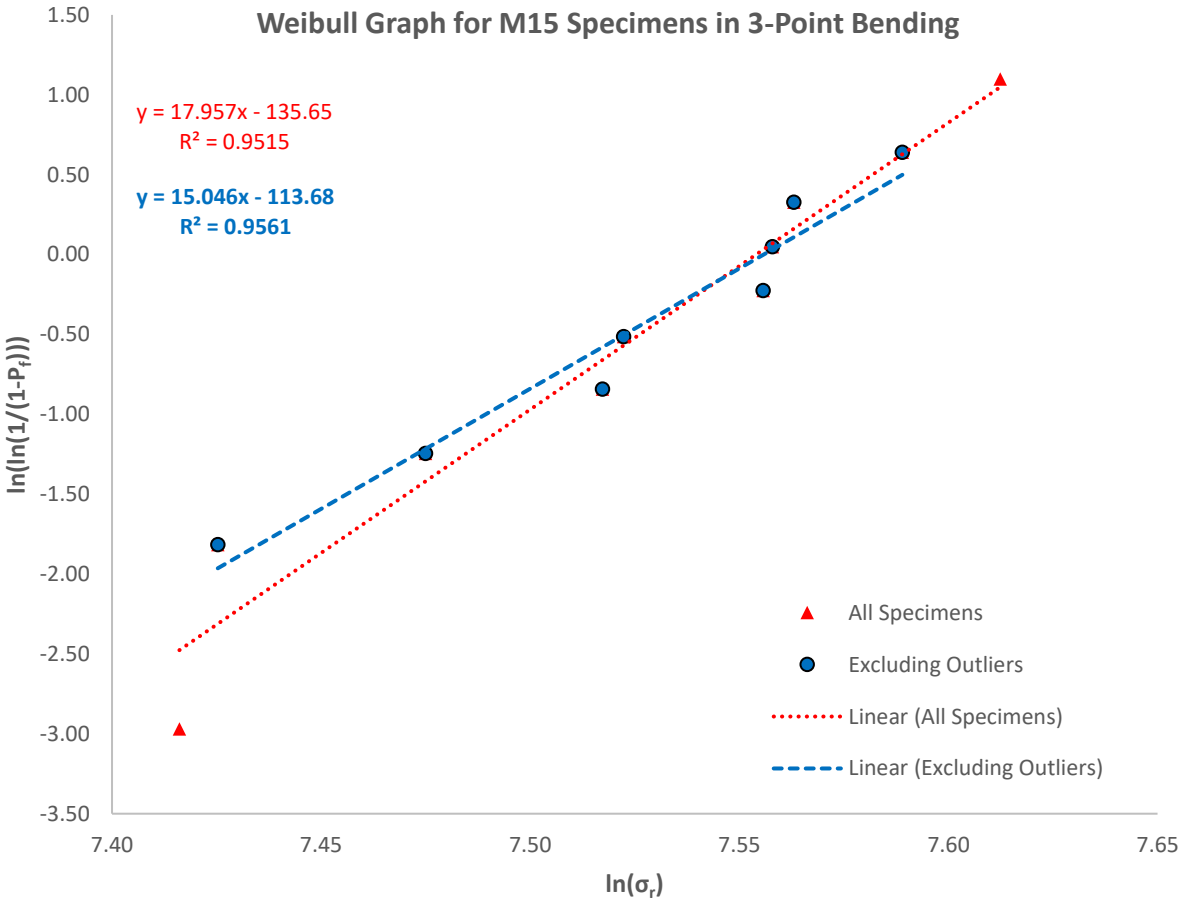

Figure D2.3: Weibull Strength Distribution Graph for M15 Specimens in 3-Point Bending

Table D2.4: Data for Weibull Strength Distribution Graph for M20 Data in 3-Point Bending

Rank, i	Test No.	Specimen No.	Rupture Modulus, σ_r (MPa)	$P_f = \frac{(i-0.5)}{n}$	$x = \ln(\sigma_r)$	$y = \ln\left(ln\left(\frac{1}{1-P_f}\right)\right)$
1	58	M20-8	1649.33	0.05	7.41	-2.97
2	59	M20-14	1673.93	0.15	7.42	-1.82
3	21	M20-1	1697.21	0.25	7.44	-1.25
4	25	M20-12	1713.71	0.35	7.45	-0.84
5	23	M20-22	1724.01	0.45	7.45	-0.51
6	57	M20-6	1757.09	0.55	7.47	-0.23
7	60	M20-10	1774.23	0.65	7.48	0.05
8	56	M20-9	1800.92	0.75	7.50	0.33
9	24	M20-19	1868.83	0.85	7.53	0.64
10	22	M20-21	1883.26	0.95	7.54	1.10
Trendline for All Specimens			m = 25.87		b = -193.81	R^2 = 0.8892
Trendline with No Outliers			**m = 21.97**		**b = -164.53**	**R^2 = 0.9063**

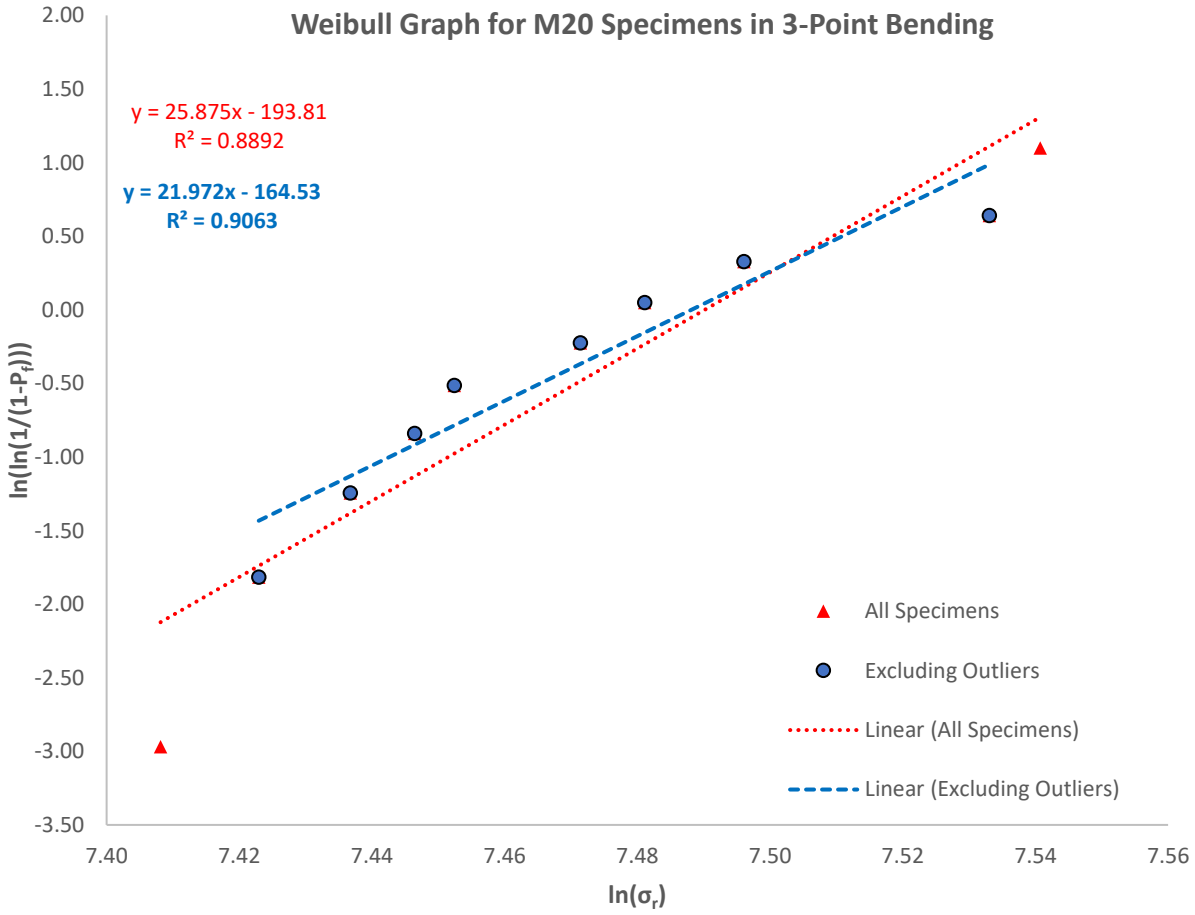

Figure D2.4: Weibull Strength Distribution Graph for M20 Specimens in 3-Point Bending

Table D2.5: Data for Weibull Strength Distribution Graph for M25 Data in 3-Point Bending

Rank, i	Test No.	Specimen No.	Rupture Modulus, σ_r (MPa)	$P_f = \frac{(i-0.5)}{n}$	$x = \ln(\sigma_r)$	$y = \ln\left(ln\left(\frac{1}{1-P_f}\right)\right)$
1	16	M25-1	1603.71	0.05	7.38	-2.97
2	49	M25-9	1611.32	0.15	7.38	-1.82
3	47	M25-15	1624.26	0.25	7.39	-1.25
4	46	M25-20	1626.08	0.35	7.39	-0.84
5	48	M25-19	1649.21	0.45	7.41	-0.51
6	50	M25-18	1660.02	0.55	7.41	-0.23
7	19	M25-12	1665.32	0.65	7.42	0.05
8	18	M25-13	1744.68	0.75	7.46	0.33
9	17	M25-2	1748.75	0.85	7.47	0.64
10	20	M25-8	1759.49	0.95	7.47	1.10
Trendline for All Specimens			m = 30.43		b = -226.36	R^2 = 0.7851
Trendline with No Outliers			**m = 23.58**		**b = -175.37**	**R^2 = 0.8122**

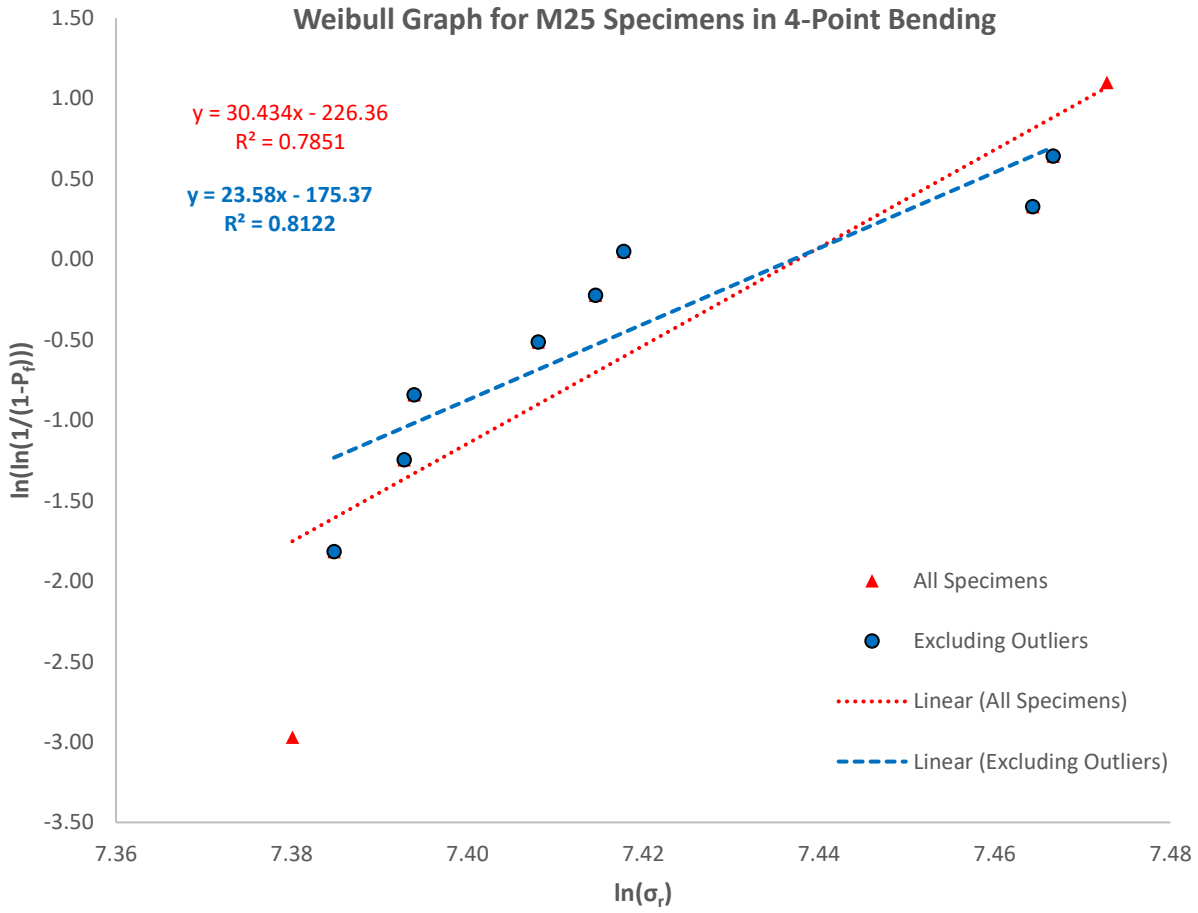

Figure D2.5: Weibull Strength Distribution Graph for M25 Specimens in 3-Point Bending

Table D2.6: Data for Weibull Strength Distribution Graph for M32 Data in 3-Point Bending

Rank, i	Test No.	Specimen No.	Rupture Modulus, σ_r (MPa)	$P_f = \frac{(i-0.5)}{n}$	$x = \ln(\sigma_r)$	$y = \ln\left(ln\left(\frac{1}{1-P_f}\right)\right)$
1	28	M32-4	1328.51	0.05	7.19	-2.97
2	51	M32-9	1510.44	0.15	7.32	-1.82
3	30	M32-5	1518.96	0.25	7.33	-1.25
4	26	M32-16	1538.84	0.35	7.34	-0.84
5	54	M32-3	1590.23	0.45	7.37	-0.51
6	55	M32-8	1617.29	0.55	7.39	-0.23
7	52	M32-15	1642.32	0.65	7.40	0.05
8	27	M32-12	1645.12	0.75	7.41	0.33
9	53	M32-20	1655.11	0.85	7.41	0.64
10	29	M32-11	1688.41	0.95	7.43	1.10
Trendline for All Specimens			m = 16.80		b = -124.16	R^2 = 0.9313
Trendline with No Outliers			**m = 21.17**		**b = -156.47**	**R^2 = 0.9335**

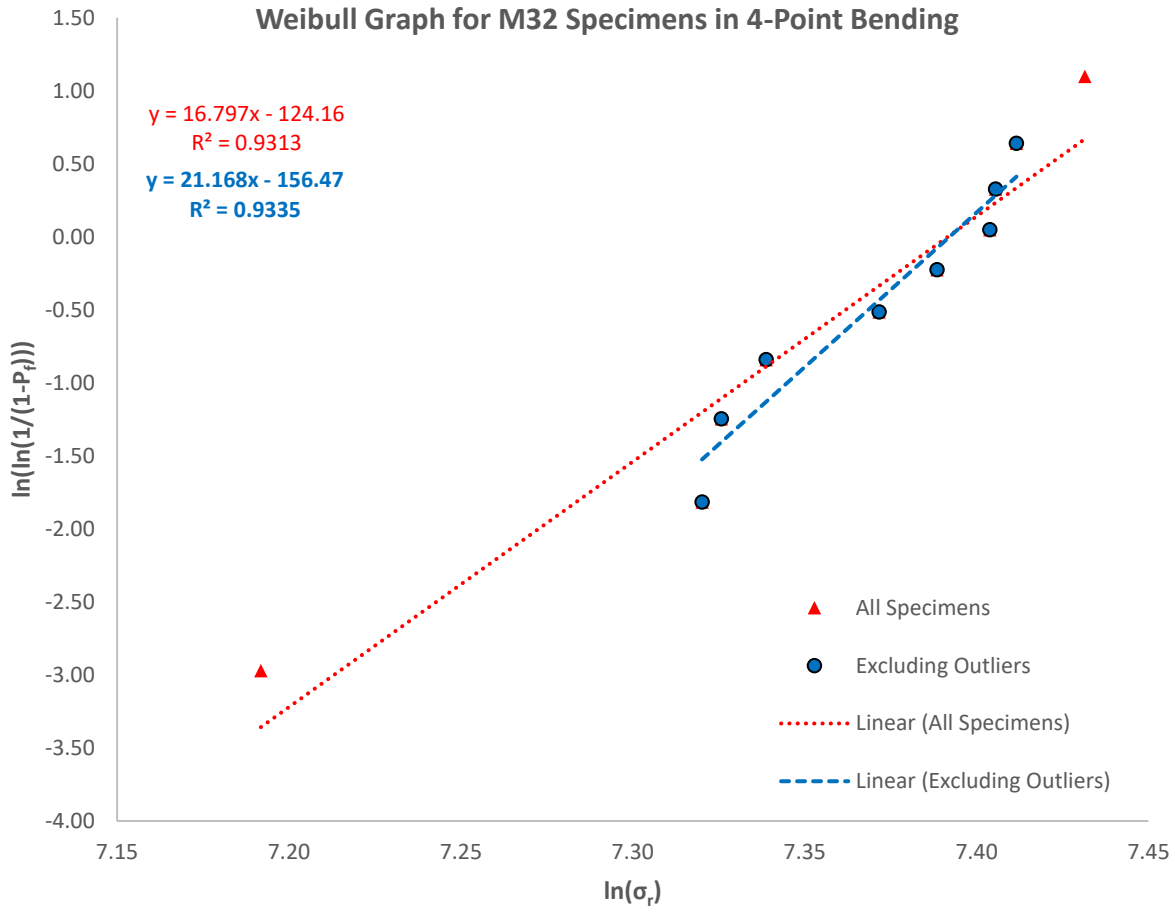

Figure D2.6: Weibull Strength Distribution Graph for M32 Specimens in 3-Point Bending

D2.2 4-Point Bending

Table D2.7: Data for Weibull Strength Distribution Graph for M8 Data in 4-Point Bending

Rank, i	Test No.	Specimen No.	Rupture Modulus, σ_r (MPa)	$P_f = \frac{(i-0.5)}{n}$	$x = \ln(\sigma_r)$	$y = \ln\left(ln\left(\frac{1}{1-P_f}\right)\right)$
1	87	M8-17	1969.60	0.05	7.59	-2.97
2	86	M8-8	2094.25	0.15	7.65	-1.82
3	84	M8-4	2097.05	0.25	7.65	-1.25
4	85	M8-15	2165.45	0.35	7.68	-0.84
5	91	M8-23	2232.28	0.45	7.71	-0.51
6	90	M8-11	2256.32	0.55	7.72	-0.23
7	88	M8-32	2297.43	0.65	7.74	0.05
8	83	M8-6	2325.86	0.75	7.75	0.33
9	92	M8-14	2346.05	0.85	7.76	0.64
10	89	M8-27	2534.16	0.95	7.84	1.10
Trendline for All Specimens			m = 16.65		b = -128.91	R^2 = 0.9460
Trendline with No Outliers			**m = 18.09**		**b = -139.84**	**R^2 = 0.9579**

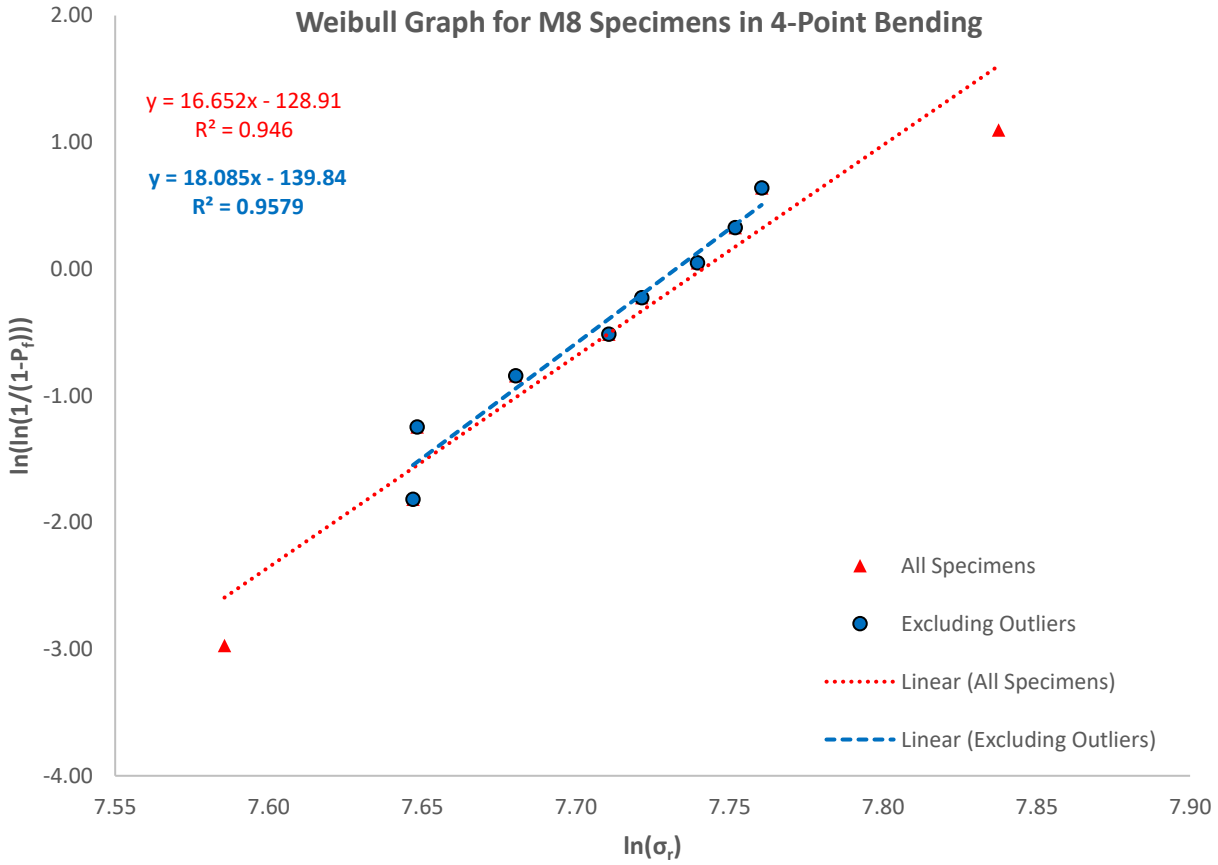

Figure D2.7: Weibull Strength Distribution Graph for M8 Specimens in 4-Point Bending

Table D2.8: Data for Weibull Strength Distribution Graph for M13 Data in 4-Point Bending

Rank, i	Test No.	Specimen No.	Rupture Modulus, σ_r (MPa)	$P_f = \frac{(i-0.5)}{n}$	$x = \ln(\sigma_r)$	$y = \ln\left(ln\left(\frac{1}{1-P_f}\right)\right)$
1	76	M13-12	1628.79	0.05	7.40	-2.97
2	78	M13-16	1646.81	0.15	7.41	-1.82
3	74	M13-4	1678.17	0.25	7.43	-1.25
4	75	M13-8	1791.51	0.35	7.49	-0.84
5	77	M13-17	1802.00	0.45	7.50	-0.51
6	79	M13-5	1824.17	0.55	7.51	-0.23
7	81	M13-9	1839.14	0.65	7.52	0.05
8	73	M13-7	1914.12	0.75	7.56	0.33
9	82	M13-19	1939.10	0.85	7.57	0.64
10	80	M13-6	2014.21	0.95	7.61	1.10
Trendline for All Specimens			m = 16.51		b = -124.37	R^2 = 0.9242
Trendline with No Outliers			**m = 14.12**		**b = -106.27**	**R^2 = 0.9560**

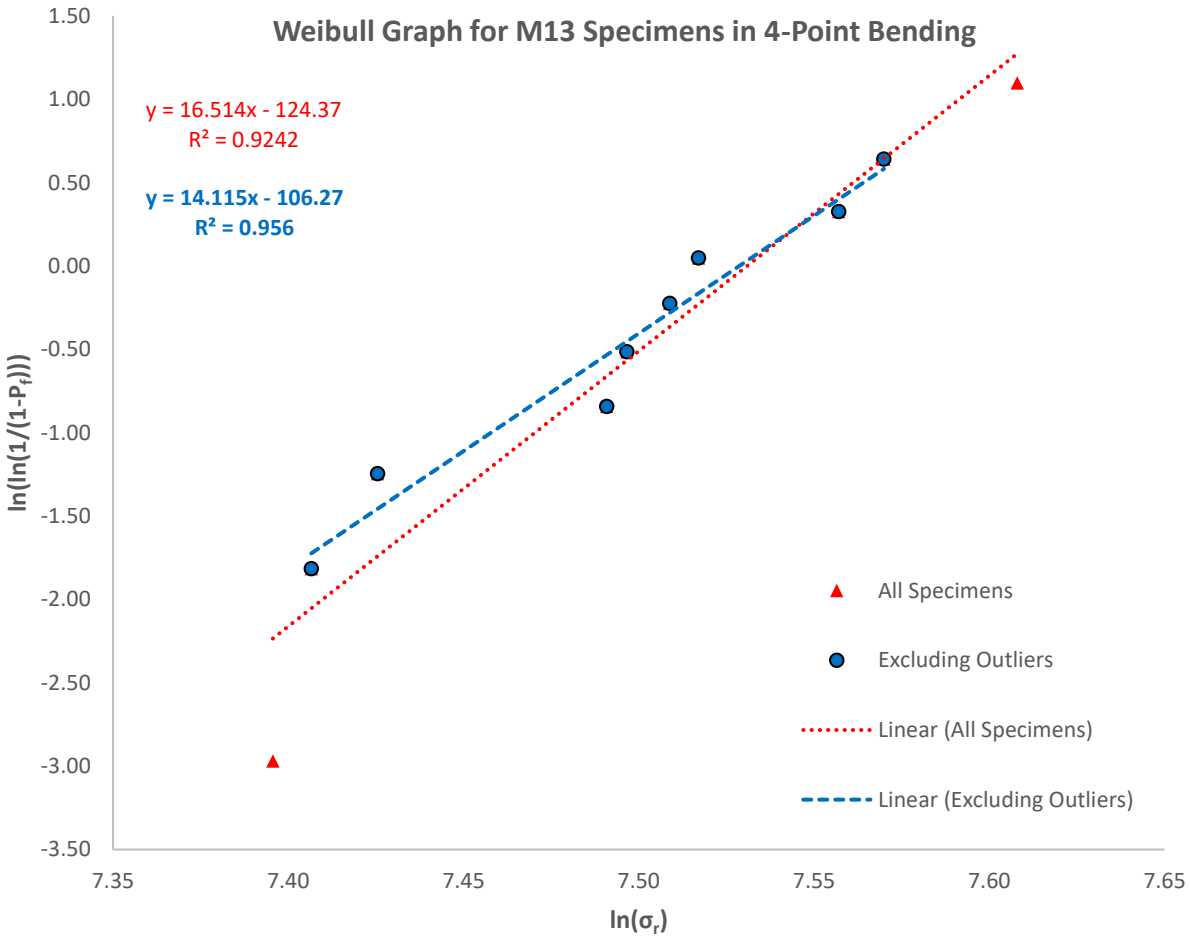

Figure D2.8: Weibull Strength Distribution Graph for M13 Specimens in 4-Point Bending

Table D2.9: Data for Weibull Strength Distribution Graph for M15 Data in 4-Point Bending

Rank, i	Test No.	Specimen No.	Rupture Modulus, σ_r (MPa)	$P_f = \frac{(i-0.5)}{n}$	$x = \ln(\sigma_r)$	$y = \ln\left(ln\left(\frac{1}{1-P_f}\right)\right)$
1	69	M15-27	1394.75	0.05	7.24	-2.97
2	63	M15-9	1590.85	0.15	7.37	-1.82
3	67	M15-10	1613.61	0.25	7.39	-1.25
4	65	M15-7	1632.73	0.35	7.40	-0.84
5	66	M15-20	1672.43	0.45	7.42	-0.51
6	68	M15-4	1699.88	0.55	7.44	-0.23
7	72	M15-15	1749.80	0.65	7.47	0.05
8	70	M15-13	1757.72	0.75	7.47	0.33
9	71	M15-21	1822.19	0.85	7.51	0.64
10	64	M15-31	1852.76	0.95	7.52	1.10
Trendline for All Specimens			m = 14.70		b = -109.70	R^2 = 0.9675
Trendline with No Outliers			**m = 17.01**		**b = -127.10**	**R^2 = 0.9501**

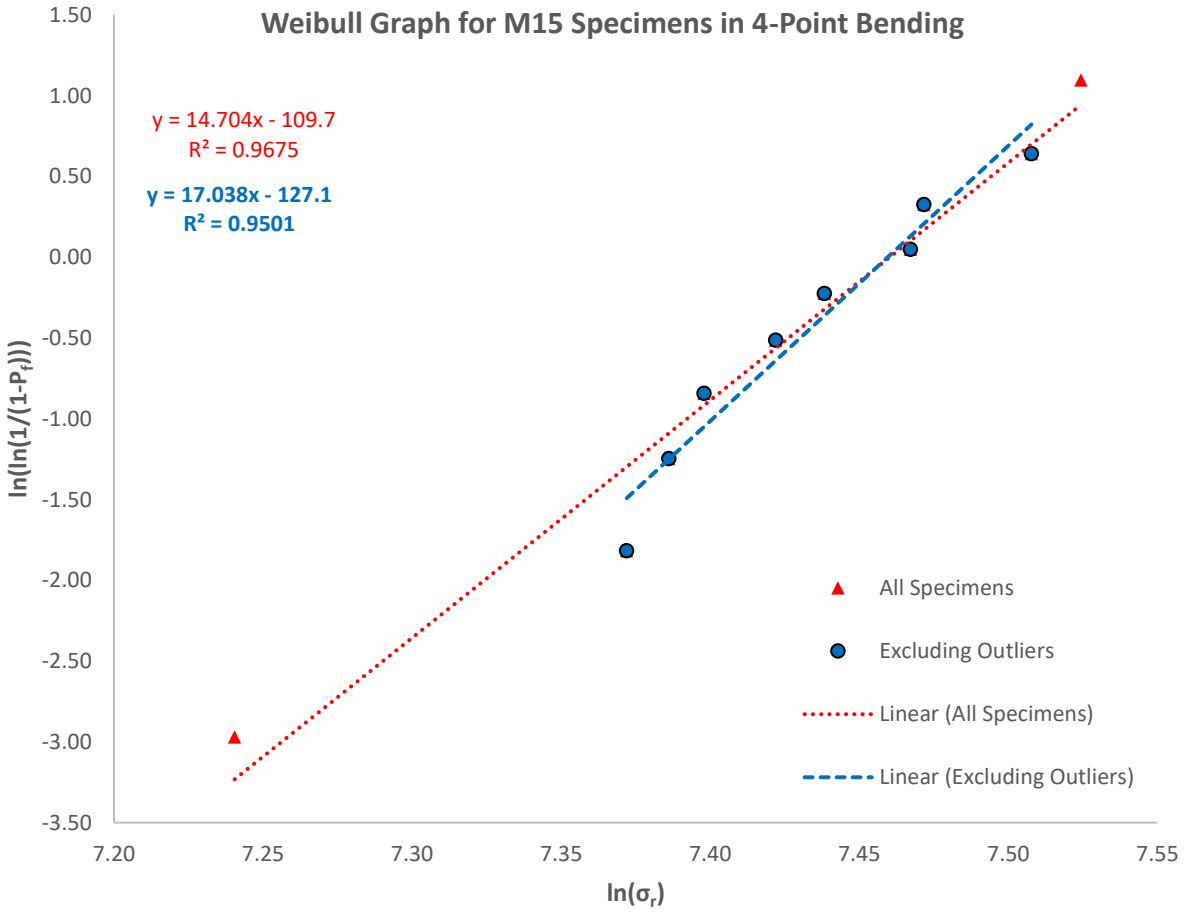

Figure D2.9: Weibull Strength Distribution Graph for M15 Specimens in 4-Point Bending

Table D2.10: Data for Weibull Strength Distribution Graph for M20 Data in 4-Point Bending

Rank, i	Test No.	Specimen No.	Rupture Modulus, σ_r (MPa)	$P_f = \frac{(i-0.5)}{n}$	$x = \ln(\sigma_r)$	$y = \ln\left(ln\left(\frac{1}{1-P_f}\right)\right)$
1	114	M20-26	1374.88	0.05	7.23	-2.97
2	115	M20-5	1422.39	0.15	7.26	-1.82
3	113	M20-18	1493.53	0.25	7.31	-1.25
4	120	M20-3	1541.10	0.35	7.34	-0.84
5	119	M20-20	1627.73	0.45	7.39	-0.51
6	118	M20-7	1636.48	0.55	7.40	-0.23
7	121	M20-23	1640.27	0.65	7.40	0.05
8	122	M20-17	1658.33	0.75	7.41	0.33
9	117	M20-24	1705.27	0.85	7.44	0.64
10	116	M20-11	1766.52	0.95	7.48	1.10
Trendline for All Specimens			m = 14.89		b = -110.26	R^2 = 0.9651
Trendline with No Outliers			**m = 13.07**		**b = -96.76**	**R^2 = 0.9455**

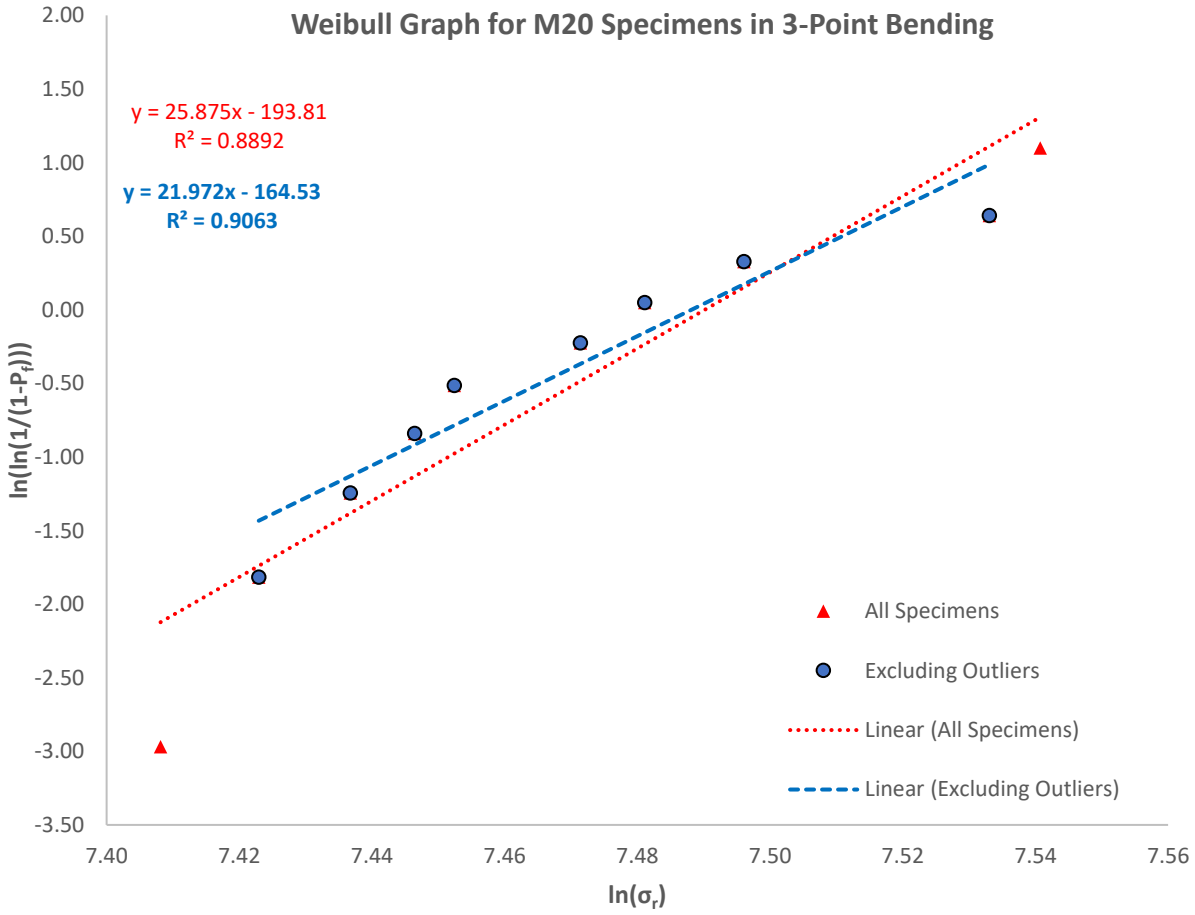

Figure D2.10: Weibull Strength Distribution Graph for M20 Specimens in 4-Point Bending

Table D2.11: Data for Weibull Strength Distribution Graph for M25 Data in 4-Point Bending

Rank, i	Test No.	Specimen No.	Rupture Modulus, σ_r (MPa)	$P_f = \frac{(i-0.5)}{n}$	$x = \ln(\sigma_r)$	$y = \ln\left(ln\left(\frac{1}{1-P_f}\right)\right)$
1	93	M25-6	1503.72	0.05	7.32	-2.97
2	98	M25-3	1563.13	0.15	7.35	-1.82
3	99	M25-10	1580.13	0.25	7.37	-1.25
4	102	M25-7	1603.87	0.35	7.38	-0.84
5	96	M25-17	1605.83	0.45	7.38	-0.51
6	97	M25-4	1617.46	0.55	7.39	-0.23
7	94	M25-11	1624.61	0.65	7.39	0.05
8	101	M25-16	1748.63	0.75	7.47	0.33
9	100	M25-5	1767.47	0.85	7.48	0.64
10	95	M25-14	1847.26	0.95	7.52	1.10
Trendline for All Specimens			m = 17.47		b = -129.89	R^2 = 0.8262
Trendline with No Outliers			**m = 15.67**		**b = -116.44**	**R^2 = 0.7550**

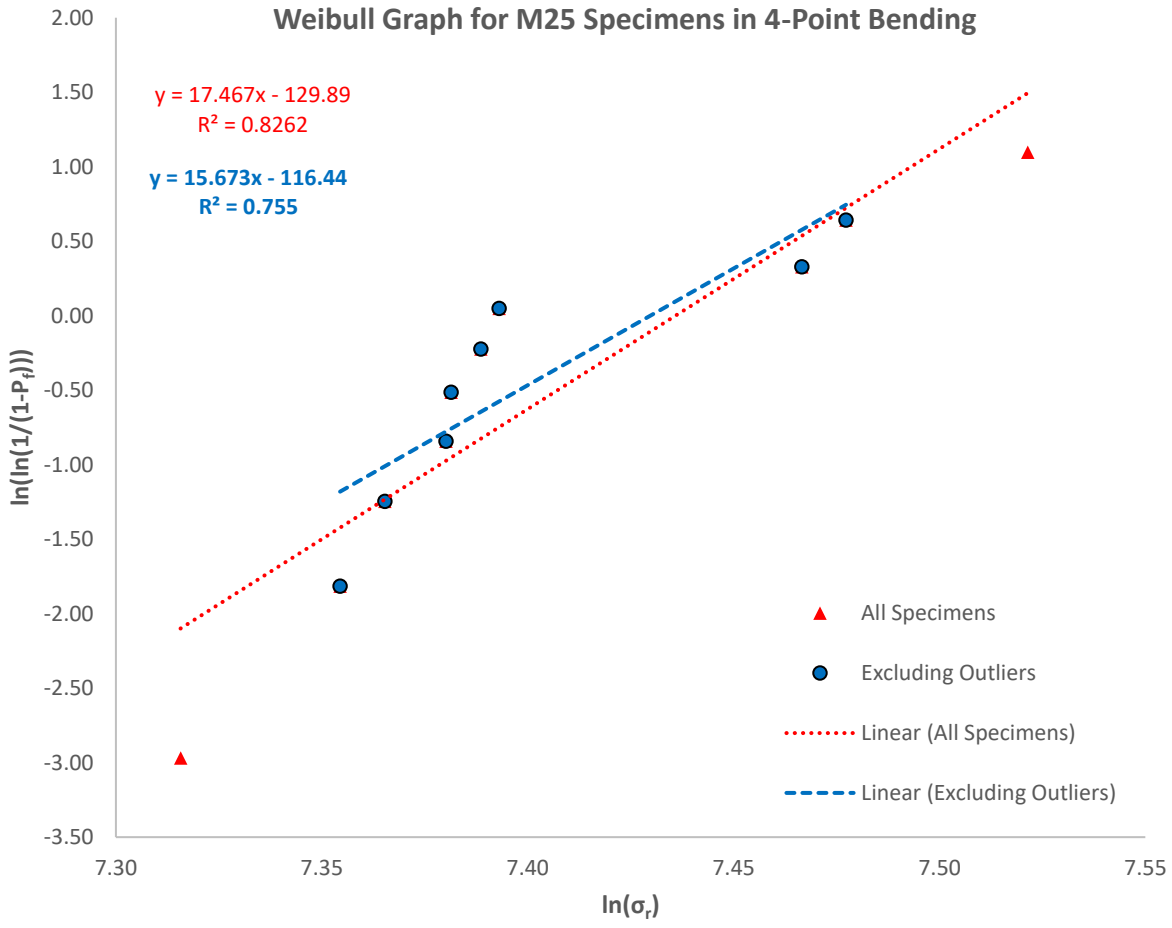

Figure D2.11: Weibull Strength Distribution Graph for M25 Specimens in 4-Point Bending

Table D2.12: Data for Weibull Strength Distribution Graph for M32 Data in 4-Point Bending

Rank, i	Test No.	Specimen No.	Rupture Modulus, σ_r (MPa)	$P_f = \frac{(i-0.5)}{n}$	$x = \ln(\sigma_r)$	$y = \ln\left(ln\left(\frac{1}{1-P_f}\right)\right)$
1	103	M32-19	882.99	0.05	6.78	-2.97
2	111	M32-6	1484.88	0.15	7.30	-1.82
3	109	M32-17	1545.45	0.25	7.34	-1.25
4	107	M32-18	1562.64	0.35	7.35	-0.84
5	104	M32-7	1572.03	0.45	7.36	-0.51
6	110	M32-14	1573.17	0.55	7.36	-0.23
7	108	M32-13	1578.70	0.65	7.36	0.05
8	106	M32-10	1629.02	0.75	7.40	0.33
9	105	M32-2	1676.68	0.85	7.42	0.64
10	112	M32-1	1718.47	0.95	7.45	1.10
Trendline for All Specimens			m = 5.30		b = -39.30	R^2 = 0.6879
Trendline for All Specimens			m = 20.16		b = -148.12	R^2 = 0.9150
Trendline with No Outliers			**m = 21.72**		**b = -160.35**	**R^2 = 0.8875**

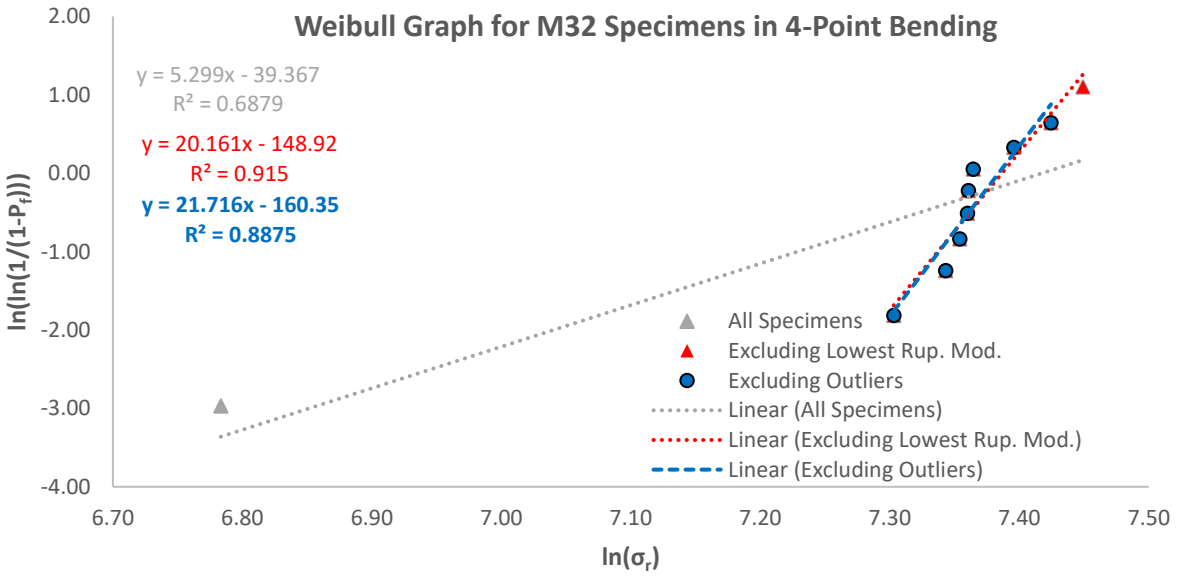

Figure D2.12: Weibull Strength Distribution Graph for M32 Specimens in 4-Point Bending

Note that the Weibull graph and data for the M32 specimen in 4-point bending, points correspond to using all specimens in the Weibull (grey triangle data points) , whereas the red triangular data correspond to using all the specimens except the first data point (which is the specimen with the lowest rupture modulus). The reason for distinguishing between the two data sets are to show that the first data point heavily skews the results from the Weibull graph for the for the gray square data points. Therefore, the red triangular data points are treated as the primary data set, similar to the rest of the graphs, even though it does not contain all data points.

Appendix E – Tensile Specimen Parameters

E.1 M8 Specimens

GFRP Parameter & Info		M8 Tensile Specimens					Using All Specimens			Excluding Outliers		
							Avg.	Std. Dev.	C.O.V.	Avg.	Std. Dev.	C.O.V.
GFRP Admin Info	Specimen Number	M8-T1	M8-T2	M8-T3	M8-T4	M8-T5						
	Test Number	10	11	12	13	14						
	Date of Test	January 13, 2021										
	Batch number & Date	Batch info unavailable										
	Additional Notes											
Specimen Dimensions	Outer Diameter (mm)	8.00	8.00	8.00	8.00	8.00	8.00	0.00	0.00	8.00	0.00	0.00
	Area (mm2)	50.27	50.27	50.27	50.27	50.27	50.27	0.00	0.00	50.27	0.00	0.00
	Free Length (mm)	314.00	314.00	313.00	314.00	316.00	314.20	1.10	0.00	314.00	0.00	0.00
	Gage Length (mm)	165.74	170.27	165.52	166.51	164.46	166.50	2.23	0.01	167.51	2.42	0.01
DOM Tube Dimensions	Outer Diameter (in)	1.375										
	Wall Thickness (in)	0.25										
	Length (mm)	500.00										
	Thread Specification	1 5/16 - 12 (thread full length)										
Used MTS V-Grips Info	Assembly Number	47-641-604										
	Allowable Clamping Size (mm)	33.0 - 42.4										
Test Data	Max Loading (kN)	69.35	66.06	70.50	67.31	55.94	65.83	5.79	0.09	67.57	1.66	0.02
Calculations	Ultimate Stress (MPa)	1379.71	1314.26	1402.47	1339.07	1112.81	1309.67	115.28	0.09	1344.35	33.04	0.02
	Elastic Modulus (MPa)	79296.01	82970.62	78883.17	80356.07	77980.09	79897.19	1918.43	0.02	80874.23	1891.31	0.02

*Orange text denotes outliers

E.2 M13 Specimens

GFRP Parameter & Info		M13 Tensile Specimens					Using All Specimens			Excluding Outliers		
GFRP Admin Info	Specimen Number	M13-T4	M13-T5	M13-T2	M13-T3	M13-T1	Avg.	Std. Dev.	C.O.V.	Avg.	Std. Dev.	C.O.V.
	Test Number	1	2	3	-	4						
	Date of Test	January 12, 2021				January 13, 2021						
	Batch number & Date	# 8033245 Date: Feb. 9, 2016	# 8033215 Date: Feb. 3, 2016	Batch info unavailable								
	Additional Notes				Not tested due to machine error	Extensometer data was not recorded						
Specimen Dimensions	Outer Diameter (mm)	13.00	13.00	13.00	13.00	13.00	13.00	0.00	0.00	13.00	0.00	0.00
	Area (mm2)	132.73	132.73	132.73	132.73	132.73	132.73	0.00	0.00	132.73	0.00	0.00
	Free Length (mm)	523.00	518.00	518.00	517.00	513.00	517.80	3.56	0.01	516.33	2.89	0.01
	Gage Length (mm)	166.01	165.33	165.33	-	166.23	165.72	0.46	0.00	165.63	0.52	0.00
DOM Tube Dimensions	Outer Diameter (in)	1.625										
	Wall Thickness (in)	0.25										
	Length (mm)	500.00										
	Thread Specification	M30 x 3.5 (thread full length)										
Used MTS V-Grips Info	Assembly Number	47-641-605										
	Allowable Clamping Size (mm)	41.9 - 51.3										
Test Data	Max Loading (kN)	158.83	159.92	165.88	N/A	164.47	162.27	3.43	0.02	163.42	3.11	0.02
Calculations	Ultimate Stress (MPa)	1196.60	1204.86	1249.73	N/A	1239.09	1222.57	25.81	0.02	1231.23	23.45	0.02
	Elastic Modulus (MPa)	N/A	76846.72	76377.19	N/A	77319.64	76847.85	471.23	0.01	76847.85	471.23	0.01

*Orange text denotes outliers

E.3 M15 Specimens

GFRP Parameters & Info		M15 Tensile Specimens					Using All Specimens			Excluding Outliers		
GFRP Admin Info	Specimen Number	M15-T4	M15-T2	M15-T5	M15-T1	M15-T3	Avg.	Std. Dev.	C.O.V.	Avg.	Std. Dev.	C.O.V.
	Test Number	5	6	7	8	9						
	Date of Test	January 13, 2021	January 13, 2021	January 13, 2021	January 13, 2021	January 13, 2021						
	Batch number & Date	# 8051973	# 8051973	Batch info	Batch info	# 8051973						
	Additional Notes											
Specimen Dimensions	Outer Diameter (mm)	16.00	16.00	16.00	16.00	16.00	16.00	0.00	0.00	16.00	0.00	0.00
	Area (mm2)	201.06	201.06	201.06	201.06	201.06	201.06	0.00	0.00	201.06	0.00	0.00
	Free Length (mm)	637.00	640.00	652.00	639.00	640.00	641.60	5.94	0.01	638.67	1.53	0.00
	Gage Length (mm)	166.02	165.89	165.28	166.40	165.92	165.90	0.41	0.00	166.11	0.25	0.00
DOM Tube Dimensions	Outer Diameter (in)	1.625										
	Wall Thickness (in)	0.25										
	Length (mm)	500.00										
	Thread Specification	M30 x 3.5 (thread full length)										
Used MTS V-Grips Info	Assembly Number	47-641-605										
	Allowable Clamping Size (mm)	41.9 - 51.3										
Test Data	Max Loading (kN)	246.82	233.90	272.15	238.09	244.39	247.07	14.92	0.06	243.10	4.50	0.02
Calculations	Ultimate Stress (MPa)	1227.57	1163.32	1353.54	1184.18	1215.48	1228.82	74.19	0.06	1209.08	22.39	0.02
	Elastic Modulus (MPa)	74988.65	76614.48	74694.94	75446.29	74470.74	75243.02	849.08	0.01	74968.56	488.08	0.01

*Orange text denotes outliers

Appendix F – Tensile Testing Graphs

This appendix includes the load-displacement and stress-strain plots derived from the direct tensile testing data. Since the extensometer (device used to track the GFRP displacement) was removed at approximately 60% to 75% of the predicted ultimate load capacity of the specimen, load-displacement plots based on the crosshead displacement data have been provided for reference for specimen behaviour during the full duration of testing. Despite this, the crosshead displacement is not used in further calculations since it does not accurately represent the displacement of the GFRP specimen. These plots are organized by the sequence of their testing number order, not their specimen number.

F1.0 M8 Specimens

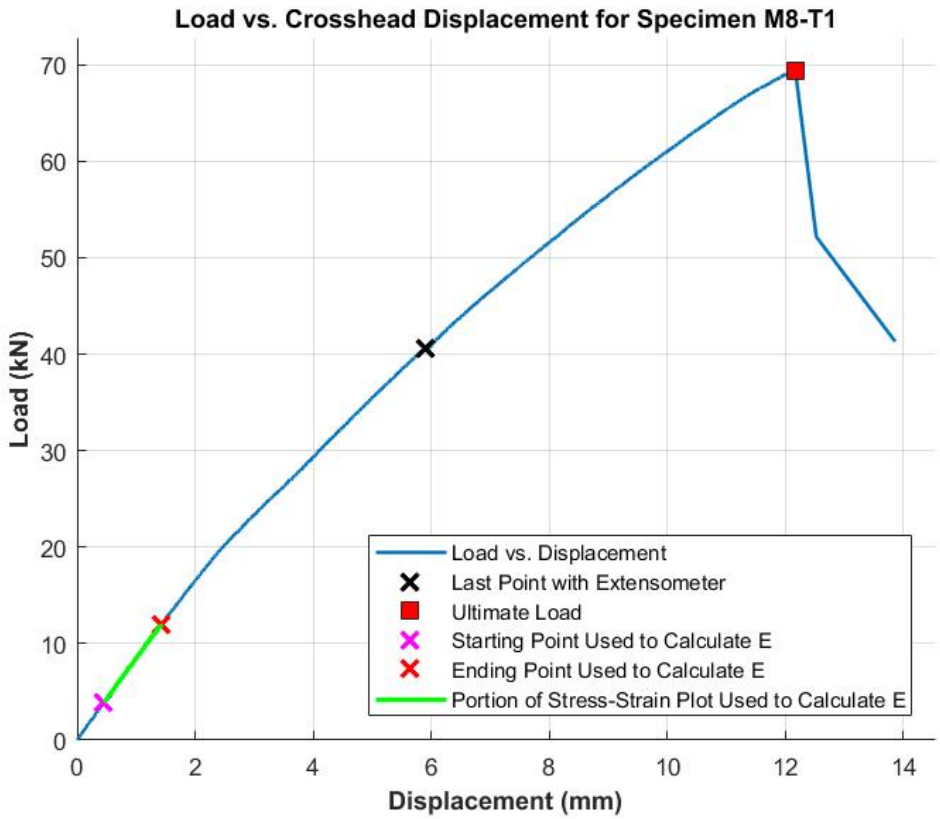

Figure F1.1: Load-displacement of Crosshead for Specimen M8-T1

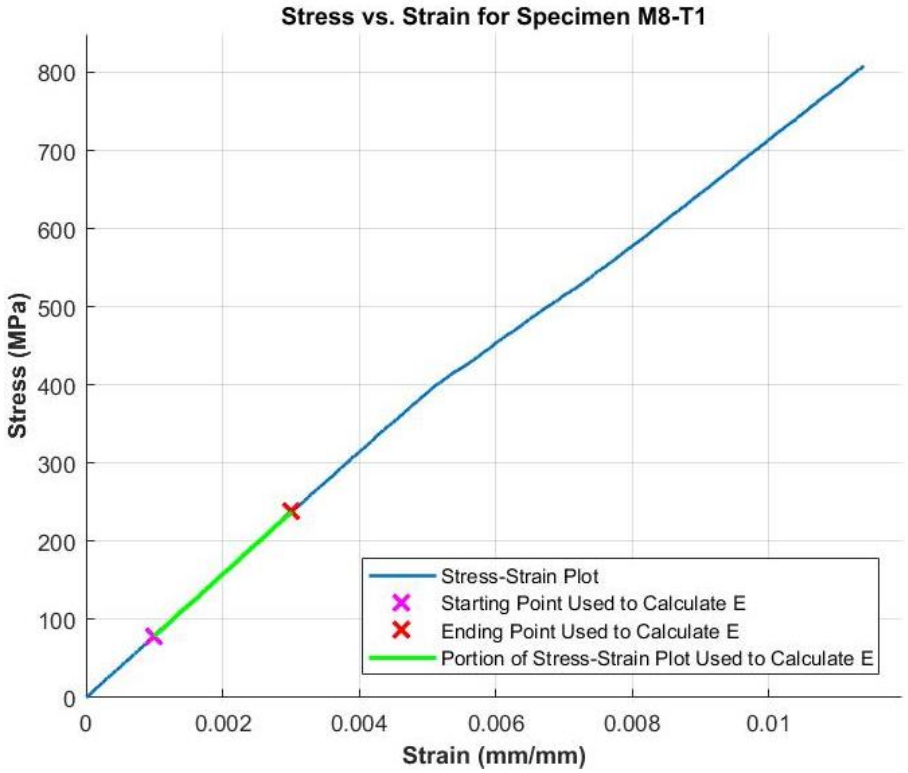

Figure F1.2: Load-displacement of Extensometer plot for Specimen M8-T1

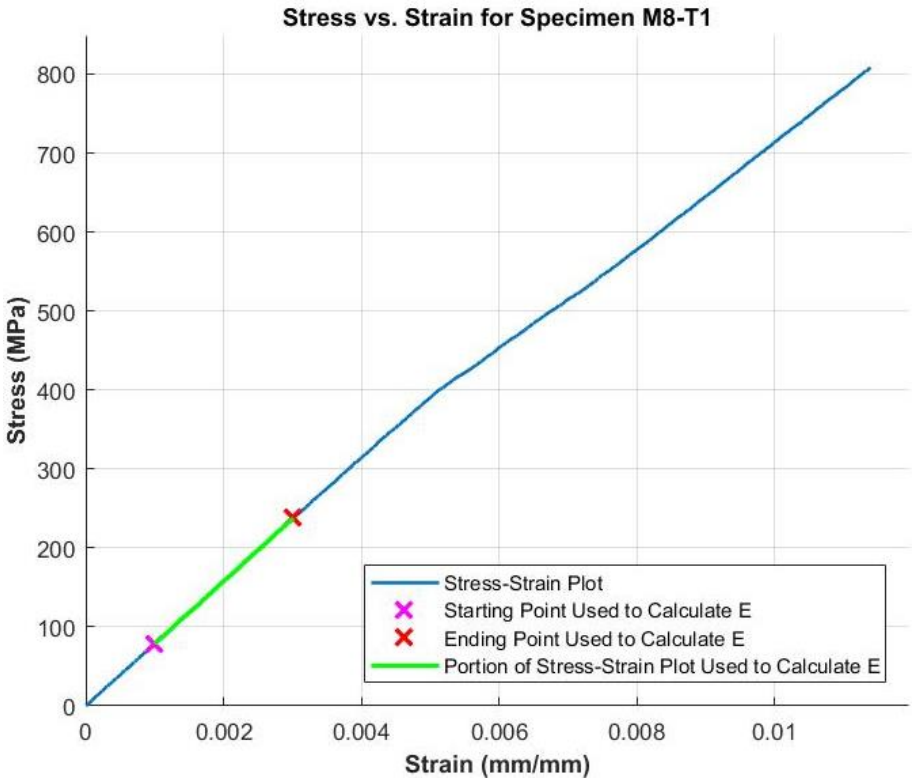

Figure F1.3: Stress-strain of Specimen M8-T1

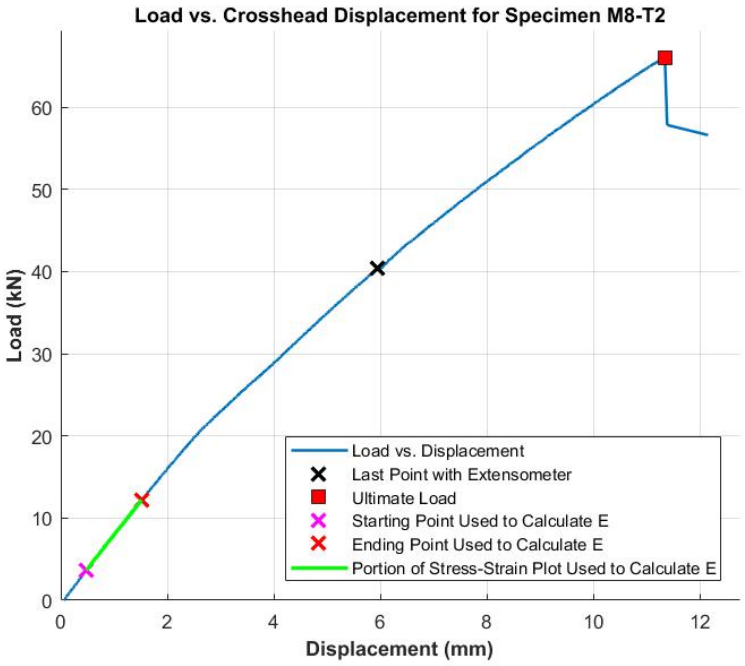

Figure F1.4: Load-displacement of Crosshead for Specimen M8-T2

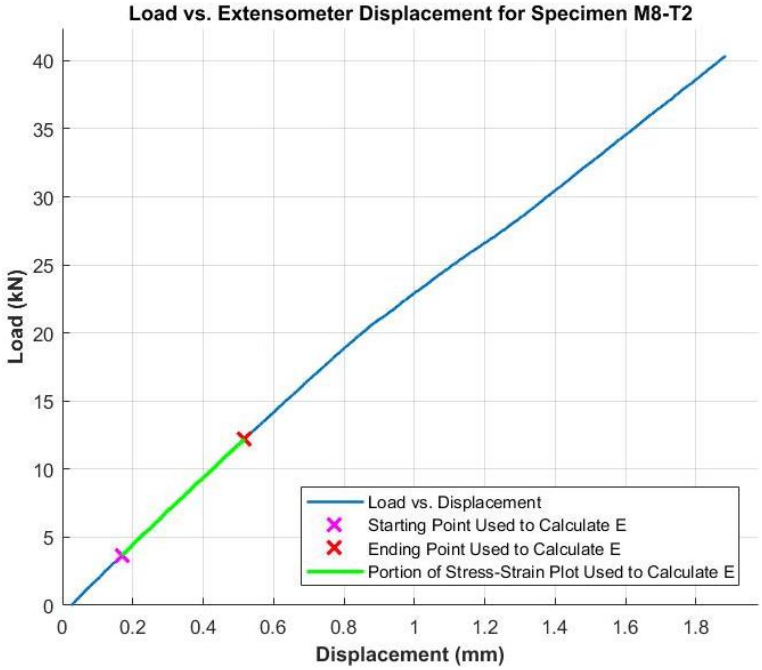

Figure F1.5: Load-displacement plot of Extensometer for Specimen M8-T2

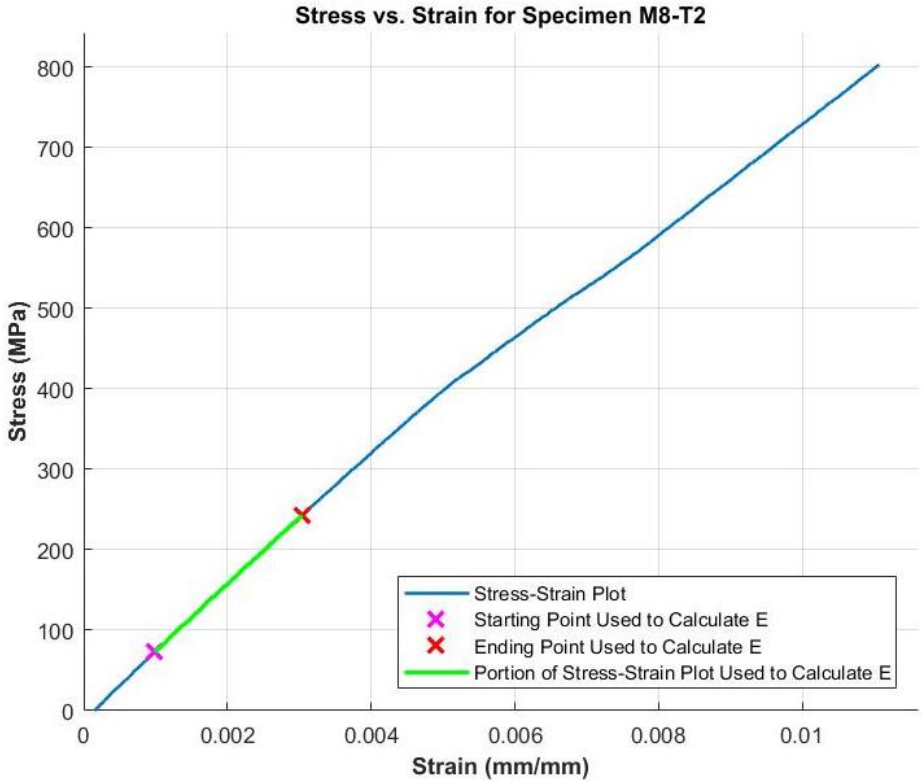

Figure F1.6: Stress-strain of Specimen M8-T2

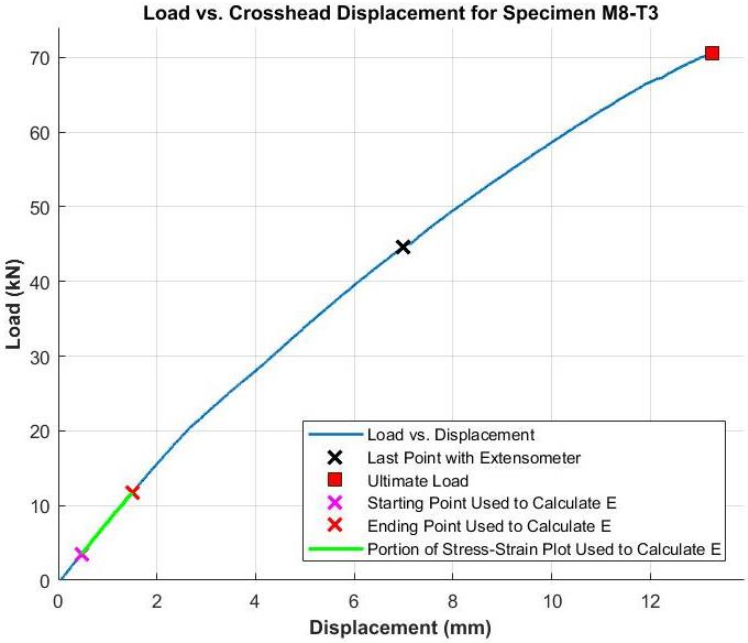

Figure F1.7: Load-displacement of Crosshead for Specimen M8-T3

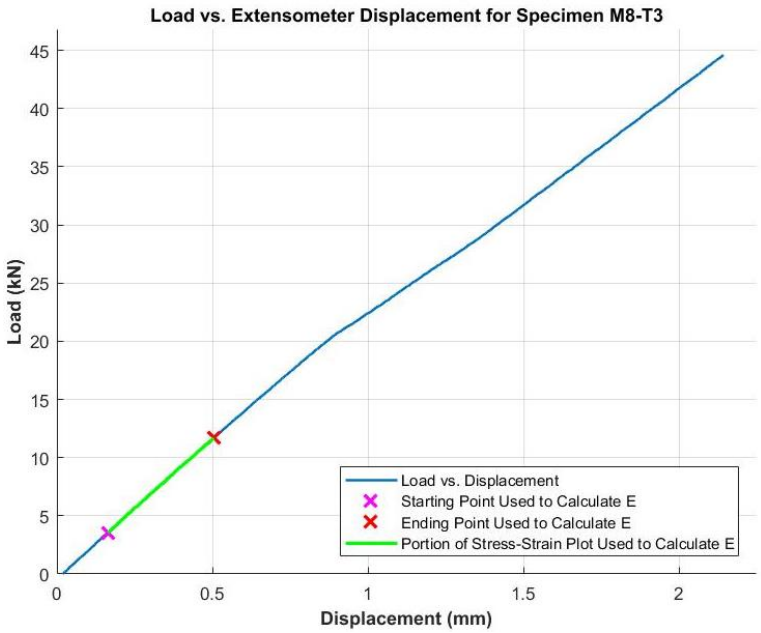

Figure F1.8: Load-displacement plot of Extensometer for Specimen M8-T3

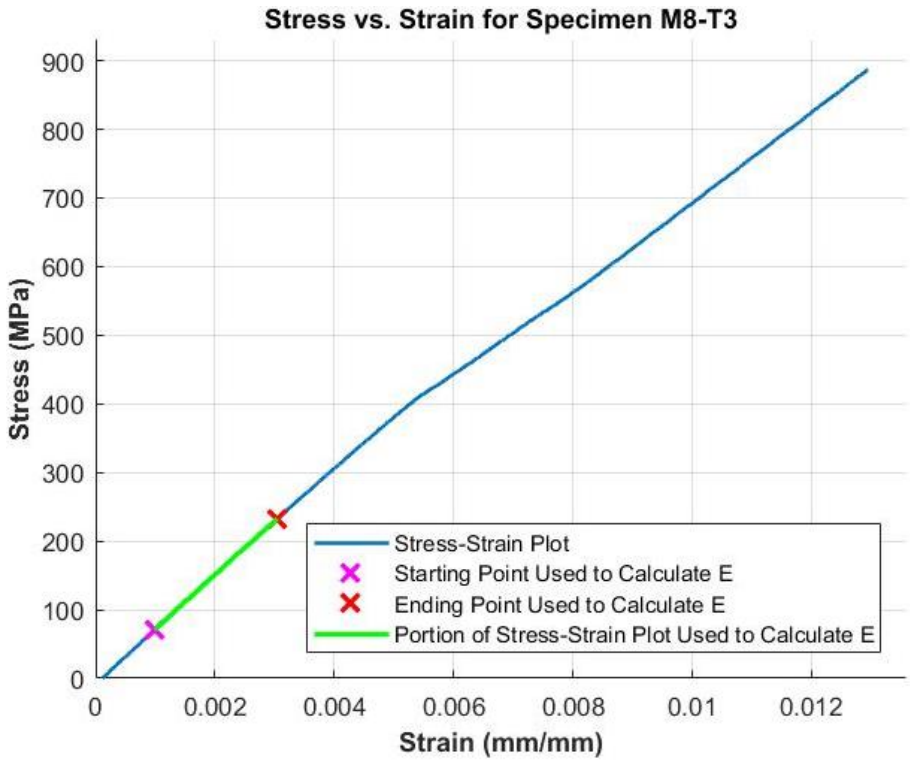

Figure F1.9: Stress-strain of Specimen M8-T3

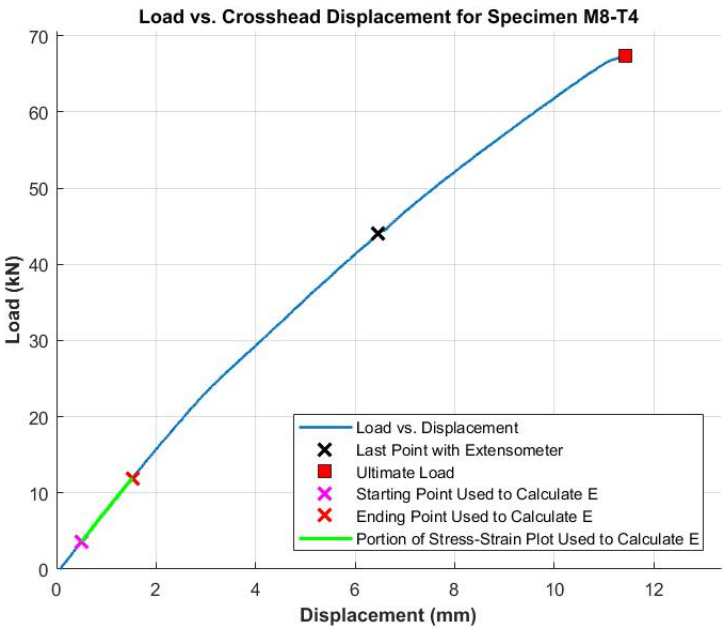

Figure F1.10: Load-displacement of Crosshead for Specimen M8-T4

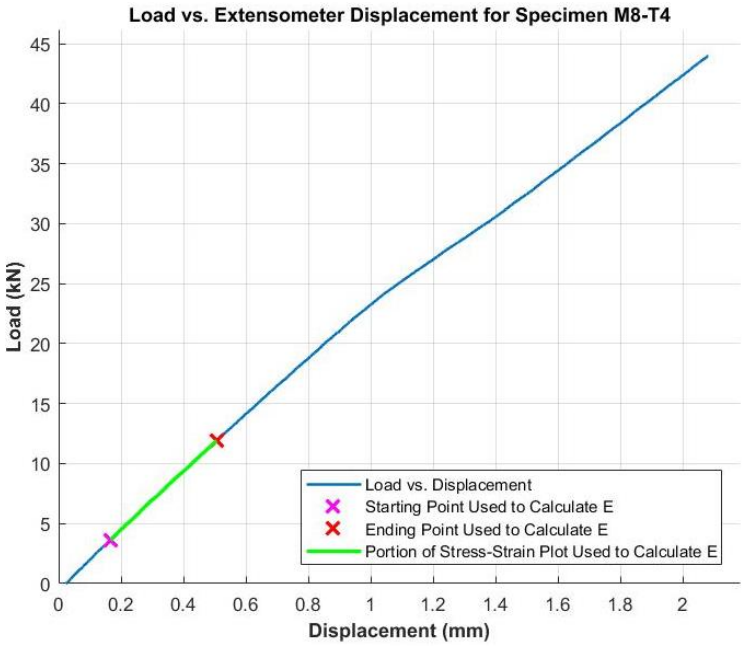

Figure F1.11: Load-displacement plot of Extensometer for Specimen M8-T4

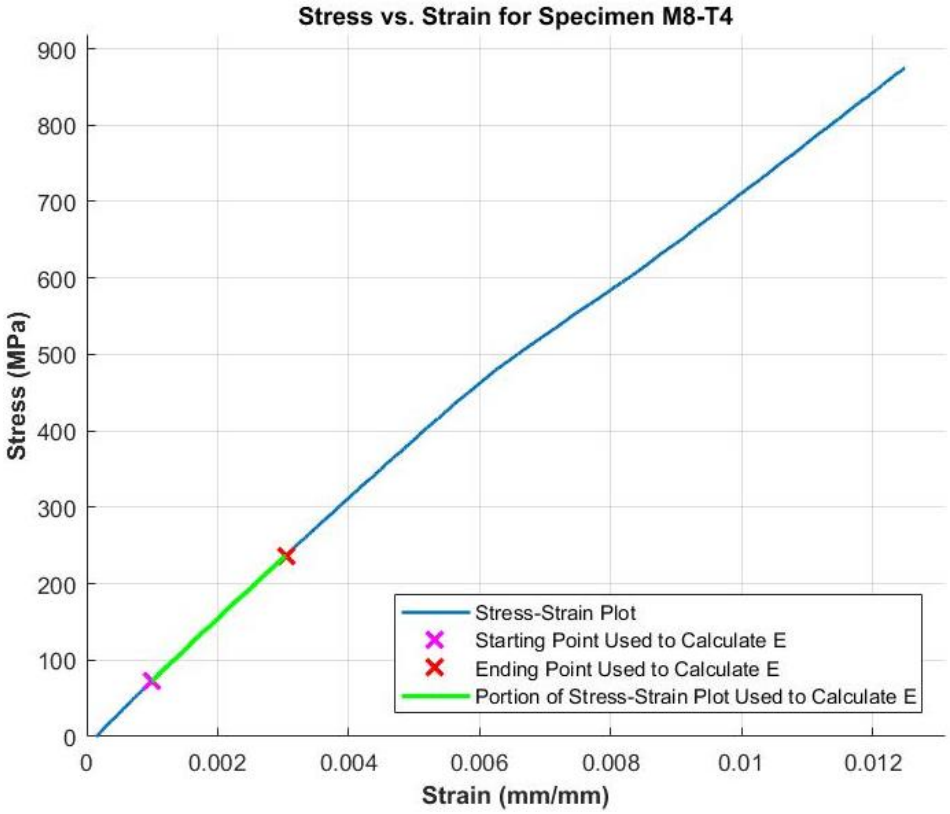

Figure F1.12: Stress-strain of Specimen M8-T4

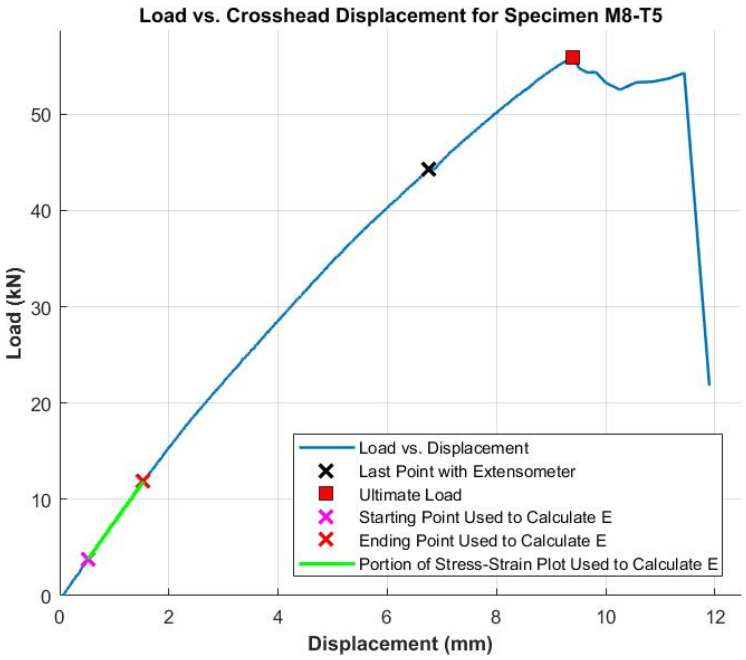

Figure F1.13: Load-displacement of Crosshead for Specimen M8-T5

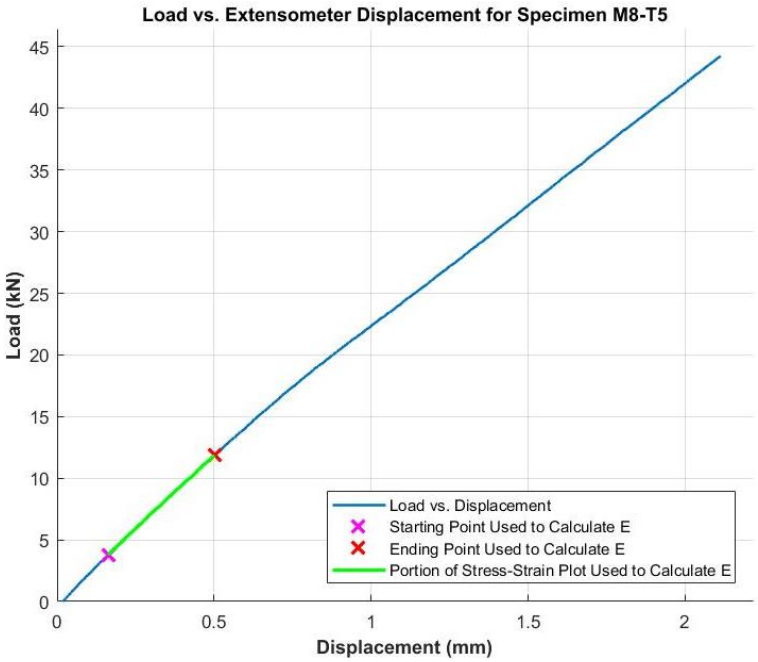

Figure F1.14: Load-displacement plot of Extensometer for Specimen M8-T5

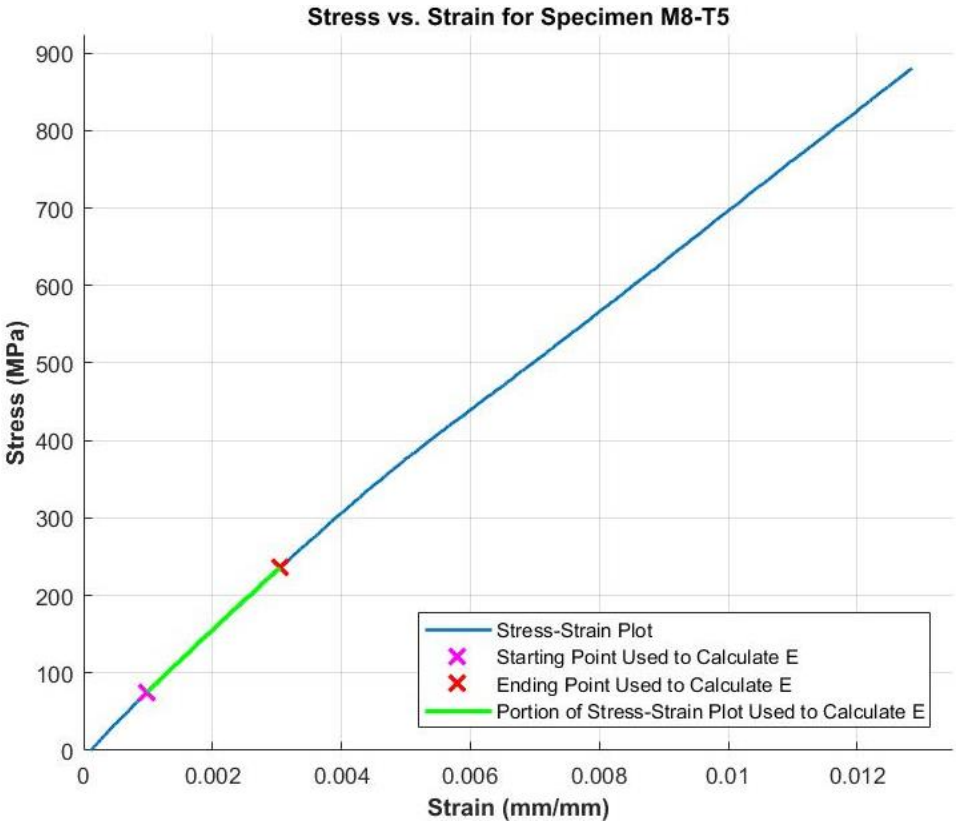

Figure F1.15: Stress-strain of Specimen M8-T5

F2.0 M13 Specimens

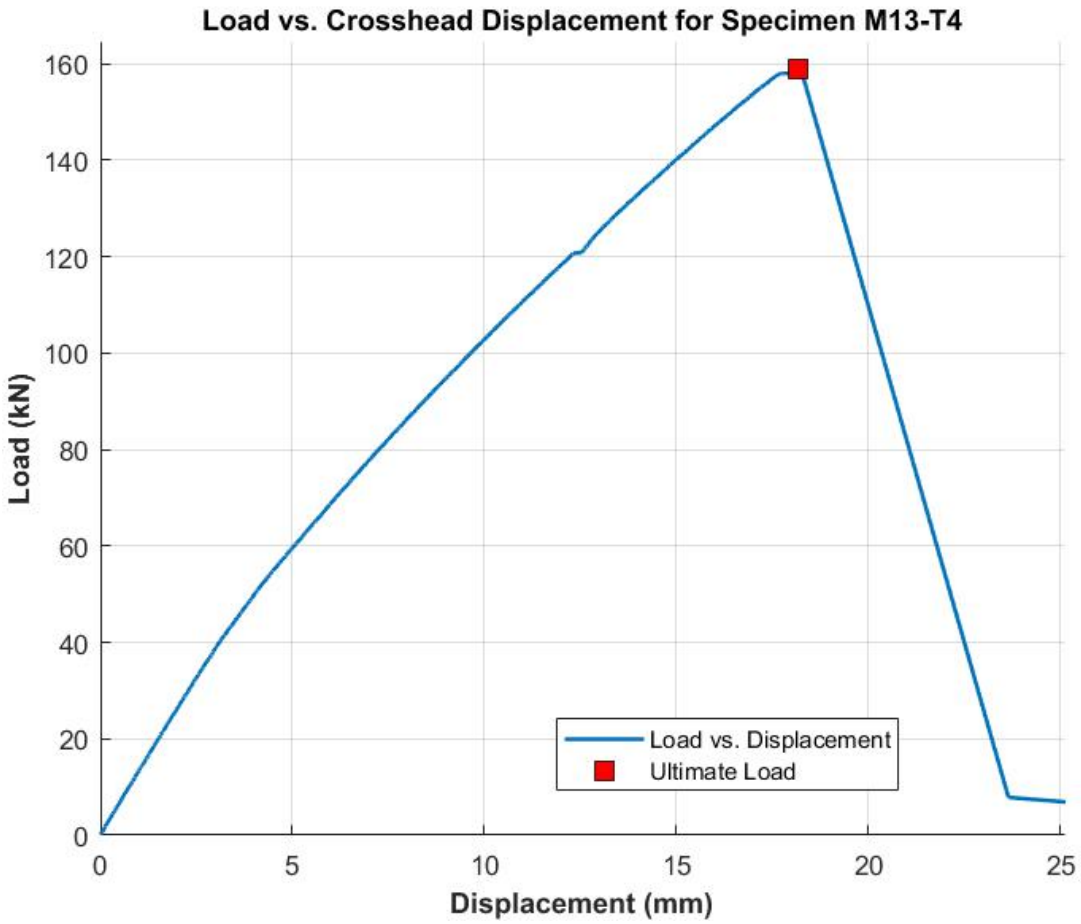

Figure F2.1: Stress-strain of Specimen M13-T4

Due to testing errors, the data from the extensometer for this specimen was not recorded. As a result, the load-displacement plot using extensometer data cannot be produced, along with the associated stress-strain plot.

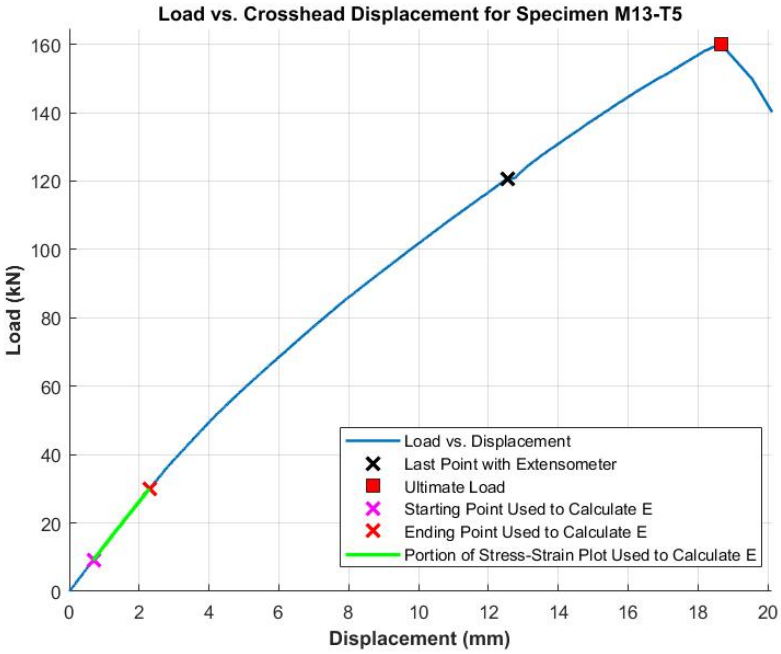

Figure F2.2: Load-displacement of Crosshead for Specimen M13-T5

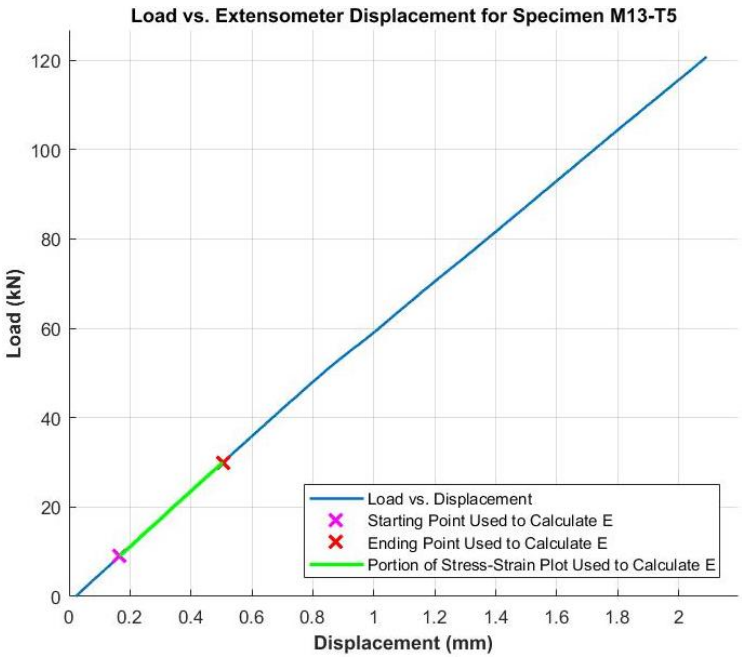

Figure F2.3: Load-displacement plot of Extensometer for Specimen M13-T5

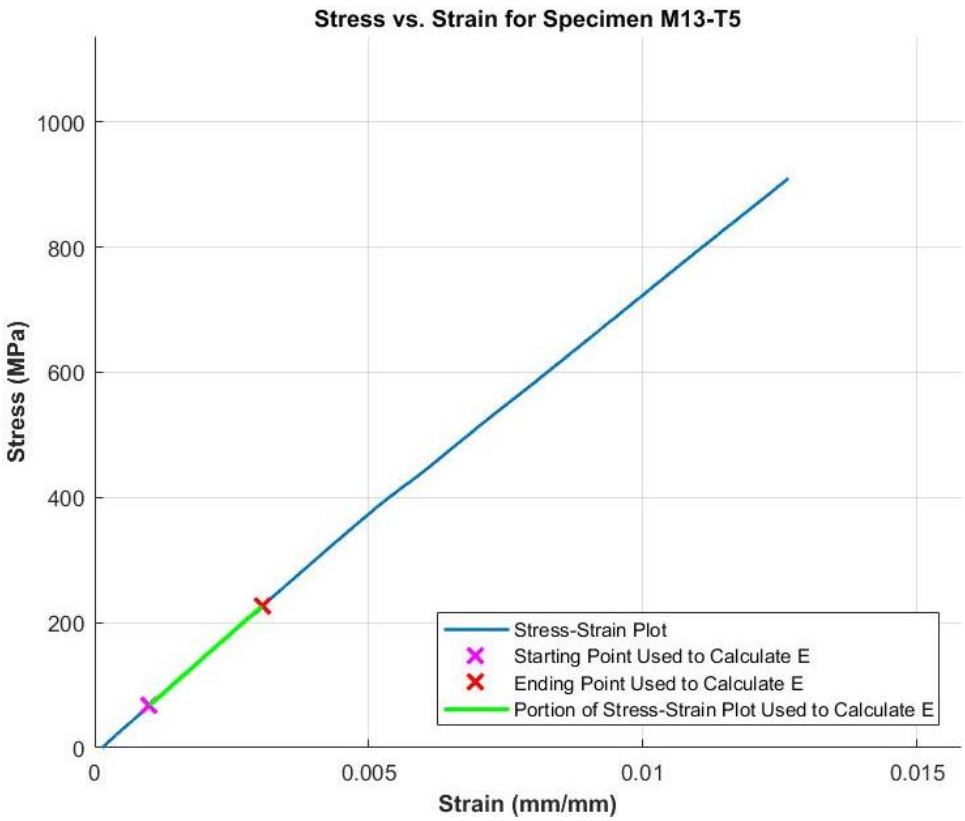

Figure F2.4: Stress-strain of Specimen M13-T5

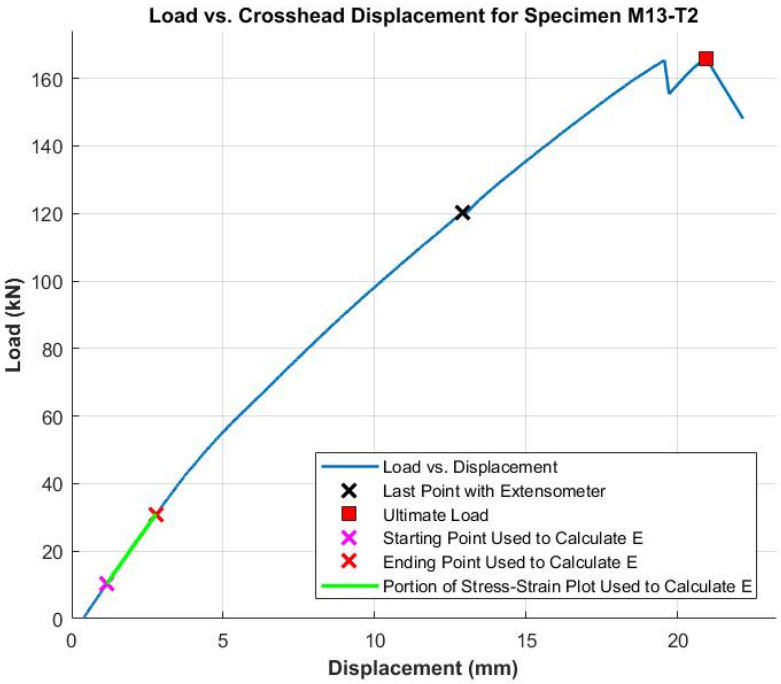

Figure F2.5: Load-displacement of Crosshead for Specimen M13-T2

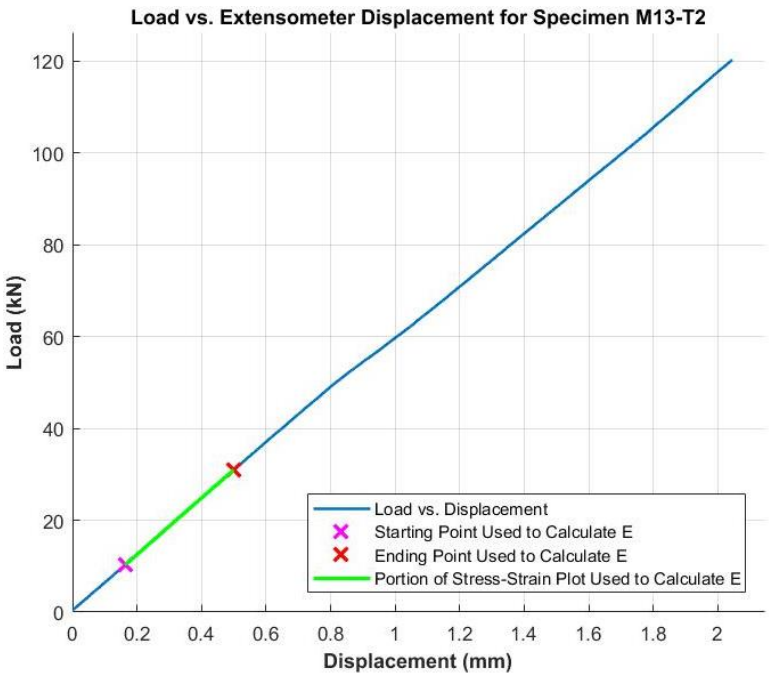

Figure F2.6: Load-displacement plot of Extensometer for Specimen M13-T2

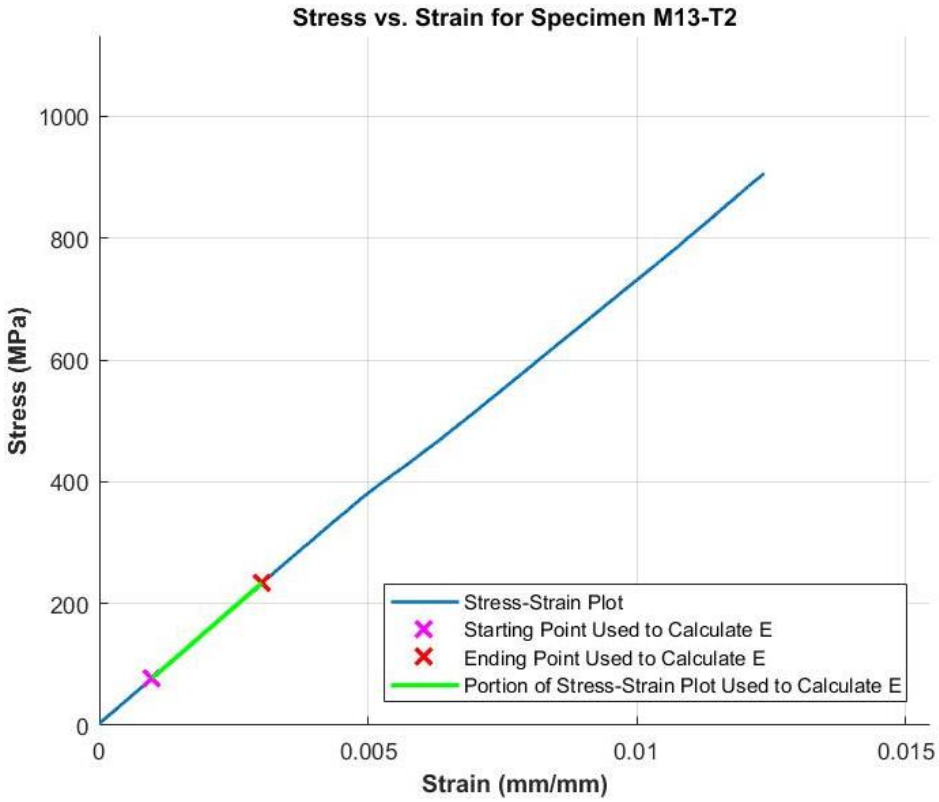

Figure F2.7: Stress-strain of Specimen M13-T2

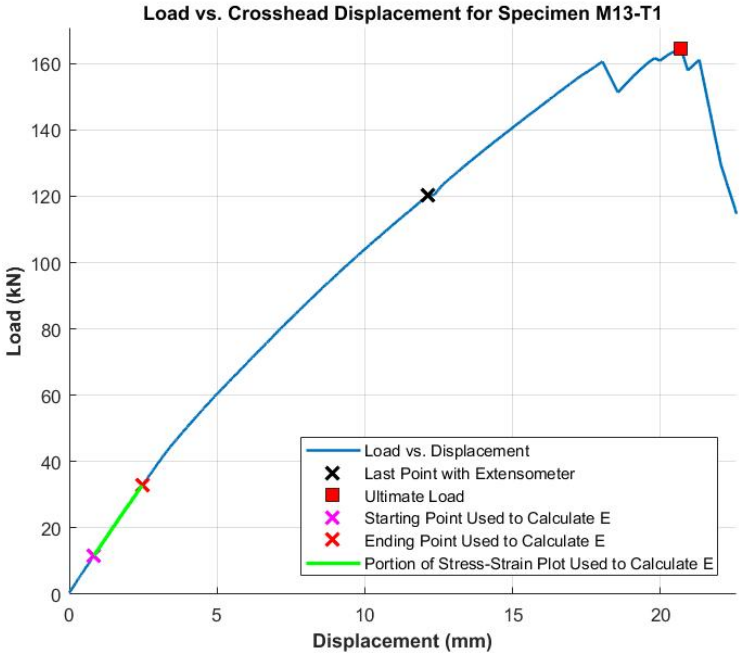

Figure F2.8: Load-displacement of Crosshead for Specimen M13-T1

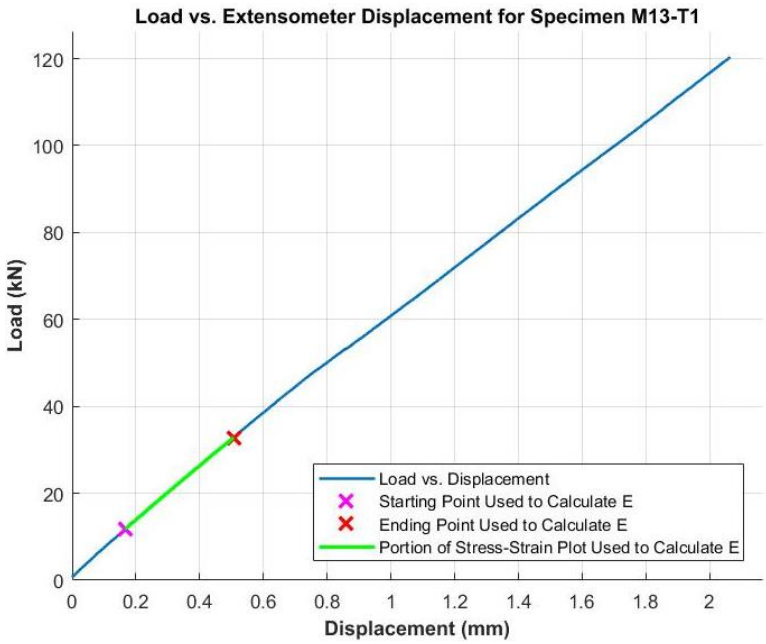

Figure F2.9: Load-displacement plot of Extensometer for Specimen M13-T1

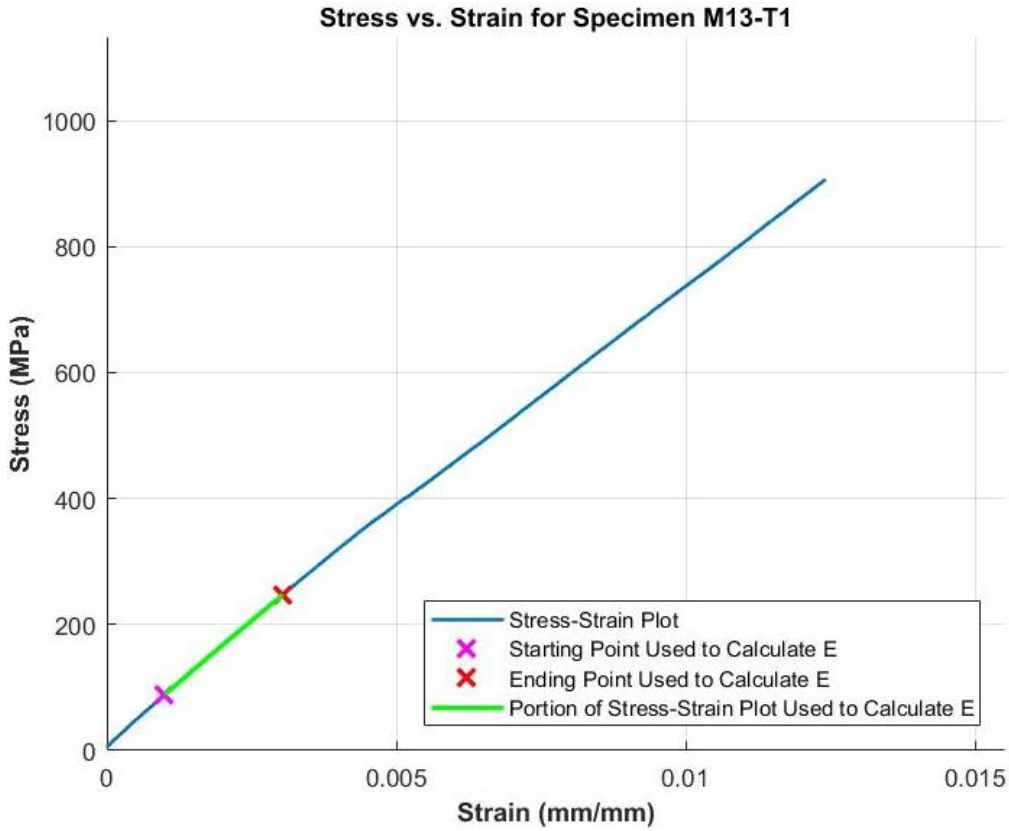

Figure F2.10: Stress-strain of Specimen M13-T1

F3.0 M15 Specimens

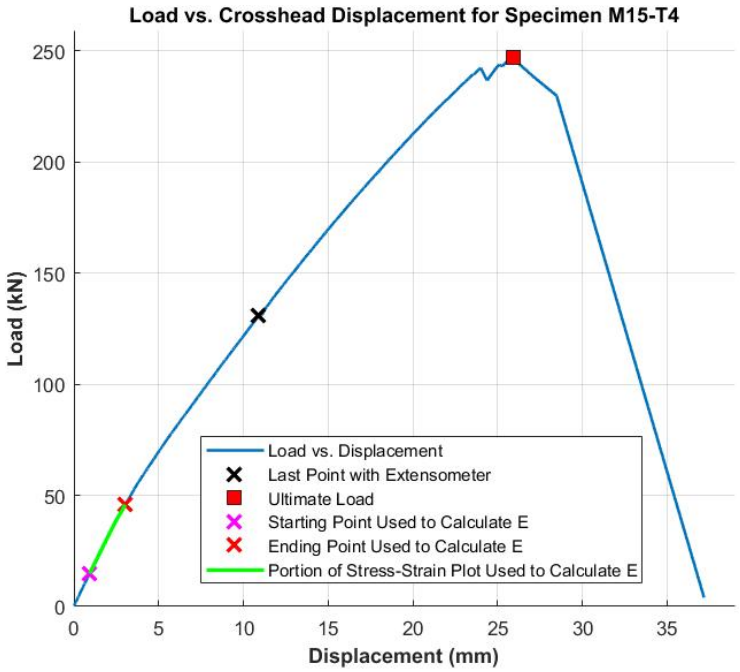

Figure F3.1: Load-displacement of Crosshead for Specimen M15-T4

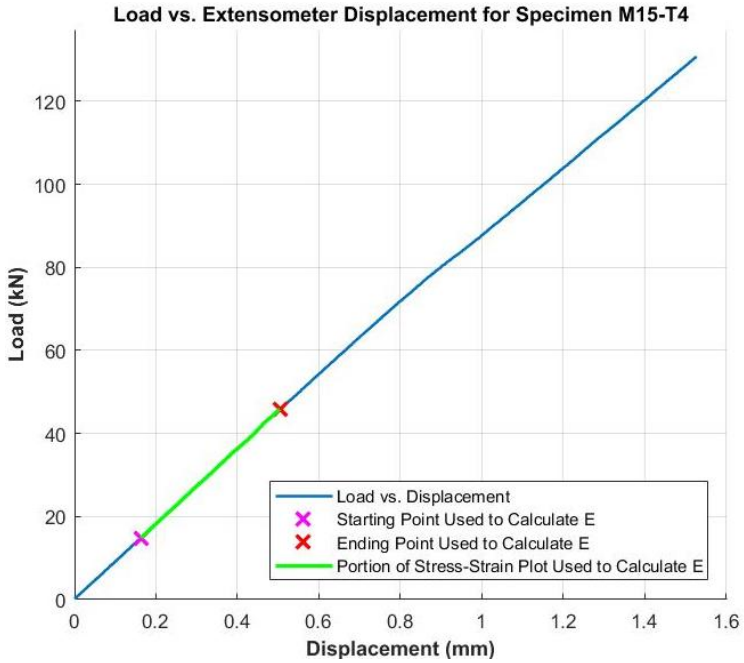

Figure F3.2: Load-displacement plot of Extensometer for Specimen M15-T4

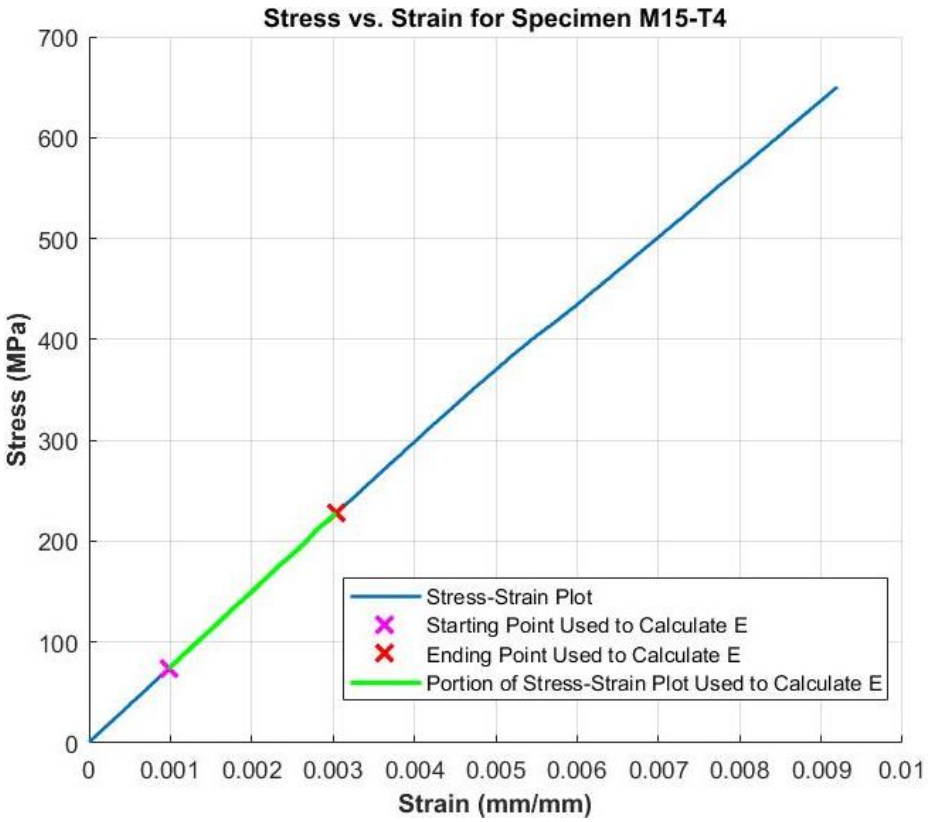

Figure F3.3: Stress-strain of Specimen M15-T4

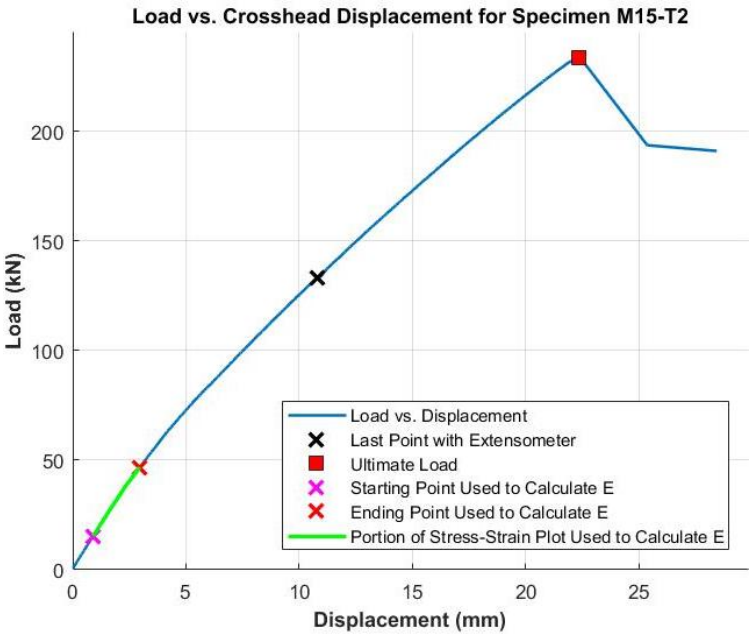

Figure F3.4: Load-displacement of Crosshead for Specimen M15-T2

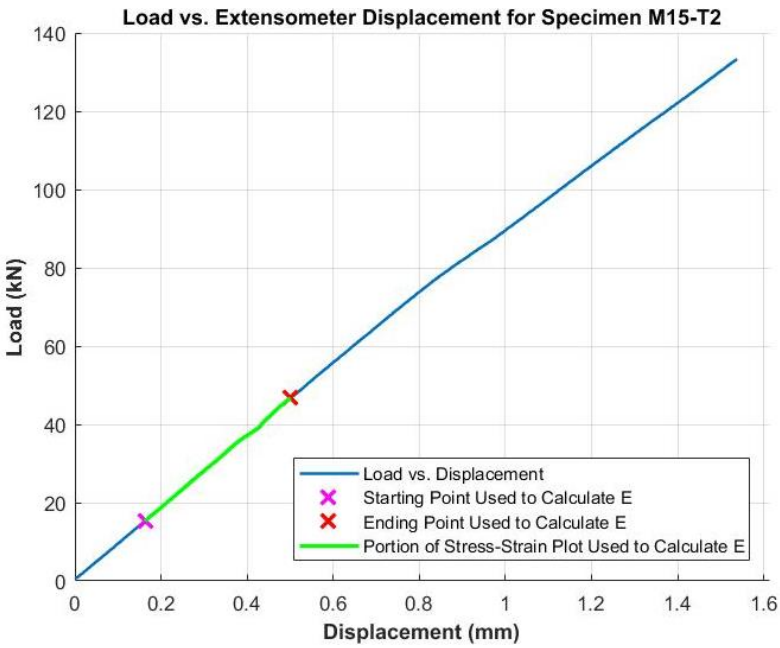

Figure F3.5: Load-displacement plot of Extensometer for Specimen M15-T2

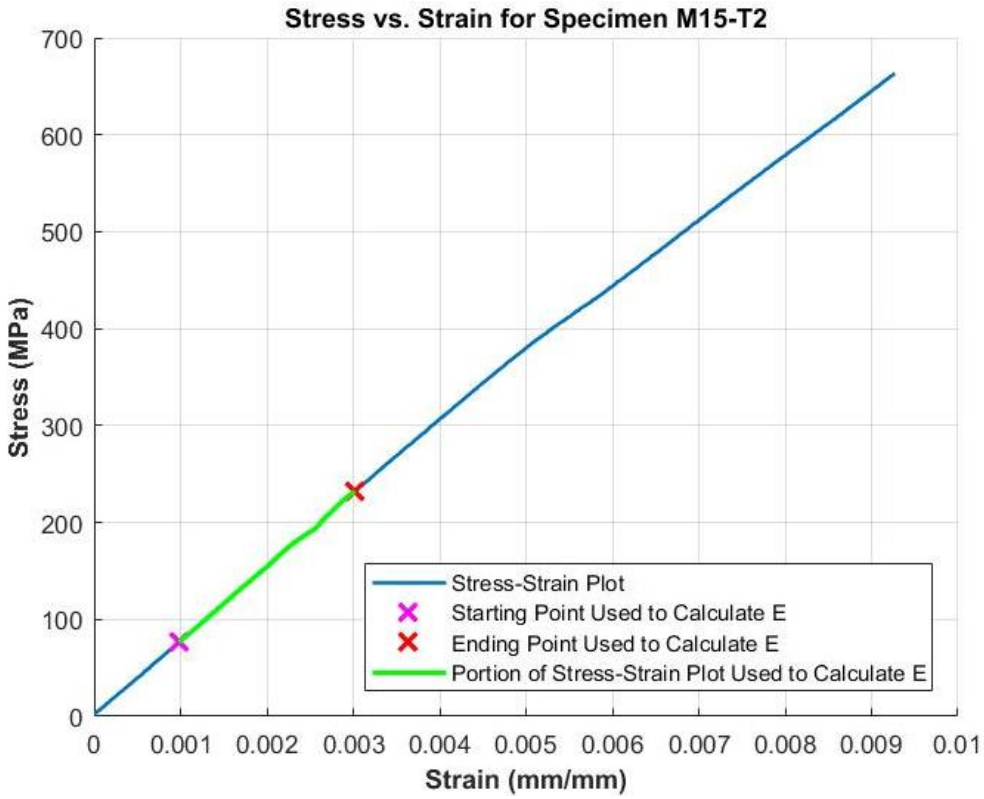

Figure F3.6: Stress-strain of Specimen M15-T2

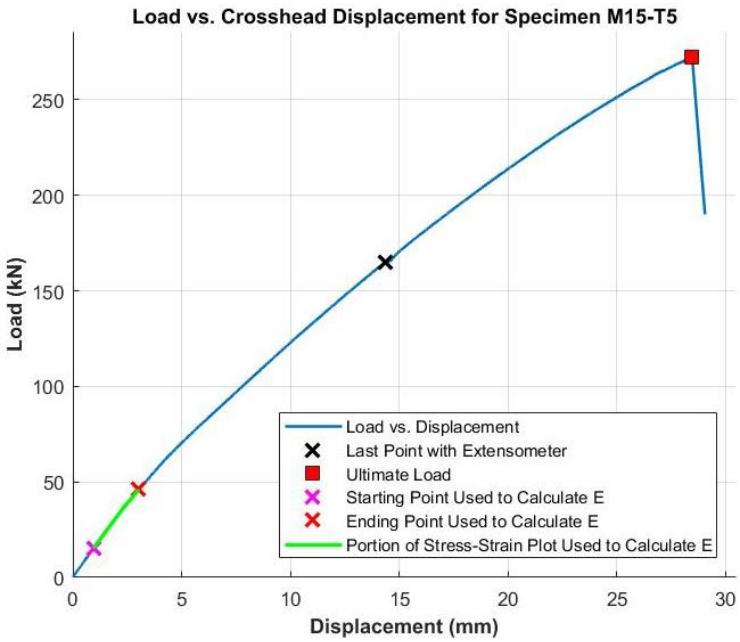

Figure F3.7: Load-displacement of Crosshead for Specimen M15-T5

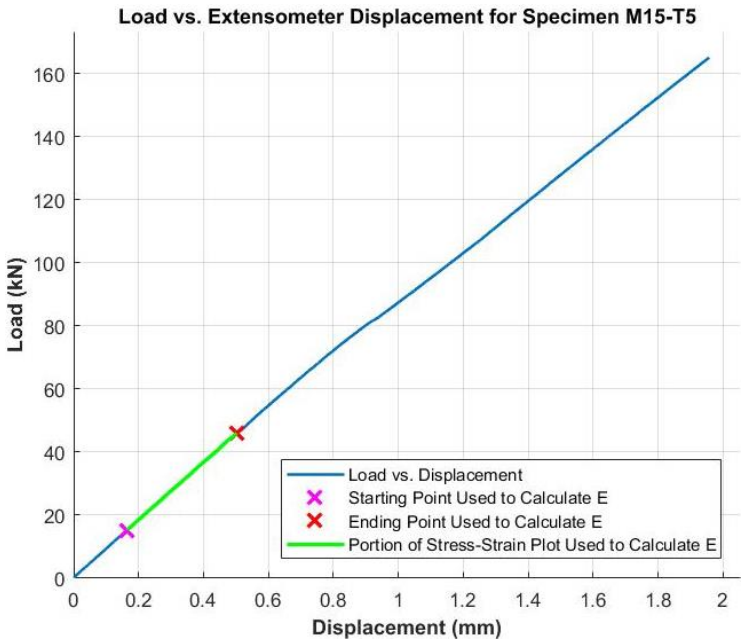

Figure F3.8: Load-displacement plot of Extensometer for Specimen M15-T5

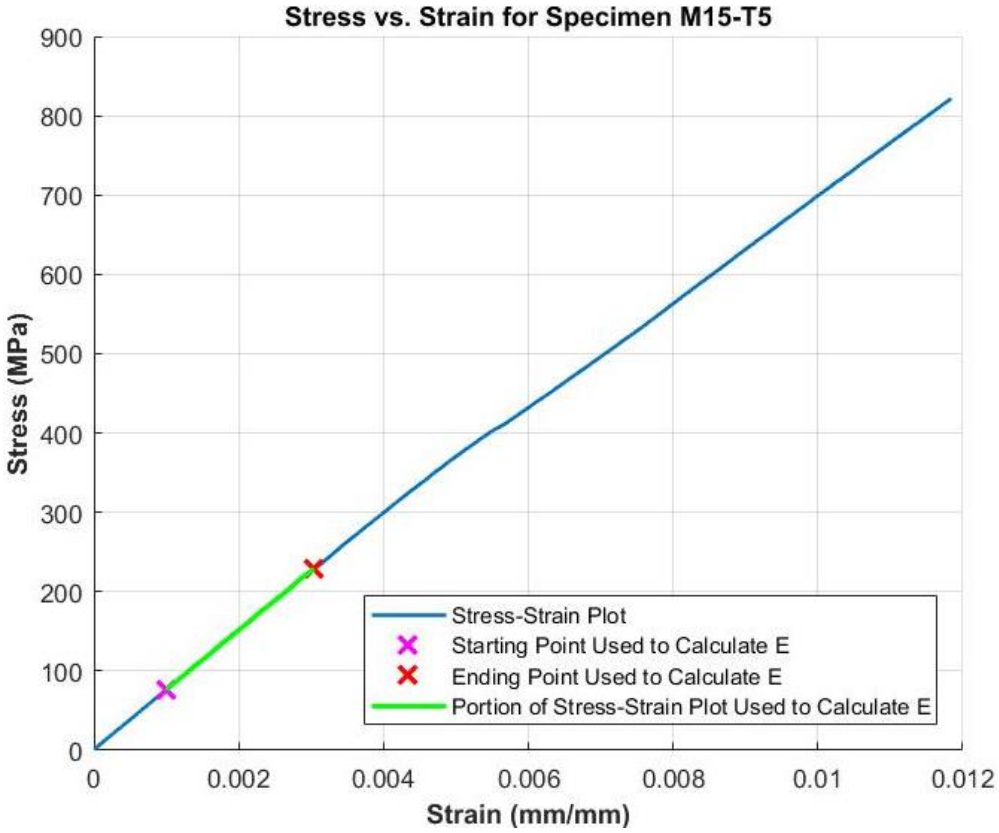

Figure F3.9: Stress-strain of Specimen M15-T5

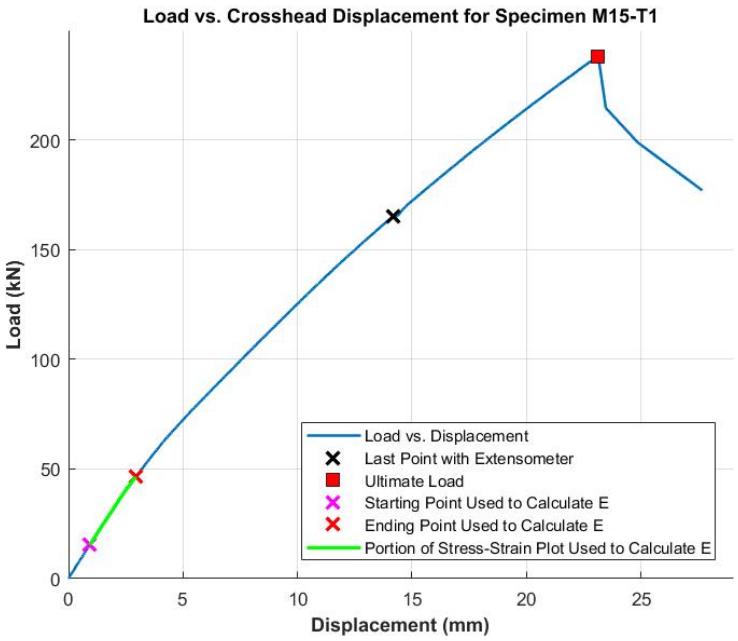

Figure F3.10: Load-displacement of Crosshead for Specimen M15-T1

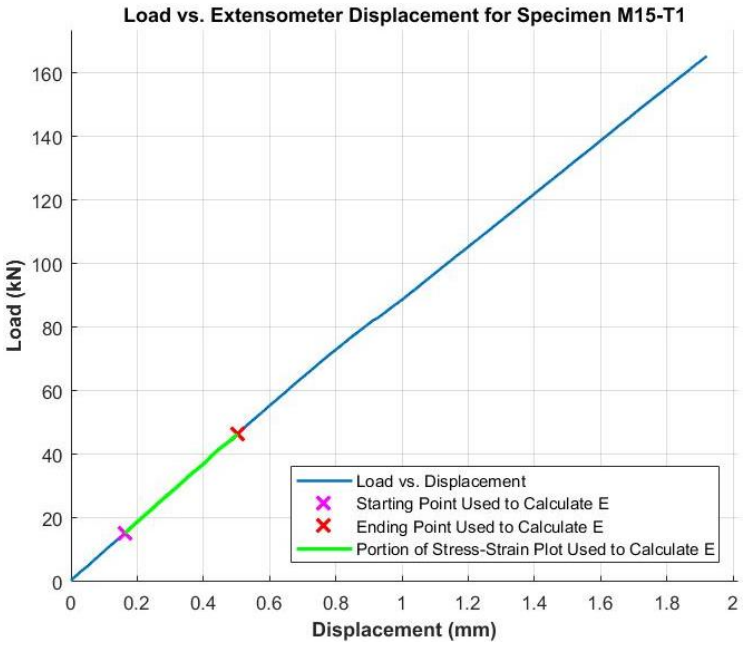

Figure F3.11: Load-displacement plot of Extensometer for Specimen M15-T1

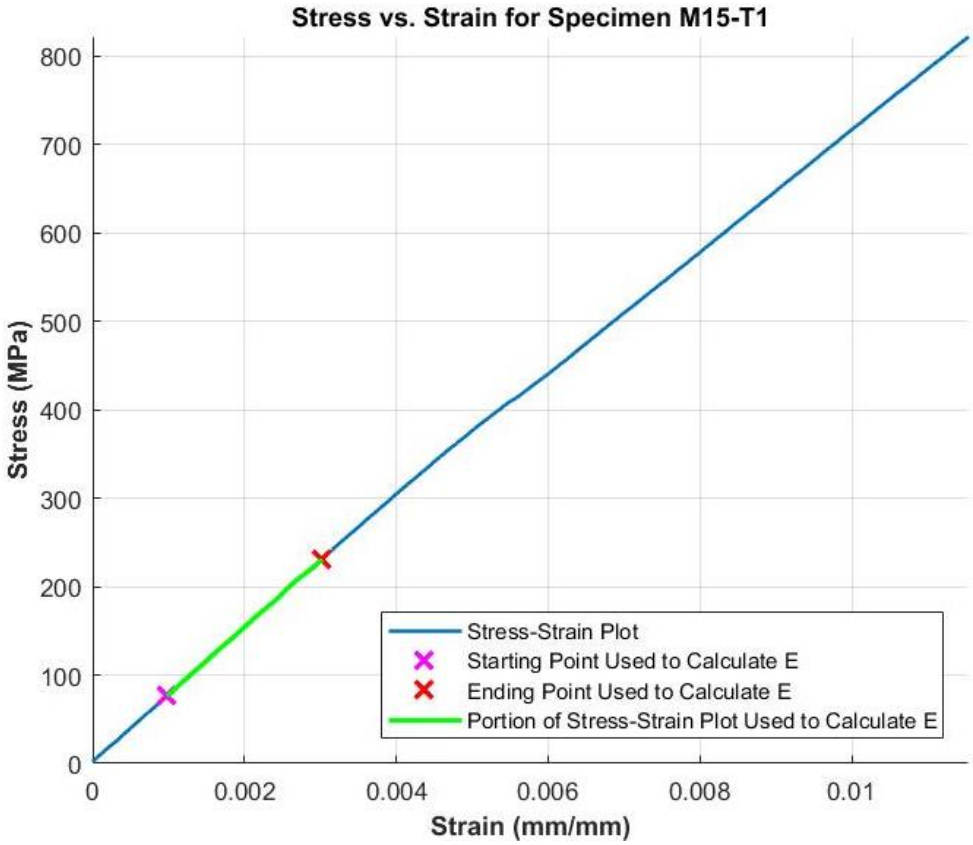

Figure F3.12: Stress-strain of Specimen M15-T1

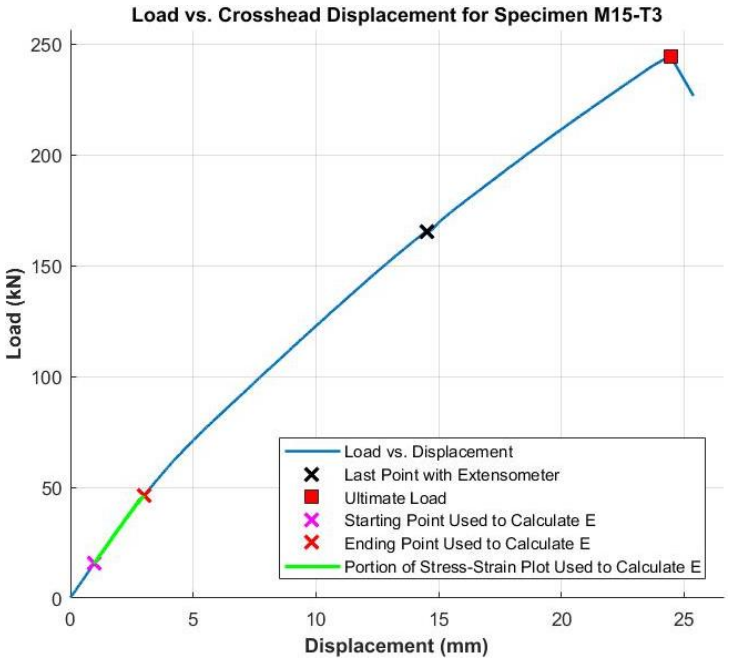

Figure F3.13: Load-displacement of Crosshead for Specimen M15-T3

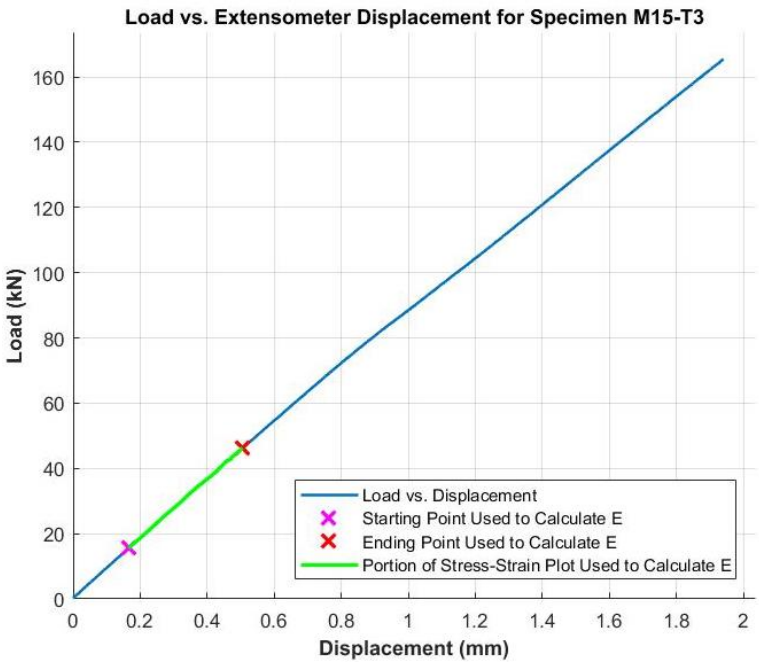

Figure F3.14: Load-displacement plot of Extensometer for Specimen M15-T3

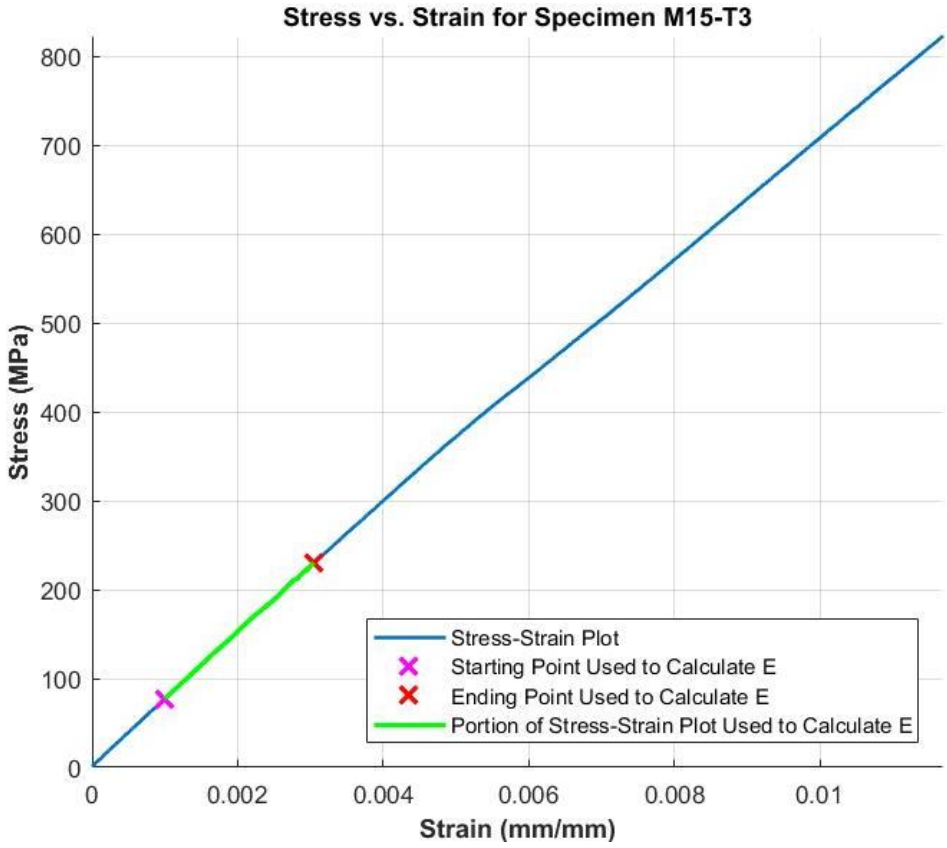

Figure F3.15: Stress-strain of Specimen M15-T3

Appendix G – Derivations

G1.0 Procedure for Calculating the Rupture Modulus

Since the analysis used in this research work considers GFRP to exhibit a bi-moduli behaviour, typical equations used in solid mechanics for beams will need to be modified accordingly. The equations outlined in section G1.0 represented the equations used in calculations from sections 5.1 to 5.2 in the main body of the thesis.

G1.1 Modified Stress-Strain Relationship

This directly affects the linear stress-strain relationship of the GFRP, where the material is assumed to be elastic. Using the **linear relationship for the strain distribution** of the GFRP **specimen along the depth of the cross-section**:

$$\frac{\varepsilon_t}{h-c} = \frac{\varepsilon_c}{c} \qquad \textit{Equation G1.1}$$

Where:

- ε_t = tensile strain in outermost fibre at bottom edge of the GFRP
- ε_c = compressive strain in outermost fibre at top edge of the GFRP
- h = height of the GFRP specimen
- c = location of neutral axis of the GFRP (measured from the top edge of the GFRP cross section depth)

Turning this relationship from the strain distribution to represent the **stress distribution** by substituting Hooke's Law for the respective portions of the different stresses in the GFRP cross section:

$$\frac{\sigma_t}{E_t(h-c)} = \frac{\sigma_c}{E_c c} \qquad \textit{Equation G1.2}$$

Where

- σ_t = tensile stress experienced by GFRP subjected to bending
- σ_c =compressive stress experienced by GFRP subjected to bending
- E_t = tensile elastic modulus for GFRP
- E_c = compressive elastic modulus for GFRP

Note that both elastic moduli for the GFRP are represented here by two distinct value

Since the specimen will be subjected to tensile and compressive stresses due to bending, resultant forces. The **equilibrium of the sum of forces** must equal zero, since there is no axial displacement present. As such, the follow equations can be applied:

$$\sum F_i = 0 \qquad \textit{Equation G1.3}$$

$$F_t + F_c = 0 \qquad \textit{Equation G1.4}$$

$$\int_{A_t} \sigma_t \, dA + \int_{A_c} \sigma_c \, dA = 0 \qquad \textit{Equation G1.5}$$

$$\sigma_t A_t + \sigma_c A_c = 0 \qquad \textit{Equation G1.6}$$

Where:

- F_t = resultant tensile force
- F_c = resultant compressive force
- A_t = portion of cross-sectional area under tensile stress
- A_c =portion of cross-sectional area under compressive stress

The next equation that will be utilized will **equilibrium of sum of moments**. The sum of the product of the resultant forces and their represent distance between a targeted point along the depth of the cross section - in this case, the location of the neutral axis at $y = 0$ – will be equal to the bending moment that the specimen is subjected to: calculates this as follows:

$$\sum \mathrm{M} = 0 \qquad \textit{Equation G1.7}$$

$$\mathrm{M_t} + \mathrm{M_c} = \mathrm{M} \qquad \textit{Equation G1.8}$$

$$\int_{\mathrm{A_t}} -\mathrm{y}\sigma_\mathrm{t}\,\mathrm{dA} + \int_{\mathrm{A_c}} -\mathrm{y}\sigma_\mathrm{c}\,\mathrm{dA} = \mathrm{M} \qquad \textit{Equation G1.9}$$

$$\sigma_\mathrm{t}\mathrm{A_t}\mathrm{y}\begin{cases}-(\mathrm{h}-\mathrm{c})\\0\end{cases} + \sigma_\mathrm{c}\mathrm{A_c}\mathrm{y}\begin{cases}\mathrm{c}\\0\end{cases} = \mathrm{M} \qquad \textit{Equation G1.10}$$

Where:

- M_t = moment produced by resultant tensile force and lever arm between resultant force and neutral axis
- M_c = moment produced by resultant compressive force and lever arm between resultant force and neutral axis
- M = total bending moment experienced by GFRP specimen
- y = variable for depth of the GFRP specimen

G1.2 Important Integrals to Solve

These integrals have been solved using Maple to evaluate the close-formed, indefinite integral. The anti-derivative expression presented from the Maple computation is used in the appropriates calculations (these antiderivatives are not indicated here due to the length and complexity of the equations).

$$\int_0^? \sqrt{\left(R^2 - \left(y - \left(R - (h-c)\right)\right)^2\right)}\,dy \;\rightarrow (INT_0)\begin{cases}?\\0\end{cases} \qquad \textit{Equation G1.11}$$

$$\int_0^? y\sqrt{\left(R^2 - \left(y - \left(R - (h-c)\right)\right)^2\right)}\,dy \;\rightarrow (INT_1)\begin{cases}?\\0\end{cases} \qquad \textit{Equation G1.12}$$

$$\int_0^? y^2\sqrt{\left(R^2 - \left(y - \left(R - (h-c)\right)\right)^2\right)}\,dy \;\rightarrow (INT_2)\begin{cases}?\\0\end{cases} \qquad \textit{Equation G1.13}$$

G1.3 Sum of Forces

As noted in Equation G1.6 and Equation G1.10, both equations involved using the **compressive and tensile area**. The computation for the area is not as simple since the cross-sectional area does not maintain the radius of the its original circular cross-section prior to being longitudinally cut; it is less due to accounting for the width of the waterjet cut. As a result, the areas for tensile and compressive areas are derived as using the neutral axis as the point of reference/origin, where:

- x is the width co-ordinate of the cross-section (i.e. left side of y-axis will be considered "negative")
- y is the height/depth co-ordinate of the cross-section (i.e. below x-axis will be considered "negative")

The expressions for of A_t and A_c will be shown below in Equation G1.14 and Equation G1.17, respectively.

Starting with Equation G1.4 and Equation G1.5:

$$\int_{A_t} \sigma_t \, dA + \int_{A_c} \sigma_c \, dA = 0$$

$$F_t + F_c = 0$$

Developing expression for A_t:

$$A_t = \int_0^{-(h-c)} \int_{-\sqrt{R^2-\left(y-\left(R-(h-c)\right)\right)^2}}^{\sqrt{R^2-\left(y-\left(R-(h-c)\right)\right)^2}} \frac{y}{-(h-c)} \, dxdy \qquad \textit{Equation G1.14}$$

Then substituting it into F_t:

$$\begin{aligned} F_t &= (A_t)(\sigma_t) \qquad \textit{Equation G1.15} \\ &= \left(\int_0^{-(h-c)} \int_{-\sqrt{R^2-\left(y-\left(R-(h-c)\right)\right)^2}}^{\sqrt{R^2-\left(y-\left(R-(h-c)\right)\right)^2}} \frac{y}{-(h-c)} \, dxdy \right) (\sigma_t) \\ &= \left(\int_0^{-(h-c)} \frac{y}{-(h-c)} \left(2\sqrt{R^2 - \left(y - \left(R - (h-c)\right)\right)^2} \right) dy \right) (\sigma_t) \\ &= \left(\frac{2\sigma_t}{-(h-c)} \right) \left(\int_0^{-(h-c)} \left(y\sqrt{R^2 - \left(y - \left(R - (h-c)\right)\right)^2} \right) dy \right) \end{aligned}$$

$$F_t = \left(\frac{2\sigma_t}{-(h-c)} \right) \left((INT_1) \begin{Bmatrix} -(h-c) \\ 0 \end{Bmatrix} \right) \qquad \textit{Equation G1.16}$$

Developing expression for A_c:

$$A_c = \int_0^{c} \int_{-\sqrt{R^2-\left(y-\left(R-(h-c)\right)\right)^2}}^{\sqrt{R^2-\left(y-\left(R-(h-c)\right)\right)^2}} \frac{y}{c} \, dxdy \qquad \textit{Equation G1.17}$$

Then substituting it into F_c:

$$F_c = (A_c)(\sigma_c)$$
$$= \left(\int_0^c \int_{-\sqrt{R^2-\left(y-\left(R-(h-c)\right)\right)^2}}^{\sqrt{R^2-\left(y-\left(R-(h-c)\right)\right)^2}} \frac{y}{c}\, dx dy \right)(\sigma_c)$$
$$= \left(\int_0^c \frac{y}{c} \left(2\sqrt{R^2-\left(y-\left(R-(h-c)\right)\right)^2} \right) dy \right)(\sigma_c)$$
$$= \left(\frac{2\sigma_c}{c}\right) \left(\int_0^c \left(y\sqrt{R^2-\left(y-\left(R-(h-c)\right)\right)^2} \right) dy \right)$$

Equation G1.18

$$F_c = \left(\frac{2\sigma_c}{c}\right)\left((INT_1)\begin{Bmatrix} c \\ 0 \end{Bmatrix}\right)$$

Equation G1.19

Starting with Equation G1.4 and substituting expressions for F_t and F_c:

$$0 = F_t + F_c$$

$$0 = \left(\frac{2\sigma_t}{-(h-c)}\right)\left((INT_1)\begin{Bmatrix} -(h-c) \\ 0 \end{Bmatrix}\right) + \left(\frac{2\sigma_c}{c}\right)\left((INT_1)\begin{Bmatrix} c \\ 0 \end{Bmatrix}\right)$$

Equation G1.20

$$0 = \sigma_t A + \sigma_c B$$

Equation G1.21

G1.4 Sum of Moments

Starting with Equation G1.8 and Equation G1.9:

$$\int_{A_t} -y\sigma_t \, dA + \int_{A_c} -y\sigma_c \, dA = M$$

$$M_t + M_c = M$$

Developing expression for M_t:

$$M_t = -y(A_t)(\sigma_t)$$
$$= -\left(\int_0^{-(h-c)} \int_{-\sqrt{R^2-\left(y-\left(R-(h-c)\right)\right)^2}}^{\sqrt{R^2-\left(y-\left(R-(h-c)\right)\right)^2}} \frac{y^2}{-(h-c)}\, dx dy \right)(\sigma_t)$$
$$= -\left(\int_0^{-(h-c)} \frac{y^2}{-(h-c)} \left(2\sqrt{R^2-\left(y-\left(R-(h-c)\right)\right)^2} \right) dy \right)(\sigma_t)$$
$$= \left(\frac{2\sigma_t}{(h-c)}\right) \left(\int_0^{-(h-c)} \left(y^2\sqrt{R^2-\left(y-\left(R-(h-c)\right)\right)^2} \right) dy \right)$$

Equation G1.22

$$M_t = \left(\frac{2\sigma_t}{(h-c)}\right)\left((INT_2)\begin{Bmatrix} -(h-c) \\ 0 \end{Bmatrix}\right)$$

Equation G1.23

Developing expression for M_c:

$$M_c = -y(A_c)(\sigma_c)$$ Equation G1.24

$$= -\left(\int_0^c \int_{-\sqrt{R^2-\left(y-\left(R-(h-c)\right)\right)^2}}^{\sqrt{R^2-\left(y-\left(R-(h-c)\right)\right)^2}} \frac{y^2}{c}\,dx\,dy\right)(\sigma_c)$$

$$= -\left(\int_0^c \frac{y^2}{c}\left(2\sqrt{R^2-\left(y-\left(R-(h-c)\right)\right)^2}\right)dy\right)(\sigma_c)$$

$$= \left(\frac{-2\sigma_c}{c}\right)\left(\int_0^c \left(y^2\sqrt{R^2-\left(y-\left(R-(h-c)\right)\right)^2}\right)dy\right)$$

$$M_c = \left(\frac{-2\sigma_c}{c}\right)\left((INT_2)\begin{Bmatrix} c \\ 0 \end{Bmatrix}\right)$$ Equation G1.25

Starting with Equation G1.8 and substituting expressions for M_t and M_c:

$$M = M_t + M_c$$

$$M = \left(\frac{2\sigma_t}{(h-c)}\right)\left((INT_2)\begin{Bmatrix} -(h-c) \\ 0 \end{Bmatrix}\right) + \left(\frac{-2\sigma_c}{c}\right)\left((INT_2)\begin{Bmatrix} c \\ 0 \end{Bmatrix}\right)$$ Equation G1.26

$$M = \sigma_t C + \sigma_c D$$ Equation G1.27

G1.5 Solving System of Equations

Using Equation G1.21, Equation G1.27, Equation G1.2 as a system of equations, the remaining unknowns can be solved for:

$$0 = \sigma_t A + \sigma_c B \rightarrow ①$$ Equation G1.21

$$M = \sigma_t C + \sigma_c D \rightarrow ②$$ Equation G1.27

$$\frac{\sigma_t}{E_t(h-c)} = \frac{\sigma_c}{E_c c} \rightarrow ③$$ Equation G1.2

Solving for σ_t by elimination:

$$② \times B - ① \times D: \quad MB = \sigma_t BC + \sigma_c BD$$
$$0 = \sigma_t AD + \sigma_c BD$$
$$MB = \sigma_t(BC - AD)$$

$$\boldsymbol{\sigma_t = \frac{MB}{BC - AD}}$$ Equation G1.28

Substituting σ_t into ①:

$$\left(\frac{MB}{BC-AD}\right)A + \sigma_c B = 0$$

$$\boldsymbol{\sigma_c = -\frac{MA}{BC - AD}}$$ *Equation G1.29*

c is found using Excel's Solver using ③ as a constraint. c, σ_t, σ_c all must be positive values (i.e. distance and magnitude of stress values would be positive; negatives should be accounted for within equation)

G1.6 Moment Equations for Flexure Testing

For 3-point and 4-point (where loading is placed as $\frac{L}{3}$), respectively:

$$M = \frac{FL}{4}$$ *Equation G1.30*

$$M = \frac{FL}{3}$$ *Equation G1.31*

G2.0 Calculating Equations for Effective Volume of Flexure Specimen Under Tensile Stress

The equations and derivations shown in this section G2.0 represent the equations used for calculations from in section 5.3.3 in the main body of the thesis. Section G2.1 will show the derivations for a 3-point bending, and section G2.2 will show the derivations for 4-point bending. For both demonstrations, the equations will be shown in application for a rectangular bar for simplicity, like as shown in Figure G2.1.

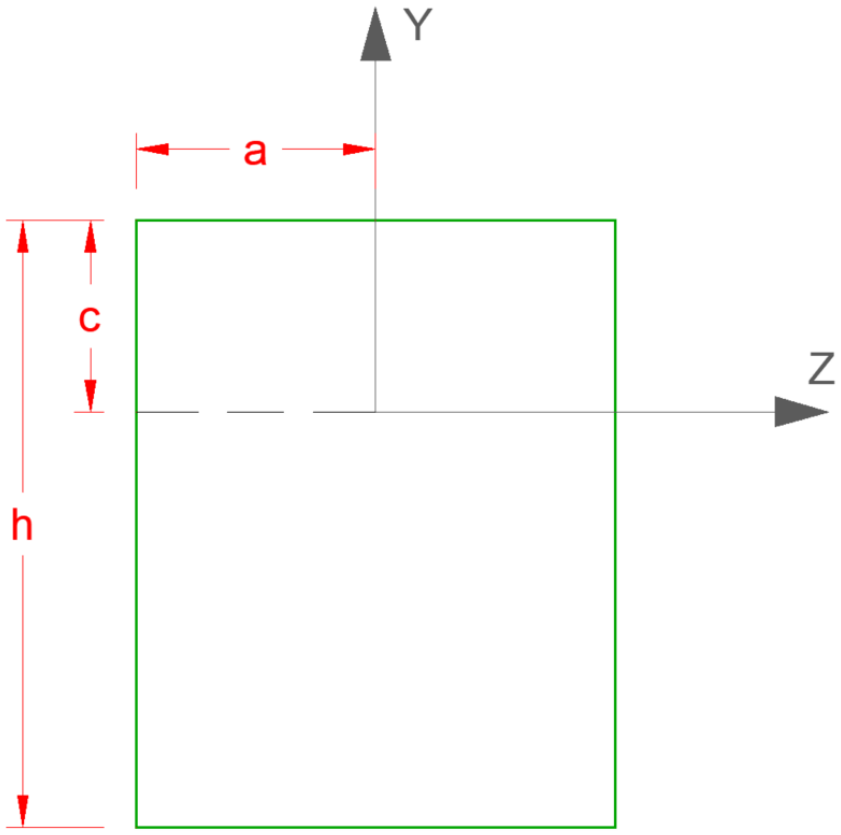

Figure G2.1: Effective Volume Analysis of Rectangular Bar

G2.1 Effective Volume for 3-Point Bending

Starting with the equation for Weibull's Effective Volume (Quinn & Quinn, 2010) (related to Equation 5.7 in main body of thesis):

$$V_E = \int_{V_b} \left(\frac{\sigma_b}{\sigma_{max}}\right)^m dV_b \qquad \textit{Equation G2.1}$$

Formatting this equation for a 3-point bending test:

$$V_E = 2\int_0^{\frac{L}{2}} \int_{A_t} \left(\frac{\sigma_b}{\sigma_{max}}\right)^m dA_t\, dx \qquad \textit{Equation G2.2}$$

Where:

- x = length of specimen

Considering the variations of stress within a specimen subjected for 3-point bending along the length of the specimen:

$$\left(\frac{x}{L/2}\right)\sigma_{t,max} = \left(\frac{2x}{L}\right)\sigma_{t,max} \qquad \textit{Equation G2.3}$$

Considering the stress variations along the height/depth of the cross section (i.e. axial stress, in reference to tensile stress only):

$$\frac{h-c}{\sigma_{max}} = -\frac{y}{\sigma_t}$$
$$\sigma_b = \sigma_t = -\left(\frac{y}{h-c}\right)\sigma_{max} \qquad \textit{Equation G2.4}$$

Combining these stress equations:

$$\sigma_b = -\left(\frac{y}{h-c}\right)\left(\frac{2x}{L}\right)\sigma_{max} \qquad \textit{Equation G2.5}$$

Substituting these stress equations into the 3-point bending effective volume equation for a rectangular bar:

$$V_E = 2\int_0^{\frac{L}{2}}\int_{A_t}\left(-\left(\frac{y}{h-c}\right)\left(\frac{2x}{L}\right)\left(\frac{\sigma_{max}}{\sigma_{max}}\right)\right)^m dA_t\,dx \qquad \text{Equation G2.6}$$

$$= 2\int_0^{\frac{L}{2}}\int_0^{-(h-c)}\int_0^{a}\left(-\left(\frac{y}{h-c}\right)\left(\frac{2x}{L}\right)\right)^m dz\,dy\,dx$$

$$= \frac{2(-1)^m(2)^m}{(h-c)^m L^m}\int_0^{\frac{L}{2}}\int_0^{-(h-c)}(y^m x^m a)\,dy\,dx$$

$$= \frac{2^{m+1}(-1)^m}{(h-c)^m L^m}\left(\left(\frac{y^{m+1}}{m+1}\right)\begin{Bmatrix}-(h-c)\\0\end{Bmatrix}\right)\left(\left(\frac{x^{m+1}}{m+1}\right)\begin{Bmatrix}L/2\\0\end{Bmatrix}\right)$$

$$= \frac{2^{m+1}(-1)^m a}{(h-c)^m L^m}\times\frac{(-1)^{m+1}(h-c)^{m+1}}{m+1}\times\frac{\left(\frac{L}{2}\right)^{m+1}}{m+1}$$

$$= \frac{2^{m+1}\times(-1)^{2m+1}\times(h-c)^{m+1}\times L^{m+1}\times a}{2^{m+1}\times(h-c)^m\times(m+1)^2\times L^m}$$

$$= \frac{(-1)^{2m+1}\times(h-c)\times L\times a}{(m+1)^2}$$

Since a rectangular bar is being considered: $L\times a\times(h-c)=\frac{V}{2}$, assuming $c=\frac{h}{2}$. Also, the negative can be ignored since volume is never "negative":

$$\therefore\ V_{Eb,3ptbnd} = \frac{(-1)^{2m+1}\times(h-c)\times L\times a}{(m+1)^2}\rightarrow\frac{V}{2(m+1)^2} \qquad \text{Equation G2.7}$$

This expression for a rectangular section has been proven in other research for brittle materials that follow the Weibull Weakest's Link Model (Quinn, 2003).

G2.2 Effective Volume for 4-Point-Bending

Note that these calculations correspond to a 4-point bending test where the 2 point loads are placed at $\frac{1}{3}$ of the clear span length of the flexure specimen.

Similar to calculating the effective volume for 3-point bending, Equation G2.1 is used to as a starting point (related to Equation 5.8 in main body of thesis):

$$V_E = \int_{V_b}\left(\frac{\sigma_b}{\sigma_{max}}\right)^m dV_b$$

Formatting this equation for a 4-point bending test, where the point loads are placed at one-third of the length from both ends of the specimen:

$$V_E = 2\int_0^{\frac{L}{6}}\int_{A_t}\left(\frac{\sigma_b}{\sigma_{max}}\right)^m dA_t\,dx + 2\int_0^{\frac{L}{3}}\int_{A_t}\left(\frac{\sigma_b}{\sigma_{max}}\right)^m dA_t dx \qquad \textit{Equation G2.8}$$

Where:

- x = length of specimen
- First term (left side of plus sign) is accounting for inner one-third of length of specimen
- Second term (right side of plus sign) accounts for outer one-third of length of specimen

Considering the variations of stress within a specimen subjected for 4-point bending along the length, they can be represented as follows:

$$\sigma_b = \sigma_{max}\; for \frac{L}{3} < x < \frac{2L}{3} \qquad \textit{Equation G2.9}$$

$$\sigma_b = \left({}^{x}\!\Big/_{\left(\frac{L}{3}\right)}\right)\sigma_{max}\; for\; 0 < x < \frac{L}{3}\;\&\frac{2L}{3} < x < L \qquad \textit{Equation G2.10}$$

For the stress variations along the height/depth of the cross section (i.e. axial stress, in reference to tensile stress only), it is the same linear relationship as a 3-point bending flexure test, as represented by Equation G2.4:

$$\frac{h-c}{\sigma_{max}} = -\frac{y}{\sigma_t}$$

$$\sigma_b = \sigma_t = -\left(\frac{y}{h-c}\right)\sigma_{max}$$

Combining these stress equations:

$$for \frac{L}{3} < x < \frac{2L}{3} \;\rightarrow\; \sigma_b = -\left(\frac{y}{h-c}\right)\sigma_{max} \qquad \textit{Equation G2.11}$$

$$for\; 0 < x < \frac{L}{3}\;\&\frac{2L}{3} < x < L \rightarrow \sigma_b = -\left(\frac{y}{h-c}\right)\left(\frac{3x}{L}\right)\sigma_{max} \qquad \textit{Equation G2.12}$$

Substituting these stress equations into the 4-point bending effective volume equation:

$$V_E = 2\int_0^{\frac{L}{6}}\int_{A_t}\left(-\left(\frac{y}{h-c}\right)\left(\frac{\sigma_{max}}{\sigma_{max}}\right)\right)^m dA_t dx + 2\int_0^{\frac{L}{3}}\int_{A_t}\left(-\left(\frac{y}{h-c}\right)\left(\frac{3x}{L}\right)\left(\frac{\sigma_{max}}{\sigma_{max}}\right)\right)^m dA_t dx$$

Equation G2.13

$$= 2\int_0^{\frac{L}{6}}\int_0^{-(h-c)}\int_0^{a}\left(-\left(\frac{y}{h-c}\right)\right)^m dz dy dx + 2\int_0^{\frac{L}{3}}\int_0^{-(h-c)}\int_0^{a}\left(-\left(\frac{y}{h-c}\right)\left(\frac{3x}{L}\right)\right)^m dz dy dx$$

$$= \frac{2(-1)^m}{(h-c)^m}\int_0^{\frac{L}{6}}\int_0^{-(h-c)}(y^m a)\,dy\,dx + \frac{2(-1)^m(3)^m}{(h-c)^m L^m}\int_0^{\frac{L}{3}}\int_0^{-(h-c)} y^m x^m a dy\,dx$$

$$= \frac{2a(-1)^m}{(h-c)^m}\left(\left(\frac{y^{m+1}}{m+1}\right)\begin{Bmatrix}-(h-c)\\0\end{Bmatrix}\right)\left(x\begin{Bmatrix}L/6\\0\end{Bmatrix}\right) + \frac{2a(-1)^m(3)^m}{(h-c)^m L^m}\left(\left(\frac{y^{m+1}}{m+1}\right)\begin{Bmatrix}-(h-c)\\0\end{Bmatrix}\right)\left(\left(\frac{x^{m+1}}{m+1}\right)\begin{Bmatrix}L/3\\0\end{Bmatrix}\right)$$

$$= \frac{La}{3(m+1)}\left(-\frac{1}{h-c}\right)^m\left(-(h-c)\right)^{m+1} + \frac{2a}{(m+1)^2}\left(-\frac{3}{L(h-c)}\right)^m\left(-\frac{L(h-c)}{3}\right)^{m+1}$$

$$= -\frac{La(h-c)}{3(m+1)} - \frac{2La(h-c)}{3(m+1)^2}$$

$$= -\frac{La(h-c)}{3(m+1)}\left(1+\frac{2}{m+1}\right)$$

$$= -\frac{La(h-c)(m+3)}{3(m+1)^2}$$

For rectangular cross section: $L \times a \times (h-c) = \frac{V}{2}$, assuming $\frac{h}{c} = \frac{h}{2}$. The negative can also be ignored.

$$\therefore\ V_{Eb} = -\frac{La(h-c)(m+3)}{3(m+1)^2} \rightarrow \frac{V(m+3)}{6(m+1)^2}$$

Equation G2.14

This expression for a rectangular section has been proven in other research for brittle materials that follow the Weibull Weakest's Link Model (Quinn, 2003).

These derivations have been shown for a rectangular bar for ease of demonstration. Please refer to equations in main body of thesis for the derivation of the cross-section of GFRP specimen of a flexure test, as shown in Figure G2.2.

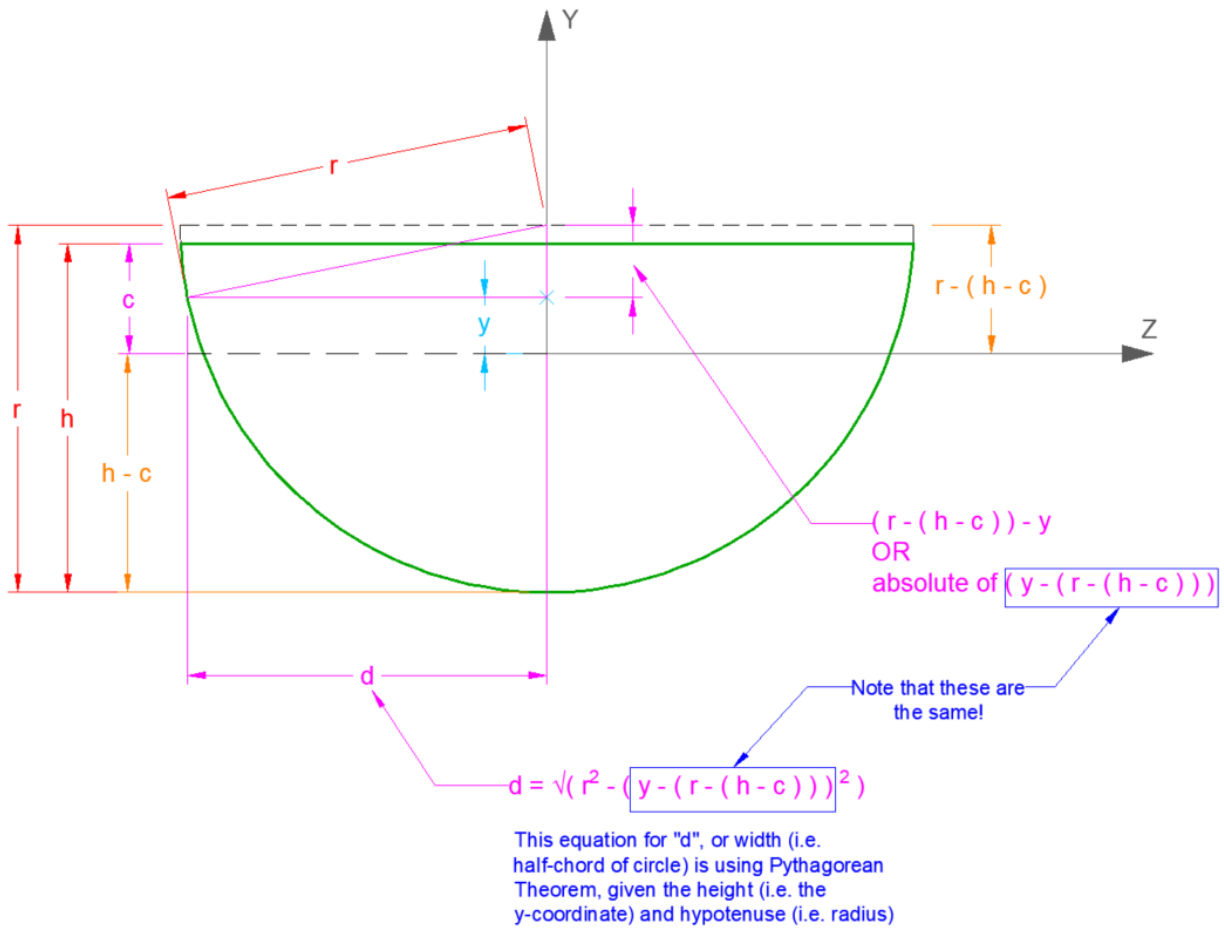

Figure G2.2: Effective Volume Analysis of GFRP Flexure Specimen

G3.0 Converting Load and Displacement for 4-Point Bending Tests

Since the testing machine used for the flexure tests have outputted the load and displacement exhibited on the crosshead of the machine, the following calculations have been used to covert the load from the crosshead to each of the loading noses, and the deflection of the crosshead to midspan of the specimen.

G3.1 Loading for 4-Point Bending Tests

The load transmitted through each loading nose is half the load recorded and applied by the testing machine's crosshead.

$$F_{loading\ nose} = \frac{F_{applied}}{2} \qquad \textit{Equation G3.1}$$

G3.2 Displacement for 4-Point Bending Tests

Assuming the deflected shape of the flexural specimen is a parabolic shape, it can be represented by the following equation and figure:

$$y = \alpha x^2 + \beta x + \gamma \qquad \textit{Equation G3.2}$$

Where:

- α, β, γ are coefficients for the parabolic equation
- x and y are the established co-ordinates to describe points along the specimen, and variables in the equation

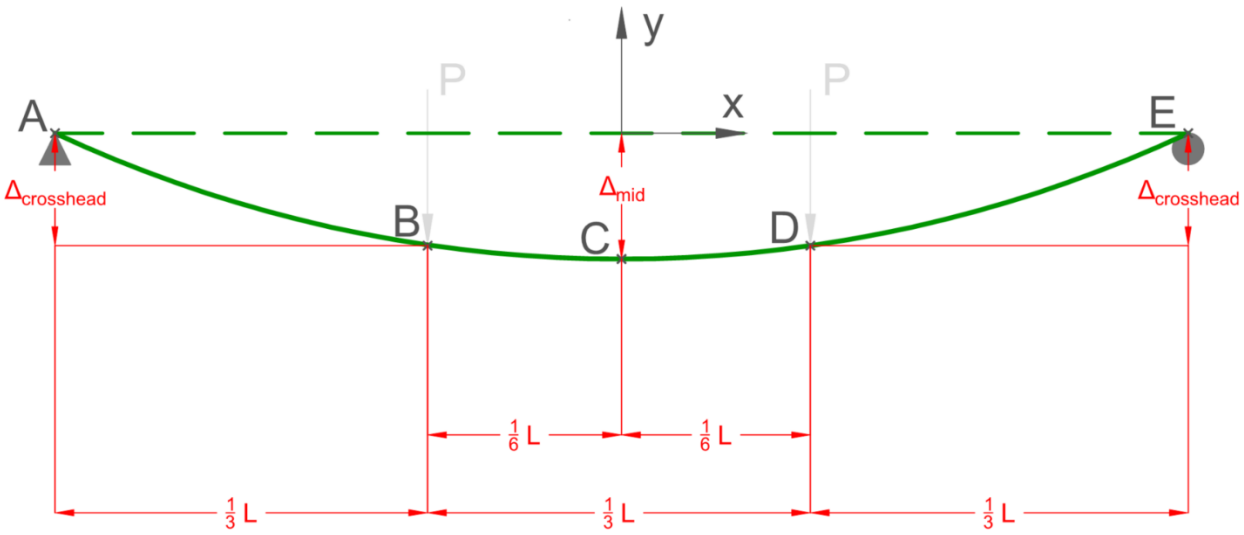

Point	Location	x-coordinate	y-coordinate (represented as positive)
A	Leftmost support/end of specimen clear span length	$-\frac{L}{2}$	0
B	Leftmost application of point-load on specimen & left one-third of specimen	$-\frac{L}{6}$	$\Delta_{crosshead}$
C	Midspan of specimen	0	Δ_{mid}
D	Rightmost application of point-load on specimen & right one-third of specimen	$\frac{L}{6}$	$\Delta_{crosshead}$
E	Rightmost support/end of specimen clear span length	$\frac{L}{2}$	0

Using Points A & E:

From Point A	From Point E
$0 = \alpha\left(-\frac{L}{2}\right)^2 + \beta\left(-\frac{L}{2}\right) + \gamma$	$0 = \alpha\left(\frac{L}{2}\right)^2 + \beta\left(\frac{L}{2}\right) + \gamma$
$0 = \frac{\alpha L^2}{4} - \frac{\beta L}{2} + \gamma$	$0 = \frac{\alpha L^2}{4} + \frac{\beta L}{2} + \gamma$

Equation G3.3

Equating these two expressions:

$$\frac{\alpha L^2}{4} - \frac{\beta L}{2} + \gamma = \frac{\alpha L^2}{4} + \frac{\beta L}{2} + \gamma$$

Equation G3.4

Simplifying these equations:

$$-\beta = \beta$$

Equation G3.5

The only way for this above equation to work, is:

$$\therefore \beta = 0$$

Equation G3.6

Substituting $\beta = 0$ into one of the simplified equations from using Point A/E:

$$0 = \frac{\alpha L^2}{4} - \frac{(0)L}{2} + \gamma$$
$$0 = \frac{\alpha L^2}{4} + \gamma$$

Equation G3.7

Rearranging for γ:

$$\rightarrow \gamma = -\frac{\alpha L^2}{4}$$

Equation G3.8

Using Points B & D, and substituting $\beta = 0$:

From Point B	From Point D
$\Delta_{crosshead} = \alpha\left(-\frac{L}{6}\right)^2 + (0)\left(-\frac{L}{6}\right) + \gamma$	$\Delta_{crosshead} = \alpha\left(\frac{L}{6}\right)^2 + (0)\left(\frac{L}{6}\right) + \gamma$
$\Delta_{crosshead} = \frac{\alpha L^2}{36} + \gamma$	$\Delta_{crosshead} = \frac{\alpha L^2}{36} + \gamma$

Equation G3.9

Substituting $\gamma = -\frac{\alpha L^2}{4}$ into Equation G3.9 one of the simplified equations for Points B & D (since they result in the same equation):

$$\Delta_{crosshead} = \frac{\alpha L^2}{36} - \frac{\alpha L^2}{4} \qquad \text{Equation G3.10}$$

$$\Delta_{crosshead} = \alpha\left(\frac{L^2}{36} - \frac{9L^2}{36}\right)$$

$$\Delta_{crosshead} = \alpha\left(\frac{-8L^2}{36}\right)$$

$$\alpha = -\frac{9\Delta_{crosshead}}{2L^2}$$

Substituting α into $\gamma = -\frac{\alpha L^2}{4}$ to solve for γ

$$\gamma = -\left(-\frac{9\Delta_{crosshead}}{2L^2}\right)\frac{L^2}{4} \qquad \text{Equation G3.11}$$

$$\gamma = \frac{9}{8}\Delta_{crosshead}$$

Finally, substituting expressions for α, β & γ, and co-ordinates for Point C into parabolic equation to r solve for $\Delta_{4pt-mid}$:

$$\Delta_{4pt-mid} = \left(-\frac{9\Delta_{crosshead}}{2L^2}\right)(0)^2 + (0)(0) + \frac{9}{8}\Delta_{crosshead} \qquad \text{Equation G3.12}$$

$$\boldsymbol{\Delta_{4pt-mid} = \frac{9}{8}\Delta_{crosshead}}$$

G4.0 Method Utilizing Deflection of Flexural Specimen to Calculate Tensile Elastic Modulus

Noted in section 6.2 of the thesis: since this research primary focuses on using flexural tests, the recorded outputs for the test are the loading and displacement on the specimen. The loading is used to calculate the rupture modulus, what the displacement is unused, as it is not a required parameter. An improvement to the correlation calculation could be to utilize the deflection it in order to find one of the two elastic moduli of a GFRP specimen (assuming bi-moduli behaviour of GFRP), based on beam equations in bending for deflection. The following calculations are used in the proposed method:

Based on research (Jones 1977, 1978):

$$\frac{E_t}{E_c} = 1.2 \; to \; 1.25 \qquad \text{Equation G4.1}$$

Based on research on determining tensile and compressive elastic moduli from flexural tests (Mujika et al., 2006):

$$E_{bend} = \beta E_t, \text{ where } \beta = \frac{4}{1+\sqrt{\frac{E_t}{E_c}}} \qquad \text{Equation G4.2}$$

Since the deflection equations from the flexural tests are going to be used, this splits the calculations up into two sections:

Description	3-Point Bending Calculations	4-Point Bending Calculations (loading placed at L/3)	
Deflection Equations for Appropriate Flexural Test	$\Delta_{midspan} = \frac{FL^3}{48E_{bend}I}$	$\Delta_{midspan} = \frac{FL}{72E_{bend}I}\left(3L^3 - \frac{4}{9}L^2\right)$	*Equation G4.3*
Substituting Equation G4.2 to have in terms of $\boldsymbol{E_t}$	$\Delta_{midspan} = \frac{FL^3}{48\beta E_t I}$	$\Delta_{midspan} = \frac{FL}{72\beta E_t I}\left(3L^3 - \frac{4}{9}L^2\right)$	*Equation G4.4*
Re-arranging to solve for $\boldsymbol{E_t}$	$E_t = \frac{FL^3}{48\beta\Delta_{midspan}I}$	$E_t = \frac{FL}{72\beta\Delta_{midspan}I}\left(3L^3 - \frac{4}{9}L^2\right)$	*Equation G4.5*
Substituting $\boldsymbol{\beta}$	$E_t = \frac{FL^3}{192\Delta_{midspan}I}\left(1 + \sqrt{\frac{E_t}{E_c}}\right)$	$E_t = \frac{FL}{288\Delta_{midspan}I}\left(1 + \sqrt{\frac{E_t}{E_c}}\right)\left(3L^3 - \frac{4}{9}L^2\right)$	*Equation G4.6*

Equations have been derived for the tensile elastic modulus. However, the issue that arose was that there was missing information in the calculations that accurately represent the testing in environment. For example, these calculations assume the supports for the flexural test are frictionless, when they are not. Therefore, the equations involved with deflection should be altered to accurately model the testing environment.

Glossary

Term	Definition	First References In
Correlation Calculations	Set of arithmetic used to calculate the correlated tensile strength from the rupture modulus calculated from flexural tests. The following equations used (in order of reference): 6.1 to 6.3, 6.16, 6.20, 6.15	Section 1.3
Method 1	The first iteration of the results from the correlation calculations that used $\frac{E_t}{E_c} = 1.25$.	Section 5.2.2
Method 2	The first iteration of the results from the correlation calculations that used $\frac{E_t}{E_c} = 1.2$.	Section 5.2.2
Cracking Load	Point of maximum load on the linear portion of load-displacement graph of a flexural test	Chapter 4
Rupture Modulus	The bending stress at which the tensile fibres begin to rupture – i.e. tensile failure of GFRP flexural specimen	Section 1.1
Variation A	A variation in the correlation calculations where all specimens were used to compute the Weibull modulus, and used in the average calculations.	Section 5.3.2
Variation B	A variation in the correlation calculations where the flexural specimens (per size and type of test) with the lowest and highest rupture modulus were not used to compute the Weibull modulus, and were not used in the average calculations.	Section 5.3.2